Unconventional reservoir geomechanics

Edited by
Jingshou Liu, Wenlong Ding, Shimin Liu, Kouqi Liu and Dadong Liu

About Frontiers

Frontiers is more than just an open access publisher of scholarly articles: it is a pioneering approach to the world of academia, radically improving the way scholarly research is managed. The grand vision of Frontiers is a world where all people have an equal opportunity to seek, share and generate knowledge. Frontiers provides immediate and permanent online open access to all its publications, but this alone is not enough to realize our grand goals.

Frontiers journal series

The Frontiers journal series is a multi-tier and interdisciplinary set of open-access, online journals, promising a paradigm shift from the current review, selection and dissemination processes in academic publishing. All Frontiers journals are driven by researchers for researchers; therefore, they constitute a service to the scholarly community. At the same time, the *Frontiers journal series* operates on a revolutionary invention, the tiered publishing system, initially addressing specific communities of scholars, and gradually climbing up to broader public understanding, thus serving the interests of the lay society, too.

Dedication to quality

Each Frontiers article is a landmark of the highest quality, thanks to genuinely collaborative interactions between authors and review editors, who include some of the world's best academicians. Research must be certified by peers before entering a stream of knowledge that may eventually reach the public - and shape society; therefore, Frontiers only applies the most rigorous and unbiased reviews. Frontiers revolutionizes research publishing by freely delivering the most outstanding research, evaluated with no bias from both the academic and social point of view. By applying the most advanced information technologies, Frontiers is catapulting scholarly publishing into a new generation.

What are Frontiers Research Topics?

Frontiers Research Topics are very popular trademarks of the *Frontiers journals series*: they are collections of at least ten articles, all centered on a particular subject. With their unique mix of varied contributions from Original Research to Review Articles, Frontiers Research Topics unify the most influential researchers, the latest key findings and historical advances in a hot research area.

Find out more on how to host your own Frontiers Research Topic or contribute to one as an author by contacting the Frontiers editorial office: frontiersin.org/about/contact

Unconventional reservoir geomechanics

Topic editors

Jingshou Liu — China University of Geosciences Wuhan, China
Wenlong Ding — China University of Geosciences, China
Shimin Liu — The Pennsylvania State University (PSU), United States
Kouqi Liu — Central Michigan University, United States
Dadong Liu — China University of Petroleum, Beijing, China

Table of contents

Editorial: Unconventional reservoir geomechanics

Jingshou Liu[1]*, Wenlong Ding[2], Shimin Liu[3], Kouqi Liu[4] and Dadong Liu[5]

[1]School of Earth Resources, China University of Geosciences, Wuhan, China, [2]School of Energy Resources, China University of Geosciences, Beijing, China, [3]Department of Energy and Mineral Engineering, G3 Center and Energy Institute, The Pennsylvania State University, University Park, PA, United States, [4]Institute of Energy, Peking University, Beijing, China, [5]State Key Laboratory of Petroleum Resources and Prospecting, China University of Petroleum, Beijing, China

KEYWORDS

reservoir geomechanics, *in situ* stress, reservoir fracture, rock mechanics, unconventional reservoir

Editorial on the Research Topic
Unconventional reservoir geomechanics

Unconventional resources, which can be regarded as an alternative for the conventional resources, have been a hot Research Topic over the past decades. Many countries, including the United States, Russia, Canada, and China, have effectively promoted the exploration and development of shale oil and gas, tight oil and gas and coalbed methane. Despite their great potential, the economic hydrocarbon production from these resources is hampered by our poor understanding of reservoir geology and limited engineering technology. In recent years, considerable progress has been made in the study of *Unconventional reservoir geomechanics* due to commercial development. *Unconventional reservoir geomechanics* encompasses the fields of structural geology, petroleum geology, rock mechanics, and petroleum engineering, aiming to solve a wide range of mechanical problems that arise during the exploitation of unconventional resources. Moreover, multiscale geomechanics-based geoengineering method have been employed in laboratories by more and more researchers.

It was a great honor to be invited to serve as the team of Guest Editors for this Research Topic. Upon the opening of this topic, it received a great response from relevant academic communities. This Research Topic collects 15 papers from different disciplines, which helps international readers deepen geological understanding and solve engineering problems through geomechanics. A wide range of research was presented, including geomechanics experiments (e.g., Cheng et al.; Wang et al.; Yang et al.), the prediction of reservoir fracture characterization (e.g., Li et al.; Yang et al.; Mi et al.), the numerical simulation of stress fields (e.g., Feng et al.; Xu et al.) and case studies (e.g., Wang Q et al.; Wang et al.; Xu et al.). The study of reservoir geomechanics is significant for guiding unconventional oil and gas exploration (e.g., stress field simulation, fault sealing evaluation, fracture activity prediction, etc.) and development (e.g., wellbore stability analysis, fracture propagation in hydraulic fracturing, casing damage prediction and protection, etc.).

At present, the exploration and development of oil and gas are moving towards deep and ultradeep reservoirs. In addition, the development of tight unconventional reservoirs is playing an increasingly important role in the oil and gas industry. For example, some wells in the Tarim Basin in China have reached more than 8,000 m, and the ultradeep rocks are in an environment of high temperature, high pressure and high *in situ* stress. Traditional reservoir geomechanics theory has limitations in guiding the development of deep resources and deep engineering (Xie et al., 2021; Xu et al., 2022). Whether it is the

development of ultradeep reservoirs or tight unconventional reservoirs, reservoir geomechanics will play an increasingly critical role (Zoback and Kohli, 2019). With the in-depth development of multidisciplinary intersections, reverse engineering, 3D printing technology, multiphysics field coupling theory, and other methods that have been introduced to reservoir geomechanics, a number of new research results and technologies have emerged. In the future, the development of reservoir geomechanics will focus on the *in situ* mechanical properties of deep to ultradeep rocks (Xie et al., 2021), evolution of rock mechanical properties and their geomechanical response (Laubach et al., 2019; Liu et al., 2022a), formation mechanism and distribution prediction of unconventional reservoir fractures (Zhang et al., 2021; Li et al., 2022), and development of commercial software for numerical simulation of *in situ* stress in complex structures (Liu et al., 2017; Liu et al., 2022b; Zou et al., 2022).

Author contributions

All authors listed have made substantial, direct, and intellectual contributions to the work and approved it for publication.

Conflict of interest

The authors declare that the research was conducted in the absence of any commercial or financial relationships that could be construed as a potential conflict of interest.

Publisher's note

All claims expressed in this article are solely those of the authors and do not necessarily represent those of their affiliated organizations, or those of the publisher, the editors and the reviewers. Any product that may be evaluated in this article, or claim that may be made by its manufacturer, is not guaranteed or endorsed by the publisher.

References

Laubach, S. E., Lander, R. H., Criscenti, L. J., Anovitz, L. M., Urai, J. L., Pollyea, R. M., et al. (2019). The role of chemistry in fracture pattern development and opportunities to advance interpretations of geological materials. *Rev. Geophys.* 57 (3), 1065–1111. doi:10.1029/2019rg000671

Li, H., Yu, F., Wang, M., Wang, Y., and Liu, Y. (2022). Quantitative prediction of structural fractures in the Paleocene lower Wenchang formation reservoir of the Lufeng Depression. *Adv. Geo-Energy Res.* 6 (5), 375–387. doi:10.46690/ager.2022.05.03

Liu, J., Chen, P., Xu, K., Yang, H., Liu, H., and Liu, Y. (2022a). Fracture stratigraphy and mechanical stratigraphy in sandstone: A multiscale quantitative analysis. *Mar. Petroleum Geol.* 145, 105891. doi:10.1016/j.marpetgeo.2022.105891

Liu, J., Ding, W., Yang, H., Wang, R., Yin, S., Li, A., et al. (2017). 3D geomechanical modeling and numerical simulation of *in-situ* stress fields in shale reservoirs: A case study of the lower cambrian niutitang formation in the cen'gong block, south China. *Tectonophysics* 712, 663–683. doi:10.1016/j.tecto.2017.06.030

Liu, J., Yang, H., Xu, K., Wang, Z., Liu, X., Cui, L., et al. (2022b). Genetic mechanism of transfer zones in rift basins: Insights from geomechanical models. *GSA Bull.* 134 (9-10), 2436–2452. doi:10.1130/b36151.1

Xie, H. P., Li, C. B., Gao, M. Z., Zhang, R., Gao, F., and Zhu, J. B. (2021). Conceptualization and preliminary research on deep *in situ* rock mechanics. *Chin. J. Rock Mech. Eng.* 40 (2), 217.

Xu, K., Yang, H., Zhang, H., Ju, W., Li, C., Fang, L., et al. (2022). Fracture effectiveness evaluation in ultra-deep reservoirs based on geomechanical method, Kuqa Depression, Tarim Basin, NW China. *J. Petroleum Sci. Eng.* 215, 110604. doi:10.1016/j.petrol.2022.110604

Zhang, Y., Zeng, L., Luo, Q., Zhu, R., Lyu, W., Liu, D., et al. (2021). Influence of natural fractures on tight oil migration and production: A case study of permian lucaogou formation in jimsar sag, junggar basin, NW China. *J. Earth Sci.* 32 (4), 927–945. doi:10.1007/s12583-021-1442-y

Zoback, M. D., and Kohli, A. H. (2019). *Unconventional reservoir geomechanics*. Cambridge, UK, England: Cambridge University Press.

Zou, C., Yang, Z., Li, G., Li, J., Liu, X., Tang, Y., et al. (2022). Why can China realize the continental "shale oil revolution". *J. Earth Sci.* 33 (5), 1324–1327. doi:10.1007/s12583-022-1745-7

Effects of Fracture Formation Stage on Shale Gas Preservation Conditions and Enrichment in Complex Structural Areas in the Southern Sichuan Basin, China

Jing Li[1], Hu Li[2,3,4,5]*, Jianliang Xu[1], Yijia Wu[1,4] and Zhi Gao[1]

[1]Institute of Geological Exploration and Development of CNPC Chuanqing Drilling Engineering, Chengdu, China, [2]Natural Gas Geology Key Laboratory of Sichuan Province, Southwest Petroleum University, Chengdu, China, [3]Shale Gas Evaluation and Exploitation Key Laboratory of Sichuan Province, Chengdu, China, [4]School of Geoscience and Technology, Southwest Petroleum University, Chengdu, China, [5]Department of Railway Engineering, Sichuan College of Architectural Technology, Chengdu, China

Fractures have significantly impacted the preservation, enrichment, and productivity of shale gas in the Longmaxi Formation in the complex structural area of the southern Sichuan Basin. Based on outcrop, core, imaging logging, inclusion analysis, acoustic emission experiments, and burial and thermal evolution history data, the formation stage, evolution and preservation conditions of structural fractures were comprehensively studied. Shear fractures are the main features of tectonic origin and are characterized by small widths, wide spacing, and high filling degrees. The structural fractures of the Longmaxi Formation can be divided into three groups in terms of their formation stage. The first-stage fractures were formed in the middle-late period of the Yanshanian tectonic movement (86.2–68.5 Ma), when the palaeotectonic stress was 68.33–71.82 MPa; and the homogenization temperature of the fluid inclusions in the corresponding fracture fillings is 150–178°C. The second-stage fractures were formed at the end of the Yanshanian-early Himalayan tectonic movement (68.5–35.2 Ma), when the palaeotectonic stress was 85.2–100.5 MPa; the homogenization temperature of the corresponding fluid inclusions is 123–148°C. The third-stage tectonic fractures formed during the middle-late period of the Himalayan tectonic movement (35.2–0 Ma), when the palaeotectonic stress was 55.6–63.8 MPa; fillings are scarce in these fractures, but the measured homogenization temperature of the corresponding fluid inclusions is 90–110°C. Shale gas preservation conditions were affected by the fracture formation stage, maximum horizontal crustal stress, fault scale, structural burial depth, formation pressure coefficient, etc. Three types of favourable preservation conditions were identified. The Type I target area is the low slope area in the middle of the syncline, which occurs more than 2.0 km from the fault. The research results have guiding significance for the evaluation of the preservation conditions of deep shale gas in the study area and similar areas.

Keywords: deep shale gas, accumulation geological conditions, formation stage, structural fracture, shale gas preservation conditions, southern Sichuan basin

1 INTRODUCTION

The Wufeng Formation-Longmaxi Formation Section One in the Sichuan Basin is rich in shale gas resources, with a geological resource volume of $21.9 \times 10^{12} \, m^3$, of which deep shale gas from the burial depths of 3,500–4,500 m accounts for 51%, i.e., $11.3 \times 10^{12} \, m^3$. The volume shale gas resources in southern Sichuan is $10 \times 10^{12} \, m^3$, of which the $8.7 \times 10^{12} \, m^3$ from burial depths of 3,500–4,500 m accounts for 87% (Ma et al., 2018; Wei et al., 2019; Ma et al., 2021; Li et al., 2022a; 2022b). Breakthroughs have been achieved in exploring and developing shale gas in the middle to shallow layers of the southern Sichuan Basin, and shale gas commercial development zones, such as Changning, Weiyuan, and Zhaotong, have been established (Liu et al., 2016; Li et al., 2019a; Fan et al., 2020a; Hou et al., 2020; Tang et al., 2020; Wang et al., 2020; Li et al., 2022a). Shale gas exploration and development is progressing in the deep (burial depths greater than 3,500 m) shale gas areas of Luzhou and Yuxi in the southern Sichuan Basin. The test gas production of Well Y 101 (Yang, vertical depth 3,577 m) is $43 \times 10^4 \, m^3$/d, representing a breakthrough of deep shale gas. The test daily gas production of Well Z202-H1 (Zu, vertical depth 3,960 m) is $46 \times 10^4 \, m^3$, and the test gas production of Well L203 (Lu) has reached $138 \times 10^4 \, m^3$/d, which indicates the great potential of deep shale gas exploration and development at depths of 3,500–4,500 m in the southern Sichuan Basin (Guo J. et al., 2021; Wang et al., 2021; Xi and Tang 2021).

Many scholars have proposed that marine shale in southern China has experienced multiple stages of tectonic activity and a lengthy evolutionary history and is characterized by an old deposition age, a complex genesis, strong tectonic activity, and variable gas-bearing properties (Fan et al., 2020b; Liu H. et al., 2022a; Zhang et al., 2022). The development of faults and fractures under effective preservation conditions is key for determining the quality of shale gas reservoirs (Xie 2021; Li et al., 2022a; Li et al., 2022b; Liu J. S. et al., 2022b). Due to the extremely low permeability of shale formations, fractures not only serve as storage spaces but also improve porosity and permeability and connect pores and microstructures, thereby playing a vital role in controlling underground gas migration (Li et al., 2022b). Qualitative and quantitative research has been conducted on naturally formed shale fractures and the fracture networks formed after fracturing stimulation, the relationship between fractures and permeability, the propagation of fractures during hydraulic fracturing, and the mechanisms of fracture formation, which are crucial features to understand to improve gas enrichment and accumulation, reservoir performance, and production capacity (Liu et al., 2018, 2020, 2021; Li H. et al., 2021a, Li H. T. et al., 2021; Qie et al., 2021; Wang et al., 2021; Wang and Wang 2021; Zhan et al., 2021). The characteristics, formation stages and genetic mechanisms of natural fractures in shale reservoirs play an important role in controlling and regulating the migration and accumulation of shale gas (Fan et al., 2018; Gao 2019; Nie et al., 2020; Kang 2021; He et al., 2022a; 2022b). Taking the Longmaxi Formation of the Luzhou area in the southern Sichuan Basin as an example, this study analyses the main tectonic evolution stages, structural fracture formation stages, and fracture formation mechanisms by using macroscopic geological methods (interpretations of outcrop, drilling, and geophysical data) and microexperimental tests (analysis of fluid inclusions from fracture fillings, acoustic emission experimental results, and the burial and thermal evolution history). The research results provide guidance for the high-quality exploration and development of deep shale gas in complex structural areas in southern Sichuan and can help improve well placement optimization, fracturing stimulation optimization, and productivity predictions.

2 REGIONAL GEOLOGIC BACKGROUND

The Luzhou block is located in a low and steeply dipping structural belt in southern Sichuan, surrounded by the gently dipping structural belt of central Sichuan, the high and steeply dipping structural belt of eastern Sichuan, the low-folded structural belt of southwestern Sichuan and the Loushan fold belt. The Luzhou block primarily contains NE-trending structures and broom-like structures from NE to SW, where the strength of the structural folds gradually weakens (Jin et al., 2018; Ma et al., 2018). The Luzhou block is primarily characterized by wide synclines and narrow anticlines, and contains three large-scale synclines. The Luzhou block has two groups of main faults that trend NE-SW and E-W, and the distance between the main faults is large, which controls the tectonic shape (**Figure 1A**). There are 32 Grade I faults in total, and Grade II and III faults are also developed in this region. The fault spacings are generally 20–170 m, and the lengths are generally 5–10 km. The Longmaxi Formation shale in the Luzhou block has multistage, multitype, and multidirectional natural fracture systems, which are important for enriching and accumulating shale gas, improving reservoir performance, and predicting productivity.

During the sedimentary period of the Longmaxi Formation, the entire southern Sichuan area was bounded by the central Sichuan palaeo-uplift and the central Guizhou palaeo-uplift, and generally was a continental shelf sedimentary environment. The Luzhou block was located in the sedimentary depocentre of the deep-water continental shelf sedimentary centre during the sedimentary period of the Wufeng Formation-Longmaxi Formation. The bottom of the Longmaxi Formation conformably contacts the Wufeng Formation, and the top of the Longmaxi Formation contacts the carbonate rocks of the lower Silurian Shiniulan Formation (Xie et al., 2019; Guo J. L. et al., 2020a; Guo X. S. et al., 2020b). The high-quality shale section at the bottom of the Longmaxi Formation is rich in biogenic siliceous minerals with a mass fraction of 60–70%, characterized by the shale total organic carbon (TOC) mass fraction of 2.8–6.0% (an average of 3.9%), a porosity of 4.0–6.5% (an average of 5.1%), and a gas saturation of 50–70% (an average of 65%) (**Figure 1B**). The total gas content tested in the field is 5.0–7.5 m^3/t with an average of 6.3 m^3/t, which is the highest in southern Sichuan.

3 FAVOURABLE TARGET PRESERVATION CONDITIONS FOR DEEP SHALE GAS

3.1 Samples

This study primarily focuses on two methods, i.e., macrogeological analysis and microexperimental testing.
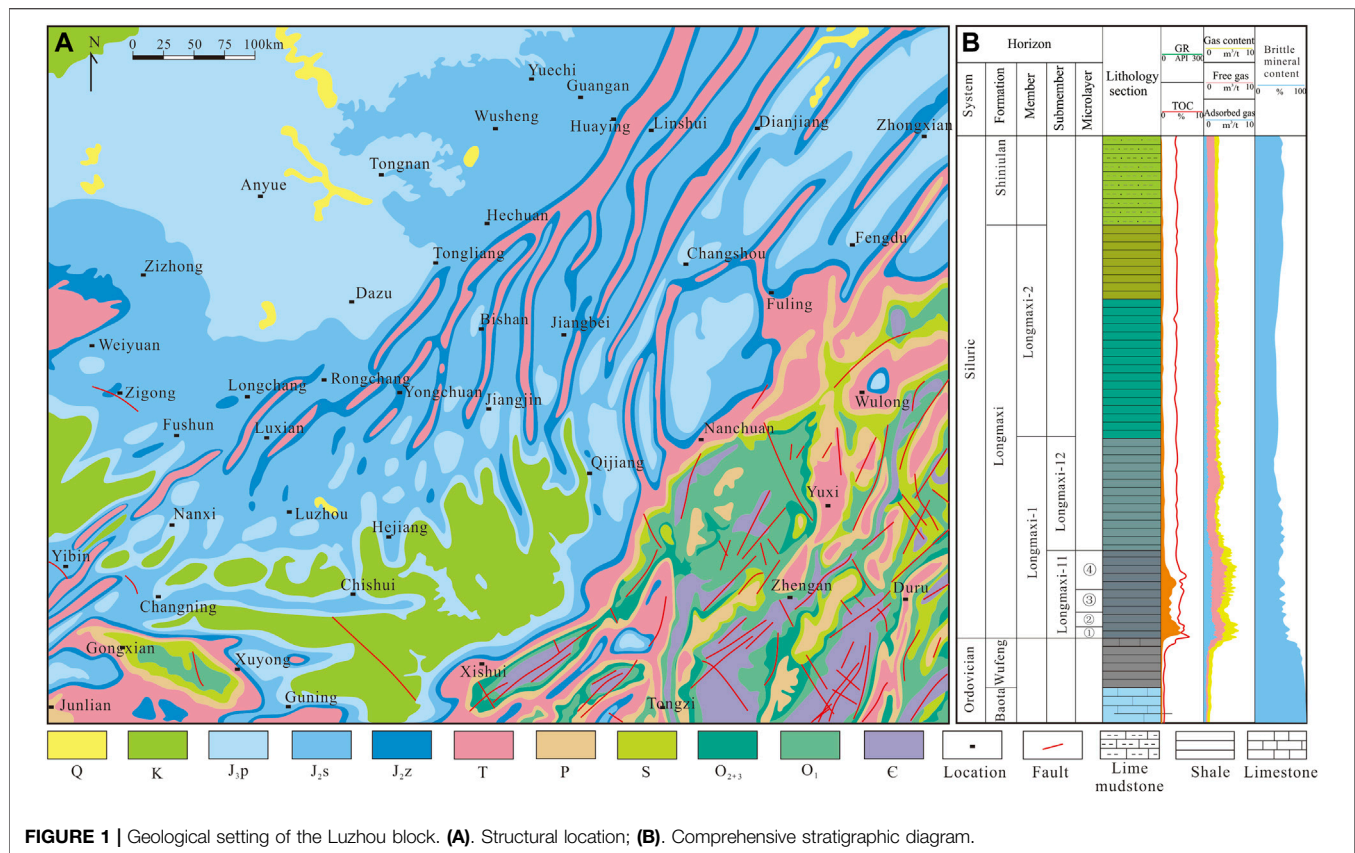
FIGURE 1 | Geological setting of the Luzhou block. **(A)**. Structural location; **(B)**. Comprehensive stratigraphic diagram.

Macroscopic geological analysis primarily uses surface structure analysis, drilling core observations, Formation Micro Imager (FMI) logging interpretations and seismic structure analysis, which were conducted in combination with the analysis of actual production data. Observations and sampling were conducted on the cores at approximately 320 m from four wells drilled in the Longmaxi Formation, including Well L201, Well L203H79-4, Well Y101H3-8, and Well Y101H41-2. A total of 48 samples of fracture fillings and 15 full-diameter samples were observed. FMI logs of the 12 wells encountering the Longmaxi Formation, including Well L206, Well L211, and Well Y101H3-8, were collected and interpreted, and 3D seismic data from the Luzhou shale gas production area (covering 1,470 km^2) were collected, analysed, and interpreted.

3.2 Macrogeological Analysis

The surface structural analysis primarily used the regional structural background to determine the fracture stage and to classify surface faults in the Luzhou area. The drilling core observations mainly included the fracture type, development degree, filling characteristics, and fracture intersection relationship, and the fracture occurrence was primarily determined and interpreted with FMI logging. The LANDMAK 2003.12.13 interpretation system and 10 × 10 density controls were used to process and interpret the 3D seismic data and to study the fault distribution, intersection relationships, and evolution processes at different stages.

3.3 Microexperimental Tests

The fracture stages were studied by macroscopic fracture analysis and the analysis of structural fractures formed at the same stage as the fractures. Rock mechanics tests on the Longmaxi Formation cores, homogenization temperature tests of the fluid inclusions in the fracture fillings, and the burial history of the study area were used to determine the fracture formation stage (Fan et al., 2020a).

Rock slices from 30 fracture fillings of five wells in the study area were placed on a Linkam THMSG600 stage at room temperature, and the microscope was focused to find the inclusions. During heating, when the inclusions were close to homogenization, the heating rate was changed to 1–3°C/min. When the gas-liquid phase in the inclusions transformed into a homogeneous phase, the homogenization temperature was obtained, and the fluid filling stage was obtained according to the homogenization temperature test of the fluid inclusions.

The rock mechanics tests were completed by the Rock Mechanics Laboratory of the State Key Laboratory of Oil and Gas Reservoir Geology and Exploitation, Southwest Petroleum University. The tests included triaxial compression tests and acoustic emission tests. The acoustic emission test primarily uses the memory characteristics of unfractured rocks. When the pressure conditions approach those of the tectonic stress that occurred during geologic history, the unfractured rocks break, resulting in acoustic emission effects, which can be used to determine the tectonic stress stage. In this study, samples were collected in three directions, i.e., 0°, 45°, and 90°, from 15 full-

FIGURE 2 | Rock acoustic emission testing experimental system. **(A)**. Sampling methods; **(B)**. Experiment process.
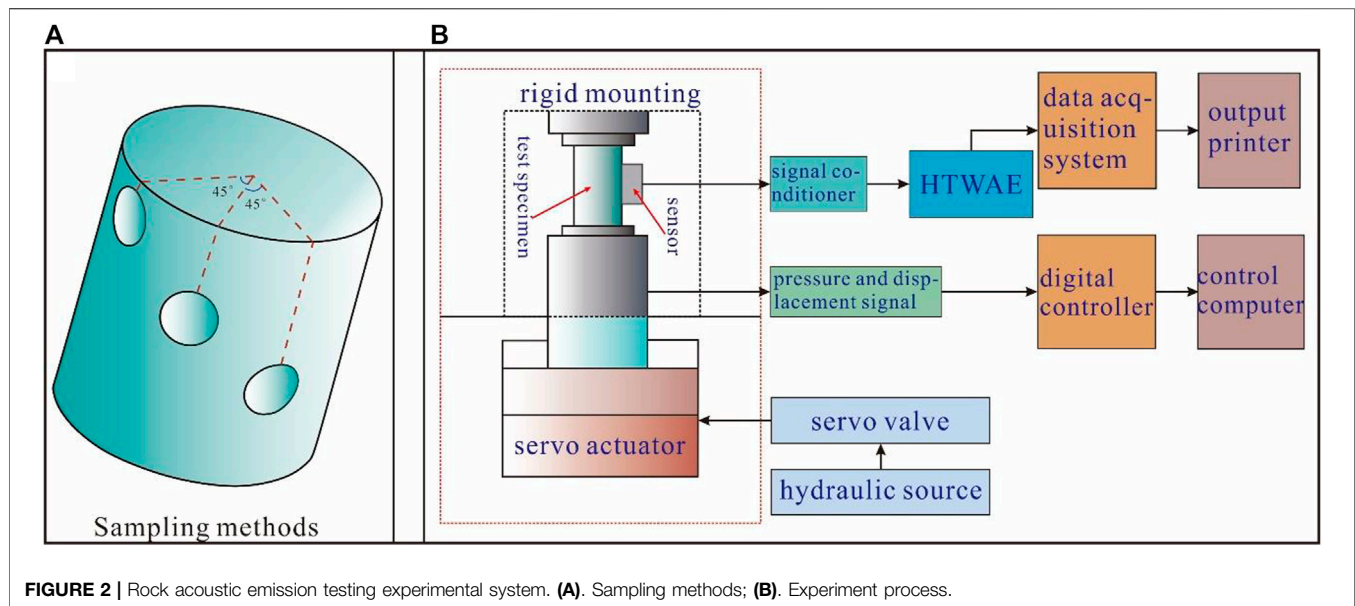
diameter cores to create cylindrical samples 50 mm × 25 mm in size (**Figure 2A**). The rock mechanical parameters of the samples were measured using the RTR-1000 high-temperature and high-pressure triaxial rock mechanics test system produced by GCTS (**Figure 2B**) (Fan et al., 2022). The tests were performed in accordance with GB/T 23561.11-2009, GB/T 50266-2013, SY/T5336-2006, and SY/T 6351-1998.

The duration and intensity of tectonic deformation were studied based on the experimental results obtained from the burial thermal evolution history of core samples from the Luzhou area, and the experimental data were provided by the Sichuan Shale Gas Exploration and Development Company.

4 FAVOURABLE TARGET PRESERVATION CONDITIONS FOR DEEP SHALE GAS

4.1 Fracture Stage Study With Macrogeological Methods

4.1.1 Analysis of Surface Structures

The southern margin of the Sichuan Basin is influenced by the Jiangnan Xuefeng uplift belt, the Daliangshan fault-fold structural belt, and the Daloushan fault-fold structural belt. The right triangular joint structural area in southern Sichuan is bounded and connected by the Changshou-Zunyi fault zone, the Gulin-Yanjin fault zone, and the Huayingshan-Qingshanling fault zone. Constrained by the surrounding structures, the boundary structure trajectory is consistent with the boundary extension orientation, and strong superposition and transformation occur inside the basin. The study area is located at the intersection of the southern Sichuan fold belt and Loushan fault-fold structural belt and has been transformed by structural activities that have occurred at different stages and in different directions; therefore, the area exhibits structural compounding and superposition characteristics in some stages (**Figure 3**).

The folds in this area are divided into three belts, i.e., E-W-trending structural belts, S-N-trending structural belts, and NE-trending structural belts. The E-W-trending structural belt primarily includes the Shengdengshan and Luoguanshan anticlines. This structural belt exhibits an E-W-trending disjointed distribution, and the W end of the main axis often shifts to the S in the WSW direction and is dominated by steeply dipping and low gently dipping tectonic types. The N-S-trending structural belt is primarily located in the Yanggaosi anticline, exhibits a N-S-trending westward protruding arc distribution, with high to low steeply dipping anticlines in the N and low and gently dipping anticlines in the S, and is characterized by a steep slope in the W and a gentle incline in the east. The NE-trending structural belt mainly includes the Gufoshan, Jiukuishan, Huangguashan, Longdongping, and Tanziba anticlines. The main trend of this tectonic belt is to the NE, and the structure is distributed in echelon, arc, and "S" shapes. The NE-trending structural belt is dominated by high overturned, high steeply dipping, and low steeply dipping, which extend to the SE. Judging from the fault development, most of the faults trend NE and near-E-W, and a few NW-trending faults are developed in and around the study area. The extension direction of each fault is approximately the same as that of the fold in which it is located. The main structure in the Luzhou area is directed approximately E-W and turns eastward to the NNW; it has obvious structural superposition characteristics. The NNW structure is superimposed onto the early EW structure, and the tectonic trajectories of adjacent areas are quite different. The NE-trending structure can be observed from the NW direction and was formed due to the influence from the Huayingshan fault zone.

4.1.2 Core Fracture Stage and Classification

The core fracture morphology, filling and intersection relationships provide an intuitive basis for the study of
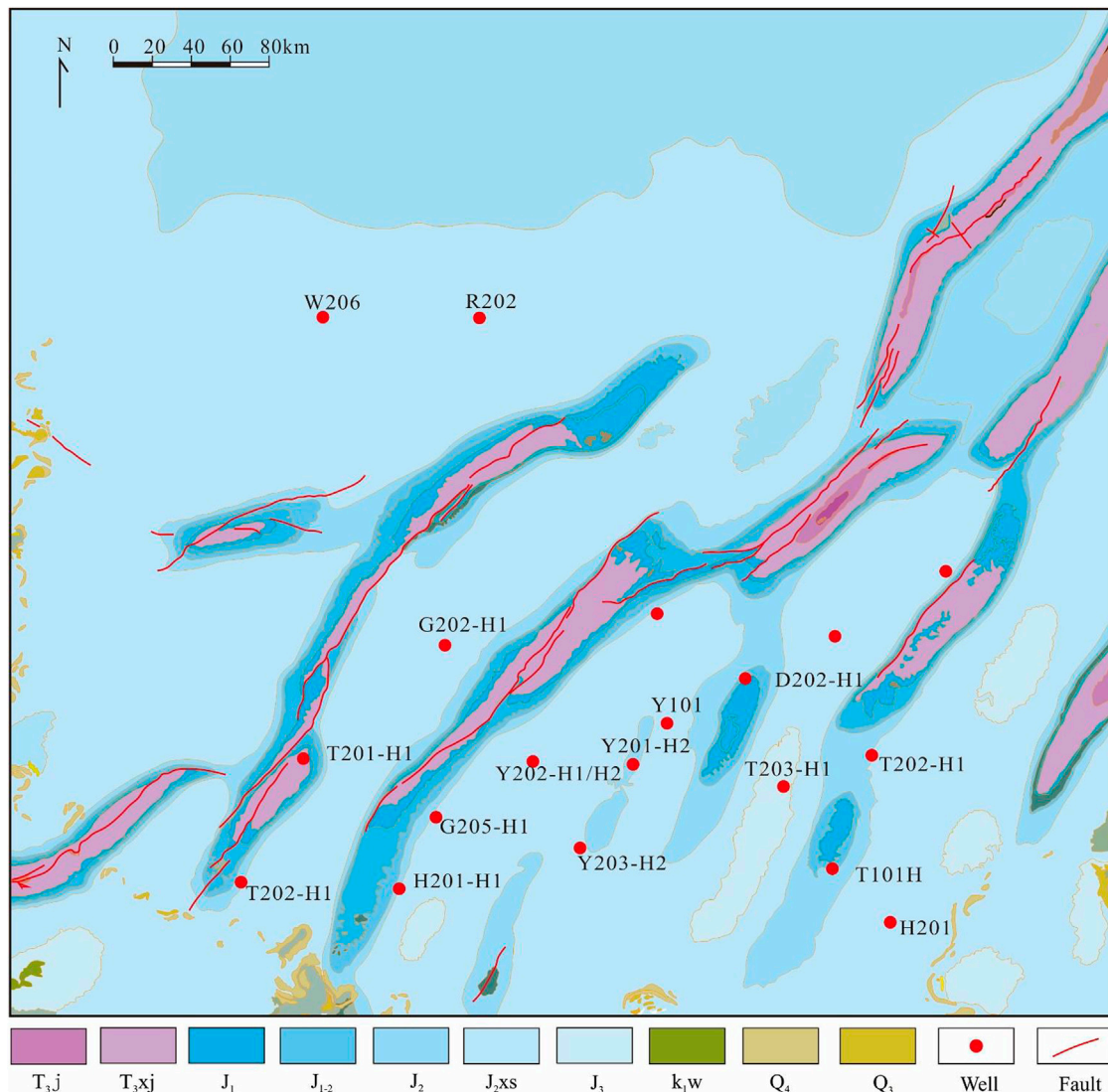
FIGURE 3 | Surface geological map of the Luzhou block.

fracture stages. In the Wufeng Formation-Longmaxi Formation, shear fractures are the primary features of tectonic origin, followed by extensional fractures, shear-tensional fractures and interlayer fractures, as well as a small number of artificially induced fractures. The shear fractures are mostly composed of high-angle shear fractures and vertical fractures, have large extension lengths and straight joint surfaces, and are mostly filled with calcite (**Figures 4A,B**) (Li et al., 2019b; Li H. et al., 2021a; Li H. T. et al., 2021). According to the mutual intersection relationships among core fractures, there are at least three stages of fractures in the Longmaxi Formation (**Figures 4C–F**).

The fractures in the Longmaxi Formation with lengths of 15–25 cm account for 34.5% of the total fractures. The fractures with lengths of 5–15 cm account for the next-largest proportion. Fractures longer than 25 cm are less common. Fractures with widths between 0.5 and 1 mm account for 50% of the total fractures;

fractures with widths <0.5 mm account for approximately 14% of the total fractures. Thus, these fractures have small widths. Additionally, they are relatively closed. The Wufeng Formation-Longmaxi Formation fracture density ranges from 3/0.5 m to 10/0.5 m. High-angle fractures (45°–75°) and near-vertical fractures (75°–90°) are dominant. The proportion of unfilled fractures is approximately 26.2%, the proportion of partially fractures is approximately 22.7%, and the proportion of fully filled fractures is approximately 51.1%. Fracture fillings include calcite, pyrite, quartz, and organic matter, etc., indicating a good sealing effect in this area.

The fracture strike orientation interpreted by FMI logging shows that the Well L206 area primarily contains reticulated fractures, mainly NW-trending (330° ± 10°) fractures, followed by NE-trending (30° ± 5°) and NEE-trending (70° ± 5°) fractures. The Well Y101 area primarily contains reticulated fractures, mainly in the NNE (20° ± 10°), NE (40° ± 10°), and ENE (80° ± 10°) directions,
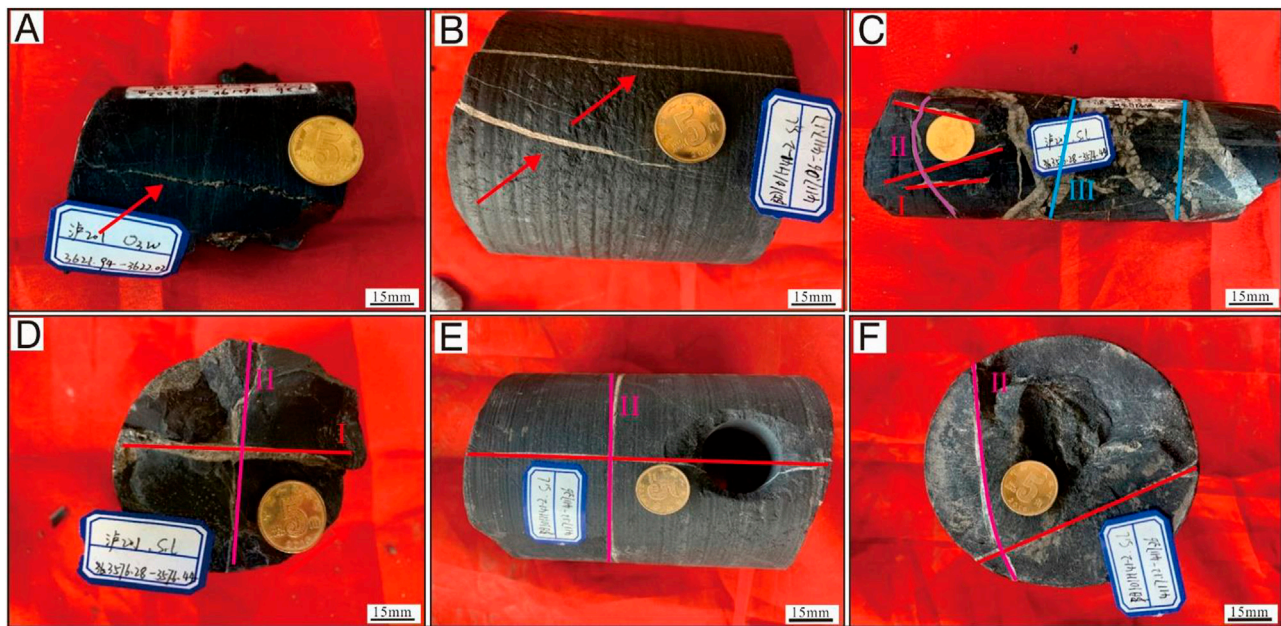
FIGURE 4 | Intersection relationship of typical core fractures of Longmaxi formation in Luzhou block.

followed by near S-N (0° ± 10°) fractures. The Well L211 area primarily contains unidirectional fractures, mainly ENE (80° ± 10°) fractures (**Figure 5**). High-angle fractures and vertical fractures are dominant, and the fracture dip angle mainly ranges from 30° to 80°, which is consistent with the core observation results. According to the fracture dip angle distribution histogram, the fractures observed in the wells in the study area are generally high-angle fractures, followed by near-vertical fractures, with fewer low-angle fractures, and virtually no horizontal fractures.

Based on the occurrence, filling characteristics and mutual intersection relationships among core fractures, at least three stages of structural fractures can be determined, indicating that fracture formation was influenced by at least three stages of tectonic movement.

4.1.3 Stage Classification of Underground Faults
Geophysical interpretations show that the faults in the study area were mostly formed in a large-scale compressional orogenic environment during the Himalayan period and are mainly reverse faults (**Figure 6**). Vertically, the transition zone is composed of the Jialingjiang Formation gypsum rock, thick Silurian Longmaxi mudstone, and Cambrian Gaotai Formation gypsum rock; therefore, three sets of fault systems were formed. The faults extension shape of the main fault system in the Luzhou block trends NE-SW and NE; ENE and NNE trends are also present, which shows that the fault systems in this area did not develop at the same time. Instead, they are the result of multiple stages of tectonic events that occurred in different directions. The bottom boundary of the Late Ordovician Wufeng Formation in the Luzhou area has experienced three stages of tectonic compression in different directions over its geological history. Combined with the morphological features of its surface structures and seismic data

from this area, it is believed that the faults, such as those exposed at Wells T40, L28, L34, L40, G11, G35, YS10, and H2, trend ENE in general, whereas those in the NW part of the area trend WE. These faults were the earliest formed and are Stage I faults that formed due to the compressive crustal stress that trends SSE. The overall strike of the L20, Q6, L18, Y35, and other faults is in the NE direction; these faults formed next and Stage II faults that occurred due to the NW compressive crustal stress. Faults, such as those encountered at Wells T15, T30, YS12, DS3, YS11, and YS12, trend N-S overall and were the last faults formed; they are Stage III faults that occurred due to the compressive crustal stress that trends E-W.

4.2 Characteristics of Fluid Inclusions in Fracture Fillings
4.2.1 Types and Homogenization Temperature Characteristics of Fluid Inclusions
The tectonic activities that occurred in different periods may have produced multistage faults. As fluid migration channels, faults can capture fluids with different properties. Inclusions retain information, such as the temperature and pressure when the fluid was captured, thereby retaining traces of tectonic activities at different stages (Nagarajan et al., 2007; He et al., 2018; Fan et al., 2020a). The fracture fluid inclusions in the Silurian Longmaxi Formation primarily include four types of single-phase liquid hydrocarbon inclusions, gas-liquid two-phase hydrocarbon inclusions, single-phase brine inclusions, and two-phase brine inclusions. Inclusions composed of liquid hydrocarbons, ranging in size from 3 μM to 6 μM, are yellow and yellow-green under fluorescence. The size of gas-liquid two-phase inclusions ranges from 4 μM to 10 μM, and the liquid phase is yellow under fluorescence, while the gas phase is colourless under fluorescence. The brine inclusions include single-
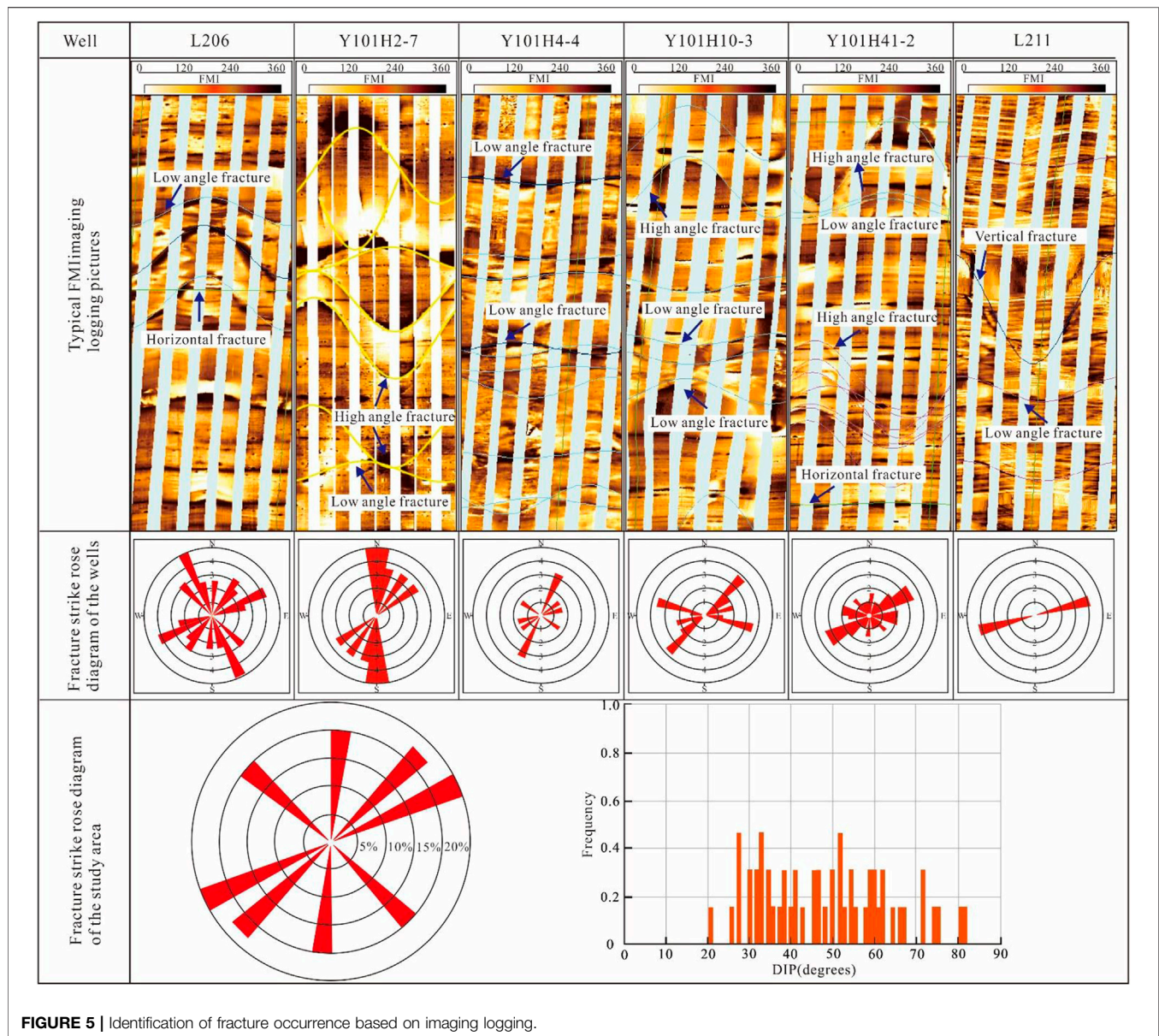
FIGURE 5 | Identification of fracture occurrence based on imaging logging.

phase brine inclusions and two-phase brine inclusions, and the size of the inclusions range from 2 μM to 10 μM (**Table 1**; **Figure 7**).

The test results of the fluid inclusion samples from fracture fillings in L201, L203H79-4, Y101H41-2, and Y101H3-8 show that fluid charging activities in the fractures experienced at least three stages (**Figure 8**). The study area experienced at least three stages of relatively strong tectonic compression before fault and fracture systems were formed, which provided migration channels and charging sites for fluids. The first stage corresponds to the first-stage structural uplift that occurred after the Luzhou area reached its maximum burial depth, and the temperature of inclusions formed at this time is the highest. The inclusions formed during this event include both gas and brine inclusions, and the homogenization temperature of these inclusions is 150–178°C. The second stage corresponds to the temporary uplift of the structure that occurred at the end of the Middle Triassic due to the Indosinian event; the inclusions formed during this event are brine inclusions from the same period of the asphalt formation, and the fluid charging homogenization temperature caused by the short-term uplift is mainly 123–148°C. The third stage corresponds to the period from the mid-Himalayan orogeny to the present day, which is the structural setting period, during which slow uplift lasted for an extended period. The inclusions formed during this stage are oil and bitumen inclusions, and the homogenization temperature of these fluid inclusions is 90–110°C.

4.2.3 Indicative Significance of Inclusions for Preservation Conditions

The inclusions in Well L201 are dominated by high-density liquid hydrocarbon inclusions and high density methane inclusions,
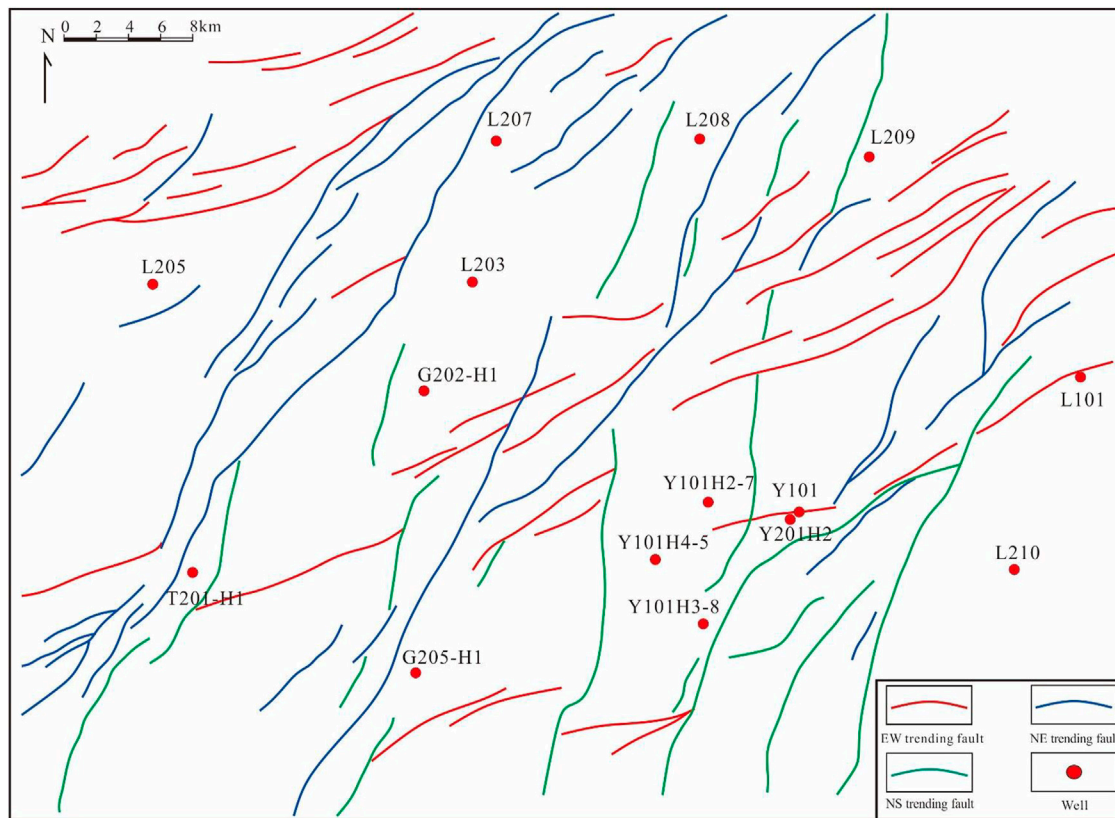
FIGURE 6 | Distribution of the fault system in the Longmaxi Formation of the Luzhou block.

indicating that the fractures in Well L201 were formed at the time of the maximum burial depth of the shale. Hydrocarbon inclusions in the high-quality shale sections are highly developed, while two-phase inclusions are very rare, and low-temperature two-phase inclusions are less rare, indicating that the fluid activity in the late stage of structural fractures was weak (Burruss et al., 1983; Mourgues et al., 2012; Han et al., 2018). The brine inclusions are dominant in Well L203H79-4 and Y101H3-8, which also include a small number of hydrocarbon inclusions and carbonaceous bitumen inclusions, indicating that 1) fluid inclusions were not developed during the stage of massive oil and gas generation, and the homogenization temperature of the hydrocarbon inclusions is between 123 and 155°C; 2) during the uplift and denudation stage, fluid inclusions were developed and influenced by filling by external water, and the homogenization temperature of brine inclusions is between 98 and 112°C. In the geologic history of Well Y101H41-2, brine inclusions are dominant and coexist with gas inclusions. These inclusions have homogenization temperatures between 90 and 114°C and are characterized by low-temperature fluids, which represent the filling of formation fluids. Oil and gas deposits were captured during the generation period, and the inclusions developed during this period were primarily brine inclusions, indicating a high degree of shale gas loss across geological history. The multistage homogenization temperatures of the shale fluid inclusions reveal subsequent multiple structural fractures and

fluid charging events. The vertical distribution of fluid inclusion types includes brine inclusions at the bottom and a small amount of hydrocarbon inclusions at the top, indicating that the deep fluids intruded upwards into the high-quality shale intervals along fractures, and that shale gas escaped from the bottom layers.

The fluid inclusion types present in L201, L203H79-4, Y101H3-8, and Y101H41-2 indicate that the preservation conditions of shale gas in this area gradually deteriorated from W to E, which is consistent with the strength of the regional tectonic deformation.

4.3 Fracture Formation Stages Determined by Acoustic Emission Experiments

The Kaiser effect of the acoustic emission test was evaluated for five groups of 15 samples in the study area, and the number of effect points that appeared on the acoustic emission experimental curve was used to determine the stages of tectonic compression experienced during the geohistorical period. The acoustic emission energy accumulation-time relationship and stress-time relationship curves were established (Suboyin et al., 2020; Qiu et al., 2021; Shan et al., 2021; Song et al., 2021; Xi et al., 2021). The energy accumulation-time relationship curve shows that as the load gradually increased, the energy suddenly increased at 50 s; after that, there were four sharp energy accumulation points,

TABLE 1 | Test data of fluid inclusions in fracture fillings of the Longmaxi Formation (partial).

Well	No.	Depth	Distribution characteristics	Distribution form	Size/μM	Gas- liquid ratio/%	Homogenization temperature/°C
L201	1	3576.28	Zonal distribution	Irregular	7	8	108
	2	3576.28			10	10	120
	3	3576.28			6	8	114
	4	3576.28			6	5	135
	5	3576.28		Strip	7	4	150
	6	3766.00		Oval	5	4	142
	7	3766.00			5	4	164
	8	3766.00			8	8	178
L203H79-4	9	3797.95		Irregular	12	6	98
	10	3816.72		Triangle	8	6	123
	11	3825.26		Irregular	7	6	115
	12	3826.88			8	6	148
	13	3846.20		Diamond	9	6	155
	14	3846.88		Strip	9	5	108.3
	15	3872.66			8	5	114.3
	16	3900.62		Irregular	7	5	128.7
Y101H3-8	17	3279.83		Oval	6	6	112
	18	3279.83		Irregular	5	5	108
	19	3754.44			6	6	135
	20	3742.48		Strip	8	6	126
	21	3772.84		Irregular	6	5	118
	22	3772.84			6	5	100
Y101H41-2	23	3779.36		Rectangle	5	6	90
	24	3782.95		Oval	5	4	114
	25	4117.12			4	5	105
	26	4126.00		Irregular	4	4	101
	27	4126.00			5	4	112
	28	4143.62			7	4	109.6

and a total of five high-energy accumulation points (**Figure 9**). Four obvious inflection points, namely, the characteristic points of the Kaiser effect, can be seen on the energy accumulation-time relationship curve. The experimental results show that five Kaiser effect points can be identified on the energy accumulation-time curve of multiple samples from the Longmaxi Formation in the Luzhou area, reflecting that the rock has experienced five microfracture events throughout geologic history. According to the stress pattern of the rock acoustic emission measurements, the palaeotectonic stresses corresponding to the five Kaiser effect points are as follows: Caledonian tectonic stress of 26.5–32.03 MPa, mid-late Yanshanian tectonic stress of 68.3–76.8 MPa, late Yanshanian-early Himalayan tectonic stress of 85.2–100.5 MPa, middle-late Himalayan tectonic stress of 55.6–63.8 MPa, and present stress field value of 46.8–56.2 MPa.

Combining with the existing research results and regional tectonic evolution history in and around the study area, the five stages of tectonic stress in this study area are as follows: the present tectonic stress, the mid-Himalayan-present tectonic stress, the late Yanshanian-early Himalayan tectonic stress, the mid-late Yanshanian tectonic stress, and the Caledonian tectonic stress stages, respectively. Because the Caledonian tectonic event included up-and-down movement throughout the entire southern Sichuan region, it had little effect on the fracture development and structural trajectory, and the tectonic motion at this stage can be excluded from the explanation of fracture development. The comprehensive analysis of the regional

tectonic evolution history shows that the study area has experienced at least three stages of tectonic motion since the Late Ordovician and at least three corresponding fracture development stages. The three periods in which these three-stage fractures developed are the middle-late Yanshanian period, the end Yanshanian period-early Himalayan period, and the middle Himalayan period-present.

5 DISCUSSION

5.1 Structure and Hydrocarbon Evolution of Shale Gas Reservoirs

In general, the Luzhou area is characterized by three stages, i.e., formation of shale gas reservoirs in the early stage, enrichment of high-pressure and ultrahigh-pressure shale gas in the middle stage, and small uplift and denudation in the later stage. The duration and magnitude of structural uplift can be obtained by analysing the burial thermal history. The maximum burial depth in the Luzhou area was 6,020–6,635 m, the uplift range was 2087–2,353 m, and the uplift occurred at 78–85 Ma. The shale has experienced three stages of burial (hydrocarbon generation) and three stages of uplift. Burial stage I of the Wufeng Formation-Longmaxi Formation shale in typical wells in the Luzhou area was the rapid burial that occurred from the Late Ordovician to late early Silurian. This stage corresponds to the early to middle stage of oil generation; the burial depth was more than 2 km, and the formation temperature was approximately
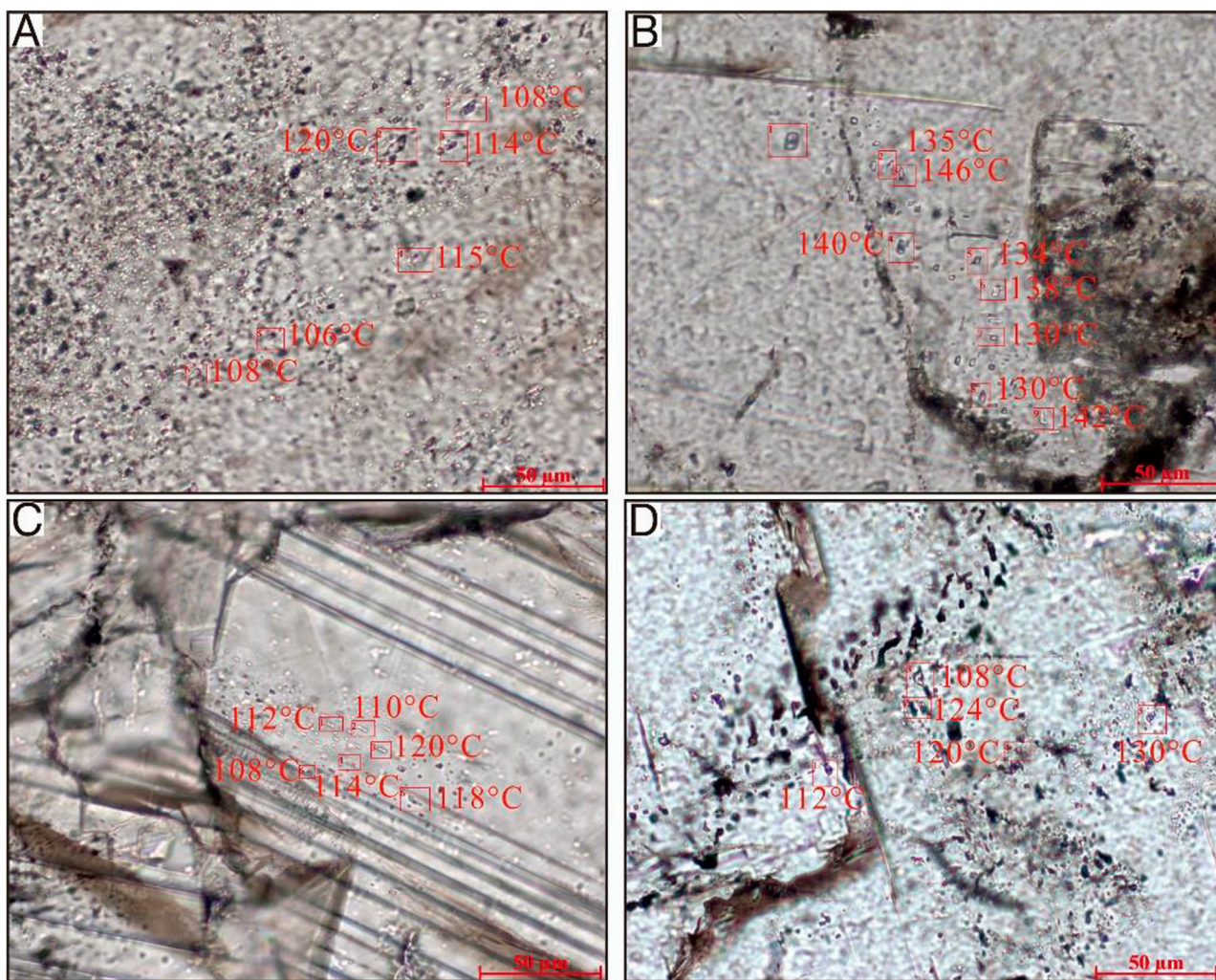
FIGURE 7 | Fluid inclusions in typical fracture fillings of the Luzhou block. **(A)**, **(B)**. Well L201, 3,576.28, Longmaxi Formation; **(C)**. Well L206, 4043.20, Longmaxi Formation; **(D)**. Well Y101H3-8, 3779.36, Longmaxi Formation.
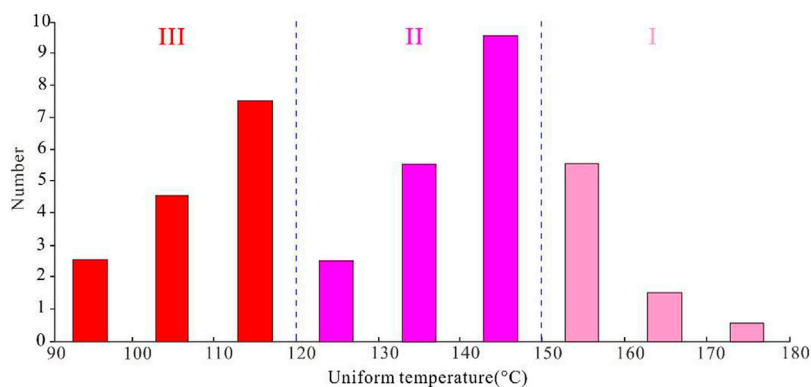
FIGURE 8 | Homogeneous temperature distribution of fluid inclusions in fracture fillings of the Luzhou block.

FIGURE 9 | Acoustic emission experimental results of the Well L203H79-4 (3842.81–3843.16 m). **(A)**, **(D)**. The sampling angle is 0°; **(B)**, **(E)**. The sampling angle is 45°; **(C)**, **(F)**. The sampling angle is 90°.
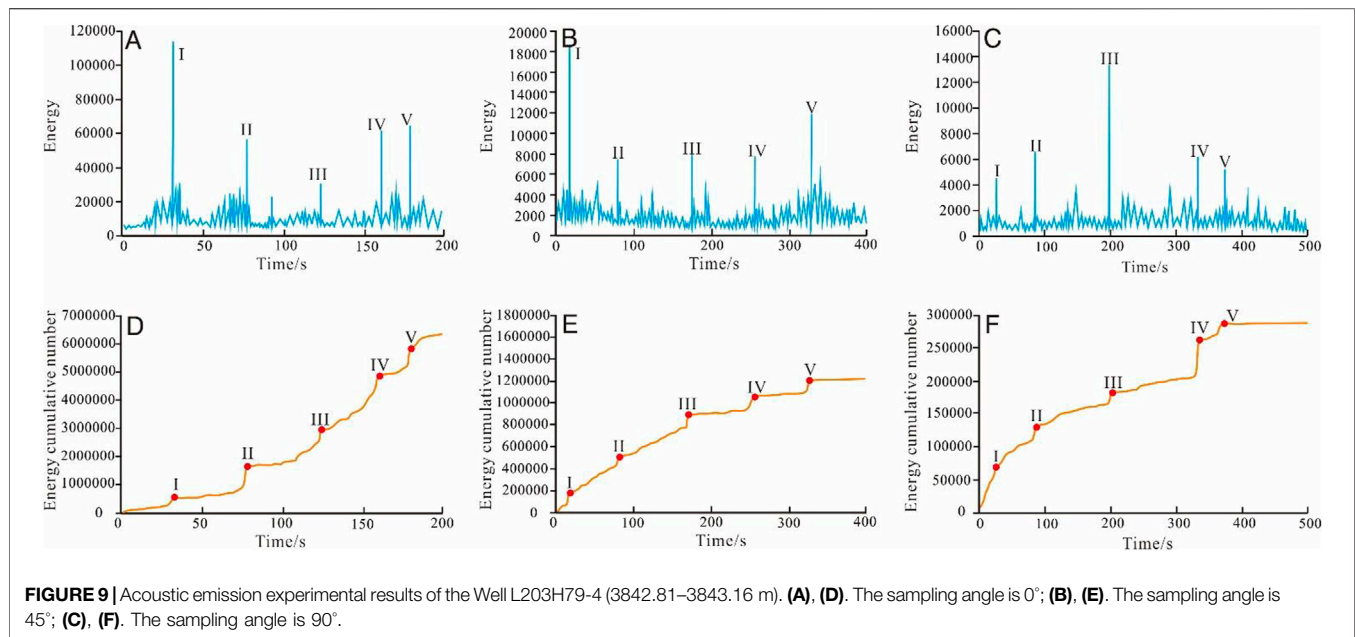
90–110°C. Uplift stage I (oscillatory uplift) included the slow uplift from the end of the middle Silurian to the Carboniferous. Burial stage II included the sedimentary deposition and subsidence that occurred during the early Permian-Early Triassic and corresponds to a burial depth of nearly 3 km and a formation temperature of approximately 130–170°C. This stage is the later stage of oil generation, during which organic matter began to generate and expel hydrocarbons in large quantities, and the vitrinite reflectance (Ro) of samples from this period was between 0.7% and 1.0%. Uplift stage II (short-term uplift) was the short-term uplift of the structure at the end of the Middle Triassic that occurred due to the influence of the Indosinian event. Burial stage III featured a rapid and deep burial from the Middle Triassic to the late Cretaceous, to a burial depth of approximately 6,273 m, and the formation temperature exceeded 200°C. The organic matter entered the high-overmature stage, and the Ro values from samples from this period are approximately 1.3%–3.0% (**Figure 10**). Various types of organic matter preserved in shale began to decompose during this period; therefore, this stage is the primary gas generation stage. Uplift stage III (transformation and uplift period) was influenced by the uplift of the Qinghai-Tibet Plateau in the Himalayas and the depression of the western Sichuan foreland basin that has occurred since the Late Cretaceous. Rapid uplift and transformation occurred from the Late Cretaceous to the Neogene, and uplift occurred at approximately 75–85 Ma. The shale is deeply buried and has developed multistage fault deformation, and the enrichment and preservation conditions of the shale gas are still optimal, with relatively large total resources and a relatively high abundance.

The degree of thermal evolution of organic matter is usually quantitatively characterized by the Ro value, and a moderate degree of thermal evolution can promote shale gas enrichment. The test results of the equivalent Ro value of organic matter in shale samples from the Luzhou area show that the thermal

evolution of organic matter generally exceeds 2.0%, and the equivalent Ro value ranges from 2.86% to 3.34% (an average of 3.16%). The organic matter in the Luzhou area is at the stage of high-overmature pyrolysis and can produce dry gas, which ensures that the organic matter has been converted into hydrocarbons. During the thermal evolution of shale, when the degree of thermal evolution and Ro values are less than the "critical point", at Ro values between 2.8 and 3.2%, the is between 0.6 and 6.3%, and the porosity is between 2.8 and 5.8%. The porosity and pore structure characteristics of shale reservoirs are controlled by other factors, such as organic carbon content, clay mineral types, and thermal evolution degree, among which the thermal evolution degree is a key factor. As the shale Ro increases, the rate of hydrocarbon generation in the shale increases, a large amount of natural gas is generated, and elliptical or stomata-shaped overpressure-induced organic pores are formed. When the thermal evolution degree (Ro) is greater than 3.2%, the porosity is between 2.7% and 5.7% (**Figure 11A**), and the TOC is between 0.4% and 5.5%; additionally, the porosity of shale slowly decreases as the Ro value increases (**Figure 11B**). The continued thermal evolution of the shale reservoirs leads to organic matter graphitization, during which the pore structure of the shale changes, organic pores collapse, the specific surface areas of several meso- to micropores in the reservoirs decrease, and the specific surface areas of organic pores in the shale decrease.

5.2 Fracture Development Stages and Evolution Models

The main fault system in the Luzhou area trends NE-SW, NE, ENE and NNE, which indicates that the fault system in this area is the result of multistage tectonic compression that occurred in different directions. By comprehensively analysing the results

FIGURE 10 | Comprehensive model of burial history, hydrocarbon generation and structural evolution of shale in the Longmaxi formation encountered in typical wells in the Luzhou area. **(A)**. Well Y101H65-5; **(B)**. Well L205; **(C)**. Well 201.

FIGURE 11 | Evolution of shale organic matter in the Longmaxi Formation of the Luzhou area. **(A)**. Relationship between R_O and porosity; **(B)**. Relationship between R_O and TOC.

from the rock acoustic emission experiments, inclusion homogenization temperature testing and burial-thermal evolution history (Li et al., 2019b), it was confirmed that the Longmaxi Formation in the Luzhou area experienced three major tectonic events; therefore, the formation of surface and underground fractures is also divided into three stages (**Figure 12**).

During the middle-late period of the Yanshan Movement (86.2–68.5 Ma), the Luzhou area was squeezed from the S to the N by the Daloushan tectonic belt, and the maximum effective principal stress was 76.8 MPa, resulting in WNW-trending conjugate plane shear fractures and NE- and near-E-W-trending conjugate shear fractures, among which the near-EW-trending conjugate shear fractures further expanded and penetrated into new areas, forming near-EW-trending faults with the earliest formation stage, i.e., the Stage I faults. The palaeotectonic stress of the tectonic motion at this stage was 68.3–76.8 MPa. The resulting fractures were formed early and have a high degree of filling. The filling material is mostly calcite, and the homogenization temperature of the fluid inclusions in these fillings is 150–178°C.

From the end of the Yanshan Movement to the middle of the Himalayan Movement (68.5–35.2 Ma), the uplift of the Qinghai-Tibet Plateau triggered the NW-SE extrusion in this area. The maximum effective principal stress was 100.5 MPa, forming NW-trending and nearly E-W-trending conjugate plane shear fractures and NE-trending conjugate shear fractures, of which the NE-trending conjugate shear fractures further expanded and penetrated, forming many NE-trending faults with the second-earliest formation stage, i.e., the Stage II fractures. The palaeotectonic stress at this stage was 86.91–99.61 MPa, and the resulting fractures have a high degree of filling. The fillings are mostly calcite, with a small amount of pyrite, and the homogenization temperature of the fluid inclusions in these fillings is 123–148°C.

From the late Himalayan Movement to the present (35.2–0 Ma), due to the combined action of the Jiangnan Xuefeng uplift and the central Sichuan uplift, the Luzhou area was squeezed by the resultant force in the E-W direction, and the maximum effective principal stress was 63.8 MPa, forming NNE-trending conjugate plane shear fractures and near-N-S-trending conjugate shear fractures, of which the near-NS-trending
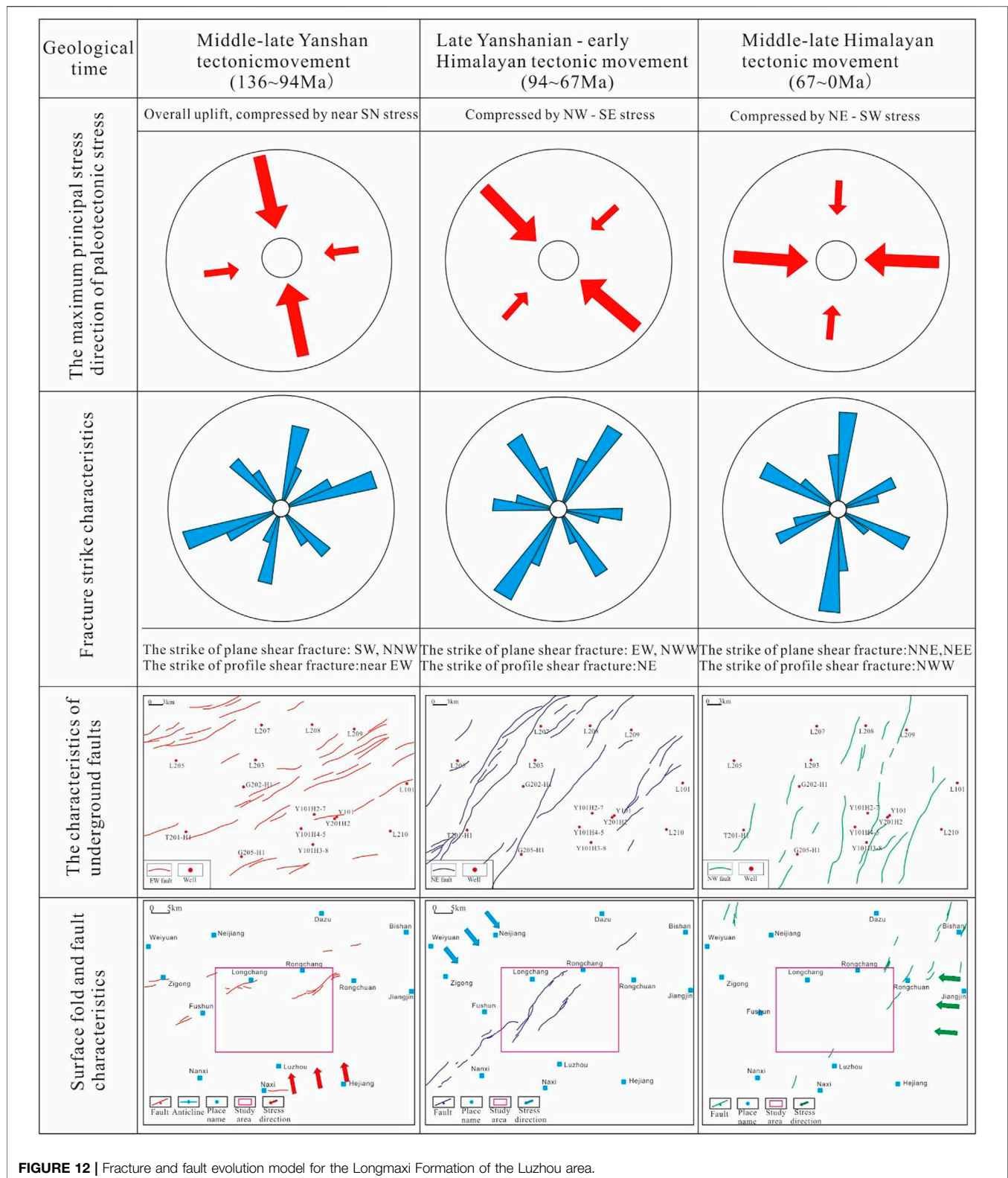
FIGURE 12 | Fracture and fault evolution model for the Longmaxi Formation of the Luzhou area.

conjugate shear fractures further extended and penetrated, forming a large number of near-N-S-trending fractures during the latest formation stage, i.e., the Stage III faults. The

palaeotectonic stress of tectonic movement at this stage was 47.76–57.64 MPa, and the resulting fractures have a low filling degree. The filling materials are mostly a small amount of calcite
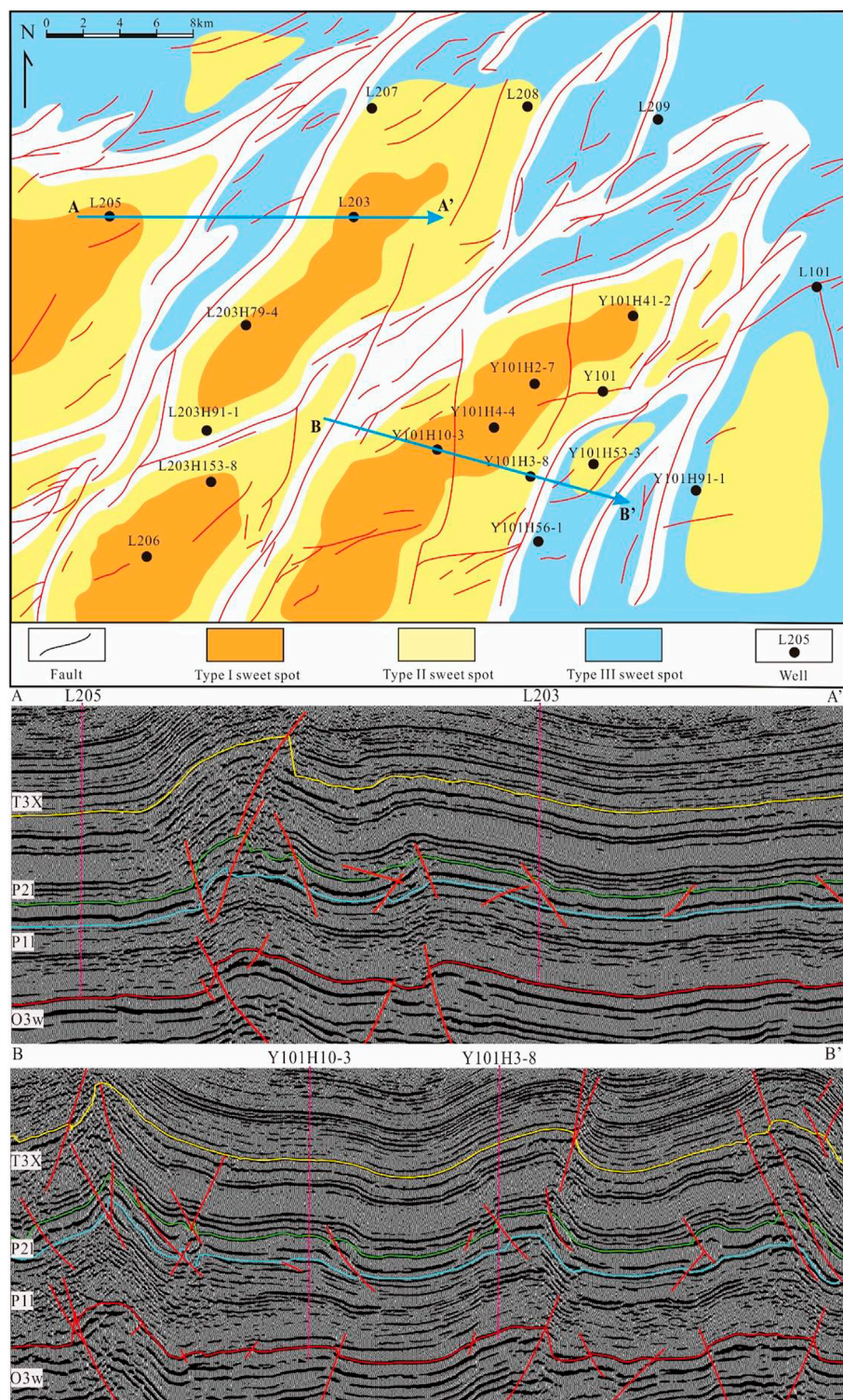
FIGURE 13 | Favourable area for shale gas preservation in the Luzhou area.

and mud, and the homogenization temperature of the fluid inclusions in these fillings is 90–110°C.

5.3 Effect of the Fracture Stage on Shale Gas Preservation and Enrichment

The tectonic movement caused fractures to form in the Longmaxi Formation. The dominant orientations and development degrees of fractures formed at different tectonic evolution stages are different, and the effects on the enrichment of the shale gas and the gas-bearing properties of the shale in the later stage are also different (Curtis 2002; Yin et al., 2019; Guo W. X. et al., 2021). The direction of the maximum horizontal principal stress in the Longmaxi Formation is ESE at each well in the Luzhou block. Within the range of 105° ± 10°, the fault stage is related to the maximum horizontal crustal stress, which is one of the important influencing factors of oil and gas preservation conditions. In general, the mid-late Yanshan tectonic movement intensity is small, mainly involving vertical up-and-down movement, and the fault scale is small. The formation of the Stage I ENE- and E-W-trending fractures occurred early, and the resulting fractures have a high degree of filling, but the angle between the fracture direction and the current crustal stress orientation is small, which has a certain influence on shale gas dissipation. The scales and distributions of Stage II NE-trending faults that formed at the end of the Yanshan Movement to the middle of the Himalayan Movement are quite different from those of the Stage I fractures. Both sides of the NE-trending faults were subjected to the ESE-trending stress, causing lateral displacement along the fault strike and forming a certain extensional environment. As a result, the sealing performance of the faults is reduced, resulting in a reduction in the ability to preserve oil and gas. Stage III N-S-trending faults that formed from the late Himalayan Movement to the middle stage of the present are squeezed and closed under the action from the ESE-trending stress, forming an overall compressive environment. The N-S-trending, NNE-trending and NE-trending fractures exhibit a large angle (>20° or more) to the current crustal stress direction (105 ± 10°) and are more likely to improve the gas-bearing properties of the shale. The development of small-scale and medium-scale fractures has little effect on the oil and gas preservation capacity in the study area.

Oil and gas preservation conditions are affected by factors such as fault stage and maximum horizontal crustal stress, fault scale, structural burial depth, and formation pressure coefficient. A quantitative target evaluation system and standard for shale gas sweet spots were established, and three types of favourable preservation conditions were identified (**Figure 13**). The Type I sweet spot area is affected by the faults and is concentrated in the southwest of the Well Lu 205, Well Lu 203, and Well Yang 101 areas; it belongs to the middle area of a broad and gentle syncline in structure, and the spacing of the Stage II NE-trending faults is more than 2.0 km; here, the shale gas preservation conditions are good, the formation pressure coefficient is between 2.0 and 2.2, the shale burial depth is between 3,500 and 4,000 m, and the stress difference coefficient is as low as 0.12–0.16. The favourable areas for oil and gas preservation in the Type II sweet spot area are

mostly distributed in a ring-shaped zone in the slope area in the transition from syncline to anticline; the spacing of the Stage II NE-trending faults is 1.0–2.0 km, the preservation conditions of shale gas are weakened to a certain extent, the pressure coefficient is 2.0–2.1, the shale burial depth is 3,500–4,000 m, and the stress difference coefficient is 0.16–0.18. The Type III sweet spot areas are mostly concentrated in the middle and northern areas of the block and the structurally high structural parts of the anticline; here, the formation pressure coefficient is between 1.9 and 2.1, the shale burial depth is 3,000–3,500 m, and the stress difference coefficient is high (0.16–0.20); faults and folds have developed in the corresponding areas, and the spacing of the Stage II NE-trending fault is less than 1.0 km. The oil and gas preservation conditions of the Longmaxi Formation in the northern Well Lu 207, Well Lu 208, and Well Lu 209 areas are generally poor.

6 CONCLUSION

(1) Due to its tectonic history, the Longmaxi Formation is primarily composed of high-angle fractures and vertical fractures. The fractures have a small width, large spacing, and high filling degree, and their conductivity is poor. The Longmaxi Formation was primarily influenced by tectonic compression in the three directions of SSE, NW, and W-E after sedimentation, and the fractures mostly developed in the NW direction (330° ± 10°), NE direction (30° ± 5°), and ENE direction (70° ± 5°).

(2) The formation of structural fractures of the Longmaxi Formation in the Luzhou area can be divided into three stages. The first-stage fractures were formed in the middle-late period of the Yanshanian tectonic movement (86.2–68.5 Ma) with a palaeotectonic stress of 68.33–71.82 MPa, and the corresponding homogenization temperature of the fluid inclusions in fracture fillings is 150–178°C. The second-stage fractures were formed at the end of the Yanshanian-early Himalayan tectonic movement (68.5–35.2 Ma) with a palaeotectonic stress of 85.2–100.5 MPa, and the corresponding homogenization temperature is 123–148°C. The formation time of the third-stage fractures is the middle-late period of the Himalayan tectonic movement (35.2–0 Ma) with a palaeotectonic stress of 55.6–63.8 MPa. The filling degree of these fractures is low, and the corresponding homogenization temperature is 90–110°C.

(3) Fractures with an early formation time, high filling degree, and a larger angle between the fracture orientation and the current crustal stress orientation are favourable for preserving shale gas. Otherwise, shale gas preservation conditions may be easily damaged. Shale gas preservation conditions are affected by the fault stage, maximum horizontal crustal stress, fault scale, structural burial depth, and formation pressure coefficient. Three types of favourable preservation conditions were identified. The Type I area belongs to the middle area of a broad and gentle syncline, which is concentrated in the southwestern part of the Well L205, Well L203, and Well Y101 areas.

DATA AVAILABILITY STATEMENT

The original contributions presented in the study are included in the article/supplementary material, further inquiries can be directed to the corresponding author.

AUTHOR CONTRIBUTIONS

JL and HL contributed in writing, reviewing, and editing, datacuration, writing—original draft preparation; JX, YW, and ZG contributed in formal analysis, validation, and reviewing.

REFERENCES

Burruss, R. C., Cercone, K. R., and Harris, P. M. (1983). Fluid Inclusion Petrography and Tectonic-Burial History of the Al Ali No. 2 Well: Evidence for the Timing of Diagenesis and Oil Migration, Northern Oman Foredeep. *Geology* 11, 567–570. doi:10.1130/0091-7613(1983)11<567:fipath>2.0.co;2

Curtis, J. B. (2002). Fractured Shale-Gas Systems. *AAPG Bull.* 86 (11), 1921–1938. doi:10.1306/61eeddbe-173e-11d7-8645000102c1865d

Fan, C. H., He, S., Zhang, Y., Qin, Q. R., and Zhong, C. (2018). Development Phases and Mechanisms of Tectonic Fractures in the Longmaxi Formation Shale of the Dingshan Area in Southeast Sichuan Basin, China. *Acta Geol. Sin.* 92 (6), 2351–2366.

Fan, C., Li, H., Zhao, S., Qin, Q., Fan, Y., Wu, J., et al. (2020a). Formation Stages and Evolution Patterns of Structural Fractures in Marine Shale: Case Study of the Lower Silurian Longmaxi Formation in the Changning Area of the Southern Sichuan Basin, China. *Energy fuels.* 34, 9524–9539. doi:10.1021/acs.energyfuels.0c01748

Fan, C., Li, H., Qin, Q., He, S., and Zhong, C. (2020b). Geological Conditions and Exploration Potential of Shale Gas Reservoir in Wufeng and Longmaxi Formation of Southeastern Sichuan Basin, China. *J. Pet. Sci. Eng.* 191, 107138. doi:10.1016/j.petrol.2020.107138

Fan, C. H., Xie, H. B., Li, H., Zhao, S. X., Shi, X. C., Liu, J. F., et al. (2022). Complicated Fault Characterization and its Influence on Shale Gas Preservation in the Southern Margin of the Sichuan Basin, China. *Lithosphere* 2022, 8035106. doi:10.2113/2022/8035106

Gao, F. Q. (2019). Use of Numerical Modeling for Analyzing Rock Mechanic Problems in Underground Coal Mine Practices. *J. Min. Strata Control Eng.* 1 (1), 013004. doi:10.13532/j.jmsce.cn10-1638/td.2019.02.009

Guo, J. L., Jia, C. Y., He, D. B., Li, L., Zhu, H. Q., Zhou, Y., et al. (2020a). Classified Evaluation of Shale Reservoirs in the Ordovician Wufeng to Silurian Longmaxi Formations in the Southern Sichuan Basin. *Geol. J. China Univ.* 26 (3), 323–332. doi:10.16108/j.issn1006-7493.2019047

Guo, X. S., Hu, D. F., Huang, R. C., Wei, Z. H., Duan, J. B., Wei, X. F., et al. (2020b). Deep and Ultra-deep Natural Gas Exploration in the Sichuan Basin: Progress and Prospect. *Nat. Gas. Ind.* 40 (5), 1–14. doi:10.1016/j.ngib.2020.05.001

Guo, J., Jia, C., He, D., and Meng, F. (2021a). Classification and Evaluation on Shale Gas Reservoir for Wufeng-Longmaxi Formation in Chuannan Area, Sichuan Basin. *Lithosphere* 2021, 3364731. doi:10.2113/2021/3364731

Guo, W. X., Tang, J. M., Ouyang, J. S., Wang, T., Wang, X., and Wang, Y. (2021b). Characteristics of Structural Deformation in the Southern Sichuan Basin and its Relationship with the Storage Condition of Shale Gas. *Nat. Gas. Ind.* 41 (5), 11–19. doi:10.3787/j.issn.1000-0976.2021.05.002

Han, Z.-Z., Liu, H., Song, Z.-G., Zhong, W.-J., Han, C., Han, M., et al. (2018). Geochronology, Geochemistry, and Tectonic Implications of Upper Silurian - Lower Devonian Meta-Sedimentary Rocks from the Jiangyu Group in Eastern Jilin Province, Northeast China. *Can. J. Earth Sci.* 55, 490–504. doi:10.1139/cjes-2017-0260

He, Z. L., Li, S. J., Nie, H. K., Yuan, Y. S., and Wang, H. (2018). The Shale Gas "Sweet Window": "The Cracked and Unbroken" State of Shale and its Depth Range. *Mar. Pet. Geo.* 101, 334–342. doi:10.1016/j.marpetgeo.2018.11.033

He, S., Qin, Q. R., Li, H., and Zhao, S. X. (2022a). Geological Characteristics of Deep Shale Gas in the Silurian Longmaxi Formation in the Southern Sichuan Basin, China. *Front. Earth Sci.* 9, 818543. doi:10.3389/feart.2021.818155

He, S., Qin, Q. R., Li, H., and Wang, S. L. (2022b). Deformation Differences in Complex Structural Areas in the Southern Sichuan Basin and its Influence on Shale Gas Preservation: A Case Study of Changning and Luzhou Area. *Front. Earth Sci.* 9, 818155. doi:10.3389/feart.2021.818534

Hou, E. K., Cong, T., Xie, X. S., and Wei, J. B. (2020). Ground Surface Fracture Development Characteristics of Shallow Double Coal Seam Staggered Mining Based on Particle Flow. *J. Min. Strata Control Eng.* 2 (1), 013521. doi:10.13532/j.jmsce.cn10-1638/td.2020.01.002

Jin, Z., Nie, H., Liu, Q., Zhao, J., and Jiang, T. (2018). Source and Seal Coupling Mechanism for Shale Gas Enrichment in Upper Ordovician Wufeng Formation - Lower Silurian Longmaxi Formation in Sichuan Basin and its Periphery. *Mar. Petroleum Geol.* 97, 78–93. doi:10.1016/j.marpetgeo.2018.06.009

Kang, H. P. (2021). Temporal Scale Analysis on Coal Mining and Strata Control Technologies. *J. Min. Strata Control Eng.* 3 (1), 013538. doi:10.13532/j.jmsce.cn10-1638/td.20200814.001

Li, H., Tang, H. M., and Zheng, M. J. (2019a). Micropore Structural Heterogeneity of Siliceous Shale Reservoir of the Longmaxi Formation in the Southern Sichuan Basin, China. *Minerals* 9, 548. doi:10.3390/min9090548

Li, H., Tang, H., Qin, Q., Zhou, J., Qin, Z., Fan, C., et al. (2019b). Characteristics, Formation Periods and Genetic Mechanisms of Tectonic Fractures in the Tight Gas Sandstones Reservoir: A Case Study of Xujiahe Formation in YB Area, Sichuan Basin, China. *J. Pet. Sci. Eng.* 178, 723–735. doi:10.1016/j.petrol.2019.04.007

Li, H., Wang, Q., Qin, Q., and Ge, X. (2021a). Characteristics of Natural Fractures in an Ultradeep Marine Carbonate Gas Reservoir and Their Impact on the Reservoir: A Case Study of the Maokou Formation of the JLS Structure in the Sichuan Basin, China. *Energy fuels.* 35, 13098–13108. doi:10.1021/acs.energyfuels.1c01581

Li, H. T., Peng, R., Du, W. S., Li, X. P., and Zhang, N. B. (2021b). Experimental Study on Structural Sensitivity and Intervention Mechanism of Mechanical Behavior of Coal Samples. *J. Min. Strata Control Eng.* 3 (4), 043012. doi:10.1638/td.20210820.001

Li, J., Qin, Q., Li, H., and Zhao, S. (2022a). Paleotectonic Stress Field Modeling and Fracture Prediction of the Longmaxi Formation in the N216 Well Block, Southern Sichuan Basin, China. *Arab. J. Geosci.* 15, 347. doi:10.1007/s12517-022-09616-z

Li, J., Qin, Q., Li, H., Wan, Y., and Wan, Y. F. (2022b). Numerical Simulation of the Stress Field and Fault Sealing of Complex Fault Combinations in Changning Area, Southern Sichuan Basin, China. *Energy Sci. Eng.* 10 (2), 278–291. doi:10.1002/ese3.1044

Li, H. (2022a). A Review of Mechanical Mechanism and Prediction of Natural Fracture in Shale. *Arab. J. Geosci.* 15 (6), 474. doi:10.1007/s12517-022-09786-w

Li, H. (2022b). Research Progress on Evaluation Methods and Factors Influencing Shale Brittleness: A Review. *Energy Rep.* 8, 4344–4358. doi:10.1016/j.egyr.2022.03.120

Liu, S. G., Deng, B., Zhong, Y., Ran, B., Yong, Z. Q., Sun, W., et al. (2016). Unique Geologic Features of Burial and Superimposition of the Lower Paleozoic Shale□gas across the Sichuan Basin and its Periphery. *Earth Sci. Front.* 23 (1), 11–28. doi:10.13745/j.esf.2016.01.002

Liu, J., Ding, W., Gu, Y., Xiao, Z., Dai, J., Dai, P., et al. (2018). Methodology for Predicting Reservoir Breakdown Pressure and Fracture Opening Pressure in Low-Permeability Reservoirs Based on an *In Situ* Stress Simulation. *Eng. Geol.* 246, 222–232. doi:10.1016/j.enggeo.2018.09.010

Liu, J. S., Yang, H. M., Wu, X. F., and Liu, Y. (2020). The *In Situ* Stress Field and Microscale Controlling Factors in the Ordos Basin, Central China. *Int. J. Rock Mech. Min.* 135, 104488. doi:10.1016/j.ijrmms.2020.104482

Liu, J., Yang, H., Bai, J., Wu, K., Zhang, G., Liu, Y., et al. (2021). Numerical Simulation to Determine the Fracture Aperture in a Typical Basin of China. *Fuel* 283, 118952. doi:10.1016/j.fuel.2020.118952

Liu, J., Ban, S., Bédard, K., and Giroux, B. (2022a). Characteristics of Precambrian Basement Intruded by Cretaceous Geological Intrusions in Monteregian Igneous Province and Their Impacts on Regional Thermal Structure. *Adv. Geo-Energy Res.* 6 (3), 206–220. doi:10.46690/ager.2022.03.04

Liu, J. S., Yang, H. M., Xu, K., Wang, Z. M., Liu, X. Y., Cui, L. J., et al. (2022b). Genetic Mechanism of Transfer Zones in Rift Basins: Insights from Geomechanical Models. *GSA Bull.* doi:10.1130/b36151.1

Ma, Y. S., Cai, X. Y., and Zhao, P. R. (2018). Chinas Shale Gas Exploration and Development: Understanding and Practice. *Pet. Explor. Dev.* 45 (4), 561–574. doi:10.1016/s1876-3804(18)30065-x

Ma, X., Wang, H., Zhou, S., Shi, Z., and Zhang, L. (2021). Deep Shale Gas in China: Geological Characteristics and Development Strategies. *Energy Rep.* 7, 1903–1914. doi:10.1016/j.egyr.2021.03.043

Mourgues, R., Bureau, D., Bodet, L., Gay, A., and Gressier, J. B. (2012). Formation of Conical Fractures in Sedimentary Basins: Experiments Involving Pore Fluids and Implications for Sandstone Intrusion Mechanisms. *Earth Planet. Sci. Lett.* 313-314, 67–78. doi:10.1016/j.epsl.2011.10.029

Nagarajan, R., Madhavaraju, J., Nagendra, R., Armstrong-Altrin, J. S., and Moutte, J. (2007). Geochemistry of Neoproterozoic Shales of the Rabanpalli Formation, Bhima Basin, Northern Karnataka, Southern India: Implications for Provenance and Paleoredox Conditions. *Rev. Mex. Cienc. Geol.* 24, 150–160.

Nie, H. K., He, Z. L., Liu, G. X., Zhang, G. R., Lu, Z. Y., Li, D. H., et al. (2020). Status and Direction of Shale Gas Exploration and Development in China. *China Univ. Min. Technol.* 49 (1), 13–35. doi:10.13247/j.cnki.jcumt.001096

Qie, L., Shi, Y. N., and Liu, J. G. (2021). Experimental Study on Grouting Diffusion of Gangue Solid Filling Bulk Materials. *J. Min. Strata Control Eng.* 3 (2), 023011. doi:10.13532/j.jmsce.cn10-1638/td.20201111.001

Qiu, Z., Song, D., Zhang, L., Zhang, Q., Zhao, Q., Wang, Y., et al. (2021). The Geochemical and Pore Characteristics of a Typical Marine-Continental Transitional Gas Shale: A Case Study of the Permian Shanxi Formation on the Eastern Margin of the Ordos Basin. *Energy Rep.* 7, 3726–3736. doi:10.1016/j.egyr.2021.06.056

Shan, S. C., Wu, Y. Z., Fu, Y. K., and Zhou, P. H. (2021). Shear Mechanical Properties of Anchored Rock Mass under Impact Load. *J. Min. Strata Control Eng.* 3 (4), 043034. doi:10.13532/j.jmsce.cn10-1638/td.20211014.001

Song, J. F., Lu, C. P., Li, Z. W., Ou, Y. G. C., Cao, X. M., and Zhou, F. L. (2021). Characteristics of Stress Distribution and Microseismic Activity in Rock Parting Occurrence Area. *J. Min. Strata Control Eng.* 3 (4), 043518. doi:10.13532/j.jmsce.cn10-1638/td.20210607.002

Suboyin, A., Rahman, M. M., and Haroun, M. (2020). Hydraulic Fracturing Design Considerations, Water Management Challenges and Insights for Middle Eastern Shale Gas Reservoirs. *Energy Rep.* 6, 745–760. doi:10.1016/j.egyr.2020.03.017

Tang, Y., Li, R., and Wang, S. (2020). Research Progress and Prospects of Coal Petrology and Coal Quality in China. *Int. J. Coal Sci. Technol.* 7 (2), 273–287. doi:10.1007/s40789-020-00322-3

Wang, J., and Wang, X. L. (2021). Seepage Characteristic and Fracture Development of Protected Seam Caused by Mining Protecting Strata. *J. Min. Strata Control Eng.* 3 (3), 033511. doi:10.13532/j.jmsce.cn10-1638/td.20201215.001

Wang, X., Tang, Y., Wang, S., and Schobert, H. H. (2020). Clean Coal Geology in China: Research Advance and its Future. *Int. J. Coal Sci. Technol.* 7 (2), 299–310. doi:10.1007/s40789-020-00321-4

Wang, B., Lu, C. L., Huang, Z. K., and Hu, S. Y. (2021). Experimental Study on Damage Evolution Characteristics of Rock under Triaxial Rheological Disturbance. *J. Min. Strata Control Eng.* 3 (4), 043028. doi:10.13532/j.jmsce.cn10-1638/td.20210525.001

Wang, B., Zhou, F., Zhou, H., Ge, H., and Li, L. (2021). Characteristics of the Fracture Geometry and the Injection Pressure Response during Near-Wellbore Diverting Fracturing. *Energy Rep.* 7, 491–501. doi:10.1016/j.egyr.2020.12.039

Wei, D., Liu, H., and Shi, K. (2019). What Are the Key Barriers for the Further Development of Shale Gas in China? A Grey-DEMATEL Approach. *Energy Rep.* 5, 298–304. doi:10.1016/j.egyr.2019.02.010

Xi, Z., and Tang, S. (2021). Geochemical Characteristics and Organic Matter Accumulation of Late Ordovician Shale in the Upper Yangtze Platform, South China. *Energy Rep.* 7, 667–682. doi:10.1016/j.egyr.2021.01.029

Xi, Y., Jiang, J., Li, J., Li, H., and Gao, D. (2021). Research on the Influence of Strike-Slip Fault Slippage on Production Casing and Control Methods and Engineering Application during Multistage Fracturing in Deep Shale Gas Wells. *Energy Rep.* 7, 2989–2998. doi:10.1016/j.egyr.2021.05.039

Xie, J., Qin, Q., and Fan, C. (2019). Quantitative Prediction of Fracture Distribution of the Longmaxi Formation in the Dingshan Area, China Using FEM Numerical Simulation. *Acta Geol. Sin. - Engl. Ed.* 93 (6), 1662–1672. doi:10.1111/1755-6724.13815

Xie, J. T., Fu, X. P., Qin, Q. R., and Li, H. (2021). Prediction of Fracture Distribution and Evaluation of Shale Gas Preservation Conditions in Longmaxi Formation in Dongxi Area. *Coal Geol. Explor.* 49 (6), 35–45. doi:10.3969/j.issn.1001-1986.2021.06.004

Yin, S., Tian, T., and Wu, Z. (2019). Developmental Characteristics and Distribution Law of Fractures in a Tight Sandstone Reservoir in a Low-Amplitude Tectonic Zone, Eastern Ordos Basin, China. *Geol. J.* 54, 1–16. doi:10.1002/gj.3521

Zhan, H., Yang, Y., Zhang, Y., Miao, X., Zhao, K., and Yue, W. (2021). Terahertz for the Detection of the Oil Bearing Characteristics of Shale. *Energy Rep.* 7, 5162–5167. doi:10.1016/j.egyr.2021.08.109

Zhang, L., Chen, L., Hu, R., and Cai, J. (2022). Subsurface Multiphase Reactive Flow in Geologic CO2 Storage: Key Impact Factors and Characterization Approaches. *Adv. Geo-Energy Res.* 6 (3), 179–180. doi:10.46690/ager.2022.03.01

Check for updates

In Situ Stress Distribution in Cretaceous Ultra-Deep Gas Field From 1D Mechanical Earth Model and 3D Heterogeneous Geomechanical Model, Kuqa Depression, Tarim Basin, NW China

Ke Xu[1]*, Hui Zhang[1], Ruixia Dong[1], Wei Ju[2], Yani Xie[1], Deyu Cui[3], Lu Fang[1], Fang Yuan[1], Shujun Lai[1], Jingrui Liang[1], Wei Zhang[1] and Bin Zhao[1]

[1]*Research Institute of Exploration and Development, Tarim Oilfield Company, PetroChina, Korla, China,* [2]*School of Resources and Geosciences, China University of Mining and Technology, Xuzhou, China,* [3]*Resource Exploration Department, Tarim Oilfield Company, PetroChina, Korla, China*

The Kuqa Depression boasts rich cretaceous ultra-deep hydrocarbon resources. However, it is in complex geological conditions. At present, sufficient understandings on the *in situ* stress distribution and influencing factors are lacking, which restricts the process of hydrocarbon exploitation. Therefore, in this study, the Bozi gas field is selected as an example, and a 1D mechanical earth model (1D MEM) is established with the drilling data and logging data through the geomechanical method to clarify the *in situ* stress distribution of the wellbore. A 3D heterogeneous geomechanical model (3D HGM) is established with the constraint of 1D HEM to clarify the distribution characteristics of the 3D *in situ* stress field in the Bozi gas field and discuss its influencing factors. The results show that: 1) the Bozi gas field is in an extremely strong *in situ* stress condition with high stress values. The minimum horizontal principal stress (S_h) of the cretaceous system is 153~180 MPa, and the maximum horizontal principal stress (S_H) is nearly 200 MPa; 2) the *in situ* stress in the Bozi gas field has obvious vertical stratification characteristics, which can be divided into three stress sequences of "low–high–low", with great differences in interlayer stress; 3) the *in situ* stress distribution of the Bozi gas field is greatly affected by the types of faulted anticline. Different types indicate different stress distribution; 4) within the influence range of overthrusts, the *in situ* stress in the footwall is lower than that of the hanging wall. The greater the fault offset, the greater the *in situ* stress difference between the hanging wall and footwall. Moreover, the lower the stress in the footwall, the higher is the degree of overthrust, and the larger is the range of footwall stress area; and 5) the means of highly deviated wells is more helpful to the Bozi gas field for hydrocarbon exploitation.

Keywords: *in situ* stress, geomechanics, numerical simulation, ultra-deep reservoir, Kuqa depression, Tarim basin

1 INTRODUCTION

At present, with the rapid development of the world economy, shallow resources are gradually exhausted, and the resource development is moving toward deep and ultra-deep layers, which have great exploration potential. The deep and ultra-deep hydrocarbon resources are an important replacement field and have become a research hotspot in the global oil and gas field (Bloch et al., 2002; Dutton and Loucks, 2010; Jia and Pang, 2015; Li et al., 2019). In recent years, important progress has been made in global deep and ultra-deep hydrocarbon exploitation. By the end of 2018, 68 oil and gas reservoirs with a depth of more than 8,000 m had been found worldwide (Li et al., 2020), with the new oil and gas reserves and production showing an obvious growth momentum (Bloch et al., 2002; Hu et al., 2013; Bai and Cao, 2014; Cao et al., 2022).

As for the boundary depth of deep and ultra-deep reservoirs in petroliferous basins, different countries, institutions, and scholars have different understandings (Glasmann, 1992; Girard et al., 2002; Hu et al., 2013; Pang et al., 2015; Hu et al., 2019). Cao et al. (2022) proposed a division by considering burial depth, geothermal gradient, burial history, thermal evolution history, and diagenetic history, which is found in cold basins with low geothermal gradient (<2.5°C/100 m); 4,500 ~ 6,000 m is defined as deep layer and more than 6,000 m is defined as ultra-deep layer; in medium warm basins with a geothermal gradient of 2.5 ~ 3.5°C/100 m, 3,500 ~ 4,500 m is defined as the deep layer, and more than 4500 m is defined as the ultra-deep layer; and in the thermal basin with a high geothermal gradient (>3.5°C/100 m), 3,000 ~ 4,000 m is defined as the deep layer, and more than 4,000 m is defined as the ultra-deep layer.

At present, the deepest large-scale clastic rock oil and gas reservoir found abroad is the Jack/St Malo deep-water turbidite oilfield of Lower Tertiary Trend in the Gulf of Mexico, with a maximum burial depth of 8,839 m, and its oil and gas reserves are 6821×10^4t (oil equivalent) at 7,620 m (25,000 ft) with a water depth of 2,133 m (7,000 ft) of Well Jack-2, and the production is 818 t/d (Meyer et al., 2007; Rains et al., 2007; He et al., 2017).

Currently, the deepest borehole in China is Well Luntan 1 in Tarim Basin (8,882 m in 2019), where high-yield industrial oil and gas flow is obtained in the Cambrian below a burial depth of 8,200 m (Yang et al., 2020). The deepest clastic rock gas field is the Kelasu gas field in Tarim Basin (Yang et al., 2018, 2019; Zeng LB. et al., 2020; Tian et al., 2020). At Well Dabei 4, high-yield natural gas flow is obtained in the year of 2022 at 8,200 m in the cretaceous sandstones.

Theoretically, in such ultra-deep background, the reservoir rocks become extremely dense due to strong diagenetic compaction and cementation. The matrix porosity is generally not more than 10%, and the permeability is even less than 1mD, making it difficult to form an efficient seepage system. However, such ultra-deep reservoirs often develop fractures and are present in strong *in situ* stress environment. The exploration and development practice of many ultra-deep fractured reservoirs shows that the high-quality fractures under the control of *in situ* stress are the optimum point of ultra-deep hydrocarbon exploitation (Zeng et al., 2008; Jiang et al., 2020). Under the control of *in situ* stress field, fractures can increase the reservoir permeability by orders of magnitude (Wang et al., 2018; Zeng QL. et al., 2020; Liu J. et al., 2022), which is an important guarantee for the existence of wells with high and stable production in ultra-deep reservoirs. *In situ* stress greatly influences the quality of ultra-deep reservoir and hydrocarbon production capacity by affecting the fracture activity and hydraulic fracturing effect (Zhang et al., 2018; Xu et al., 2022). Therefore, it is necessary to carry out systematic research on the *in situ* stress in ultra-deep reservoirs, clarifying the orientation and magnitude of *in situ* stress, and finding the main factors affecting its distribution. The results are expected to provide suggestions and supports for well location deployment and optimization fracturing scheme.

This study takes the Bozi gas field in Tarim Basin as an example to study the *in situ* stress. The Bozi gas field is a typical ultra-deep gas field with a burial depth of 6,000 ~ 8,000 m. At present, the existing research of the Bozi gas field mainly focuses on sedimentation, structure, and petroleum geological conditions (Yang et al., 2019; Wang et al., 2022) and understandings on the *in situ* stress distribution characteristics and influencing factors are lacking, which restricts the hydrocarbon exploitation in this area. Therefore, a one-dimensional mechanical earth model (1D MEM) and a three-dimensional heterogeneous geomechanical model (3D HGM) were conducted and analyzed. It plays an important role in better understanding the geomechanical properties and provides references for the efficient development of natural gas.

2 GEOLOGICAL SETTING

2.1 Location

The Kuqa Depression is located in the north of Tarim Basin. It is connected with the South Tianshan fault fold belt by the thrust fault in the north, Tabei Uplift in the south, Yangxia sag in the east, and Wushi sag in the West. It is a superimposed foreland basin dominated by Mesozoic and Cenozoic sedimentation and can be divided into seven secondary structural units (**Figure 1A**). Among them, the Kelasu tectonic belt is a typical deep and ultra-deep natural gas resource enrichment area. From west to east, it can be divided into Awate segment, Bozi segment, Dabei segment, and Keshen–Kela segment. The Kelasu tectonic belt develops four first-order faults from north to south, which are divided into Bozi–Kela fault tectonic belt, Keshen fault tectonic belt, Baicheng fault tectonic belt, and Baicheng South fault tectonic belt. Multiple secondary thrust faults are developed between the faults.

The Bozi gas field is located in the west of Kelasu tectonic belt and is characterized by rows of faulted anticlines. The strike of anticline is generally the same, which is in the NE–SW direction. The northern Bozi gas field is a pop-up structure sandwiched by two thrust faults F1 and F2, and the southern part is a series of imbricate structures, with gradually increasing burial depth (**Figures 1B,C**). From east to west, the overlapping degree of the imbricate structure increases gradually.
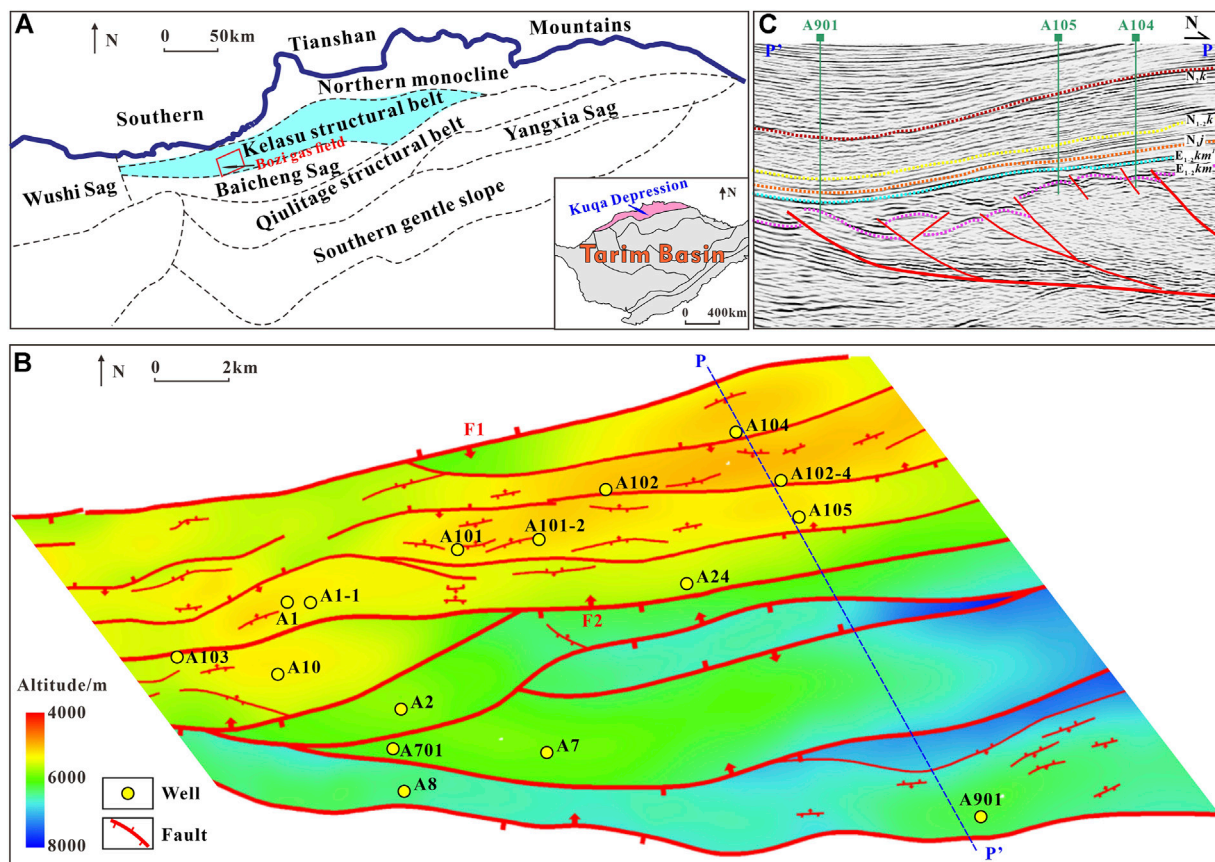
FIGURE 1 | Field location, seismic profile, and top structure of the target layer in the Bozi gas field. **(A)** The Kuqa Depression is the northernmost first level unit in Tarim Basin. The Kuqa depression can be further divided into seven secondary tectonic units. The Kelasu tectonic belt is located in the second-row structure from the north, and the Bozi gas field is located in the west of the Kelasu tectonic belt; **(B)** the Cretaceous top structure map of the Bozi gas field comprises several rows of faulted anticline structures divided by thrust faults. The strike of the anticline structure is basically the same, which is in the NE–SW direction; and **(C)** the typical thrust imbricate structure and pop-up structure of the Bozi gas field can be seen through the seismic section of PP'.

2.2 Stratigraphy

The drilling of the Bozi gas field shows that the drilling strata from the top to bottom are: Quaternary Xiyu Formation (Q_1x), Neogene Kuqa Formation (N_2k), Kangcun Formation ($N_{1-2}k$), Jidike Formation (N_1j), Paleogene Suweiyi Formation ($E_{2-3}s$), Kumugeliemu Group ($E_{1-2}km$), Cretaceous Bashijiqike Formation (K_1bs), and Baxigai Formation (K_1bx). Among them, The $E_{1-2}km$ is a set of gypsolith rock formation with great thickness distribution and plastic flow characteristics. In the process of compression deformation, layered shrinkage deformation occurs, and the strata above this plastic stratum folds, thrusts, and rises sharply, forming a "roof like" structure. Under the control of "roof" structure, salt rock flow results in the characteristics of abovementioned salt Kelasu tectonic belt, salt body, and subsalt differential structural deformation.

The target strata of the study are the Cretaceous K_1bs and K_1bx. The K_1bs can be divided into three lithologic segments. The first lithologic segment is missing due to the influence of paleosedimentary environment. The second lithologic segment mainly comprises medium thick ~ super thick layered brown and grayish brown medium sandstone and fine sandstone, which is deposited at the front of braided river delta. The third lithologic segment mainly comprises medium thick ~ thick layered brown fine sandstone, thin ~ medium thick layered siltstone, and argillaceous siltstone, which are deposited at the front of fan delta. The K_1bx comprises thin medium thick brown mudstone and medium thick layered brownish gray, grayish brown fine sandstone, siltstone, and argillaceous siltstone, which are interbedded in an isopachous-slight isopachous manner and are deposited at the front of braided river delta (**Figure 2**).

2.3 Reservoir

Reservoir pore types in the Bozi gas field are mainly primary intergranular pores, with a small amount of microfractures and micropores. The porosity of Bashijiqike formation mainly ranges between 4% and 10.0%, with an average of 6.30%, and the permeability mainly ranges between 0.1 and 0.5 mD, with an average of 0.256 mD. The porosity of Baxigai formation sandstone ranges between 4 and 9%, with an average porosity of 6.06%, and the permeability mainly ranges between 0.035 and

0.1 mD, with an average permeability of 0.067 mD. The reservoir fractures are relatively developed, mostly being partially filled—unfilled, high angle, and shear fractures. The fracture strike is mainly near E–W, and the fracture density ranges between 0.2/m and 0.4/m.

3 METHODS

3.1 *In Situ* Stress State Interpreted From Wells

At present, there are many methods to measure and test *in situ* stress, including the drill-based borehole collapse method, relaxation strain measurement, stress relief technique, acoustic emission, and differential strain method (Zang and Stephansson, 2010). The Bozi gas field is deep buried and has high bottom hole temperature and high pressure. Hence, the measuring instrument has poor applicability, and there is no constraint of confining pressure after core removal, causing rapid stress relief. In mild cases, it may lead to inaccurate measurement, and in serious cases, it may lead to possible core fracture. Therefore, it is not suitable to use downhole measurement and core testing to obtain the *in situ* stress state.

This article utilizes the drilling and logging data to obtain the *in situ* stress state. Different basins are in different states, and scholars have put forward a variety of *in situ* stress calculation models considering more comprehensive factors. As a result, the accuracy of the calculation has gradually improved, and the applicability has become more extensive. At present, there is little dispute about the calculation of vertical stress (S_v). It is considered that its magnitude is equal to the gravity of the overlying rock mass, which can be obtained by integrating the density curve from the ground to the target depth such as **Eq. 1**:

$$S_V = \int_0^z \rho(z)g\,dz, \tag{1}$$

where g is the gravitational acceleration (m/s^2), $\rho(z)$ is the density as a function of burial depth (kg/m^3), and z is the burial depth (m).

There are many calculation models for obtaining horizontal principal stress magnitudes, including the uniaxial strain model, Mohr–Coulomb failure model, Coulomb–Navier failure model, Huang's model, combined spring model, porous elastic strain model, and biaxial strain model (Li and Zhang, 1997; Liu and Luo, 1999; Rasouli and Sutherland, 2014; Li et al., 2017). In this article, the calculation model is as follows (Li et al., 1997):

$$\begin{cases} S_H = \dfrac{\mu}{1-\mu}\left(S_V - \alpha P_P\right) + \dfrac{E\xi_H}{1-\mu^2} + \dfrac{\mu E\xi_h}{1-\mu^2} + \alpha P_P \\[2mm] S_h = \dfrac{\mu}{1-\mu}\left(S_V - \alpha P_P\right) + \dfrac{E\xi_h}{1-\mu^2} + \dfrac{\mu E\xi_H}{1-\mu^2} + \alpha P_P \end{cases}, \tag{2}$$

where S_H is the maximum horizontal principal stress, MPa; S_h is the minimum horizontal principal stress, MPa; S_V is the vertical principal stress, MPa; P_P is the pore pressure, MPa; μ is Poisson's ratio, dimensionless; E is the modulus of elasticity, GPa; α is the

Biot coefficient, dimensionless; and ξ_H ξ_h are the maximum and minimum principal stress coefficient, respectively, dimensionless.

The method of calculating the mechanical parameters with the logging data is as follow (Lu et al., 2015):

$$E_d = \frac{\rho_b}{\Delta t_s^2} \cdot \frac{3\Delta t_s^2 - 4\Delta t_p^2}{\Delta t_s^2 - \Delta t_p^2}, \tag{3}$$

$$\mu_d = \frac{\Delta t_s^2 - 2\Delta t_p^2}{2\left(\Delta t_s^2 - \Delta t_p^2\right)}, \tag{4}$$

where ρ_b is the rock density, kg/m^3, and Δt_p and Δt_s are the P-wave time difference and S-wave time difference, respectively, μs/ft.

Generally, we may determine S_h at a specific location through the hydraulic fracturing construction data, which can be used as the constraint and scale basis to determine the value of ξ_h. However, the maximum horizontal principal stress (S_H) of ultra-deep wells cannot be determined through hydraulic fracturing (Hickman, 1983; Zoback, 2007). In this article, the S_H is determined with the wellbore fracture information. In the process of drilling, as the borehole is drilled, the borehole wall may produce stress concentration under the action of confining pressure. When the stress concentration exceeds the fracture strength of the rock around the borehole, the borehole wall will collapse (Bell and Gough, 1979; Zoback et al., 2003).

Because wells in different structural locations have different stress distributions (stress concentration and tensile range) around the well in different lithologic sections, and with the increase of radial depth, the stress effect will decrease and the degree of borehole wall collapse will also vary. Therefore, it is a more intuitive method to distinguish the direction of *in situ* stress by analyzing the changes of formation characteristics around the borehole from the scanning images of formation micro resistivity (FMI). The collapse width of the borehole wall can be judged from FMI, and the collapse width has the following mathematical calculation relationship with rock uniaxial compressive strength and *in situ* stress state (Zoback, 2007):

$$S_H = \frac{(C_0 + 2P_p + \Delta p + \sigma^{\Delta T}) - Sh \cdot [1 + 2\cos(\pi - W_{BO})]}{1 - 2\cos(\pi - W_{BO})}, \tag{5}$$

where C_0 is the uniaxial compressive strength, P_P is the pore pressure, Δp is the difference between pore pressure and bottom hole pressure, W_{BO} is the collapse width, and $\sigma^{\Delta T}$ is the thermal stress, which can be ignored generally.

Therefore, the gradient of the maximum horizontal principal stress and the minimum horizontal principal stress can be inverted according to the collapse width W_{BO} and the uniaxial compressive strength (C_0) of the borehole wall collapse position.

3.2 3D Geomechanical Modeling of *In Situ* Stress
3.2.1 Principles of the Finite Element Method

The distribution of *in situ* stress field was predicted using a popular finite element method (Liu et al., 2017a; Liu et al., 2017b; Ju et al., 2021). To begin with, the geological mass was discretized

into several finite units that were connected to each other by nodes. Rock mechanical parameters were assigned to the corresponding units. The primary variables of the field functions for the study area included displacement, stress, and strain. The equation set where the node displacement served as the unknown quantity and the total stiffness matrix as the coefficient was solved based on the boundary stress condition and the node balance condition. The displacement at each node was then obtained. Finally, the stress and strain of each unit were calculated.

Generally, based on elastic mechanics, the relationship between strain and displacement follows **Eq. 6** (Ju et al., 2021):

$$\begin{cases} \varepsilon_{xx} = \dfrac{\partial i}{\partial x}, \ \gamma_{xy} = \gamma_{yx} = \dfrac{\partial i}{\partial y} + \dfrac{\partial j}{\partial x} \\[2mm] \varepsilon_{yy} = \dfrac{\partial j}{\partial y}, \ \gamma_{yz} = \gamma_{zy} = \dfrac{\partial j}{\partial z} + \dfrac{\partial k}{\partial y}, \\[2mm] \varepsilon_{zz} = \dfrac{\partial k}{\partial z}, \ \gamma_{zx} = \gamma_{xz} = \dfrac{\partial k}{\partial x} + \dfrac{\partial i}{\partial z} \end{cases} \tag{6}$$

where ε_{xx}, ε_{yy}, and ε_{zz} are the linear strain components and γ_{xy}, γ_{yz}, and γ_{zx} are the shear strain components.

The matrix form can be derived as follows:

$$[\varepsilon] = [B][\delta], \tag{7}$$

where $[\delta]$ is the nodal displacement matrix and $[B]$ is the geometric matrix.

From the physical equation, stress and strain can be expressed as follows:

$$[\sigma] = [D][\varepsilon], \tag{8}$$

where $[D]$ is the elasticity matrix.

3.2.2 Geological Model and 3D Heterogenous Rock Mechanical Parameters

The Bozi gas field is featured by fault developed and complex fault intersection. This article adopts the volume element based (VBM) structural framework modeling method. The grid established is continuously distributed, but it is discontinuous at the fault. Compared with the traditional corner grid modeling, the established complex structure model is more realistic and has higher accuracy. In order to consider the heterogeneity of rock, the "logging + seismic" combination method is used to establish the 3D heterogeneous rock mechanics field (Xu et al., 2018a; Xu et al., 2018b; Ju et al., 2021).

3.2.3 Boundary Conditions

The surface of the Bozi gas field is relatively flat and mostly covered by vegetation and Gobi. However, due to the complex lithology, the shallow Kuqa and Kangcun Formations gravel layer and the plastic Kumugeliemu group gypsolith rock have a certain impact on the distribution of *in situ* stress in the target layer. Therefore, when establishing the model, this article considers the surface fluctuation morphology and different rock mechanical properties of the surrounding rock, rather than just treat the rock body above the target layer as a homogeneous cube. As shown in **Figure 3**, an outer frame is established outside the Bozi gas field model as the surrounding rock. The surrounding rock is divided into five layers, representing loose rock on the surface, shallow gravel, mudstone layer, gypsum salt rock, and Cretaceous rock layer, which are given by the rock mechanical parameters of different lithology, respectively. The rock mechanical parameters of each layer are obtained according to the mechanical test of field samples in Kuqa Depression and corrected according to the vertical stress calculated by density logging of the target layer (Xu et al., 2020). The target layer model is assigned with 3D heterogeneous rock mechanical parameters, among which the elastic modulus mostly ranges between 20 and 30 GPa, locally as high as 40 GPa; the Poisson's ratio is mainly concentrated in 0.24 ~ 0.27; and the value of rock density in 3D space is mainly between 2.3 and 2.6 g/cm3 (**Figure 3**). Using the distance scanning method (that is, calculate the distance between a unit and its surrounding rock mechanical parameters one by one and select the rock mechanical parameters with the smallest distance to load on the unit), this article assigns the heterogeneous rock mechanical parameters in the constructed 3D rock mechanical field to each finite element grid of the target layer model.

With the *in situ* stress state of seven wells in the Bozi gas field as the constraints, the iterative optimization process is carried out for the stress boundary loading to optimize and determine the reasonable boundary conditions. Through repeated attempts, the following boundary conditions are finally determined (**Figure 3**): a compression magnitude of 210 MPa is applied in the N–S direction and 163 MPa is applied in the E–W direction of the model.

4 RESULTS

4.1 1D Mechanical Earth Model

In this article, a 1D mechanical earth modeling has been carried out in the Bozi gas field. **Figure 4** shows the 1D MEM result along the well section of A2–A101-2–A102-4–A105, which indicates the distribution and changes of Cretaceous geomechanical parameters in one dimension of the wellbore.

Taking Well A2 as an example, Young's modulus is 20 ~ 30 GPa, the average uniaxial compressive strength is approximately 100 MPa, and Poisson's ratio changes little, at 0.25 ~ 0.30. The minimum horizontal, maximum horizontal, and vertical principal stress gradients are 2.11 ~ 2.18 MPa/100 m, 2.55 ~ 2.72 MPa/100 m, and 2.45 MPa/100 m, respectively, which are in strike–slip stress regime ($S_H > S_V > S_h$). For a better comparison, the S_h is filled with colors, with warm color representing low value and cold color for high value. It can be seen that the *in situ* stress shows obvious stratification vertically. The stress in the upper part of K_1bs_2 and K_1bs_3, that is, 7456 ~ 7555 m is low, and the S_h magnitude is approximately 165 MPa. The stress in the lower part of K_1bs_3, the upper part of K_1bx_1 and K_1bx_2, that is, 7555 ~ 7700 m is high, and the S_h magnitude is approximately 175 MPa, and local areas can reach 180 MPa. The stress in the lower part of

Formation	Description	Formation	Depth/m	Lithology
Q_1x	Medium thick-thick layered fine conglomerate and glutenite, locally intercalated with thin layered mudstone and siltstone	K_1bs_2	7200 – 7240	
N_2k	Medium thick-thick layered fine conglomerate, locally intercalated with thin-medium thick layered mudstone and argillaceous siltstone			
$N_{1-2}k$	The middle and upper part is dominated by extremely thick layered sandy conglomerate, intercalated with medium thick layered siltstone and mudstone; The bottom is dominated by medium thick layered sandy conglomerate, intercalated with thin-medium thick layered siltstone and mudstone	K_1bs_3	7240 – 7315	
N_j	The upper part is mainly medium thick-thick layered pebbly fine sandstone, and the middle part is brown mudstone mixed with thin layer pebbly fine sandstone and siltstone; The lower part is dominated by mudstone. From the upper part to the lower part, the particle size gradually becomes finer and the mudstone gradually develops			
$E_{2-3}s$	The upper part is mainly medium thick layered mudstone, the lower part is mainly medium thick - thick layered mudstone, intercalated with thin-medium thick layered gypsum mudstone, and the bottom is intercalated with argillaceous siltstone			
$E_{1-2}km$	Medium thick layered mudstone, gypsum containing mudstone and gypsum mudstone are mainly mixed with thin layers of argillaceous gypsum rock, gypsum siltstone and argillaceous siltstone in the middle, and thin to medium thick layered gypsum mudstone, argillaceous gypsum rock and gypsum fine sandstone	K_1bx_1	7315 – 7385	
K_1bs	The first setion is missing; The second section: medium thick ~ super thick layered fine sandstone, argillaceous fine sandstone, medium sandstone and gravelly sandstone, locally intercalated with thin and medium thick layered mudstone. The third section: medium thick thick layered fine sandstone and medium sandstone, followed by siltstone, intercalated with thin ~ medium thick layered mudstone and silty mudstone. There are more mudstone Intercalations in this section than in the second lithologic section			
K_1bx	The first section: the upper thin ~ medium thick layered mudstone is interbedded with fine sandstone and siltstone, and the lower lithology is mainly thin ~ medium thick layered mudstone and silty mudstone, mixed with fine sandstone. The second section: fine sandstone, fine sandstone with mud gravel, mudstone and silty mudstone are interbedded with unequal thickness.	K_1bx_2	7385 – 7435	
K_1s	Mainly medium thick layered mudstone		7435 – 7440	

FIGURE 2 | Stratigraphic histogram and lithology description in the Bozi gas field.

K_1bx_2 decreases, and the S_h magnitude is approximately 170 MPa. This shows the distribution characteristics of "low–high–low".

The *in situ* stress of single wells in the Bozi gas field has certain similar characteristics. The stress has the distribution characteristics of "low–high–low " in the Cretaceous system. That is, the stress in the upper part of K_1bs_2 and K_1bs_3 is low, the stress in the lower part of K_1bs_3, and the upper part of K_1bx_1 and K_1bx_2 is high, and the stress in the lower part of K_1bx_2 is
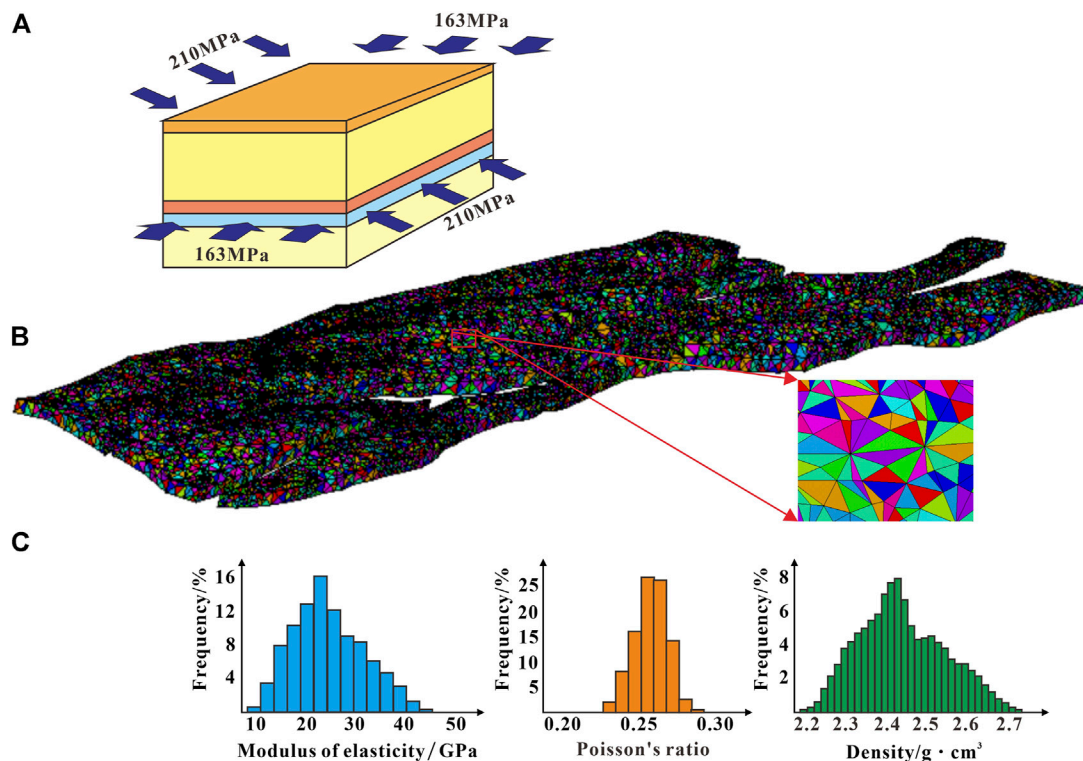
FIGURE 3 | (A) Outer frame established outside the Bozi gas field model as the surrounding rock. The surrounding rock is divided into five layers. A compression magnitude of 210 MPa is applied in the N–S direction and 163 MPa is applied in the E–W direction of the model; **(B)** Target layer model is assigned with 3D heterogeneous rock mechanical parameters, and the heterogeneous rock mechanical parameters are assigned to each grid of the finite element model. Each triangular grid represents a material, including an array comprising elastic modulus, Poisson's ratio, density, and other parameters. Different colors represent different numbers of materials, and the grid color does not represent the distribution of rock mechanical parameters; **(C)** Distribution histogram of rock mechanical parameters.

reduced. In addition, compared with the Baxigai Formation, the stress characteristics of Bashijiqike Formation are lower, and stress difference between the layers is relatively small. The interlaminar stress difference in the Baxigai Formation is large, resulting in a stronger interlaminar property.

4.2 3D Stress Distribution

The 3D distribution of the *in situ* stress in the Cretaceous layes of Bozi gas field is shown in **Figure 5**. The distributions of three principal stresses are similar, showing a trend of low in the north and high in the south. The S_h is mainly $153 \sim 180$ MPa, and S_H is $180 \sim 200$ Pa, and S_V is $175 \sim 200$ MPa, which is a strike slip stress state. There are great differences in stress distribution among the different fault blocks. The S_h in A104 and A102 fault blocks is $153 \sim 160$ MPa and the S_H is approximately $180 \sim 188$ MPa, while the S_h in A8 and A9 fault blocks is as high as 175 MPa and the S_H even exceeds 200 MPa.

Figure 6 shows the *in situ* stress distribution of five typical sections in the Bozi gas field. It can be seen that the *in situ* stress distribution is evidently related to the tectonic form. Each fault block in the Bozi gas field is basically a fault anticline structure, and different structural styles vary in terms of stress distribution. **Figure 7** summarizes the structural style of the fault anticline in the Bozi gas field and the corresponding *in situ* stress distribution mode. The structural style of the fault anticline is divided into five

categories: north steep and south gentle type (A8 and A10), north gentle and south steep type (A7), symmetrical imbricate type (A104), complete pop-up structure (A7), and semi complete pop-up structure (A1). Generally, the *in situ* stress distribution of symmetrical imbricate faulted anticline and pop-up structure is regular and symmetrical. The stress is low at the top of the anticline and high at the wings. In north steep and south gentle type, the stress is high in the north wing and low in the south wing. In the north gentle and south steep type, the stress in low in the north wing and high in the south wing.

5 DISCUSSION

5.1 Error Analysis

The *in situ* stress prediction results of seven wells in different fault blocks of the Bozi gas field are compared with the logging calculation results (**Table 1**). The calculation method of error (r) is as follows:

$$r = S_c - S_m, \qquad (9)$$

where S_m is the *in situ* stress value actually calculated, MPa and S_c is the *in situ* stress predicted by numerical simulation, MPa. It can
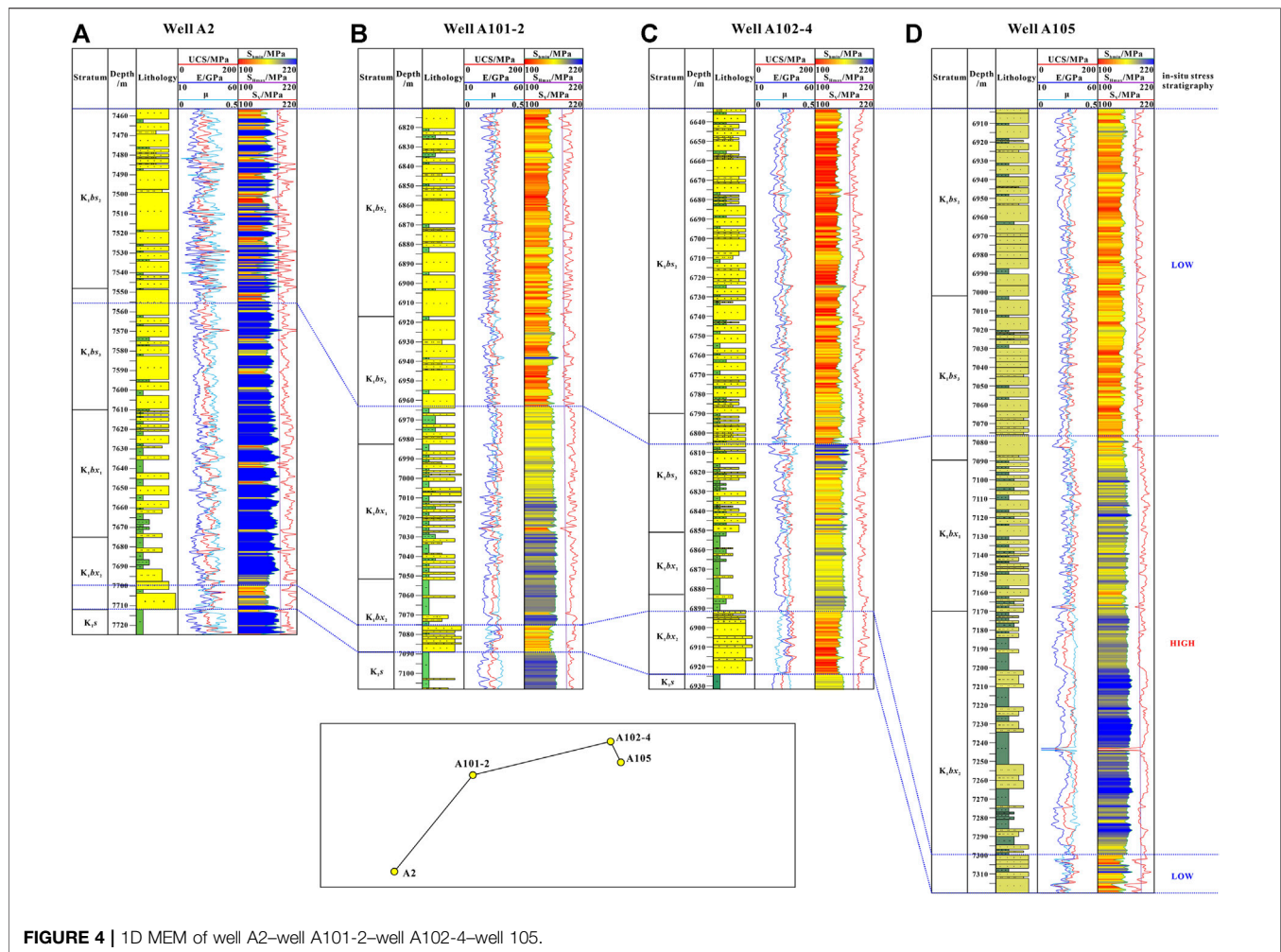
FIGURE 4 | 1D MEM of well A2–well A101-2–well A102-4–well 105.

be seen that the average error of the S_H value is 6.5 MPa, and the average error of the S_h value is 6.3 MPa. Both the errors are within 10%, indicating that the *in situ* stress simulation results have high reliability.

5.2 Influence of Thrust Imbricate Structure on *in situ* Stress

The *in situ* stress distribution of the thrust imbricate structure is complex, especially the disturbance effect of the fault on the *in situ* stress (Meyer et al., 2007; Rasouli and Sutherland, 2014). In this study, the *in situ* stress shows a special distribution feature in the thrust imbricate structure (**Figure 6**). In the area around a fault, the *in situ* stress in the footwall is lower than that of the hanging wall, even if the footwall is buried deeper. Moreover, the greater the fault offset, the greater is the stress difference between the hanging wall and footwall, that is, the *in situ* stress value within the control range of the footwall is lower. According to the statistics of stress values from the hanging wall and the footwall of 20 faults (**Figure 8**), when the fault offset is less than 50 m, the stress difference is less than 5 MPa, and while it exceeds 500 m, the stress difference exceeds 15MPa, and there is a good

correlation between the fault distance and stress difference between the hanging wall and footwall. In addition, the footwall of the overthrust generally shows low stress value. The higher the degree of overthrust, the larger is the range of low stress area of the footwall.

5.3 Support for Well Location

Previous studies (Liu et al., 2004; Li et al., 2012; Liu JS. et al., 2022) indicate that the wellbore trajectory is the most stable along the direction of the S_H under the strike–slip stress regime. The practice of Tarim Oilfield also confirms that under the ultra-deep strike–slip stress regime, highly deviated wells have fewer complex drilling accidents and shorter drilling cycle compared with the vertical wells (Xu et al., 2020; Cai et al., 2022). Therefore, in the Bozi gas field, highly deviated wells or horizontal wells have better wellbore stability.

The *in situ* stress field in the Bozi gas field is heterogeneous, and the *in situ* stress distributes in the belt horizontally and stratified vertically. The directional wells (inclined or horizontal wells) are more likely to drill in favorable low-stress zones than the vertical wells, and the directional trajectory or sidetrack
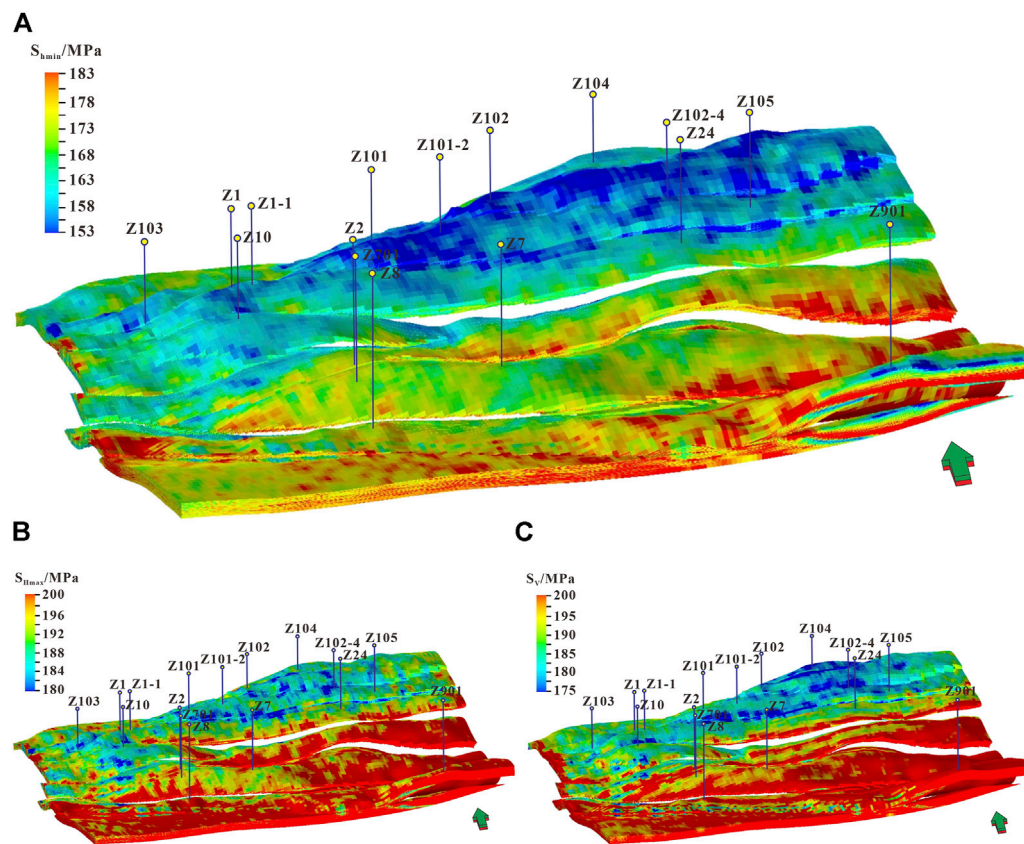
FIGURE 5 | 3D heterogenous *in situ* stress field in the Bozi gas field. **(A)** S_h; **(B)** S_H; and **(C)** S_v.
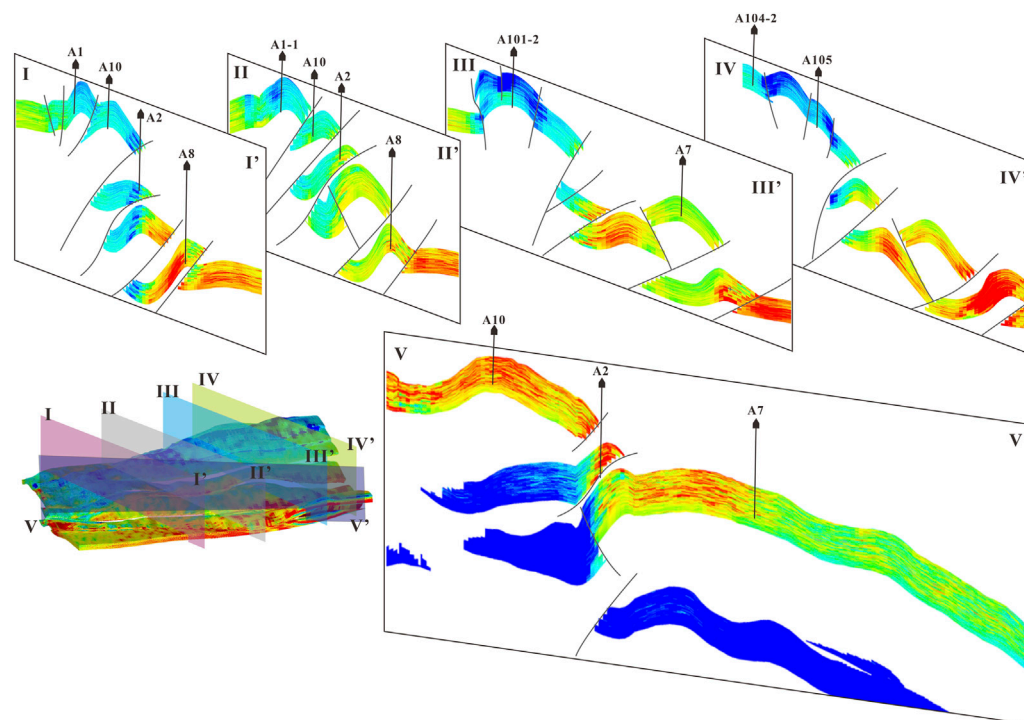
FIGURE 6 | *In situ* stress distribution in a typical section of the Bozi gas field.
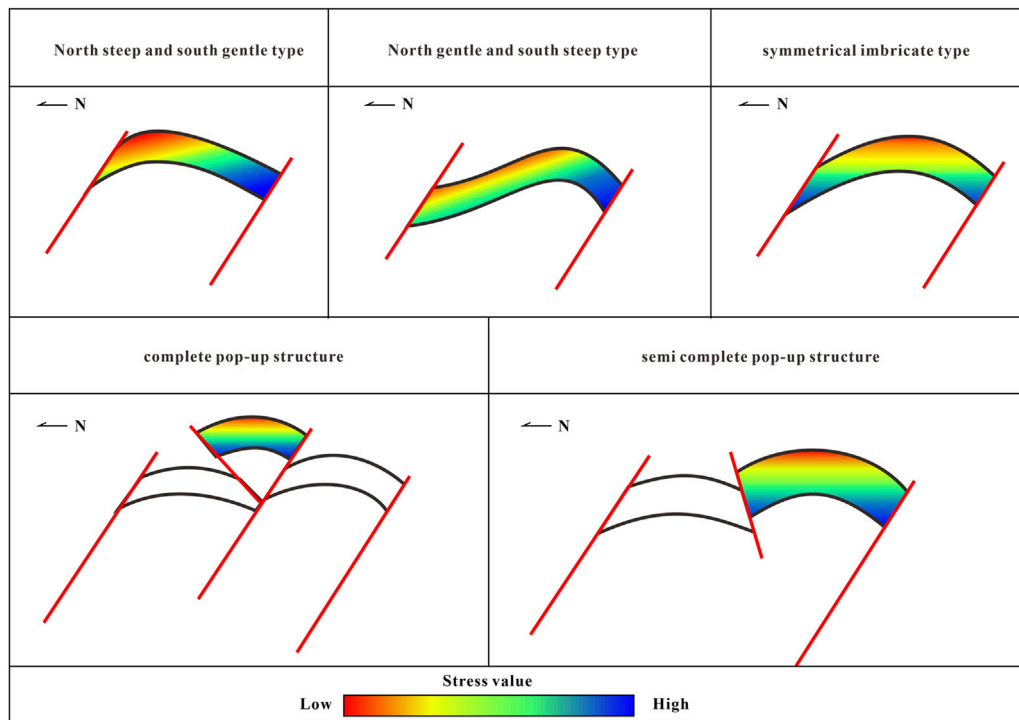
FIGURE 7 | Structural style and corresponding *in situ* stress distribution mode.

TABLE 1 | Analysis of numerical simulation results of *in situ* stress.

Well	Depth (m)	S_H			S_h		
		Measured (MPa)	Predicted (MPa)	Error (MPa)	Measured (MPa)	Predicted (MPa)	Error (MPa)
A1	7043	184.8	193.6	8.8	157.5	150.2	−7.3
A101	6998	179.3	190.5	11.2	148.3	148.8	0.5
A102	6832	175.5	176.8	1.3	143.2	148.7	5.5
A104	6774	179.4	171.2	−8.2	144.1	136.7	−7.4
A2	7500	202.1	191.4	−10.7	158.0	170.5	12.5
A8	8125	202.2	200.0	−2.2	174.4	176.2	1.8
A901	7800	202.8	200.0	−2.8	169.0	178.4	9.4
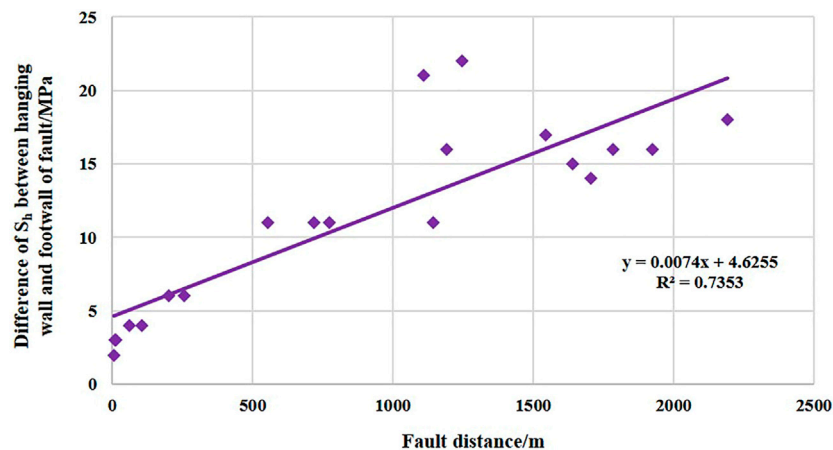
FIGURE 8 | Relationship between thrust fault distance and the difference of minimum horizontal principal stress between the hanging wall and footwall.

drilling may be adjusted during the drilling based on *in situ* stress field.

Due to the high degree of overthrust in the Bozi gas field and the favorable low-stress area is often in the footwall, the vertical well method cannot meet the drilling conditions, while the directional well method can avoid the obstacles of nontarget layer and drill into the favorable area of target layer. The existing practice in Tarim Oilfield also proves that the production of directional wells is higher than that of the vertical wells. Therefore, it is considered that the highly deviated wells are more suitable for hydrocarbon exploitation in the Bozi gas field.

6 CONCLUSION

1) The Bozi reservoir is in extremely strong *in situ* stress environment, which is featured by high *in situ* stress and horizontal minimum principal stress (S_h) of the Cretaceous reservoir ranging between 153 and 180 MPa, and horizontal maximum principal stress generally exceeds 200 MPa. It is dominant by the strike–slip stress regime.

2) The *in situ* stress of the Bozi gas field has obvious stratification characteristics vertically, and it can be divided into three stress sequences of "low–high–low". The upper part of K_1bs_2 and K_1bs_3 is a low-stress segment, the lower part of K_1bs_3, K_1bx_1, and K_1bx_2 are high-stress segments, and the lower part of K_1bx_2 is a low-stress segment, resulting in great difference in interlayer stress.

3) The *in situ* stress distribution of the Bozi gas field is greatly affected by the structural style of the fault anticline. The symmetrical imbricate faulted anticline and pop-up structure show regular and symmetrical *in situ* stress distribution, with low stress at the top of anticline and high stress at the wings. The stress is low at the top of anticline and high at the wings. In the north steep and south gentle type, the stress is high in the north wing and low in the south wing. In the north gentle and south steep type, the stress is low in the north wing and high in the south wing.

4) The overthrust structure has an obvious influence on the *in situ* stress distribution. In the area around a fault, *in situ* stress in the footwall is lower than that of the hanging wall. The greater the fault offset, the greater is the stress difference between the hanging wall and footwall. The footwall of the overthrust generally shows low stress value. The higher the degree of overthrust, the larger is the range of low stress area of footwall.

5) In the Bozi gas field, under the strike–slip stress regime, the directional wells have multiple advantages such as safety and stability, crossing more favorable parts and avoiding nontarget formation obstacles. The highly deviated wells are more suitable for the Bozi gas field to carry out hydrocarbon exploitation.

DATA AVAILABILITY STATEMENT

The original contributions presented in the study are included in the article/Supplementary Material. Further inquiries can be directed to the corresponding author.

AUTHOR CONTRIBUTIONS

KX, Conceptualization, Investigation, Writing—Original Draft; HZ, Supervision, Methodology, Validation; RD, Software, Visualization; WJ, Formal Analysis; YX, Data Curation; DC, Writing—revised manuscript; LF, Formal Analysis; FY, Formal Analysis; SL, Software; JL, Software; WZ, Software; BZ, Software.

FUNDING

REFERENCES

Anderson, E. M. (1951). *The Dynamics of Faulting and Dyke Formation with Applications to Britain*. second ed. Edinburgh: Oliver, 206.

Bai, G. P., and Cao, B. F. (2014). Characteristics and Distribution Patterns of Deep Petroleum Accumulations in the World. *Oil Gas Geol.* 35 (1), 19–25. doi:10.11743/ogg20140103

Bell, J. S., and Gough, D. I. (1979). Northeast-southwest Compressive Stress in Alberta Evidence from Oil Wells. *Earth Planet. Sci. Lett.* 45, 475–482. doi:10.1016/0012-821X(79)90146-8

Bloch, S., Lander, R. H., and Bonnell, L. (2002). Anomalously High Porosity and Permeability in Deeply Buried Sandstone Reservoirs: Origin and Predictability. *AAPG Bull.* 86 (2), 301–328. doi:10.1306/61eedabc-173e-11d7-8645000102c1865d

Cai, Z. Z., Xu, K., Zhang, H., Wang, Z. M., Yin, G. Q., and Liu, X. Y. (2022). ROP Improvement and Production Enhancement for Ultra‐Deep Wells Based on Geology‐Engineering Integration: A Case in Kuqa Depression, Tarim Basin. *Xinjiang Pet. Geol.* 43 (2), 206–213. doi:10.7657/XJPG20220212

Cao, Y. C., Yuan, G. H., Yang, H. J., Wang, Y. Z., Liu, K. Y., Zan, N. M., et al. (2022). Current Situation of Oil and Gas Exploration and Research Progress of the Origin of High-Quality Reservoirs in Deep-Ultra-Deep Clastic Reservoirs of Petroliferous Basins. *Acta Pet. Sin.* 43 (1), 112–140. doi:10.7623/syxb202201010

Dutton, S. P., and Loucks, R. G. (2010). Diagenetic Controls on Evolution of Porosity and Permeability in Lower Tertiary Wilcox Sandstones from Shallow to Ultradeep (200-6700m) Burial, Gulf of Mexico Basin, U.S.A. *Mar. Petroleum Geol.* 27 (1), 69–81. doi:10.1016/j.marpetgeo.2009.08.008

Girard, J.-P., Munz, I. A., Johansen, H., Lacharpagne, J.-C., and Sommer, F. (2002). Diagenesis of the Hild Brent Sandstones, Northern North Sea: Isotopic Evidence for the Prevailing Influence of Deep Basinal Water. *J. Sediment. Res.* 72 (6), 746–759. doi:10.1306/040102720746

Glasmann, J. R. (1992). The Fate of Feldspar in Brent Group Reservoirs, North Sea: A Regional Synthesis of Diagenesis in Shallow, Intermediate, and Deep Burial Environments. *Geol. Soc. Lond. Spec. Publ.* 61 (1), 329–350. doi:10.1144/GSL.SP.1992.061.01.17

He, Z. L., Zhang, J. T., Ding, Q., You, D. H., Peng, S. T., Zhu, D. Y., et al. (2017). Factors Controlling the Formation of High-Quality Deep to Ultra-deep

Carbonate Reservoirs. *Oil Gas Geol.* 38 (4), 633–644. doi:10.11743/ogg20170401

Hickman, S. H. (1983). "The Interpretation of Hydraulic Fracturing Pressure-Time Data for In-Situ Stress Determination," in *Proc. Of Workshop on Hydraulic Fracturing Stress Measurements*. Editors D.C. Washington and B.C. Zoback (Monterey: National Academy Press).

Hu, S. B., Long, Z. L., Zhu, J. Z., Hu, D., Huang, Y. P., Shi, Y. L., et al. (2019). Characteristics of Geothermal Field and the Tectonic-Thermal Evolution in Pearl River Mouth Basin. *Acta Pet. Sin.* 40 (S1), 178–187. doi:10.7623/syxb2019S1015

Hu, W., Bao, J., and Hu, B. (2013). Trend and Progress in Global Oil and Gas Exploration. *Petroleum Explor. Dev.* 40 (4), 439–443. doi:10.1016/s1876-3804(13)60055-5

Jia, C. Z., and Pang, X. Q. (2015). Research Processes and Main Development Directions of Deep Hydrocarbon Geological Theories. *Acta Pet. Sin.* 36 (12), 1457–1469. doi:10.7623/syxb201512001

Jia, C. Z., Zheng, M., and Zhang, Y. F. (2012). Unconventional Hydrocarbon Resources in China and the Prospect of Exploration and Development. *Petroleum Explor. Dev.* 39 (2), 129–136. doi:10.1016/s1876-3804(12)60026-3

Jiang, T. W., Zhang, H., Xu, K., Wang, Z. M., and Wang, H. Y. (2020). Reservoir Geomechanical Characteristics and the Influence on Development in Keshen Gas Field. *J. Southwest Petroleum Univ. (Science&Technology Ed.* 42 (04), 1–12. doi: 10.11885j.issn.1674-5086.2020.04.09.01

Ju, W., Shen, J., Qin, Y., Wang, G., Xu, K., Li, G., et al. (2021). Stress Distribution in the Upper Shihezi Formation from 1D Mechanical Earth Model and 3D Heterogeneous Geomechanical Model, Linxing Region, Eastern Ordos Basin, Central China. *Acta Geol. Sin. - Engl. Ed.* 95 (03), 976–987. doi:10.1111/1755-6724.14411

Li, C. L., Zhu, S. Y., Wang, F. L., Du, Q. L., You, C. M., Zhu, L. H., et al. (2017). Some Topics about Reservoir Sensitivity Evaluation. *Xinjiang Pet. Geol.* 38, 488–491. doi:10.7657/XJPG20170419

Li, J., She, Y. Q., Gao, Y., Yang, G. R., Li, M. P., and Yang, S. (2019). Onshore Deep and Ultra-deep Natural Gas Exploration Fields and Potentials in China. *China Pet. Explor.* 24 (04), 403–417. doi:10.3969/j.issn.1672-7703.2019.04.001

Li, Y., Xue, Z. J., Cheng, Z., Jiang, H. J., and Wang, R. Y. (2020). Progress and Development Directions of Deep Oil and Gas Exploration and Development in China. *China Pet. Explor.* 25 (1), 45–57. doi:10.3969/j.issn.1672-7703.2020.01.005

Li, Y. F., Fu, Y. Q., Tang, G., She, C. Y., and Zhang, J. Y. (2012). Laws of the Effects of Earth Stress Patterns on Wellbore Stability in a Directional Well. *Nat. Gas. Ind.* 32 (3), 78–80. doi:10.3787/j.issn.1000-0976.2012.03.018

Li, Z. M., and Zhang, J. Z. (1997). *In-situ Stress and Exploration and Development of Oil and Gas.* Beijing: Petroleum Industry Press.

Liu, J., Ding, W., Wang, R., Yin, S., Yang, H., and Gu, Y. (2017a). Simulation of Paleotectonic Stress Fields and Quantitative Prediction of Multi-Period Fractures in Shale Reservoirs: A Case Study of the Niutitang Formation in the Lower Cambrian in the Cen'gong Block, South China. *Mar. Petroleum Geol.* 84, 289–310. doi:10.1016/j.marpetgeo.2017.04.004

Liu, J., Ding, W., Yang, H., Wang, R., Yin, S., Li, A., et al. (2017b). 3D Geomechanical Modeling and Numerical Simulation of In-Situ Stress Fields in Shale Reservoirs: A Case Study of the Lower Cambrian Niutitang Formation in the Cen'gong Block, South China. *Tectonophysics* 712-713, 663–683. doi:10.1016/j.tecto.2017.06.030

Liu, J. S., Mei, L. F., Ding, W. L., Xu, K., Yang, H. M., and Liu, Y. (2022b). Asymmetric Propagation Mechanism of Hydraulic Fracture Networks in Continental Reservoirs. *GSA Bull.* doi:10.1130/B36358.1

Liu, J., Yang, H., Xu, K., Wang, Z., Liu, X., Cui, L., et al. (2022a). Genetic Mechanism of Transfer Zones in Rift Basins: Insights from Geomechanical Models. *GSA Bull.* doi:10.1130/B36151.1

Liu, X. J., Luo, P. Y., and Meng, Y. F. (2004). Influence of Ground Stress Field on Borehole Trajectory Design and Well-Face Stability. *Nat. Gas. Ind.* (9), 57–59+8.

Liu, X. J., and Luo, P. Y. (1999). *Oil Logging and Wellbore Stability.* Beijing: Petroleum Industry Press.

Lu, S. K., Wang, D., Li, Y. K., Meng, X. J., Hu, X. Y., and Chen, S. W. (2015). Research on Three-Dimensional Mechanical Parameters' Distribution of the Tight Sandstone Reservoirs in Daniudi Gasfield. *Nat. Gas. Geosci.* 26, 1844–1850. doi:10.11764/j.issn.1672-1926.2015.10.1844

Meyer, D., Zarra, L., and Yun, J. (2007). From BAHA to Jack, Evolution of the Lower Tertiary Wilcox Trend in the Deepwater Gulf of Mexico. *Sed. Rec.* 5 (3), 4–9. doi:10.2110/sedred.2007.3.4

Pang, X.-Q., Jia, C.-Z., and Wang, W.-Y. (2015). Petroleum Geology Features and Research Developments of Hydrocarbon Accumulation in Deep Petroliferous Basins. *Pet. Sci.* 12 (1), 1–53. doi:10.1007/s12182-015-0014-0

Rains, D. B., Zarra, L., and Meyer, D. (2007). The Lower Tertiary Wilcox Trend in the Deepwater Gulf of Mexico. *Houst. Geol. Soc. Bull.* 50 (2), 24.

Rasouli, V., and Sutherland, A. (2014). Geomechanical Characteristics of Gas Shales: A Case Study in the North Perth Basin. *Rock Mech. Rock Eng.* 47, 2031–2046. doi:10.1007/s00603-013-0531-3

Tian, J., Yang, H. J., Wu, C., Mo, T., Zhu, W. H., and Shi, L. L. (2020). Discovery of Well Bozi 9 and Ultra-deep Natural Gas Exploration Potential in the Kelasu Tectonic Zone of the Tarim Basin. *Nat. Gas. Ind.* 40 (01), 11–19. doi:10.3787/j.issn.1000-0976.2020.01.002

Wang, K., Yang, H. J., Zhang, H. L., Li, Y., Zhang, R. H., Yang, X. J., et al. (2018). Characteristics and Effectiveness of Structural Fractures in Ultra-deep Tight Sandstone Reservoir: A Case Study of Keshen-8 Gas Pool in Kuqa Depression, Tarim Basin. *Oil Gas Geol.* 39 (4), 719–729. doi:10.11743/ogg20180409

Wang, K., Zhang, R. H., Zeng, Q. H., Wang, J. P., Xia, J. F., and Mo, T. (2022). Characteristics and Formation Mechanism of Lower Cretaceous Deep and Ultra-deep Reservoir in Bozi-Dabei Area, Kuqa Depression. *J. China Univ. Min. Technol.* 51 (02), 311–328. doi:10.13247/j.cnki.jcumt.001337

Xu, K., Dai, J. S., Feng, J. W., Shang, L., and Ren, Q. Q. (2018a). Prediction of 3D Heterogeneous In-Situ Stress Field of Northern Area in Gaoshen, Nanpu Sag, Bohai Bay Basin, China. *J. China Univ. Min. Technol.* 47 (6), 1276–1286. doi:10.13247/j.cnki.jcumt.000869

Xu, K., Dai, J. S., Shang, L., Feng, J. W., and Fang, L. (2018b). Prediction of Current In Situ Stress Field and its Application of Southern Area of Deep Reservoir in Gaoshangpu Oilfield. *J. China Univ. Petroleum(Edition Nat. Sci.* 42 (6), 19–29. doi:10.3969/j.issn.1673-5005.2018.06.003

Xu, K., Tian, J., Yang, H. J., Zhang, H., Ju, W., Liu, X. Y., et al. (2022). Effects and Practical Applications of Present-Day In-Situ Stress on Reservoir Quality in Ultra-deep Layers of Kuqa Depression,Tarim Basin. *Nat. Gas. Geosci.* 33 (1), 13–23. doi:10.11764/j.issn.1672-1926.2020.09.002

Xu, K., Tian, J., Yang, H. J., Zhang, H., Wang, Z. M., Yuan, F., et al. (2020). Prediction of Current In Situ Stress Field and its Application of Deeply Buried Tight Reservoir, a Case Study of Keshen 10 Gas Reservoir in Kelasu Structural Belt, Tarim Basin. *J. China Univ. Min. Technol.* 49 (4), 708–720. doi:10.13247/j.cnki.jcumt.001134

Yang, H. J., Chen, Y. Q., Tian, J., Du, J. H., Zhu, Y. F., Li, H. H., et al. (2020). Great Discovery and its Significance of Ultra-deep Oil and Gas Exploration in Well Luntan-1 of the Tarim Basin. *China Pet. Explor.* 25 (02), 62–72. doi:10.3969/j.issn.1672-7703.2020.02.007

Yang, H. J., Li, Y., Tang, Y. G., Lei, G. L., Zhou, L., and Zhou, P. (2019). Discovery of Kelasu Subsalt Deep Large Gas Field, Tarim Basin. *Xinjiang Pet. Geol.* 40 (01), 12–20.

Yang, H. J., Zhang, R. H., Yang, X. Z., Wang, K., Wang, J. P., Tang, Y. G., et al. (2018). Characteristics and Reservoir Improvement Effect of Structural Fracture in Ultra-deep Tight Sandstone Reservoir: A Case Study of Keshen Gasfield,Kuqa Depression, Tarim Basin. *Nat. Gas. Geosci.* 29 (7), 942–950. doi:10.11764/j.issn.1672-1926.2018.06.018

Zang, A., and Stephansson, O. (2010). *Stress Field of the Earth's Crust.* Netherlands: Springer Netherlands.

Zeng, L. B., Lyu, P., Qu, X. F., and Fan, J. M. (2020a). Multi-scale Fractures in Tight Sandstone Reservoirs with Low Permeability and Geological Conditions of Their Development. *Oil Gas Geol.* 41 (3), 449–454. doi:10.11743/ogg20200301

Zeng, L. B., Qi, J. F., Wang, C. G., and Li, Y. L. (2008). The Influence of Tectonic Stress on Fracture Formation and Fluid Flow. *Earth Sci. Front.* 15 (3), 292–298.

Zeng, Q. L., Mo, T., Zhao, J. L., Tang, Y. L., Zhang, R. H., Xia, J. F., et al. (2020b). Characteristics,genetic Mechanism and Oil and Gas Exploration Significance of High-Quality Sandstone Reservoirs Deeper Than 7 000 M: a Case Study of the Bashijiqike Formation of Lower Cretaceous in the Kuqa Depression. *Nat. Gas. Ind.* 40 (1), 38–47. doi:10.3787/j.issn.1000-0976.2020.01.005

Zhang, H., Yin, G. Q., and Wang, H. Y. (2018). Effects of Natural Fractures Geomechanical Response on Gas Well Productivity in Kuqa Depression, Tarim Basin. *Nat. Gas. Geosci.* 30 (3), 379–388. doi:10.11764/j.issn.1672-1926.2018.10.020

Zoback, M. D. (2007). *Reservoir Geomechanics*. Cambridge: Cambridge University Press, 206–265.

Zoback, M. D., Barton, C. A., Brudy, M., Castillo, D. A., Finkbeiner, T., Grollimund, B. R., et al. (2003). Determination of Stress Orientation and Magnitude in Deep Wells. *Int. J. Rock Mech. Min. Sci.* 40 (7-8), 1049–1076. doi:10.1016/j.ijrmms.2003.07.001

Check for updates

Proactive stress interference mechanism and its application in the Mahu oil area, Junggar basin

Shuo Wang[1]*, Xiaoshan Li[1], Lihua Hao[2], Xiaogong Zhang[1], Lifeng Zhang[1], Junqiang Song[1], Rongjun Liu[1], Hong Pan[1], Kaifang Gu[1], Ting Li[1], Guanxing Luo[1], Xin Wang[1] and Shihong Li[1]

[1]Research Institute of Exploration and Development, PetroChina Xinjiang Oilfield, Karamay, XJ, China, [2]Research Institute of Engineering Technology, PetroChina Xinjiang Oilfield, Karamay, XJ, China

There exists a large horizontal principal stress difference (11−38 MPa) in the tight conglomerates in the Mahu oil area, China. It is difficult to form a complex fracture network *via* hydraulic fracturing under these conditions. To improve reservoir stimulation, the fracture formation mechanism of the complex conglomerate fracture networks was explored. Based on the geomechanics theory of fracture formation, the mechanism of the "stress wall" formed by fracturing in horizontal wells was analyzed in this paper. The inhibitory effect of the stress wall on the formation of tensile and shear fractures was studied. The reason for the decrease in the stress difference coefficient caused by fracturing fluid was analyzed through numerical simulation, which suggested that the complexity of a fracturing network is mainly controlled by the interference of externally applied stress and the reduction in the coefficient of internal stress difference. In this paper, innovative technologies were developed by proactively introducing stress interference in the application of the Ma131 small-well-spacing pilot area. The core technologies include optimization of the 3-D staggered small-well-spacing pattern, and synergetic optimization of multiple elements and zipper fracturing. The positive effects of proactive stress interference on improving fracturing volume, reserve utilization rate and recovery were discussed. Based on the concept of proactive stress interference, the "serial fracturing mode" of horizontal wells was proposed to reduce drilling and fracturing interference and improve the development effect.

KEYWORDS

Mahu tight conglomerate, stress wall, proactive stress interference, complex fracture network, sequence of fracturing
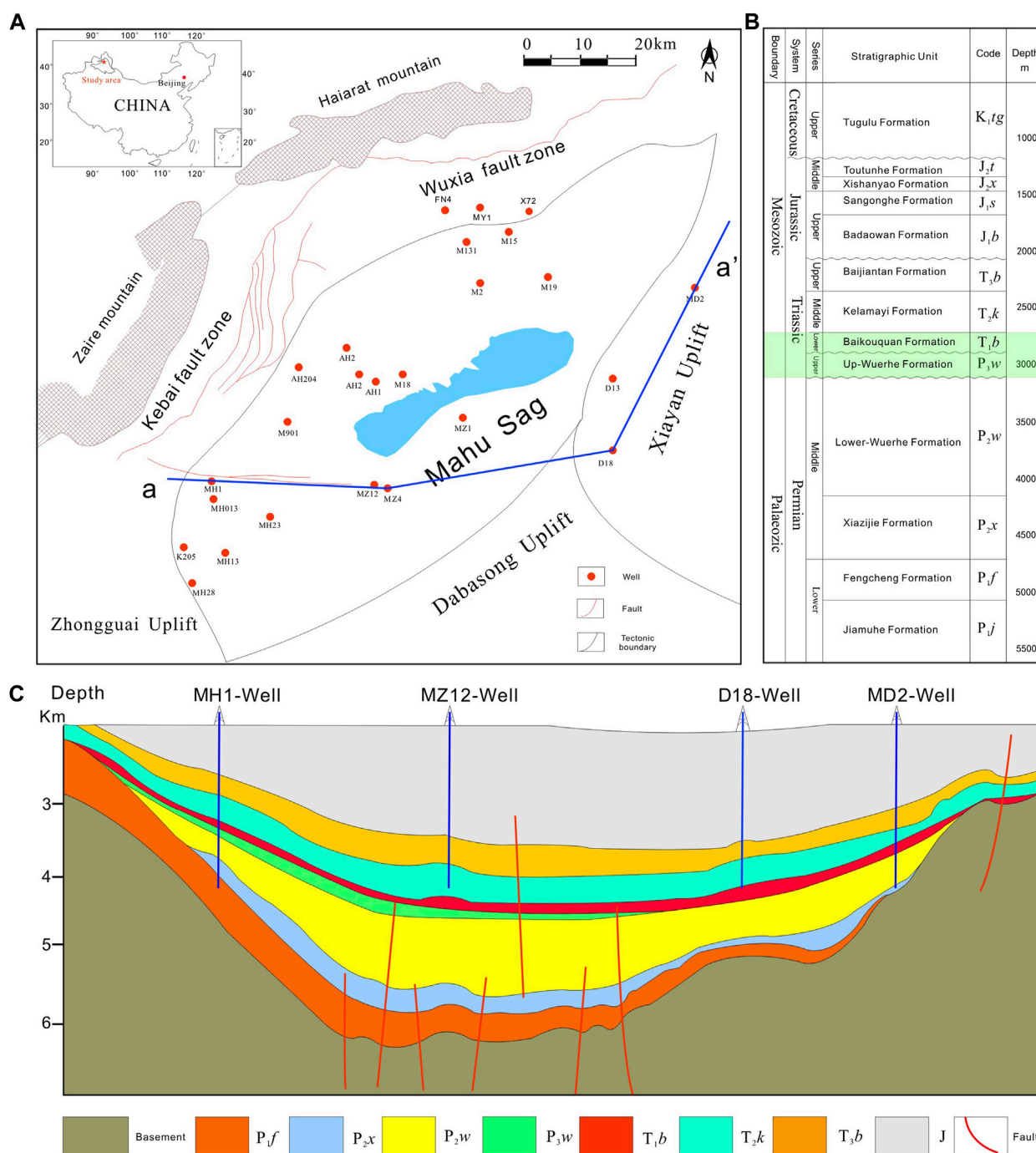
FIGURE 1
(A) Location of the Mahu; **(B)** stratigraphic column of the study area; **(C)** cross-section through the Mahu sag.

1 Introduction

An extremely large integrated conglomerate reservoir with reserves up to a billion tons has been discovered in the Mahu Sag, Junggar Basin, western China (Cao et al., 2015; Feng et al., 2020;

Zhang et al., 2020). Ten oil-bearing series have been found longitudinally. The main oil-bearing strata are the Baikouquan Formation and the overlying Wuerhe Formation (Figure 1). After 8 years of continuous development since the exploration breakthrough of the M131 well in 2012, the main

development model of horizontal well fracturing was established, which improves the efficiency of oil and gas exploration and development in the Mahu area (Jia et al., 2016; Li et al., 2018; Huang et al., 2019).

Due to unique sedimentary and accumulation conditions, The Mahu tight conglomerate has a unique lithology. This deposition is significantly different from the widespread deposition in North American. Its efficient development has the following difficulties. First, due to the strong heterogeneity of the reservoir, the sweet spot was difficult to identify. The conglomerate has a multimodal structure, which is similar to concrete with a large difference in particle size and composition. With the sudden lateral changes in the reservoir and relatively dispersed vertical stacking of the hydrocarbon-rich layers, the superior sweet spot is difficult to target. Second, the reservoir has relatively poor quality, the horizontal well output decreases rapidly, and it is difficult to maintain stable production. The reservoir has a porosity of (7.6%–11.8%). The permeability under overburden pressure is (0.02–0.45) $\times 10^{-3}$ μm (Cao et al., 2015). The reservoir has a low abundance of (22.3–47.1) $\times 10^4$ m^3/km^2. A horizontal well targeting this reservoir has a risk of low primary recovery and production. Third, it is difficult to form a complex fracture network due to the large horizontal principal stress difference and lack of natural fractures. The horizontal principal stress difference of the Mahu tight conglomerate is 11–38.2 MPa. Based on the experience of unconventional oil and gas development in North America and the research results of commercial simulators, hydraulic fractures have the characteristic of long bilateral wings under a large principal stress difference (Adachi et al., 2007; Jin and Roy, 2017; Lecampion et al., 2018; Gao and Ghassemi, 2020a). Fourth, the reservoir is deeply buried, the conglomerate has poor drillability, and the drilling cycle is too long, which leads to a high investment required to drill a single horizontal well and increases the difficulty of economic development under the scenario of a low oil price. The unique geological conditions bring great challenges to the efficient development of the tight conglomerate reservoir in Mahu. Due to the limited ability of fluids to percolate through tight conglomerates, the concept of "fracture-controlled development" has gradually formed. The contact area between the fracture surface and the matrix can be expanded by the method of large-scale pumping and high-density fracturing. The difference in percolation pressure will decrease, and the distance of fracturing fluid percolation will be shortened, which can increase the estimated ultimate recovery (EUR) of a horizontal well. In addition, optimizing the fracturing sequence between wells and using the local high-stress field formed by the earlier fracturing of wells to proactively interfere with the fractures stimulated by subsequently completed hydraulic fracturing wells aims at enhancing the complexity of the fracture network, which is an effective method to enhance the production of horizontal wells. The process does not need to increase the cost of drilling and

completion and is easy to implement, so it is a significant development strategy to improve economic efficiency. This technique has gradually been considered more seriously by reservoir engineers.

At present, a large number of studies and field tests have been carried out to improve the complexity of fracture networks by using stress interference (Jin and Roy, 2017). In the 1980s, researchers found that earlier formed hydraulic fractures can increase the stress of subsequent fractures, and that the geometry of the hydraulic fractures and the elastic effect of the pores can affect the growth of nearby hydraulic fractures (Adachi et al., 2007; Pan et al., 2014; Lecampion et al., 2018; Gao and Ghassemi, 2020a). Bunger et al. (2011) further verified this phenomenon in their research of Barnet shale gas in 2010 and defined it as a stress shadow (Zhou et al., 2017; Ju et al., 2020; Wang et al., 2022; Bunger et al., 2011). With the innovation and progress of hydraulic fracturing methods, the stress shadow effect can be used to improve the effect of reservoir stimulation through zipper fracturing or simultaneous fracturing methods. However, the technique is mainly applied to clusters of parallel fractures in adjacent wells. With the transformation of the development mode from conventional single-layer sequential fracturing to three-dimensional development, the interference value of stress should be further explored and fully applied to platforms or wells to improve the effect of reservoir stimulation.

To solve the problem that a complex fracture network is difficult to form under a large horizontal stress difference in the Mahu tight conglomerate reservoir, the geomechanics mechanism of proactive stress interference between wells and its application in a pilot area with a small well spacing are expounded, and the characterization method of increasing complexity of the fracture network is analyzed. Second, based on proactive stress interference, the serial fracturing mode of horizontal wells is proposed to reduce drilling and fracturing interference and improve the development effect.

2 Mechanism of proactive stress interference

Due to the unique characteristics of the tight conglomerate reservoir and a lack of development experience, the advanced development theories applied in North America cannot be fully applied to the Mahu Oilfield. In the early stage of the development of the Mahu tight conglomerate reservoir, a series of tests were carried out, such as advanced water injection tests in vertical wells, depletion development tests in vertical wells, water injection tests in vertical wells, conventional development tests in horizontal wells and stereo development tests with a small well spacing. Our exploration of efficient development technologies has led to the following summary of the related theories on the mechanical mechanism of the formation of a complex fracture network.

Based on the development process of horizontal wells and the practice of small well spacing in the Mahu Oilfield, Guoxin Li (Li et al., 2020) innovatively proposed the "steered-by-edge" fracturing mechanism (SBEFM) and the "proactive fracturing interference" mechanism (PFIM). However, the theory of PFIM is not further discussed. Based on previous studies, the concept of a stress wall (or "pressure wall") is innovatively proposed in this paper. The mechanical mechanism of the formation of a complex fracture network by proactive stress interference is expounded in detail, and the proactive stress interference theory is enriched and developed.

2.1 Proactive stress interference

Laboratory experiments on tight conglomerate cores show that the difference in horizontal stress has an essential effect on the propagation of hydraulic fractures (Meng et al., 2013; Zhang et al., 2018; Zhao et al., 2018). Due to the large horizontal stress difference of the tight conglomerate in the Mahu Oilfield, it is difficult to form a complex hydraulic fracture network with the conventional fracturing method there. The fracturing scale of the Mahu tight conglomerate horizontal well is very large. The initial formation pressure and *in-situ* stress are increased by injecting a large amount of fracturing fluid into the formation. In this paper, we define the stress wall as the reservoir pressure, which is higher than the initial formation pressure after fracturing. Affected by the stress wall of the fracturing well, it is difficult for the fracturing fluid in the hydraulic fractures of adjacent wells to penetrate the high-pressure area, which leads to the resistance of the fracture propagation. The backflow of fracturing fluid results in increasing pressure, which reduces the effective stress, and promotes the Mohr stress circle to move toward the failure envelope and enter the shear failure state, causing hydraulic fracture diversion. The method of promoting the diversion of hydraulic fractures by setting up a stress wall between horizontal wells is called proactive stress interference.

2.2 Geo-mechanical mechanism of proactive stress interference

Hydraulic fracture propagation is a very complex process that is affected by the heterogeneity of rocks and the uncertainty of *in-situ* stress. In addition, complex physical processes are involved. The conglomerate has a multimodal structure, which consists of gravel, matrix, and planes of weakness are also present. Hydraulic fractures have complex propagation mechanisms, such as SBEFM, conglomerate-piercing mechanism, and conglomerate-ending mechanism. The classical theory of two-dimensional fracture propagation cannot meet the requirement of hydraulic fracturing of tight conglomerate reservoirs. The mechanism of fracture propagation needs to be further studied to provide theoretical guidance for the design of complex fracture networks.

2.2.1 The relationship between pore pressure and *in-situ* stress

In the process of oilfield development, the pore pressure of the formation decreases due to production. The fractures will asymmetrically propagate in the direction of the adjacent older wells. This phenomenon is widely observed in unconventional reservoirs during hydraulic fracturing. The change in pore pressure during hydraulic fracturing is regarded as the inverse of that during production.

During hydraulic fracturing, the pore pressure of the rock increases because a large amount of fluid is injected into the formation, which changes the state of the *in-situ* stress (Thiercelin and Plumb, 1994; Yi et al., 2018). It is assumed that the mechanical parameters (Young's modulus E, Poisson' ratio μ) and structural stress coefficients (ε_h, ε_H) remain constant during fracturing ($0 < \mu < 0.5$), and that the maximum and minimum horizontal principal stresses increase with increasing pore pressure, which is the mechanical basis for the formation of a stress wall (Liu et al., 2017; Liu et al., 2021; Liu et al., 2022a; Liu et al., 2022b)

$$\begin{cases} \sigma_H = \dfrac{\mu}{1-\mu}\sigma_V + \dfrac{E}{1-\mu^2}\varepsilon_H + \dfrac{\mu E}{1-\mu^2}\varepsilon_h + \dfrac{1-2\mu}{1-\mu}\alpha P_p \\[2mm] \sigma_h = \dfrac{\mu}{1-\mu}\sigma_V + \dfrac{E}{1-\mu^2}\varepsilon_h + \dfrac{\mu E}{1-\mu^2}\varepsilon_H + \dfrac{1-2\mu}{1-\mu}\alpha P_p \\[2mm] \sigma_V = \rho_0 g H_0 + \displaystyle\int_{H_0}^{H} \rho g \, dh \end{cases} \quad (1)$$

In these equations, σ_v is the stress of the overlying strata; σ_H and σ_h are the maximum and minimum horizontal principal stresses, respectively; μ and E are Poisson's ratio and Young's modulus, respectively; P_P is the pore pressure; α is the Biot coefficient; ρ_0 and ρ are the average formation density determined without density logging and the formation density from density logging, respectively; and H_0 and H are the starting and reference depths of density logging, respectively.

The pore pressure plays an important role in forming tensile and shear fractures during hydraulic fracturing. We discuss the mechanism of the stress wall, which inhibits fracture propagation and promotes fracture diversion, in detail.

2.2.2 Inhibition mechanism of tensile fracture

A tensile fracture in rock is formed when the normal stress acting on the fracture surfaces and the tensile strength of the rock are overcome (Tong and Yin, 2011; Sone and Zoback, 2013; Tong et al., 2014; Tong et al., 2021). During the fracturing process, the pore pressure at the fracture tip is increased by pumping fracturing fluid into the formation. When the pore pressure at the fracture tip is greater than the sum of the normal stress on the fracture and the tensile strength of the rock, tensile fractures form in the rock. Due to the high pore pressure formed at the end of the secondary fractures generated around the earlier fractured horizontal wells, the fracture has to overcome the additional pore
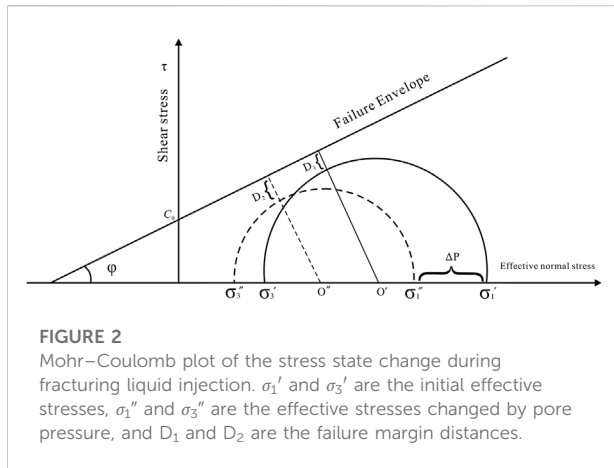
FIGURE 2
Mohr–Coulomb plot of the stress state change during fracturing liquid injection. σ_1' and σ_3' are the initial effective stresses, σ_1'' and σ_3'' are the effective stresses changed by pore pressure, and D_1 and D_2 are the failure margin distances.

pressure difference during the propagation process. The maximum tensile stress criterion is used as the basis for judging the tensile fracture of rock, and the tensile fracture factor σ_T is introduced, whose expression is as follows:

$$\sigma_T = P - \Delta P - \sigma_h - T_0, \tag{2}$$

where P is the pressure transmitted by the fracturing fluid to the fracture surface; ΔP is the difference between the pore pressure outside the fracture and the original formation pressure inside the fracture; and T_0 is the tensile strength of the rock.

In essence, whether the fracture can expand is determined by a comparison of $P - \Delta P$ and $\sigma_h + T_0$: ① when $P - \Delta P > \sigma_h + T_0$, fracture extension occurs, and ② when $P - \Delta P \leq \sigma_h + T_0$, the fracture is in the critical or inhibited state of propagation. As the secondary fracture expands in the direction of the rock where the stress wall has been formed in the earlier stage of hydraulic fracturing, ΔP gradually increases, and $P - \Delta P$ gradually decreases, resulting in a weaker ability to overcome the normal stress at the fracture and the tensile strength of the rock. Therefore, the tensile extension of the artificially formed fractures to the zone with high pore pressure is inhibited.

2.2.3 Inhibition mechanism of shear fracture

Porous elastic theory is used to predict the stress changes with reservoir depletion (Zoback, 2007). In isotropic, linear elastic, and porous media, the change in horizontal stress relative to pore pressure may be written as:

$$\chi = \alpha \frac{1 - 2\mu}{1 - \mu} = \frac{\Delta S_{Hor}}{\Delta P_P}, \tag{3}$$

where χ is the theoretical change in horizontal stress with depletion, generally in the range of 0.5–0.7.

In this paper, the classical Mohr–Coulomb criterion is used to describe rock failure, expressed as: (Hubbert and Rubey, 1959)

$$\tau = \sigma \tan(\varphi) + c, \tag{4}$$

where ϕ is the friction angle, and c is the cohesion of the rock.

To better understand the effect of pore pressure on shear fracture, the Mohr stress circle is introduced (Figure 2). The vertical and horizontal principal stresses are defined as σ_1, σ_2, and σ_3. According to the core experimental results of *in-situ* stress, the true stress state in the Mahu Oilfield is $\sigma_3 < \sigma_2 < \sigma_1$.

Assuming that the formation pore pressure changes by ΔP during hydraulic fracturing, the gravity of the overlying rock is constant. The new maximum effective stress is given as:

$$\sigma''_1 = \sigma'_1 - \Delta P. \tag{5}$$

The new minimum effective stress is given as:

$$\sigma_3'' = \sigma_3' - \Delta P + \chi \Delta P. \tag{6}$$

Before and after the change in pore pressure, the distance between the Mohr–Coulomb circle and the failure envelope is given as:

$$D_1 = \frac{1}{2}\sin\varphi\left(\sigma'_1 + \sigma'_3\right) - \frac{1}{2}\left(\sigma'_1 - \sigma'_3\right) + C_0 \cos\varphi, \tag{7}$$

$$D_2 = \frac{1}{2}\sin\varphi\left(\sigma''_1 + \sigma''_3\right) - \frac{1}{2}\left(\sigma''_1 - \sigma''_3\right) + C_0 \cos\varphi. \tag{8}$$

Combining Eqs 5–8, the difference between the two failure margin distances is given as:

$$D_1 - D_2 = \Delta P\left(\sin\varphi\left(1 - \frac{\chi}{2}\right) - \frac{\chi}{2}\right). \tag{9}$$

According to Eqs 3, 9, to calculate the difference between D_1 and D_2, the Poisson's ratio, internal frictional angle, and Biot coefficient of the rock in the Mahu Oilfield need to be determined. Therefore, three cores from the Ma131 oilfield are selected to carry out the triaxial rock mechanical experiment. The samples are machined into a cylindrical shape with a diameter of 25 mm and a height of 50 mm. The average Young's modulus of the conglomerate in the Ma131 oilfield is 27.0 GPa, the average Poisson's ratio is 0.18, and the average internal frictional angle is 31.5° (Table 1).

According to the conglomerate test results (Table 2), the Biot coefficient is 0.89, and the increasing coefficient χ is 0.69. The difference between the two failure margin distances is calculated as $-0.0066\Delta P$, which is consistent with the literature published by Dohmen (Dohmen et al., 2014; Wang et al., 2019), Norbeck and Horne (Norbeck and Horne, 2016).

3 Results and discussion

3.1 Formation mechanism of a complex fracture network by proactive stress interference

3.1.1 External factor: Proactive stress interference

Under the effects of diagenesis, hydrocarbon expulsion and the mechanical property differences between the gravel and matrix, a large number of gravel margin fractures are

TABLE 1 Triaxial mechanical experimental data of Ma131.

Well	Depth/m	Confining pressure/MPa	Compressive strength/MPa	Young's modulu/GPa	Poisson's ratio	Cohesion/MPa	Internal frictional angle(°)
X723	2,670–2,742	10	103.6	20.1	0.18	22.2	30.1
		20	140.0	24.1	0.18		
		30	164.1	26.0	0.18		
Ma139	3,262–3,310	10	123.4	24.2	0.16	27.9	30.1
		20	163.0	25.5	0.19		
		30	186.6	26.2	0.17		
Ma154	3,003–3,061	10	153.4	27.6	0.14	31.8	34.5
		20	193.1	28.0	0.15		
		30	243.1	28.9	0.19		
Average	2,670–3,310	10	126.8	23.9	0.16	27.3	31.5
		20	165.4	25.8	0.17		
		30	198.0	27.0	0.18		

TABLE 2 Published geomechanical data and Ma131 oilfield data related to the failure margin coefficient (Dohmen et al., 2017).

Reference	Increasing coefficient χ	Cohesion (°)	Failure margin coefficient
Dohmen (2014)	0.62	26.56	$-0.0016\Delta P$
Norbeck and Horne (2016)	0.49	16.70	$-0.026\Delta P$
Ma131 oilfield	0.69	31.5	$-0.0066\Delta P$
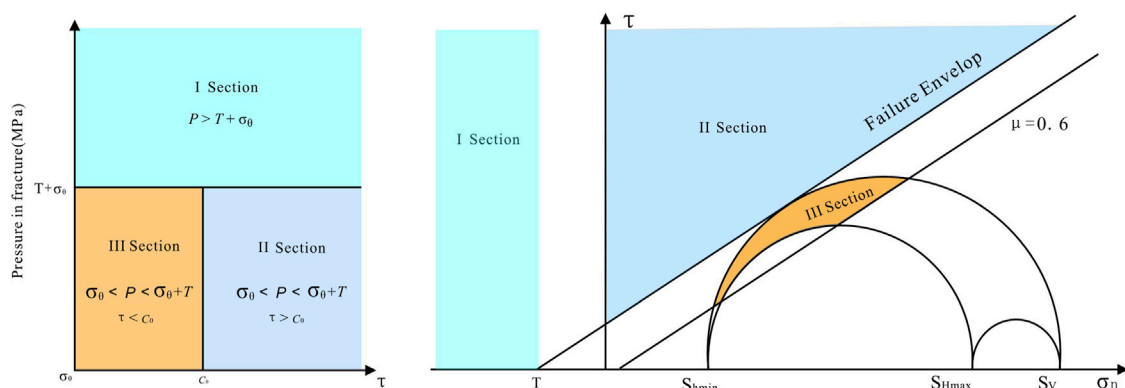
FIGURE 3
The stress mechanism controlling the formation of multiple types of fractures in tight conglomerates.

observed in the microscopic thin sections of this conglomerate rock.

Influenced by the natural weak surface of the conglomerate, three types of fractures are mainly developed in the process of artificial fracture propagation: extensional fractures, shear fractures, and gravel margin fractures. According to the relationship between the fluid pressure, the *in-situ* stress, and the tensile strength of the rock, the stress mechanism controlling
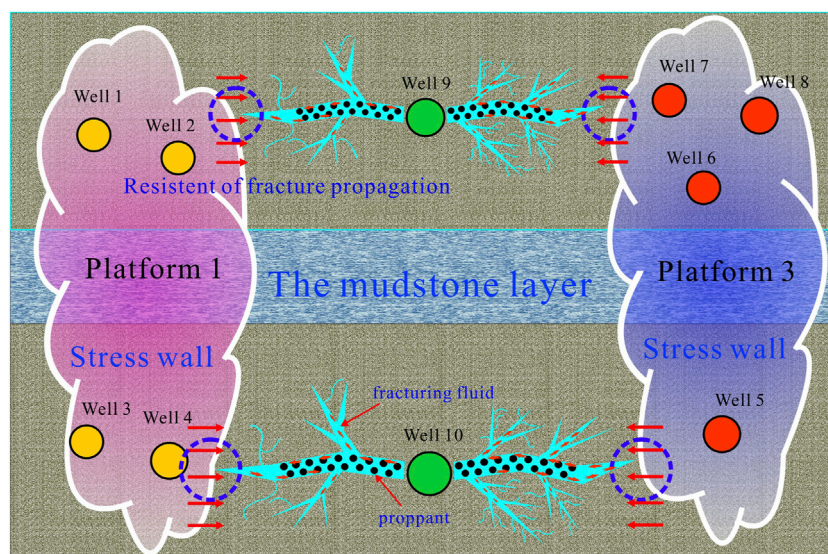
FIGURE 4
Diagram of the formation mechanism of proactive stress interference in a complex fracture network.

the formation of fractures with different properties is established, and the corresponding stress chart is formulated (Figure 3). ① If the fluid pressure is greater than the sum of the normal stress and the tensile strength of the rock surface, a tensile fracture will form. ② If the fluid pressure is smaller than the sum of the normal stress and the tensile strength of the rock surface, and the shear stress is greater than the rock cohesion, a tensile fracture will be form.③ If the fluid pressure is smaller than the sum of the normal stress and the tensile strength of the rock surface, and the shear stress is smaller than the rock cohesion, a gravel margin fracture will be form.

According to the research above, the stress wall can inhibit the propagation of tensile and shear fractures during hydraulic fracturing. During hydraulic fracturing, the pore pressure in the fracture is increased, and the effective stress on the fracture surface is reduced. At this time, the interior of the fracture during fracturing is an open space that will not be affected by the elastic effect of the pore; however, when the effective stress decreases, the Mohr stress circle shifts to the left and enters the shear state, promoting the formation of a large number of shear fractures around the main fracture. In the process of the branched fractures extending forward, as the energy decreases but does not decrease enough to form new shear fractures, the fractures will propagate along gravel edges, forming gravel margin fractures (Figure 4).

Through proactive stress interference, the propagation of tensile fractures is inhibited, and shear fractures and gravel margin fractures are promoted. Finally, high-density fracture networks are formed, including tensile fractures, shear fractures, and gravel margin fractures.

3.1.2 Internal factor: Stress difference coefficient

To form complex fractures, unique *in-situ* stress conditions need to be satisfied. The lower the degree of the *in-situ* stress anisotropy is, the higher the complexity of the hydraulic fractures. The influence of the *in-situ* stress on the fracture is quantitatively evaluated by the horizontal stress difference coefficient (Eq. 10). It is difficult to form complex branched fractures under a large horizontal stress difference coefficient. Compared with those in homogeneous reservoirs, the hydraulic fracture propagation paths in this conglomerate reservoir are more tortuous, and the hydraulic fracture morphology is more complex. According to the test results of the conglomerate cores, if the coefficient of the horizontal stress difference is larger than 0.2, the hydraulic fracture morphology tends to be simple; if the coefficient of the horizontal stress difference is less than 0.2, it is difficult to form complex fracture networks (Figure 5A).

$$K_h = \frac{S_H - S_h}{S_h}, \tag{10}$$

where K_h is the horizontal stress difference coefficient, S_H is the maximum principal stress and S_h is the minimum principal stress.

$$K'_h = \frac{(S_H + S'_H) - (S_h + S'_h)}{S_h + S'_h} = \frac{\Delta\sigma - \Delta\sigma'}{S_h + S'_h} < K_H. \tag{11}$$

If the pore pressure increases during the fracturing process, the original horizontal principal stress changes due to the interference of induced stress, and the horizontal stress difference coefficient gradually decreases (Eq. 11).
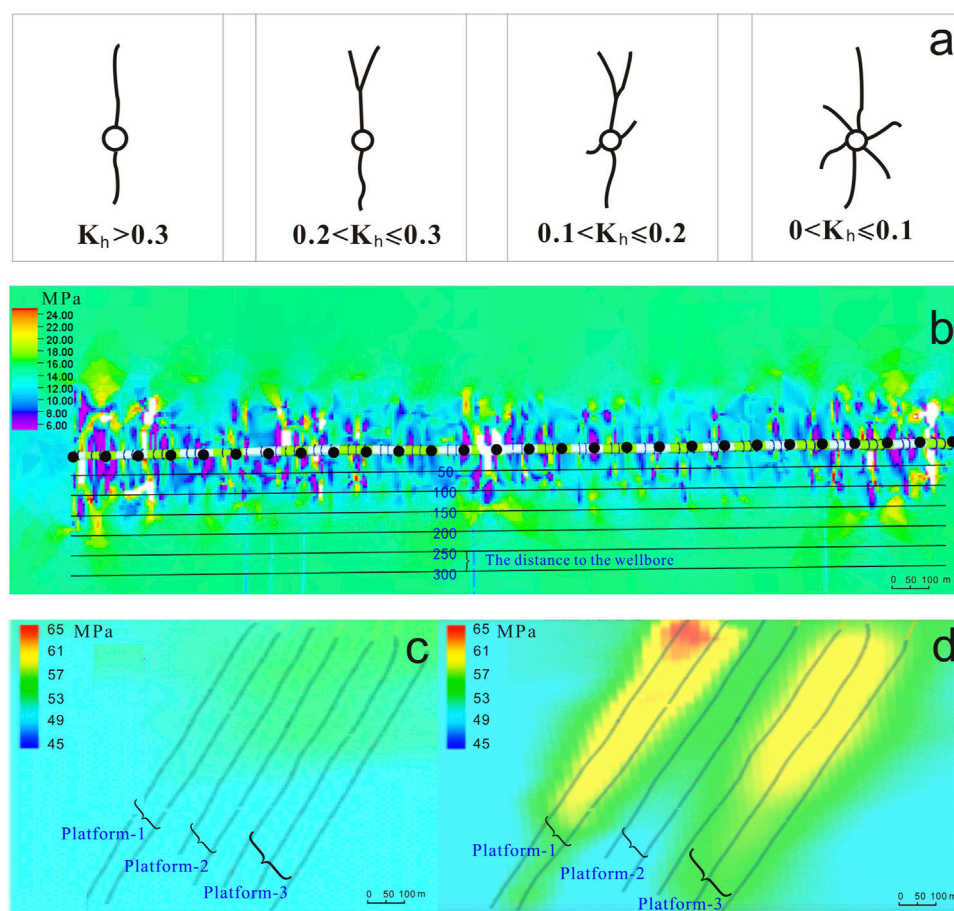
FIGURE 5
(A) The relationship between the stress difference coefficient and the complex fracture network; **(B)** numerical simulation result in the difference of horizontal stress; **(C)** minimum principal stress before hydraulic fracturing; **(D)** minimum principal stress after hydraulic fracturing.

$$K'_h = \frac{(S_H + S'_H) - (S_h + S'_h)}{S_h + S'_h} = \frac{\Delta\sigma - \Delta\sigma'}{S_h + S'_h} < K_H, \qquad (12)$$

where K'_h is the coefficient of stress difference; S'_H and S'_h are the induced stresses of the pore elasticity effect in the direction of maximum and minimum principal stress, respectively, and $\Delta\sigma$ and $\Delta\sigma'$ are the initial horizontal stress difference and the horizontal stress difference after pore pressurization, respectively.

The test results of Ma131 cores show that, the horizontal stress difference is approximately 17 MPa, the minimum horizontal principal stress is 55 MPa, and the horizontal stress difference coefficient is 0.31. According to the relationship between the horizontal stress difference coefficient and the complexity of fracture networks, it is difficult to form a complex fracture network. The numerical simulation results show that the horizontal stress difference decreases during fracturing (Figure 5B),

which can be reduce by 2–10 MPa in the range of 150 m. The reduction decreases with increasing distance from the wellbore (Figure 5C). With an increased pore pressure, the shut-in pressure in wells after fracturing increases significantly, and the minimum horizontal principal stress can increase by 5–10 MPa (Figure 5D). Therefore, the high pore-pressure will change the *in-situ* stress of later fracturing wells, and the horizontal stress difference coefficient will decrease to 0.16–0.3 (Eq. 10), which benefits the formation of complex fracture networks.

In conclusion, the complexity of hydraulic fractures is affected by multiple factors. The proactive stress interference inhibits the extension of the main fractures by changing the initial *in-situ* stress, and improves the complexity of the fracture network by reducing the difference in the horizontal stress coefficient. In this paper, the formation mechanism of a complex fracture network is described in detail.

TABLE 3 Statistics of the small-well-spacing pilot area in the Ma131 oilfield.

Platform number	Well number	Layer	Well space/ m	Horizontal segment length/m	Drilling ratio/%	Fracturing stage	Cluster number	Cluster spacing/ m	Sanding amount/ m3	Fracturing fluid volume/m3	Sanding rate/ m³ m⁻¹	Shut-in pressure/ MPa
1	M1241	T_1b_2	150	1,800	94.6	26	78	24.8	2,125.0	34,521	1.18	24.3
	M1242	T_1b_2	150	1,802	99.9	24	144	13.0	3,245.0	48,790	1.80	28.8
	M1246	T_1b_3	100	1,802	99.5	33	99	20.0	1900.0	24,275	1.05	24.9
	M1247	T_1b_3	100	1,803	100.0	29	58	29.3	1890.0	23,052	1.05	26.6
2	M1243	T_1b_2	150	1,802	99.9	29	174	10.7	3,380.0	54,122	1.88	30.3
	M1244	T_1b_2	150	1,801	95.6	29	174	11.1	3,250.0	51,134	1.80	32
	M1248	T_1b_3	100	1,489	98.3	26	52	29.9	1770.0	21,622	1.19	27.2
	M1249	T_1b_3	100	1,606	96.2	27	81	21.5	1,670.0	21,111	1.04	29.1
3	M1245	T_1b_2	150	1765	96.0	27	81	22.8	2,190.0	36,098	1.24	21
	M1250	T_1b_3	100	1,600	97.6	27	81	21.3	2,510.0	28,765	1.57	22.7
	M1251	T_1b_3	100	1,622	94.4	26	78	21.6	2,700.0	29,221	1.66	25.3
	M1252	T_1b_3	100	1780	99.9	28	84	21.7	1,678.0	20,664	0.94	23.1

3.2 Application of proactive stress interference in the Ma131 small-well-spacing pilot area

Further improvements are highly desirable, such as those in the reserve utilization rate, recovery rate, drilling and completion efficiency, and investment requirements. To explore a new efficient development mode of tight conglomerates, the development test of long lateral length, tight well spacing, big well clusters, fine perforation clustering, and factory operation is carried out in the Ma131 pilot area under the guidance of proactive stress interference theory.

3.2.1 Design and implementation of proactive stress interference for a small well spacing
3.2.1.1 General situation of the pilot area and the designation of hydraulic fracture parameters

The pilot area is 1.2 km (Cao et al., 2015), with proven geological reserves of approximately 100.0×10^4 t. Two sets of oil reservoirs (T_1b_3 and T_1b_2) were developed with a span of 35–40 m in the longitudinal direction, and developed mudstone intercalations of 13–20 m in the middle direction. The reservoir porosity is 8.6%–10.1%, permeability is 1.1×10^{-3} µm (Cao et al., 2015), oil saturation is 50.3%–59.4%, and brittleness is 70–80. A total of 12 horizontal wells were developed, including seven wells in the T_1b_3 layer and five wells in the T_1b_2 layer. The horizontal section length is 1,200–2000 m, the sanding rates are 0.9–1.6 m³/m, and the cluster spacing is 20 m (Table 3). The fracturing mode of drilling plugs, current-limiting fracturing, and temporary plugging fracturing were adopted. Twelve wells were designed with three factory-type platforms, and four wells were drilled by one rig. Three rigs operated at the same time to improve the efficiency.

3.2.1.2 Active stress interference technique

First, a 3-D staggered well pattern is adopted in the pilot area. The W-type stereo staggered mode, in which the vertical horizontal well space is designed 50 m apart, can strengthen the positive vertical interference between wells. During the fracturing progress, based on the regularity of extension, the vertical operation procedure is determined to enhance vertical interference, which is favorable (Figure 6A).

In addition, an intermittent fracturing project is designed. According to the fracture sequence of platform 1, platform 2 and platform 3, the stress wall of platform 1 and platform 3 is formed to promote the formation of a complex fracture network in the fracturing process of platform 2, which enhances the plane favorable interference (Figure 6B).

Finally, zipper fracturing is adopted. The two sets of reservoirs are targeted with the staggered well pattern. The staggered fracture spacing in the longitudinal direction is 10 m. The fracture network is more complicated due to the

FIGURE 6
(A) The well pattern of small well spacing in the Ma131 oilfield; **(B)** lithofacies and design of the platform; **(C)** zipper fracturing sequence of the platform.
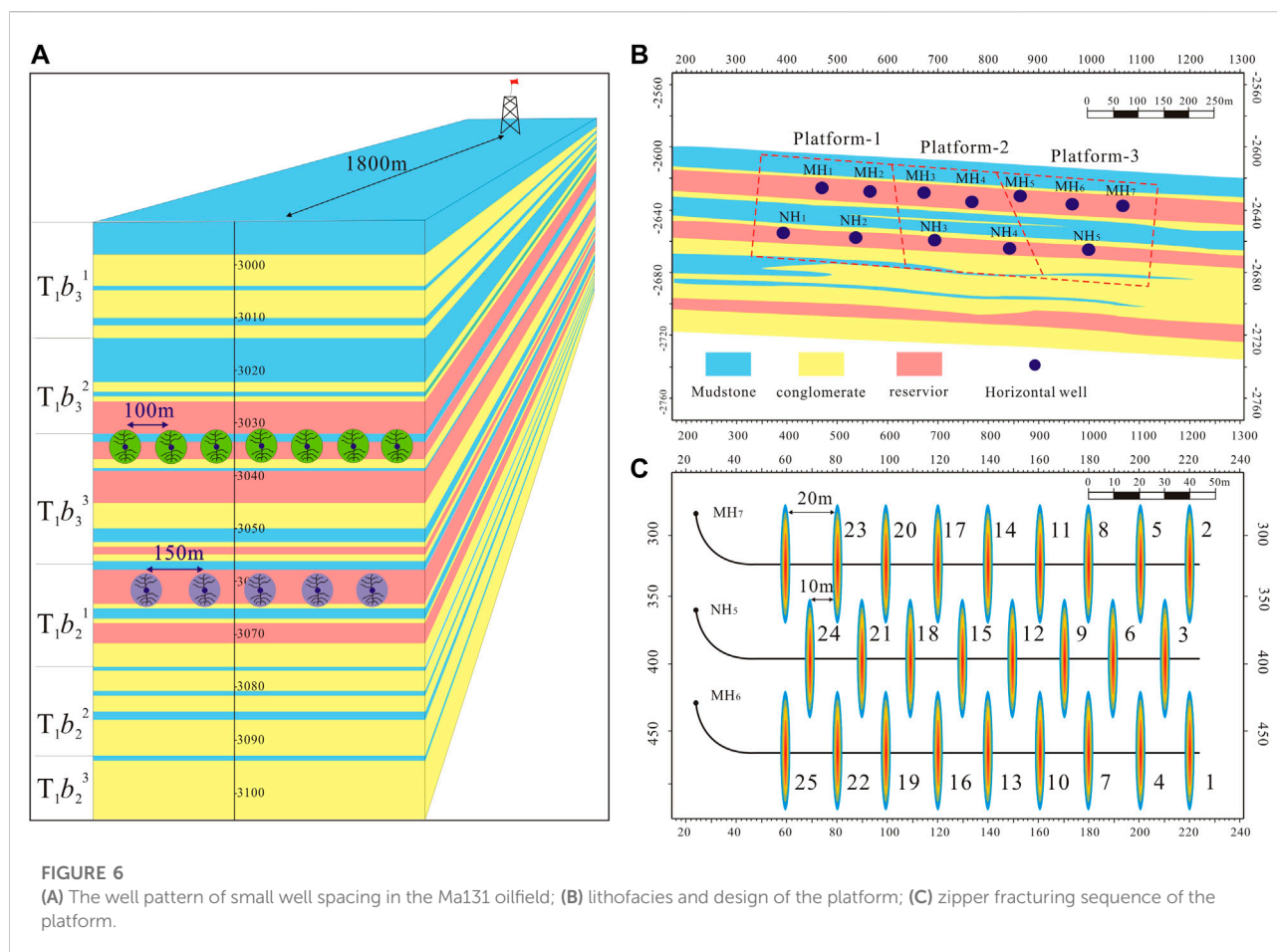
adoption of the asynchronous fracturing method, which creates cluster-to-cluster stress interference (Figure 6C).

3.2.2 Evaluation of the fracture network characteristics of proactive stress interference

3.2.2.1 Shut-in pressure characteristics

Due to the large amount of fracturing fluid injected into the formation, the pore pressure of the formation initially increases, and the pump-off pressure of the subsequently completed fracturing wells increases. More completion energy is spent on generating fractures, which leads to complex fracture networks during subsequent completions. The shut-in pressure of platform 2 is increased by 8 MPa compared to that of platform 1, which fractured earlier (Figure 7A), indicating that platform 2 has a higher energy for fracture formation.

3.2.2.2 Production diagnosis

Production diagnosis is a reliable method of measuring the complexity of fracture networks. During the early linear flow of the horizontal well, the slope of the flow curve is equal to the reciprocal of the product of the contacted surface area of the reservoir and the

square root of permeability (Eq. 12). A shallower slope equates to a greater surface area, which is indicative of more complex fracture networks. The production diagnostic result (Figure 7B) illustrates the relationship between the productivity index ($\Delta p/q$) and the square root of time. The shallower slope of the small-well-spacing data indicates that the proactive interference of stress creates a more complex fracture network than the typical hydraulic fracture technique does in the Ma131 oilfield (Figure 7C).

$$T = \frac{1}{h_f n_f x_f \sqrt{k}},\qquad(13)$$

where T is the slope of the unit pressure drop with the square root of time, h_f is the fracture height, x_f is the fracture half-length, n_f is the fracture number, and k is the fracture permeability.

3.2.2.3 Initial production characteristics

The production law in the Mahu Oilfield shows that the horizontal wells mainly have two periods of flow: an early linear flow and a late pseudo flow. The duration of the early linear flow is generally 3 months. To reduce the influence of the single-well-controlled reserves of the single well on
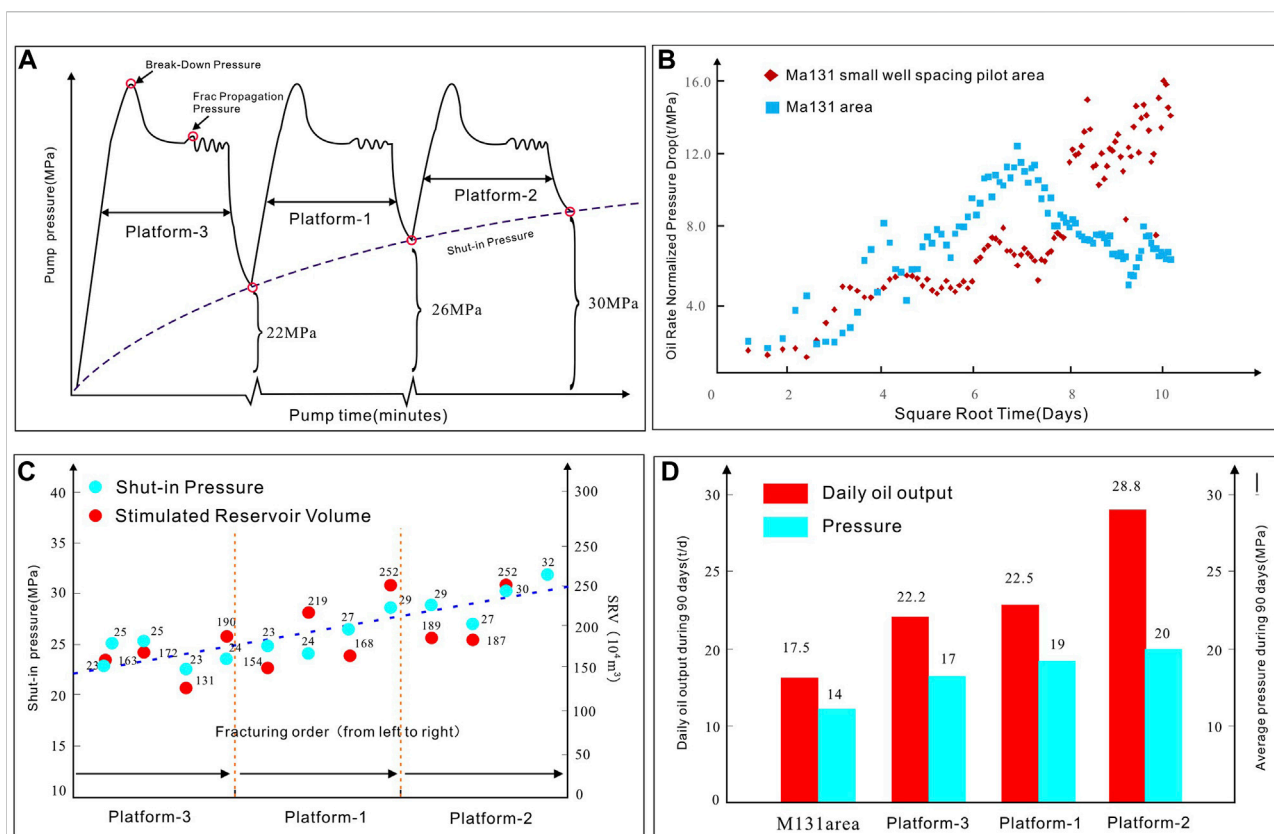
FIGURE 7
(A) Shut-in pressure of different platform plots; **(B)** reciprocal productivity index plot of the average of Ma131 small-well-spacing pilot wells compared to a typical well; **(C)** shut-in pressure and stimulated reservoir volume in Ma131 small-well-spacing pilot wells; **(D)** daily oil output of Ma131 small-well-spacing pilot wells compared to typical wells.

production, the average daily oil production and oil pressure in the first 3 months of the small-well-spacing pilot are selected as the parameters of the complex fracture network characteristics. In terms of initial production, the average daily oil output of the small-well-spacing pilot wells in the first 3 months is higher than that of other horizontal wells in the Ma131 oilfield (Figure 7D). The daily output of platform 2 is higher than those of platform 1 and platform 3. This shows that under proactive stress interference, the complexity of the fracture network near the well zone is improved, the conductivity of the formation is improved, and the initial production is significantly increased.

3.2.2.4 Microseismic monitoring characteristics

At present, microseismic monitoring is an effective method to evaluate the effect of reservoir stimulation in oilfield development. The microseismic monitoring results in the small-well-spacing pilot area show that compared with the 400 m spacing hydraulic fracturing well, the small-well-spacing pilot wells have a denser microseismic response (Figure 8A), larger stimulated reservoir volume and more complexity of the fracture network (Figure 8B).

4 Discussion

4.1 Application prospect of proactive stress interference in preventing WOB interference

Considering the particularity of tight conglomerate reservoirs, the mature horizontal well development model of shale oil and tight oil reservoirs in the North American Permian basin cannot be used for reference in the Mahu Oilfield. To further improve oilfield development, conventional fracturing (Figure 9A), group fracturing (Figure 9B), and well factory fracturing modes have been explored (Ajani and Kelkar, 2012; Kurtoglu and Salman, 2015; Bommer et al., 2017; Jacobs, 2018a). However, there are still two urgent problems that need to be solved in the development process: 1) Affected by the strong heterogeneity of conglomerates, hydraulic fracture propagation is asymmetrical, resulting in fracture hits. Mahu Oilfield data show that the longest distance of fracture hits is 2 km. Fracture hits cause serious production interference, which not only affects the reservoir fracture network

FIGURE 8
(A) Ma131 early horizontal well with a well spacing of 400 m; **(B)** Ma131 small-well-spacing pilot area.

FIGURE 9
(A) Conventional single-layer fracturing model; **(B)** group fracturing model; **(C)** serial fracturing model; **(D)** step-by-step implementation of the serial fracturing model.
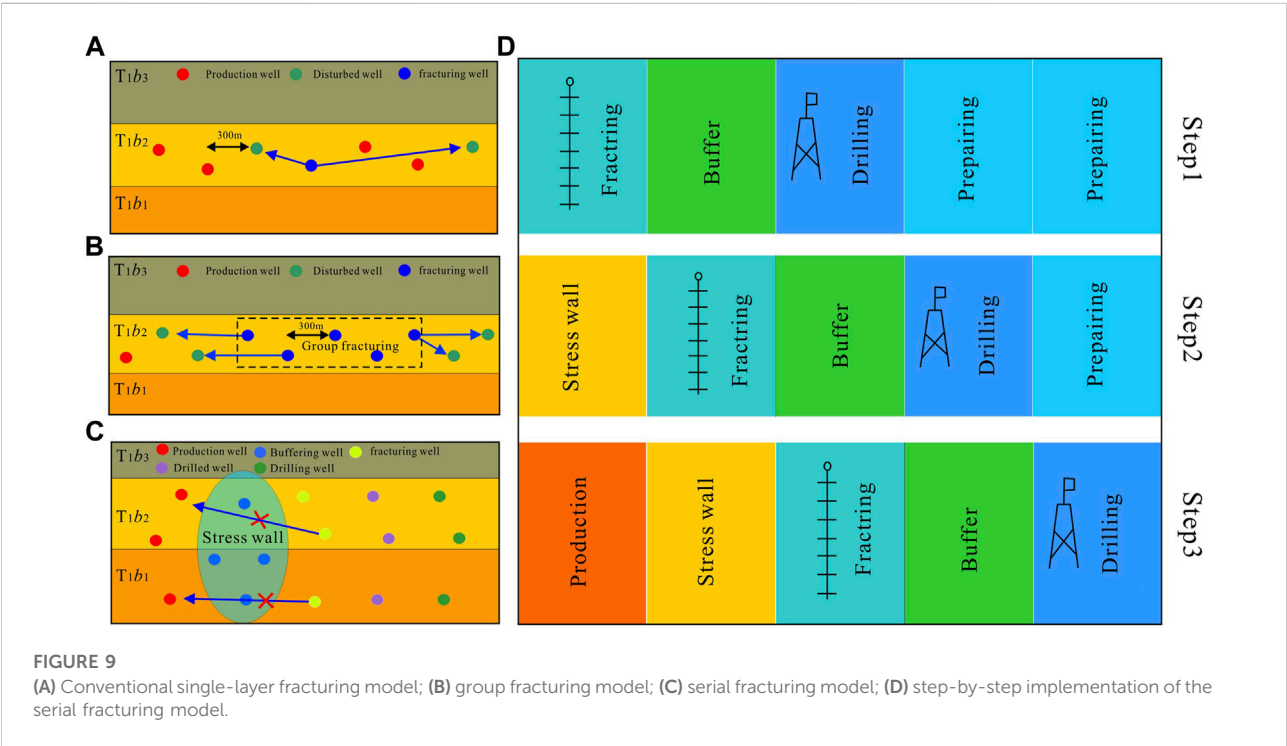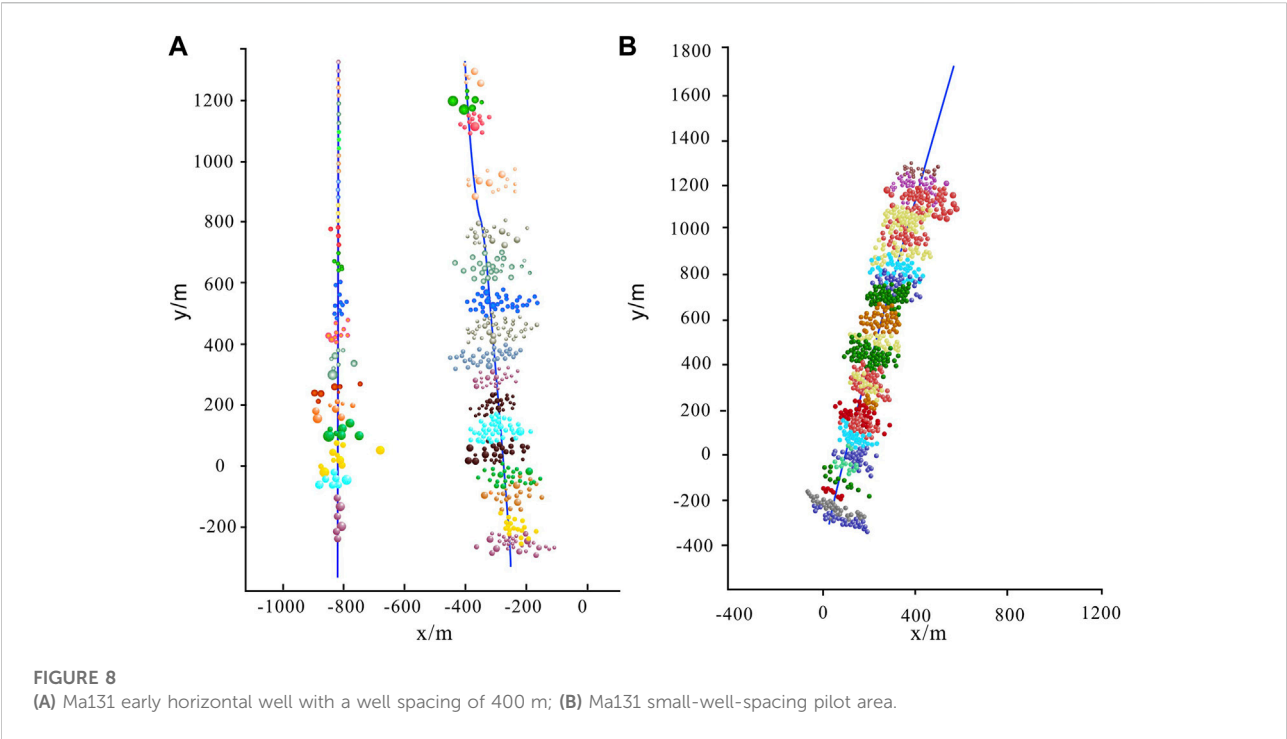
construction quality, but also affects the production of the adjacent well (Hao et al., 2017; Kumar et al., 2018; Thompson et al., 2018). 2) In the process of fracturing, high-density drilling muds cause irreversible damage to the artificially formed fracture of the adjacent well, resulting in a significant EUR reduction of the adjacent well.

FIGURE 10
(A) The production difference between small-spacing wells and conventional wells in the Ma131 oilfield; **(B)** the daily output and predicted cumulative oil production of small-well-spacing pilot wells; **(C)** the relationships between recovery and cumulative oil production with well space; **(D)** the relationships between NPV and recovery with well space.
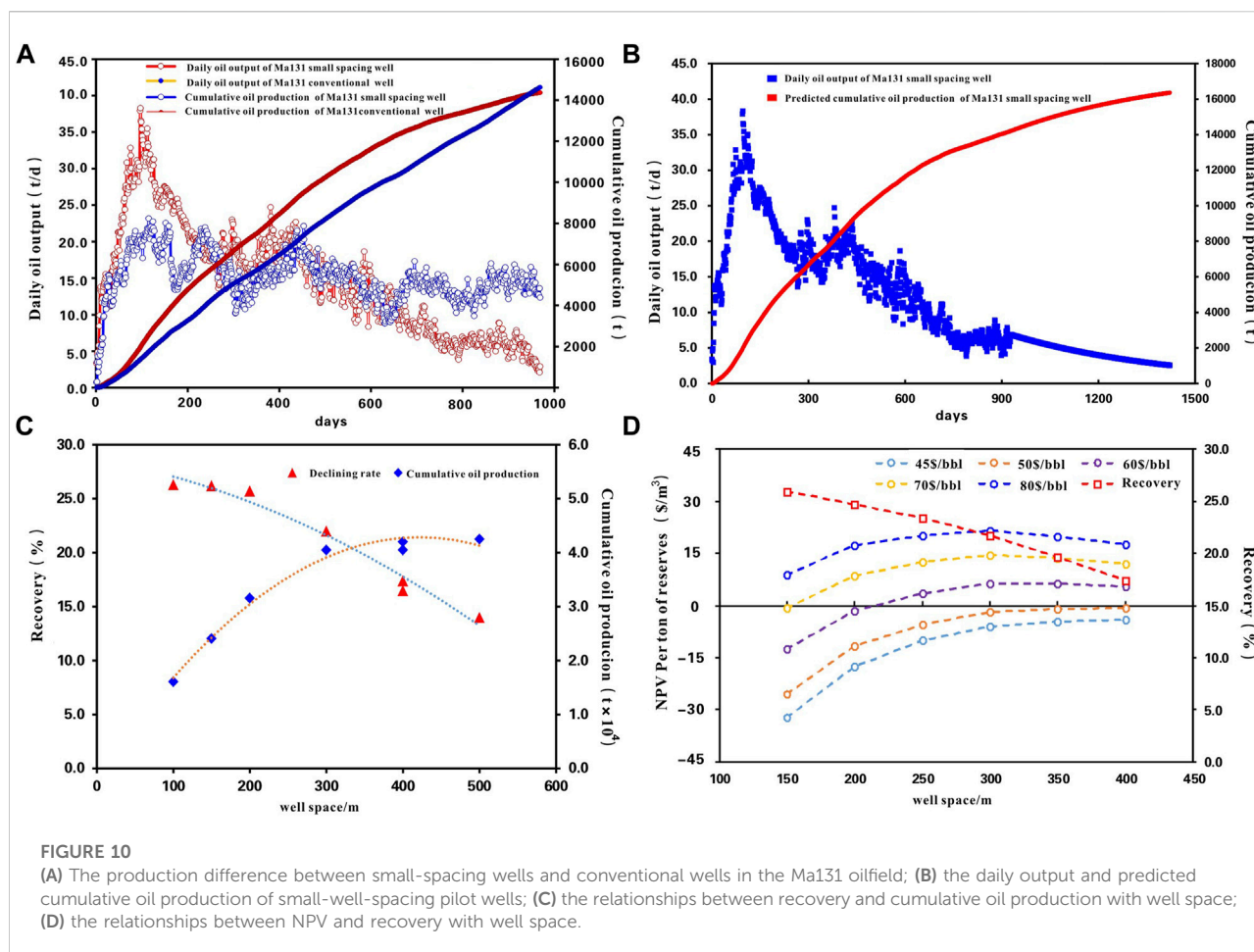
According to the theory of proactive stress interference, this paper uses the stress wall formed by an earlier fractured well to suppress hydraulic fracture propagation and promote fracture diversion in subsequently completed wells, and the serial fracturing mode is innovatively proposed, which can reduce drilling and fracturing hits (Figures 9C,D). The advantages are as follows: 1) The stress barrier formed by the fractured well, which is not produced, can reduce the interference of the subsequently completed fracturing well to the producing well. 2) The established drilling completion buffer zone can reduce the interference of drilling hits to the fracturing well. The development efficiency of the oilfield is improved through the six steps: production, soaking, fracturing, buffering, drilling and preparation.

4.2 Influence of proactive stress interference in the Ma131 well area on well spacing design

In the process of horizontal well fracturing, the effect of reservoir fracture network construction can be improved by reducing the well spacing and using proactive stress interference. However, in the design process of well spacing in tight conglomerate reservoirs, we should not only pursue the complexity of fracture networks but also ignore the potential negative impact of a well spacing that is too small. The production practice of horizontal well spacing in Ma131 shows that (Figure 10A), large well spacing is conducive to improving the production of single wells, but the recovery is relatively low. However, if the well spacing is too small, the geological reserves and EUR controlled by the single well decrease, which increases the benefit risk. Compared with the result of conventional horizontal wells in the same block, in less than 400 days, the Ma131 small-well-spacing pilot wells show higher production and decline rates. In more than 400 days, the production of the small-well-spacing wells is less than that of conventional horizontal wells (Figure 10B). By using the Arps decreasing method, the EUR of the small-well -spacing horizontal wells is determined to be less than 20,000 tons (Figure 10C), which is far below its economic production limit.

The net present value (NPV) is the factor used to optimize the well spacing in this work. With the investment data of horizontal wells in the Ma131 oilfield, a chart of the relationship between well spacing and NPV of different oil prices is developed. Figure 10D indicates that when the oil price is $60 BBL, the limit for economic well spacing is 200 m. Therefore, in the process of developing and

designing horizontal wells in tight conglomerate reservoirs, it is important to optimize the economic well spacing.

5 Conclusion

(1) In this paper, we put forward proactive stress interference theory in a tight conglomerate oilfield and reveal its geo-mechanical mechanism. The mechanism of the stress wall and its inhibitory effect on tensile and shear fracture propagation in subsequently completed hydraulic fracturing wells are analyzed in detail. It is proposed that the formation of complex fracture networks with a small well spacing is the result of proactive stress interference and the reduction in the difference in the horizontal stress coefficient.

(2) Based on the application of proactive stress interference of staggered cube pads with a small well spacing at Ma131, the technical method and steps required to implement proactive stress interference are introduced in detail, and the characterization method of judging fracture complexity by means of shut-in pressure, linear flow characteristics, initial production characteristics and microseismic monitoring is proposed.

(3) A sequence development mode based on proactive stress interference is proposed. In view of the contradiction between drilling and fracturing interference and efficient production in the Mahu Oilfield, the stress wall formed by previously completed fracturing wells is used to reduce the interference of later fracturing wells. At the same time, the drilling buffer zone is designed to reduce the interference between the fracturing well and the production well. The development sequence is as follows: production, closing in, fracturing, buffering, drilling, and preparation.

Data availability statement

The original contributions presented in the study are included in the article/Supplementary Material, further inquiries can be directed to the corresponding author.

Author contributions

SW: Conceptualization, data curation, formal analysis, Writing—original draft, Writing—review and editing. XL: Validation, resources. LH: Formal analysis, investigation. XZ: Resources, validation. LZ: Resources, validation. JS: Methodology. RL: Methodology. PH: investigation. KG: Resources. TL: Methodology. GL: Methodology. XW: Resources. SL: Resources.

Funding

Conflict of interest

All authors were employed by PetroChina Xinjiang Oilfield.

Publisher's note

All claims expressed in this article are solely those of the authors and do not necessarily represent those of their affiliated organizations, or those of the publisher, the editors and the reviewers. Any product that may be evaluated in this article, or claim that may be made by its manufacturer, is not guaranteed or endorsed by the publisher.

Supplementary material

The Supplementary Material for this article can be found online at: https://www.frontiersin.org/articles/10.3389/feart.2022.948932/full#supplementary-material

References

Adachi, J., Siebrits, E., Peirce, A., and Desroches, J. (2007). Computer Simulation of Hydraulic Fractures[J]. *Int. J. Rock Mech. Min. Sci.* 44 (5), 739–757. doi:10.1016/j.ijrmms.2006

Ajani, A. A., and Kelkar, M. G. (2012). "Interference study in shale plays." in Paper presented at the SPE Hydraulic Fracturing Technology Conference (Texas: The Woodlands). SPE-151045-MS. 6–8. doi:10.2118/151045-MS

Bommer, P., Bayne, M., Mayerhofer, M., Machovoe, M., and Staron, M. (2017). "Re-designing from scratch and defending offset wells: case study of a six-well bakken zipper project, McKenzie county, ND." in Paper presented at the SPE Hydraulic Fracturing Technology Conference and Exhibition. Texas: The Woodlands. SPE-184851-MS. doi:10.2118/184851-MS

Bunger, A. P., Zhang, X., and Jeffrey, R. G. (2011). "Parameter affecting the interaction among closely spaced hydraulic fractures[C]." in paper 140426 presented at the SPE Hydraulic Fracturing Technology Conference, 24-26 January, the Woodlands (Texas, New York: The Woodlands). doi:10.2118/140426-PA

Cao, J., Lei, D. W., Li, Y. W., Tang, Y., AbulimitChang, Q. S., et al. (2015). Ancient high-quality alkaline lacustrine source rocks discovered in the lower permian fengcheng formation, junggar basin. *Acta Pet. Sin.* 36 (7), 781–790. doi:10.7623/syxb201507002

Dohmen, T., Blangy, J. P., and Zhang, J. (2014). Microseismic depletion delineation. *Interpretation* 2 (3), SG1–SG13. doi:10.1190/int-2013-0164.1

Dohmen, T., Zhang, J., Barker, L., and Blangy, J. P. (2017). Microseismic magnitudes and b-Values for delineating hydraulic fracturing and depletion. *SPE J.* 22 (05), 1–624. doi:10.2118/186096-pa

Feng, C., Li, T., He, W., and Zheng, M. (2020). Organic geochemical traits and paleo-depositional conditions of source rocks from the carboniferous to permian sediments of the northern mahu sag, junggar basin, china. *J. Petroleum Sci. Eng.* 191, 107117. doi:10.1016/j.petrol.2020.107117

Gao, Q., and Ghassemi, A. (2020a). Finite element simulations of 3D planar hydraulic fracture propagation using a coupled hydro-mechanical interface element. *Int. J. Numer. Anal. Methods Geomech.* 44 (15), 1999–2024. doi:10.1002/nag.3116

Hao, S., Dengen, Z., Adwait, C., and Baosheng, L. (2017). "Understanding the 'frac-hits' impact on a midland basin tight-oil well production," in in Paper presented at the SPE Unconventional Resources Technology Conference, Austin, Texas, July 24. doi:10.15530/urtec-2017-2662893

Huang, L., Cao, J., Guo, J., Ma, Y., Wang, G., and Zhang, H. (2019). The forming mechanism of high quality glutenite reservoirs in Baikouquan formation at the eastern slope of mahu sag of the Junggar basin,c. *Petroleum Sci. Technol.* 37 (14), 1665–1674. doi:10.1080/10916466.2019.1602638

Hubbert, M. K., and Rubey, W. W. (1959). Role of fluid pressure in mechanics of overthrust faulting: I. Mechanics of fluid-filled porous solids and its application to overthrust faulting. *Geol. Soc. Am. Bull.* 70 (2), 115–166. doi:10.1130/0016-7606(1959)70[115:rofpim]2.0.co;2

Jacobs, T. (2018a). In the battle against frac hits, shale producers go to new extremes. *J. Pet. Technol.* 70 (8), 35–38. SPE-0818-0035-JPT. doi:10.2118/0818-0035-JPT

Jia, H., Ji, H., Li, X., Zhou, H., Wang, L., and Gao, Y. (2016). A retreating fan-delta system in the Northwestern Junggar Basin, northwestern China-Characteristics, evolution and controlling factors. *J. Asian Earth Sci.* 123, 162–177. doi:10.1016/j.jseaes.2016.04.004

Jin, G., and Roy, B. (2017). Hydraulic-fracture geometry characterization using low-frequency DAS signal [J]. *Lead. Edge* 36 (12), 975–980. doi:10.1190/tle36120975.1

Ju, Y., Li, Y., Wang, Y. L., and Yang, Y. M. (2020). Stress shadow effects and microseismic events during hydrofracturing of multiple vertical wells in tight reservoirs: A three-dimensional numerical model. *J. Nat. Gas Sci. Eng.* 84, 2020. doi:10.1016/j.jngse.2020.103684

Kumar, D., Masouleh, S. F., Gassami, A., Riley, S., and Elliott, B. (2018). "A 3D geomechanical analysis of horizontal well refracturing and "frac" its." in paper presented at the 52nd U.S. Rock Mechanics/Geomechanics Symposium ARMA-2018-729. 17–20 June. Seattle, WA.

Kurtoglu, B., and Salman, A. (2015). "How to utilize hydraulic fracture interference to improve unconventional development" in Paper presented at the AbuDhabi International Petroleum Exhibition and Conference (Abu Dhabi: UAE). SPE-177953-MS. doi:10.2118/177953-MS

Lecampion, B., Bunger, A. P., and Zhang, X. (2018). Numerical methods for hydraulic fracture propagation: a review of recent trends [J]. *J. Nat. Gas Sci. Eng.* 49, 66–83. doi:10.1016/j.jngse.2017.10.012

Li, G. X., Qin, J. H., Xian, C. G., Fan, X. B., Zhang, J., and Ding, Y. (2020). Theoretical understandings, key technologies and practices of tight conglomerate oilfield efficient development: a case study of the mahu oilfield, junggar basin, NW china[J]. *Petroleum Explor. Dev.* 47 (6), 1185–1197. doi:10.1016/s1876-3804(20)60135-0

Li, H., Tang, H.-m., Qin, Q.-r., Fan, C.-h., Han, S., Yang, C., et al. (2018). Reservoir characteristics and hydrocarbon accumulation of carboniferous volcanic weathered crust of zhongguai high area in the western junggar basin, china. *J. Cent. South Univ.* 25 (11), 2785–2801. doi:10.1007/s11771-018-3953-y

Liu, J., Ding, W., Yang, H., and Liu, Y. (2021). Quantitative multiparameter prediction of fractured tight sandstone reservoirs: a case study of the yanchang formation of the ordos basin, central china. *SPE J.*, 1–32. doi:10.2118/205495-pa

Liu, J., Ding, W., Yang, H., Wang, R., Yin, S., Li, A., et al. (2017). 3D geomechanical modeling and numerical simulation of *in-situ* stress fields in shale reservoirs: a case study of the lower cambrian niutitang formation in the cen'gong block, south cChina. *Tectonophysics* 712, 663–683. doi:10.1016/j.tecto.2017.06.030

Liu, J., Mei, L., Ding, W., Xu, K., Yang, H., and Liu, Y. (2022b). Asymmetric propagation mechanism of hydraulic fracture networks in continental reservoirs. *GSA Bull.* doi:10.1130/B36358.1

Liu, J. S., Yang, H. M., Xu, K., Wang, Z. M., Liu, X. Y., Cui, L. J., et al. (2022a). Genetic mechanism of transfer zones in rift basins: insights from geomechanical models. *GSA Bull.* doi:10.1130/b36151.1

Meng, C., Maerten, F., and Pollard, D. D. (2013). Modeling mixed-mode fracture propagation in isotropic elastic three dimensional solid. *Int. J. Fract.* 179, 45–57. doi:10.1007/s10704-012-9771-6

Norbeck, J. H., and Horne, R. N. (2016). Physical mechanisms related to microseismic-depletion-delineation field tests with application to reservoir surveillance. *SPE J.* 21 (04), 1–279. doi:10.2118/178926-pa

Pan, L. H., Zhang, S. C., Cheng, L. J., Lu, Z. H., and Lliu, K. Y. (2014). A numerical simulation of the inter-cluster interference in multi-cluster staged fracking for horizontal wells [J]. *Nat. Gas. Ind.* 34 (1), 74–79. doi:10.3787/j.issn.1000-0976.2014.01.011

Sone, H., and Zoback, M. D. (2013). Mechanical properties of shale-gas reservoir rocks—Part 1: static and dynamic elastic properties and anisotropy. *Geophysics* 78 (5), D381–D392. doi:10.1190/geo2013-0050.1

Thiercelin, M. J., and Plumb, R. A. (1994). A core-based prediction of lithologic stress contrasts in east texas formations [J]. *SPE Form. Eval.* 9 (4), 251–258. doi:10.2118/21847-pa

Thompson, J., Franciose, N., Schutt, M., Hartig, K., and Mckenna, J. (2018). "Tank development in the midland basin, texas: a case study of super-charging a reservoir to optimize production and increase horizontal well densities." in SPE-2902895 presented at the Unconventional Resources Technology Conference held in Houston, 23. doi:10.15530/urtec-2018-2902895

Tong, H. M., Zhang, P., Zhang, H. X., Liu, Z. P., Ren, X. H., Xiao, K. Z., et al. (2021). Geomechanical mechanisms and prevention countermeasures of casing deformation in shale gas horizontal wells[J]. *Nat. Gas. Ind.* 41 (1), 189–197. doi:10.3787/j.issn.1000-0976.2021.01.017

Tong, H. M., and Yin, A. (2011). Reactivation tendency analysis: a theory for predicting the temporal evolution of pre-existing weakness under uniform stress state. *Tectonophysics* 503, 195–200. doi:10.1016/j.tecto.2011.02.012

Tong, H. M., Wang, J. J., Zhao, H. T., Li, B., Hao, H. H., and Wang, M. Y. (2014). Mohr space and its application to the activation prediction of pre-existing weakness. *Sci. China Earth Sci.* 57, 1595–1604. doi:10.1007/s11430-014-4860-1

Wang, L. C., Duan, K., Zhang, Q. Y., Li, X. Y., and Jiang, R. H. (2022). Study of the dynamic fracturing process and stress shadowing effect in granite sample with two holes based on SCDA fracturing method. *Rock Mech. Rock Eng.* 55, 1537–1553. doi:10.1007/s00603-021-02728-0

Wang, S. G., Tan, Y. H., Sangnimnuan, An., Khan, S., Liang, B. S., and Rijken, P. (2019). "Learnings from the hydraulic fracturing test site (hfts) #1, midland basin, west Texas - a geomechanics perspective," in in Paper presented at the SPE Unconventional Resources Technology Conference. URTEC-2019-1570-MS., Denver, Colorado, July 22. doi:10.15530/urtec-2019-1570

Yi, C., Johansson, D., and Greberg, J. (2018). Effects of *in-situ* stresses on the fracturing of rock by blasting. *Comput. Geotechnics* 104, 321–330. doi:10.1016/j.compgeo.2017.12.004.9

Zhang, B., Ji, B., and Liu, W. (2018). The study on mechanics of hydraulic fracture propagation direction in shale and numerical simulation. *Geomech. Geophys. Geo-energ. Geo-resour.* 4, 119–127. doi:10.1007/s40948-017-0077-z

Zhang, C. M., Song, X. M., Wang, X. J., Wang, X. L., Zhao, K., and Shuang, Q. (2020). Origin and depositional characteristics of supported conglomerates [J]. *Petroleum Explor. Dev.* 47 (2), 272–285. doi:10.1016/s1876-3804(20)60047-7

Zhao, J. Z., Ren, L., Shen, C., and Li, Y. M. (2018). Latest research progresses in network fracturing theories and technologies for shale gas reservoirs [J]. *Nat. Gas. Ind.* 38 (3), 1–14. doi:10.3787/j.issn.1000-0976.2018.03.001

Zhou, L., Chen, J., Gou, Y., and Feng, W. (2017). Numerical investigation of the time-dependent and the proppant dominated stress shadow effects in a transverse multiple fracture system and optimization. *Energies* 10 (1), 83. doi:10.3390/en10010083

Zoback, M. D. (2007). *Reservoir geomechanics [M]*. New York: Cambridge University Press

Laboratory investigation and evaluation of the hydraulic fracturing of marine shale considering multiple geological and engineering factors

Lei Wang[1]*, Jun Zhou[2,3], Yintong Guo[1], Xuehang Song[4] and Wuhao Guo[1]

[1]State Key Laboratory of Geomechanics and Geotechnical Engineering, Institute of Rock and Soil Mechanics, Chinese Academy of Sciences, Wuhan, China, [2]CNOOC Research Institute Co., Ltd., Beijing, China, [3]State Key Laboratory of Offshore Oil Exploitation, Beijing, China, [4]CAS Key Lab of Low-Carbon Conversion Science and Engineering, Shanghai Advanced Research Institute, Chinese Academy of Sciences, Shanghai, China

Hydraulic fracturing is widely implemented in the exploration of marine shale gas. Affected by various geological and engineering factors, gas production after stimulation is not always satisfactory. To reveal the influential effect of multiple factors, laboratory hydraulic fracturing experiments are performed on Longmaxi marine shales by considering key parameters (deviatoric stress, confining pressure, pumping rate, fracturing fluid type, and bedding angle). The variation of breakdown pressures and the characteristics of hydraulic fractures are recorded and analyzed. The results show that the breakdown pressure increases with increasing deviatoric stress, confining pressure, pumping rate, and viscosity of the fracturing fluid. As the bedding angle varies from 0° to 90°, the breakdown pressure declines first and increases again. Furthermore, parameter sensitivity analysis indicates that geological factors (confining pressure, bedding angle, and deviatoric stress) would largely determine the breakdown pressure, while engineering factors (pumping rate, fracturing fluid type) could only affect it to a lesser extent. Computed tomography measurements show that natural fractures, originating from tectonic shear failure, could possess greater width than tension-dominated hydraulic and bedding fractures. Statistical analysis shows that the length of the hydraulic fractures alone is only approximately 150 mm. However, the fully activated natural and/or bedding fractures could help substantially increase the total fracture length to 600 mm. Low deviatoric stress, low confining pressure, low viscous slick-water, and high bedding angle are conducive to activating natural and bedding fractures and forming

---

a complex fracture network. The aforementioned findings are valuable for the optimal design of field hydraulic fracturing.

1 Introduction

Organic-rich shales are important hydrocarbon-bearing source rocks and thus are targets for shale oil and gas exploration worldwide. In China, the geological resources of shale gas are estimated to be approximately 110×10^{12} m³, with recoverable gas reserves of ca. 20×10^{12} m³ (Zou et al., 2019). According to the sedimentary environment, organic-matter-rich shales can be further divided into three types: marine, transitional, and lacustrine shales. Shales of marine origin, with a ca. total of 9×10^{12} m³ of recoverable resources is the most promising type to make a breakthrough. After 10 years of exploration and practice in the marine shales of the Wufeng–Longmaxi Formation, China, has become one of the few countries achieving industrial shale gas exploitation (Ma et al., 2018). By the end of 2020, the annual production of shale gas exceeded 200×10^8 m³ (Zhang et al., 2021).

In view of the fact that the porosity and permeability of shale reservoirs are extremely low, hydraulic fracturing is an effective technology to achieve commercial development (Zou et al., 2017). Ideally, hydraulic fractures initiate from the borehole at an acceptable breakdown pressure and propagate into the reservoir, fully activating natural fractures and bedding and forming a complex fracture network (Xu et al., 2018). The fracturing effects are controlled by various factors, which can be roughly divided into geological and engineering categories. *In-situ* stress, the development of natural fractures, and the bedding structure are major geological factors closely related to hydraulic fracturing. The pumping procedure and fracturing fluid type are key engineering factors that can be controlled to regulate hydraulic fracture propagation.

To reveal the influence of various factors on the initiation and propagation of hydraulic fractures in marine shales, former researchers performed laboratory hydraulic fracturing tests. In the work of Tan et al. (2017), the vertical propagation behavior of hydraulic fractures in laminated shale formations was investigated. *In situ* stress, injection rate, and fluid viscosity were included in the experimental design. Hou et al. (2019) proposed a novel alternating fluid injection method with guar fluid and slick water to form a large, complex fracture network. In addition, Hou et al. (2018) also focused on the condition of a high horizontal stress difference in deep shale formations. Zhang et al. (2019) and Cai et al. (2020) both discussed the anisotropic effects of shale on fracturing. In the aspect of fracture morphology analysis, an optical scanner was used to reconstruct the rough fracture surface at the macroscale (Song et al., 2019; Yang et al., 2022), while scanning electron microscopy (SEM) was applied to observe hydraulic fractures at the local microscale (He et al., 2020). Computed tomography (CT) scanning is another powerful tool for 3-D hydraulic fracture characterization (Guo et al., 2014; Zhang et al., 2017; Li et al., 2019). Referring to the concept of "Stimulated Reservoir Volume" (SRV) (Fisher et al., 2004; Mayerhofer et al., 2010), "Stimulated Rock Area" (SRA) is proposed to quantitatively evaluate the laboratory hydraulic fracture networks (Hou et al., 2014). The aforementioned literature review showed that previous research mainly focused on one or some factors affecting hydraulic fractures. Few studies have compared and analyzed multiple factors at the same time. Parameter sensitivity analysis of the breakdown pressure is also rarely reported. The contributions of natural fractures and bedding structures to improving the stimulation effects need to be further evaluated.

In this study, an outcrop of the Longmaxi marine shale is collected. Laboratory hydraulic fracturing experiments are performed, involving multiple factors, such as deviatoric stress, confining pressure, pumping rate, fracturing fluid type, and bedding angle. The breakdown pressure and fracture morphology are recorded and analyzed, comparatively. Based on the fracture classification, width and length measurements are implemented. Parameter sensitivity analysis on the breakdown pressure, contribution of natural/bedding fractures, and influence of heterogeneity are discussed.

2 Materials and test methods

2.1 Outcrop collection

The sampling site of the marine shale outcrop is located in Wulong District, Chongqing, China (Figure 1A), approximately 70 km from the Fuling gas field, the first large-scale shale gas field in China. The outcrop is the natural extension of the Lower Silurian Longmaxi Formation, which is one of the main targeted shale gas reservoirs in southern China. Stratigraphic consistency guaranteed the representativeness and effectiveness of the mineral composition, mechanical properties, and laboratory hydraulic fracturing results derived in this study. Considering that long-term atmospheric and microbiological factors would exert a deterioration effect on the outcrop shale, making it softer and more broken, the upper-weathered layer is removed as much as possible and the bottom fresh shale is collected during sampling.
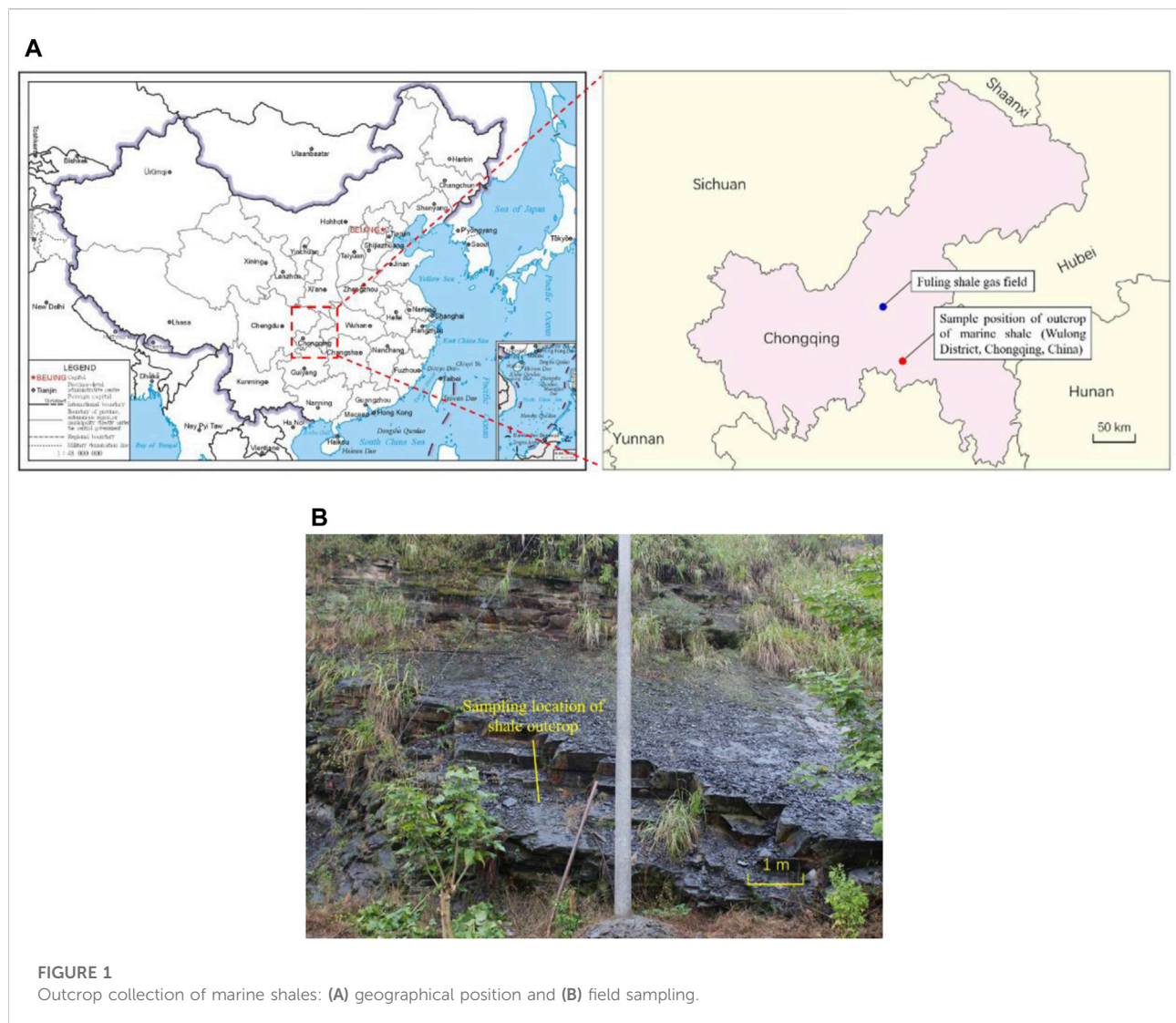
FIGURE 1
Outcrop collection of marine shales: **(A)** geographical position and **(B)** field sampling.

2.2 Sample preparation

To reveal the mineral composition of the collected outcrop, shale fragments are ground into a powder sample for X-ray diffraction (XRD) analysis. In addition, two types of cylindrical specimens ($\varphi50\times100$ mm and $\varphi50\times25$ mm) are also prepared for rock mechanical tests. Specifically, five samples with dimensions of $\varphi50\times100$ mm are designed for uniaxial compressive tests, which can provide the mechanical properties of uniaxial compressive strength, Young's modulus, and Poisson's ratio. It should be noted that the bedding of the shale is perpendicular to the axis of the cylinder for this type of specimen. Ten specimens ($\varphi50\times25$ mm) were used for Brazilian indirect tensile experiments, which could evaluate the tensile strength of the shale matrix and bedding. The shale bedding is parallel to the axis of the cylinder for this type of sample.

The sample preparation for hydraulic fracturing tests is relatively complex. First, approximately twenty cylindrical specimens, with a diameter of 100 mm and height of 200 mm are prepared from shale outcrops. Here, the bedding angle (β) is considered, which is the angle between the bedding plane and the vertical axis of the cylinder. For most of the specimens, the bedding is along the horizontal plane ($\beta=90°$), while the bedding planes of several other specimens are inclined with different bedding angles. Detailed information on the sample orientation is provided in Table 1. Second, a small hole, with a diameter of 12 mm and depth of 120 mm, is drilled into the center of one end face by using a special slender drill bit (Figure 2A). Third, the steel pipe (Figure 2B), with a diameter of 6 mm and height of 110 mm, is placed in the small hole to a depth of 100 mm. The surface of the steel pipe is spirally prefabricated to increase the bonding strength with the sealant. Then, the epoxy resin sealant (Figure 2C) is poured into the annulus. After the sealant is set, an

TABLE 1 Experimental scheme of laboratory hydraulic fracturing considering multiple factors.

σ_3	$\sigma_1-\sigma_3$	Q	β	Fracturing fluid	Sample number
Confining pressure (MPa)	Deviatoric stress (MPa)	Pumping rate (ml/s)	Bedding angle (°)		
0	*3*	0.02	90	Slick-water	W-1
	6				W-2
	9				W-3
	12				W-5
0	3	0.02	90	Slick-water	*W-1*
25					*W-11*
30					*W-7*
25	3	0.02	90	*Slick-water*	W-11
				Guar-gum	W-22
25	6	*0.01*	90	Slick-water	W-13
		0.02			W-18
		0.04			W-16
25	3	0.02	*0*	Slick-water	W-17
			30		W-19
			60		W-20
			90		W-11

open hole with a height of 20 mm is reserved inside the specimen. Some prepared specimens and the detailed dimensions are provided in Figure 2D and Figure 2E, respectively. It should be noted that the steel pipe is 10 mm higher than the end face of the specimen, and a sealing ring is added to guarantee the sealing performance between the steel pipe and indenter.

2.3 Experimental system and scheme

2.3.1 Experimental system

The mineral composition analysis was implemented on a D8 Advance X-ray diffractometer. Uniaxial compressive and Brazilian indirect tensile tests were conducted on MTS815 and RMT-150C rock test systems (Wang et al., 2020), respectively. Considering that the aforementioned experimental systems are conventional test instruments, the detailed introduction is omitted. A specific description of the laboratory hydraulic fracturing system is provided in the following section.

As shown in Figure 3A, the laboratory hydraulic fracturing system mainly consists of three parts. The first part is a servo-controlled triaxial testing machine, which can provide steady axial compressive stress (σ_1) and confining pressure (σ_3) on the specimen to simulate vertical and horizontal *in-situ* stresses, respectively. The designed maximum axial force is 2,000 kN, and the limit of confining pressure is 140 MPa. The second part is a plunger pump, which can transport the fracturing fluid into the specimen at a given flow rate and achieve the initiation and

propagation of hydraulic fractures (Guo et al., 2020). The controlled flow rate range is 0.01–10 ml/min, the maximum output pumping pressure is 70 MPa, and the maximum storage volume is 300 ml. The third part is the control and data acquisitions system, which is responsible for the control and acquisition of key parameters, such as axial stress, confining pressure, and pumping pressure. The aforementioned three parts cooperate with each other and perform their own functions.

The main test procedures are as follows:

1) The assembly of the prepared specimens. As illustrated in Figure 3B, the prepared specimen was placed between the upper and lower indenters. Wrap up the combined indenters and the specimen with a heat shrinkable tube. Connect the fracturing pipeline to the upper indenter. Deploy the related sensors.
2) The exertion of axial and confining stresses. The triaxial chamber was placed, and the inside was filled with hydraulic oil. The confining pressure was exerted to the set value and then the axial force was applied to the set value (Figure 3C). The axial stress and confining pressure would remain stable during the next hydraulic fracturing stage.
3) The injection of the fracturing fluid. With the displacement of the plunger, the fracturing fluid flows into the specimen along the pipeline at a constant rate. The pressure inside the specimen gradually increases and reaches the peak value, along with the formation of hydraulic fractures. The whole pressure–time curve is recorded.

FIGURE 2
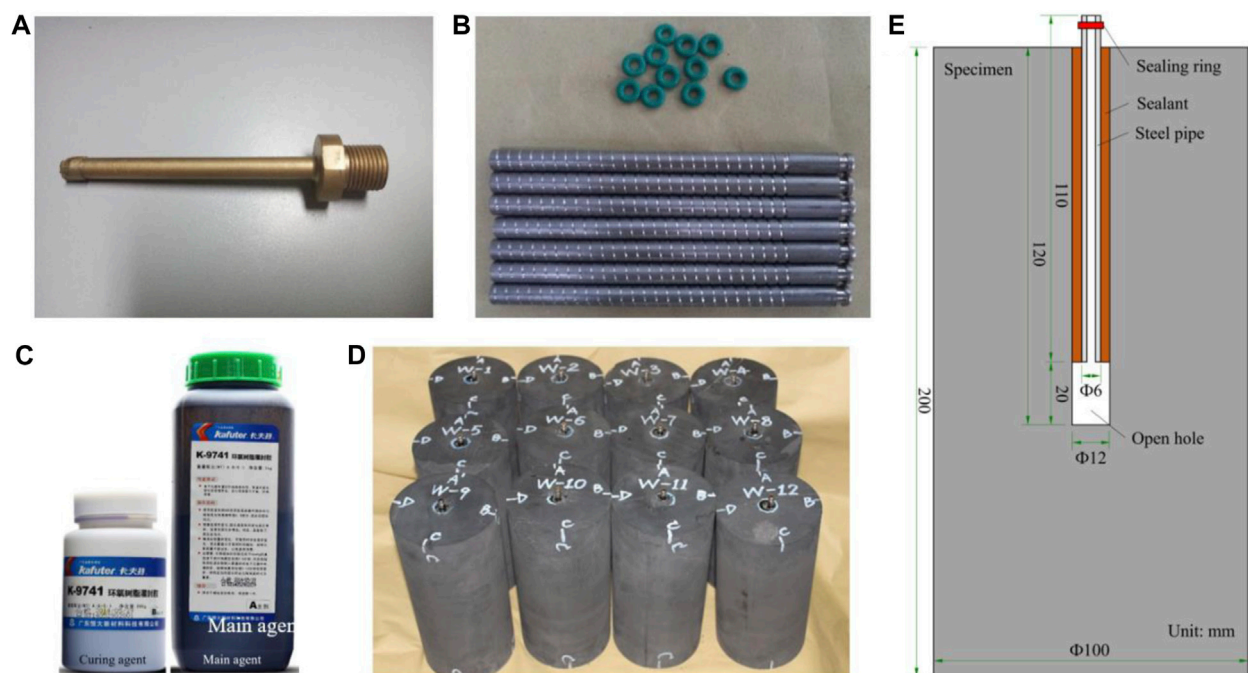Sample preparation for hydraulic fracturing: **(A)** drilling bit, **(B)** spirally prefabricated steel pipes and sealing rings, **(C)** epoxy resin sealant, **(D)** some prepared specimens, and **(E)** dimensional details of the specimen.
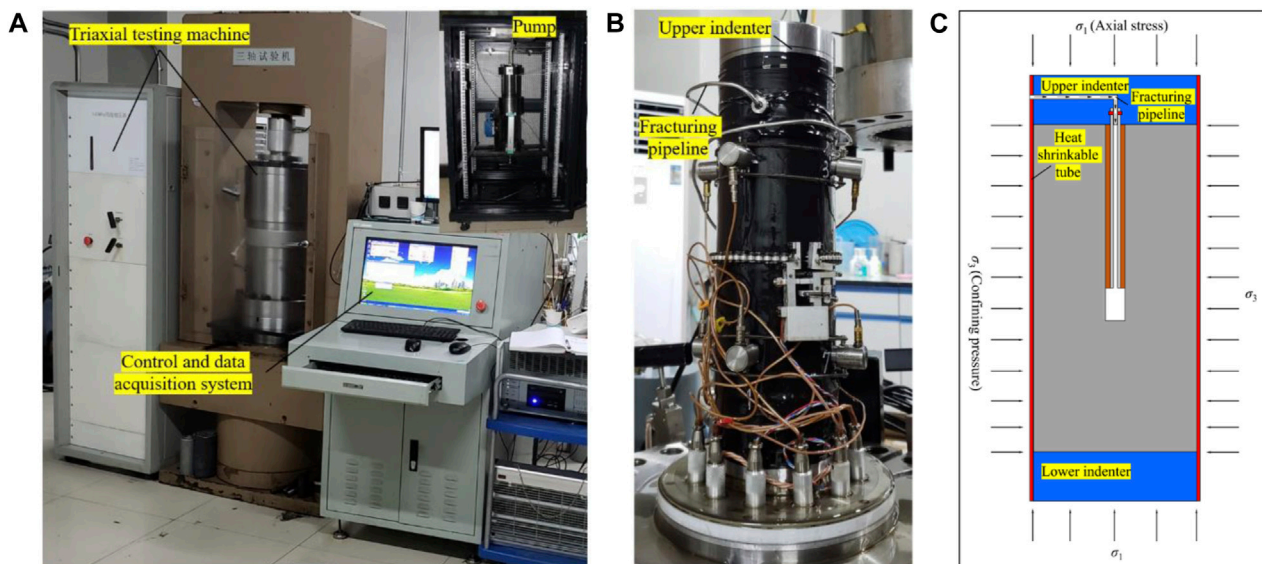

FIGURE 3
Laboratory hydraulic fracturing system: **(A)** main experimental equipment, **(B)** assembled sample, and **(C)** stress state and fluid transportation.

4) The characterization of hydraulic fractures. After the drop in pumping pressure and the full extension of the hydraulic fractures, the post-test specimen was removed, and the characteristics of the induced hydraulic fractures were recorded, described, and analyzed in detail. CT scanning was implemented on specimens with typical hydraulic fracture morphologies.

2.3.2 Experimental scheme

In uniaxial compressive experiments, five samples are tested by controlling a constant axial displacement rate of 0.12 mm/min. The uniaxial compressive strength, Young's modulus, and Poisson's ratio could be measured. In Brazilian indirect tensile tests, the ten specimens are divided into two equal groups. Samples in one group are loaded along the bedding structure, while the other group is loaded perpendicular to the bedding. Therefore, the tensile strengths of both the bedding and matrix could be acquired.

Considering that the primary objective of this study is to investigate the features of the hydraulic fractures in marine shales, five primary controlling factors are selected in the experimental design. They are the deviatoric stress (σ_1-σ_3), confining pressure (σ_3), pumping rate (q), fracturing fluid type, and bedding angle (β). Comprehensively considering the *in situ* geological and field-fracturing operation parameters, the similarity criterion (De Pater et al., 1994; Crosby et al., 2002), and the capacity of the laboratory hydraulic fracturing system, the detailed experimental scheme is designed and listed in Table 1.

3 Experimental results and analysis

3.1 Basic physical and mechanical parameters

3.1.1 Mineral composition

From the XRD results, the outcrop shale mainly contained quartz, accounting for 69.78%. The content of albite ranked second and was 11.40%. The illite content was 10.93%, which was in the third place after quartz and albite. In addition, small amounts of calcite, pyrite, and dolomite were also detected (Table 2). The total content of brittle minerals (quartz+albite+calcite+dolomite) was nearly 90%, exhibiting great brittleness (Jarvie et al., 2007; Jin et al., 2015; Rahimzadeh Kivi et al., 2018).

3.1.2 Basic mechanical parameters

Laboratory mechanical tests show that the values of uniaxial compressive strength are distributed between 81.6 and 108.4 MPa, and the average value is 98.5 MPa. The values of Young's modulus and Poisson's ratio are 22.29–26.96 GPa (average value 24.11 GPa) and 0.17–0.24 (average value 0.20), respectively. Brazilian indirect tensile tests indicated that the tensile strengths of the matrix and bedding were 13.0 and 8.5 MPa, respectively, with a specific value of 1.5. This type of marine shale shows high strength, high Young's modulus, and low Poisson's ratio, which reflect strong brittleness. The collection of mechanical parameters is provided in Supplementary Table A1.

3.2 Breakdown pressure and fracture morphology under different factors

3.2.1 Deviatoric stress

Deviatoric stress (σ_1-σ_3) is defined as the difference between axial stress (σ_1) and confining pressure (σ_3). Under a normal fault stress state ($\sigma_V > \sigma_H > \sigma_h$), vertical stress ($\sigma_V$) could be simulated by axial stress (σ_1), and horizontal principal stress (σ_H, σ_h) could be represented by confining pressure (σ_3) in the experimental context. When the value of confining pressure remains constant, the variation in deviatoric stress could influence the interaction between hydraulic fractures and bedding structures.

As depicted in Figure 4, the pumping pressure increases slowly in the initial pumping stage, and then gradually accelerates with the continuous injection of the fracturing fluid. After reaching the peak point, the pressure curve drops sharply to zero in the absence of the confining pressure constraint. The breakdown pressure (pressure value at the peak point) (Yew, 1997) grows approximately linearly with increasing deviatoric stress. Specifically, at a deviatoric stress of 3 MPa, the breakdown pressure is 16.4 MPa. The value of p_b nearly doubles and reaches 30.95 MPa, when the deviatoric stress is set to 12 MPa.

The fracture morphology is also sensitive to the variation in deviatoric stress. At a deviatoric stress of 3 MPa (Figure 4C), double wing hydraulic fractures are formed in the vertical direction, with one side extending more fully. In addition, four bedding planes are also completely disturbed to crack. The hydraulic fractures and opened bedding planes are interconnected to present a relatively complex fracture morphology. As the deviatoric stress increases to 6 MPa, the main hydraulic cracks are still double wing-shaped. However, the opening of bedding structures is significantly inhibited. Although four bedding fractures can be observed, they are sparsely distributed and partially opened. It is noteworthy that a small portion of the filled natural fractures is activated and connected with the main hydraulic fractures. When the deviatoric stress reaches further to 9 MPa, the cracking of the bedding planes is further restricted in both quantity and degree. Only one bedding plane is partially opened. Under the condition of σ_1-σ_3=12 MPa, hydraulic fractures only propagate in the vertical direction, and the bedding structure remains intact throughout the whole hydrofracturing process. Therefore, the increase in deviatoric stress could observably hinder the cracking of bedding and reduce the complexity of the hydraulic fracture morphology.

TABLE 2 Mineral composition of outcrop shales.

Mineral type	Quartz	Albite	Calcite	Dolomite	Pyrite	Illite
Content (%)	69.78	11.40	2.80	2.16	2.93	10.93

The deviatoric stress usually grows with increasing burial depth. For deep shale gas resources (burial depth ≥3500 m), the absolute value of the vertical *in situ* stress could exceed 87.5 MPa (assuming a stress gradient of 2.5 MPa/100 m in the vertical direction), and the deviatoric stress would easily exceed 10 MPa. It could be inferred from the experimental results that the opening of the bedding fractures would be severely restricted, and the morphology of the hydraulic fractures would tend to be simple in deep shale formations. It would be difficult to form a complex fracture network similar to that in the shallow strata. The reservoir stimulation strategy should pay more attention to cyclic injection (Zhou et al., 2017; Zhou et al., 2019) and cluster spacing reduction.

3.2.2 Confining pressure

The exertion of confining pressure could be regarded as underground horizontal *in situ* stress. With increasing burial depth, the horizontal *in situ* stress grows synchronously, which inevitably affects the breakdown pressure and geometry of the hydraulic fractures.

As provided in Figure 5, the effect of confining pressure could greatly improve the pressure required to fracture the specimen. In the unconfined situation (σ_3=0 MPa), the breakdown pressure is just 16.42 MPa. When the confining pressure is set to 25 MPa, the breakdown pressure increases by more than double and reaches 51.36 MPa. As the confining pressure continuously increases to 30 MPa, the breakdown pressure reaches a new peak value of 60.80 MPa. Under the condition of confining pressure, the initiation of hydraulic fracture would have to overcome the tensile strength and two times the confining pressure, leading to a significant increase in the breakdown pressure.

Regarding fracture morphology, the amount and complexity of hydraulic fractures shows a declining trend with increasing confining pressure (Figure 5C). At a confining pressure of 25 MPa, specimen W-11 is well developed with cemented natural fractures. During the propagation of hydraulic fractures, these natural fractures are fully activated and connected. The interconnected hydraulic–bedding–natural fracture network is presented. In addition, it is worth noting that a sufficient opening of the bedding structure could be seen under all three conditions. Therefore, it could be inferred that confining pressure would not remarkably restrain the cracking of bedding planes.

3.2.3 Pumping rate

The pumping rate is one of the few controllable parameters in hydraulic fracturing. A large pumping rate could produce a high net pressure and promote the full extension of the hydraulic fractures into the formation. As the pumping rate increases from 0.01 ml/s to 0.04 ml/s, the breakdown pressure increases from 51.40 to 61.78 MPa (Figures 6A,B). The pressurizing rate (slope of the linear part of the pressure–time curve) also increases almost linearly (Figure 6C).

As photographed and depicted in Figure 6D, only double-wing hydraulic fractures are formed in all specimens. At a pumping rate of 0.01 ml/s, the trace of hydraulic fractures is subtle and not easy to observe with the naked eye. When the pumping rate increases to 0.04 ml/s, the fracture width becomes obvious. No bedding fractures are observed under any of the three conditions, which might be attributed to two aspects. One is the relatively large deviatoric stress (6 MPa), and the other is the locally undeveloped bedding structure.

3.2.4 Fracturing fluid type

Slick water and guar gum are two major injection fluids widely and heavily used in shale gas hydraulic fracturing. Slick water has low viscosity (usually below 10 mPa s) and can penetrate into tiny fractures, which is conducive to the formation of complex fractures. In contrast, guar gum bears high viscosity (10^1~10^2 mPa s), and its main duty is producing wide main fractures.

As shown in Figure 7A, pumping guar gum brings about a higher breakdown pressure than injecting slick water. Specifically, the peak value grows from 51.36 to 57.40 MPa, increasing by 11.8%. The fracture morphology also exhibits significant differences. The specimen, fractured by slick water, has not only the main hydraulic fractures, but also activated bedding and natural fractures. The final fracture morphology is relatively complex (Figure 7B). For the specimen stimulated by guar gum, only the main hydraulic fractures were formed, and the fracture geometry was very simple.

3.2.5 Bedding angle

Shale has a special bedding structure. The well trajectory is not always strictly vertical or horizontal to the bedding. As portrayed in Figure 8, with an increasing bedding angle, the breakdown pressure ascends after an initial declining trend. The minimum value is taken at a bedding angle of 30°. The curve shape of the pumping pressure *vs* time at β= 30° is also special, and does not exhibit significant post-peak drop
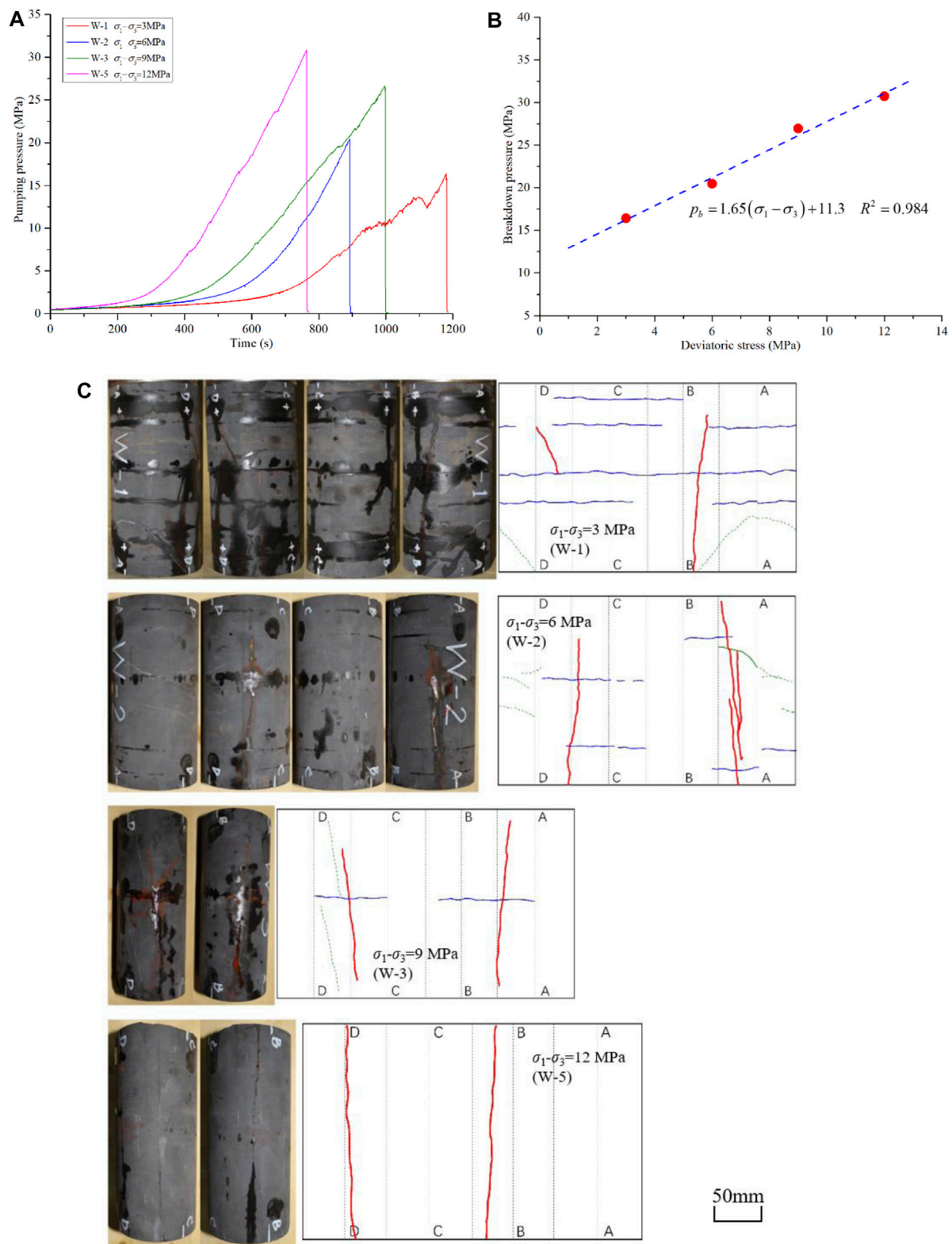
FIGURE 4
Pumping pressure and fracture morphology under different deviatoric stresses: **(A)** pumping pressure vs. time, **(B)** breakdown pressure vs. deviatoric stress, and **(C)** photographed and depicted surface distributions of the hydraulic fractures. (Red solid curves denote the main hydraulic fractures. Blue solid curves represent the opened bedding structures induced by hydraulic fracturing. Green dotted lines are closed natural fractures, and the part activated by hydraulic fracturing is replaced by green solid lines. Black dotted lines divide the whole area into eight equal parts, which are used to locate the relative position of the fractures.).
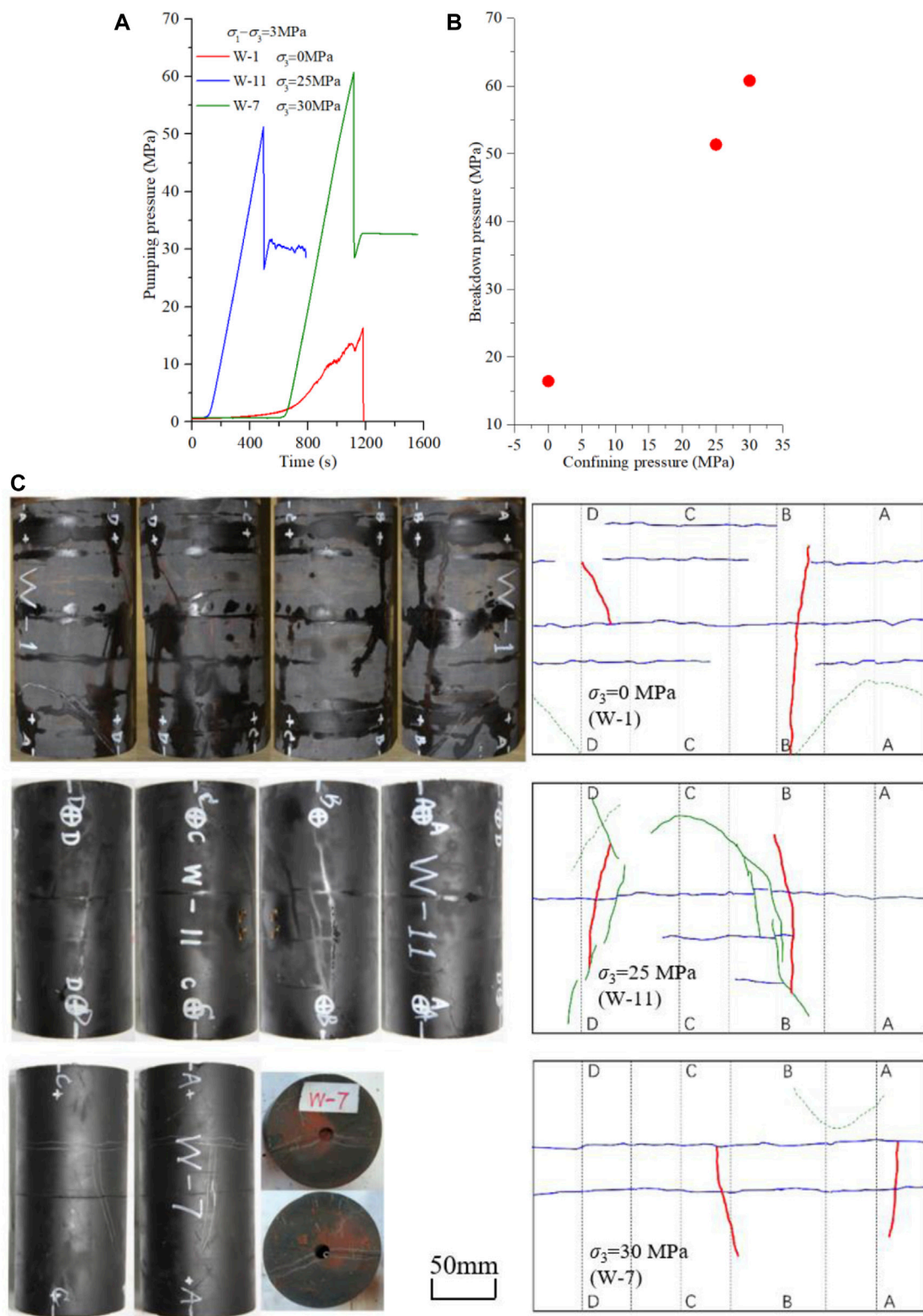
FIGURE 5
Pumping pressure curves and fracture morphologies at different confining pressures: **(A)** pumping pressure vs. time, **(B)** breakdown pressure vs. confining pressure, and **(C)** photographed and depicted surface distributions of hydraulic fractures.
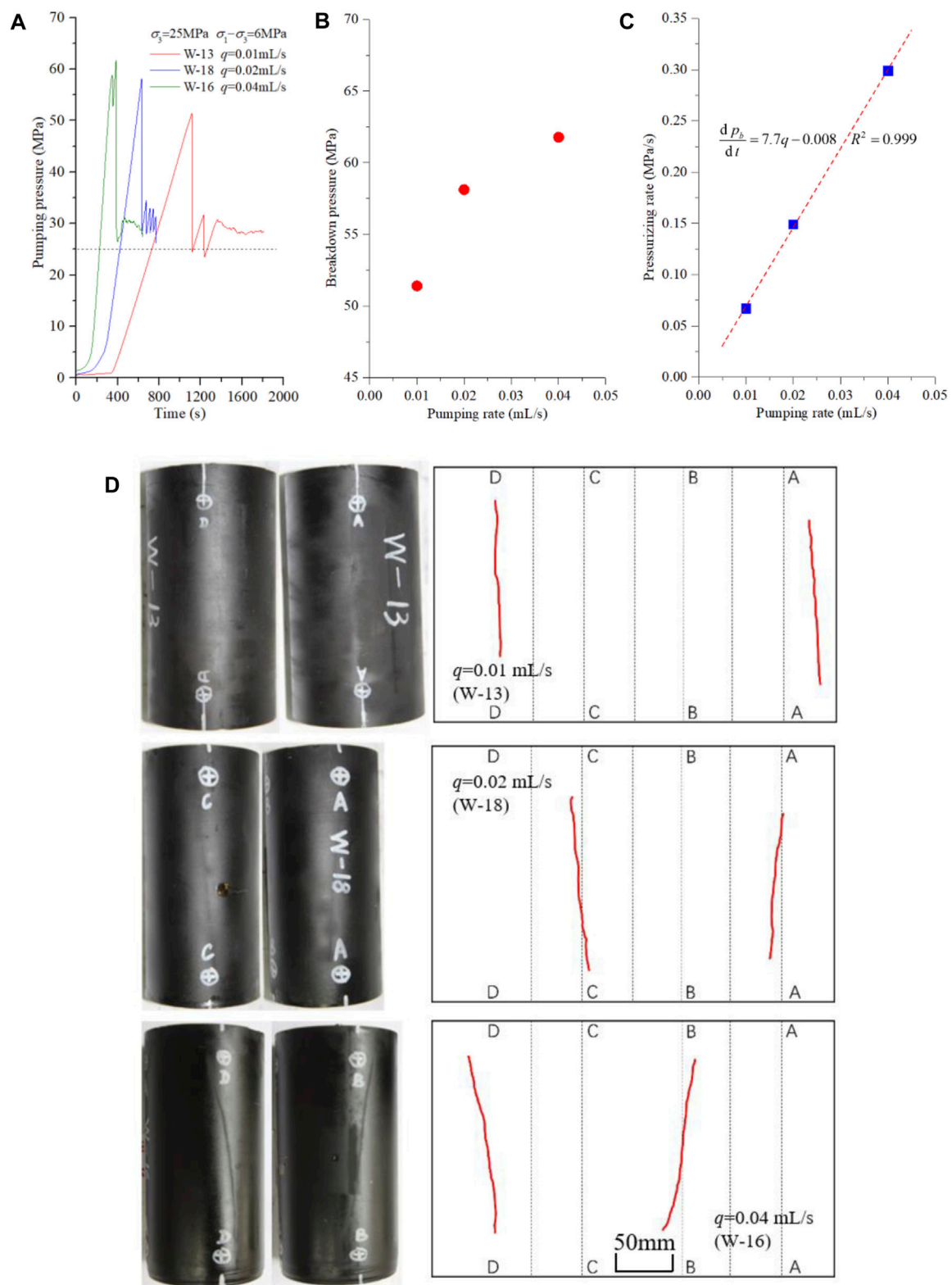
FIGURE 6
Pumping pressure curves and fracture morphologies at different pumping rates: **(A)** pumping pressure vs. time, **(B)** breakdown pressure vs. pumping rate, **(C)** pressurizing rate vs. pumping rate, and **(D)** photographed and depicted surface distributions of hydraulic fractures.
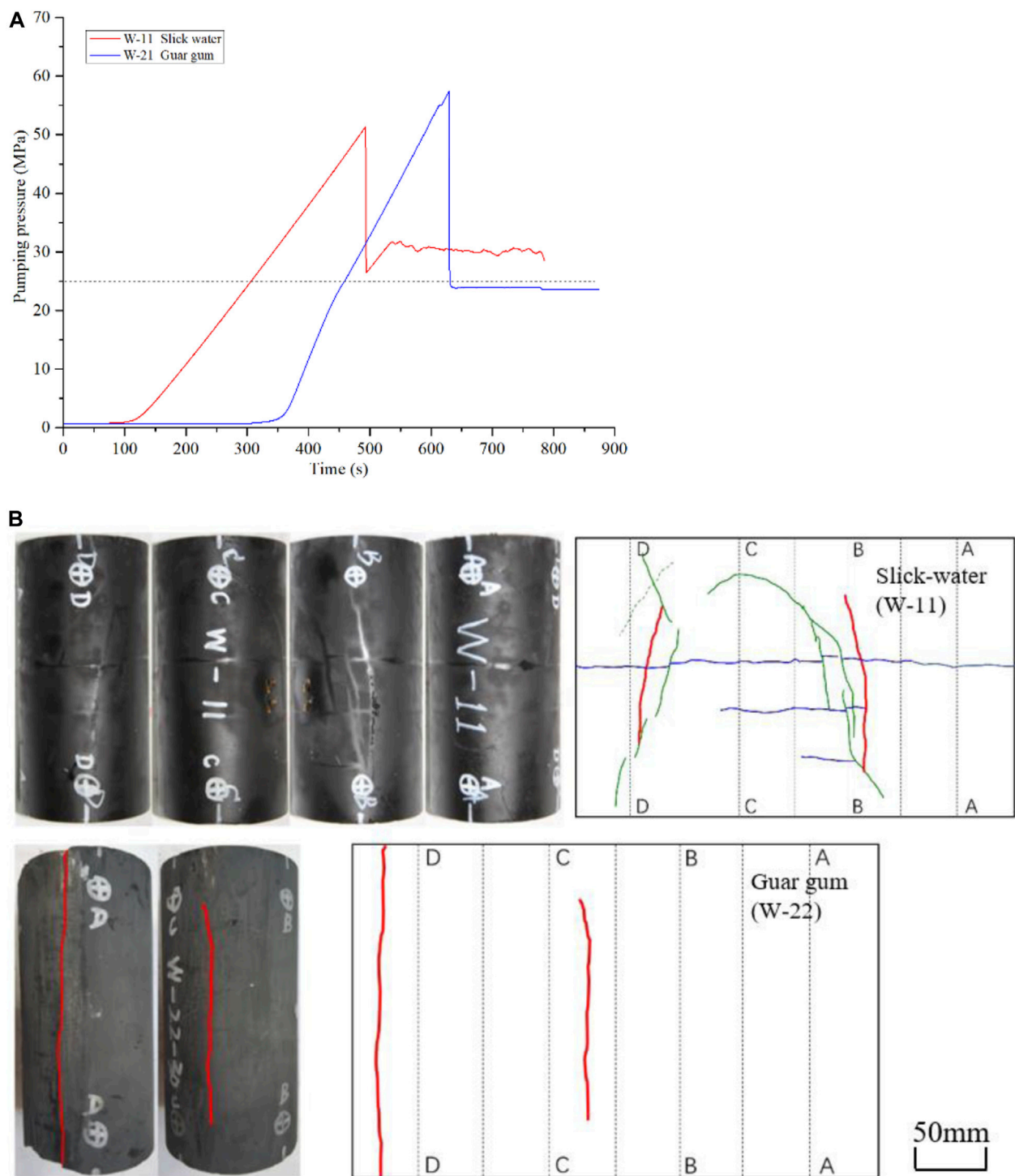
FIGURE 7
Pumping pressure curves and fracture morphologies at different fracturing fluid types: **(A)** pumping pressure vs. time, and **(B)** photographed and depicted surface distributions of hydraulic fractures.
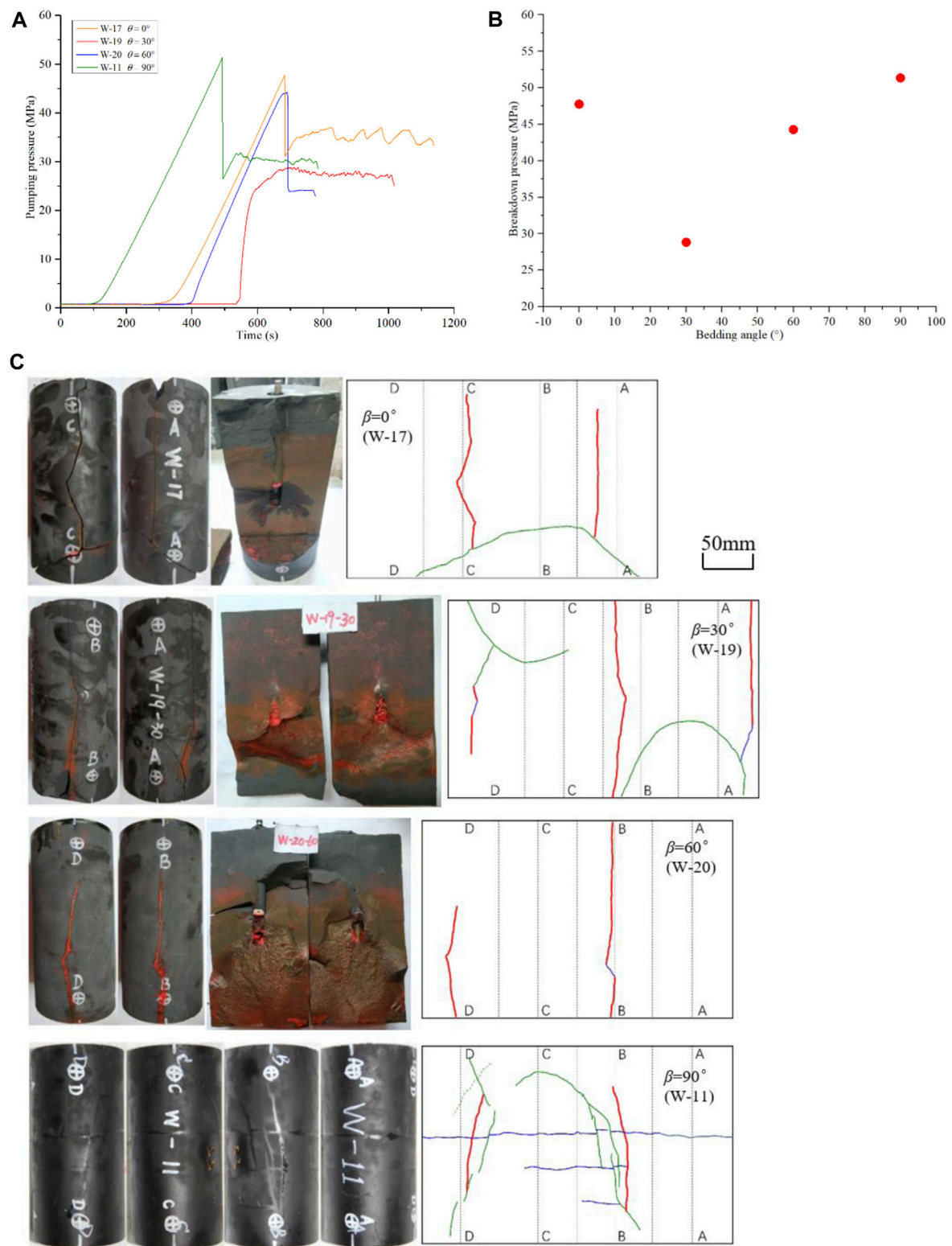
FIGURE 8
Pumping pressure curves and fracture morphology at different bedding angles: **(A)** pumping pressure vs. time, **(B)** breakdown pressure vs. bedding angle, and **(C)** photographed and depicted surface distributions of hydraulic fractures.

features. The reason might be that the initial hydraulic fractures quickly communicate with weak bedding or/and natural fractures.

The fracture morphology is also remarkably influenced by the bedding angle. For specimen W-17, at a bedding angle of 0° (Figure 8C), the drilling hole is coplanar with the bedding plane. Hydraulic cracks initiate from the open hole section and propagate along the bedding structure. In addition, a natural fracture is activated and opened. When the bedding angle is set to 30°, the propagation of the hydraulic fractures is still affected by the bedding structure. A main hydraulic fracture first initiates and propagates. Then, it reorients to the inclined bedding plane. The extended bedding fracture further activates a natural fracture. The final interconnected hydraulic–bedding–natural fractures are formed. At a bedding angle of 60°, the fracture morphology is relatively simple, but the bedding structure also participates in the formation of hydraulic fractures. A main hydraulic fracture is divided into two parts by a short path of bedding fracture, implying that the fracture has temporarily changed its direction to a bedding plane. At a bedding angle of 90°, the main hydraulic cracks pass through the bedding and continue to propagate along their previous vertical direction. However, they are finally arrested by natural fractures with a relatively small approaching angle.

The data of the breakdown pressures and various fracture lengths for all specimens can be found in Supplementary Table A2.

3.3 Fracture characterization by CT scanning

Based on the description of fracture geometry in Section 3.2.1–3.2.5, specimen W-11 is selected to implement CT scanning for its relatively complex fracture morphology (containing an interconnected hydraulic–bedding–natural fracture network).

As shown in Figure 9, three slice images of CT scanning are presented. In Figure 9A, the slice image is perpendicular to the axis of the borehole and in the open hole section. The main hydraulic fractures initiate from two opposite positions at the borehole wall and propagate to the boundary of the cylinder. The measured widths of the two hydraulic fractures are distributed in 155.4–211.3 μm (mean value 177.0 μm) and 143.7–185.4 μm (mean value 170.6 μm). This minor difference in the fracture width indicates a balanced extension in both directions. Another finding is that the crack width decreases as the fracture gradually moves away from the borehole.

In Figure 9B, the slice is along the axis of the borehole. Two natural fractures are recognized and measured. The first natural fracture is adjacent to the open hole section, and the values of the measured width vary largely between 367.1 and 621.4 μm, with an average value of 467.9 μm. The second fracture is in the

FIGURE 9
CT scanning images and fracture width measurement for specimen W-11: **(A)** slice image perpendicular to the axis of the borehole, **(B)** slice along the axis of the borehole, and **(C)** slice image parallel to the axis of the borehole with a certain offset.

lower part of the specimen. Its measured fracture width is 307.8–572.6 μm (mean value 430.8 μm). In Figure 9C, the slice image is parallel to the axis of the borehole with a certain offset. Three types of fractures (hydraulic, bedding, and natural fractures) are presented together. Hydraulic fracture 5 is vertical, and the average value of the fracture width is 203.7 μm. The opened bedding plane 6 is horizontal, with a mean width of 120.7 μm. Natural fracture 7 is gently oblique and has an average width of 203.2 μm. Different from the inclined natural fractures 3 and 4, natural fracture 7 extends nearly in the vertical direction. This implies that the formation mechanism of fracture 7 is tensile dominated, and the corresponding fracture width would be smaller, compared with shear-dominated fractures 3 and 4. Based on the aforementioned fracture classificat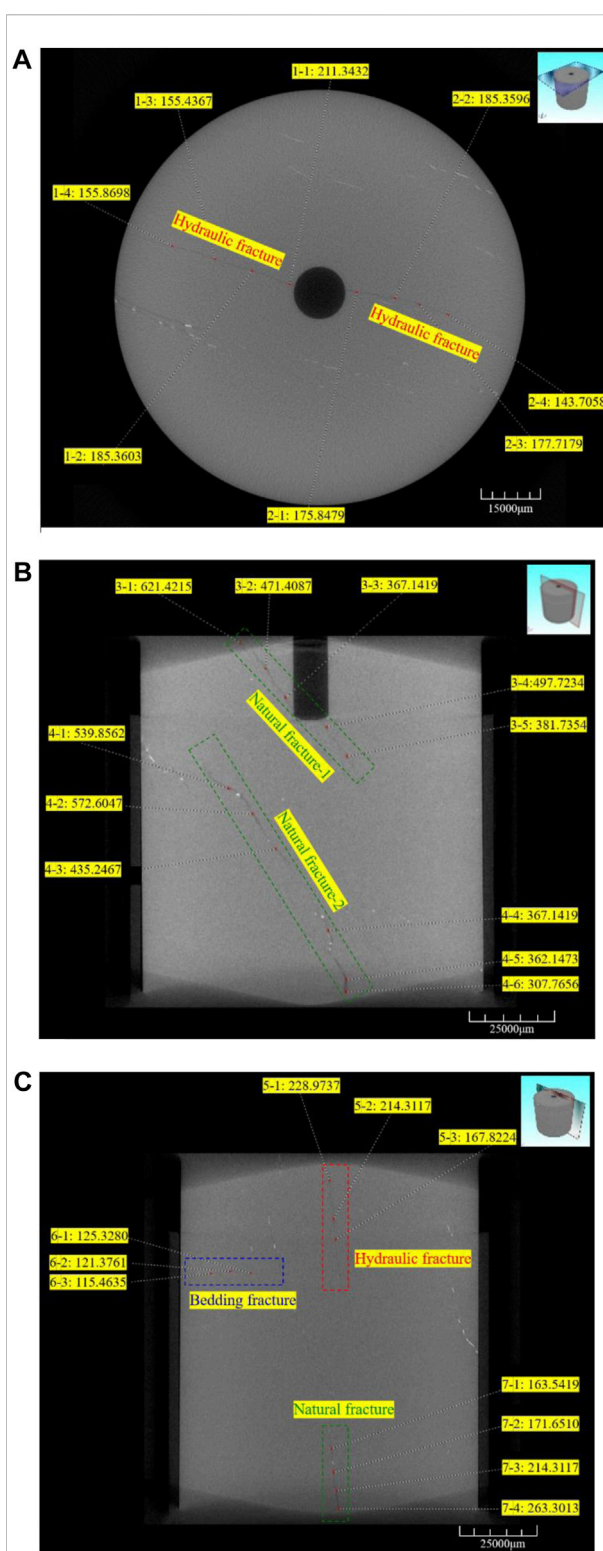ion and width measurement, the fracture width sorting is natural fracture > hydraulic fracture > bedding fracture. Natural fractures usually originate from tectonic shear failure. The mutual dislocation of fracture surfaces maintains a relatively large fracture width, even under compressive stress. The main hydraulic fracture is a kind of tension crack, which could gain a relatively better closure. The opened bedding is activated by hydraulic fractures. Because of the compression of overburden stress and low internal pressure, its width is the minimum among the three. The data of the measured fracture width from the CT images are listed in Supplementary Table A3.

4 Discussion

4.1 Parameter sensitivity analysis of breakdown pressure

The breakdown pressures under the five influencing factors are shown in Figure 10A. The variation ranges induced by each factor are different. Superficially, the alteration of confining pressure could bring about a substantial change in the breakdown pressure. The effect of deviatoric stress and bedding angle ranks second. The pumping rate and fracturing fluid type are in the last place. However, one thing worth noting is that these five influencing factors are not in unit consistency. Therefore, the aforementioned inference might not be correct, and parameter sensitivity analysis is needed.

Here, the relative change rate is applied to evaluate the parameter sensitivity of the breakdown pressure. The sensitivity index is expressed by:

$$S_i = \frac{(K_{i\max} - K_{i\min})}{(K_{i\max} + K_{i\min})/2} \bigg/ \frac{(X_{i\max} - X_{i\min})}{(X_{i\max} + X_{i\min})/2} \qquad (1)$$

where S_i is the breakdown pressure sensitivity index of parameter i; $K_{i\max}$ is the maximum value of breakdown pressure in parameter i; $K_{i\min}$ is the minimum value of breakdown pressure in parameter i; $X_{i\max}$ is the maximum value of parameter i; $X_{i\min}$ is the minimum value of parameter i; and i represents the five influencing factors: deviatoric stress, confining pressure, pumping rate, fracturing fluid type, and bedding angle.

By calculating the sensitivity index of each factor, we drew Figure 10B. It should be noted that viscosity was used to quantify the influence of slick water (5 mPa s) and guar gum (100 mPa s) in the sensitivity analysis. The sequence of factors that influence the variation range of the breakdown pressure is confining pressure, bedding angle, deviatoric stress, pumping rate, and fracturing fluid type. The sensitivity of confining pressure, bedding angle, and deviatoric stress is much greater than that of pumping rate and the fracturing fluid type. Confining pressure, bedding angle, and deviatoric stress should be classified as geological factors, which are inherent and usually uncontrollable. The pumping rate and fracturing fluid type are engineering factors that can be regulated and controlled. This demonstrates that geological factors would largely determine the breakdown pressure and engineering factors could only affect it to a lesser extent.

4.2 Statistical analysis of fracture length

The fracture length of each specimen is measured and recorded, according to the different fracture types. As shown in Figure 11, without considering the contribution of natural and bedding fractures, the length of the hydraulic fractures is only approximately 60–210 mm (average value 150 mm). In comparison, if the natural and/or bedding fracture could be fully activated under certain conditions, the total fracture length could increase up to 4 times and reach approximately 600 mm, greatly improving the fracture complexity and stimulated volume. Factors, such as low deviatoric stress, low confining pressure, low viscous slick water, and high bedding angle are conducive to activating natural and bedding fractures and forming a complex fracture network.

4.3 Influence of heterogeneity

Owing to the irregular development of natural fractures, the cylindrical specimens exhibit certain heterogeneity, which could inevitably affect the comparative analyses of the results. We tried to minimize the influence of heterogeneity from sample preparation to result analysis. During outcrop sampling, we selected shale blocks with relatively few natural fractures. Before hydraulic fracturing, a small value of pressure (0.5-1 MPa) is held to
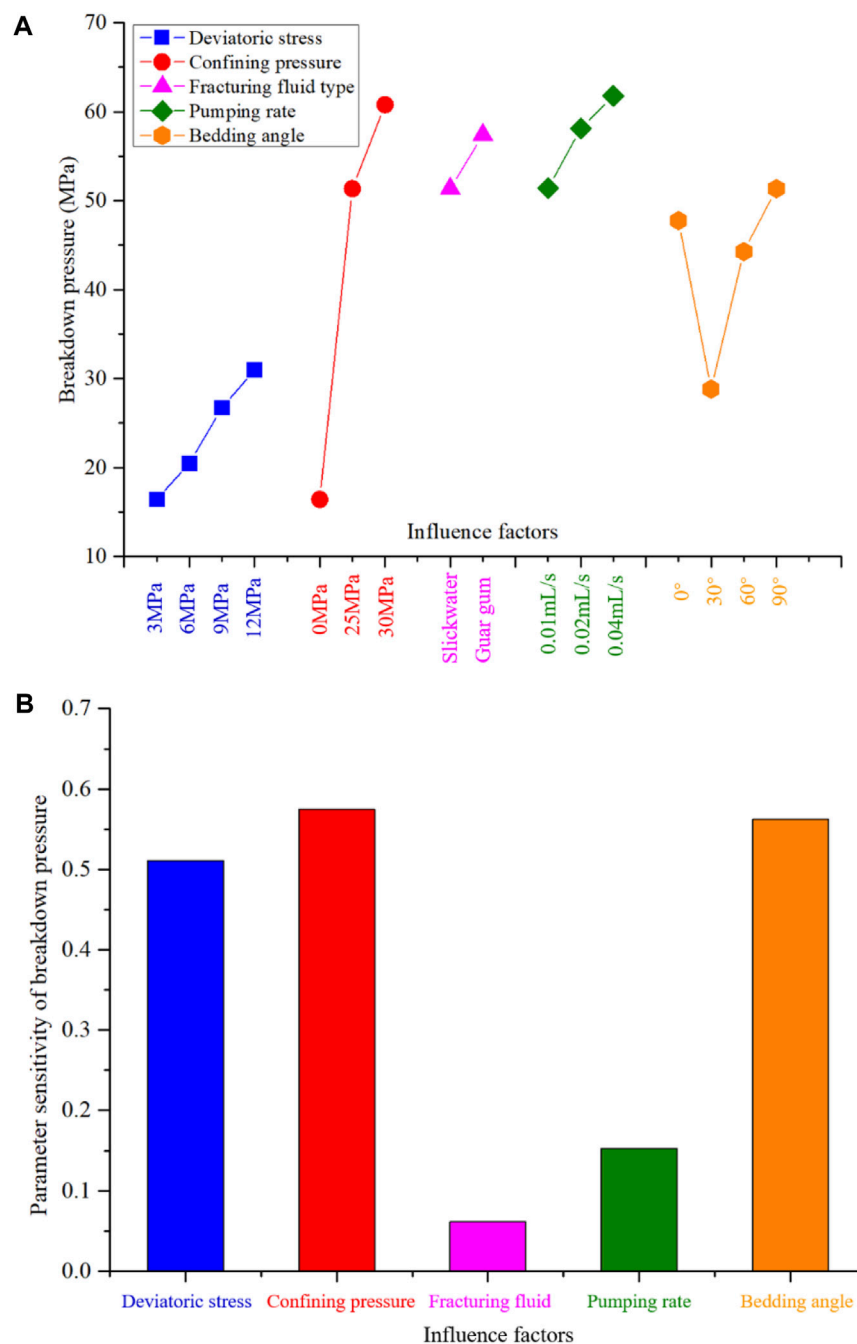
FIGURE 10
Breakdown pressures under various influence factors: **(A)** comparison of absolute values and **(B)** parameter sensitivity analysis.

check the tightness and integrity of the specimen. In this way, we could guarantee that the rock in the vicinity of the open hole is in a relatively intact state for all specimens. The initiation of hydraulic fractures can be regarded as being in a comparable state. The sharp pressure decline after the peak value demonstrates the initial intact state around the open

hole. Therefore, the test values of the breakdown pressures are little affected by the heterogeneity. During the propagation of hydraulic fractures, natural fractures affect the final morphology of the hydraulic fractures. The influence of natural fractures was depicted and quantitatively analyzed.
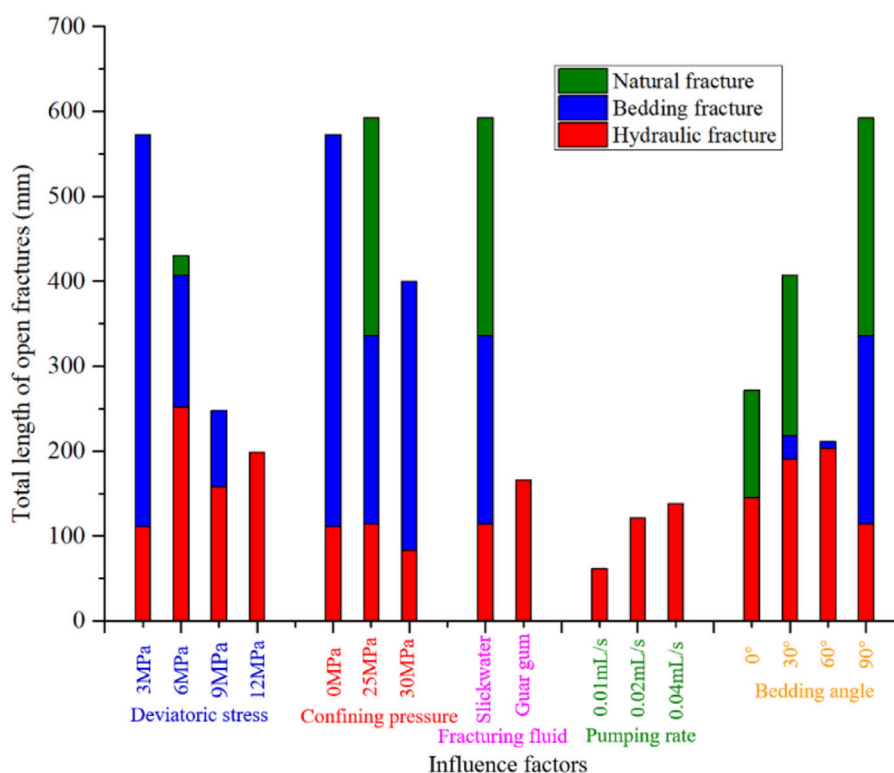
FIGURE 11
The total length of open fractures under various influence factors.

5 Conclusion

By considering the major geological and engineering factors, laboratory hydraulic fracturing experiments are implemented. Statistical analyses of breakdown pressure, fracture morphology, and parameter sensitivity are conducted. The conclusions are as follows:

1) The increase in deviatoric stress could significantly improve breakdown pressure and observably hinder the cracking of bedding planes, reducing the complexity of the hydraulic fracture morphology.
2) The width of the activated natural fractures (approximately 430 μm) is much greater than that of hydraulic fractures (170 μm) and opened bedding planes (120 μm), implying that the mutual dislocation of shear fracture surfaces could maintain a relatively large fracture width than the crack created by the tension mechanism.
3) By using the sensitivity analysis, the sequence of factors that influence the variation range of breakdown pressures is confining pressure, bedding angle, deviatoric stress, pumping rate, and fracturing fluid type. Geological factors would largely determine the breakdown pressure,

while engineering factors could only affect it to a lesser extent.
4) The length of the pure hydraulic fracture is quite limited. Low deviatoric stress, low confining pressure, low viscous slick water, and a high bedding angle are conducive to activating natural and bedding fractures and forming a complex fracture network.

Data availability statement

The original contributions presented in the study are included in the article/Supplementary Material; further inquiries can be directed to the corresponding author.

Author contributions

LW and JZ contributed to the conception and design of the study. JZ performed the statistical analysis. LW wrote the draft of the manuscript. XS and WG wrote sections of the manuscript. YG was responsible for review and editing. All authors contributed to manuscript revision, read, and approved the submitted version.

Funding

Conflict of interest

JZ was employed by the company CNOOC Research Institute Co., Ltd.

The remaining authors declare that the research was conducted in the absence of any commercial or financial relationships that could be construed as a potential conflict of interest.

Publisher's note

All claims expressed in this article are solely those of the authors and do not necessarily represent those of their affiliated organizations, or those of the publisher, the editors, and the reviewers. Any product that may be evaluated in this article, or claim that may be made by its manufacturer, is not guaranteed or endorsed by the publisher.

Supplementary material

The Supplementary Material for this article can be found online at: https://www.frontiersin.org/articles/10.3389/feart.2022.952655/full#supplementary-material

References

Cai, C., Kang, Y., Yang, Y., Wang, X., Li, Y., Huang, M., et al. (2020). The effect of shale bedding on supercritical CO2 jet fracturing: A experimental study. *J. Pet. Sci. Eng.* 195, 107798. doi:10.1016/j.petrol.2020.107798

Crosby, D. G., Rahman, M. M., Rahman, M. K., and Rahman, S. S. (2002). Single and multiple transverse fracture initiation from horizontal wells. *J. Pet. Sci. Eng.* 35, 191–204. doi:10.1016/S0920-4105(02)00243-7

De Pater, C. J., Cleary, M. P., Quinn, T. S., Barr, D. T., Johnson, D. E., and Weijers, L. (1994). Experimental verification of dimensional analysis for hydraulic fracturing. *SPE Prod. Facil.* 9, 230–238. doi:10.2118/24994-pa

Fisher, M. K., Heinze, J. R., Harris, C. D., Davidson, B. M., Wright, C. A., and Dunn, K. P. (2004). Optimizing horizontal completion techniques in the barnett shale using microseismic fracture mappina. *Proc. - SPE Annu. Tech. Conf. Exhib.*, 1099–1109. doi:10.2523/90051-ms

Guo, T., Zhang, S., Qu, Z., Zhou, T., Xiao, Y., and Gao, J. (2014). Experimental study of hydraulic fracturing for shale by stimulated reservoir volume. *Fuel* 128, 373–380. doi:10.1016/j.fuel.2014.03.029

Guo, Y., Hou, L., Yao, Y., Zuo, L., Wu, Z., and Wang, L. (2020). Experimental study on influencing factors of fracture propagation in fractured carbonate rocks. *J. Struct. Geol.* 131, 103955. doi:10.1016/j.jsg.2019.103955

He, J., Li, X., Yin, C., Zhang, Y., and Lin, C. (2020). Propagation and characterization of the micro cracks induced by hydraulic fracturing in shale. *Energy* 191, 116449. doi:10.1016/j.energy.2019.116449

Hou, B., Chang, Z., Fu, W., Muhadasi, Y., and Chen, M. (2019). Fracture initiation and propagation in a deep shale gas reservoir subject to an alternating-fluid-injection hydraulic-fracturing treatment. *SPE J.* 24, 1839–1855. doi:10.2118/195571-PA

Hou, B., Chen, M., Li, Z., Wang, Y., and Diao, C. (2014). Propagation area evaluation of hydraulic fracture networks in shale gas reservoirs. *Petroleum Explor. Dev.* 41, 833–838. doi:10.1016/S1876-3804(14)60101-4

Hou, B., Zhang, R., Zeng, Y., Fu, W., Muhadasi, Y., and Chen, M. (2018). Analysis of hydraulic fracture initiation and propagation in deep shale formation with high horizontal stress difference. *J. Pet. Sci. Eng.* 170, 231–243. doi:10.1016/j.petrol.2018.06.060

Jarvie, D. M., Hill, R. J., Ruble, T. E., and Pollastro, R. M. (2007). Unconventional shale-gas systems: The Mississippian Barnett Shale of north-central Texas as one model for thermogenic shale-gas assessment. *Am. Assoc. Pet. Geol. Bull.* 91, 475–499. doi:10.1306/12190606068

Jin, X., Shah, S. N., Roegiers, J. C., and Zhang, B. (2015). An integrated petrophysics and geomechanics approach for fracability evaluation in shale reservoirs. *SPE J.* 20, 518–526. doi:10.2118/168589-PA

Li, S., Liu, L., Chai, P., Li, X., He, J., Zhang, Z., et al. (2019). Imaging hydraulic fractures of shale cores using combined positron emission tomography and computed tomography (PET-CT) imaging technique. *J. Pet. Sci. Eng.* 182, 106283. doi:10.1016/j.petrol.2019.106283

Ma, Y., Cai, X., and Zhao, P. (2018). China's shale gas exploration and development: Understanding and practice. *Petroleum Explor. Dev.* 45, 589–603. doi:10.1016/S1876-3804(18)30065-X

Mayerhofer, M. J., Lolon, E. P., Rightmire, C., Walser, D., Cipolla, C. L., and Warplnskl, N. R. (2010). What is stimulated reservoir volume? *SPE Prod. Oper.* 25, 89–98. doi:10.2118/119890-PA

Rahimzadeh Kivi, I., Ameri, M., and Molladavoodi, H. (2018). Shale brittleness evaluation based on energy balance analysis of stress-strain curves. *J. Pet. Sci. Eng.* 167, 1–19. doi:10.1016/j.petrol.2018.03.061

Song, X., Guo, Y., Zhang, J., Sun, N., Shen, G., Chang, X., et al. (2019). Fracturing with carbon dioxide: From microscopic mechanism to reservoir application. *Joule* 3, 1913–1926. doi:10.1016/j.joule.2019.05.004

Tan, P., Jin, Y., Han, K., Hou, B., Guo, X., Gao, J., et al. (2017). Analysis of hydraulic fracture initiation and vertical propagation behavior in laminated shale formation. *Fuel* 206, 482–493. doi:10.1016/j.fuel.2017.05.033

Wang, L., Guo, Y., Yang, C., Xiao, J., Lu, C., and Song, Y. (2020). Mechanical characterization of continental shale in Sichuan Basin of China and its potential impact on reservoir stimulation. *J. Nat. Gas. Sci. Eng.* 79, 103346. doi:10.1016/j.jngse.2020.103346

Xu, Y., Lei, Q., Chen, M., Wu, Q., Yang, N., Weng, D., et al. (2018). Progress and development of volume stimulation techniques. *Petroleum Explor. Dev.* 45, 932–947. doi:10.1016/S1876-3804(18)30097-1

Yang, H., Guo, Y., Wang, L., Bi, Z., Guo, W., Zhao, G., et al. (2022). *Study on the Stimulation Effectiveness Evaluation of Large- Scale Hydraulic Fracturing Simulation Experiment Based on Optical Scanning Technology*, 1–19.

Yew, C. H. (1997). *Mechanics of hydraulic fracturing*. Houston, Texas: Gulf Publishing Company.

Zhang, J., Shi, M., Wang, D., Tong, Z., Hou, X., Niu, J., et al. (2021). Fields and directions for shale gas exploration in China. *Nat. Gas. Ind.* 41, 69–80. doi:10.3787/j.issn.1000-0976.2021.08.007

Zhang, X., Lu, Y., Tang, J., Zhou, Z., and Liao, Y. (2017). Experimental study on fracture initiation and propagation in shale using supercritical carbon dioxide fracturing. *Fuel* 190, 370–378. doi:10.1016/j.fuel.2016.10.120

Zhang, Y., He, J., Li, X., and Lin, C. (2019). Experimental study on the supercritical CO2 fracturing of shale considering anisotropic effects. *J. Pet. Sci. Eng.* 173, 932–940. doi:10.1016/j.petrol.2018.10.092

Zhou, Z. Le, Zhang, G. Q., Dong, H. R., Liu, Z. Bin, and Nie, Y. X. (2017). Creating a network of hydraulic fractures by cyclic pumping. *Int. J. Rock Mech. Min. Sci.* 97 (1997), 52–63. doi:10.1016/j.ijrmms.2017.06.009

Zhou, Z. Le, Zhang, G. Q., Xing, Y. K., Fan, Z. Y., Zhang, X., and Kasperczyk, D. (2019). A laboratory study of multiple fracture initiation from perforation clusters by cyclic pumping. *Rock Mech. Rock Eng.* 52, 827–840. doi:10.1007/s00603-018-1636-5

Zou, C., Ding, Y., Lu, Y., Liu, X., Chen, J., Wang, X., et al. (2017). Concept, technology and practice of "man-made reservoirs" development. *Petroleum Explor. Dev.* 44, 146–158. doi:10.1016/S1876-3804(17)30019-8

Zou, C., Zhu, R., Chen, Z. Q., Ogg, J. G., Wu, S., Dong, D., et al. (2019). Organic-matter-rich shales of China. *Earth. Sci. Rev.* 189, 51–78. doi:10.1016/j.earscirev.2018.12.002

Adaptability of hydraulic fracturing packers and optimization of their sealing performance for three common clastic rock reservoirs based on finite element analysis

Yusen Kang[1]*, Zhilin Long[1]*, Tengfang Kang[2], Zhuohang Ren[1], Tianzi Shi[1] and Xinrui Zhang[1]

[1]College of Civil Engineering and Mechanics, Xiangtan University, Xiangtan, China, [2]College of Mechanical and Transportation Engineering, China University of Petroleum, Beijing, China

In this paper, the adaptability characteristics of the packer to three types of common clastic rock reservoirs (mudstone, shale, sandstone) are analyzed systematically. Moreover, the identification and structural design of the packer in hydraulic fracturing are systematically conducted based on the finite element calculation. Finally, the nonlinear mathematical models of the packing safety factor and the pressure under the packer and the conditions of casing, mudstone, shale and sandstone are obtained. The results show that the maximum stress of the rubber cylinder in the three formation models of mudstone, shale and sandstone is lower than the compression set strength of the rubber cylinder, indicating that the rubber cylinder will not cause stress damage. At the same time, by analyzing the common rubber materials and constitutive models of the packers, the structure of the packer rubber cylinder and a new anti-shoulder protrusion device were redesigned. The Nitrile-butadiene rubber (NBR) meets the performance requirements of the rubber tube under the allowable pressure difference and temperature difference. The designed new anti-protrusion device can ensure the structural integrity and stress uniformity of the rubber tube, thereby ensuring good sealing performance. Under the three formation conditions of mudstone, shale and sandstone, the rubber cartridge can be in a safe working state, and its sealing width is close to the contact length of the rubber cartridge. In addition, the rubber cartridge is in a good elastic deformation range. The design of the packer in this study satisfies the third strength theory and the safety requirements. The deformation and sealing performance of the rubber cylinder are relatively stable, and the size of the rubber cylinder also meets the field requirements.

KEYWORDS

fracturing, packer, structural optimization of rubber cylinder, finite element analysis, performance optimization

Introduction

The measurement of initial stress of underground rock mass has very important practical value to improve the development efficiency of tight oil and gas resources. In addition, the test of *in-situ* stress is also of great significance to the safe utilization of urban space, disaster reduction and prevention. Packers are the basic equipment for obtaining *in-situ* stress in hydraulic fracturing tests (Yohannes., 2017; Huang et al., 2020). The research object of this study is the Jurassic Ziliujing Formation in the X area of the Sichuan Basin, China. Typically, the rocks encountered by packers in the formation are mainly mudstone, shale, and sandstone. Hydraulic fracturing is one of the methods for measuring *in-situ* stress specified by the International Professional Committee of Rock Mechanics Testing Technology, and it is also the most effective method for measuring deep *in-situ* stresses. At present, the differential pressure of some newly developed bridging packers in the world is around 35 MPa, which cannot fully meet the temperature and pressure conditions required for deep hole geostress testing (Wakuda et al., 2002; Zhao et al., 2021a; Zhao et al., 2021b; Liu et al., 2022; Zhao et al., 2022; Zheng et al., 2022). Packers are important tools for downhole stress measurements. The sealing rubber material of the packer is prone to have problems such as stress relaxation and shoulder protrusion under high temperature and high pressure or tough

environment, furthermore, it will lead to sealing failures (Akhtar et al., 2012). Shale is developed in the Jurassic Ziliujing Formation in the Sichuan Basin, and the shale has strong toughness or creep characteristics. It is easy to soften and expand after soaking with annotation, and it has small deformation modulus and poor sliding stability. There are a large number of interlayer pores and micro-fractures developed in shale rocks (Figure 1), thus higher requirements for deep hole *in-situ* stress testing are needed.

In order to improve the performance of the rubber cartridge, some scholars have carried out related research on the selection and design of the packer (Lan et al., 2019; Liu et al., 2020; Zheng et al., 2022). However, in the research on the improvement of the rubber tube structures of the packer and the selection of rubber materials, there is no systematic analysis of the influence of different lithologies on the adaptability of the packer. Existing models mainly assume that rubber is a linear elastic material with a fixed elastic modulus, which ignores the highly nonlinear and hyperelastic properties between the rubber barrel and the casing. Furthermore, these studies generally did not consider the effect of the anti-shoulder structure on sealing performance.

Based on the current problems in the research of packers in hydraulic fracturing, this study systematically analyzes the influence of three common lithologies on the contact pressure of packers. The outburst prevention device contacts directly with
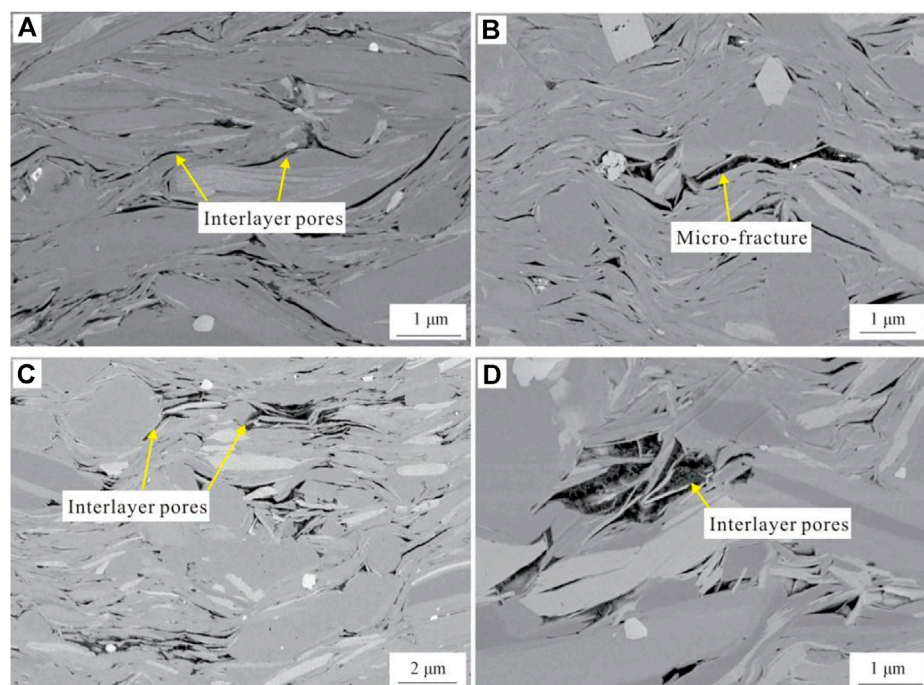
FIGURE 1
Development characteristics of interlayer pores and microfractures in the Ziliujing Formation shale in the Sichuan Basin (Liu et al., 2021). Notes: **(A)** Well F1, 2736.3 m; **(B)** Well X101, 2149.77 m; **(C)** WellX101, 2269.94 m; **(D)**Well Y30, 4007.13 m.

TABLE 1 Comparison of properties of different types of rubber materials.

Materials	Advantage	Disadvantage
Fluororubber	Good heat resistance and aging resistance	Poor plasticity, not easy to be processed and formed
Nitrile rubber	High tensile strength, easy molding, low cost	Easy to fail under high temperature and high pressure
Hydrogenated nitrile rubber	Good heat resistance and high wear resistance	High viscosity, poor processability

TABLE 2 Physical properties of nitrile rubber.

Elongation (%)	525-450
Tensile strength (MPa)	19.0-17.6
Tear strength (MPa)	1.8-1.4
Hardness (Shore A)	70°

the rubber materials. We have designed a novel outburst prevention device according to high nonlinearity and superelasticity of rubber materials. Then, a finite element model of the packer is established based on the highly nonlinear and hyperelastic properties of the rubber material. The results of finite element analysis show that the sealing performance of the rubber cylinder with the new anti-outburst device has been significantly improved.

Materials and methods

Selection of cartridge material

The maximum working pressure difference and temperature of the packer are mainly limited by the material of the rubber barrel, and the choice of material is a key factor in the design of the packer tube (Luo et al., 2002; Bu et al., 2011; Li et al., 2013; Dorokhov et al., 2016). The main rubber materials of compression packers are fluorine rubber, nitrile rubber, and hydrogenated nitrile rubber. The advantages and disadvantages of these materials are shown in Table 1. By comparing these materials, nitrile rubber (NBR) has the following advantages: high tensile strength and elastic modulus, easy molding, and low cost. At the same time, it can be applied to the three clastic rock lithologic formations in this paper, and its physical properties are shown in Table 2.

Constitutive models

Rubber material is a typical nonlinear material, its elastic properties are related to hardness, load size, load frequency and other factors, therefore it cannot be represented by a simple elastic modulus. In the study of constitutive relation of rubber, the phenomenological theory is used to describe its stress-strain relation. It assumes that rubber is isotropic in undeformed state and considers rubber as an incompressible material, it is difficult to obtain a reasonable structure of the sealing unit through theoretical calculation when designing the structure of the rubber cylinder (Guo et al., 2011; Polonsky and Tyurin., 2015; Zhang et al., 2017). In the analysis and calculation of rubber components, the highly nonlinear and superplastic models include Mooney-Rivlin model, Yeoh model and Gent model. The applicability of these models is shown in Table 3.

The Yeoh model and the Gent model cannot be used for moderate and small deformation, while the Mooney-Rivlin model can better fit the stress-strain relationship of incompressible rubber materials at moderate deformation. Therefore, the Mooney-Rivlin model is selected in this study.

The strain energy density function in the Mooney-Rivlin model is expressed as:

$$W = C_{10}(I_1 - 3) + C_{01}(I_2 - 3) \tag{1}$$

where W is the strain potential energy, I_1 and I_2 are the deformation tensors, and C_{10} and C_{01} are the Mooney material coefficients.

The Poisson's ratio of incompressible rubber materials can generally be set to 0.5. When the rubber material is in the small strain region, the relationship between its elastic modulus E_0, shear modulus G_0 and material coefficient can be expressed as:

$$G_0 = \frac{E_0}{3} = 2(C_{10} + C_{01}) \tag{2}$$

According to the fitting results of the experimental data of rubber hardness and elastic modulus, the relationship between rubber hardness H and elastic modulus E_0 can be obtained:

$$\lg E_0 = 0.0198H - 0.5432 \tag{3}$$

From Eqs 2, 3, the relationship between hardness and material coefficient can be expressed as:

$$6C_{10}\left(1 + \frac{C_{10}}{C_{01}}\right) = 10^{0.0198H - 0.5432} \tag{4}$$

The ratio of C_{10} to C_{01} is usually between 0.3 and 0.7. In this study, C10/C01=0.5. The mechanical properties of the rubber material constitutive model are shown in Table 4.

TABLE 3 Comparison of different constitutive models.

Model	Advantage	Disadvantage
Yeoh model	It can simulate the mechanical behavior of rubber materials under large deformation	Not suitable for medium and small deformation
Gent model	It can simulate the strain energy of rubber materials under large deformation	Not suitable for medium and small deformation
Mooney-Rivlin model	It can fit the stress-strain relationship of incompressible rubber materials, and is suitable for medium and small deformation	Undetermined parameters are difficult to obtain from manuals or references

TABLE 4 Mechanical properties of rubber materials.

Serial number	Hardness (IRHD)	Elastic modulus (MPa)	Mooney material factor	
			C10	C01
1	60	4.42	0.491	0.294
2	65	5.54	0.616	0.307
3	70	6.96	0.774	0.387
4	75	8.75	0.972	0.486
5	80	10.98	1.221	0.610
6	85	13.80	1.533	0.767
7	90	17.33	1.926	0.963
8	95	21.77	2.420	1.410

Finite element simulation

The finite element method is a principle of the finite element method, which uses an electronic computer to solve the numerical solution of problems such as static and dynamic characteristics of complex structures. It has high precision, strong adaptability and wide application range. At present, the finite element analysis software used to solve nonlinear material problems mainly includes ANSYS and ABAQUS.

ANSYS (Analysis System) is a large-scale CAE general finite element analysis software that integrates structure, heat, fluid, electromagnetic and acoustics, and has powerful and extensive geomechanical analysis functions. It is widely used in linear and nonlinear problems with multi-physical fields such as structure, heat, fluid, electromagnetic, acoustics, and multi-field coupling.

ABAQUS software is a relatively powerful finite element software in the field of engineering simulation, especially in solving complex nonlinear problems. The ABAQUS operation interface is simple and user-friendly, and complex problems can be "simplified" through the combination of various option blocks, so that highly nonlinear problems can be simulated.

Compared with ANSYS, ABAQUS adopts the parametric modeling method, which provides a powerful tool for parameter design and optimization of actual engineering structures and structural modification. Moreover, ABAQUS adopts CAD modeling and visualization window system, which has good human-computer interaction characteristics. Based on the

above analysis, the ABAQUS software was selected for the nonlinear finite element analysis of the packer cylinder group in this study.

Results

Influence of lithology on the contact pressure of packer

Different lithologic formations have different pore structures and rock mechanical properties. The scanning electron microscope images and rock mechanical parameters of typical mudstone, shale and sandstone of the artesian well formation in the study area are shown in Figure 2. Sandstone has the highest compressive strength and elastic modulus (uniaxial condition), followed by shale and mudstone, respectively. Cohesion represents the degree of aggregation between particles within a rock. The results show that loose mudstone has the lowest cohesion value, while sandstone with dense massive structure has the highest cohesion value.

Due to the different lithology of the formation, the packing performance of the packer and the formation is also different. Under the pressure environment of the downhole packer, the contact pressure between the rubber cylinder and the formation should be greater than the gas channeling pressure on either side, so that the gas channeling channel can be cut off. Only by

FIGURE 2
Microstructures of clastic rock formations of different types
of lithology based on SEM observations. Notes: **(A)** Mudstone, Well
S1, 2243 m; **(B)** Shale, Well S1, 2247 m; **(C)** Sandstone, Well S1,
2255 m.

FIGURE 3
Relationship between the isolation safety factor and the
pressure under the rubber cylinder.
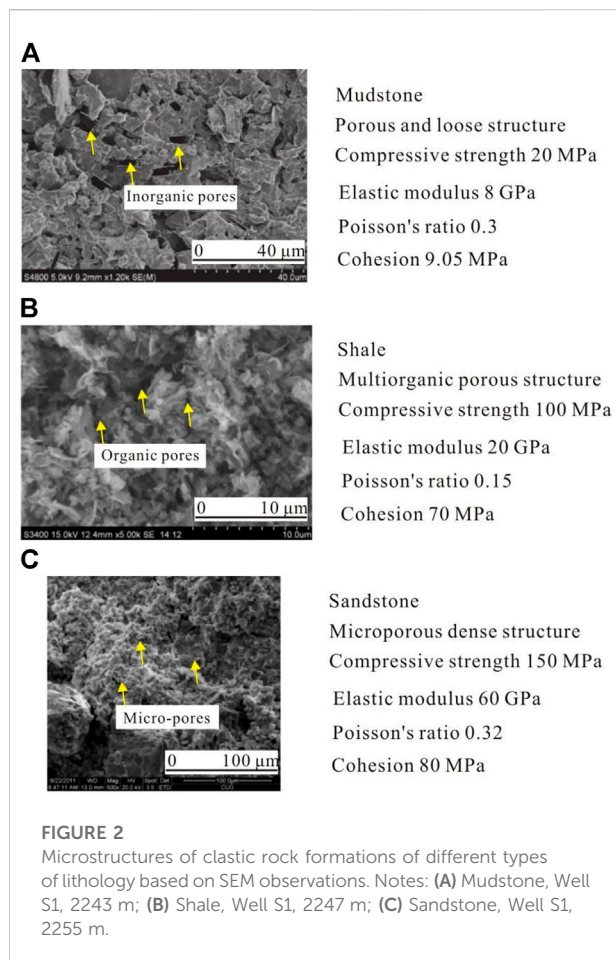
ensuring that the upper or lower gas channeling cannot pass through the contact surface between the rubber cylinder and the formation, can the packer be able to absolutely effectively seal the upper and lower pressures. Therefore, as long as the contact pressure between the rubber cylinder and the well wall is greater than the pressure below the rubber cylinder, it can be determined that the rubber cylinder can effectively seal the upper and lower pressure differences in this case.

In this study, a parameter to characterize effective containment, the packer safety coefficient (S), was introduced. It is defined as the ratio of the maximum contact pressure of the packer cartridge to the pressure below the cartridge. It assumes that the pressure below the packer is greater than the pressure above it. If the obtained packing safety factor is greater than 1, it can be determined that the packer can effectively pack the upper and lower pressure difference in the downhole.

According to the lithological parameters in Figure 2, the casing material takes yield strength σ=835 MPa, elastic modulus E=210 GPa, and Poisson's ratio μ=0.28. By keeping the pressure above the packer rubber cylinder at 40 MPa, the contact pressure between the packer and the formation can be calculated using finite element, under different lithologic
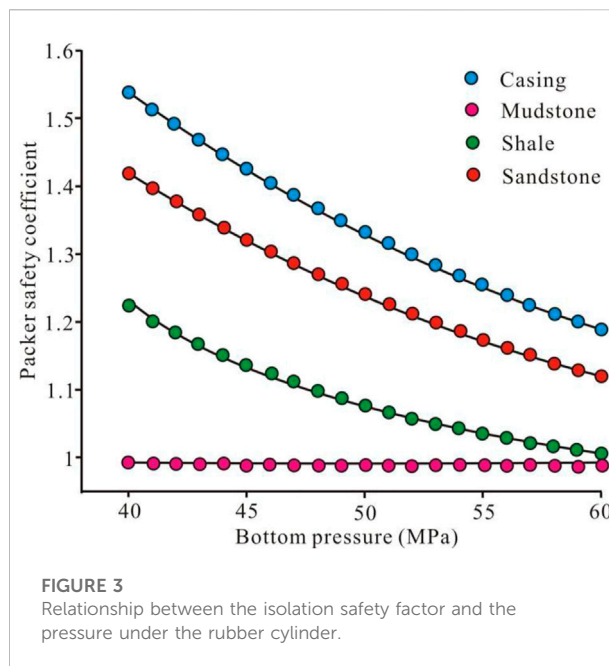
formations and different pressure conditions below the rubber cylinder. The length of the rubber barrel is 0.8 m, and the interference thickness is 3 mm. The interference thickness is the value of the interference fit between the rubber cylinder and the formation after expansion. In turn, the containment safety factor is obtained (Figure 3).

Using the least squares fitting curve, the nonlinear mathematical model of the packing safety factor and the pressure under the packer can be obtained respectively under the formation conditions of casing, mudstone, shale and sandstone.

Casing:

$$S = 2.83116e^{-\frac{x}{28.26663}} + 0.848 \tag{5}$$

Mudstone:

$$S = 52.791.67e^{-\frac{x}{2.87485}} + 0.989 \tag{6}$$

Shale:

$$S = 4.64994e^{-\frac{x}{14.3954}} + 0.933 \tag{7}$$

Sandstone:

$$S = 2.57172e^{-\frac{x}{26.2973}} + 0.855 \tag{8}$$

In above formulas, S is the packer safety coefficient; x is the pressure under the rubber cylinder, where 40 MPa $< x <$ 60 MPa.

The above formulas (5–8) are empirical formulas established when the pressure below the packer rubber cylinder is 40–60 MPa. The application range of this empirical formula is further extended, that is, the pressure under the packer rubber cylinder is 40 ~ x MPa ($x \geq 40$). When S=1, that is, when it can just

FIGURE 4
Variation curve of the isolation safety factor with the pressure under the rubber cylinder under different formation models.

FIGURE 5
Variation of maximum formation shear stress under different contact pressures.

$$\sigma_{\max} = 7.10779^{-\frac{x}{199.9056}} - 5.89419 \qquad (12)$$

where $\sigma_{\max}$ is the rubber barrel stress, MPa; x is the bottom pressure, MPa.

After the above calculation of the stress of the rubber cylinder, the maximum stresses in the above four formation models are 7.146, 2.575, 2.740 and 3.707 MPa, which are lower than the compression set strength of the rubber material of the rubber cylinder of 23.9 MPa. This means that the rubber cartridge will not be damaged by stress under the pressure (40 MPa $< x <$ 60 MPa) under the rubber cylinder. Therefore, when the pressure above the rubber cylinder is 40 MPa and the pressure below the rubber cylinder is 40–60 MPa, the packer can safely seal the upper and lower pressure differences.

Cylinder stress under different lithology

In order for the packer to achieve the expected packing effect in the downhole, it must be ensured that the rubber tube of the packer does not undergo stress damage under the downhole pressure difference. The stress of the rubber cylinder under different formation models was calculated by finite element analysis, and the results are shown in Figure 4.

After the least squares curve fitting, the nonlinear mathematical models of the maximum stress under the casing, mudstone, shale, and sandstone under the pressure of 40–60 MPa were obtained.

Casing:

$$\sigma_{\max} = -19.1315e^{-\frac{x}{15.6194}} + 7.5241 \qquad (9)$$

Mudstone:

$$\sigma_{\max} = 30285.46e^{\frac{x}{870435.63}} - 30285.025 \qquad (10)$$

Shale:

$$\sigma_{\max} = 1.00439e^{\frac{x}{55.08032}} - 0.29937 \qquad (11)$$

Sandstone:

be sealed, the maximum safe lower pressure of the rubber cylinder under the four models is calculated respectively: casing $p_T=$ 82.704 MPa > sandstone $p_S=$ 75.772 MPa > shale $p_Y =$ 60.988 MPa > mudstone $p_N=$ 44.28 MPa.

Influence of packer working state on formation

The influence of the packer on the formation mainly refers to the influence of the contact pressure between the packer and the formation on the formation: ① If the contact pressure between the packer and the formation is too small, the packer cannot effectively seal the upper and lower pressure difference; ② If the contact pressure between the packer and the formation is too large, the formation or formation rock will be fractured and shear stress damage will occur.

This study assumes that only vertical wells are considered, and the effects of well inclination and azimuth on *in-situ* stress are ignored. Moreover, the horizontal *in-situ* stress is non-uniform, and the formation pore pressure is considered in the sandstone layer. Since the wellbore diameter is much smaller

than the well depth, the vertical wellbore model can be simplified as a plane strain problem. That is, the maximum horizontal principal stress σ_H acts at infinite distance in the X direction, the minimum horizontal principal stress σ_h acts at infinite distance in the Y direction, the packer contact pressure P acts on the inside of the wellbore, and the sandstone has the effect of overlying rock pressure.

In this study, considering that the packer is driven to a depth of 4 000 m, the triaxial stress state of the rock in the downhole is σ_H = 30 MPa, σ_h = 20 MPa, and the overburden pressure is 40 MPa. Furthermore, under this assumption, the formation shear stress under different lithologic formations and under different contact pressures is calculated by the finite element method. Figure 5 shows the change curves of the maximum formation shear stress under different lithologic formations and different contact pressures. It can be seen from Figure 5 that the maximum shear stress of the borehole formation under the action of triaxial stress increases linearly with the increase of the contact pressure of the rubber.

In addition, it can also be seen from Figure 5 that the straight line slope of the sandstone formation is the largest, followed by shale and mudstone. The slope represents the rate at which formation shear stress varies with packer contact pressure. Therefore, the maximum formation shear stress under different lithologic formations is proportional to the increasing rate of the packer contact pressure and the elastic modulus of the formation.

Thus, the relational models of formation shear stress and contact pressure under different lithologic formations and under different contact pressures are established.

Sandstone:

$$\tau = 0.6427p - 12.01 \tag{13}$$

Shale:

$$\tau = 0.627p - 11.84 \tag{14}$$

Mudstone:

$$\tau = 0.498p - 7.605 \tag{15}$$

where τ is the formation shear stress, MPa; p is the contact stress, MPa.

These models can be used to calculate the maximum safe contact pressure for shear stress failure in different lithologic formations. It provides the basic conditions for the structural optimization of the packer.

Calculation of cartridge parameters

In order to verify the sealing performance and bearing capacity of the compression packer, the basic size parameters and setting pressure of the packer cartridge are calculated as follows:

In order to facilitate installation and interchangeability, the inner diameter of the rubber barrel should be larger than the outer diameter of the central pipe, and it should contact and close the well wall quickly during the setting process. Therefore, the gap between the rubber barrel and the central tube should not be too large. The outer diameter of the central tube was 35 mm, and the inner diameter of the rubber cartridge was determined to be 35.5 mm.

The height of the rubber barrel determines the contact length between the rubber barrel and the hole wall, which is an important factor in determining the sealing performance. The relevant empirical formulas are:

$$\sigma_z = \frac{2ER_3}{1+\mu} \cdot \frac{R_3 - R_2}{R_3^2 - R_2^2} \tag{16}$$

$$F_\varepsilon = \int_{R_2}^{R_3} \sigma_z \cdot 2\pi r \mathrm{d}r \tag{17}$$

$$h = \frac{\Delta P(R_3^2 - R_1^2)}{2R_1[\tau] + R_3 f \cdot \frac{F_\varepsilon}{A} \cdot \frac{\mu}{1-\mu}} \tag{18}$$

In the formula, σ_z is the axial stress of the rubber tube; E is the elastic modulus of the rubber tube material; μ is the Poisson coefficient; R_3 is the inner diameter of the casing; R_2 is the outer diameter of the rubber tube; R_1 is the inner diameter of the rubber tube; h is the rubber The height of the pipe; f is the friction coefficient; $[\tau]$ is the allowable shear force of the rubber cylinder; A is the annular cross-sectional area between the central pipe and the well wall.

Since R_3=76 mm, R_2=72 mm, R_1=35.5 mm and ΔP=35 MPa, the axial stress and the height of the rubber cylinder can be calculated: F_ε=19.11 kN and h=100 mm.

The differential equation of radial displacement of elastic body is expressed as:

$$\frac{\mathrm{d}^2u}{\mathrm{d}r^2} + \frac{1}{r}\frac{\mathrm{d}u}{\mathrm{d}r} - \frac{u}{r^2} = 0 \tag{19}$$

where u is the radial displacement and r is the radius of curvature.

Its general solution can be expressed as:

$$u = Ar + \frac{B}{r} \tag{20}$$

where u is the radial displacement and r is the radius of curvature.

According to the boundary conditions, the definite integral can be calculated as:

$$u|_{r=R_0} = 0; u|_r = R_3 = R_3 - R_2 \tag{21}$$

Therefore,

$$A = \frac{(R_3 - R_2)R_3}{R_3^2 - R_1^2} \tag{22}$$
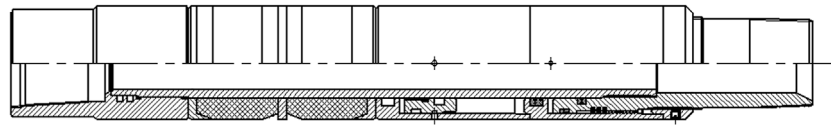
FIGURE 6
Schematic of a compression packer.
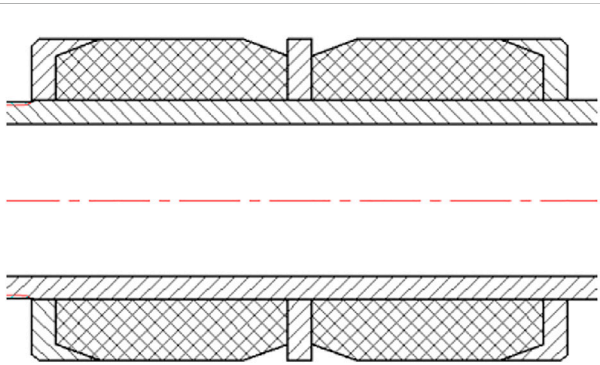
FIGURE 7
Schematic diagram of the rubber barrel structure.
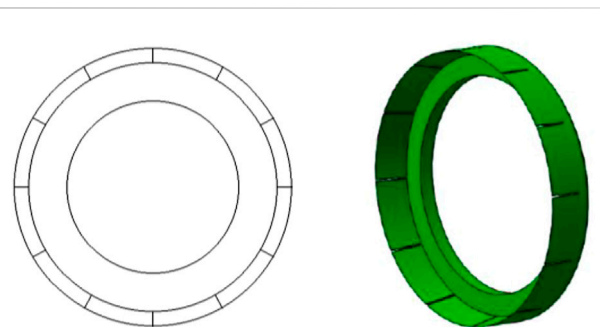
FIGURE 8
Schematic diagram of the shoulder pad structure.

$$B = -\frac{(R_3 - R_2)R_1^2 R_3}{R_3^2 - R_1^2} \tag{23}$$

In the formula, R_3 is the inner diameter of the casing, R_2 is the outer diameter of the rubber cylinder, and R_1 is the inner diameter of the rubber cylinder.

Substituting Eqs 22, 23 into the definite integral (20), the relative radial elongation ε_r and relative tangential elongation ε_θ can be obtained:

$$\varepsilon_r = \frac{\mathrm{d}u}{\mathrm{d}r} = \frac{(R_3 - R_2)R_3}{R_3^2 - R_1^2} + \frac{(R_3 - R_2)R_1^2 R_3}{r^2 (R_3^2 - R_1^2)} \tag{24}$$

$$\varepsilon_\theta = \frac{u}{r} = \frac{(R_3 - R_2)R_3}{R_3^2 - R_1^2} - \frac{(R_3 - R_2)R_1^2 R_3}{r^2 (R_3^2 - R_1^2)} \tag{25}$$

where u is the radial displacement, r is the radius of curvature, R_3 is the inner diameter of the casing, R_2 is the outer diameter of the rubber cylinder, and R_1 is the inner diameter of the rubber cylinder.

The change in volume of an elastomer θ can be expressed as:

$$\theta = \varepsilon_r + \varepsilon_\theta + \varepsilon_z \tag{26}$$

where ε_z is the relative axial elongation, ε_r is the relative radial elongation and ε_θ is the relative tangential elongation.

Assuming that the sealing element is incompressible, that is, $\theta = 0$, Eq. 26 can be expressed as:

$$\varepsilon_z = -(\varepsilon_r + \varepsilon_\theta) \tag{27}$$

where ε_z is the relative axial elongation, ε_r is the relative radial elongation and ε_θ is the relative tangential elongation.

Substituting Eqs 24, 25 into Eq. 27, the relative axial elongation ε_s can be obtained:

$$\varepsilon_z = \frac{2R_3 (R_3 - R_2)}{R_3^2 - R_1^2} \tag{28}$$

where R_3 is the inner diameter of the casing, R_2 is the outer diameter of the rubber cylinder, and R_1 is the inner diameter of the rubber cylinder.

According to generalized Hooke's law, radial, tangential, and axial normal components can be calculated:

$$\sigma_r = \frac{E}{(1 - 2\mu)(1 + \mu)} \left[(1 - \mu)\varepsilon_r + \mu (\varepsilon_\theta + \varepsilon_z) \right] \tag{29}$$

$$\sigma_\theta = \frac{E}{(1 - 2\mu)(1 + \mu)} \left[(1 - \mu)\varepsilon_\theta + \mu (\varepsilon_r + \varepsilon_z) \right] \tag{30}$$

$$\sigma_z = \frac{E}{(1 - 2\mu)(1 + \mu)} \left[(1 - \mu)\varepsilon_z + \mu (\varepsilon_\theta + \varepsilon_r) \right] \tag{31}$$

where ε_z is the relative axial elongation; ε_r is the relative radial elongation; and ε_θ is the relative tangential elongation; σ_r is the radial stress; σ_θ is the radial stress; σ_z is the radial stress; μ is the Poisson's coefficient; E is the elasticity modulus.

Further, the above three expressions can be transformed into:

$$\sigma_r = \frac{ER_3}{(1 + \mu)} \left(\frac{R_3 - R_2}{R_2^2 - R_1^2} \right) \left(1 + \frac{R_1^2}{r^2} \right) \tag{32}$$

FIGURE 9
Schematic diagram of the rubber barrel structure.

TABLE 5 Mechanical parameters of materials in key parts of packer.

Name	Elastic modulus (MPa)	Poisson's ratio	Material parameters
Rubber cartridge	10.98	0.490	$C_{01} = 0.610$ $C_{10} = 1.221$
Central tube	2.16×10^5	0.286	—
Spacer	2.06×10^5	0.300	—
Shoulder pads	2.06×10^5	0.300	—

$$\sigma_\theta = \frac{ER_3}{(1+\mu)} \left(\frac{R_3 - R_2}{R_3^2 - R_1^2} \right) \left(1 - \frac{R_1^2}{r^2} \right) \quad (33)$$

$$\sigma_z = \frac{-2ER_3}{1+\mu} \left(\frac{R_3 - R_2}{R_3^2 - R_1^2} \right) \quad (34)$$

where R_3 is the inner diameter of the casing; R_2 is the outer diameter of the rubber cylinder; R_1 is the inner diameter of the rubber cylinder; ε_z is the relative axial elongation; ε_r is the relative radial elongation; ε_θ is the relative tangential elongation; σ_r is the radial stress; σ_θ is the radial stress; σ_z is the radial stress; μ is the Poisson's coefficient; E is the elasticity modulus.

Substitute Eq. 34 into $F_\varepsilon = \int_{R_1}^{R_3} \sigma_z \cdot 2\pi r dr$, and the compressive force F_ε in plane deformation can be obtained:

$$F_\varepsilon = -2\pi \frac{ER_3}{1+\mu} (R_3 - R_2) \quad (35)$$

where R_3 is the inner diameter of the casing; R_2 is the outer diameter of the rubber cylinder; μ is the Poisson's coefficient; E is the elasticity modulus.

By analyzing the relationship between the force and deformation of the rubber cylinder under uniaxial compression, the equilibrium conditions of the force can be obtained:

$$\Delta P \cdot A_2 = f \left(P'_k S_1 + P_k S_2 \right) \quad (36)$$

In the formula, ΔP is the packer pressure difference; A_2 is the annular cross-sectional area between the packer center pipe and the well wall; f is the friction coefficient; P_k' and P_k are the pressures of the axial load acting on the inner and outer surfaces of the rubber cylinder; S_1 and S_2 are the lateral areas of the inner and outer sealing surfaces after the rubber tube is deformed.

The simplified calculation is as follows:

$$P'_k S_1 \approx P_k S_2 \, (a) \quad (37)$$

$$P'_k = P_k \quad (38)$$

where P_k' and P_k are the pressures of the axial load acting on the inner and outer surfaces of the rubber cylinder; S_1 and S_2 are the lateral areas of the inner and outer sealing surfaces after the rubber tube is deformed.

Therefore,

$$S_1 = S_2 = 2\pi R_1 (h - \Delta h) \quad (39)$$

where S_1 and S_2 are the lateral areas of the inner and outer sealing surfaces after the rubber tube is deformed; R_1 is the inner diameter of the rubber cylinder; h is the height of rubber tube.

Substituting Eq. 28 into Eq. 39, it can be transformed into $S_1 = S_2 = 2\pi R_1 h (1 - \varepsilon_z)$. Then, substituting it into formula (36), we can get:
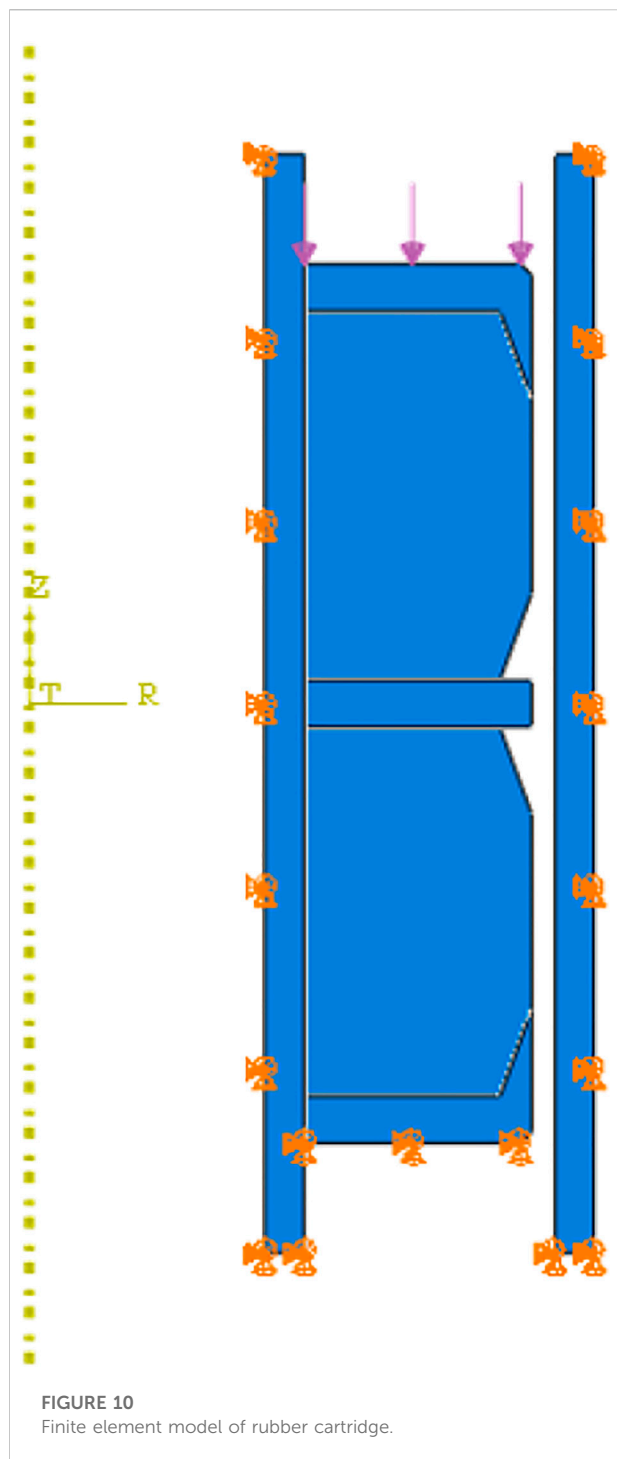
$$P_1 = \frac{\Delta P \left(R_3^2 - R_1^2 \right)}{4 f R_1 h \left(1 - \varepsilon_z \right)} \tag{40}$$

where R_3 is the inner diameter of the casing; R_1 is the inner diameter of the rubber cylinder; ΔP is the packer pressure difference; f is the friction coefficient; h is the height of rubber tube; ε_z is the relative axial elongation.

At the same time, when the axial load acts on the inner and outer sealing surfaces of the rubber cylinder, the radial pressure and the axial pressure are equal:

$$P_1 = \frac{F}{\pi \left(R_2^2 - R_1^2 \right)} \tag{41}$$

where F is the total compressive force; R_1 is the inner diameter of the rubber cylinder; R_2 is the outer diameter of the rubber cylinder;

The compressive load required for the packer to work in a sealed state is:

$$F_{\Delta P} = \frac{\pi \Delta P \left(R_3^2 - R_1^2 \right) \left(R_2^2 - R_1^2 \right)}{4 f R_1 h \left(1 - \varepsilon_z \right)} \tag{42}$$

where ΔP is the packer pressure difference; R_3 is the inner diameter of the casing; R_2 is the outer diameter of the rubber cylinder; R_1 is the inner diameter of the rubber cylinder; f is the friction coefficient; h is the height of rubber tube; ε_z is the relative axial elongation.

By substituting the known database into the above formula, the relative axial elongation ε_s, the compressive load $F_{\Delta P}$ in the sealed state, the compressive force F_ε in the plane deformation and the total compressive force F can be obtained:

$$\varepsilon_z = 0.135 \tag{43}$$

$$F_{\Delta P} = 66.06 kN \tag{44}$$

$$F_\varepsilon = -19.11 kN \tag{45}$$

$$F = F_\varepsilon + F_{\Delta P} = 46.95 kN \tag{46}$$

Furthermore, the pressure on the cartridge unit:

$$S = \pi \left(R_3^2 - R_1^2 \right) \tag{47}$$

$$P = \frac{F}{S} = 13.05 MPa \tag{48}$$

where S is the stress area of the total compressive force, mm2; P is the pressure on the cartridge unit, MPa.

Structural design of compression packer and rubber cylinder

The compression packer" is one that compresses the packer by axial force and enlarges the diameter of the packer to seal it. It's widely applicable and can be used in various conditions of deep Wells, ultra-deep Wells, directional Wells, horizontal Wells and window-side drilling. The compression packer cartridge consisting of two cartridges in this paper was selected as the study object. Its overall structure consists of a connecting device, a setting device, an anti-midway setting device, a locking device, a sealing device, etc., (Figure 6). The working principle is as follows: the piston and the central pipe are connected by threads, and
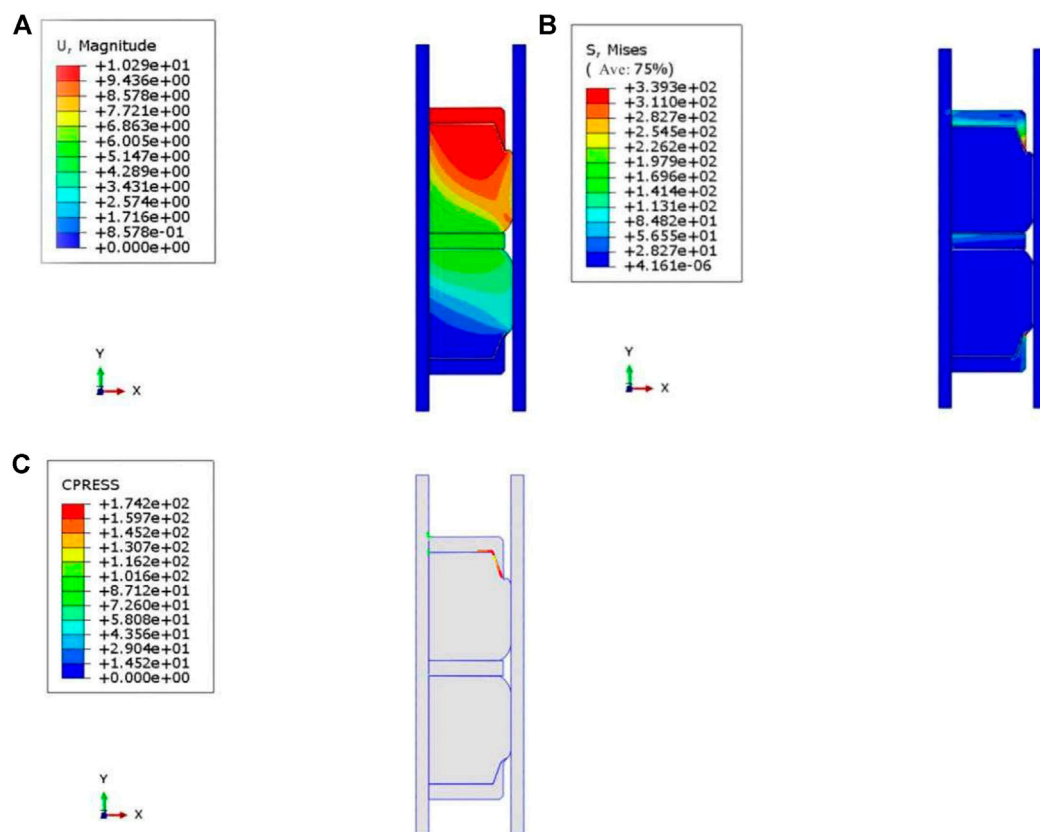
FIGURE 11
Simulation results of the stress distribution of the rubber cylinder. Notes: **(A)** Deformation cloud of the rubber cylinder; **(B)** Stress cloud of the rubber cylinder; **(C)** Contact stress cloud of the rubber cylinder.
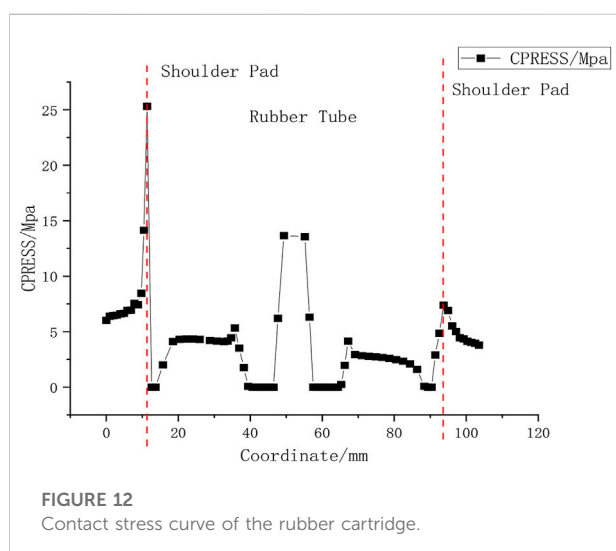
FIGURE 12
Contact stress curve of the rubber cartridge.

the inner and outer sides are sealed with the central pipe and the liquid cylinder respectively through O-rings. When working, the piston is fixed on the central tube, and the

high-pressure liquid enters the cylinder through the central small hole between the piston and the liquid cylinder. In turn, it pushes the cylinder to the left and forms a seal condition in the compressed rubber cartridge.

The structure of the rubber cylinder is shown in Figure 7. The difference from the general packer is that it has an anti-protrusion structure and adopts steel with lower rigidity. Compared with red copper, it reduces the cost, in addition, it can use the radial extension of the rubber barrel to closely contact the outer diameter of the rubber barrel, thereby effectively preventing the possibility of shoulder protrusions. Therefore, it improves the contact stress between the rubber cylinder and the pipe wall, and ensures the good sealing performance of the packer.

Discussion

Design of a new anti-shoulder structure

The direct contact between the rubber barrel and the casing will directly lead to structural deformation and performance

degradation of the rubber hose, especially under high temperature and high pressure. Therefore, the existence of an anti-shoulder structure is very necessary. A new type of anti-shoulder structure is designed using the conical surface shape of the double rubber cylinder. The structure is shown in Figure 8, and its working principle is shown in Figure 9.

The material used for the shoulder pads is low-strength steel. Its low stiffness allows a slight radial deformation of the cartridge, thereby effectively reducing contact stress, and reducing the possibility of cartridge failure and effectively preventing shoulder protrusions. Furthermore, the contact stress between the rubber cylinder and the pipe wall is increased, which ensures the good sealing performance of the packer.

Finite element analysis of rubber cartridge

The finite element software ABAQUS contains most constitutive models of hyperelastic materials. In the Mooney-Rivlin model selected in this paper, $C_{01} = 0.610$, $C_{10} = 1.221$. The mechanical parameters of the key components of the packer are shown in Table 5.

In the process of finite element analysis, the following assumptions are made in this study without affecting the use function of the packer:

① The packer is located in the center of the wellbore before and after setting, and is symmetrical about the centerline of the bottom hole;
② The effect of the packer's own weight on the results is ignored;
③ The influence of the irregularities of the wellbore on the analysis is ignored, and the casing is used instead of the wellbore to conduct the test;
④ In the analysis, only the part of the rubber cylinder is taken, the lower spacer ring, the central pipe and the well wall are fixed, and only the rubber cylinder is compressed.

The finite element analysis mainly analyzes the deformation of the rubber cylinder. Since both the spacer ring and the center tube are alloy steel, the elastic modulus is large, so the distance ring and the center tube are set as rigid bodies. According to the structure and size of the rubber cylinder in the assembled state, the contact design between the rubber tube and the metal part is established: the outer tube and the inner ring are fixed, the lower shoulder pad is fixed, and the upper shoulder pad is set as the loading reference point. The finite element model of the rubber tube was established by the finite element analysis software ABAQUS. The material of the central tube is 42CrMo, the Young's modulus and Poisson's ratio are 2.16e5 MPa and 0.286, respectively; the casing material is 45 steel, the material of the anti-outburst ring is 20 steel, the Young's modulus and Poisson's ratio are both 2.06e5 MPa and 0.3. The cartridge

material parameters are designed to be $C_{01} = 0.610$, $C_{10} = 1.221$. The solid model is shown in Figure 10.

The axial load of the rubber cartridge is 13.05 MPa (from Figure 8), and the bottom and lower shoulders of the model are restrained. The deformation, stress and contact stress cloud of the rubber cylinder are shown in Figure 11. In the deformation cloud, it can be seen that the stress is evenly distributed on the gluing cylinder. The cartridge is in close contact with the casing without excessive stress concentration. This shows that the anti-shoulder structure can make the stress uniform, and it also meet the energy requirements of the structure using low-strength steel. Its proper deformation makes the deformation degree of the rubber cartridge more elastic.

The contact pressure curve is shown in Figure 12. On the contact pressure curve, the maximum contact stress is near the two shoulder guards, and the contact pressure on the rubber tube is very uniform. Therefore, the rubber tube is protected by shoulder guards at both ends, thereby ensuring the structural integrity and uniformity of the force of the rubber tube. According to the stress cloud calculation results, the packer does not reach the maximum safe contact pressure when the lithological stratum is damaged by shear stress in the contact stratum.

Conclusion

In this study, in order to optimize the sealing performance of the conventional compression packer, the packing performance of the packer and the formation was systematically studied according to the different lithology of the formation. Empirical equations for packer suitability under three formation conditions were derived. A new anti-shoulder protrusion device is designed by comparing the commonly used rubber materials for packers and constitutive models. The main conclusions obtained in this paper are as follows:

1) The maximum stress of the rubber cylinder in the three formation models of mudstone, shale and sandstone is lower than the compression set strength of the rubber cylinder, indicating that the rubber cylinder will not cause stress damage.
2) At the same time, by analyzing the common rubber materials and constitutive models of packers, the structure of the packer rubber cylinder and a new anti-shoulder protrusion device were redesigned. Nitrile-butadiene rubber (NBR) meets the performance requirements of the rubber tube under the allowable pressure difference and temperature difference. The designed new anti-protrusion device can ensure the structural integrity and stress uniformity of the rubber tube, thereby ensuring good sealing performance.
3) Under the three formation conditions of mudstone, shale and sandstone, the rubber cartridge can be in a safe working state,

and its sealing width is close to the contact length of the rubber cartridge. In addition, the rubber cartridge is in a good elastic deformation range.

4) The design of the packer in this study satisfies the third strength theory and safety requirements, the deformation and sealing performance of the rubber cylinder are relatively stable, and the size of the rubber cylinder also meets the field requirements.

Data availability statement

The original contributions presented in the study are included in the article/supplementary material, further inquiries can be directed to the corresponding authors.

Author contributions

Authors YK and ZL are responsible for the idea and writing of this paper and authors TK, ZR, TS, and XZ are responsible for the simulation.

Conflict of interest

The authors declare that the research was conducted in the absence of any commercial or financial relationships that could be construed as a potential conflict of interest.

Publisher's Note

All claims expressed in this article are solely those of the authors and do not necessarily represent those of their affiliated organizations, or those of the publisher, the editors and the reviewers. Any product that may be evaluated in this article, or claim that may be made by its manufacturer, is not guaranteed or endorsed by the publisher.

References

Akhtar, M., Qamar, S. Z., Pervez, T., Khan, R., and Al-Kharusi, M. (2012). Elastomer seals in cold expansion of petroleum tubulars: Comparison of material models. *Mater. Manuf. Process.* 27 (7), 715–720. doi:10.1080/10426914.2011.648036

Bu, Y., Ma, M., and Li, J. (2011). Study on sealing property criterion and structure design method of packer. *Lubr. Eng.* 36 (11), 75–78. doi:10.1002/clc.20818

Dorokhov, M., Kostriba, I., and Biletskyi, V. (2016). Experimental research on the sealing ability of borehole packers. *Eastern-European J. Enterp. Technol.* 4, 56–62. doi:10.15587/1729-4061.2016.74831

Guo, Z., Li, Q., and Wang, Y. (2011). "Analysis and structural improvement of the rubber part in packer in a way of non-linearity finite element," in 2011 Second International Conference on Mechanic Automation and Control Engineering, Inner Mongolia, China, 15-17 July 2011 (IEEE), 73–76. doi:10.1109/MACE.2011.5986860

Huang, Y., Li, Y., Zhao, H., and Wen, H. (2020). Research on constitutive models of hydrogenated nitrile butadiene rubber for packer at different temperatures. *J. Mech. Sci. Technol.* 34 (1), 155–164. doi:10.1007/s12206-019-1217-x

Lan, W., Wang, H., Zhang, X., and Chen, S. S. (2019). Sealing properties and structure optimization of packer rubber under high pressure and high temperature. *Pet. Sci.* 16, 632–644. doi:10.1007/s12182-018-0296-0

Li, Z., Liu, J., and Ding, Y. (2013). Finite element analysis of the packer at fracturing. *Appl. Mech. Mater.* 385-386, 159–162. doi:10.4028/www.scientific.net/AMM.385-386.159

Liu, H., Zhang, W., Cao, Y., and Dou, Y. (2020). Analysis of the performance improvement effect of combined packing for oil and gas well packer. *IOP Conf. Ser. Earth Environ. Sci.* 514, 022017–22025. doi:10.1088/1755-1315/514/2/022017

Liu, J., Mei, L., Ding, W., Xu, K., Yang, H., and Liu, Y. (2022). Asymmetric propagation mechanism of hydraulic fracture networks in continental reservoirs. *GSA Bull.* doi:10.1130/B36358.1

Liu, Z., Hu, Z., Liu, G., Liu, Z., Liu, H., Hao, J., et al. (2021). Pore characteristics and controlling factors of continental shale reservoirs in the Lower Jurassic Ziliujing

Formation, northeastern Sichuan Basin. *Oil Gas Geol.* 42 (1), 136–145. doi:10.11743/ogg20210112

Luo, R. K., Zhou, X., and Tang, J. (2002). Numerical prediction and experiment on rubber creep and stress relaxation using time-dependent hyperplastic approach. *Polym.D. Snoke, Sci.* 298, 1368. doi:10.1016/j.polymertesting.2016.03.026

Polonsky, V. L., and Tyurin, A. P. (2015). Design of packers for sealing of the inter-tube space in equipment used for recovery of oil and gas. *Chem. Pet. Eng.* 51 (1-2), 37–40. doi:10.1007/s10556-015-9994-2

Wakuda, M., Yamauchi, Y., and Kanzaki, S. (2002). Effect of workpiece properties on machinability in abrasive jet machining of ceramic materials. *Precis. Eng.* 10, 193–198. doi:10.1016/S0141-6359(01)00114-3

Yohannes, Y. (2017). Hydraulic *in situ* testing for mining and engineering design: Packer test procedure, preparation, analysis and interpretation. *Geotech. Geol. Eng. (Dordr).* 35, 29–44. doi:10.1007/s10706-016-0112-9

Zhang, G., Zhang, Z., and Xin, Y. Y. (2017). Creep and stress relaxation of pine material polyethylene. *Adv. Eng. Sci.* 2, 232–239. doi:10.15961/j.jsuese.201601123

Zhao, P., He, B., Zhang, B., and Liu, J. (2022). Porosity of gas shale: Is the NMR-based measurement reliable? *Petroleum Sci.* 19 (2), 509–517. doi:10.1016/j.petsci.2021.12.013

Zhao, P., Xie, L., Fan, Z., Deng, L., and Liu, J. (2021b). Mutual interference of layer plane and natural fracture in the failure behavior of shale and the mechanism investigation. *Pet. Sci.* 18 (2), 618–640. doi:10.1007/s12182-020-00510-5

Zhao, P., Xie, L., He, B., and Liu, J. (2021a). Anisotropic permeability influencing the performance of free CH_4 and free CO_2 during the process of CO2 sequestration and enhanced gas recovery (CS-egr) from shale. *ACS Sustain. Chem. Eng.* 9 (2), 914–926. doi:10.1021/acssuschemeng.0c08058

Zheng, X., Li, B., and Fei, G. (2022). Evaluation of sealing performance of a compression packer at high temperature. *Sci. Prog.* 105 (1), 003685042210791–003685042210799. doi:10.1177/00368504221079180

Microstructure and heterogeneity of coal-bearing organic shale in the southeast Ordos Basin, China: Implications for shale gas storage

Rui Yu[1], Zetang Wang[2]*, Cheng Liu[3], Wenli Zhang[4]*, Yuxuan Zhu[2], Mengmeng Tang[2] and Qianjin Che[2]

[1]School of Mines, China University of Mining and Technology, Xuzhou, Jiangsu, China, [2]School of Resources and Earth Sciences, China University of Mining and Technology, Xuzhou, Jiangsu, China, [3]Key Laboratory of Unconventional Exploration and Development, CNOOC Energy Development Co, LTD, Tianjin, China, [4]School of Management, Xi'an University of Science and Technology, Xi'an, Shaanxi, China

In recent years, the eastern margin of Ordos Basin has attracted much attention as a key base for unconventional natural gas exploration. The pore-fracture structure is an important physical property of shale and provides places and channels for methane storage and migration. In this study, an integrated method of X-ray diffraction, total organic carbon (TOC), vitrinite reflectance (Ro), scanning electron microscopy (SEM), and low-temperature N_2 adsorption was performed to reveal the microstructure and heterogeneity of coal-bearing organic shale in the southeast Ordos Basin. The result indicated that the studied shale belongs to the category of organic-rich shale with an average TOC content of 8.1% and reaches the dry gas stage with a mean Ro value of 2.41%. Hysteresis loop suggests the shapes of pore structure in shale samples are dominated by inkbottle, cylindrical pores or parallel-plate. A positive correlation between kaolinite and pore surface area indicates that kaolinite contributes greatly to micropores with a large specific surface area. Intense hydrocarbon generation promotes gas to escape from organic components' surfaces, thereby increasing the pore volume. Coal-bearing shales with high brittleness may contain more natural microfractures, increasing specific surface area and pore volume. The bocking effect of minerals in microfractures may reduce pore connectivity and connectivity and enhance shale heterogeneity. The pore volume and specific surface area of coal-bearing shale are closely related to the fractal dimensions. The high complexity of the shale microstructure may lead to the formation of more micropores, resulting in a decrease in the average pore size. Besides, organic and clay-hosted pores in coal-bearing shale with high maturity may well be the main storage space for methane, but the methane is mainly stored in organic pores in marine shale.

Introduction

Due to the exhaustion of fossil energy and the deterioration of environment, the exploitation and utilization of coal measures co-associated resources have attracted great attention of coal geologists and energy enterprises in recent years (Hamawand et al., 2013; Zou et al., 2019; Wang et al., 2020; Li et al., 2022a). Coal and its associated resources are mainly composed of solid and fluid resources. Coal-bearing unconventional natural gas is low-carbon clean energy with extensive distribution and outstanding resource potential (Uysal et al., 2000; Dai et al., 2012; Huang et al., 2016; Yu et al., 2022). Therefore, it is of great practical significance to develop unconventional gas resources in coal to supply fossil energy and improve the environment. The two kinds of natural gas occurring in coal measures are mainly composed of coalbed methane and shale gas, and the latter is primarily distributed in organic-rich shale reservoirs (Jarvie et al., 2007; Ross and Bustin, 2009; Hao et al., 2013). Organic shale is a heterogeneous material composed of organic matter and mineral components, and methane molecules exist in shale's microscopic pore structure in free and adsorbed states (Bowker, 2007; Heller and Zoback, 2014). The shale porosity and the nature of pore-fracture connections are the key factors determining the shale gas seepage and migration (McGlade et al., 2013). Although the pore size of the shale matrix is very small, the large specific surface area of the pores is conducive to methane adsorption. Under suitable pressure and fracture conditions, the pores can promote the migration of shale (Shan et al., 2015). Meanwhile, Shale has a heterogeneous structure and composition, mainly manifested in the difference between mineral composition and organic structure (Klaver et al., 2015; Tang et al., 2015; Yang et al., 2017). These heterogeneities determine the pore networks and connectivity of the pore-fracture system in the gas shale reservoir. Therefore, understanding the microstructure and heterogeneity of coal-bearing shale plays an important role in revealing the occurrence of methane.

Recently, a lot of substantial progress has been made in the characterization and analysis of the microstructure of organic shale and coal reservoirs (Valenza et al., 2013; Li et al., 2015; Saif et al., 2017; Yang et al., 2018; Zhu et al., 2019; Yang et al., 2020; Arif et al., 2021). On the one hand, the characterization of reservoir microstructure by fluid injection experiment is recognized as a reliable method to reveal pore structure parameters quantitatively. On the other hand, observing pore types and distribution at the micro/nanoscale by electron microscope is a key technique for qualitative characterization of shale microstructure. Loucks et al. (2009) suggested that the volume and distribution of organic matter and its relationship with pore volume and permeability are helpful to understand the petrophysical properties of mudstone better. Curtis et al. (2012) used a combined focused ion beam and scanning

electron microscopy to study the evolution model of secondary organic pores in the Woodford Shale with different degrees of thermal maturity. Tang et al. (2015) studied the effect of material composition on the pore structure of marine shale with high maturity, indicating that the high organic matter content in marine shale will enhance the heterogeneity of the pore system. Yu et al. (2019) stated the contribution of the molecular structure of clay minerals and organic matter to microscopic pores in coal-bearing shale. Liu et al. (2018) used an NMR fluid typing method to build a classification of pore size in shale reservoirs. Kuila et al. (2014) indicated that porosity in clay is the fundamental contribution of mudstone nanostructure, and no open nanoscale porosity existed in the immature mudstone. Studied the effect of lithofacies on the nanopore structure of marine shale, suggesting that Organic matter is likely to be the main contributor to nanopores rather than clay minerals. In addition to the above studies, there are still plenty of petroleum geologists who have done a lot of work on the microstructure of organic shale (Clarkson et al., 2012a; Pan et al., 2017; Gao et al., 2020; Garum et al., 2020). However, some controversies related to the origin and main influencing factors of pores in shale still exist in petroleum geology.

As the largest superimposed basin in China, Ordos Basin has long been considered a multi-energy basin with abundant fossil energy and mineral resources. A set of upper Paleozoic coal-bearing shales in the southeast Ordos Basin is widely considered a potential area for shale gas exploration and development (Li et al., 2022b; Zhang et al., 2022). The coal-bearing shale gas resources of the Shanxi-Taiyuan Formation are in the range of $2800–3200*10^8 \text{ m}^3$ in the Daning-Jixian block, southeastern Ordos Basin (Zeng et al., 2022). Therefore, it is of great application value to study the microstructure of coal-bearing shale reservoir and its shale gas enrichment in this area. Given this, in this study, we first clarify the material composition of coal-bearing shales from the Shanxi Formation in southeast Ordos Basin using X-ray diffraction (XRD), total organic carbon content (TOC), and vitrinite reflectance (Ro). Then, we characterize the pore structures of shale samples using scanning electron microscopy (SEM), low-temperature N_2 adsorption, and fractal technology. Finally, we discuss the influences of shale material composition on pore type, size and distribution and their implications for methane storage.

Samples and methods

Samples

In this work, a total of 10 coal-bearing shale samples were obtained from a shale gas well in the Daning-Jixian block, southeast Ordos Basin (Figure 1A). The burial depth of these samples ranges from 2118 m to 2209 m, and this depth interval is the main

FIGURE 1
Geological map **(A)**, after Ju et al. (2021) and stratigraphic information **(B)** of the southeast Ordos Basin.
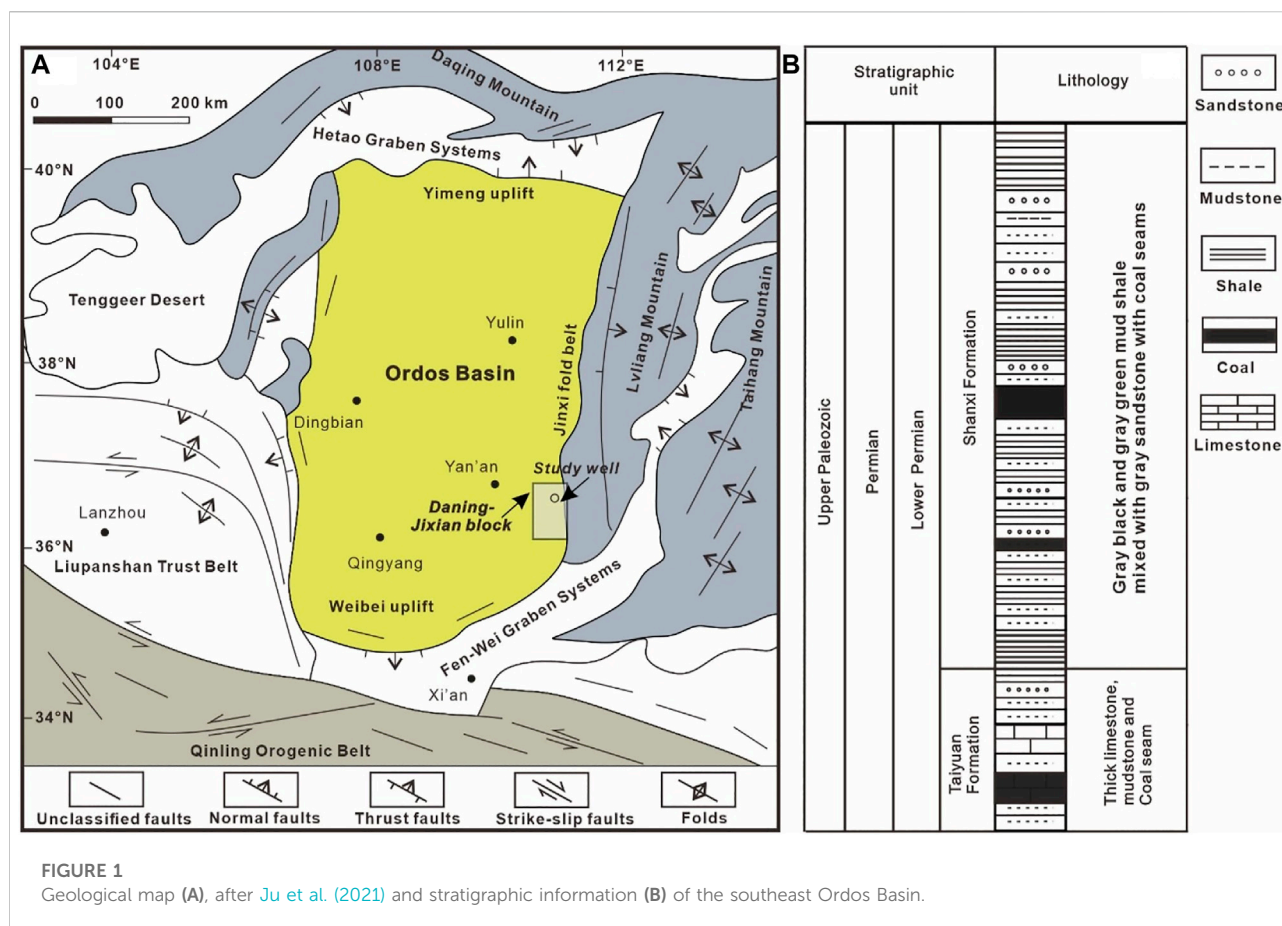
TABLE 1 Geological information and major mineral composition of shale samples.

Samples	Depth (m)	TOC (wt%)	Quartz (%)	Clay (%)	Feldspar (%)	Calcite (%)	Dolomite (%)	Siderite (%)	Pyrite (%)	Anatase (%)
SY1	2118	0.80	34.9	57.8	4.4	0.0	0.0	2.9	0.0	0.0
SY2	2127	5.40	29.4	58.3	2.2	0.0	0.0	2.8	5.0	2.4
SY3	2128	5.00	28.0	62.0	1.0	0.0	0.0	2.7	6.2	0.0
SY4	2134	0.10	58.6	23.4	6.5	0.0	10.6	0.8	0.0	0.0
SY5	2146	36.70	17.6	32.2	0.4	3.5	18.3	1.3	25.1	1.7
SY6	2152	1.70	38.8	48.8	7.0	0.0	2.4	3.1	0.0	0.0
SY7	2165	9.40	48.1	45.8	1.3	0.0	0.0	0.0	3.3	1.5
SY8	2166	10.80	43.9	44.3	1.0	0.0	4.1	0.0	5.2	1.5
SY9	2168	8.30	41.3	48.8	0.9	0.0	0.0	0.0	7.4	1.5
SY10	2209	2.70	65.1	28.6	3.7	0.0	0.0	1.1	0.0	1.5

concentration horizon of coal-bearing shale. All samples belong to the Lower Permian Shanxi Formation of late Paleozoic, representing potential source rocks consisting of dispersed organic matters during the sedimentary period of coal measures (Figure 1B). All

fresh samples are sealed and stored in airtight bags to prevent weathering before the experiment. The samples were performed on a comprehensive mineralogical and petrophysical testing method, including XRD experiment, TOC analysis, Ro measurement, SEM

test, and N$_2$ adsorption. The detailed geological information of coal-bearing shale samples is listed in Table 1.

Materials and methods

Quantitative whole rock analysis was applied to reveal the mineral composition of the shale samples, which was performed on X-ray diffraction based on the Chinese Oil and Gas Industry Standard (SY/T5163-2010). TOC analysis was conducted in PetroChina Research Institute of Petroleum Exploration and Development using a Leco CS-230 analyzer referring to the Chinese National Standard (GB/T476-2008). Vitrinite reflectance measurement was conducted by an AXIO Imager Mlm microphotometer produced by the ZEISS company at the China University of Mining and Technology. Approximately 30 values were measured for each shale sample and then averaged to ensure the accuracy of the experimental results.

FE-SEM imaging of shale samples was conducted using a HITACHI SU8020 field emission scanning electron microscopy. The sample was cut into ~10×10×5 mm blocks, and carbon plating was carried out on the sample surface to improve electrical conductivity. Then, the equipment was repeatedly adjusted to make the images of the microscopic pore-fracture structure of shale clearer and more readable. Low-pressure N$_2$ adsorption was performed in PetroChina Research Institute of Petroleum Exploration and Development using an automatic specific surface area analyzer developed by Quantachrome company, according to the Chinese National Standard (GB/T19587-2004). The specific surface area, pore size, and pore volume of samples were calculated using the Barrett–Joyner–Halenda (BJH) model (Groen et al., 2003).

Fractal theory and technology of porous media have also been used to characterize the pore-fracture structure of shale samples to describe the connectivity and density of porous media quantitatively. Detailed principles and calculation methods of shale samples were illustrated in Yang et al. (2014) and Cai et al. (2017).

Results and analysis

Mineral and organic composition

According to the XRD results, the mineral composition and clay mineral ratio of the shale samples are listed in Tables 1, 2. The minerals of coal-bearing shales from the Shanxi Formation consist of quartz, clay, feldspar, dolomite, siderite, pyrite, together with a few anatase and calcite (Table 1; Figure 2A). Precisely, the quartz content ranges from 17.6 to 65.1%, averaging 40.6%; the clay content ranges from 23.4 to 62%, averaging 45%. The feldspar content varies from 0.4 to 2.8%, with a mean value of 2.8%; the siderite content has an average value of 1.5%. Calcite and dolomite occur only in a few shale

samples and are present in very low concentrations. Pyrite is developed in most shale samples with an average of 5.2%, and anatase also appears in some samples with a low average content of 1.0% (Table 2; Figure 2A). As for the clay minerals, the mixed-layer illite-smectite (I/S) content range from 16 to 59%, averaging 31.6%, and the illite content varies from 15 to 35.6%, with a mean value of 25.4%. Kaolinite content ranges from 3.7 to 50% averaging 38.3%, and smectite content varies from 1.7 to 8.0%, having a mean value of 4.7% (Figure 2B).

TOC content of shale samples ranges from 0.1 to 36.7%, with an average of 8.1% (Figure 3). The TOC results suggest that the studied shale belongs to organic-rich shale (TOC > 2.0%). Ro values of some shale samples vary from 2.32 to 2.48% averaging 2.41%, indicating coal-bearing shale has reached the stage of dry gas generation with a potential for hydrocarbon generation.

Pore type and morphology

The typical N$_2$ adsorption-desorption curves of the studied samples are shown in Figure 4, and the isothermal curves are similar to the inverse "S" shape. These representative curves show that different samples developed different pore types, which resulted in a diverse variation trend of the curves. When the relative pressure is high, the isothermal adsorption curve rises rapidly, showing a downward concave trend, and the adsorption and desorption process has irreversibility. Subsequently, the adsorption and desorption curves are separated to form hysteresis loops (Bu et al., 2015; Yu et al., 2020). Based on the classification of Sing and Williams (2004), the adsorption-desorption curves of shale samples in the study area can be roughly divided into two types, namely, type B and type C. Type B refers to an adsorption-desorption curve with an obvious hysteresis loop (Figure 4C). Type C is the adsorption curve and desorption curve approximately consistent, and a slight hysteresis loop exists (Figures 4A,B,D). Generally, the shape of the hysteresis loop can be applied to interpret the morphology of pores in shale samples (Clarkson et al., 2012b; Yang et al., 2021). The shape of the hysteresis loop is relatively wide, indicating that the pore type is mainly the shape of a thin neck and wide-body inkbottle (such as SY1). While the shape of the hysteresis loop is not obvious, indicating that the pore type is mainly cylindrical pore or parallel plate (such as SY5).

SEM images show that the pores in coal-bearing shale can be divided into three types: intergranular pores, intragranular pores and organic pores (Loucks et al., 2012). Organic pores are generally round or oval, distributed independently in shale matrix, and have relatively poor connectivity (Zeng et al., 2022; Figure 5A). Intergranular pores and intragranular pores are commonly developed in clay minerals, and pores are generally irregular and narrow in shape (Figures 5B–E). Some pores and fractures in clay minerals form several microchannels in the shale matrix

TABLE 2 Clay mineral composition, pore parameters, and Ro values of shale samples.

Samples	I/S (%)	Illite (%)	Kaolinite (%)	Smectite (%)	I/S ratio	Surface area (m²/g)	Pore volume (cm³/g)	Average pore size (nm)	Ro (%)
SY1	39.3	30.1	26.3	4.3	16	11.5	0.037	12.9	
SY2	36.0	19.0	37.0	8.0	10	6.636	0.005	1.173	2.48
SY3	35.0	23.0	37.0	5.0	10	8.517	0.006	1.167	
SY4	59.0	35.6	3.7	1.7	12	6.66	0.02	12.14	
SY5	16.0	30.0	50.0	4.0	12	4.639	0.003	0.818	2.32
SY6	31.6	26.6	37.0	4.7	11	9.524	0.03	12.76	
SY7	28.0	20.0	49.0	3.0	14	8.731	0.007	1.155	
SY8	18.0	27.0	50.0	5.0	11	7.511	0.006	1.17	2.44
SY9	21.0	28.0	45.0	6.0	8	0.294	0.001	3.487	
SY10	32.0	15.0	48.0	5.0	9	0.587	0.002	1.024	
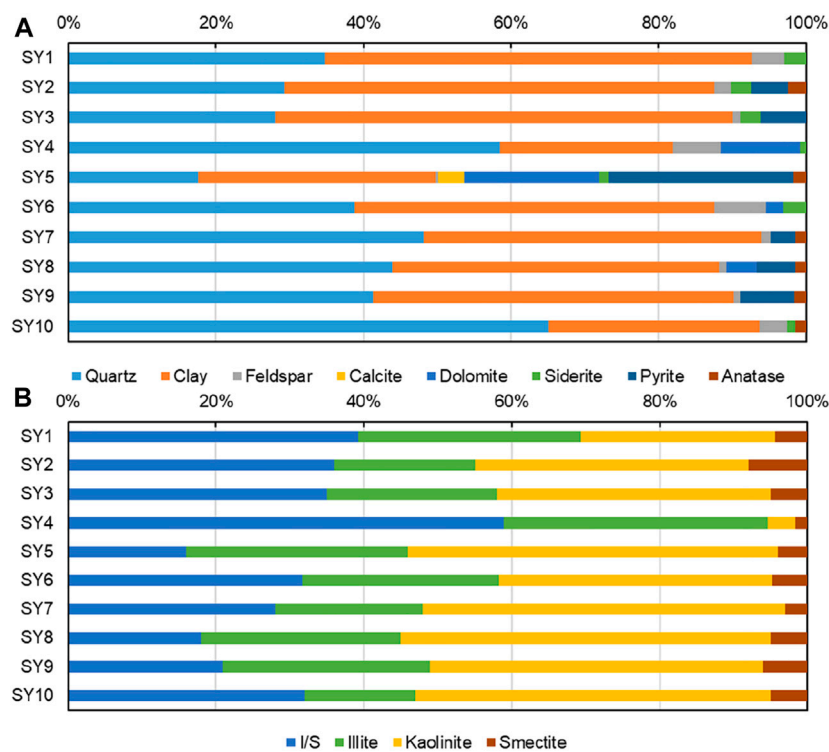
FIGURE 2
Major mineral **(A)** and clay mineral **(B)** composition of shale samples.

with good connectivity (Figures 5B,D). Organic pores are formed by hydrocarbon generation and expulsion of organic matter under a proper temperature and pressure environment. Besides, we also found that a large number of microscopic fractures developed in the shale matrix. On the whole, the connectivity between fractures is poor, and some fractures are filled with clay minerals. The shape of some fractures is arc or root, which indicates that they are affected by tectonic stress to a certain extent (Figures 5B,F). Microfractures in shale are mainly caused by matrix
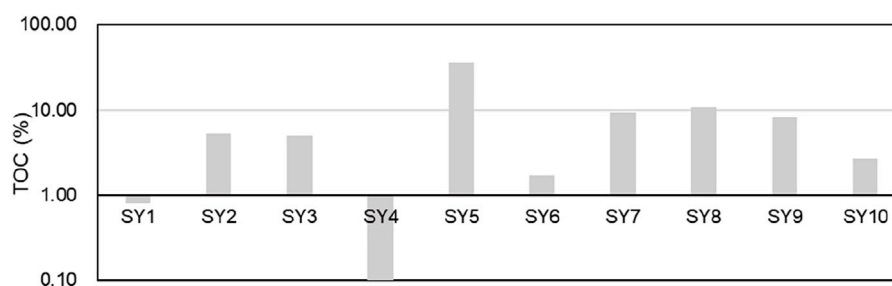
FIGURE 3
TOC content of shale samples.
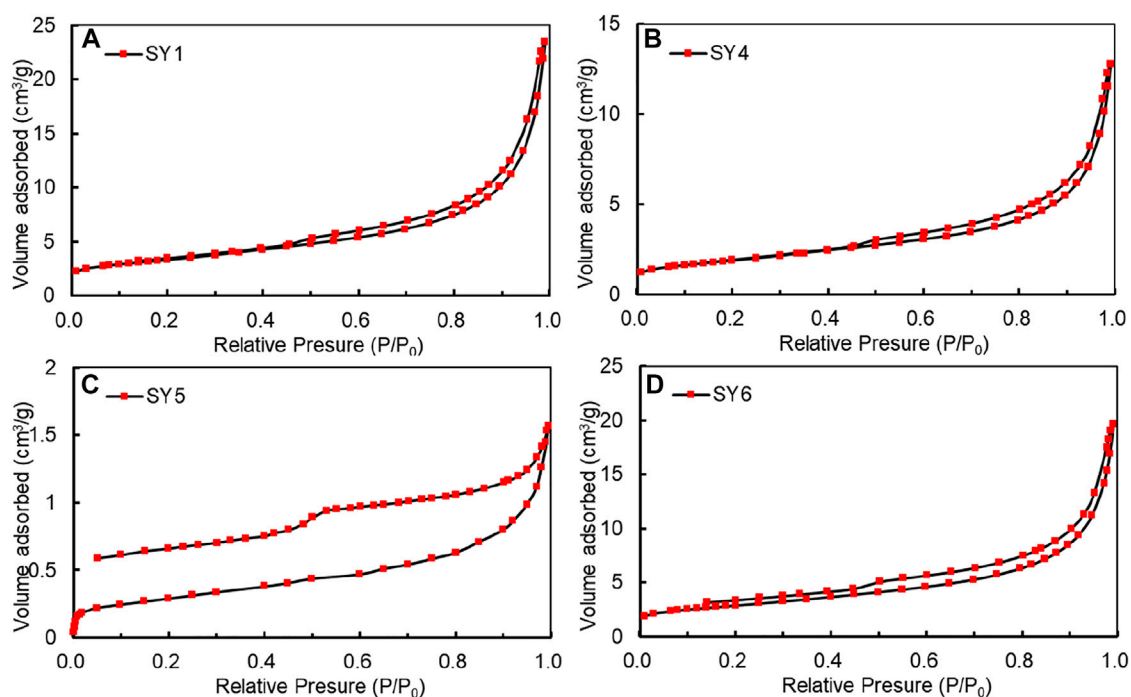
FIGURE 4
Typical low-temperature N_2 adsorption-desorption curves of the studied shale samples.

shrinkage during diagenesis or tectonic compression stress in the later stage. Meanwhile, some regular octahedral pyrite particles are enriched in the shale matrix, confirmed by the pyrite content in the whole rock component (Figure 5E).

Pore size distribution

Based on the N_2 adsorption, the curves of incremental pore volume versus pore size from the typical shale samples are presented in Figure 6. The pore volume and average pore size

of the studied shale samples ranged from 0.001 cm^3/g to 0.037 cm^3/g and from 0.82 nm to 12.76 nm, averaging 0.012 cm^3/g 4.78 nm, respectively (Table 2). Within the effective pore size characterized by N_2 adsorption (1–100 nm), the curves of pore size distribution are mostly multi-peak distribution but also appear single-peak distribution. The pore volume of most samples increased sharply in the range of 10–100 nm, and the variation curve of the pore volume of a few samples was not obvious (Figures 6A–D). The pore surface area of samples varies from 0.294 m^2/g to 11.5 m^2/g, with a mean value of 6.46 m^2/g (Table 2). The curves of pore surface area
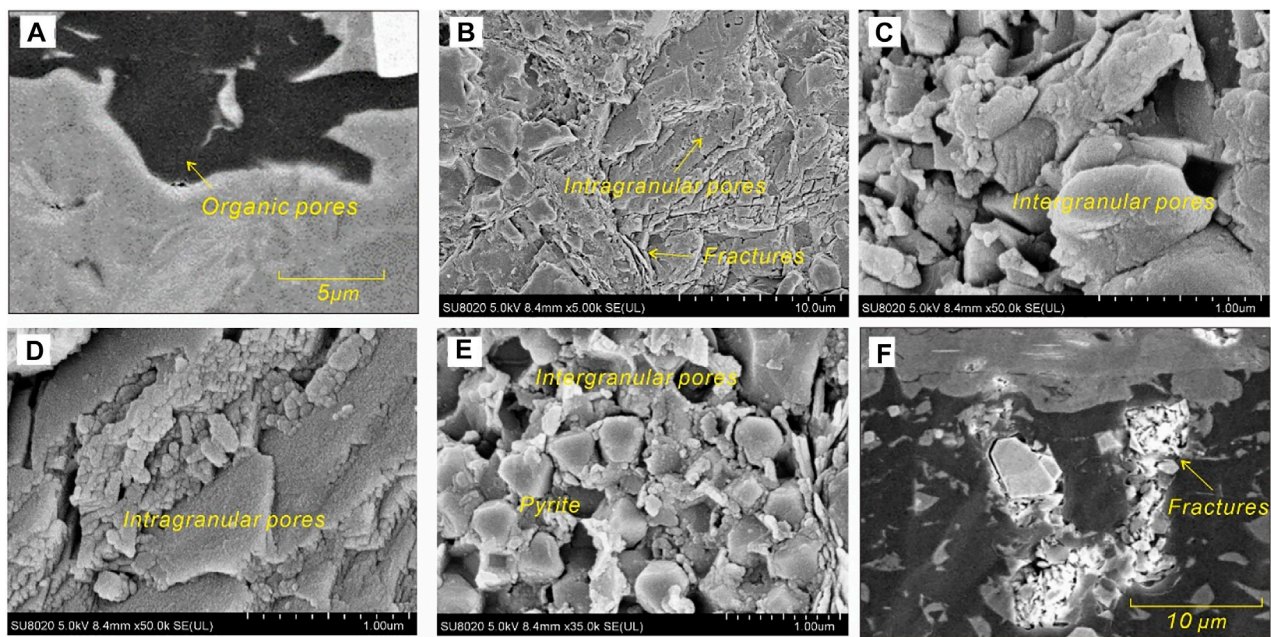
FIGURE 5
Microstructure images of coal-bearing shale in the eastern Ordos Basin, **(A)** Organic pores, **(B)** pore-fracture system in shale matrix, **(C,D)** pores in clay minerals, **(E)** intergranular pores of pyrite, **(F)** fractures in shale matrix.
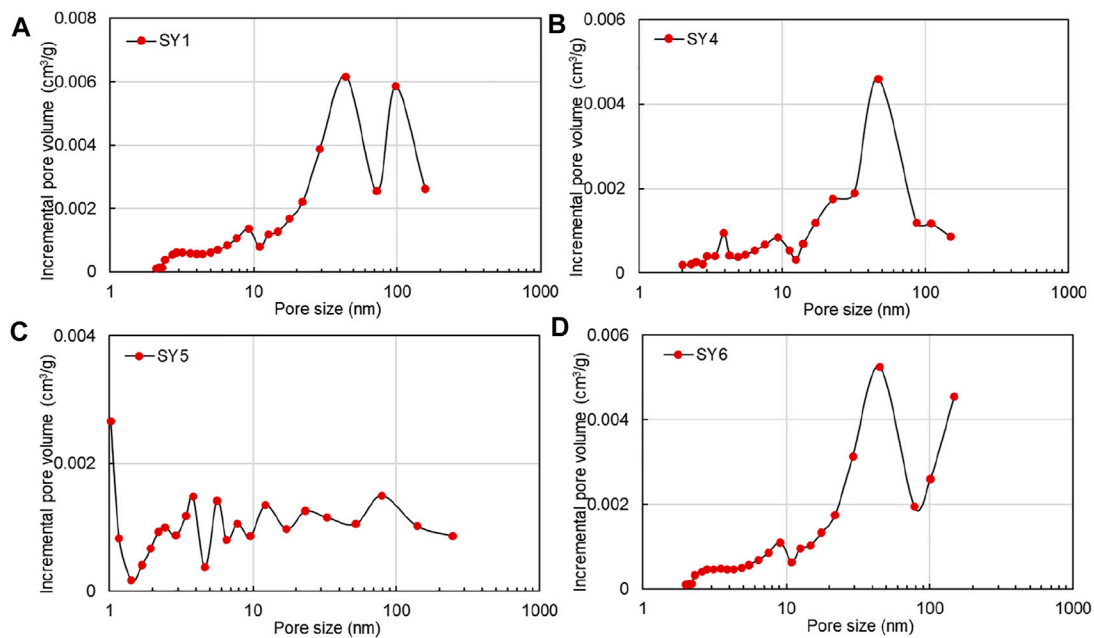
FIGURE 6
Incremental pore volume versus pore size of typical shale samples.
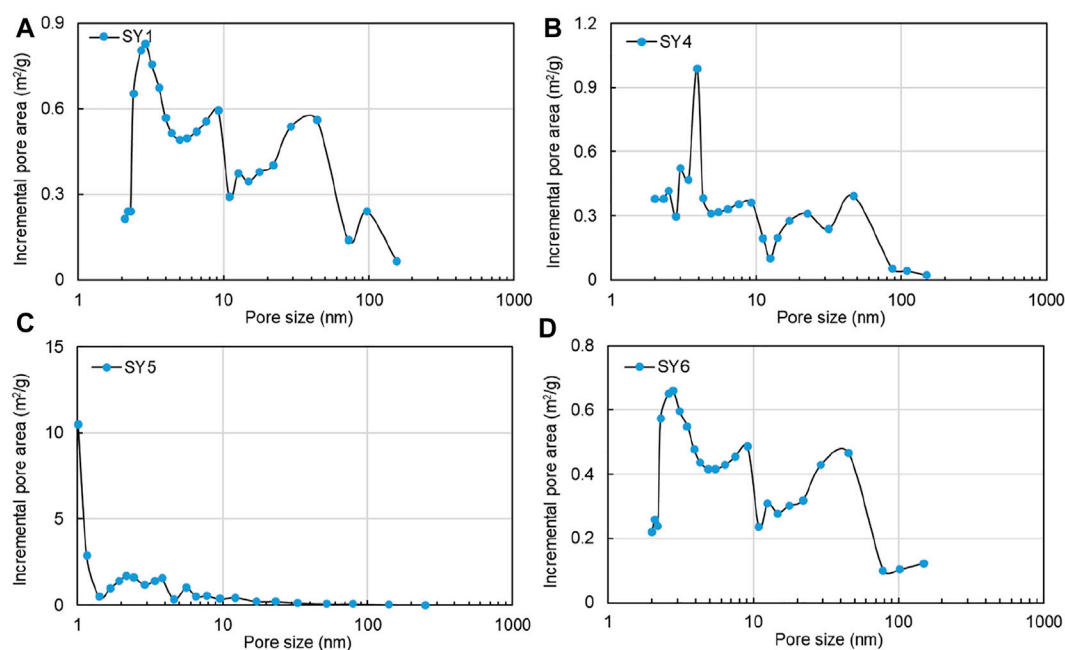
FIGURE 7
Incremental pore area versus pore size of typical shale samples.

versus pore size show that the increment of specific surface area decreases with the increase of pore size. The pore surface area increment is the largest in the range of 1–10 nm, indicating that the smaller the pore size is, the larger the specific surface area is. Meanwhile, the peak value of the increment of pore surface area is also concentrated in the range of 1–10 nm (Figure 7). According to pore surface area and volume distribution curves, pores in shale represented by SY5 are mainly pores with a pore size less than 10 nm, while pores in shale defined by SY1 are mainly pore with pore size between 10–100 nm.

Fractal analysis

In this work, based on the fractal theory (FHH model), we used the equation described to calculate shale fractal dimensions. The linear fitting coefficients (R^2) of all shale samples are greater than 0.95, indicating that the studied samples possess fractal characteristics (Table 3; Figure 8). Besides, all detailed linear equations and fractal dimensions of the studied samples are listed in Table 3. Generally, the values of fractal dimension D range from 2 to 3, and D values are affected by the geometric irregularity and roughness of the surface. The fractal dimensions of the first part (D1) vary from 2.0524 to 2.6325, averaging 2.3641, and that of the second part (D2) range from 2.4061 to 2.8177 with a mean value of 2.7006. These results indicate that the pore structure of the studied shales is complex

with strong heterogeneity. More importantly, the larger the D1 value is, the more irregular and rougher the pore surface is. The larger the D2 value is, the more complex the pore structure is (Yang et al., 2017).

Discussion

Influence of mineral and organic composition on pore structure

Organic matter content and mineral composition in shale are the key factors affecting pore structure and distribution in shale matrix. The relationships between pore structure and shale composition are presented in Figure 9. Clay mineral contents show a good correlation with pore specific surface area, especially kaolinite and I/S contents (Figures 9A,B). Kaolinite is positively correlated with specific surface area (R^2=0.5433), while I/S is negatively correlated with specific surface area (R^2=0.6318). Kaolinite derived from feldspar usually occurs in coal-bearing shales as layered aggregates, with many nanopores developed between the layers, increasing specific surface area. I/S usually present a folded section with few nanopores, and its spatial pore structure is affected by the I/S ratio. As for the pore volume, TOC and quartz contents present a positive relationship with pore volume, and no correlation exists between clay content and pore volume (Figures 9C,D). In the high-maturity shales, the

TABLE 3 Fitting equation and fractal dimensions of shale samples.

Samples	Eq. 2	R^2	D2	Eq. 1	R^2	D1
SY1	y = −0.3968x + 1.4207	0.9988	2.6032	y = −0.3675x + 1.3742	0.9988	2.6325
SY2	y = −0.184x + 0.3213	0.993	2.8160	y = −0.7051x + 0.2444	0.9589	2.2949
SY3	y = −0.1823x + 0.5189	0.9839	2.8177	y = −0.8268x + 0.487	0.9601	2.1732
SY4	y = −0.3773x + 0.8548	0.9984	2.6227	y = −0.4093x + 0.8178	0.9998	2.5907
SY5	y = −0.2899x - 0.9166	0.9895	2.7101	y = −0.506x - 0.9838	0.9922	2.494
SY6	y = −0.3758x + 1.2817	0.9976	2.6242	y = −0.3866x + 1.2452	0.9998	2.6134
SY7	y = −0.1986x + 0.6326	0.9895	2.8014	y = −0.6892x + 0.5816	0.9791	2.3108
SY8	y = −0.1942x + 0.3574	0.9856	2.8058	y = −0.6767x + 0.2953	0.97	2.3233
SY9	y = −0.2011x + 0.3265	0.9698	2.7989	y = −0.8441x + 0.3635	0.9944	2.1559
SY10	y = −0.5939x - 2.9052	0.9773	2.4061	y = −0.9476x - 2.8117	0.9521	2.0524
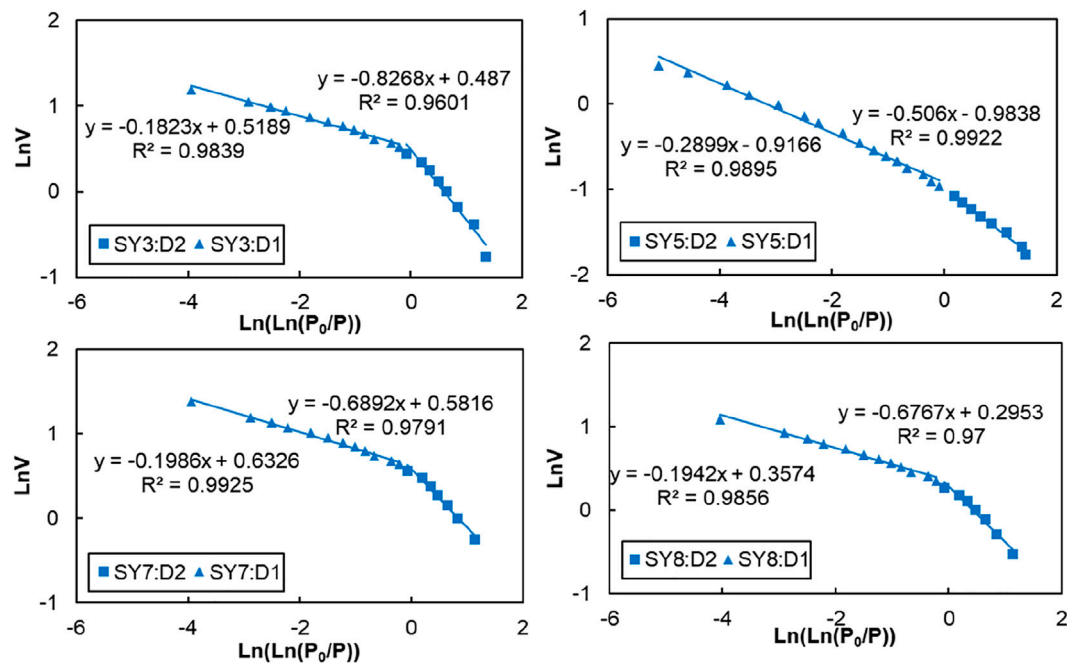
FIGURE 8
Fractal results calculated by N_2 adsorption of typical shale samples.

molecular structure of organic matter is pyrolyzed to generate methane. Gases escape from the surface of organic components, producing a large number of gas pores. The increase of quartz content may lead to brittle fracture of shale and an increase in pore volume. I/S content shows a positive relationship with average pore size, while kaolinite negatively correlates with the average pore size (Figures 9E,F). These relationships suggest that kaolinite is conducive to developing small pores, while more large pores exist in I/S. This understanding is consistent with the correlation between clay minerals and specific surface area.

Relationship between shale brittleness and pore structure

The brittleness of shale determines the development of natural fractures and the formation of a complex network, probably related to pore structure parameters. Shale brittleness was calculated by the following equation described in Rybacki et al. (2016).

$$BRIT = \frac{V_{quartz}}{V_{quartz} + V_{Calcite} + V_{Clay}} \times 100\% \qquad (1)$$
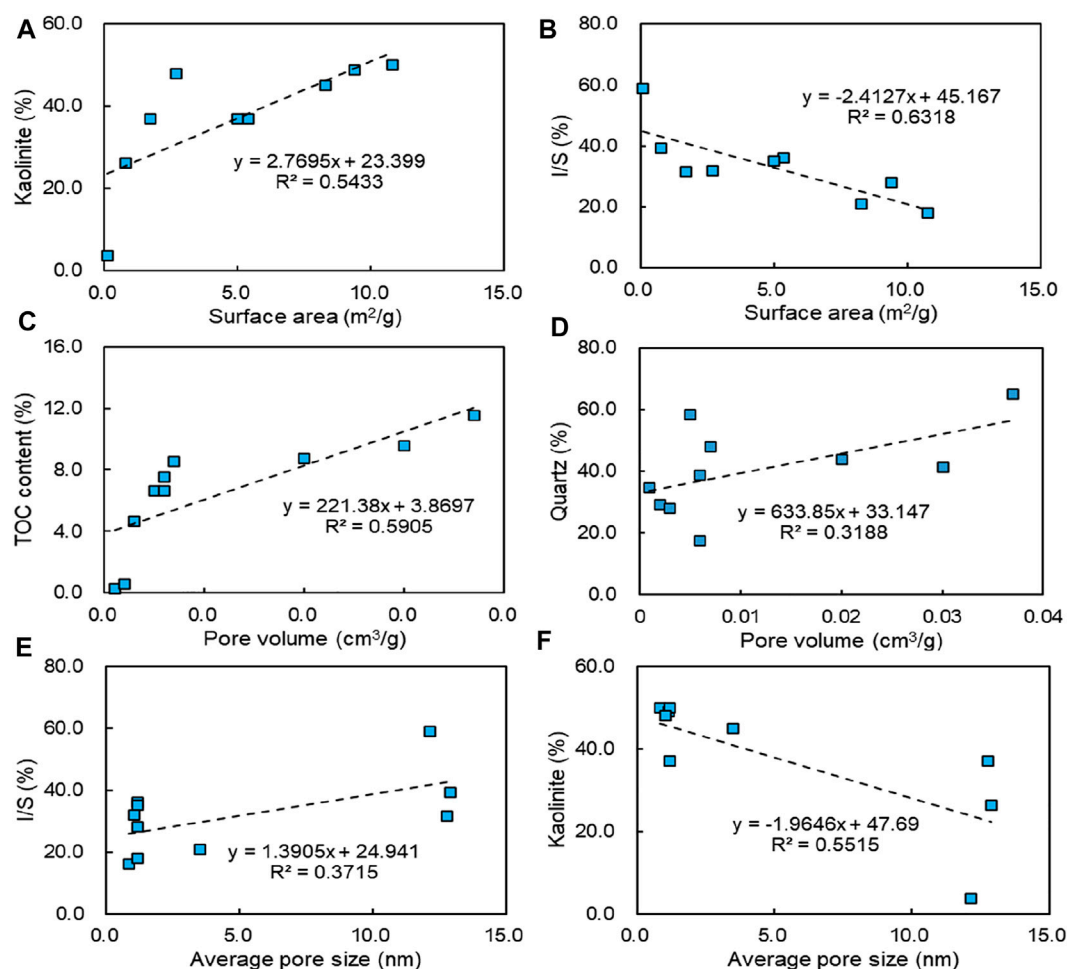
FIGURE 9
Pore structure parameters versus shale composition.

Where V stands for mineral mass fraction, BRIT stands for brittleness index of shale.

The brittleness indexes of all samples ranged from 31.1 to 71.5%, with a mean value of 46.7%. The average brittleness index is higher than 45%, indicating that the reservoir has a certain potential for fracturing and reconstruction. In this study, shale brittleness shows a positive relationship with specific surface area (Figure 10A), indicating the more brittle the shale is, the more microcracks are likely to develop in the matrix thus increasing the specific surface area of the pores. Similarly, there is a positive correlation between brittleness and pore volume (Figure 10B). This trend indicates that fracture channels are commonly developed in shale with high brittleness, increasing pore volume. However, no correlation between shale brittleness and average pore size suggests that shale brittleness has no direct effect on pore size distribution in the studied samples (Figure 10C).

Effect of shale composition and brittleness on fractal dimension

To reveal the influence of shale composition on the fractal dimension, the relationship between fractal dimension and organic matter and mineral contents is shown in Figure 11. Due to the abnormally high TOC value in the SY5 sample, this point was removed for correlation analysis in this study. TOC content positively correlated with D2 characterizing the pore structure complexity, and has a negative relationship with D1 representing the pore surface irregularity (Figures 11A,B), suggesting the increase of organic matter content results in a more complex pore structure and more regular surface. Additionally, quartz and feldspar contents negatively correlate with D2 values, and no relationship exists between quartz, feldspar, and D1 values (Figures 11C,D). These relationships suggest that the increase of homogeneous
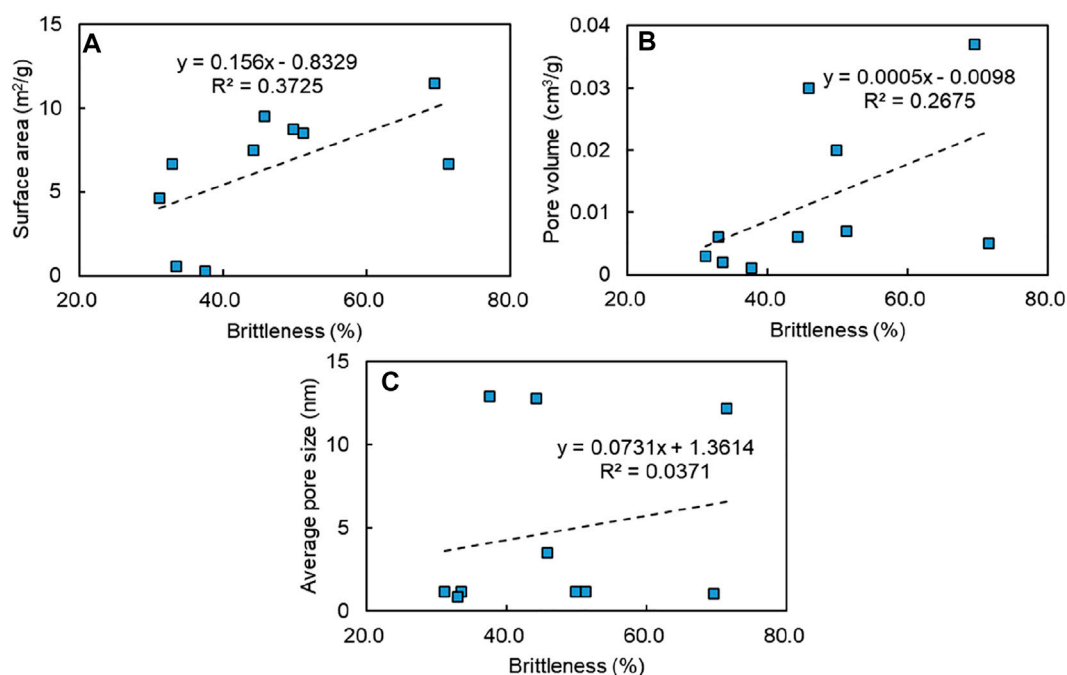
FIGURE 10
Pore structure parameters versus brittleness index in shale.

minerals such as quartz and feldspar probably play a pore-blocking role in the pore system and reduces the shale pore structure's complexity. However, clay minerals possess a positive relationship with D2 values and no obvious correlation with D1 values (Figures 11E,F). This suggests that clay minerals have a more complex structure and thereby increase the heterogeneity and complexity of shale pore structure. Besides, the brittleness indexes exhibit a negative correlation with D2 values, indicating that brittle shales produce more natural microfractures and have a more effective pore system. This relationship increases the spatial connectivity of the pore structure, which in turn naturally decreases D2 values. Overall, the more developed the microscopic pore-fracture system for porous shale, the more homogeneous the reservoir. However, the blocking effect of minerals in the pore-fracture system will reduce the connectivity of the reservoir, which will complicate the fractal dimension of the pore structure.

Heterogeneity of shale microstructure and its implication for methane storage

For understanding the heterogeneity of shale microstructure, the relationship between fractal dimension and pore structure parameters of coal-bearing shale samples is presented in Figure 12. The average pore size shows a negative association with D1 values (Figure 12A), suggesting the mesopore has a rougher and more irregular pore surface than the micropore. This fact is because micropores are round or oval pores formed by hydrocarbon generation, while mesopores are intergranular and intragranular pores of minerals. However, a negative correlation exists between average pore size and D2 values (removed outlier, Figure 12B), indicating that the complexity of shale microstructure may lead to the formation of more micropores, resulting in a decrease in the average pore size. Besides, a negative correlation occurs between pore volume and D1 values, suggesting the more irregular the shale surface, the more pores with small size develop, thus reducing the total pore volume of shale (Figure 12C). There was no obvious correlation between the D2 values and the pore volume, indicating that the complexity of shale pore structure is not necessarily related to pore volume (Figure 12D). It is worth noting that there is no significant correlation between specific surface area and fractal dimensions in this study, which is likely limited by the number and nature of shale samples.

On the other hand, the D1 values on behalf of the pore surface of coal-bearing shale (averaging 2.36) are lower than that
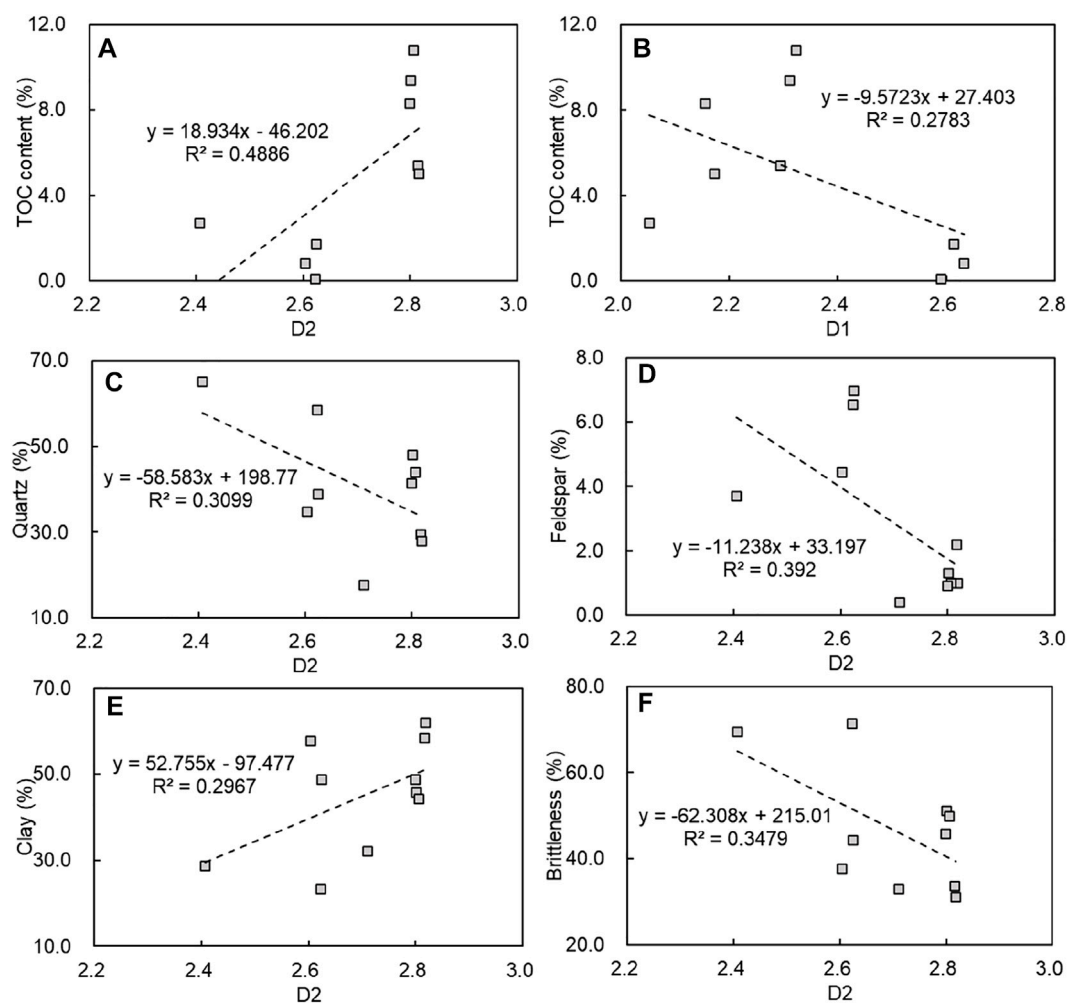
FIGURE 11
Relationship between shale composition, brittleness and fractal dimension.

of marine shale from South China (Longmaxi shale with a mean value of 2.79, Yang et al., 2016). This fact shows that the pores of marine shale with high maturity have more irregular surfaces than coal-bearing shale. Organic pores are developed in marine shale with high maturity, and the surface of organic pores is rougher than that of clay-hosted pores. Additionally, the marine shale has an average D2 value of 2.57 (Liang et al., 2015; Zhang et al., 2017), and the average D2 value of coal-bearing shales is 2.70. Similar D2 values indicate that the pore structures of marine shale and coal-bearing shale are equally

complex. In nature, due to the intense hydrocarbon generation of marine shale in South China, many organic pores are generated, which is enhanced the complexity of pore structure. However, the coal-bearing shales in North China have high clay content and numerous clay-hosted pores, making up for the lack of organic pores and presenting a high D2 value. As for the shale gas storage, organic and clay-hosted pores in coal-bearing shale with high maturity may be the main storage space for methane, while the methane is mainly stored in organic pores in marine shale.
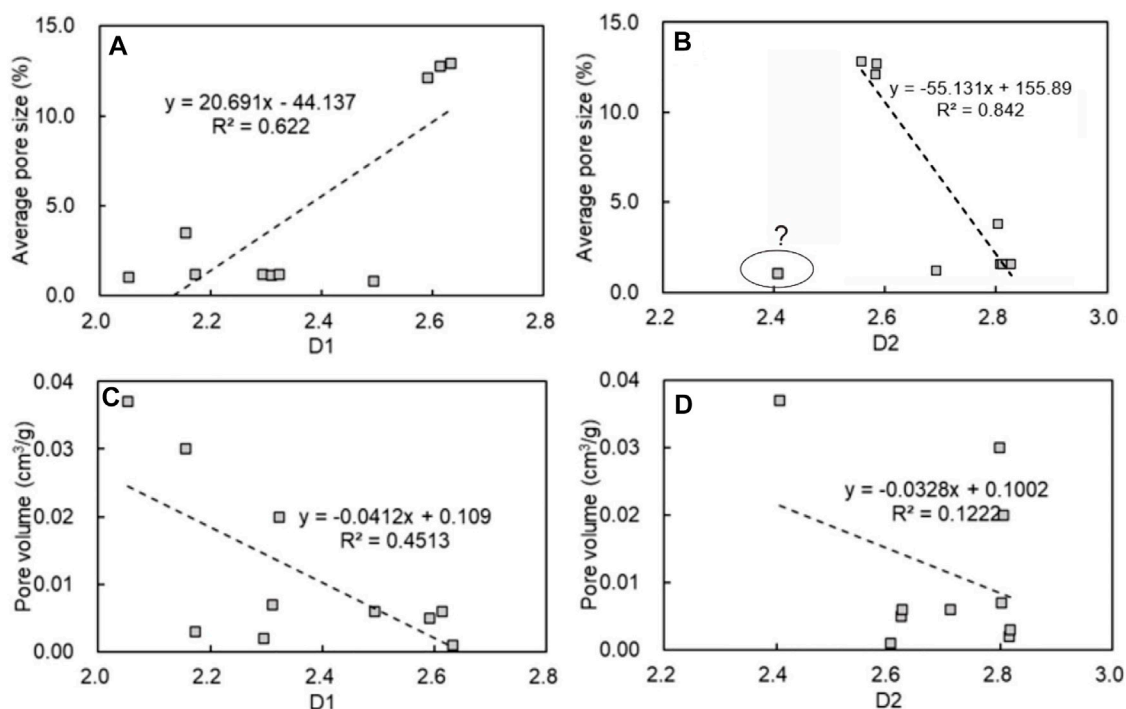
FIGURE 12
Relationship between pore structure and fractal dimension of shale samples.

Conclusion

(a) Kaolinite positively correlates with pore surface area, suggesting that many nanopores formed between the layers result in an increase in specific surface area. The positive relationship between organic matter and pore volume indicates that hydrocarbon generation promotes the formation of gas pores and increases pore volume.

(b) Coal-bearing shales with a high brittleness are probably rich in natural microfractures, which contribute to the increase of specific surface area and pore volume. However, no obvious relationship exists between average pore size and brittleness index.

(c) The more developed the pore-fracture system for porous shale, the more homogeneous the reservoir is. However, the blocking effect of minerals in the pore-fracture system decreases pore connectivity, complicating pore arrangement and enhancing shale heterogeneity.

(d) The pore volume and specific surface area of coal-bearing shale are closely related to the fractal dimensions. The high complexity of the shale microstructure may lead to the formation of more micropores, resulting in a decrease in the average pore size.

(e) By comparing the pore fractal characteristics of marine and coal-bearing shales, organic and clay-hosted pores in coal-bearing shale with high maturity may be the main storage space for methane. In contrast, methane is mainly stored in organic pores in marine shale.

Data availability statement

The datasets presented in this study can be found in online repositories. The names of the repository/repositories and accession number(s) can be found in the article/Supplementary Material.

Author contributions

Investigation, RY, and ZW; methodology, YZ, CL, and WZ; review and editing ZW; data curation, MT, and QC; writing original draft, RY.

Funding

This study was funded by the National Natural Science Foundation of China (No. 41772129).

Acknowledgments

This work was supported by the PetroChina Research Institute of Petroleum Exploration and Development. The authors thank PetroChina Research Institute of Petroleum Exploration and Development for their help and guidance in sample collection, experimental testing and data analysis.

Conflict of interest

Author CL is employed by the CNOOC Energy Development Co., LTD.

The remaining authors declare that the research was conducted in the absence of any commercial or financial relationships that could be construed as a potential conflict of interest.

Publisher's note

All claims expressed in this article are solely those of the authors and do not necessarily represent those of their affiliated organizations, or those of the publisher, the editors and th reviewers. Any product that may be evaluated in this article, or claim that may be made by its manufacturer, is not guaranteed or endorsed by the publisher.

References

Arif, M., Mahmoud, M., Zhang, Y., and Iglauer, S. (2021). X-Ray tomography imaging of shale microstructures: A review in the context of multiscale correlative imaging. *Int. J. Coal Geol.* 233, 103641. doi:10.1016/j.coal.2020.103641

Bowker, K. A. (2007). Barnett shale gas production, fort worth basin: Issues and discussion. *Am. Assoc. Pet. Geol. Bull.* 91 (4), 523–533. doi:10.1306/06190606018

Bu, H., Ju, Y., Tan, J., Wang, G., and Li, X. (2015). Fractal characteristics of pores in non-marine shales from the Huainan coalfield, eastern China. *J. Nat. Gas Sci. Eng.* 24, 166–177. doi:10.1016/j.jngse.2015.03.021

Cai, J., Wei, W. E. I., Hu, X., Liu, R., and Wang, J. (2017). Fractal characterization of dynamic fracture network extension in porous media. *Fractals* 25 (02), 1750023. doi:10.1142/s0218348x17500232

Clarkson, C. R., Jensen, J. L., Pedersen, P. K., and Freeman, M. (2012a). Innovative methods for flow-unit and pore-structure analyses in a tight siltstone and shale gas reservoir. *Am. Assoc. Pet. Geol. Bull.* 96 (2), 355–374. doi:10.1306/05181110171

Clarkson, C. R., Nobakht, M., Kaviani, D., and Ertekin, T. (2012b). Production analysis of tight-gas and shale-gas reservoirs using the dynamic-slippage concept. *SPE J.* 17 (01), 230–242. doi:10.2118/144317-pa

Curtis, M. E., Cardott, B. J., Sondergeld, C. H., and Rai, C. S. (2012). Development of organic porosity in the Woodford Shale with increasing thermal maturity. *Int. J. Coal Geol.* 103, 26–31. doi:10.1016/j.coal.2012.08.004

Dai, S., Ren, D., Chou, C. L., Finkelman, R. B., Seredin, V. V., and Zhou, Y. (2012). Geochemistry of trace elements in Chinese coals: A review of abundances, genetic types, impacts on human health, and industrial utilization. *Int. J. Coal Geol.* 94, 3–21. doi:10.1016/j.coal.2011.02.003

Gao, Z., Fan, Y., Xuan, Q., and Zheng, G. (2020). A review of shale pore structure evolution characteristics with increasing thermal maturities. *Adv. Geo-Energy Res.* 4 (3), 247–259. doi:10.46690/ager.2020.03.03

Garum, M., Glover, P. W., Lorinczi, P., Drummond-Brydson, R., and Hassanpour, A. (2020). Micro-and nanoscale pore structure in gas shale using Xμ-CT and FIB-SEM techniques. *Energy fuels.* 34 (10), 12340–12353. doi:10.1021/acs.energyfuels.0c02025

Groen, J. C., Peffer, L. A., and Pérez-Ramírez, J. (2003). Pore size determination in modified micro-and mesoporous materials. Pitfalls and limitations in gas adsorption data analysis. *Microporous mesoporous Mater.* 60 (1-3), 1–17. doi:10.1016/s1387-1811(03)00339-1

Hamawand, I., Yusaf, T., and Hamawand, S. G. (2013). Coal seam gas and associated water: A review paper. *Renew. Sustain. energy Rev.* 22, 550–560. doi:10.1016/j.rser.2013.02.030

Hao, F., Zou, H., and Lu, Y. (2013). Mechanisms of shale gas storage: Implications for shale gas exploration in China. *Am. Assoc. Pet. Geol. Bull.* 97 (8), 1325–1346. doi:10.1306/02141312091

Heller, R., and Zoback, M. (2014). Adsorption of methane and carbon dioxide on gas shale and pure mineral samples. *J. Unconv. oil gas Resour.* 8, 14–24. doi:10.1016/j.juogr.2014.06.001

Huang, B., Zhao, X., and Zhang, Q. (2016). Framework of the theory and technology for simultaneous mining of coal and its associated resources. *J. China Univ. Min. Technol.* 45 (4), 653–662.

Jarvie, D. M., Hill, R. J., Ruble, T. E., and Pollastro, R. M. (2007). Unconventional shale-gas systems: The Mississippian Barnett Shale of north-central Texas as one model for thermogenic shale-gas assessment. *Am. Assoc. Pet. Geol. Bull.* 91 (4), 475–499. doi:10.1306/12190606068

Ju, Y., Yu, K., Wang, G., Li, W., Zhang, K., Li, S., et al. (2021). Coupling response of the Meso–Cenozoic differential evolution of the North China Craton to lithospheric structural transformation. *Earth-Science Rev.* 223, 103859. doi:10.1016/j.earscirev.2021.103859

Klaver, J., Desbois, G., Littke, R., and Urai, J. L. (2015). BIB-SEM characterization of pore space morphology and distribution in postmature to overmature samples from the Haynesville and Bossier Shales. *Mar. Petroleum Geol.* 59, 451–466. doi:10.1016/j.marpetgeo.2014.09.020

Kuila, U., McCarty, D. K., Derkowski, A., Fischer, T. B., Topór, T., and Prasad, M. (2014). Nanoscale texture and porosity of organic matter and clay minerals in organic-rich mudrocks. *Fuel* 135, 359–373. doi:10.1016/j.fuel.2014.06.036

Li, J., Yin, J., Zhang, Y., Lu, S., Wang, W., Li, J., et al. (2015). A comparison of experimental methods for describing shale pore features—A case study in the bohai bay basin of eastern China. *Int. J. Coal Geol.* 152, 39–49. doi:10.1016/j.coal.2015.10.009

Li, Y., Pan, S., Ning, S., Shao, L., Jing, Z., and Wang, Z. (2022a). Coal measure metallogeny: Metallogenic system and implication for resource and environment. *Sci. China Earth Sci.* 65, 1211–1228. doi:10.1007/s11430-021-9920-4

Li, Y., Chen, J., Elsworth, D., Pan, Z., and Ma, X. (2022b). Nanoscale mechanical property variations concerning mineral composition and contact of marine shale. *Geosci. Front.* 13. doi:10.1016/j.gsf.2022.101405

Liang, L., Xiong, J., and Liu, X. (2015). An investigation of the fractal characteristics of the Upper Ordovician Wufeng Formation shale using nitrogen adsorption analysis. *J. Nat. Gas Sci. Eng.* 27, 402–409. doi:10.1016/j.jngse.2015.07.023

Liu, Y., Yao, Y., Liu, D., Zheng, S., Sun, G., and Chang, Y. (2018). Shale pore size classification: An NMR fluid typing method. *Mar. Petroleum Geol.* 96, 591–601. doi:10.1016/j.marpetgeo.2018.05.014

Loucks, R. G., Reed, R. M., Ruppel, S. C., and Jarvie, D. M. (2009). Morphology, Genesis, and distribution of nanometer-scale pores in siliceous mudstones of the Mississippian Barnett Shale. *J. Sediment. Res.* 79 (12), 848–861. doi:10.2110/jsr.2009.092

Loucks, R. G., Reed, R. M., Ruppel, S. C., and Hammes, U. (2012). Spectrum of pore types and networks in mudrocks and a descriptive classification for matrix-related mudrock pores. *Am. Assoc. Pet. Geol. Bull.* 96 (6), 1071–1098. doi:10.1306/08171111061

McGlade, C., Speirs, J., and Sorrell, S. (2013). Methods of estimating shale gas resources–Comparison, evaluation and implications. *Energy* 59, 116–125. doi:10.1016/j.energy.2013.05.031

Pan, J., Peng, C., Wan, X., Zheng, D., Lv, R., and Wang, K. (2017). Pore structure characteristics of coal-bearing organic shale in Yuzhou coalfield, China using low pressure N2 adsorption and FESEM methods. *J. Petroleum Sci. Eng.* 153, 234–243. doi:10.1016/j.petrol.2017.03.043

Ross, D. J., and Bustin, R. M. (2009). The importance of shale composition and pore structure upon gas storage potential of shale gas reservoirs. *Mar. Petroleum Geol.* 26 (6), 916–927. doi:10.1016/j.marpetgeo.2008.06.004

Rybacki, E., Meier, T., and Dresen, G. (2016). What controls the mechanical properties of shale rocks?–Part II: Brittleness. *J. Petroleum Sci. Eng.* 144, 39–58. doi:10.1016/j.petrol.2016.02.022

Saif, T., Lin, Q., Bijeljic, B., and Blunt, M. J. (2017). Microstructural imaging and characterization of oil shale before and after pyrolysis. *Fuel* 197, 562–574. doi:10.1016/j.fuel.2017.02.030

Shan, C., Zhang, T., Guo, J., Zhang, Z., and Yang, Y. (2015). Characterization of the micropore systems in the high-rank coal reservoirs of the southern Sichuan Basin, China. *Am. Assoc. Pet. Geol. Bull.* 99 (11), 2099–2119. doi:10.1306/07061514240

Sing, K. S., and Williams, R. T. (2004). Physisorption hysteresis loops and the characterization of nanoporous materials. *Adsorpt. Sci. Technol.* 22 (10), 773–782. doi:10.1260/0263617053499032

Tang, X., Jiang, Z., Li, Z., Gao, Z., Bai, Y., Zhao, S., et al. (2015). The effect of the variation in material composition on the heterogeneous pore structure of high-maturity shale of the Silurian Longmaxi formation in the southeastern Sichuan Basin, China. *J. Nat. Gas Sci. Eng.* 23, 464–473. doi:10.1016/j.jngse.2015.02.031

Uysal, I. T., Golding, S. D., and Glikson, M. (2000). Petrographic and isotope constraints on the origin of authigenic carbonate minerals and the associated fluid evolution in Late Permian coal measures, Bowen Basin (Queensland), Australia. *Sediment. Geol.* 136 (3-4), 189–206. doi:10.1016/s0037-0738(00)00097-x

Valenza, J. J., Drenzek, N., Marques, F., Pagels, M., and Mastalerz, M. (2013). Geochemical controls on shale microstructure. *Geology* 41 (5), 611–614. doi:10.1130/g33639.1

Wang, X., Tang, Y., Wang, S., and Schobert, H. H. (2020). Clean coal geology in China: Research advance and its future. *Int. J. Coal Sci. Technol.* 7 (2), 299–310. doi:10.1007/s40789-020-00321-4

Yang, F., Ning, Z., and Liu, H. (2014). Fractal characteristics of shales from a shale gas reservoir in the Sichuan Basin, China. *Fuel* 115, 378–384. doi:10.1016/j.fuel.2013.07.040

Yang, R., He, S., Yi, J., and Hu, Q. (2016). Nanoscale pore structure and fractal dimension of organic-rich Wufeng-Longmaxi shale from Jiaoshiba area, Sichuan Basin: Investigations using FE-SEM, gas adsorption and helium pycnometry. *Mar. Petroleum Geol.* 70, 27–45. doi:10.1016/j.marpetgeo.2015.11.019

Yang, J., Hatcherian, J., Hackley, P. C., and Pomerantz, A. E. (2017). Nanoscale geochemical and geomechanical characterization of organic matter in shale. *Nat. Commun.* 8 (1), 2179–9. doi:10.1038/s41467-017-02254-0

Yang, W., Song, Y., Jiang, Z., Luo, Q., Wang, Q., Yuan, Y., et al. (2018). Whole-aperture characteristics and controlling factors of pore structure in the Chang 7th continental shale of the Upper Triassic Yanchang Formation in the southeastern Ordos Basin, China. *Interpretation* 6 (1), T175–T190. doi:10.1190/int-2017-0090.1

Yang, W., Wang, Q., Wang, Y., Jiang, Z., Song, Y., Li, Y., et al. (2020). Pore characteristic responses to categories of depositional microfacies of delta-lacustrine tight reservoirs in the Upper Triassic Yanchang Formation, Ordos Basin, NW China. *Mar. Petroleum Geol.* 118, 104423. doi:10.1016/j.marpetgeo.2020.104423

Yang, W., Xu, L., Chen, D. X., Jiang, Z. X., Zhang, Z. Y., Hao, B., et al. (2021). How argillaceous reservoirs exhibit better quality than silty mudstones? Anomalous

behavior of shale gas-bearing properties of continental fine-grained sediments in southwest China and its possible forcing mechanisms. *Petroleum Sci.* 18 (6), 1589–1610. doi:10.1016/j.petsci.2021.09.032

Yu, K., Shao, C., Ju, Y., and Qu, Z. (2019). The Genesis and controlling factors of micropore volume in transitional coal-bearing shale reservoirs under different sedimentary environments. *Mar. Petroleum Geol.* 102, 426–438. doi:10.1016/j.marpetgeo.2019.01.003

Yu, K., Ju, Y., and Shao, C. (2020). Structure characteristics and evolution mechanism of nanopore in transitional coal-bearing shale. *J. Petroleum Sci. Eng.* 184, 106545. doi:10.1016/j.petrol.2019.106545

Yu, K., Ju, Y., Wan, Z., and Zhao, K. (2022). Paleoenvironment, provenance, and hydrocarbon potential of lower permian coal-bearing source rocks in the southern north China basin: A case study of the pingdingshan coalfield. *ACS Earth Space Chem.* 6 (5), 1299–1310. doi:10.1021/acsearthspacechem.2c00003

Zeng, X., Wang, W., Cao, Q., Zhou, S., Dong, G., Wang, A., et al. (2022). *Evaluation of the accumulation conditions and favorable areas of shale gas in the upper palaeozoic marine-continental transitional facies in the daning-jixian area*. Geofluids: Ordos Basin.

Zhang, J., Li, X., Wei, Q., Sun, K., Zhang, G., and Wang, F. (2017). Characterization of full-sized pore structure and fractal characteristics of marine–continental transitional Longtan Formation shale of Sichuan Basin, South China. *Energy fuels.* 31 (10), 10490–10504. doi:10.1021/acs.energyfuels.7b01456

Zhang, Q., Qiu, Z., Zhao, Q., Zhang, L., Dong, D., Wang, Y., et al. (2022). Composition effect on the pore structure of transitional shale: A case study of the permian Shanxi Formation in the daning–jixian block at the eastern margin of the Ordos Basin. *Front. Earth Sci. (Lausanne).* 9, 1407. doi:10.3389/feart.2021.802713

Zhu, H., Ju, Y., Huang, C., Han, K., Qi, Y., Shi, M., et al. (2019). Pore structure variations across structural deformation of silurian longmaxi shale: An example from the chuandong thrust-fold belt. *Fuel* 241, 914–932. doi:10.1016/j.fuel.2018.12.108

Zou, C. N., Yang, Z., Huang, S. P., Ma, F., Sun, Q. P., Li, F. H., et al. (2019). Resource types, formation, distribution and prospects of coal-measure gas. *Petroleum Explor. Dev.* 46 (3), 451–462. doi:10.1016/s1876-3804(19)60026-1

frontiers | Frontiers in Earth Science

Pore structure and fractal characteristics of the marine shale of the longmaxi formation in the changning area, Southern Sichuan Basin, China

Hu Li[1,2,3,4]*, Jiling Zhou[5], Xingyu Mou[6], Hongxi Guo[6], Xiaoxing Wang[6], Hongyi An[6], Qianwen Mo[6], Hongyu Long[5], Chenxi Dang[7], Jianfa Wu[8], Shengxian Zhao[8], Shilin Wang[2,4], Tianbiao Zhao[2,3,4] and Shun He[2,4]

[1]Shale Gas Evaluation and Exploitation Key Laboratory of Sichuan Province, Chengdu, China, [2]Natural Gas Geology Key Laboratory of Sichuan Province, Chengdu, China, [3]Sichuan College of Architectural Technology, Chengdu, China, [4]School of Geoscience and Technology, Southwest Petroleum University, Chengdu, China, [5]Exploration and Development Research Institute, PetroChina Southwest Oil and Gas Field Company, Chengdu, China, [6]Exploration Division, PetroChina Southwest Oil and Gas Field Company, Chengdu, China, [7]Northwest Sichuan Gas District, PetroChina Southwest Oil and Gas Field Company, Jiangyou, China, [8]Shale Gas Institute, PetroChina Southwest Oil and Gas Field Company, Chengdu, China

The pore structure is an important factor affecting reservoir capacity and shale gas production. The shale reservoir of the Longmaxi Formation in the Changning area, Southern Sichuan Basin, is highly heterogeneous and has a complex pore structure. To quantitatively characterize the shale's pore structure and influencing factors, based on whole rock X-ray diffraction, argon ion polishing electron microscopy observations, and low-temperature nitrogen adsorption-desorption experiments, the characteristics of the shale pore structure are studied by using the Frenkel-Halsey-Hill (FHH) model. The research reveals the following: 1) The pores of the Longmaxi Formation shale mainly include organic pores, intergranular pores, dissolution pores and microfractures. The pore size is mainly micro-mesoporous. Both ink bottle-type pores and semiclosed slit-type pores with good openness exist, but mainly ink bottle-type pores are observed. 2) The pore structure of the Longmaxi Formation shale has self-similarity, conforms to the fractal law, and shows double fractal characteristics. Taking the relative pressure of 0.45 ($P/P_0 = 0.45$) as the boundary, the surface fractal dimension D_{sf} and the structural fractal dimension D_{st} are defined. D_{sf} is between 2.3215 and 2.6117, and the structural fractal dimension D_{st} is between 2.8424 and 2.9016. The pore structure of micropores and mesopores is more complex. 3) The mineral components and organic matter have obvious control over the fractal dimension of shale, and samples from different wells show certain differences. The fractal dimension has a good positive correlation with the quartz content but an obvious negative correlation with clay minerals. The higher the total organic carbon content is, the higher the degree of thermal evolution, the more complex the pore

structure of shale, and the larger the fractal dimension. The results have guiding significance for the characterization of pore structure of tight rocks.

Introduction

Shale gas is a high-quality unconventional natural gas resource under the "carbon peaking and carbon neutralization" policy and has the characteristics of enormous resources, cleanness, and efficiency. Sichuan Basin is a key target area for shale gas exploration and development in China. The marine shale of the Wufeng-Longmaxi Formation has the characteristics of a high TOC value, large thickness, high maturity, good brittleness, and high gas content and is the preferred horizon for shale gas exploration and development (Jin et al., 2018; Fan et al., 2020a, 2020b; Ma et al., 2021; Qiu et al., 2021). Currently, three national shale gas demonstration areas, Fuling, Weiyuan-Changning, and Zhaotong, have been built for the shale gas of the Wufeng-Longmaxi Formation in the Sichuan Basin. These areas mentioned above mainly contain medium-shallow shale gas reservoirs with a buried depth of less than 3,500 m. Organic rich shale generally has the characteristics of low porosity and permeability (porosity less than 8% and permeability less than 10 nD) and mainly develops micron to nanometre pores (He et al., 2021, 2022a; Li et al., 2022a, 2022b; Fan et al., 2022). The pore structure is complex, and the specific surface area is large. The complex internal surface area can store a large amount of gas by adsorption. The proportion of free gas and adsorbed gas in shale is affected by the pore structure of the shale. The more complex the pore structure is, the stronger the adsorption capacity of hydrocarbon gas. The complex pore structure and heterogeneity of shale increase the level of difficulty for shale gas development (Liu J. et al., 2018; Li H. T. et al., 2021, Li et al., 2021 H.; Wang et al., 2021; Zhan et al., 2021). Quantitative characterization of the shale pore structure is of great significance for the effective development of shale gas.

For qualitative or quantitative characterization of the shale pore structure, environmental scanning electron microscopy, argon ion polishing technology, transmission electron microscopy, the mercury intrusion method, and the low-pressure gas adsorption method are mainly used at present. However, because the heterogeneity of the shale pore structure does not conform to the traditional European geometric law, these methods cannot be directly used to characterize the heterogeneity of the pore structure. Fractal geometry theory was proposed by Mandelbrot and can be used to characterize special structures that do not conform to European geometric laws and have certain self-similarity (Mandelbrot, 1978, 1984, 1985). In recent years, it has been widely used in the shale pore structure field (Li et al., 2019a; Liu et al., 2020; Li, 2021; Liu et al.,

2021). Pore image data, gas or liquid flow test data (such as nitrogen adsorption and mercury intrusion tests), and NMR data can be used to study the pore fractal characteristics (Yang et al., 2017; Liu J. S. et al., 2018; Tang et al., 2019; Wei et al., 2019). For different types of shale reservoir spaces, researchers have attempted to use different models such as the Frenkel-Halsey-Hill (FHH) model, Newton-Kantorovich (NK) model, and Neimark model to carry out fractal research on the shale pore structures (Ahmad and Mustafa, 2006; Pan et al., 2021; Chang et al., 2022). The FHH model is more suitable for rocks with porous media than other models. Also, the FHH model is the most accurate for rock with microporous - mesoporous. In addition, among the various calculation models, the FHH fractal model is widely used in shale pore structure, which is simple to calculate and has strong applicability (Zhang et al., 2018; Li et al., 2019a; Tang et al., 2022).

The Changning area in the Southern Sichuan Basin is close to the basin's edge. The Longmaxi Formation shale has complex sedimentation and structural evolution, forming a large number of multiscale pore and fracture systems, so the heterogeneity of the reservoir pore structure is strong. Based on scanning electron microscopy (SEM), X-ray diffractometry (XRD), and related geochemical experiments, combined with low-temperature nitrogen adsorption experiments, this study quantitatively characterized the pore structure of the Longmaxi Formation shale in the study area by using the commonly used FHH model and analyzed the main influencing factors of the fractal dimension. The research results have guiding significance for the characterization of the pore structure of marine shale and evaluation of the shale gas reservoir capacity.

Geological setting

The Changning area is located at the southern edge of the Sichuan Basin, and its geographical location is located in the south of Changning County, northeast of Junlian County, west of Gao County, and east of Xuyong County. The structure is located at the end of the southwest extension of the high and steep fold belt in Eastern Sichuan, at the junction of the Southern Sichuan fault fold belt and the Loushan fault fold belt, and adjacent to the Southern Huaying Mountain fault fold belt in the west (Figure 1A). The surface of the study area mainly develops NE, NW, EW, and other multidirectional faults and related folds (Fan et al., 2020b; He et al., 2022b). The long axis of the Changning anticline is WNW-ESE, the NE wing is steep, the SW

FIGURE 1
Regional geological overview of the Changning area (Wu et al., 2021). **(A)**. Tectonic position (He et al., 2019); **(B)**. Surface geological map; **(C)**. Comprehensive stratigraphic histogram (Feng et al., 2016).
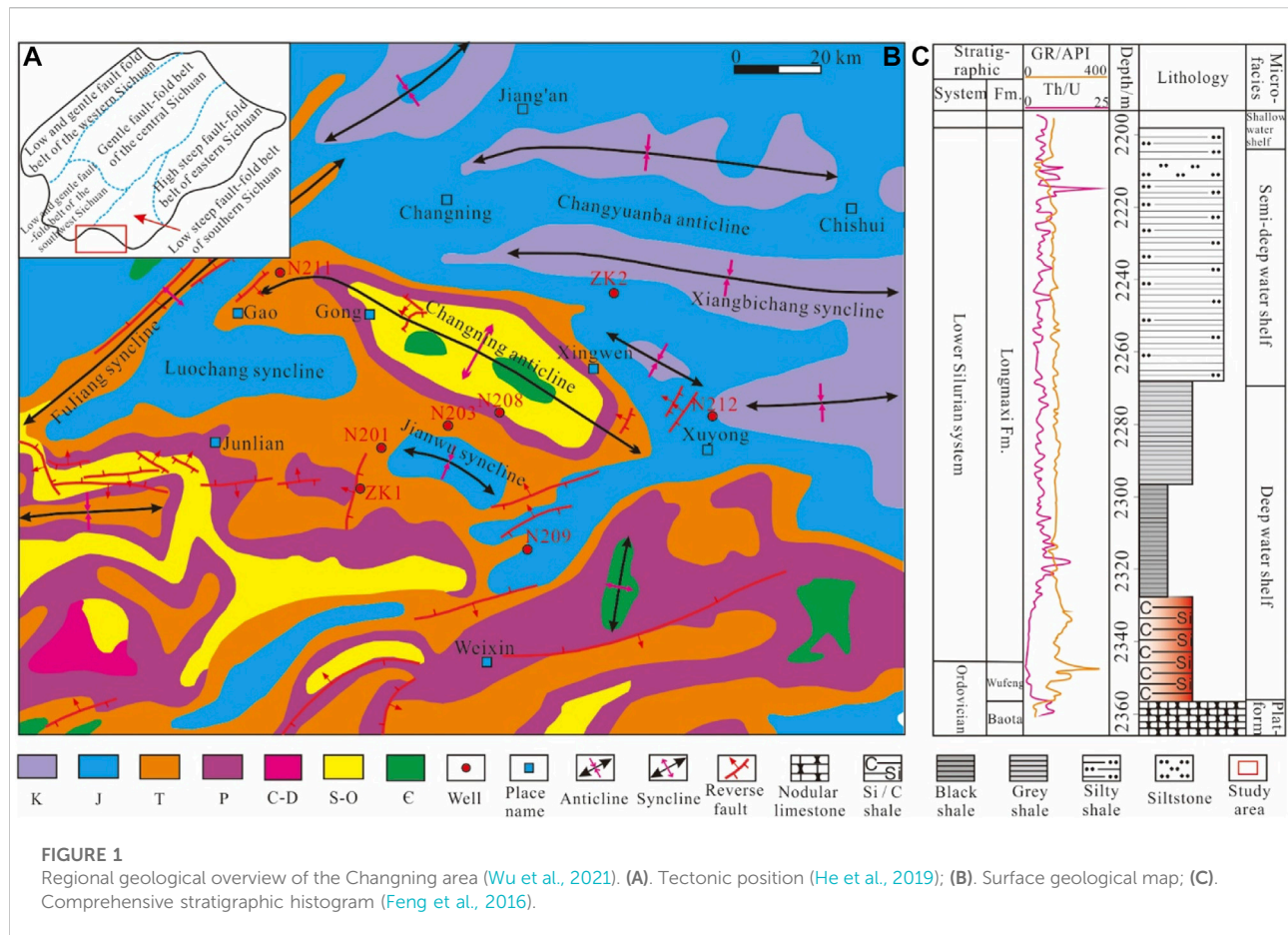
wing is gentle, and the axial plane at the NW end of the anticline is curved, plunging to the south of Gao County, reaching the Jin'e area in the east, and disappearing in the Xuyong syncline. The core of the anticline is exposed to the lower Ordovician, and the two wings of the anticline are exposed to the Silurian, Permian, Triassic, Jurassic, and Cretaceous, along with the Middle Devonian and Carboniferous systems (Figure 1B) (Li et al., 2022c).

From the late Ordovician to the Early Silurian, affected by the Duyun tectonic movement, most areas of the Sichuan Basin were trapped by the subaqueous uplift in Sichuan, the Niushou Mountain-Central Guizhou uplift, and the Jiangnan-Xuefeng uplift, forming a large-scale deep-water depression dominated by the continental shelf. Rapid transgression occurred in the depression, forming a large-scale oxygen-poor/anoxic deep-water shelf environment (Wang et al., 2019). Organic matter and silica are enriched and continuously distributed at the bottom of the Longmaxi Formation, forming an area of $10.7 \times 10^4 \ km^2$ of organic-rich (TOC greater than 2%) cumulative shale facies belt, in which the thickness of the high-quality shale interval is greater than 35 m (Figure 1C).

Samples and methods

Samples and experiments

Due to the influence of weathering, the pore structure of the outcrop samples may change, which cannot reflect the real pore structure characteristics. Therefore, the shale samples were taken from 12 Longmaxi Formation drilling cores from two evaluation wells (ZK_1 and ZK_2) in the study area, and the sampling depth covered Member one of the Longmaxi Formation from bottom to top. The lithology of the sample was mainly black and greyish black organic-rich shale, and the type of organic kerogen was mainly type I and a small amount of type II_1.

The experimental test included organic carbon content (TOC), vitrinite reflectance (Ro), whole rock X-ray diffraction analysis, scanning electron microscopy observations, and low-temperature nitrogen adsorption-desorption experiments. These tests were mainly conducted at the State Key Laboratory of Oil and Gas Reservoir Geology and Development Engineering, and some data were obtained from the Shale Gas Research Institute of PetroChina Southwest Oil and Gas Field Company. The organic carbon content of shale was tested by a CS230SH carbon and

sulfur analyzer produced by Leco company located in the United States, using the solid-state infrared absorption method and following the Standard for the Determination of Total Organic Carbon in Sedimentary Rocks (GB/T 19145-2003). The mineral composition of the whole rock was analyzed according to the SY/T5163-2010 standard and determined by an X'Pert MPD PRO X-ray diffractometer produced by Panaco company in the Netherlands. A Quanta 450 environmental scanning electron microscope made by FEI Company in the United States was used for the Argon ion polishing scanning electron microscopy observations. The working voltage of the instrument was set to 15 kV and 15 nA, and the maximum pore resolution was 3 nm. According to the GB/T16594-2008 standard, an Ilion II 697 argon ion polishing instrument and a Merlin Compact field emission scanning electron microscope were used to determine.

A six-station automatic specific surface area and porosity analyzer (Quantachrome Instruments, United States) was used for the low-temperature nitrogen adsorption experiments. The measured pore size range was 0.35–500 nm. Before the experiment, the samples were placed in deionized water for ultrasonic cleaning to remove surface impurities, and the samples were dried and pretreated after decontamination. Then, the dried samples were manually ground to 20–50 mesh in an agate mortar, and the ground powder samples were vacuum dried for 14 h under a high temperature of 120°C. During the experiment, liquid nitrogen with a purity greater than 99.999% was used as the adsorption medium. Under a constant temperature liquid nitrogen condition of 77 K, the gas adsorption capacity under the gradual increase in the relative pressure and the desorption capacity when the pressure decreased were measured to obtain the isothermal adsorption and desorption data for the sample.

Calculation of the fractal dimension based on nitrogen adsorption and desorption data

According to the International Union of Pure and Applied Chemistry (IUPAC) classification standard of pore size, the pores of shale can be divided into micropores (<2 nm) and mesopores (2–50 nm), and macropores (>50 nm) (Li et al., 2019a; Yang et al., 2022). Organic-rich shale mainly develops micron to nanometre pores, and pores with a diameter of 2–50 nm are the main contributors to shale porosity and the main space for gas enrichment. Research has revealed that the low-temperature liquid nitrogen adsorption-desorption method can better characterize micropores (<2 nm) and mesopores (2–50 nm). Therefore, this study mainly analyses the fractal characteristics of these two types of pores. The fractal dimension of shale is calculated based on the low-temperature nitrogen adsorption

curve data for the sample, and the commonly used FHH model is applied:

$$\ln V = K \ln \left[\ln \left(P_0 / P \right) \right] + C \qquad (1)$$

$$D = K + 3 \qquad (2)$$

$$D = 3K + 3 \qquad (3)$$

Where V is the volume of adsorbed gas under different relative pressures, cm^3/g; P_0 refers to the saturated steam pressure, MPa; K is the slope of the equation fitting curve; C is a constant; and D is the fractal dimension.

Different publicity calculations are used to calculate the fractal dimension according to the morphological characteristics of the low-temperature nitrogen adsorption curve. If the surface tension of liquid/gas is the more important factor, the capillary force tends to reduce the interface area, and the fractal dimension is calculated by Formula (2). Suppose the van der Waals force between the solid and the adsorption layer is the main factor, and the adsorption is mainly affected by the surface roughness of the gas/adsorption layer interface. In that case, Formula (3) is used to calculate the fractal dimension. When quantifying the complexity of shale pores, the fractal dimension is between 2 and 3. The larger the fractal dimension is, the more complex the shale pore structure. The object does not have fractal characteristics if the fractal dimension is less than 2 or greater than 3 (Tang et al., 2022).

Results

Pore types and characteristics of shale

Generally speaking, the pores of organic-rich shale mainly include three types: inorganic pores, organic pores, and microfractures. These three types of pores are developed in the Longmaxi Formation shale in the Changning area. Shale has a complex mineral composition and various inorganic pores, including intergranular pores, intragranular pores, intercrystalline pores, and dissolution pores (Wang et al., 2018; Li et al., 2020; Wang and Wang, 2021). Shale has a high degree of the thermal evolution of organic matter, and primary organic pores and hydrocarbon generation shrinkage pores are widely developed. Due to the extrusion of mineral particles and the action of tectonic stress, mineral edge fractures and tectonic microfractures are developed.

Intergranular pores are mostly residual primary pores, the residual intergranular pore space after compaction and water loss transformation in diagenesis (Wang et al., 2020). This type of pore is similar to the residual primary intergranular pores of conventional reservoirs and usually shrinks with the increase in burial depth. Quartz and feldspar minerals are highly brittle, and mineral particles support each other, often forming mineral
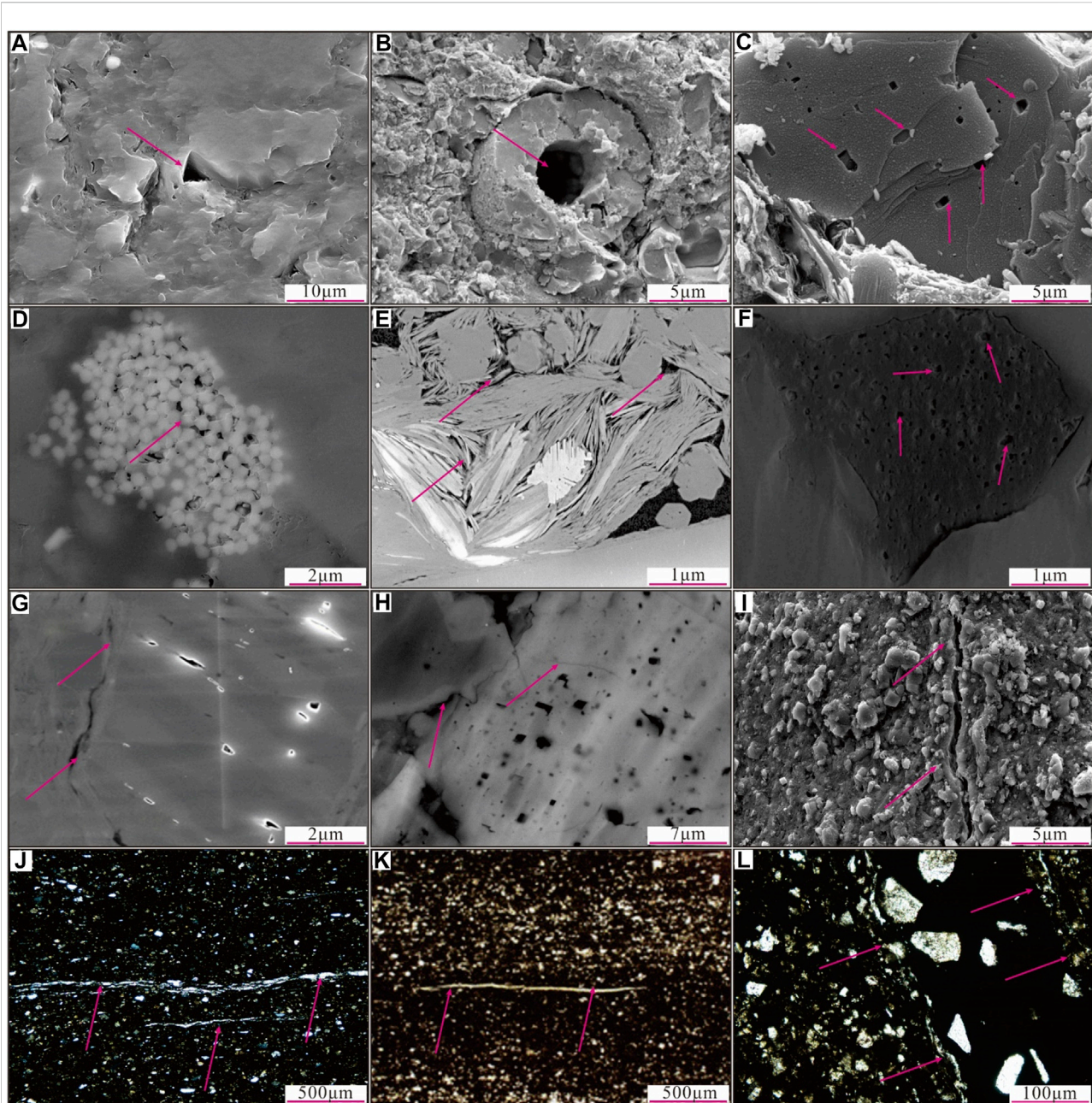
FIGURE 2
Microscopic pore types and characteristics of the Longmaxi Formation shale in the Changning area. **(A)** N216, 2,302.5 m, clay mineral particles supporting residual pores; **(B)** N216, 2,316.7 m, biological cavities developed inside biological particles; **(C)**. ZK$_2$, 2,233.8 m, intragranular dissolution pores; **(D)**. ZK$_2$, 233.95 m, intracrystalline pores of strawberry pyrite; **(E)**. N216, 2,308.2 m, intracrystalline pores developed between the crystals of clay minerals; **(F)**. ZK$_2$, 2,214.37 m, organic pores with a honeycomb distribution; **(G)**. N201, intracrystalline fracture; **(H)**. N216, fracture in the crystal; **(I)**. N216, diagenetic contraction fracture; **(J)**. N216, bedding fracture; **(K)**. N216, hydrocarbon expulsion contraction fracture; **(L)**. N216, dissolution fracture.

intergranular pores, which are mainly produced in a slit or irregular shape (Figure 2A). Intragranular pores are developed in the interior of clastic particles, such as biological cavity pores (Figure 2B) and wall pores of organisms developed in biological particles, and intragranular pores developed in quartz, feldspar, clay, and other particles, some of which form intragranular dissolved pores under the action of an acidic fluid (Figure 2C). Intercrystallite pores are micropores formed by mineral crystallization under the condition of a stable environment and appropriate medium conditions, including

TABLE 1 Mineral composition and vertical changes in the Wufeng-Longmaxi Formation shale in the Changning area.

Well	Sample	Depth (m)	Quartz (%)	Potash feldspar (%)	Plagioclase (%)	Calcite (%)	Dolomite (%)	Pyrite	Clay minerals (%)	TOC (%)	Ro (%)
ZK1	ZK1-1	2,393.51	23.8	1	4.5	26.1	5.5	1.1	38	0.89	2.24
	ZK1-2	2,467.35	35.4	2.5	12.3	8.1	3.3	1.5	36.9	1.56	2.52
	ZK1-3	2,473.58	31	2.3	17.6	11.4	2.7	1.4	33.6	1.11	2.5
	ZK1-4	2,487.10	37.4	1	4.8	12.4	1.9	2.4	40.1	2.1	2.53
	ZK1-5	2,496.31	39.8	1.6	5.2	9.5	4	2.7	37.2	4.89	2.62
	ZK1-6	2,499.29	30.8	0.2	4.1	17.2	12.1	6.4	29.2	4.05	2.48
ZK2	ZK2-1	2,235.60	52.00	1.18	3.78	11.96	18.90	0.95	11.23	4.08	2.75
	ZK2-2	2,223.80	58.88	0.76	3.07	4.90	12.90	1.4	18.10	3.87	2.78
	ZK2-3	2,221.25	49.58	1.32	6.08	9.94	8.80	0.97	23.30	4.13	2.69
	ZK2-4	2,209.20	36.57	1.01	5.75	5.15	2.20	1.02	48.30	2.30	2.65
	ZK2-5	2,188.55	33.22	2.71	9.20	9.09	3.10	0.99	41.70	1.59	2.54
	ZK2-6	2,160.80	27.35	2.79	13.94	10.27	3.40	0.04	42.20	1.19	2.46

pyrite, clay minerals, dolomite, etc., and the pore diameters are mostly distributed between 10 and 500 nm. The most common intercrystallite pores in the study area are strawberry pyrite (Figure 2D) formed in the deep water and anoxic reduction environment and pores developed between the crystals of clay minerals (Figure 2E). The study area mainly develops intergranular organic pores and pyrite-associated organic pores, mainly micropores and mesopores, which contribute greatly to the specific surface area and pore volume of shale and are the main reservoir space of adsorbed natural gas. The content of clastic particles is high, and organic matter fills between the clastic particles and forms organic pores (Figure 2F), which are mainly round and oval.

In addition, the fractures in the study area are widely developed, mainly including three types of microfractures (Wu et al., 2021): 1) mineral intracrystalline fractures and intragranular fractures formed by tectonic action, in which the intracrystalline fractures are also called mineral crystal edge fractures or paste grain fractures (Li et al., 2019a; 2019b). Mineral crystals are deformed and displaced to varying degrees by early tectonic action, forming a certain degree of fractures with the surrounding, and the fracture surfaces are mostly crystal surfaces. The fracture shape coordinates with the crystal boundary, and the opening is approximately 0.01–0.10 μm (Figure 2G). Intragranular fractures, also known as mineral joint fractures, are caused by lattice dislocation or fracture in the crystal under tectonic action (Figure 2H) (Ameen, 2016; Cheng et al., 2021; Shan et al., 2021; Song et al., 2021; Liu et al., 2022a; Wang et al., 2022). 2) Diagenetic contraction fractures and bedding fractures are formed by diagenesis, in which diagenetic contraction fractures are formed by a series of physical and chemical actions such as dehydration, contraction, dry cracking, phase transformation, or recrystallization of

sediments during diagenesis, which is characterized by a long extension distance and large opening variation range (Figure 2I). The most prominent feature of bedding fractures is that they are oriented with clay minerals and other minerals, and the opening of fractures can be large or small locally, with a width of approximately 0.01–23.3 μm, which is mostly filled with minerals (Figure 2J). 3) Abnormal high-pressure fractures, hydrocarbon expulsion contraction fractures, and dissolution fractures formed by hydrocarbon generation and expulsion of organic matter, in which abnormal high-pressure fractures are generally developed in shale rich in organic matter, which is mostly controlled by the morphology of kerogen and mineral crystals. Kerogen as the centre extends radially along the surface of the mineral particles and is considered the main transportation channel for the lateral migration of oil and gas. Hydrocarbon expulsion contraction fractures are mainly developed from the interior of organic matter to the edge of organic matter and mineral particles (Gao, 2019; Fan et al., 2020c; Li, 2022). For long-axis organic matter, contraction fractures divide it into multiple sections, most of which are arc-shaped, and the width of the fracture is up to 20 μm in the middle of the fracture arc (Figure 2K). The fracture can also show a slender "hair" shape, bending and pinching out at the end, formed by the volume contraction caused by the dehydration of organic matter at the later stage (Figure 2L) (Ambrose et al., 2010; Li et al., 2018, 2019c).

Mineral composition and organic geochemical characteristics

According to the experimental test data for 12 samples from the two evaluation wells, ZK_1 and ZK_2, in the study area, the shale

FIGURE 3
Low-temperature nitrogen adsorption-desorption curves of the Longmaxi Formation shale in the Changning area. **(A–F)** is from ZK$_1$, and **(G–L)** is from ZK$_2$.
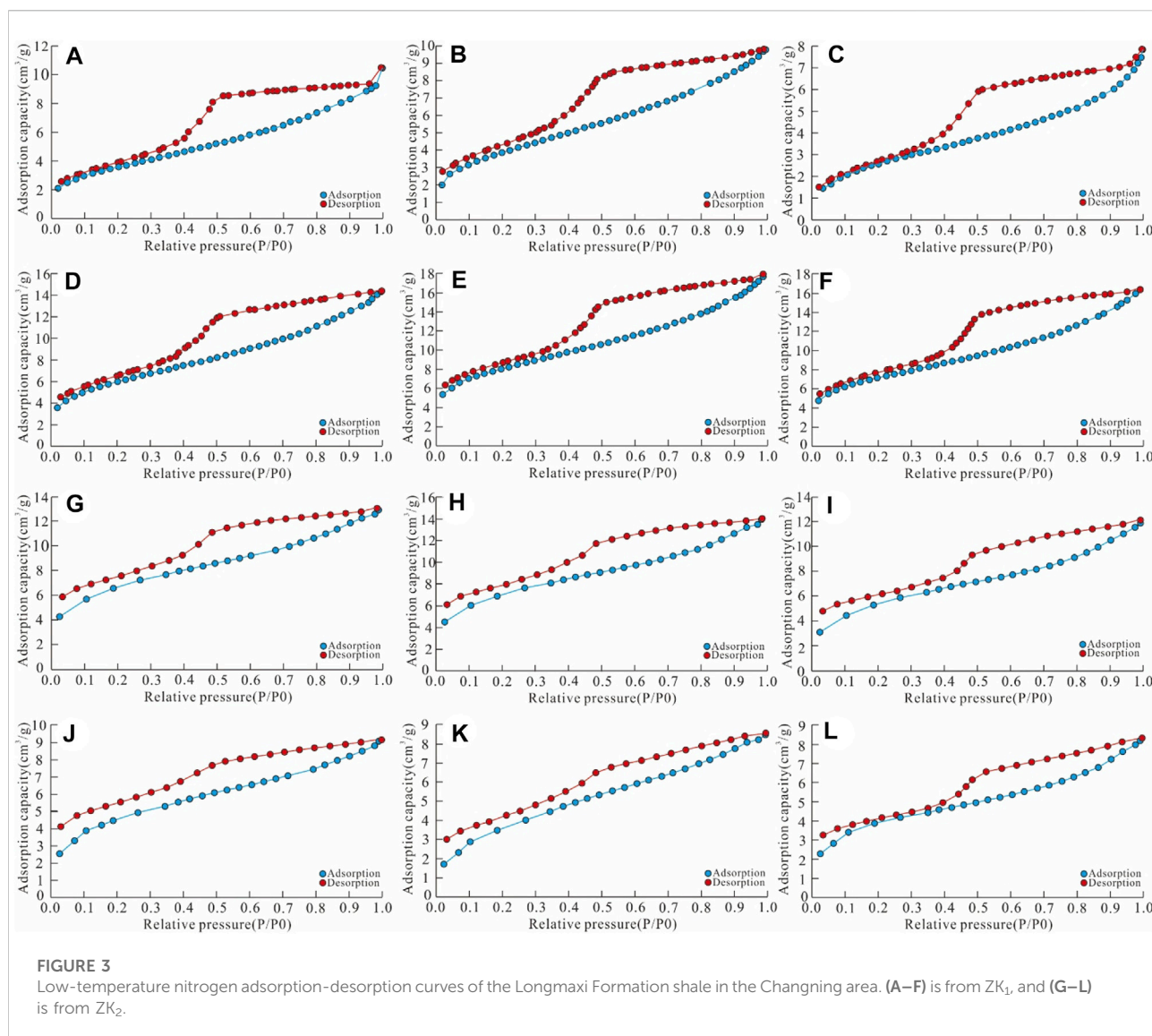
mineral components mainly include quartz, feldspar (potassium feldspar and plagioclase), calcite, dolomite, pyrite, clay minerals, etc. The quartz content of well ZK$_1$ is between 23.8 and 39.8%, with an average of 33.03%, and that of well ZK$_2$ is between 27.35 and 58.88%, with an average of 42.93%. The feldspar content of well ZK$_1$ is between 4.3 and 19.9%, with an average of 9.52%, and that of well ZK$_2$ is between 3.83 and 16.73%, with an average of 8.60%. The content of carbonate minerals (calcite and dolomite) in well ZK$_1$ is between 11.4 and 31.6%, with an average of 19.03%, and that in well ZK$_2$ is between 7.35 and 30.86%, with an average of 16.77%. The clay minerals include mainly illite, along with illite/montmorillonite mixed layer and chlorite. The content of well ZK$_1$ is between 29.2 and 40.1%, with an average of 35.83%, and that of well ZK$_2$ is between 11.23 and 48.30%, with an average of 30.81% (Table 1). According to the

organic sulfur carbon test results, the TOC and Ro in the study area are both high. The TOC of well ZK$_1$ is between 0.89 and 4.89%, with an average of 2.43%, and the Ro is between 2.24 and 2.62%, with an average of 2.48%. The TOC of well ZK$_2$ is between 1.19 and 4.13%, with an average of 2.86%, and the Ro is between 2.46 and 2.78%, with an average of 2.65% (Table 1). Overall, with the increase in depth, the content of quartz and brittle minerals gradually increases, while the content of clay minerals gradually decreases. The content of brittle minerals reaches the maximum at the bottom of the Longmaxi Formation. In addition, the maximum values of TOC and Ro are also at the bottom of the Longmaxi Formation. Due to the different structural positions of the two wells, there are large differences in the mineral components, but the variation rules are the same.

FIGURE 4
ln (V) vs ln [ln (P$_0$/P)] curves of the Longmaxi Formation shale in the Changning area. **(A–F)** is from ZK$_1$, and **(G–L)** is from ZK$_2$.
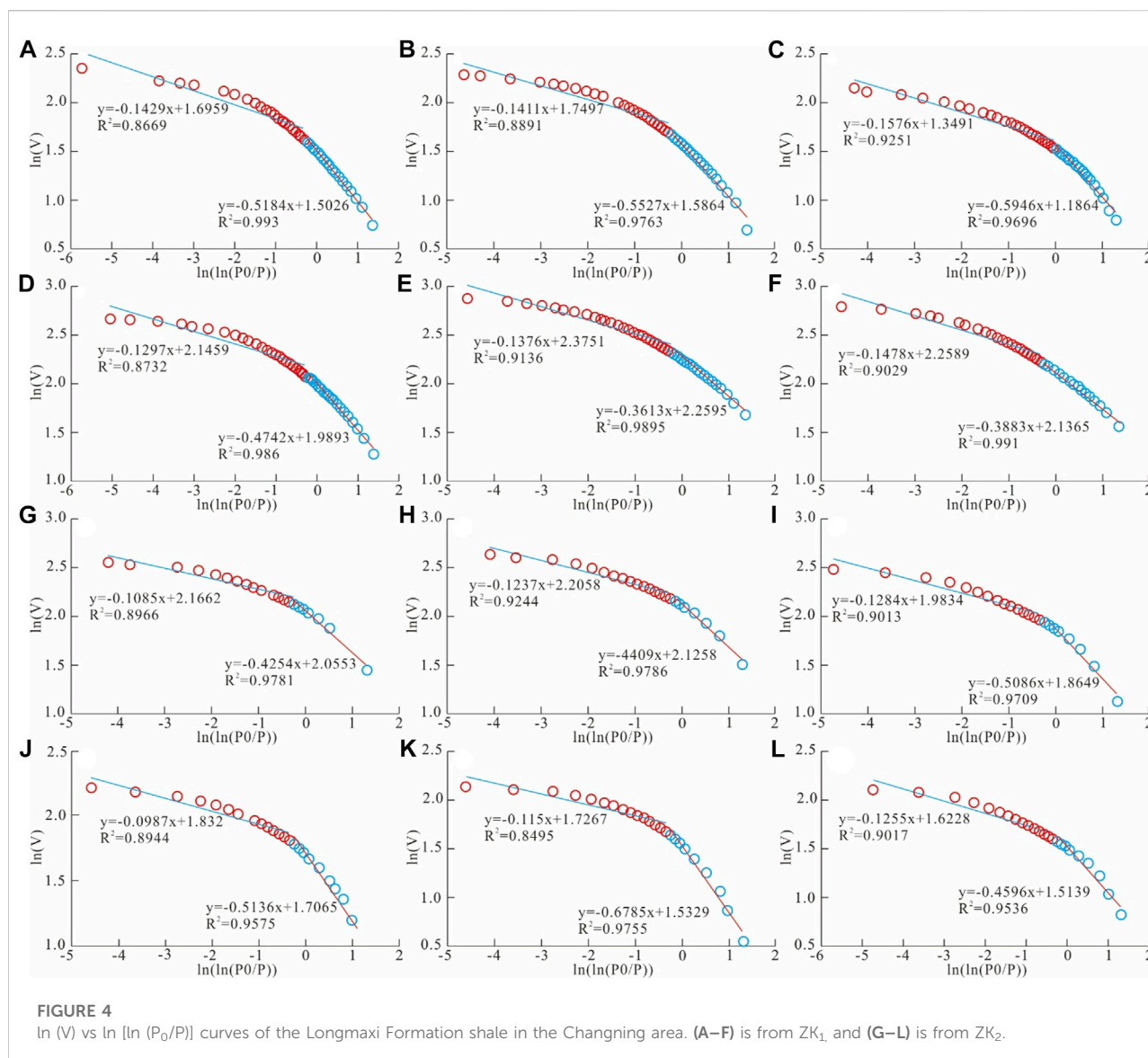
Pore morphological characteristics

Low-temperature nitrogen adsorption-desorption experiments were carried out on the 12 samples from the two wells in the study area. With the increase in relative pressure, nitrogen was gradually adsorbed on the pore surface of shale, and capillary condensation occurred (Li et al., 2015; Ma et al., 2022). After reaching the maximum pressure, the pressure began to decrease, and the nitrogen adsorbed on the pore surface of shale gradually began to evaporate in the capillary, resulting in desorption. Because the phenomenon of nitrogen desorption is obviously later than that of adsorption at the same pressure, a hysteresis loop is formed (Xu et al., 2017). According to the IUPAC classification of isothermal adsorption curves and hysteresis loops, pores can be divided into four different categories, i.e., cylindrical pores, ink bottle pores, parallel plate pores, and slit pores.

From the low-temperature nitrogen adsorption-desorption curves of the 12 samples (Figure 3). In the relatively low-pressure stage (P/P$_0$<0.45), the shapes of the adsorption curve and desorption curve are the same, but the two do not coincide. The curve rises slowly and presents an upward slightly convex shape. This stage is the transition from adsorption monolayer to multi-molecular layer. In the relatively high-pressure stage (P/P$_0$>0.45), the adsorption capacity increases slowly with the increase of pressure, and this stage is a multi-layer adsorption process, the adsorption curve shows obvious hysteresis. According to the shape of the nitrogen adsorption-desorption curve, we believe that the pore morphology in the study area is of two types: mainly ink bottle-type pores along with semiclosed

TABLE 2 Fractal dimension of the Wufeng-Longmaxi Formation shale based on the FHH theoretical model.

Well	Sample	P/Po < 0.45			P/Po > 0.45		
		Fractal fitting equation	R^2	D_1	Fractal fitting equation	R^2	D_2
ZK1	ZK1-1	y = −0.5184x + 1.5026	R^2 = 0.993	2.4816	y = −0.1429x + 1.6959	R^2 = 0.8669	2.8571
	ZK1−2	y = −0.5527x + 1.5864	R^2 = 0.9763	2.4473	y = −0.1411x + 1.7497	R^2 = 0.8891	2.8589
	ZK1-3	y = −0.5946x + 1.1864	R^2 = 0.9696	2.4054	y = −0.1576x + 1.3491	R^2 = 0.9251	2.8424
	ZK1-4	y = −0.4742x + 1.9893	R^2 = 0.9860	2.5258	y = −0.1297x + 2.1495	R^2 = 0.8732	2.8703
	ZK1-5	y = −0.3913x + 2.2595	R^2 = 0.9895	2.6087	y = −0.1376x + 2.3751	R^2 = 0.9136	2.8624
	ZK1-6	y = −0.3883x + 2.1365	R^2 = 0.9910	2.6117	y = −0.1478x + 2.2589	R^2 = 0.9029	2.8522
ZK2	ZK2-1	y = −0.4254x + 2.0553	R^2 = 0.9781	2.5746	y = −0.1085x + 2.1662	R^2 = 0.8966	2.8915
	ZK2-2	y = −0.4409x + 2.1258	R^2 = 0.9786	2.5591	y = −0.1237x + 2.2058	R^2 = 0.9244	2.8763
	ZK2-3	y = −0.5086x + 1.8649	R^2 = 0.9709	2.4914	y = −0.1284x + 1.9834	R^2 = 0.9013	2.8716
	ZK2-4	y = −0.5136x + 1.7065	R^2 = 0.9575	2.4864	y = −0.0987x + 1.8320	R^2 = 0.8944	2.9013
	ZK2-5	y = −0.6785x + 1.5329	R^2 = 0.9755	2.3215	y = −0.1115x + 1.7267	R^2 = 0.8495	2.8885
	ZK2-6	y = −0.4596x + 1.5139	R^2 = 0.9536	2.5404	y = −0.1255x + 1.6228	R^2 = 0.9017	2.8745

slit-type pores with good openness, indicating that micropores, mesopores, and macropores are developed in the shale, but mainly micropores and mesopores occur, which is also why this study only uses low-temperature nitrogen adsorption experiments. Compared with previous studies, there is a big difference in the stage of the high-pressure ratio (Bu et al., 2015; Xi et al., 2018; Liu et al., 2019). We think there may be the following two reasons: first, there are maybe certain errors in the experimental results, but considering the uniqueness of the rocks, we still use these data; the second is that the high-pressure section is mainly filled with macropores, and the proportion of macropores in Longmaxi formation shale in Changning area is small (mainly microporous and mesoporous). Therefore, in the relatively high-pressure stage, the amount of nitrogen filled in the macropores is small, and there will be no sudden increase.

Pore fractal dimension

As mentioned above, when P/P$_0$ = 0.45, most samples' adsorption and desorption curves begin to become inconsistent. Therefore, we take the relative pressure of 0.45 as the boundary, divide the curve into a "relatively low-pressure section curve" and a "relatively high-pressure section curve", and calculate the fractal dimension of each section. In the relatively low-pressure stage (P/P$_0$<0.45), the fractal dimension mainly reflects the single molecule and multiple molecule adsorption and filling in the pores, which can be used to indicate the irregularity, roughness, and complexity of the pore surface or can also be used to indicate the complexity of the relatively large pores (mesopores), which we define as the surface fractal dimension D$_{sf}$. In the relatively high-pressure

stage (P/P$_0$>0.45), gas capillary condensation occurs with increased gas pressure. The fractal dimension usually indicates the complexity of the pore space and structural irregularity, or it can also be used to indicate the complexity of the relative micropores. We define this as the structural fractal dimension D$_{st}$. Formula (1) is used to create the correlation diagram of ln (V) and ln [ln (P$_0$/P)] (Figure 4), and linear fitting for different relative pressure sections is conducted. Then, the fractal dimension of the sample pores in the relatively low-pressure and relatively high-pressure stages is calculated through Formula (2). The results show that the surface fractal dimension D$_{sf}$ of well ZK$_1$ is between 2.4054 and 2.6117, and the structural fractal dimension D$_{st}$ is between 2.8424 and 2.8703. The surface fractal dimension D$_{sf}$ of well ZK$_1$ is between 2.3215 and 2.5746, and the structural fractal dimension D$_{st}$ is between 2.8716 and 2.9013 (Table 2). Overall, the fractal dimension of the shale pore structure of the Wufeng-Longmaxi Formation in the study area is large, indicating that the shale pore structure is relatively complex. At the same time, the structural fractal dimension D$_{st}$ is greater than the surface fractal dimension D$_{sf}$, demonstrating that the microporous structure's complexity is significantly greater than that of the mesoporous structure.

Discussion

Relationship between the fractal dimension and shale mineral composition

There are many types of organic shale minerals, including quartz, feldspar, calcite, dolomite, clay minerals, pyrite, etc. There
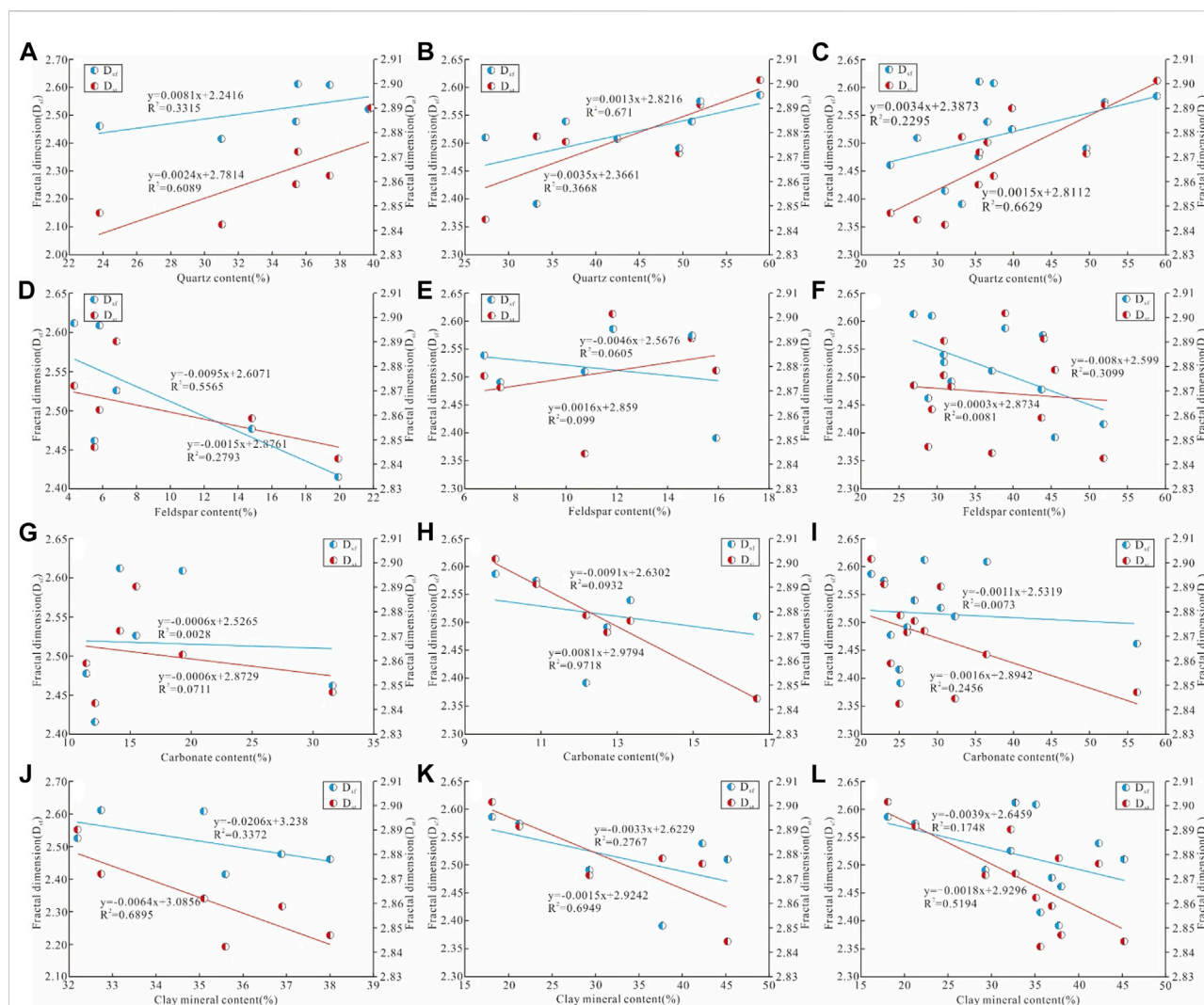
FIGURE 5
Correlation between the shale mineral composition and fractal dimension of the Longmaxi Formation in the Changning area. **(A–F)** is from ZK1, and **(G–L)** is from ZK2.

are certain differences in the content of mineral components in different regions, and their effects on the fractal dimension are also different (Kennedy et al., 2002; Liu et al., 2022b). Here, the relationship between the fractal dimension and quartz, feldspar (potassium feldspar + plagioclase), carbonate rock (calcite + dolomite), and clay minerals are analyzed (Figure 5).

There are positive correlations between the quartz content and fractal dimensions D_{sf} and D_{st}, among which the correlation coefficients of the quartz content in well ZK_1 and D_{sf} and D_{st} are 0.3315 and 0.6089, respectively (Figure 5A). The correlation coefficients of the quartz content in well ZK_2 and D_{sf} and D_{st} are 0.671 and 0.3668, respectively (Figure 5B), and the correlation coefficients of all samples with D_{sf} and D_{st} are 0.2295 and 0.6629, respectively (Figure 5C). Quartz is the most important brittle mineral, and its content is significant for the exploration and

development of shale gas. The fractal dimension of shale and the quartz content in the Changning area are positively correlated, which is mainly related to the source of silica in the shale. The shale in Longmaxi Formation was deposited in a deep-water shelf environment. The deposition of a low siliceous biological framework formed a large number of biogenic quartzes, which increased the pores of organic matter, the number of micropores, and the fractal dimension of the shale. However, in sedimentary diagenesis, a small amount of terrigenous clastic siliceous materials inevitably enters, and the sorting and rounding degree is greater than the biogenic degree, reducing the complexity of the pores and the correlation coefficient.

The relationship between the feldspar content and fractal dimension in different wells is obviously different (Figures 5D–F). The feldspar content in well ZK_1 has a weak medium
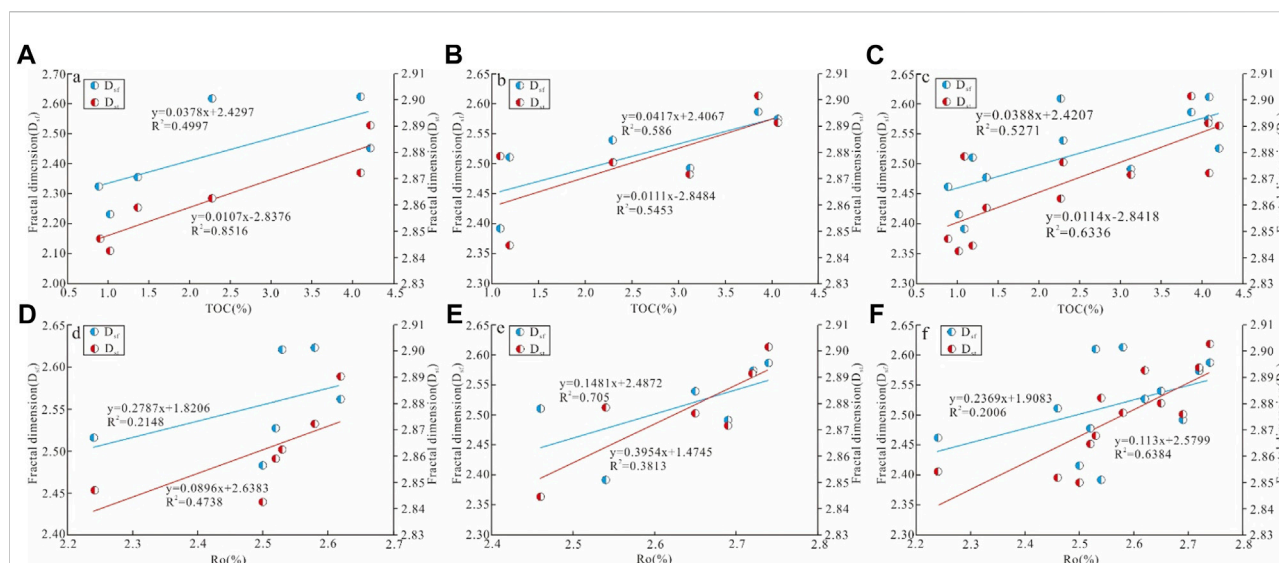
FIGURE 6
Correlation between the organic matter content and maturity and fractal dimension of the shale.

negative correlation with D_{sf} and D_{st}, with correlation coefficients of 0.5565 and 0.2793, respectively (Figure 5D). The feldspar after handling has a good sorting performance, which mainly plays a good role in the intergranular pores and dissolution pores, and the pore size formed is large, leading to the negative correlation between the feldspar content and fractal dimension. The feldspar content of well ZK_2 is weakly correlated with D_{sf} and D_{st}, with correlation coefficients of only 0.0605 and 0.099 (Figure 5E). The content of feldspar is very low (obviously lower than that of quartz), thus providing fewer pores. At the same time, feldspar mostly comes from terrigenous clasts, so it has little effect on the fractal dimension.

The correlation between the content of carbonate rock minerals and fractal dimension is generally very weak. The correlation coefficients of the carbonate rock content with D_{sf} and D_{st} in well ZK_1 are 0.0028 and 0.0711, respectively (Figure 5G), and those in well ZK_2 are 0.0932 and 0.9718, respectively (Figure 5H), while the correlation coefficients of all samples with D_{sf} and D_{st} are 0.0073, and 0.2456, respectively (Figure 5I). Some carbonate rocks exist in the form of cement, which fills and blocks the pores and reduces the connectivity of the pores. The negative correlation becomes stronger if the content is large and the filling is regular. In addition, carbonate rocks are soluble minerals, which often form large dissolution pores and have a weak contribution to the development of micropores. In general, the dual effect of carbonate rocks on pore development leads to the poor correlation between carbonate rocks and the microporous structure.

Compared with carbonate rock minerals, the negative correlation between clay minerals and the fractal dimension is

obvious. The correlation coefficients between the clay mineral content of well ZK_1 and D_{sf} and D_{st} are 0.3372 and 0.6895 (Figure 5J), respectively. The correlation coefficients between clay mineral content of well ZK2 and D_{sf} and D_{st} are 0.2767 and 0.6949, respectively (Figure 5K). In contrast, the correlation coefficients between all samples and D_{sf} and D_{st} are 0.1748, and 0.5194, respectively (Figure 5L). Clay minerals have strong plasticity. During long-term diagenesis, clay minerals are strongly compacted, which reduces the porosity of the reservoir, especially the number of micropores. In addition, the deformation and filling of clay minerals also reduce the connectivity of pores, thereby reducing the complexity of the pore structure.

Relationship between the fractal dimension and organic matter

Organic matter is the material basis for the formation of hydrocarbon gases. At the same time, it significantly impacts the pore structure of shale, mainly the content of TOC and the degree of thermal evolution (Ro). The former mainly affects the development of organic pores, while the latter affects the size and morphology of organic pores, thus affecting the fractal dimension of shale pores (Burruss et al., 1983; Gao et al., 2020; Sun et al., 2022).

The TOC content and fractal dimension show a good positive correlation. The correlation coefficients between the TOC content of well ZK_1 and D_{sf} and D_{st} are 0.4997 and 0.8516, respectively (Figure 6A), and the correlation coefficients between the TOC content of well ZK_2 and D_{sf} and D_{st} are 0.586 and

0.5453, respectively (Figure 6B), and the correlation coefficients between the TOC content of all samples and D_{sf} and D_{st} are 0.5271 and 0.6336, respectively (Figure 6C). With the increase in the TOC content, micropores, mesopores, and macropores increase, improving shale adsorption capacity for hydrocarbon gases. In contrast, with the increase in the TOC content, the increase in the fractal dimension D_{st} is more obvious (especially in well ZK_1), indicating that organic micro-mesopores are developed in the Changning area and that well ZK_1 is more developed than well ZK_2. With the increase in the organic carbon content, the number of micro-mesopores increases, and the pore structure tends to be more complex, which indicates that organic pores have a significant impact on the pore structure of shale.

The decomposition of kerogen or asphalt mainly forms the pores produced by organic matter during the ripening process, so the development of organic pores is related to the Ro of organic matter, which then affects the size of the fractal dimension. Ro and the fractal dimension are also positively correlated. The correlation coefficients of Ro in well ZK_1 with D_{sf} and D_{st} are 0.2148 and 0.4738, respectively (Figure 6D). The correlation coefficients of Ro in well ZK2 with D_{sf} and D_{st} are 0.705 and 0.3813, respectively (Figure 6E). The correlation coefficients of Ro in all samples with D_{sf} and D_{st} are 0.2006 and 0.6384, respectively (Figure 6F). The samples are high over the mature stage, the maturity increases, and the aromatization degree of organic matter intensifies, making the interior of the organic pores rougher. At the same time, the increase in organic matter will also reduce the support capacity. Under the overlying strata, the internal pore deformation of organic matter intensifies, reducing the connectivity between pores, increasing pore complexity, and increasing the fractal dimension.

Conclusion

In this paper, taking the organic-rich shale of Longmaxi formation in the Changning area as an example, based on whole rock X-ray diffraction, argon ion polishing electron microscopy observations, and low-temperature nitrogen adsorption-desorption experiments, the pore structure of shale was quantitatively characterized by using Frenkel Halsey Hill (FHH) model. The main conclusions are as follows:

1) The pores of the organic-rich shale in the Longmaxi Formation in the Changning area of southern Sichuan are mainly organic, intergranular pores, dissolution pores, and microfractures, with mainly micropores and mesopores. The pore morphology is ink bottle-type and semiclosed slit-type with good openness. Calculating the fractal dimension reveals that the shale has good dual fractal characteristics. The surface fractal dimension D_{sf} is between 2.3215 and 2.6117, the

structural fractal dimension D_{st} is between 2.8424 and 2.9013, and the structural fractal dimension is greater than the surface fractal dimension.

2) The fractal dimension of the shale is affected by both inorganic minerals and organic matter. The fractal dimension has a good positive correlation with the quartz content but an obvious negative correlation with clay minerals. The correlation between the feldspar content and fractal dimension is either poor or nonexistent, and the relationship between carbonate minerals and the fractal dimension is a very weak negative correlation. The higher the total organic carbon content and thermal evolution degree are, the greater the number of micro-mesopores and the larger the pore fractal dimension.

3) The pore size distribution is wide for different types of shale. The pore structure of shale is quantitatively characterized by the low-temperature nitrogen adsorption-desorption experiment and the FHH model. The experimental methods and fractal calculation models are different for different pore sizes of shale. Therefore, the main research direction of shale pore quantitative characterization is to carry out the quantitative characterization of shale pores through high-pressure mercury injection, liquid nitrogen adsorption, carbon dioxide adsorption, and other experiments and to select different fractal dimensions models.

Data availability statement

The original contributions presented in the study are included in the article/supplementary material, further inquiries can be directed to the corresponding author.

Author contributions

HL, JZ, XM, SW, TZ, and SH contributed in writing, reviewing, and editing, datacuration, writing—original draft preparation; HG, XW, HA, QM, HL, CD, JW, and SZ contributed in formal analysis, validation, and reviewing.

Funding

Acknowledgments

We thank all editors and reviewers for their helpful comments and suggestions.

Conflict of interest

Authors JZ, HL, XM, HG, XW, HA, QM, CD, JW, and SZ are employed by the PetroChina Southwest Oil and Gas Field Company.

The remaining authors declare that the research was conducted in the absence of any commercial or financial

relationships that could be construed as a potential conflict of interest.

Publisher's note

All claims expressed in this article are solely those of the authors and do not necessarily represent those of their affiliated organizations, or those of the publisher, the editors and the reviewers. Any product that may be evaluated in this article, or claim that may be made by its manufacturer, is not guaranteed or endorsed by the publisher.

References

Ahmad, A. L., and Mustafa, N. N. N. (2006). Pore surface fractal analysis of palladium-alumina ceramic membrane using frenkel-Halsey-Hill (FHH) model. *J. Colloid Interface Sci.* 301 (2), 575–584. doi:10.1016/j.jcis.2006.05.041

Ambrose, R. J., Hartman, R. C., Campos, M. D., Akkutlu, I. K., and Sondergeld, C. (2010). New pore-scale considerations for shale gas in place calculations. *Soc. Pet. Eng.* 17 (1), 219–229. doi:10.2118/131772-PA

Ameen, M. S. (2016). Fracture modes in the silurian qusaiba shale play, northern Saudi Arabia and their geomechanical implications. *Mar. Pet. Geol.* 78, 312–355. doi:10.1016/j.marpetgeo.2016.07.013

Bu, H. L., Ju, Y. W., Tan, J. Q., Wang, G. C., and Li, X. S. (2015). Fractal characteristics of poresin non-marine shales from the huainan coalfield, eastern China. *J. Nat. Gas. Sci. Eng.* 24, 166–177. doi:10.1016/j.jngse.2015.03.021

Burruss, R. C., Cerone, K. R., and Harris, P. M. (1983). Fluid inclusion petrography and tectonic-burial history of the A1 Ali No.2 well:evidence for the timing of diagenesis and oil migration, northern Oman Foredeep. *Geology* 11, 567

Chang, J. Q., Fan, X. D., Jiang, Z. X., Wang, X. M., Chen, L., Li, J. T., et al. (2022). Differential impact of clay minerals and organic matter on pore structure and its fractal characteristics of marine and continental shales in China. *Appl. Clay Sci.* 216, 106334. doi:10.1016/j.clay.2021.106334

Cheng, G. X., Jiang, B., Li, M., Li, F. L., and Zhu, M. (2021). Structural evolution of southern sichuan basin (South China) and its control effects on tectonic fracture distribution in longmaxi shale. *J. Struct. Geol.* 153, 104465. doi:10.1016/j.jsg.2021.104465

Fan, C. H., Li, H., Qin, Q. R., He, S., and Zhong, C. (2020a). Geological conditions and exploration potential of shale gas reservoir in wufeng and longmaxi formation of southeastern sichuan basin, China. *J. Pet. Sci. Eng.* 191, 107138. doi:10.1016/j.petrol.2020.107138

Fan, C. H., Li, H., Qin, Q. R., Shang, L., Yuan, Y. F., and Li, Z. (2020c). Formation mechanisms and distribution of weathered volcanic reservoirs: A case study of the carboniferous volcanic rocks in northwest junggar basin, China. *Energy Sci. Eng.* 8, 2841–2858. doi:10.1002/ese3.702

Fan, C. H., Li, H., Zhao, S. X., Qin, Q. R., Fan, Y., Wu, J. F., et al. (2020b). Formation stages and evolution patterns of structural fractures in marine shale: Case study of the lower silurian Longmaxi formation in the changning area of the southern Sichuan Basin, China. *Energy fuels.* 34 (8), 9524–9539. doi:10.1021/acs.energyfuels.0c01748

Fan, C. H., Xie, H. B., Li, H., Zhao, S. X., Shi, X. C., Liu, J. F., et al. (2022). Complicated fault characterization and its influence on shale gas preservation in the southern margin of the Sichuan Basin, China. *China. Lithosphere* 2022, 8035106. doi:10.2113/2022/8035106

Feng, Z. Q., Liu, D., Huang, S. P., Wu, W., Dong, D. Z., Peng, W. L., et al. (2016). Carbon isotopic composition of shale gas in the silurian Longmaxi formation of the changning area, Sichuan Basin. *Petroleum Explor. Dev.* 43 (5), 769–777. doi:10.1016/S1876-3804(16)30092-1

Gao, F. Q. (2019). Use of numerical modeling for analyzing rock mechanic problems in underground coal mine practices. *J. Min. Strata Control Eng.* 1 (1), 013004. doi:10.13532/j.jmsce.cn10-1638/td.2019.02.009

Gao, Z., Fan, Y., Xuan, Q., and Zheng, G. (2020). A review of shale pore structure evolution characteristics with increasing thermal maturities. *Adv. Geo-Energy Res.* 4 (3), 247–259. doi:10.46690/ager.2020.03.03

He, D. F., Liu, R. Q., Huang, H, Y., Wang, X. S., Jiang, H., and Zhang, W. K. (2019). Tectonic and geological setting of the earthquake hazards in the Changning shale gas development zone, Sichuan Basin, SW China. *Petroleum Explor. Dev.* 46 (5), 1051–1064. doi:10.1016/S1876-3804(19)60262-4

He, S., Li, H., Qin, Q. R., and Long, S. X. (2021). Influence of mineral compositions on shale pore development of Longmaxi Formation in the Dingshan area, southeastern Sichuan Basin, China. *Energy fuels.* 35 (13), 10551–10561. doi:10.1021/acs.energyfuels.1c01026

He, S., Qin, Q. R., Li, H., and Wang, S. L. (2022b). Deformation differences in complex structural areas in the southern Sichuan Basin and its influence on shale gas preservation: A case study of changning and luzhou areas. *Front. Earth Sci. (Lausanne).* 9, 818155. doi:10.3389/feart.2021.818534

He, S., Qin, Q. R., Li, H., and Zhao, S. X. (2022a). Geological characteristics of deep shale gas in the silurian Longmaxi formation in the southern Sichuan Basin, China. *Front. Earth Sci. (Lausanne).* 9, 818543. doi:10.3389/feart.2021.818155

Jin, Z. J., Nie, H. K., Liu, Q. Y., Zhao, J. H., and Jiang, T. (2018). Source and seal coupling mechanism for shale gas enrichment in upper ordovician wufeng formation - lower silurian longmaxi formation in sichuan basin and its periphery. *Mar. Pet. Geol.* 97, 78–93. doi:10.1016/j.marpetgeo.2018.06.009

Kennedy, M. J., Pevear, D. R., and Hill, R. J. (2002). Mineral surface control of organic carbon in black shale. *Science* 295 (5555), 657–660. doi:10.1126/science.1066611

Li, H. (2021). Quantitative prediction of complex tectonic fractures in the tight sandstone reservoirs: A fractal method. *Arab. J. Geosci.* 14, 1986. doi:10.1007/s12517-021-08344-0

Li, H., Qin, Q. R., Zhang, B. J., Ge, X. Y., Hu, X., Fan, C. H., et al. (2020). Tectonic fracture formation and distribution in ultradeep marine carbonate gas reservoirs: A case study of the maokou formation in the jiulongshan gas field, Sichuan Basin, southwest China. *Energy Fuels.* 34 (11), 14132–14146. doi:10.1021/acs.energyfuels.0c03327

Li, H. (2022). Research progress on evaluation methods and factors influencing shale brittleness: A review. *Energy Rep.* 8, 4344–4358. doi:10.1016/j.egyr.2022.03.120

Li, H., Tang, H. M., Qin, Q. R., Fan, C. H., Han, S., Yang, C., et al. (2018). Reservoir characteristics and hydrocarbon accumulation of Carboniferous volcanic weathered crust of Zhongguai high area in the Western Junggar Basin, China. *J. Cent. South Univ.* 25 (11), 2785–2801. doi:10.1007/s11771-018-3953-y

Li, H., Tang, H. M., Qin, Q. R., Wang, Q., and Zhong, C. (2019c). Effectiveness evaluation of natural fractures in Xujiahe Formation of Yuanba area, Sichuan basin, China. *Arab. J. Geosci.* 12 (6), 194. doi:10.1007/s12517-019-4292-5

Li, H., Tang, H. M., Qin, Q. R., Zhou, J. L., Qin, Z. J., Fan, C. H., et al. (2019b). Characteristics, formation periods and genetic mechanisms of tectonic fractures in the tight gas sandstones reservoir: A case study of xujiahe formation in YB area, Sichuan Basin, China. *J. Petroleum Sci. Eng.* 178, 723–735. doi:10.1016/j.petrol.2019.04.007

Li, H., Tang, H. M., and Zheng, M. J. (2019a). Micropore structural heterogeneity of siliceous shale reservoir of the Longmaxi Formation in the southern Sichuan Basin, China. *Minerals* 9, 548. doi:10.3390/min9090548

Li, H. T., Peng, R., Du, W. S., Li, X. P., and Zhang, N. B. (2021a). Experimental study on structural sensitivity and intervention mechanism of mechanical behavior of coal samples. *J. Min. Strata Control Eng.* 3 (4), 043012. doi:10.13532/j.jmsce.cn10-1638/td.20210820.001

Li, H., Wang, Q., Qin, Q. R., and Ge, X. Y. (2021b). Characteristics of natural fractures in an ultradeep marine carbonate gas reservoir and their impact on the reservoir: A case study of the maokou formation of the jls structure in the Sichuan Basin, China. *Energy fuels.* 35 (16), 13098–13108. doi:10.1021/acs.energyfuels.1c01581

Li, J. J., Qin, Q. R., Li, H., and Wan, Y. F. (2022c). Numerical simulation of the stress field and fault sealing of complex fault combinations in Changning area, Southern Sichuan Basin, China. *Energy Sci. Eng.* 10, 278–291. doi:10.1002/ese3.1044

Li, J. J., Yin, J. X., Zhang, Y. N., Lu, S. F., Wang, W. M., Li, J. B., et al. (2015). A comparison of experimental methods for describing shale pore features - a case study in the Bohai Bay Basin of eastern China. *Int. J. Coal Geol.* 152, 39–49. doi:10.1016/j.coal.2015.10.009

Li, J., Li, H., Xu, J. L., Wu, Y. J., and Gao, Z. (2022a). Effects of fracture formation stage on shale gas preservation conditions and enrichment in complex structural areas in the southern sichuan basin, china. *Front. Earth Sci. (Lausanne).* 9, 823855. doi:10.3389/feart.2022.921988

Li, J., Li, H., Yang, C., Wu, Y. J., Gao, Z., and Jiang, S. L. (2022b). Geological characteristics and controlling factors of deep shale gas enrichment of the Wufeng-Longmaxi Formation in the southern Sichuan Basin, China. *Lithosphere* 2022, 4737801. doi:10.2113/2022/4737801

Liu, J. S., Ding, W. L., Gu, Y., Xiao, Z. K., Dai, J. S., Dai, P., et al. (2018b). Methodology for predicting reservoir breakdown pressure and fracture opening pressure in low-permeability reservoirs based on an *in situ* stress simulation. *Eng. Geol.* 246, 222–232. doi:10.1016/j.enggeo.2018.09.010

Liu, J. S., Yang, H. M., Bai, J. P., Wu, K. Y., Zhang, G. J., Liu, Y., et al. (2021). Numerical simulation to determine the fracture aperture in a typical basin of China. *Fuel* 283, 118952. doi:10.1016/j.fuel.2020.118952

Liu, J. S., Yang, H. M., Wu, X. F., and Liu, Y. (2020). The *in situ* stress field and microscale controlling factors in the ordos basin, central china. *Int. J. Rock Mech. Min. Sci. (1997).* 135, 104482. doi:10.1016/j.ijrmms.2020.104482

Liu, J. S., Yang, H. M., Xu, K., Wang, Z. M., Liu, X. Y., Cui, L. J., et al. (2022a). Genetic mechanism of transfer zones in rift basins: Insights from geomechanical models. *GSA Bull.* doi:10.1130/B36151.1

Liu, J. S., Zhang, G. J., Bai, J. P., Ding, W. L., Yang, H. M., and Liu, Y. (2022b). Quantitative prediction of the drilling azimuth of horizontal wells in fractured tight sandstone based on reservoir geomechanics in the Ordos Basin, central China. *Mar. Pet. Geol.* 136, 105439. doi:10.1016/j.marpetgeo.2021.105439

Liu, J., Yao, Y. B., Liu, D. M., Cai, Y. D., and Cai, J. C. (2018a). Comparison of pore fractal characteristics between marine and continental shales. *Fractals* 26 (2), 1840016. doi:10.1142/s0218348x18400169

Liu, K. Q., Ostadhassan, M., and Kong, L. Y. (2019). Fractal and multifractal characteristics of pore throats in the bakken shale. *Transp. Porous Media* 126 (3), 579–598. doi:10.1007/s11242-018-1130-2

Ma, X. H., Wang, H. Y., Zhou, S. W., Shi, Z. S., and Zhang, L. F. (2021). Deep shale gas in China: Geological characteristics and development strategies. *Energy Rep.* 7, 1903–1914. doi:10.1016/j.egyr.2021.03.043

Ma, Y. Z., Wang, M., Zhao, X. Z., Dai, X. G., and He, Y. (2022). Study of the microstructural characteristics of low-rank coal under different degassing pressures. *Energies* 15 (10), 3691. doi:10.3390/en15103691

Mandelbrot, B. B. (1978). Fractal objects. *Recherche* 9 (85), 5.

Mandelbrot, B. B. (1984). Fractals in physics - squig clusters, diffusions, fractal measures, and the unicity of fractal dimensionality. *J. Stat. Phys.* 34 (5-6), 895–930. doi:10.1007/BF01009448

Mandelbrot, B. B. (1985). Self-affine fractals and fractal dimension. *Phys. Scr.* 32 (4), 257–260. doi:10.1088/0031-8949/32/4/001

Pan, S. X., Zha, M., Gao, C. H., Qu, J. X., and Ding, X. J. (2021). Pore structure and fractal characteristics of organic-rich lacustrine shales of the kongdian formation, cangdong sag, bohai bay basin. *Front. Earth Sci.* 9, 760538. doi:10.3389/feart.2021.760583

Qiu, Z., Song, D. J., Zhang, L. F., Zhang, Q., Zhao, Q., Wang, Y. M., et al. (2021). The geochemical and pore characteristics of a typical marine-continental transitional gas shale: A case study of the permian shanxi formation on the eastern margin of the ordos basin. *Energy Rep.* 7, 3726–3736. doi:10.1016/j.egyr.2021.06.056

Shan, S. C., Wu, Y. Z., Fu, Y. K., and Zhou, P. H. (2021). Shear mechanical properties of anchored rock mass under impact load. *J. Min. Strata Control Eng.* 3 (4), 043034. doi:10.13532/j.jmsce.cn10-1638/td.20211014.001

Song, J. F., Lu, C. P., Li, Z. W., Ou, Y. G. C., Cao, X. M., and Zhou, F. L. (2021). Characteristics of stress distribution and microseismic activity in rock parting occurrence area. *J. Min. Strata Control Eng.* 3 (4), 043518. doi:10.13532/j.jmsce.cn10-1638/td.20210607.002

Sun, Y., Ju, Y., Zhou, W., Qiao, P., Tao, L., and Xiao, L. (2022). Nanoscale pore and crack evolution in shear thin layers of shales and the shale gas reservoir effect. *Adv. Geo-Energy Res.* 6 (3), 221–229. doi:10.46690/ager.2022.03.05

Tang, L., Song, Y., Jiang, Z. X., Jiang, S., and Li, Q. W. (2019). Pore structure and fractal characteristics of distinct thermally mature shales. *Energy fuels.* 33 (6), 5116–5128. doi:10.1021/acs.energyfuels.9b00885

Tang, X., Zheng, F. Z., Liang, G. D., Ma, Z. J., Zhang, J. Z., Wang, Y. F., et al. (2022). Fractal characterization of pore structure of cambrian niutitang shale in northern Guizhou Province, southwestern China. *Earth Sci. Front. Online.* doi:10.13745/j.esf.sf.2022.5.36

Wang, B., Zhou, F. J., Zhou, H., Ge, H., and Li, L. Z. (2021). Characteristics of the fracture geometry and the injection pressure response during near-wellbore diverting fracturing. *Energy Rep.* 7, 491–501. doi:10.1016/j.egyr.2020.12.039

Wang, J., and Wang, X. L. (2021). Seepage characteristic and fracture development of protected seam caused by mining protecting strata. *J. Min. Strata Control Eng.* 3 (3), 033511. doi:10.13532/j.jmsce.cn10-1638/td.20201215.001

Wang, R. Y., Hu, Z. Q., Long, S. X., Liu, G. X., Zhao, J. H., Dong, L., et al. (2019). Differential characteristics of the Upper Ordovician-Lower Silurian Wufeng-Longmaxi shale reservoir and its implications for exploration and development of shale gas in/around the Sichuan Basin. *Acta Geol. Sin.* 93 (3), 520–535. doi:10.1111/1755-6724.13875

Wang, R. Y., Hu, Z. Q., Sun, C. X., Liu, Z. B., Zhang, C. C., Gao, B., et al. (2018). Comparative analysis of shale reservoir characteristics in the wufeng-longmaxi (O_3w-S_1l) and niutitang ($Є_1n$) formations: A case study of wells JY1 and TX1 in the southeastern sichuan basin and its neighboring areas, southwestern China. *Interpretation* 6 (4), SN31–SN45. doi:10.1190/int-2018-0024.1

Wang, R. Y., Nie, H. K., Hu, Z. Q., Liu, G. X., Xi, B. B., and Liu, W. X. (2020). Controlling effect of pressure evolution on shale gas reservoirs: A case study of the Wufeng-Longmaxi formation in the Sichuan Basin. *Nat. Gas. Ind.* 40 (10), 1–11. doi:10.3787/j.issn.1000-0976.2020.10.001

Wang, S. L., Li, H., Lin, L. F., and Yin, S. (2022). Development characteristics and finite element simulation of fractures in tight oil sandstone reservoirs of Yanchang Formation in Western Ordos Basin. *Front. Earth Sci. (Lausanne).* 9, 823855. doi:10.3389/feart.2021.823855

Wei, D., Gao, Z. Q., Zhang, C., Fan, T. L., Karubandika, G. M., and Meng, M. M. (2019). Pore characteristics of the carbonate shoal from fractal perspective. *J. Pet. Sci. Eng.* 174, 1249–1260. doi:10.1016/j.petrol.2018.11.059

Wu, J. F., Zhao, S. X., Fan, C. H., Xia, Z. Q., Ji, C. H., Zhang, C. L., et al. (2021). Fracture characteristics of the Longmaxi Formation shale and its relationship with gas-bearing properties in Changning area, southern Sichuan. *Acta Pet. Sin.* 42 (4), 428–446. doi:10.7623/syxb202104002

Xi, Z. D., Tang, S. H., Wang, J., Yi, J. J., Guo, Y. Y., and Wang, K. F. (2018). Pore structure and fractal characteristics of niutitang shale from China. *Minerals* 8 (4), 163. doi:10.3390/min8040163

Xu, Q. L., Liu, B., Ma, Y. S., Song, X. M., Wang, Y. J., and Chen, Z. X. (2017). Geological and geochemical characterization of lacustrineshale: A case study of the jurassic da'anzhai membershalein the central Sichuan Basin, southwest China. *J. Nat. Gas. Sci. Eng.* 47, 124–139. doi:10.1016/j.jngse.2017.09.008

Yang, C., Zhang, J. C., Wang, X. Z., Tang, X., Chen, Y. C., Jiang, L., et al. (2017). Nanoscale pore structure and fractal characteristics of a marine-continental transitional shale: A case study from the lower permian shanxi shale in the southeastern ordos basin, China. *Mar. Pet. Geol.* 88, 54–68. doi:10.1016/j.marpetgeo.2017.07.021

Yang, Y. Y., Zhang, J. C., Xu, L. F., Li, P., Liu, Y., and Dang, W. (2022). Pore structure and fractal characteristics of deep shale: A case study from permian shanxi formation shale, from the ordos basin. *ACS Omega* 7 (11), 9229–9243. doi:10.1021/acsomega.1c05779

Zhan, H. L., Yang, Y. Q., Zhang, Y., Miao, X. Y., Zhao, K., and Yue, W. Z. (2021). Terahertz for the detection of the oil bearing characteristics of shale. *Energy Rep.* 7, 5162–5167. doi:10.1016/j.egyr.2021.08.109

Zhang, P., Huang, Y. Q., Zhang, J. C., Liu, H. Y., and Yang, J. W. (2018). Fractal characteristics of the Longtan formation transitional shale in northwest GuizhouJ. *China Coal Soc.* 43 (6), 1580–1588. doi:10.13225/j.cnki.jccs.2018.4046

Application of the *in-situ* stress testing technology for the design of operating pressure of underground gas storage reservoir

Qun-yi Wang, Lin Shang*, Chun-yan Xin, Yan-chun Sun, Guang-liang Gao, Miao Wang and Xiao Gu

Jidong Oilfield Company, PetroChina, Tangshan, China

The appropriate design of the operating pressure of underground gas storages (UGSs) is of great significance to their safe and profitable operation. *In situ* stress is basic data for determining the upper limit pressure of UGSs, analyzing fault stability in reservoir areas, and evaluating trap tightness. Generally, the design of the upper limit gas injection pressure of UGSs is a comprehensive geomechanical problem. After research and comparison of measurement methods, it is believed that the measurement of *in situ* stress induced by hydraulic fracturing can accurately obtain the *in situ* stress value near the wellbore, and having knowledge about the reservoir stress path will considerably decrease the risk of reservoir and cap rock instability during gas injection and production. Taking Well C1, an oil reservoir-type UGS in Block M, eastern China as an example, this paper introduces the use of hydraulic fracturing (HF) *in situ* stress testing technology to obtain the minimum principal stress values of the caprock, reservoir and floor intervals of Well C1. The measured minimum principal stress of the caprock is 32.8−36.8 MPa. Because it is an old well, the minimum principal stress of the reservoir is 33.7−34.2 MPa after correction of the *in situ* stress measurement according to the theory of elasticity. Based on the comprehensive analysis of the measured *in situ* stress data, it is believed that the safe upper limit of the reservoir-type gas storage in Block M is 27.2 MPa.

KEYWORDS

underground gas storage, hydraulic fracturing, in situ stress test, operating pressure, oil reservoirs

1 Introduction

Confirmed by research findings, natural gas will become the most demanded fossil fuel in the world in the future, and its production will reach its maximum in 2060 (Zou et al., 2018). Underground gas storage (UGS) is an important and inseparable part of the upstream and downstream of the natural gas industry. With the rapid development of China's natural gas

industry, the demand for UGSs will become increasingly urgent. China's UGS construction began in 1999, and 26 UGSs have been built in China after 20 years, with a designed storage capacity of 41.5 billion square and working gas volume of 180 billion square (Ding et al., 2010). There are contradictions between the geological storage sites and the natural gas demand market in China. Gas fields are mainly located in central and western China, and demand markets are located in the central and eastern regions, while the oil-bearing basins in the east are dominated by oil reservoirs. Therefore, the use of oil reservoirs to build UGSs has gradually developed in China (Jiang et al., 2021).

During a high rate of multicycle operation of underground gas storage, high-flow gas is injected, and high-flow gas is produced in the short term, which brings about a force change in the fault block trap and affects the dynamic sealing integrity and is completely different from conventional oil and gas reservoir development methods. The underground gas storages that are converted form oil reservoirs and are different from gas reservoirs. The process of building UGSs is a high-speed interactive displacement process of gas, oil and water, and the three-phase seepage mechanism, spatial production characteristics and capacity expansion laws are complex. For gas storage, the purpose is to maintain the maximum gas in the reservoir without escaping it. In geological storage, gas can be stored by several physical and chemical trapping mechanisms (Benson and Cole, 2008; Gunter et al., 2004). Physical storage involves storing injected gas in structural traps and storing it as residual gas in the pore volume. As a result, geomechanical considerations have a vital impact on the short- and long-term performance of gas injection.

With gas injection and production, the pore pressure and *in situ* stress are altered in the different stages of UGS life (Ferretti, 2005; Vasco et al., 2001; Zhou and Burbey, 2014). The fatigue effect caused by multicycle injection-withdrawal changed the pore-throat and microcrack structures of the caprock and enhanced the sealing capacity at the *in situ* effective stress. The dynamic breakthrough pressure is lower than the caprock fracture pressure, so capillary sealing failure is more likely than mechanical failure (Zhu et al.). Gas injection increases the reservoir pore pressure and decreases the integrity of faults close to gas well locations (Rutqvist et al., 2014). The probability of fault reactivation is soared up because of enhancing the pore pressure. This reactivation can be monitored by parameters such as friction, cohesion, and orientation of the fault (Scholz, 2019). Thus, variations in stresses applied to the reservoir can potentially threaten the integrity of the reservoir. Additionally, the activation of faults might increase the permeability of the reservoir's unsuitable sections. The faults and traps near the wellbore have the weakest sealing ability, so it is important to evaluate their sealing performance in the scheme design.

The appropriate design of the operating pressure of UGSs is of great significance to the safe and profitable operation of UGSs.

In situ stress is basic data for determining the upper limit pressure of UGSs, analyzing fault stability in reservoir areas, and evaluating trap tightness. Generally, the design of the upper limit gas injection pressure of UGSs is a comprehensive geomechanical problem. After research and comparison of measurement methods, it is believed that the measurement of *in situ* stress induced by hydraulic fracturing can accurately obtain the *in situ* stress value near the wellbore, and having knowledge about the reservoir stress path will considerably decrease the risk of reservoir and cap rock instability during gas injection and production.

This paper introduces the use of hydraulic fracturing (HF) *in situ* stress testing technology to obtain the minimum principal stress values of the caprock. Example taken from the C1 Well M Block, Nanpu Sag. We combine the imaging and dipole acoustic logging data of nearby wells, the horizontal maximum principal stress and its direction are estimated, and the upper limit pressure of the M gas storage is determined.

2 Data and methods

2.1 Geological background of the study area

According to the requirement of the *in situ* stress test for UGS construction, well C1 of UGS A is selected as the test well. The porosity of gas storage reservoir A is 27.1%, and the permeability is 619.9 mD. The temperature of the oil reservoir in the gas storage is 85 ˚C, the original formation pressure is 22.53 MPa, the current formation pressure coefficient is approximately 0.6, and the formation pressure is approximately 13.5 MPa. Well C1 is located at the higher part of the M fault block, with an artificial bottom of 2923 m, a vertical depth of 2341 m and a maximum well deviation of 44.66˚. Based on the cementing quality, casing collar and original perforation section of the well, the *in situ* stress test section is determined as shown in Table 1.

2.2 Test process

The principle of *in situ* stress measurement of hydraulic fracturing is based on elastic mechanics. According to the closure pressure of the fracturing fracture, a relatively reliable minimum principal stress can be obtained. For near-vertical wells, a relatively reliable horizontal minimum principal stress can be obtained.

Different from generalized *in situ* stress testing methods such as small-scale fracturing testing technology in the field of oil and gas fields, the classical hydraulic fracturing *in situ* stress testing method uses hydraulic expansion type bridging packers or bridge plugs + packers to separate the test section. It is sealed to realize

TABLE 1 Test information of the C1 well used for hydraulic fracturing.

Interval NO.	Depth(m)	Attribute	Perforation
1	2790–2792	Basalt caprock	New perforation
2	2814–2816	Direct mudstone caprock	New perforation
3	2834–2836	Reservoir	New perforation
4	2881.6–2884.6	Reservoir	Original production layer
5	2910–2912	Backplane layer	New perforation

the continuous measurement of small flow in the caprock. The purpose of the small flow is to minimize the influence of pore elasticity on the measurement results without forming a complex network of fractures, and the pressure in the pressure fractures can quickly reach equilibrium after the pump is turned off. The minimum principal stress is determined by the fracture closure pressure on the fracturing curve, which has the characteristics of repeatable measurement results.

The test plan is formulated according to the characteristics of the reservoir. The sequence of preparations before the test is perforation, scraping, lowering the bridge plug, lowering the *in situ* stress test string, etc. A schematic diagram of the hydraulic fracturing stress measurement system is shown in Figure 1. The specific steps of the *in situ* stress test are as follows: 1) the pipe string is kept still, and the change in the suspension weight of the pipe string is observed during the *in situ* stress test. During the pressurization process, due to the pressure sensor installed in the

high-pressure circuit, the pressure value on the digital acquisition instrument and the pressure gauge will increase rapidly with the pumping of the high-pressure liquid. Under the action of ground stress and pore pressure, according to the drilling cycle and the principle of stress concentration, when the pressure reaches the critical condition of tangential stress failure of the rock, the rock mass on the hole wall will rupture, and the maximum pressure value P_b recorded at this time is the rupture pressure. 2) After the rock cracks, turn off the high-pressure pump and stop injecting into the test section. After the pump is turned off, the pressure drops; after that, the pressure slowly drops as the liquid is lost to the formation. Under the action of *in situ* stress, the cracks tend to close. The pressure recorded when the fracture is in a critical closed state is the closure pressure Ps, which is the minimum principal stress that needs to be obtained in this test. 3) When the pressure in the fracturing section becomes stable or no longer drops significantly, the pressure in the isolation section can be

FIGURE 1
Schematic diagram of the hydraulic fracturing stress measurement system.
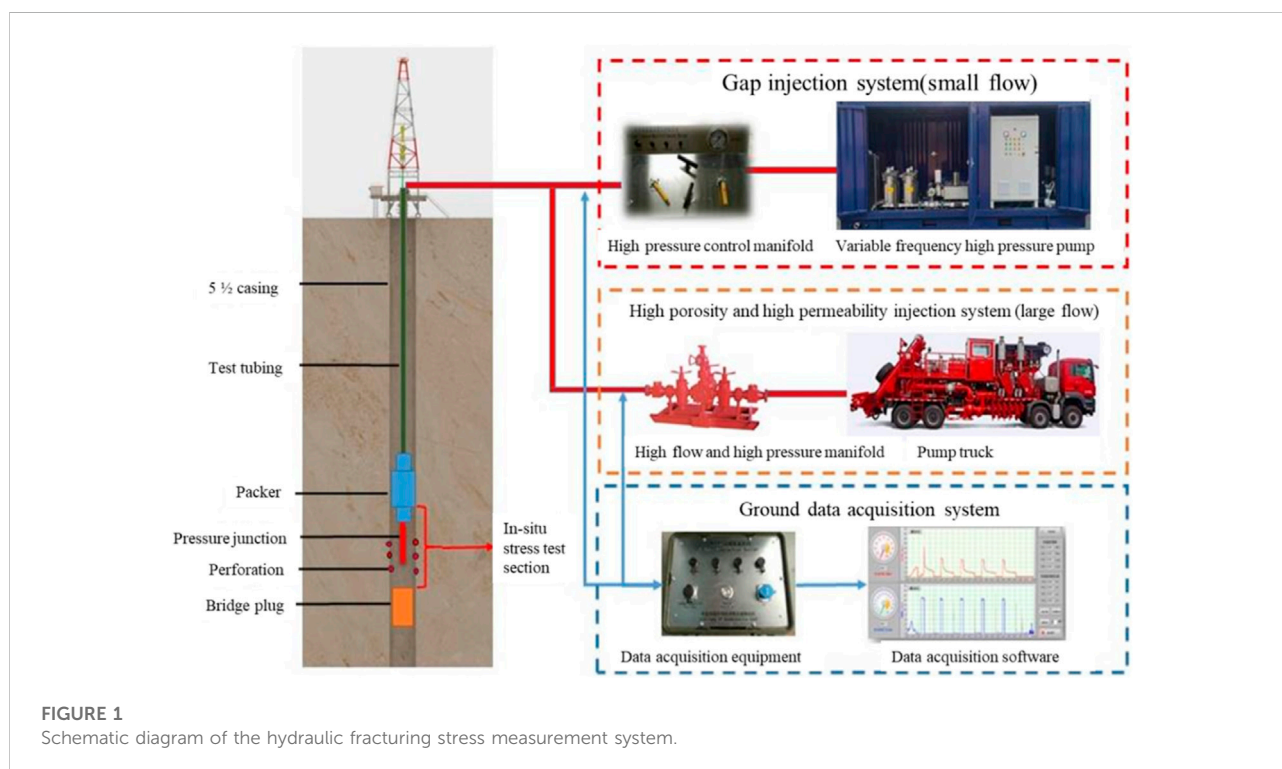
released, the pressure at the wellhead can be released, and the current test can be completed. 4) After the surface pressure drops to zero, the wellhead return valve is closed, the high-pressure pump is restarted, high-pressure fluid is injected into the test section to reopen the fractures that have occurred in the rock body, and then the pump is turned off to record the closure pressure of the fractures. The above process was repeated 3–4 times to obtain a reliable minimum principal stress. 5) For ultralow permeability formations, when the pump is stopped after rupture or retension, when the surface pressure does not drop, auxiliary backflow measures can be used to speed up the fracture closure process to obtain the fracture closure pressure, that is, the minimum principal stress. Whether to adopt auxiliary backflow measures is determined by the on-site engineer according to the pressure drop curve. This on-site test uses a small flow injection test, so no auxiliary return measures are used. 6) Lift the pipe string directly for 2 m, stabilize for 15 min, unpack the packer, and pull out the test string. The abovementioned *in situ* stress testing process is repeated, and *in situ* stress testing of other layers is performed in sequence.

From the pressure–time record curve, the fracture pressure (P_b) of the rock, the instantaneous closure pressure (P_s) and the estimated fracture retention pressure (P_r) can be directly obtained. According to the above parameters, the minimum principal stress can be determined, the maximum principal stress can be estimated, and the interpretation of specific characteristic pressure parameters and the calculation method is as follows:

Fracturing pressure (P_b). The fracturing pressure (P_b) is generally easy to determine; that is, the peak pressure of the first cycle during the fracturing process is called the fracturing pressure of the rock. The fractures are connected, and the fracture pressure is generally not obvious.

Retension pressure (P_r). The retension pressure (P_r) is the pressure when the rock mass in the fracturing section is broken, and the pressure is reopened to reopen the existing fractures. Usually, the corresponding point on the pressure–time curve when the slope changes significantly is the pressure value of rupture reopening.

Close the pressure (P_s). The determination of the shut-off pressure P_s is very important for hydraulic fracturing stress measurement. The closure pressure P_s is equal to the minimum principal stress or the horizontal minimum principal stress σ_h, and the more commonly used and popular methods for the value of Ps include the inflection point method, single tangent and double tangent method, dt/dp method, dp/dt method, Mauskat method, flow-pressure method, G-function method, etc.

Pore pressure (P_o). The formation pore pressure P_o is obtained from the measured data after the oil production well is shut in to restore the formation pressure.

3 Test results and applications

3.1 Test result

According to the pressure–time curve recorded by the downhole pressure gauge, combined with the flow data recorded on the surface, the pressure–time-flow and cumulative flow curves of Well C1 are drawn as shown in Figure 2, and the abovementioned method for determining the closure pressure of fracturing fractures is adopted, using the single tangent method, dP/dT method, Muskat method and G-Function method to obtain the minimum principal stress in the first round of 2790–2792 m. The calculation results are shown in Figure 3, Figure 4, Figure 5, and Figure 6, and the average value of the value results is used as the final minimum principal stress. Table 2 is a summary table of the data processing results for the direct mudstone caprock (2790–2792 m).

Using hydraulic fracturing *in situ* stress test technology, the *in situ* minimum main stress of the five test intervals within the depth range of 2790–2912 m (vertical depth 2244.8–2331.5 m) of reservoir-type gas storage well C1 in Block M was obtained. The *in situ* stress measurement results of the five layers from top to bottom are shown in Table 3. The measured results show that the minimum principal stress value of the overlying mudstone caprock is the highest.

3.2 Design of the operating pressure of the underground gas storages

1) *In situ* stress measurement results after pore pressure correction

The test hole of Well C1 is an old well. After years of production, the formation pressure coefficient (pore pressure) of the reservoir drops significantly. According to the theory of poroelasticity, a decrease in formation pore pressure will lead to a decrease in stress in the reservoir. For transversely isotropic reservoirs, the relationship between the variation in the horizontal minimum principal stress and the variation in pore pressure is:

$$\frac{\Delta S_h}{\Delta P_P} = \alpha \frac{(1 - 2v)}{(1 - v)} \tag{1}$$

where ΔS_h is the minimum principal stress change, ΔP_P is the pore pressure change, α is the Biot coefficient, which is 1, and v is Poisson's ratio, which is 0.2 in the calculation.

The Biot coefficient of the reservoir in Well C1 are approximately 0.6 and 0.8. During the operation of the gas storage, during the gas injection cycle, the pore pressure in the reservoir increases, which will cause the minimum principal stress in the reservoir to increase. When the
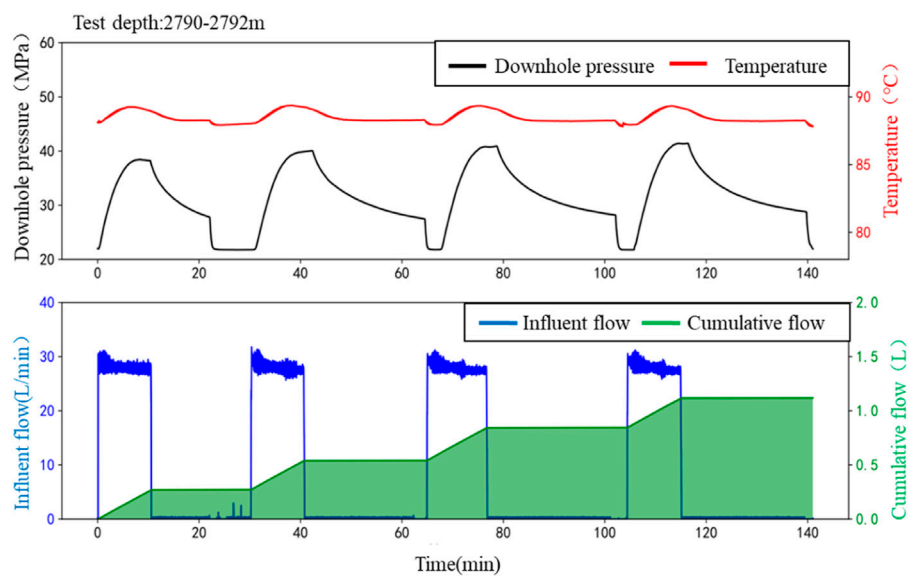
FIGURE 2
Downhole pressure–time and surface flow and cumulative flow curves.
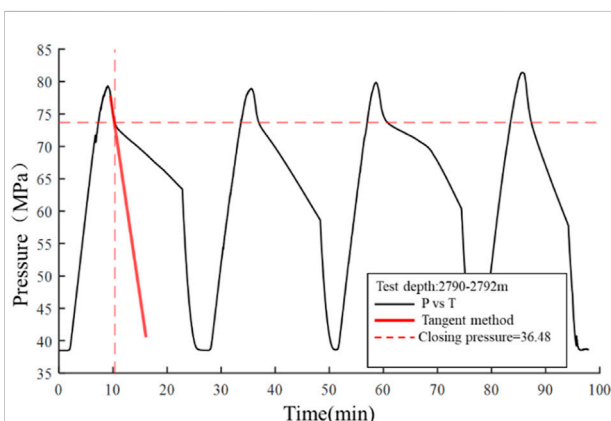
FIGURE 3
Calculation of the 1st minimum principal stress by the single tangent method.
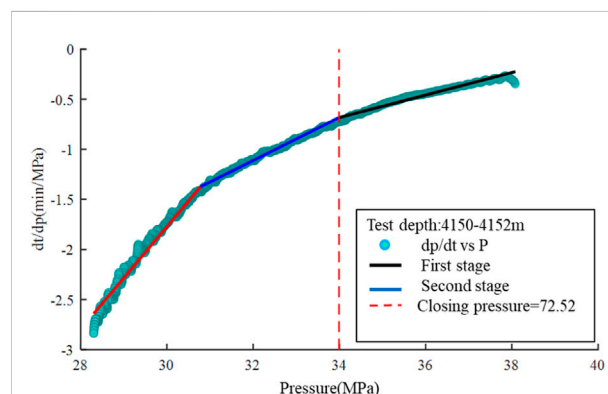
FIGURE 4
Calculation of the 1st minimum principal stress by the dp/dt method.

formation pressure of the reservoir increases when the coefficient rises to 1.0, the corrected results of the minimum principal stress in the reservoir are shown in Table 4.

2) Evaluation of the ultimate bearing capacity of the caprock

The ultimate pressure evaluation based on the mechanical integrity of the caprock mainly includes two aspects: tensile failure and shear failure resistance. My country has not officially published the national standard for determining the

upper limit pressure of gas storage. Referring to the method for determining the upper limit pressure of gas storage in Canada, the upper limit pressure of gas storage = minimum principal stress of formation × 0.8.

1) Critical fluid pressure for caprock tensile failure

For the tensile failure capacity of the caprock, the critical formation fluid pressure should be greater than the sum of the horizontal minimum principal stress σh and the tensile strength T. Based on the above measured results of the *in situ* stress, the

FIGURE 5
Calculation of the 1st minimum principal stress by the Muskat method.

FIGURE 6
Calculation of the 1st minimum principal stress by the G-function method.

principal stress. According to this method, the maximum safe gas injection pressure of the caprock is calculated as 27.2.

2) Critical fluid pressure for caprock shear failure

The shear failure risk assessment of caprock is based on the experimental study of rock mechanics, and based on the rock shear failure criterion (such as the Mohr–Coulomb criterion), the shear failure index is calculated, and the risk quantitative evaluation is realized. At present, the most classic method for evaluating the risk of caprock shear failure is based on the Mohr–Coulomb criterion in rock mechanics. Based on this criterion, the caprock safety factor is calculated by the following formula:

$$x = 1 - \frac{(\sigma_1 - \sigma_3)/2}{c \cos \varnothing + (\sigma_1 + \sigma_3) \sin \varnothing/2} = 1 - \frac{\tau_m}{\tau_m^*} \qquad (2)$$

where: σ_1 is the maximum principal stress;

σ_3 is the minimum principal stress;

τ_m is the maximum shear stress under a certain stress state;

τ_m^* is the critical shear stress when shear failure occurs;

c is the cohesive force, and ϕ is the angle of internal friction;

It can be seen from the above formula that the maximum and minimum effective principal stresses are the main factors affecting the risk of shear failure of the caprock, which are closely related to th Mohr–Coulomb e change in formation pressure. The three-dimensional *in situ* stress field of the trap before the construction of the gas reservoir is inverted according to the mine field test and the numerical simulation of geomechanics. If the local maximum and minimum effective principal stresses of the caprock are quite different, the shear safety index calculated by the above formula is ve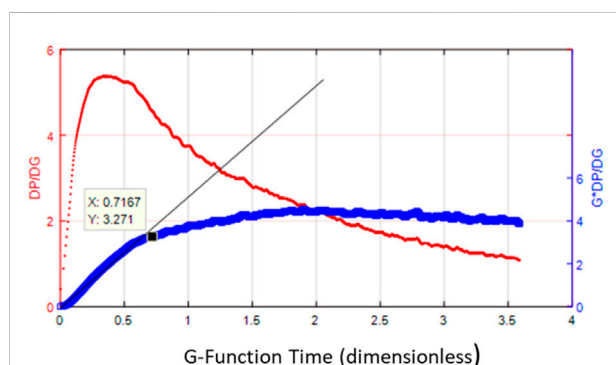ry small or even close to 0, indicating that a certain shear failure has occurred in the caprock before the construction of the library. In the experimental test, the average compressive strength of the caprock under the net overlying confining pressure is as high as 304.1 MPa, and the shear strength is 136.6 MPa, which is much higher than the current three-dimensional *in situ* stress. Based on the effective stress theory, the calculation formula of the maximum ultimate bearing pressure is as follows:

minimum horizontal principal stress at the interface of the reservoir cap rock of gas storage M is calculated to be 34.2 MPa. The European Union, Canada, Australia and other national gas storage standards stipulate that the maximum gas injection pressure must be less than 80% of the minimum

TABLE 2 Summary of data processing results of overlying mudstone caprock (2790−2792 m).

Closed pressure analysis/MPa	Tangent method/MPa	Muskat/MPa	DT/DP/MPa	G-function/MPa	Mean/MPa	Standard deviation	Error/% (m-M)/M
Times-1	36.48	35.73	33.99	34.82	35.26	0.94	-4.29%
Times-2	37.46	36.92	37.21	36.07	36.92	0.52	0.22%
Times-3	38.58	/	36.36	36.81	37.25	0.96	1.11%
Times-4	38.82	/	37.95	36.96	37.91	0.76	2.90%
Mean	/	/	/	/	36.84	/	/

TABLE 3 Summary of the measurement results of *in situ* stress caused by hydraulic fracturing in Well C1.

Numbering	Top death/m	Bottom death/m	Vertical depth of the midpoint of the measurement segment/m	Minimum principal stress/MPa	Vertical stress/MPa	Remark
1	2790	2792	2244.8	36.84	49.39	Basalt caprock
2	2814	2816	2262.3	32.79	49.77	Direct mudstone caprock
3	2834	2836	2276.8	27.36	50.09	Reservoir
4	2881.6	2884.6	2314.8	30.25	50.93	Reservoir
5	2910	2912	2331.5	34.46	51.29	Backplane layer

TABLE 4 *In situ* stress measurement results after pore pressure correction.

Numbering	Top death/m	Bottom death/m	Vertical depth of the midpoint of the measurement segment/m	Minimum principal stress/MPa	Vertical stress/MPa
1	2790	2792	2244.8	36.84	49.39
2	2814	2816	2262.3	32.79	49.77
3	2834	2836	2276.8	34.16	50.09
4	2881.6	2884.6	2314.8	33.72	50.93
5	2910	2912	2331.5	34.46	51.29

$$P_{max} < \frac{1}{4}\left(2c\cos\varnothing + S_1 + 3S_3\right) \qquad (3)$$

Considering the critical fluid pressure of the caprock tensile failure and shear failure, the ultimate pressure bearing capacity of the caprock is considered to be 38.3 MPa, and after considering the 80% safety factor, the safe pressure bearing capacity is 30.6 MPa.

3) Design of upper limit pressure of UGSs

According to the dynamic sealing evaluation results of the gas storage geological body of gas storage M, from the perspective of the static and dynamic ultimate pressures of the caprock, the ultimate pressure bearing capacity of the oil reservoir is comprehensively evaluated to be 27.2 MPa, and the main controlling factors are fault slip and lateral closure, as shown in Table 5.

TABLE 5 M UGS geological body pressure bearing capacity evaluation table.

Classification	Sealing factor	Evaluation indicators	Results	Ultimate pressure(MPa)	Safe pressure(MPa)	Recommended upper limit pressure(MPa)
Static	Geological features	Lithology/thickness	Basalt/ 400 m		–	27.2
	Capillary seal	Dynamic breakout pressure	12 MPa	34.4	34.4	
Dynamic	Tensile failure	Minimum horizontal principal stress	34.2 MPa	34.2	27.2	
	Shear failure	Sheer safety index	0.37	38.3	30.6	

4 Conclusion

The evaluation of the ultimate pressure bearing capacity of the gas storage geological body in the construction of oil and gas storage gas storage is a key issue in the design of the upper limit pressure of the gas storage operation. The main evaluation objects include caprocks and faults. For the conversion of oil and gas reservoirs to gas storage, the most basic requirement for the ultimate pressure bearing capacity of gas storage geological bodies is to ensure that the caprocks and faults do not undergo macroscopic rupture and slippage and to optimize the design for the upper limit pressure of the gas storage operation and the dynamic monitoring system.

This paper introduces in detail the equipment, procedures and data processing of *in situ* stress measurements using hydraulic fracturing technology. The test interval has high reliability, each interval has at least three measurements, and the fracture closure pressure of different test times has high consistency. The relative error of each measurement interval is less than 5%, and the test results of the hydraulic fracturing *in situ* stress measurement method have high accuracy and are basically consistent with the interpretation results of *in situ* stress in this area, which can meet the evaluation requirements of the ultimate pressure-bearing capacity of the geological body of underground gas storage.

Based on the measured *in situ* stress data, the ultimate pressure-bearing capacity of the caprock of the UGS geological body was evaluated. The comprehensive analysis concluded that the safe upper limit of the reservoir-type UGS in Block M is 27.2 MPa. There is a lack of experience and precedents for building complex fault-block reservoirs, and

there are still certain uncertainties in terms of the limitations of geological understanding.(Arree et al., 2009), (CCST, 2018).

Data availability statement

The original contributions presented in the study are included in the article/supplementary material, further inquiries can be directed to the corresponding author.

Author contributions

LS was responsible for the conception and design of the study, while others were responsible for analyzing and interpreting the data.

Conflict of interest

Authors QW, LS, CX, YS, GG, MW, and XG were employed by Jidong Oilfield Company, PetroChina.

Publisher's note

All claims expressed in this article are solely those of the authors and do not necessarily represent those of their affiliated organizations, or those of the publisher, the editors and the reviewers. Any product that may be evaluated in this article, or claim that may be made by its manufacturer, is not guaranteed or endorsed by the publisher.

References

Anna, M., Vítězová, M., Vitez, T., Buriankova, I., Huber, H., Dengler, L., et al. (2021). Underground gas storage as a promising natural methane bioreactor and reservoir. *J. Energy Storage* 47, 103631. doi:10.1016/j.est.2021.103631

Arree, B., Barree, V., and Craig, D. (2009). Holistic fracture diagnostics: Consistent interpretation of prefrac injection tests using multiple analysis methods[J]. *SPE Prod. operations* 24 (3), 396–406. doi:10.2118/107877-PA

Bakhtiari, M., Shad, S., Zivar, D., and Razaghi, N. (2021). Coupled hydromechanical analysis of underground gas storage at Sarajeh field, Qom formation, Iran. *J. Nat. Gas. Sci. Eng.* 92, 103996. doi:10.1016/j.jngse.2021.103996

CCST (2018). *Long term viability of underground natural gas storage in California: An independent review of scientific and technical information California council on science and technology (CCST).* Sacramento, USA: CCST. AvaliableAt: http://ccst.us/projects/natural_gas_storage/publications.php.

Dehghan, A. N., Goshtasbi, K., Ahangari, K., and Jin, Y. (2016). Mechanism of fracture initiation and propagation using a tri-axial hydraulic fracturing test system in naturally fractured reservoirs. *Eur. J. Environ. Civ. Eng.* 20, 560–585. doi:10.1080/19648189.2015.1056384

Ding, G. (2010). Development and driving force of globle underground gas storage. *Natural Gas Industry* 30 (8), 59–61. doi:10.3787/j.issn.1000-0976.2010.08.016

Gilbert, G., Backé, R., Puspitasari, Z., Pallikathekathil, J., Maney, B., and Dewhurst, D. (2013). Model. geomechanics gas storage a case study Iona gas field, *Aust. J. Greenh. Gas Control* 13, 138–148. doi:10.1016/j.ijggc.2012.12.009

Haimson, B., and Cornet, F. (2003). ISRM suggested methods for rock stress estimation—Part 3: Hydraulic fracturing (HF) and/or hydraulic testing of pre-existing fractures (HTPF). *Int. J. Rock Mech. Min. Sci.* 40 (7-8), 1011–1020. doi:10.1016/j.ijrmms.2003.08.002

Jeanne, P., Zhang, Y., and Rutqvist, J. (2020). Influence of hysteretic stress path behavior on seal integrity during gas storage operation in a depleted reservoir. *J. Rock Mech. Geotechnical Eng.* 12, 886–899. doi:10.1016/j.jrmge.2020.06.002

Jia, S., Fu, X., and Wang, J. (2020). *Trap integrity evaluation of porous underground gas storage.* Science Press.

Jiang, T., Wang, J., Wang, Z., and Zhou, D. (2021). Practice and understanding of collaborative construction of underground gas storge and natural gas flooding. *Nat. Gas. Ind.* 41 (9), 66–74. doi:10.3787/j.issn.1000-0976.2021.09.007

Jin, Z., Yuan, Y., Sun, D., Liu, Q., and Li, S. (2014). Models for dynamic evaluation of mudstone/shale cap rocks and their applications in the Lower Paleozoic sequences, Sichuan Basin, SW China. *Mar. Pet. Geol.* 49, 121–128. doi:10.1016/j.marpetgeo.2013.10.001

Kano, Y., Fujii, T., Uehara, S., Honda, K., and Sorai, M. (2014). Experimental study of sealing performance: Effects of particle size and particle-packing state on threshold pressure of sintered compacts. *J. Geophys. Res. Solid Earth* 119, 5482–5496. doi:10.1002/2014jb011177

Lin, W., Xiong, S., Liu, Y., He, Y., and Liu, S. (2021). Spontaneous imbibition in tight porous media with different wettability: Pore-scale simulation phys. *Fluids (1994)* 33 (3), 032013. doi:10.1063/5.0042606

Liu, J., Ding, W., Yang, H., Wang, R., Yin, S., Li, A., et al. (2017). 3D geomechanical modeling and numerical simulation of *in situ* stress fields in shale reservoirs: A case study of the lower cambrian niutitang formation in the cen'gong block, south China. *Tectonophysics* 712, 663–683. doi:10.1016/j.tecto.2017.06.030

Liu, J., Mei, L., Ding, W., Xu, K., Yang, H., and Liu, Y. (2022b). Asymmetric propagation mechanism of hydraulic fracture networks in continental reservoirs. *GSA Bull.* doi:10.1130/B36358.1

Liu, J., Yang, H., Xu, K., Wang, Z., Liu, X., Cui, L., et al. (2022a). Genetic mechanism of transfer zones in rift basins: Insights from geomechanical models. *GSA Bull.* 134, 2436–2452. doi:10.1130/B36151.1

Lynch, T., Fisher, Q., Angus, D., and Lorinczi, P. (2013). Investigating stress path hysteresis in a CO2 injection scenario using coupled geomechanical-fluid flow modeling. *Energy Procedia* 37, 3833–3841. doi:10.1016/j.egypro.2013.06.280

Mahdi, D. S., Al-Khdheeawi, E. A., Yuan, Y., Zhang, Y., and Iglauer, S. (2021). Hydrogen underground storage efficiency in a heterogeneous sandstone reservoirciency in a heterogeneous sandstone reservoir. *Adv. Geo-Energy Res.* 5 (4), 437–443. doi:10.46690/ager.2021.04.08

Mitaim, S., and Detournay, E. (2004). Damage around a cylindrical opening in a brittle rock mass. *Int. J. Rock Mech. Min. Sci.* 41, 1447–1457. doi:10.1016/j.ijrmms.2004.09.009

Mou, P., Pan, J., Wang, K., Wei, J., Yang, Y., and Wang, X. (2020). Influences of hydraulic fracturing on microfractures of high-rank coal under different *in-situ* stress conditions. *Fuel* 287, 119566. doi:10.1016/j.fuel.2020.119566

Mukherjee, S., Rajabi, M., Esterle, J., and Copley, J. (2020). Subsurface fractures, *in-situ* stress and permeability variations in the Walloon coal measures, eastern surat basin, queensland, Australia. *Int. J. Coal Geol.* 222, 103449. doi:10.1016/j.coal.2020.103449

Pijnenburg, R., Hangx, S., and Spiers, C. (2019). Inelastic deformation of the slochteren sandstone: Stress-strain relations and implications for induced seismicity in the groningen gas field. *J. Geophys. Res. Solid Earth* 124, 5254–5282. doi:10.1029/2019JB017366

Sadeghi, S., and Sedaee, B. (2021). Mechanistic simulation of cushion gas and working gas mixing during underground natural gas storage. *J. Energy Storage* 46, 103885. doi:10.1016/j.est.2021.103885

Schmitt, D. R., Currie, C. A., and Zhang, L. (2012). Crustal stress determination from boreholes and rock cores: Fundamental principles. *Tectonophysics* 580, 1–26. doi:10.1016/j.tecto.2012.08.029

Soeder, D. J. (2021). Greenhouse gas sources and mitigation strategies from a geosciences perspective. *Adv. Geo-Energy Res.* 5 (3), 274–285. doi:10.46690/ager.2021.03.04

Sui, Y., Lin, T., Liu, X., Dong, C., Cheng, W., Zhang, G., et al. (2011). Numerical simulation for the effect of cyclic stress on microstructure and mechanical properties of reservoir rocks during operations of gas storage. *J. China Univ. Petroleum(Edition Nat. Sci.* 44 (2), 78–84. doi:10.1016/j.proeng.2011.05.040

Sun, J., Zheng, D., Wang, J., Liu, J., Shi, L., Xu, H., et al. (2018). Development trend and driving force of global underground gas storage. AvaliableAt: http://onepetro.org/SPEEURO/proceedings-pdf/18EURO/2-18EURO/D022S013R001/1209055/spe-190838-ms.pdf/1 (Accessed June 19, 2022).

Wang, B., Li, D., Xu, B., Wang, Q., Zhang, F., Wang, Q., et al. (2021). Probabilistic-based geomechanical assessment of maximum operating pressure for an underground gas storage reservoir, NW China. *Geomechanics for Energy and the Environment* 31, 100279. doi:10.1016/j.est.2021.100279

Wang, J., Feng, X., Wanyan, Q., Zhao, Q., Pei, Z., Zie, G., et al. (2021). Hysteresis effect of three-phase fluids in the high-intensity injectioneproduction process of sandstone underground gas storages. *Energy* 242. doi:10.1016/j.energy.2012.123058

Xu, K., Tian, J., Yang, H., Zhang, H., Ju, W., Liu, X., et al. (2022). Effects and practical applications of present-day *in-situ* stress on reservoir quality in ultra-deep layers of Kuqa Depression, Tarim Basin, China. *J. Nat. Gas Geoscience* 7, 85–94. doi:10.1016/j.jnggs.2022.04.002

Xu, T., Tian, H., Zhu, H., and Cai, J. (2022). China actively promotes CO2 capture, utilization and storage research to achieve carbon peak and carbon neutrality. *Adv. Geo-Energy Res.* 6 (1), 1–3. doi:10.46690/ager.2022.01.01

Zhang, G., Zeng, D., Fan, Z., Mi, L., Wang, D., Yang, X., et al. (2021). Method and application of *in situ* stress field to evaluate fault sealing of underground gas storage traps. *Nat. Gas. Geosci.* 32, 923–930. doi:10.11764/j.issn.1672-1926.2021.01.014

Zhu, S., Zheng, D., Sun, J. G., Wu, Z., Wang, J., Guan, C., et al. (2022). Experimental study on dynamic sealing capacity and safe threshold of caprock in underground gas storges. *J. Nat. Gas. Sci. Eng.* 101, 104521. doi:10.1016/j.jngse.2022.104521

Zoback, M., Barton, C., Brudy, M., Castilo, D., Finkbeiner, T., Grollimund, B., et al. (2003). Determination of stress orientation and magnitude in deep wells. *Int. J. Rock Mech. Min. Sci.* 40, 1049–1076. doi:10.1016/j.ijrmms.2003.07.001

Analysis of fault characteristics and oil and gas enrichment differences in the No. 2 structural belt, Nanpu Sag, Bohai Bay Basin, East China

Juan Zou[1]*, Guoyong Liu[2], Qian Ma[1], Fusheng Yu[3], Lingjian Meng[1] and Bo Tian[1]

[1]PetroChina Jidong Oilfield, Tangshan, China, [2]PetroChina Xinjiang Oilfield, Kelamayi, China, [3]China University of Petroleum, Beijing, China

There are great differences in oil and gas enrichment at different locations in petroliferous basins, and faults are an important factor affecting the differential enrichment of oil and gas. In this paper, taking the No. 2 structure in the Nanpu Sag, Bohai Bay Basin, East China, as an example, based on the analysis of fault geometry and kinematics characteristics, the determination of oil source faults, the analysis of fault trap origin and effectiveness, and the analysis of fault caprock combinations are carried out to study the differences and mechanisms of oil and gas enrichment east and west of the Nanpu No. 2 structure. The results show that the fault-source contact relationship affects the direction of oil and gas migration. The No. 2 structure in the Nanpu Sag has a dual-source hydrocarbon supply. The western structure supplies hydrocarbons from the north and east, with oil and gas migrating along the direction parallel and perpendicular to the fault strike. The east structure supplies hydrocarbons from the south and north, with oil and gas migrating along the direction perpendicular to the fault strike. The effectiveness of fault traps affects the scale of oil and gas accumulation. Most of the traps of the Nanpu No. 2 structure formed before hydrocarbon expulsion, which are all effective traps and are conducive to oil and gas accumulation. The relationship between fault and caprock determines the vertical accumulation layers of oil and gas: The faulted thickness of the east structure is large, the fault is vertically closed, and oil and gas are enriched mainly in the deep layer. The faulted thickness of the west structure is small, and oil and gas are enriched in both deep and shallow layers.

1 Introduction

Oil and gas accumulation conditions in petroliferous basins are complex, and the enrichment differences are large. Different sags, different structural belts in the same sag, and different structural positions in the same structural belt have different oil and gas reservoir types, different key control elements, and different accumulation characteristics. As one of the most important structures in petroliferous basins, the fault is the main factor controlling oil and gas migration, accumulation and dispersion. They are not only oil and gas migration channels but also oil and gas sealing surfaces (Wan et al., 2010, 2012), controlling oil and gas sources, traps, oil and gas migration and accumulation, and adjustment and destruction of oil and gas reservoirs. Oil and gas reservoirs have been found in many structural belts in the Nanpu Sag, Bohai Bay Basin, with great exploration potential. However, due to the superposition of three tectonic activities in Es, Ed, and the late Nm, the fault characteristics are complex, especially various fault combination styles, and multiphase and multisegment fault activities control oil and gas enrichment with great differences. In this paper, taking the No. 2 structure in the Nanpu Sag as an example, the characteristics and mechanism of hydrocarbon enrichment differences are analyzed from the study of fault activity.

2 Geological setting

2.1 Location

The Nanpu Sag is located in the northeastern Huanghua Depression, the northern Chengning Uplift and the southwestern Liaodong Bay Depression in the Bohai Bay Basin. It is adjacent to the Yanshan fold belt in the north and the Bohai Sea in the south. It is further divided into seven secondary positive structural belts and four negative subsags according to structural differences.

The No. 2 structure is located in the middle south of the Nanpu Sag, adjacent to the Linque subsag in the north, the Caofeidian subsag in the southeast, the No. 1 structure in the west, and the No. 4 structure in the east, controlled by a series of NE-striking and nearly E−W-striking faults (Figure 1).

2.2 Stratigraphy

The Nanpu Sag is a multicycle Mesozoic and Cenozoic fault basin formed on the basis of the North China platform under the background of multiple tectonic movements: the stable development period of the Paleozoic platform, the disintegration period of the Mesozoic platform, and the formation and development period of the Cenozoic basin. Its geological conditions are complex, and its oil and gas resources are rich (Cui et al., 2018). Five sets of strata, including Archean,
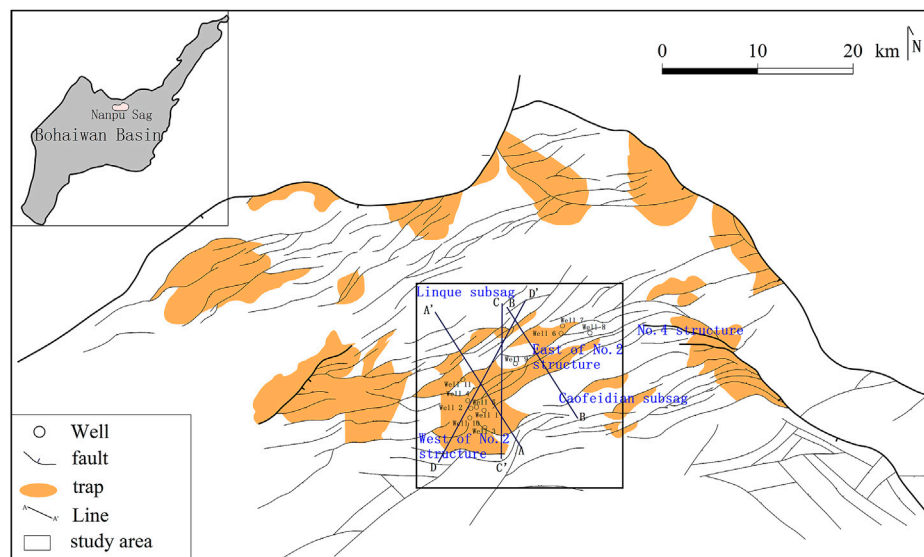
FIGURE 1
Regional structure location of the Nanpu No. 2 structure.

FIGURE 2
Stratigraphic column of the Nanpu No. 2 structure.
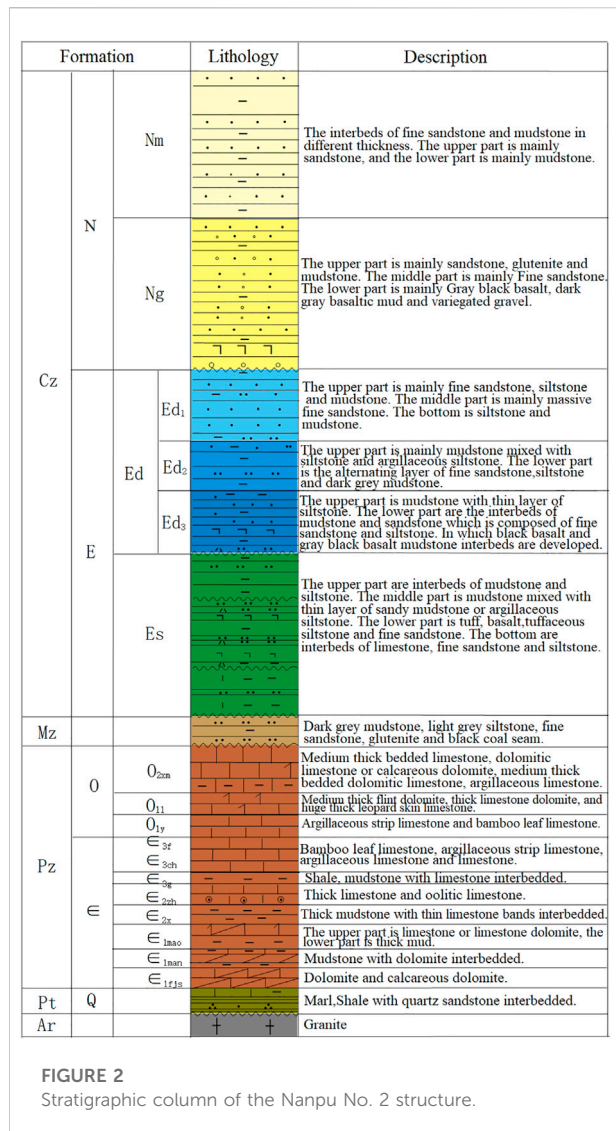
Proterozoic, Paleozoic, Mesozoic and Cenozoic strata, are developed from bottom to top in the Nanpu No. 2 structure (Figure 2). Hydrocarbon source rocks are developed in the Cenozoic Paleogene, including the Es_3, Es_1, and Ed_3 Formations (Wang et al., 2020). The reservoirs include clastic rock (sandstone) reservoirs (Kashif et al., 2019), carbonate rock reservoirs and volcanic rock reservoirs, among which sandstone reservoirs are the main reservoirs.

2.3 Reservoir

The Nanpu Sag has long oil-bearing intervals, multiple exploration strata, rich reservoir types and multiple oil and gas accumulations (Jiang et al., 2018; Wang et al., 2019). Oil and gas have been found in the Neogene Nm and Ng Formations,

the Paleogene Ed and Es Formations, the Mesozoic Jurassic, and the Paleozoic Cambrian and Ordovician strata, concluding above-source, intrasource and below-source accumulation models.

3 Methods

3.1 Analysis of fault geometry and kinematics characteristics

The faults in the Nanpu No. 2 structure are complex, and fault identification has multiple solutions. Based on the latest seismic processing data, combined with the fault development model and the prediction of low-order faults by stress field simulation, the faults are identified in detail (Liu et al., 2018). The faults in the Nanpu No. 2 structure are characterized by mixed scales, different fault distances, different extension lengths, and obvious hierarchical sequences. The fault grade is divided according to the fault extension length and cutting depth. In combination with the fault occurrence of different levels and the contact relationship of the fault plane and profile, the structure style is recognized. On this basis, the fault displacement–distance curve and section buried depth contour are used to quantitatively characterize and analyze the segmented growth process of the main faults in the Nanpu No. 2 structure, to identify the distribution and evolution of segmented points and complete segments and to determine the plane and vertical segmentation of the main fault (Wang et al., 2014; Liu J et al., 2022).

3.2 Analysis of the relationship between faults and reservoirs

On the basis of fault analysis, the relationship between faults and reservoirs is studied. First combined with the seismic data interpretation scheme of multiple rounds of processing, the oil source fault is determined by analyzing the cutting relationship and contact area between the fault and the source rock. Then, the fault displacement–distance curve is used based on the analysis of fault kinematics characteristics to restore fault activity during the hydrocarbon expulsion period to determine the effectiveness of traps. Finally, for more than 50 drilled wells in the Nanpu No. 2 structure, stratigraphic correlation is conducted according to lithological combinations and logging curves, a thick mudstone section at the top of Ed_2 is identified, and the mudstone thickness at the top of Ed_2 of each well drilled into Ed_2 is counted. The fault distance of each fault at the top of Ed_2 is calculated by using the fault drop method, and then the faulted thickness is obtained by calculating the difference in fault distance and mudstone thickness to analyze the vertical sealing property of the fault. To further clarify the differences in oil and gas accumulation.
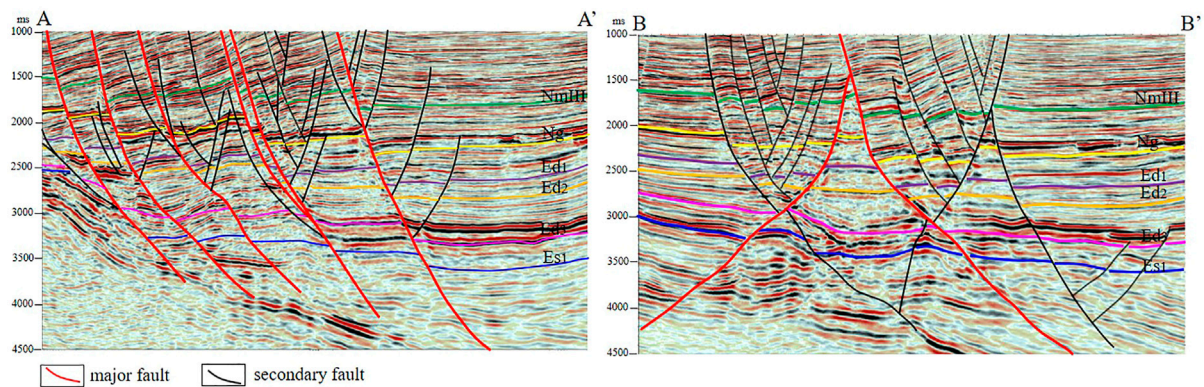
FIGURE 3
Structural Style Profile of the Nanpu No. 2 structure. **(A)** Fault terrace style formed by a series of north-dipping faults cutting the basement in the west of the Nanpu No. 2 structure. **(B)** Two compound "Y" styles formed by two major faults with opposite dips and several secondary faults in the east of the Nanpu No. 2 structure.
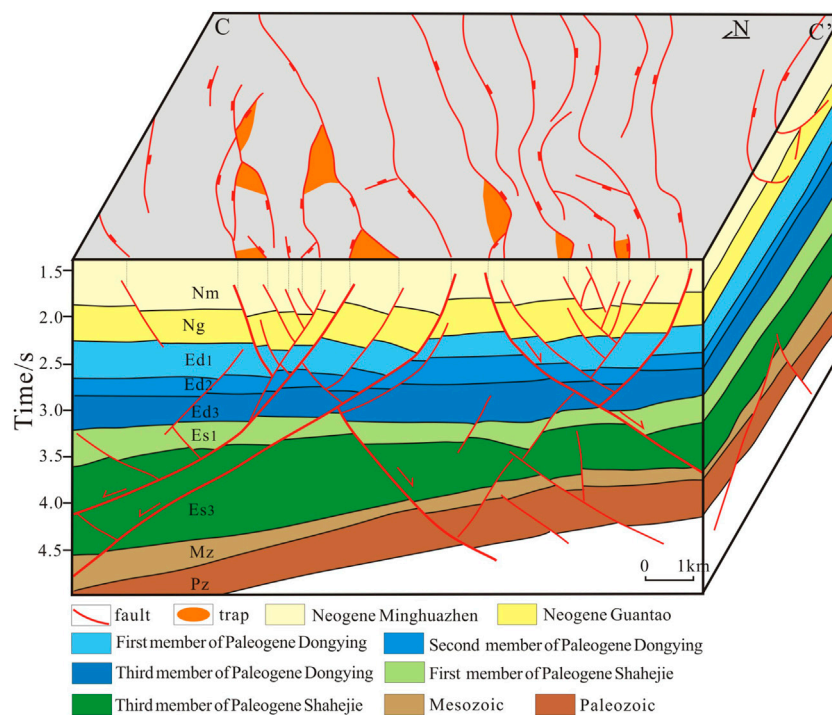
FIGURE 4
Structural distribution in the east of the Nanpu No. 2 structure. The faults have a basically NE strike, which controls the crosscut fault block trap and fault nose trap. It developed a wide and gentle anticline structure in Es_3 and compound "Y" styles in Ed.

4 Results

4.1 Differences in fault characteristics

The Nanpu No. 2 structure has experienced three periods of intense activity since the Paleogene (Liu and Zhang, 2011;

Zhao et al., 2019): Es_3, the end of Ed and the end of Nm. During the Es periods, it was subjected to NW-SE extension and developed NE-striking large faults. During the Ed periods, it was subjected to NNW-SSE extension, and NE-striking faults continued to grow. At the same time, NEE-SWW strike faults were developed. In the Neogene periods, it

became nearly NS extension. Some old faults inherited, and some near-EW strike small faults newly developed with parallel or oblique combination in the plane. The large fault is characterized by multiple episodes in the vertical direction and multiple sections in the plane (Peacock and Sanderson, 1991; Trudgill and Cartwright, 1994; Cartwright et al., 1995; Kim and Sanderson, 2005). There are NE-striking and nearly E-W-striking faults in the west structure, which are in fault terrace style (Figure 3A) controlled by the development of a series of north-dipping faults cutting the basement on the buried hill background. The faults in the east structure have a basically NE strike. The Mesozoic sedimentary rocks represent a buried hill background. It developed a wide and gentle anticline structure in the Es_3 period. During the Ed period, the activities of the reverse faults, which are deep basement, controlled the development of one horst structure and two compound "Y" styles (Figure 3B) in the north and south (Figure 4).

4.2 Relationship between faults and reservoirs

4.2.1 Fault-source feature

The Nanpu No. 2 structure is adjacent to the Linque subsag and Caofeidian subsag in the north and south, which have a two-way oil source. Three sets of hydrocarbon source rocks are developed in Es_3, Es_1 and Ed_3. The oil source is sufficient. Whether the fault can connect the hydrocarbon source rocks is the key to determining the oil source fault. Based on the analysis of the vertical episodic nature of the fault activity, the oil source faults are determined by combining the cutting relationship and contact area between the faults and the source rock. The faults cut into one or more sets of hydrocarbon source rocks and developed during the hydrocarbon expulsion period can be regarded as the main oil source faults.

At the end of the Ed, there was a large amount of oil generation for the bottom hydrocarbon source rocks in Es_3. At the end of Nm, the hydrocarbon source rocks at the bottom of Es_1 and Ed_3 entered the peak of oil generation (Sun et al., 2015), and the period of fault activity matched the period of hydrocarbon expulsion, linking the oil source well. The main oil source faults in the west structure are NW-dipping and NE-striking faults, which developed from Es_3 to the end of Nm. The main oil source faults in the east structure are NEE strikes, which developed from Ed to the end of Nm, and some cut into Es. The oil source faults cut into both the Caofeidian subsag and Linque subsag and developed at the end of Nm, in which hydrocarbons expulsed.

4.2.2 Fault-trap mechanism

The influence of faults on traps is shown in many aspects: fault combination controls trap type, fault activity controls trap development time, and fault activity controls trap transformation form. The Nanpu No. 2 structure is controlled by fault activity and mainly develops fault block traps and fault nose traps, including reverse fault traps located at the fault rising side and syndromic fault traps located at the fault falling side. The fault activity causes the uplift plate strata to tilt in the opposite direction to form a reverse fault trap, which is developed at the beginning of the fault activity. The fault descending wall strata moves downward, and the displacement of the connection part is small, forming the syndromic fault trap, so the syndromic fault trap is developed in the period of hard connection of segmented faults. The fault displacement-distance curve is used to carry out back stripping of fault activity, restore the fault activity intensity and extension length in the reservoir forming period, determine the formation time and scale of fault traps, and then determine the effectiveness of traps (Figure 5) (Liu L et al., 2022).

4.2.3 Fault-cap combination

Faults play a dual role in the process of oil and gas migration and accumulation, which can not only become a channel for oil and gas migration from deep to shallow but also provide sealing conditions for oil and gas accumulation. Caprock plays an important role in hindering the vertical transmission of oil and gas. When the thickness of the caprock is large and the scale of the fault that breaks through the caprock is small, the caprock is not pulled off, the shear mudstone coating layer is thick, and the oil and gas are completely blocked in the vertical direction. In contrast, when the thickness of the caprock is small and the fault scale is large, the caprock is completely pulled off, with the fault opening vertically, and oil and gas continue to migrate upward. The Nanpu No. 2 structure develops three sets of stable caprocks, namely, the mudstone at the bottom of the Nm Formation, the volcanic rock in the middle of the Ng Formation, and the mudstone at the top of the Ed_2 Formation. The mudstone at the top of Ed_2 is thick, with differences from east to west. It is thicker in the east, with a maximum thickness of 310 m, and thinner in the west (Figure 6). Both the thickness of the mudstone caprock and the fault distance of Ed_2 determine the difference in the faulted thickness of Ed_2 in the Nanpu No. 2 structure. The greater the faulted thickness is, the more difficult it is for oil and gas to continue to migrate upward.

5 Discussion

5.1 Differences in fault source

The Nanpu No. 2 structure is adjacent to the Caofeidian subsag in the southeast and the Linque subsag in the north. The main oil source faults in the west structure are NW dipping and
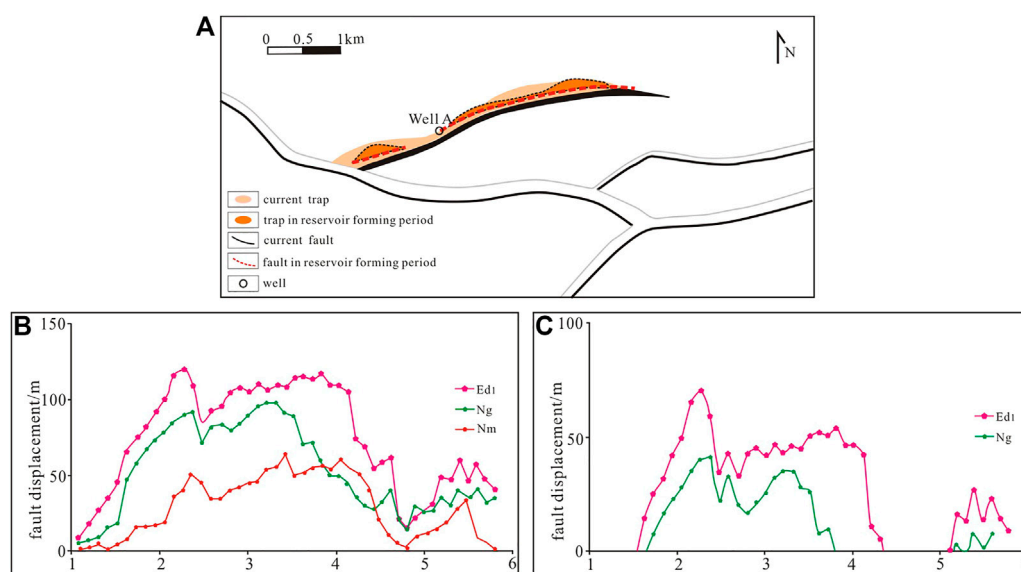
FIGURE 5
Control of fault segmentation activities on trap development. **(A)** Fault and trap distribution: The current fault is continuous, and Well A is in the current trap; The fault in the reservoir forming period is discontinuous, and Well A is not in the effective trap. **(B)** Current fault displacement-distance curve shows the fault segmentation. **(C)** Stripping the fault displacement-distance in the reservoir forming period in order to restore the trap in the reservoir forming period which is effective trap.

NE strike, connecting the oil source of the Linque subsag in the north to migrate along the direction perpendicular to the fault strike and connecting the oil source of the Caofeidian subsag in the east to migrate along the direction parallel to the fault strike to the west. The main oil source faults in the east structure have an NEE strike. The NW-dipping oil source fault in the north connects the oil source of the Linque subsag, and the SE-dipping oil source fault in the south connects the oil source of the Caofeidian subsag, both of which migrate oil and gas to the tectonic horst along the direction perpendicular to the fault strike (Figure 7). Influenced by the relationship between the oil source fault strike and the middle shallow ancient landform in which the Nanpu No. 2 east structure is located in the low-lying area between the Nanpu No. 2 west structure and the Nanpu No. 4 structure (Figure 8), the oil and gas may continue to migrate to the higher part of the Nanpu No. 2 west structure and the Nanpu No. 4 structure on both sides along the direction of the NE fault strike after migrating to the middle shallow layer of the Nanpu No. 2 east structure. In addition, a few deep faults in the east structure are "conjugate", with relatively poor longitudinal connectivity, resulting in relatively poor vertical oil and gas transmission capacity.

5.2 Effectiveness of the fault traps

Multiple fault combination styles of the Nanpu No. 2 structure control the development of multiple types of fault-related structural traps, which are mainly reverse fault block traps, and a small number of syndromic fault traps are also developed. Taking the trap in Ed_1 as an example, the reverse fault trap on the upthrown block developing in the Es and Ed periods developed in Ed_1, the same direction fault trap on the downthrown block developing in the Es and Ed periods developed at the fault hard connection period, and the reverse fault trap on the upthrown block developing in NmⅢ developed in NmⅢ. That is, most traps in Ed_1 of the Nanpu No. 2 structure were formed in Ed_1, and some were formed in NmⅢ. Moreover, particle fluorescence analysis also indicates that fault traps formed in the late Nm Formation sedimentation, and the QGF-E is generally greater than 40. The main filling period of the Ed_1 traps of the Nanpu No. 2 structure is 2–3 Ma, which is the end of Nm. Therefore, the traps that formed in the Ed_1 and NmⅢ stages are effective traps.

5.3 Differences in fault caps

The mudstone caprock at the top of Ed_2 of the Nanpu No. 2 structure affects the vertical transmission of oil and gas. The thickness of the mudstone caprock is 94–310 m, and it gradually increases from west to east. The fault displacement is 60–500 m. The faulted thickness of Ed_2 in the east structure is more than 35 m, and the caprock is not damaged. The
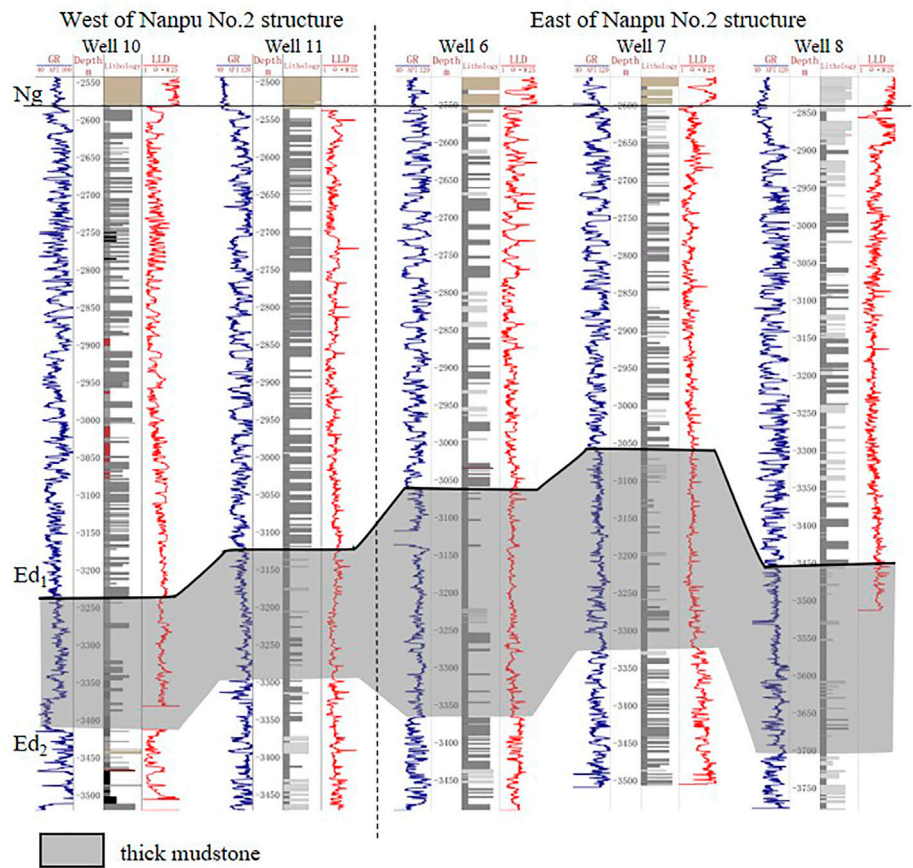
FIGURE 6
Stratigraphic correlation profile of the Nanpu No. 2 structure. Well 10 and well 11 are west of the Nanpu No. 2 structure (located in Figure 1), whose mudstone thickness at the top of Ed_2 is 160 m. Well 6, well 7 and well 8 are east of the Nanpu No. 2 structure, whose mudstone thickness at the top of Ed_2 is 250–300 m.
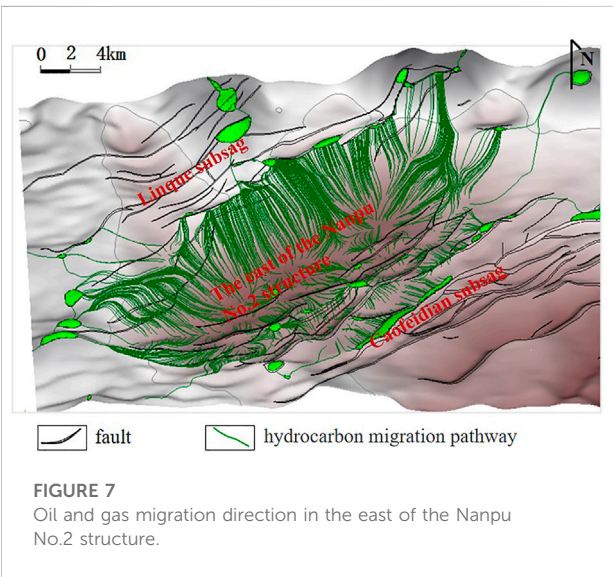
FIGURE 7
Oil and gas migration direction in the east of the Nanpu No.2 structure.
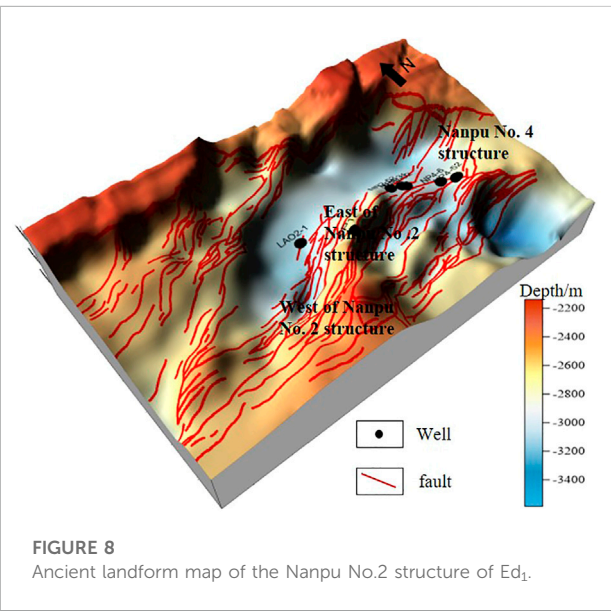
FIGURE 8
Ancient landform map of the Nanpu No.2 structure of Ed_1.
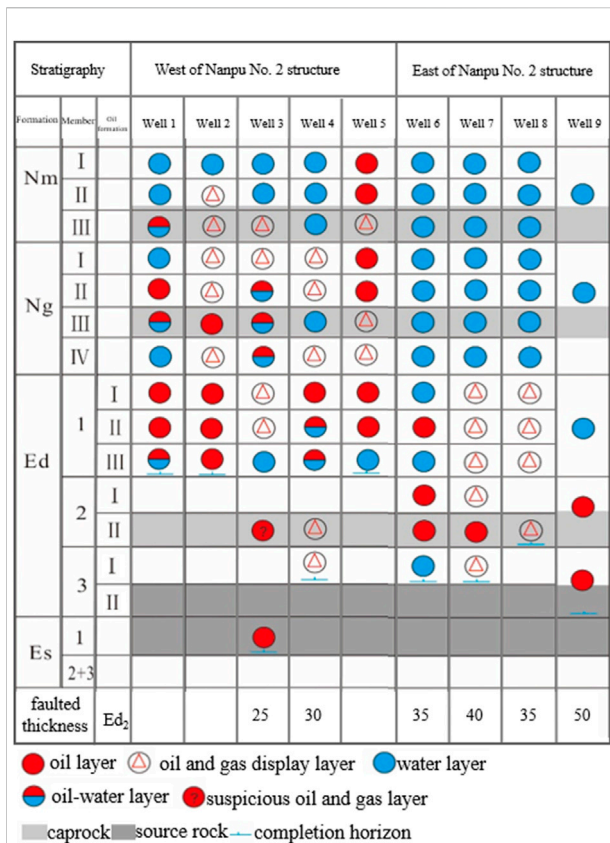
FIGURE 9
Faulted thickness and hydrocarbon distribution of the Nanpu No. 2 structure. The faulted thickness of Ed$_2$ is generally less than 35 m, and the oil layer develops in the Es, Ed, Ng and Nm Formations in the west structure; the faulted thickness of Ed$_2$ is generally more than 35 m, and the oil layer develops mainly below the Ed$_2$ Formations in the east structure.
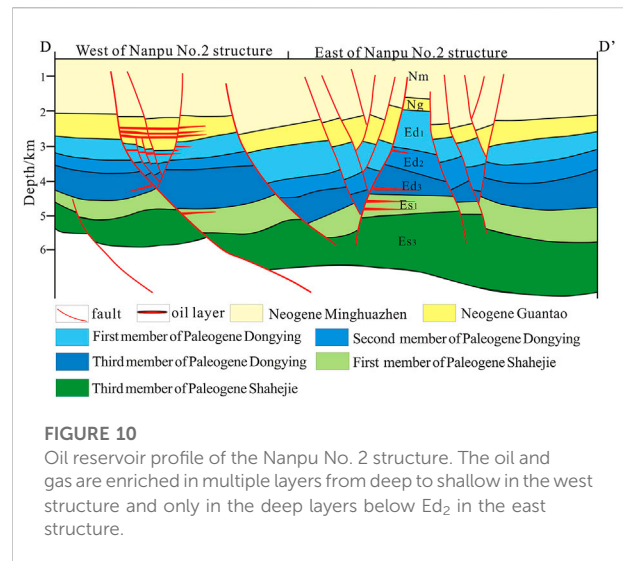
FIGURE 10
Oil reservoir profile of the Nanpu No. 2 structure. The oil and gas are enriched in multiple layers from deep to shallow in the west structure and only in the deep layers below Ed$_2$ in the east structure.

greater the faulted thickness of the caprock is, the greater the hindrance to oil and gas. In addition, the source rock has overpressure plugging, and the vertical sealing of the fault is good. Therefore, it is difficult for oil and gas to continue to migrate upward to the stratum above Ed$_2$ in the east. The faulted thickness of Ed$_2$ in the west structure is generally less than 35 m, which causes the vertical sealing property of the fault in the west structure to be poor, and the conductivity to be strong. Some oil and gas migrate upward to the Ed$_1$, Ng and Nm reservoirs (Figure 9).

5.4 Differences in oil and gas enrichment

The Nanpu No. 2 structure has many oil layers and complicated oil-water relationships. Influenced by fault-source, fault-trap and fault-cap, the oil and gas enrichment are different between the west structure and the east structure. In the western structure, oil and gas are found in the Ordovician buried hill, Es,

Ed, Ng, and Nm. The buried hill oil layer is developed in the Ordovician lower Majiagou Formation. The oil layer is enriched in the weathering crust at the high part of the buried hill, and the thickness of the oil and gas layer is 1.3–35.5 m. The Es Formation develops volcanic rock oil and gas reservoirs, and the Ed, Ng and Nm Formations are enriched in conventional sandstone oil and gas; that is, the oil and gas in the west structure are enriched in multiple layers from deep to shallow. The eastern structure mainly developed shale oil and gas reservoirs in the Es and Ed Formations and developed volcanic rock oil and gas reservoirs in the Ed Formation. The oil and gas are mainly enriched in the deep layer, and the oil- and gas-bearing properties are poor above the thick mudstone at the top of Ed$_2$ (Figure 10).

6 Conclusion

1) The fault-source contact relationship affects the direction of oil and gas migration. The No. 2 structure in the Nanpu Sag has a dual-source hydrocarbon supply. The west structure supplies hydrocarbons from the north and east, with oil and gas migrating along the direction parallel and perpendicular to the fault strike. The east structure supplies hydrocarbons from the south and north, with oil and gas migrating along the direction perpendicular to the fault strike. The east and west structures of the No. 2 structure in the Nanpu Sag have favorable oil source conditions. Influenced by the relationship between the oil source fault strike and the middle shallow ancient landform and the fault longitudinal connectivity, the oil source condition of the middle shallow structure in the west is better than that in the east.

2) The effectiveness of fault traps affects the scale of oil and gas accumulation. The middle deep traps and shallow traps are both developed in the west and east structures of the Nanpu No. 2 structure. Most traps formed before hydrocarbon

expulsion, which are all effective traps and are conducive to oil and gas accumulation.

3) The relationship between fault and caprock determines the vertical accumulation layers of oil and gas: A set of thick mudstone is developed at the top of Ed$_2$ sedimentation, which controls the difference in oil- and gas-enriched strata. The faulted thickness of the east structure is large, the fault is vertically closed, and oil and gas are enriched mainly in the deep layer. The faulted thickness of the west structure is small, and oil and gas are enriched in both deep and shallow layers.

Data availability statement

The original contributions presented in the study are included in the article/Supplementary Material, further inquiries can be directed to the corresponding author.

Author contributions

JZ, GL, and QM contributed to conception and design of the study. JZ and FY performed the statistical analysis. JZ, LM, and BT wrote and revised the manuscript. All authors approved the submitted version.

Conflict of interest

The authors JZ, QM, LM and BT were employed by the company PetroChina Jidong Oilfield. The author GL was employed by the company PetroChina Xinjiang Oilfield.

The remaining author declares that the research was conducted in the absence of any commercial or financial relationships that could be construed as a potential conflict of interest.

Publisher's note

All claims expressed in this article are solely those of the authors and do not necessarily represent those of their affiliated organizations, or those of the publisher, the editors and the reviewers. Any product that may be evaluated in this article, or claim that may be made by its manufacturer, is not guaranteed or endorsed by the publisher.

References

Cartwright, J. A., Trudgill, B. D., and Mansfield, C. (1995). Fault growth by segment linkage: An explanation for scatter in maximum displacement and trace length data from the canyonlands grabens of SE Utah. *J. Struct. Geol.* 17 (9), 1319–1326. doi:10.1016/0191-8141(95)00033-a

Cui, L., Yang, L., and Wang, S. (2018). Tense-shearing characteristics and formation mechanism of basin edge—an example of in liuzan area in Nanpu sag[J]. *Sci. Technol. Eng.* 18 (22), 15–20. doi:10.3969/j.issn.1671-1815.2018.22.002

Jiang, F., Pang, X., Li, L., Wang, Q., Dong, Y., Hu, T., et al. (2018). Petroleum resources in the Nanpu sag, Bohai Bay Basin, eastern China. *Am. Assoc. Pet. Geol. Bull.* 102 (7), 1213–1237. doi:10.1306/0906171608017148

Kashif, M., Cao, Y. C., Yuan, G. H., Asif, M., Javed, K., Mendez, J. N., et al. (2019). Pore size distribution, their geometry and connectivity in deeply buried Paleogene Es1 sandstone reservoir, Nanpu Sag, East China. *Pet. Sci.* 16 (5), 981–1000. doi:10.1007/s12182-019-00375-3

Kim, Y. S., and Sanderson, D. J. (2005). The relationship between displacement and length of faults: A review. *Earth. Sci. Rev.* 68 (68), 317–334. doi:10.1016/j.earscirev.2004.06.003

Liu, J., Ding, W., Dai, J., Wu, Z., and Yang, H. (2018). Quantitative prediction of lower order faults based on the finite element method: A case study of the M35 fault block in the western hanliu fault zone in the gaoyou sag, east China. *Tectonics* 37 (10), 3479–3499. doi:10.1029/2017TC004767

Liu, X. F., and Zhang, C. M. (2011). Nanpu sag of the Bohai Bay Basin: A transtensional fault-termination basin. *J. Earth Sci.* 22 (06), 755–767. doi:10.1007/s12583-011-0225-2

Liu, J. J., Yang, H., Xu, K., Wang, Z., Liu, X., Cui, L., et al. (2022). Genetic mechanism of transfer zones in rift basins: Insights from geomechanical models. *GSA Bull.* 134 (9-10), 2436–2452. doi:10.1130/b36151.1

Liu, L. L., Sun, Y. H., Chen, C., Lou, R., and Wang, Q. (2022). Fault reactivation in No.4 structural zone and its control on oil and gas accumulation in Nanpu sag, Bohai Bay Basin, China. *Petroleum Explor. Dev.* 49 (04), 824–836. doi:10.1016/S1876-3804(22)60313-6

Peacock, D. C., and Sanderson, D. J. (1991). Displacements, segment linkage and relay ramps in normal fault zones. *J. Struct. Geol.* 13 (6), 721–733. doi:10.1016/0191-8141(91)90033-f

Sun, B., Tang, D., Li, X. M., et al. (2015). Hydrocarbon-generation Evolution of Source Rock and Oil-gas Source in Nanpu Depression, Bohai Bay Basin[J]. *Sci. Technol. Eng.* 15 (19), 67–73. doi:10.3969/j.issn.1671-1815.2015.19.013

Trudgill, B. D., and Cartwright, J. A. (1994). Relay-ramp forms and normal-fault linkages, Canyonlands National Park, Utah. *Geol. Soc. Am. Bull.* 106 (9), 1143–1157. doi:10.1130/0016-7606(1994)106<1143:rrfanf>2.3.co;2

Wan, T., Jiang, Y. L., Dong, Y. X., et al. (2012). Relationship between fault activity and hydrocarbon accumulation and enrichment in Nanpu depression[J]. *J. China Univ. Petroleum* 36 (2), 60–67. doi:10.3969/j.issn.1673-5005.2012.02.010

Wan, T., Jiang, Y. L., Lin, H. X., et al. (2010). Quantitative Evaluation of Fault Activity and Fault Sealing Property and Its Relationship with Hydrocar-bon Migration and Accumulation—By Taking Caojiazhuang Step-fault Zone in Chexi Sag for Example[J]. *J. Oil Gas Technol.* 32 (4), 18–24. doi:10.3969/j.issn.1000-9752.2010.04.004

Wang, E., Liu, G., Pang, X., Li, C., Zhao, Z., Feng, Y., et al. (2020). An improved hydrocarbon generation potential method for quantifying hydrocarbon generation and expulsion characteristics with application example of Paleogene Shahejie Formation, Nanpu Sag, Bohai Bay Basin. *Mar. Petroleum Geol.* 112, 104106–106. doi:10.1016/j.marpetgeo.2019.104106

Wang, E., Wang, Z., Pang, X., Zhang, Z., Wang, Z., Wu, Z, et al. (2019). Key factors controlling hydrocarbon enrichment in a deep petroleum system in a terrestrial rift basin—A case study of the uppermost member of the upper Paleogene Shahejie Formation, Nanpu Sag, Bohai Bay Basin, NE China. *Mar. Petroleum Geol.* 107, 572–590. doi:10.1016/j.marpetgeo.2019.05.027

Wang, H. X., Li, M. H., Shen, Z. S., Fu, X. F., Cheng, Z. Y., and Wang, B. (2014). The Establishment and Geological Significance of Quantitative Discrimination Criterion of Fault Segmentation Growth—An Example from Saertu Reservoir in Xingbei Development Area of Songliao Basin[J]. *Geol. Rev.* 60 (06), 1259–1264. doi:10.16509/j.georeview.2014.06.005

Zhao, R., Chen, S., Wang, H., Gan, H. J., Wang, G. H., and Ma, Q. (2019). Intense faulting and downwarping of Nanpu Sag in the Bohai Bay Basin, eastern China: Response to the Cenozoic Stagnant Pacific Slab. *Mar. Petroleum Geol.* 109, 819–838. doi:10.1016/j.marpetgeo.2019.06.034

Check for updates

Relationship between the heterogeneity of low-permeability reservoirs and the dynamic evolution of fractures under uniaxial compression conditions by CT scanning: A case study in the jiyang depression of Bohai Bay Basin, China

Li Li[1]*, Guangyao Shi[1,2], Yixin Zhang[1] and Xiangwei Liu[1]

[1]School of Geosciences, China University of Petroleum (East China), Qingdao, China, [2]Henan Geological Investigation and Designing Institute Co., Ltd., Zhengzhou, China

Based on an analysis of core fractures and computed tomography scanning by X-ray under uniaxial compression tests with loading and unloading, this study investigated the three-dimensional evolution of fracture initiation and propagation in different heterogeneity conditions of low-permeability reservoirs. Reservoir heterogeneity affected the 3D dynamic development of fractures. With increasing loading value, fractures with strong heterogeneity in low-permeability reservoirs followed the development sequence from shallow to deep depth in the profile. When the fracture tip reached the incompetent layer, propagation stopped. Subsequently, when the deformation continued to increase, the fracture crossed the incompetent layer and initiated a new fracture at the front end. Therefore, the across-bedding and through-going macro fractures formed in conjugate sets or were Y-shaped, with roughly equal spacing. In the plane, the fractures initiated along the pre-existing bedding parallel fracture and further propagated into large fractures. Consequently, they formed a net-shaped fracture from the edge to the center, with a long development period. These fractures intersected to form a complex, interconnected, and high-fracture-density system in three dimensions. Under the same loading value, owing to uniform lithology, the formation of micro-fractures in the weak heterogeneity of low-permeability reservoirs is difficult. Furthermore, long shear fractures were only produced in a relatively short formation period with a low fracture density. In the plane, the fractures stepped in an en-énchelon and terminated with horse-tailing microfractures. Moreover, the strong heterogeneity of low-permeability reservoirs was more favorable for producing fractures. The fracture volume was 13.17% of the total sample volume compared to 0.67% in the weak-heterogeneity reservoir under

the same loading compression. Furthermore, a better fracturing effect was achieved by fracturing along the direction >50° with the natural fracture and under the condition of small differential horizontal stresses.

Introduction

The rocks in low permeability-tight reservoirs produce more fractures during deformation owing to their tight and brittle nature. Consequently, fractures play a crucial role in these reservoirs (Zeng and Xiao 1999; Zhou et al., 2006; Ding et al., 2015; Li et al., 2017). To exploit low-permeability tight reservoirs, hydraulic fracturing is frequently used to increase oil and gas production. The factors affecting the fracture effects include fracture attitude (strike and dip angle), size, and number, as well as aperture and its angle with maximum principal stress (Zeng, 2004; Jin et al., 2005; Gale et al., 2007). Therefore, a detailed understanding of static fractures is required to improve permeability without increasing the water cut of the oil well.

The formation and evolution of fractures include a large amount of information related to rock mechanics and determine the physical properties and oil-gas properties of low-permeability reservoirs (Germanovich et al., 1994; Wang et al., 2008; Li et al., 2019; Li et al., 2019; Zhang et al., 2020; Li et al., 2022). Rock strength, petrology, and tectonic stress influence the development of natural fractures in low-permeability reservoirs (Li et al., 2019; Li et al., 2022), and fracture density and opening directly controlled gas productivity. Microfractures with apertures less than 50 μm improve porosity and permeability in these reservoirs (Wang et al., 2008). However, owing to their small size, they are rarely identified using relevant logging and geophysical methods and their initiation and development remain unknown. Experimental results have demonstrated that when the load reaches one-third of the compressive strength, wing cracks start to propagate from the tip of the plexiglass preset crack and wrap the initial crack at a stable speed. The wing crack tip shows the largest propagation length and initially reaches 1 to 1.5 times the crack radius (Germanovich et al., 1994). Experiments on cement sand specimens showed that the propagation direction of the main crack was related to the mechanical properties of the crack and was affected by the distribution of cracks, pores, and microcracks (Chen et al., 2005). When the crack is perpendicular to the load direction, the main crack primarily extends along the edge of the crack.

In the plane perpendicular to the loading direction, cracks in tight sandstone extend along the fracture axis or increase the fracture diameter. Cracks easily lead to the penetration of pores during loading (Li et al., 2019). CT imaging by X-ray can be used to reveal the pore structure and relative density inside the core rock. Therefore, the three-dimensional evolution characteristics of fractures can be observed under different loading (Ketcham and Carlson 2001; Cao, 2005; Renard et al., 2009; Sun et al., 2020; Zhang et al., 2020). Furthermore, the analysis of dynamic fracture evolution of tight sandstone under uniaxial compression showed that fractures underwent compaction, linear elastic behavior, and non-linear and residual deformation (Zhang et al., 2020). In addition, the mineral composition and mesostructure play a significant role in the mechanical properties, fracture pattern, and crack morphology. Secondary cracks propagate parallel to the direction of axial stress. The above-mentioned fracture development studies were mostly based on CT scans of sandstone intermediate zoning layers and tight sandstone. However, studies on fracture development in low-permeability reservoirs and the influence of reservoir heterogeneity on the fracture mechanism are scarce.

Low-permeability-tight reservoir fractures have the characteristics of complex distribution and high heterogeneity, which leads to poor physical properties of the reservoir, large differences in oil and gas well productivity, and low recovery. The C41 fault block is located in the Liangjialou oil field, whose main oil and gas producing intervals include the Fourth Member of the Shahejie Formation (E_2s_4). Previous research analyzed the present ground stress, fracture characteristics, and development period (Liu et al., 2003; Shi et al., 2021). The results showed a maximum horizontal principal stress of 52–74 MPa trending toward near east-west within the fault block. The minimal horizontal principal stress was 41–52 MPa in the south-north direction (Liu et al., 2003). The Upper E_2s_4 included shear fractures with small apertures and low filling in the C41 block that developed during the periods of E_2s_{3-2} and Late E_3d deposition (Shi et al., 2021). However, these previous studies lacked information on detailed fracture evolution and mechanisms. To solve these problems and better reveal the distribution of cracks, research on the causes and development of cracks is essential. Therefore, the present study investigated the development of fractures in a low-permeability reservoir. The research method mainly included two parts: observation of core fractures and physical simulation of the three-dimensional evolution of fractures in real time. For the latter, first, a MicroXCT-510 scanner was used to scan the core sample in real-time under uniaxial compression conditions. Subsequently, based on the CT images and data obtained from the test, the fracture initiation and propagation process in was
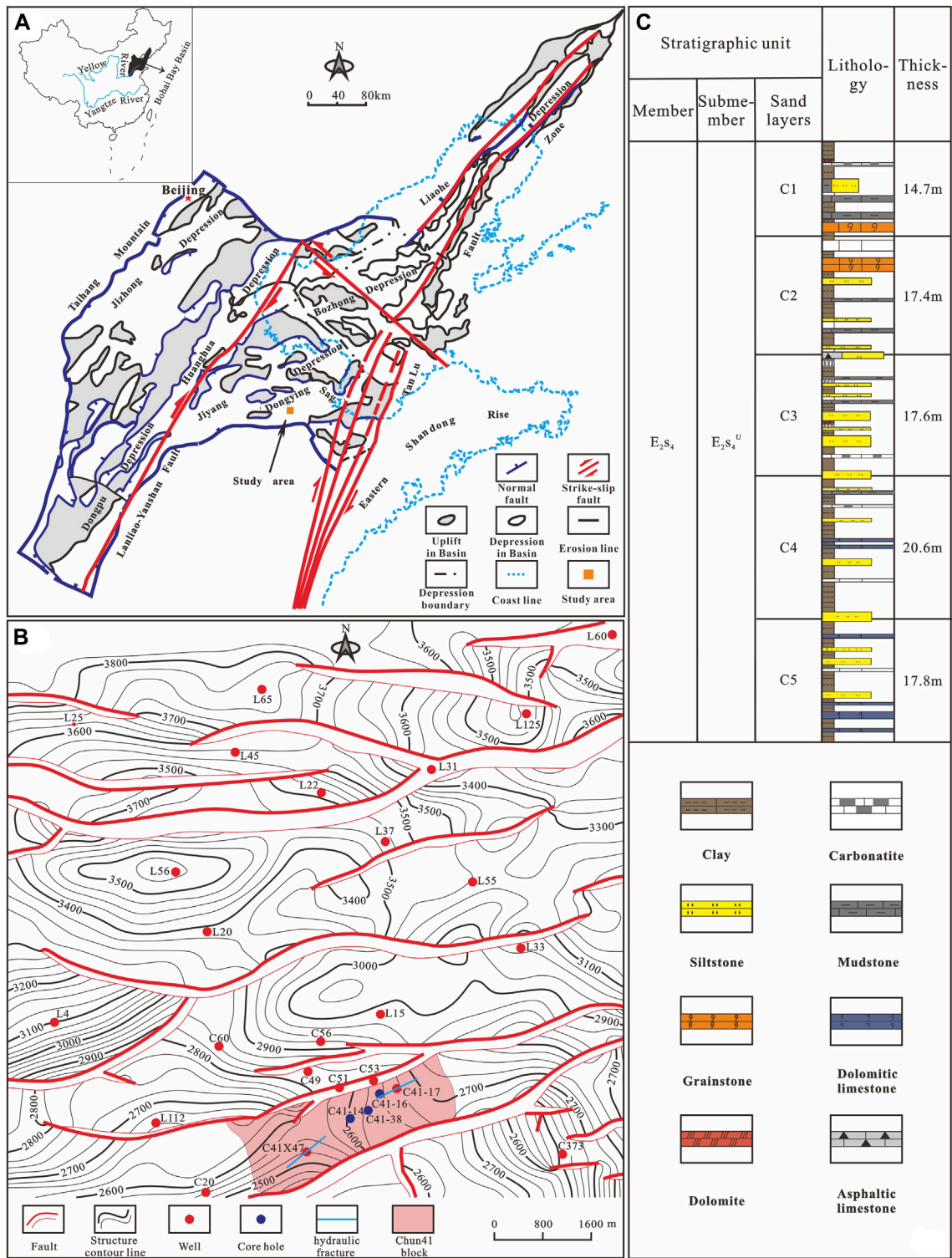
FIGURE 1
Basinal location, geological setting, well locations and strata of the study area. **(A)** Location of the Bohai Bay Basin and the study area. **(B)** Well locations and the top surface structure map of the Upper Fourth Member of Shahejie Formation (length of the hydraulic fractures exaggerated). **(C)** Stratigraphic histogram.

TABLE 1 Basic characteristics of the observation sections.

Well number	Lithology	Sand layer	Depth
C41-38	Fne sandstone, muddy limestone, limestone siltstone, and silty mudstone	C1-C3	2650.2–2707.11, of which ①: 2650.20–2680.00 ②: 2680.40–2696.78 ③: 2703.61–2707.11
C41-16	Fine sandstone, muddy siltstone, and shale	C3	2668.00–2720.90
C41-14	Silt sandstone, muddy siltstone, and mudstone	C4	2695.7–2695.7

analyzed three dimensions. Finally, the differential evolution mechanisms of fractures in different heterogeneous reservoirs were explored and the relationships of fractures with oil and gas were analyzed to provide a reliable geological basis for improving the development effects.

Study area

The study area was located in the southern Dongying Sag of the Jiyang Depression in Bohai Bay Basin (Figure 1A). The detailed study area was fault block C41, in the southern portion of the Liangjialou oilfield (Figure 1B). The Cenozoic strata of the Liangjialou oilfield comprise the Paleocene-Eocene Shahejie Formation ($E_{1-2}s$), the Oligocene Dongying Formation (E_3d), the Miocene Guantao Formation (N_1g), and the Pliocene Minghuazhen Formation (N_2m), of which the Shahejie Formation was further subdivided into four Members. The main reservoir was $E_2s_4{}^u$. $E_2s_4{}^u$ is a ladder-shaped structure composed of a series of near east-west trending faults (Figure 1B). Most of the faults dipped to the north, and the oil fault blocks controlled by them showed a gradually decreasing oil ladder from south to north. Controlled by two main NEE trending faults, the C41 fault block was high in the southwest and low in the northeast. The kick-off point of $E_2s_4{}^u$ studied here was mainly composed of fine sandstone and siltstone, in which the strata dip and dip angle changed a lot (Figure 1B).

When the $E_2s_4{}^u$ was deposited 43-40 Ma, the study area was a shallow lake with an underwater low uplift. The lake water transgression and regression affected the reservoir formation and type. Terrigenous debris transported by waves and lake currents was deposited at the site of energy reduction on the shoreline, resulting in a typical shore-shallow lake-beach bar. As the overlying sediment thickened, the pressure also increased and minerals filling the pores of the sediment cemented the dispersed grains together. Thus, diagenesis such as compaction and cementation reduced the primary pores in the sandstone, like the thinning of a piece of bread in a vertical press, rendering it a low-porosity and low-permeability reservoir. The thickness of the well sections of $E_2s_4{}^u$ range from 61 to 91 m, with an average of 81 m. $E_2s_4{}^u$ is divided into five sand layers (C1–C5) (Figure 1C), with a thin reservoir thickness and an average sand body thickness of 26.8 m. The lithology of the sand body is mainly feldspathic siltstone, fine sandstone, dolomitic siltstone, argillaceous limestone, and argillaceous dolomite

(Figure 1C). The sandstone consists of 40–45% quartz, 35–37% feldspar, and 20–24% rock debris. It has a low composition and structure maturity. The cementation between grains is mainly contact-pore type, with a few pore types. The sorting coefficient is 1.4–1.9. The roundness is subangular. The median and average particle sizes are 0.05–1 mm and 0.09 mm, respectively. The physical properties vary considerably between layers. The total average permeability is 9.2×10^{-3} μm², ranging between 14.2×10^{-3} and 5.37×10^{-3} μm². In addition, the average carbonate content in C1–C4 is 17, 23.11, 15.96, and 78.3%, respectively. The permeability difference and dart coefficient of $E_2s_4{}^u$ are 76 and 1.2, respectively; thus, the $E_2s_4{}^u$ reservoir is low-permeability with strong heterogeneity (Li, 1997). Moreover, this reservoir is widely distributed and shows great planar connectivity; however, the planar heterogeneity is severe and the areas of high permeability show zonal division.

Fracture characteristics of the core

E_2S_4 in the C41 fault block contains three core holes (Figure 1B). The attitude, type, width, opening, and filling materials of fractures can be obtained by core observation. These characteristics are shown in Table 1. The fracture attitude was measured in two steps: first, the actual attitude of the $E_2S_4{}^u$ strata was measured and calculated according to the structural contour map for $E_2S_4{}^u$. The results showed a 90°C dip with a dip angle of 6°–10° in the three core holes and gently inclined to near-horizontal strata dipping east. Second, the real attitude of the fracture in E_2S_4 was obtained. The bedding surface was found and the core was arranged according to the dip of the core to the east and a dip angle of 6°–10° so that the true occurrence of fractures could be directly measured. The fracture characteristics of the three core holes are as follows.

Core fracture characteristics of single wells

Fracture characteristics of Well C41-38

The core hole included three sections: ①, ②, and ③ (Table 1). The fracture characteristics are shown in Figures 2A–J. Most (88%) of the fractures were shear fractures; the remaining were tensile joints. The high-angle (Figure 2A) and gentle-angle fractures (Figure 2D) were small, while the
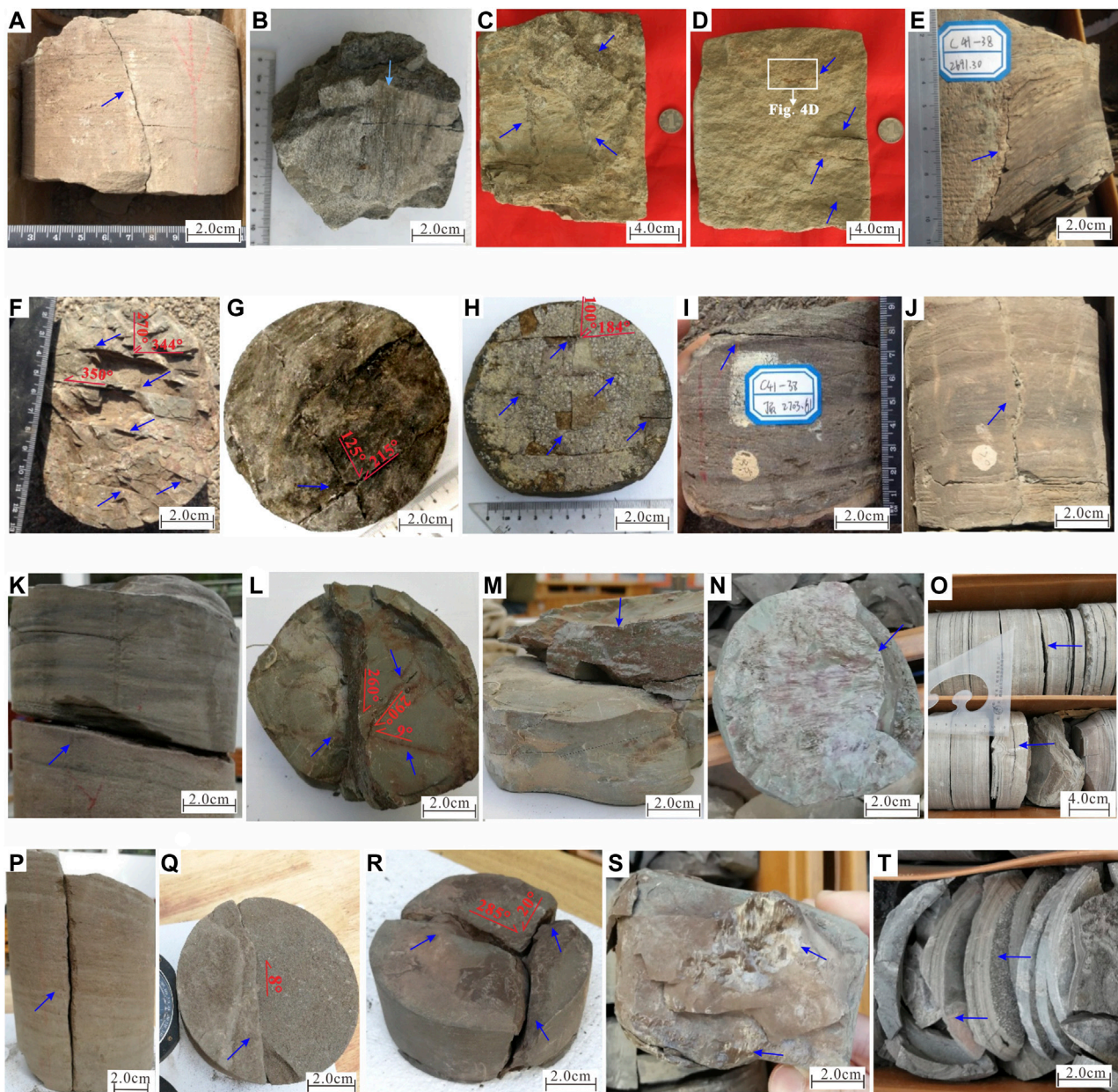
FIGURE 2
Core fracture characteristics of $E_2s_4^u$ in the C41 fault block in the Jiyang Depression of Bohai Bay Basin. From left to right are **(A–T)**: **(A)** high angle-shear fractures with no fillings, Well C41-38, 2650.2 m (arrow: drilling direction). **(B)** Vertical shear fractures, with scratches and calcite fibers on the fracture surfaces, Well C41-38, 2652.815 m. **(C)** Many groups of high-angle fractures and filling with mud and oil, well C41-38, 2680.00 m, coin diameter 2.0 cm. **(D)** Five groups, low-angle shear fractures, with the development of cross-bedding in the upper part with oil filling, well C41-38, 2680 m. **(E)** Bedding fractures in silt mudstone and a high-angle shear fracture along the junction of silt and silt mudstone, without fillings, Well C41-38, 2691.30 m. **(F)** Sub-parallel (lower part) and conjugate (upper part) shear fractures (top view), top in 2684.10 m. **(G)** High-angle shear fractures (top view) filled with oil, Well C41-38, top in 2665.41 m. **(H)** Grid-shaped shear fracture system (top view), no filling, Well C41-38, top in 2691.21 m. **(I)** Bedding and low-angle shear fractures without filling, Well C41-38, 2703.61 m. **(J)** Vertical tension fractures without filling, Well C41-38, 2707.11 m. **(K)** Low-angle opening shear fracture, Well C41-16, 2688.74–2688.81 m. **(L)** Vertical shear fractures (top view) with iron filling in the restricted fractures, Well C41-16, 2691.77 m. **(M)** Vertical shear fractures showing the development of a friction mirror on the fracture surface, Well C41-16, 2691.81 m. **(N)** Scratches on bedding-parallel fractures, Well C41-16, 2690.94 m. **(O)** Diagenetic and bedding shear fractures without filling, Well C41-16, 2669.77 m. The acute angle of the right triangular ruler indicates the direction of drilling. **(P)** Long vertical shear fracture without filling, Well C41-14, 2705.05–2705.26 m. **(Q)** Vertical shear fractures (top view) without filling, Well C41-14, 2702.60 m. **(R)** High-angle shear fractures without filling, Well C41-14, 2778.49–2778.53 m. **(S)** Friction mirror in a vertical shear fracture, Well C41-14, 2778.49 m. **(T)** Diagenetic fractures without filling, Well C41-14, 2702.78 m. The right indicates the drilling direction.
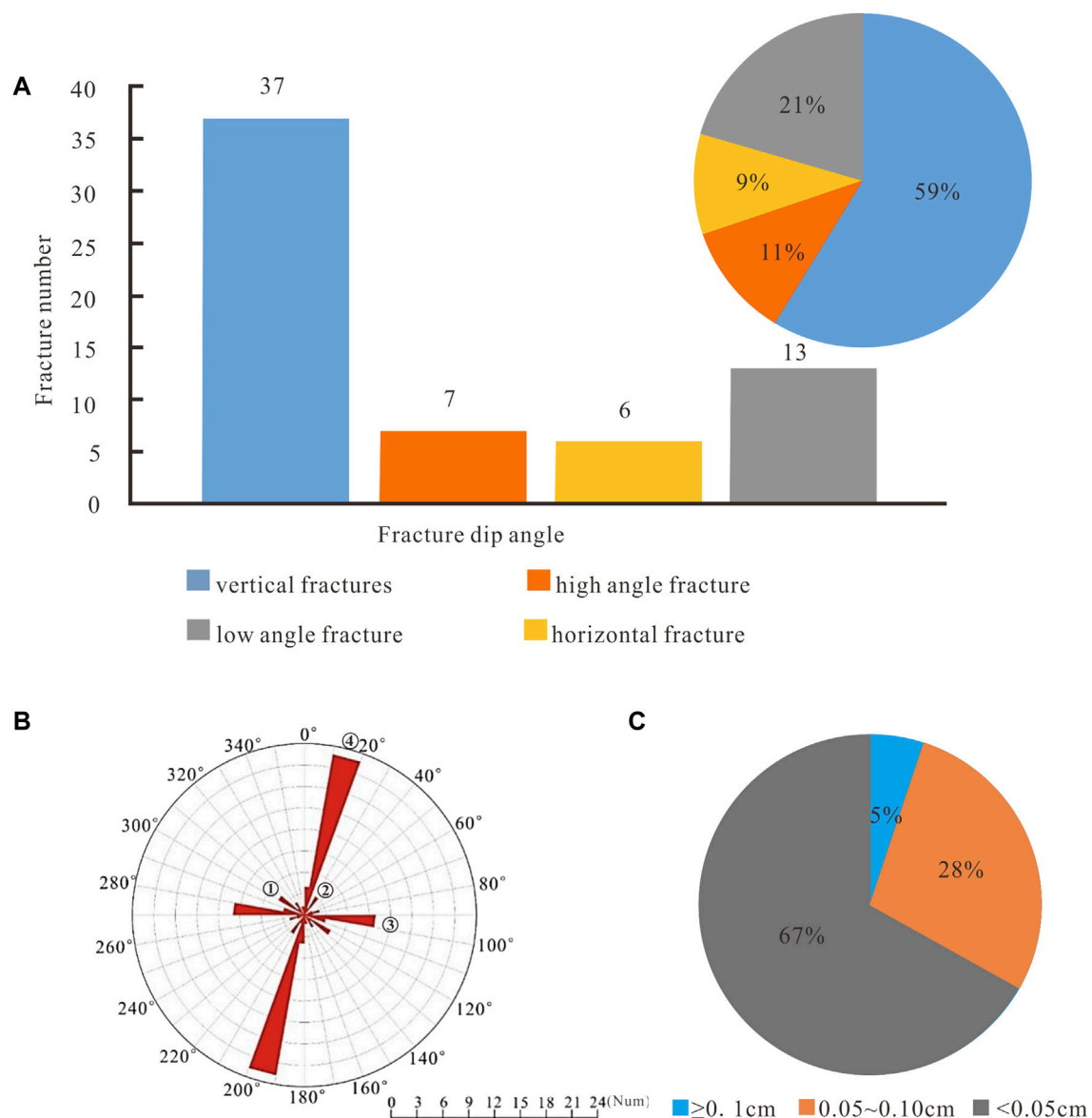
FIGURE 3
Fracture type, strike, and aperture of $E_2s_4{}^u$ in the C41 fault block of the Jiyang Depression in Bohai Bay Basin. **(A)** Type of core fracture dip angle. **(B)** Fracture strike rose diagram. **(C)** Fracture aperture.

vertical fracture showed significant development (Figures 2B–C, E–J).

Some high-angle fractures developed with small fracture widths and no filling materials (Figure 2A); however, others were filled with oil (Figure 2C). Scratches were observed on the vertical cracks surface, along which fibrous calcite crystals developed (Figure 2B). Most of the vertical cracks had no filling materials, while some fractures showed oil filling (Figure 2G). Furthermore, the low-angle fractures often had large crack widths filled with calcite. The observation of oil

filling in low-angle, high-angle, and vertical fractures indicated oil and gas migration or accumulation along the fracture system. Therefore, fractures are the channels or spaces for oil and gas migration in low-permeability reservoirs.

Some shear fractures showed fracture groups with fracture sets that were parallel to each other (Figure 2F) or X conjugate sets (Figures 2G,H). The tensile fractures were mostly vertical with a zig-zag shape in profile (Figure 2J). Generally, the fracture length was 0.4–18 cm and fracture width was 0.01–1.5 cm. Moreover, most of the tensile
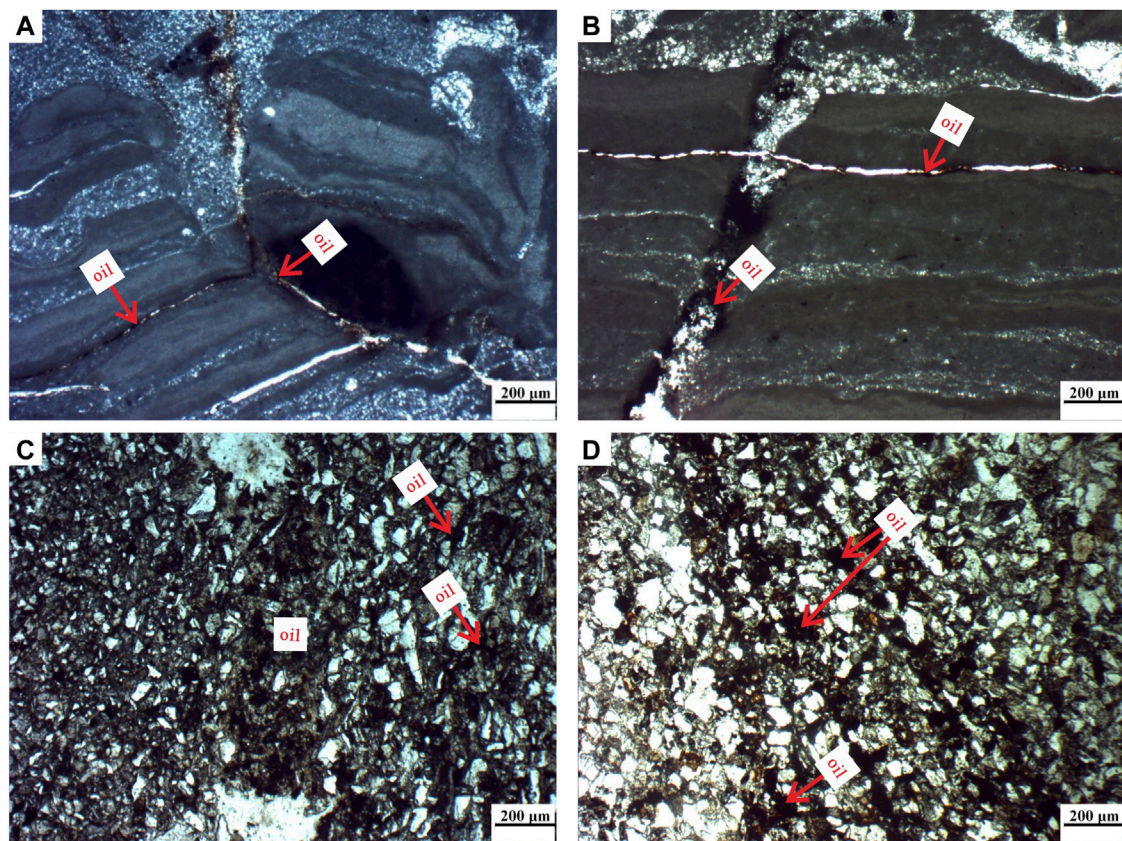
FIGURE 4
Oil fillings (dark brown) in microfractures of $E_2s_4^u$ in the C41 fault block of the Jiyang Depression in Bohai Bay Basin. From left to right from top to bottom are: **(A–D)**: **(A)** oil filling in both high-angle and interlayer fractures of muddy limestone, Well C41-38, 2680 m, PPL×50. **(B)** Oil stored in the high-angle fracture that has migrated to the bedding-parallel fracture, Well C41-38, 2680 m, PPL×50. **(C)** A wide fracture in muddy siltstone partially filled with oil, with two small branched fractures filled with oil, Well C41-38, 2656.21 m, PPL×50. **(D)** Oil fillings in the bedding-parallel fracture group of muddy siltstone (location in Figure 2), Well C41-38, 2656.21 m, PPL×50.

fractures had no filling, although occasional mud filling was observed.

Apart from the fracture cut across the bedding surface, several bed-parallel fractures were observed in the core (Figure 2E), most of which developed along the bedding surface. Some were diagenetic or contracted fractures, while others resulted from the structural replacement of the bedding surface under tectonic action (Li et al., 2009).

Fracture characteristics of Well C41-16

Well C41-16 had fewer fractures in the core compared to Well C41-38. The core fracture characteristics are shown in Figures 2K–O. All structural fractures were shear fractures, including low-angle (Figure 2K), vertical (Figures 2L,M), and bed-parallel (Figures 2N,O) fractures. The across-bedding was 4–13 cm in length and 1–3 mm wide. Most fracture surfaces were closed with no filling, while some showed iron oxide filling (Figure 2J). Friction mirrors on the crack surfaces were

occasionally observed (Figure 2M). Bed-parallel fractures were also observed in the core, with the development of slickensides and mirrors (Figure 2N), which caused the rock to be crushed (Figure 2O).

Fracture characteristics of Well C41-14

Compared to the fractures in Wells C41-38 and C41-16, the core fracture was extremely undeveloped in Well C41-14 (Figures 2P–T). Only five high-angle structural fractures were observed, including three vertical and two oblique. The length and width of these fractures were 8–31 cm and 1–7 mm, respectively. No filling was observed inside the fracture. Moreover, the bed-parallel fractures developed in sections 2699.26–2706.86 m (Figure 2T).

The core observation showed that the fractures were generally not developed in the C41 block. They comprised structural and non-structural fractures. The structural fractures were mainly across-bedding shear fractures but were
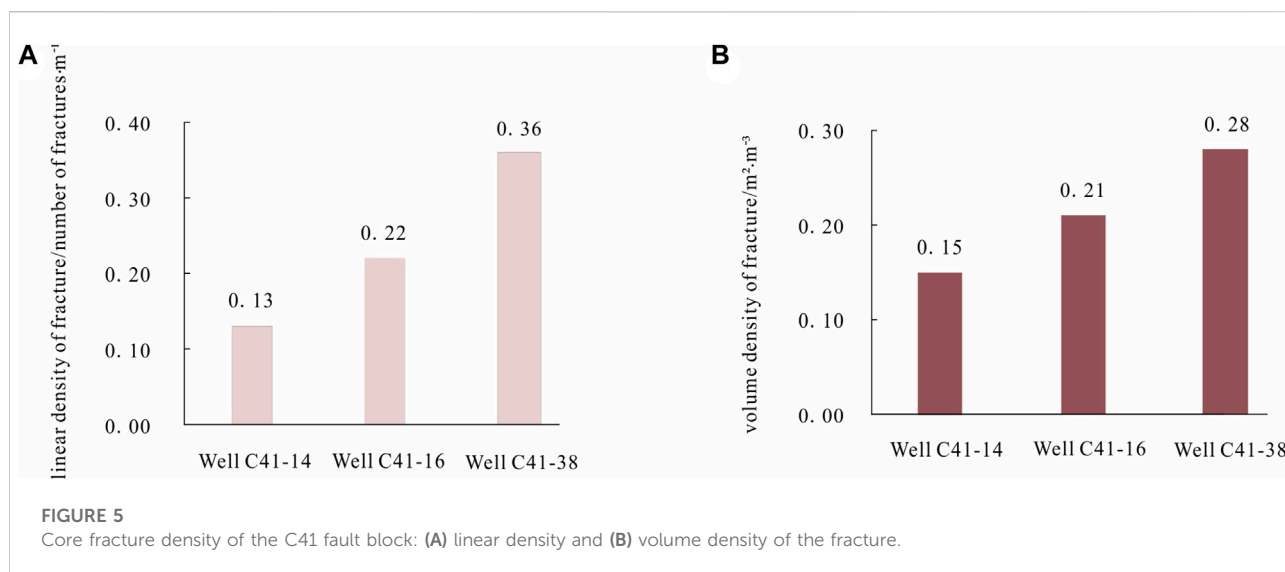
generally not as well developed. Most of the fractures were observed independently, with a few fractures developed in systems. The bed-parallel fractures were also developed. Among the three wells, the fractures in Well C41-38 were the most developed, while those in Well C41-14 were the least developed.

Quantitative characterization of the core fractures

Type, strike, aperture, and mineral filling of the structural fractures

Fracture types and strikes

The core fractures of the above three wells included structural and non-structural fractures, the former of which were significantly developed. Most of the structural fractures (90%) were shear fractures. The remaining were tensile fractures.

The angle between the fracture dip angle and the bedding surface revealed the following five fracture types: vertical (dip angle >75°), high-angle (45° ≤ dip angle <75°), low-angle (15° < dip angle <45°), horizontal (<15°), and bedding-parallel shear fractures (Figure 3A). The first four are referred to as shear fractures across-bedding. More vertical and horizontal fractures were observed in the bedding cut fractures, accounting for 59 and 21% of total fractures, respectively. Relatively fewer high- and low-angle fractures were observed, accounting for 11 and 9% of total fractures, respectively. The bedding-parallel and across-bedding fractures affect the propagation, termination, and diversion of hydraulic fractures (HFs) (Huang et al., 2018).

The strike rose diagrams of the structural fractures (Figure 3B) revealed four dominant directions in the $E_2s_4^u$

reservoir. Fractures ④ in an average direction of 15° were most common, followed by fractures ③ with an average strike of 95°. Fractures ① and ② were less developed, with average strikes of 315° and 35°, respectively.

Fracture apertures

The core fracture aperture is usually larger than its real aperture owing to rock unloading; thus, correction is required (Van Golf-Racht and Chen, 1989). The real fracture aperture buried in strata was corrected using Eq. 1, where B is the real fracture aperture, B_i is the measured aperture in section i, n is the fracture number in the same group, and $2/\pi$ provides empirical correction.

$$B = \frac{1}{n}\frac{2}{\pi}\sum_{i=1}^{n}B_i. \tag{1}$$

The calculated results of the fracture aperture in $E_2s_4^u$ showed that most fracture apertures were less than 0.05 cm (67% of total fractures) (Figure 3C). While fractures with apertures of 0.05–0.10 cm accounted for 28% of total fractures, only 5% of fracture apertures were larger than 0.10 cm. Hence, the evidence indicated relatively weak tectonic stress when fractures were formed. Here, the high proportion (67%) of fracture apertures less than 0.05 cm may explain the low permeability of the $E_2s_4^u$ reservoir and the low productivity in the study area. In addition, the narrow aperture of these thin fractures can cause HF cross-over (Lee et al., 2015).

Fracture mineral fills

Overall, the structural fractures in the study area showed poor mineral filling. Most fractures (93.1% of total fractures) did not contain mineral fill (Figure 2). Owing to the lack of mineral fills, the

TABLE 2 Characteristics of the samples for CT scanning.

Well number	Sample	Lithology	Sand layer	Height(mm)	Diameter (mm)	Primary structure
C41-38		Muddy siltstone	C3	46	25	Horizontal bedding ripple bedding
C41-14		Siltstone	C4	50	25	_

FIGURE 6
Method of CT scanning with X-ray.
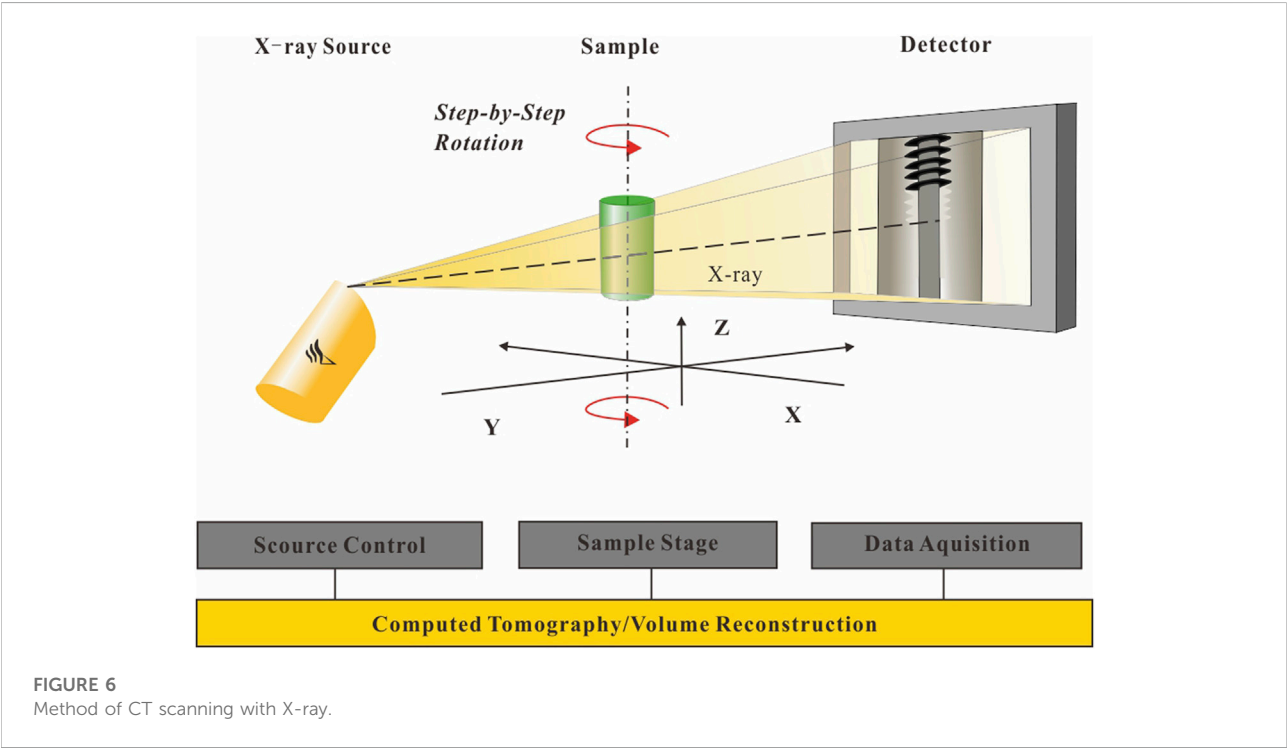
mechanical strength of the mineral fill bond was not considered in hydraulic fracturing (Kolawole and Ispas 2020). The filling materials were oil, calcite, or iron oxide in 6.9% of the observed fractures (Figures 2C,F,J), with calcite the most common. The oil traces in the fractures were evidence of oil-gas once migration and accumulation. Thin section observation also revealed this phenomenon (Figure 4). Fractures can store and migrate oil and gas (Figure 4A), high-angle fracture reservoir oil and gas, and low-angle fractures as migration channels (Figure 4B). Large fracture and branch small fractures, as

well as bedding-parallel fractures connected to the fracture net to store oil and gas (Figures 4C,D).

Density of the core structural fractures

The fracture line density (the number of fractures in the core per meter) and volume density (the area of cracks in the core per cubic meter) of the three wells were calculated. The results are as

TABLE 3 Scanning information of the samples.

Well number	Sample number	Scan size (mm)	Resolution (μm)	Voltage/Power (kV/W)	Lab temperature(°C)	Scan time (h)
C41-38	CC05	25	51.2	148/0.89	23	2
C41-14	CC02	25	57.2	148/0.89	23	2

TABLE 4 Mechanic characteristics of the samples.

Sample number	Top of sample (m)	Top of overburden (m)	z (m)	ρ (kg.m^{-3})	g (m·s^2)	P (MPa)
CC05	2690.94	310	—	2600	9.8	61
CC02	2765.60	310	—	2600	9.8	62

follows (Figure 5). Among the three core wells, the fractures in Well C41-14 were the least developed, while the fractures in Well C 41–38 were the most developed. Table 1 shows to which sand group the cores belonged. Thus, the fractures in the middle and upper C1-3 were the most developed, whereas those in the lower C4 were poorly developed. This result was obtained in a small area of 445 m east-west, 278 m north-south, and a depth of 10–62 m from west to east. As mentioned above, the primary porosity of the low-permeability reservoir rock was not developed and the rock was relatively tight. Therefore, the difference in fracture density demonstrates the heterogeneity in the reservoir of the study area.

Core fracture analysis revealed obvious differences in fracture characteristics, particularly in C3 of Well C41-38 and C4 of Well C41-14. These differences in fracture development indicated differences in reservoir heterogeneity. The lithology of the reservoir in Well C41-38 was fine sandstone and siltstone with uneven grain size, connecting with mudstone in sand layer C3. In addition, the bedding was well developed in the core of Well C41-38 (Table 1). Thus, the core in Well C41-38 indicated strong reservoir heterogeneity with more fractures. In contrast, the lithology of sand layer C4 in Well C41-14 was tight siltstone and the bedding was almost invisible (Table 1), representing weak reservoir heterogeneity with fewer fractures.

Dynamic development and evolution of fractures in low-permeability reservoirs

The effect of reservoir heterogeneity on the characteristics and evolution of fractures is an important research topic. The initiation, propagation, and termination of fractures with different reservoir heterogeneities contribute to hydraulic fracturing for further exploitation. Consequently, hydraulic fracturing can cause more fractures in low-permeability reservoirs. CT scanning with X-ray under uniaxial compression in real time can reveal the fracture evolution in three dimensions (Zabler et al., 2008; Cnudde et al., 2011; Zhang et al., 2020). The triaxial compression requires strict sample conditions, which cannot be placed into the instrument once removed. The present study applied uniaxial compression to simulate fracture initiation and propagation.

Samples, methods, and facilities

Sample characteristics

Two tight core rocks (samples CC05 and CC02) of different heterogeneity from fault block Chun 41 were selected. Their detailed characteristics are shown in Table 2. Their strata are $E_2s_4^u$, whose sedimentary facies were the beach-bar of the shore-shallow lake. The lithology of sample CC05 is muddy siltstone, with mostly horizontal or ripple beddings (Table 2); thus, it represented a reservoir with strong heterogeneity. In contrast, CC02 showed no bedding development (Table 2); thus, it represented a reservoir with weak heterogeneity.

The rock in particular layers reflects the physical changes that the sediment has experienced throughout its history of burial, lithification, and uplift (Fossen, 2016). Confining pressure is important in fracture evolution. Hence, it should be calculated. The top depths of the two samples are shown in Table 2. The uppermost strata of the two samples were Pliocene Minghuazhen Formation (N_2m), top of 310 m in depth. Therefore, the difference between the two
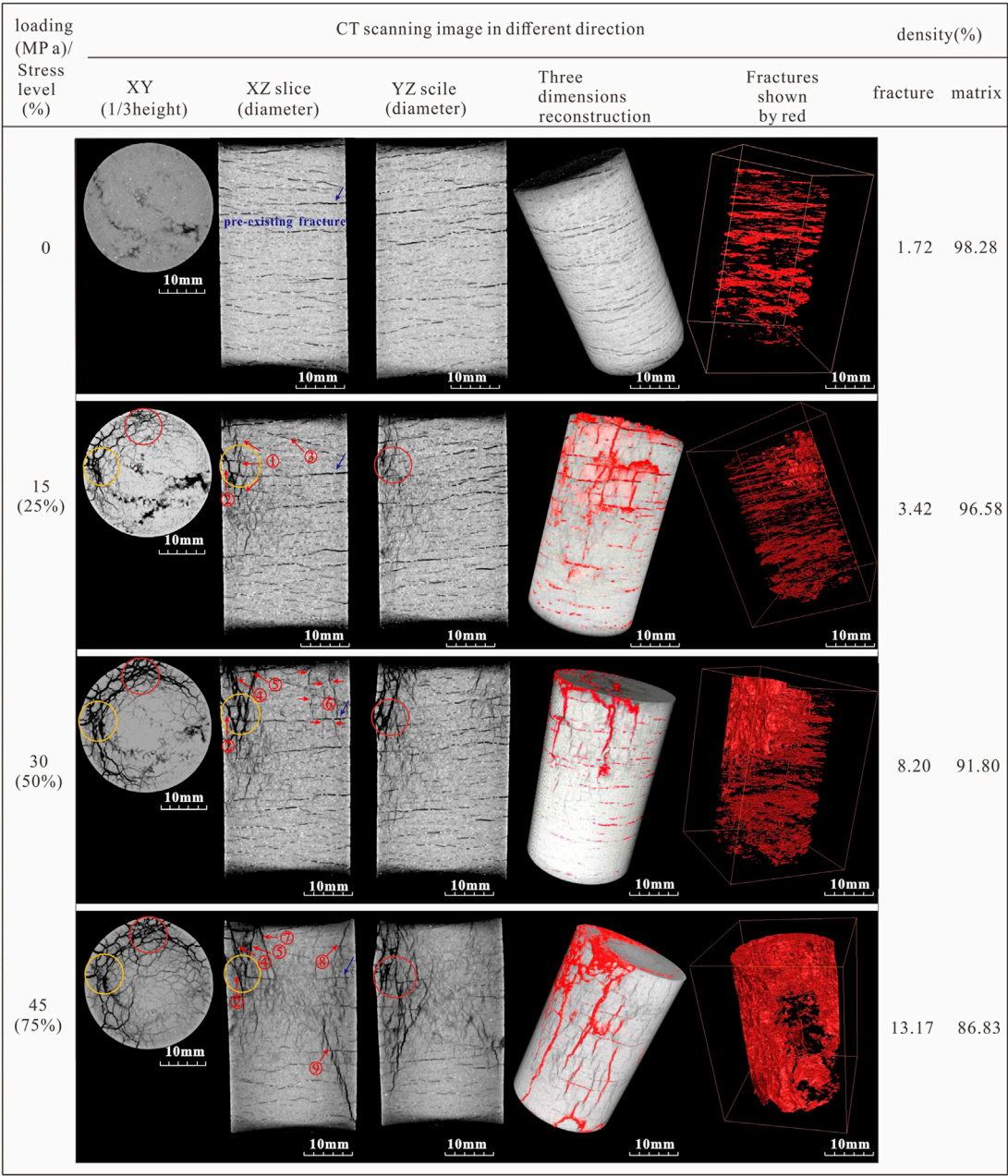
FIGURE 7
CT image of the fracture evolution of sample CC05 in a strong-heterogeneity reservoir. The yellow and red circles in the horizontal XY slice correspond to the yellow circle in the XZ slice and the red circle in the YZ slice, respectively.

depths was the depth of sample overburden. The rock density was 2600 kg/m³ for siltstone, and g was 9.8 (ms²). Thus, the confining pressure (P) was calculated using Eq. 2, where P is the confining pressure (MPa), ρ is the density (kg/m³), g is the gravitational acceleration (ms²), and z is the overburden depth of sample (m).

$$P = 10^{-6} \rho g z. \qquad (2)$$

The confining pressures of the two samples were 61 MPa and 62MPa, respectively, which were close in value (Table 2). This is an important factor in determining the maximum stress of loading.

Methods and facilities
Experimental facilities

CT scanning with X-ray can be used to fully display the small features of core rock through a massive image without destroying

the sample (Zabler et al., 2008; Cnudde et al., 2011). As the cone-shaped X-ray penetrates the sample, a three-dimensional model of the sample is reconstructed *via* amplified images. During this process, different magnifications are used and several attenuated X-ray images are formed by 360° rotation (Figure 6). A CT image can truly reflect the pore structure and relative density inside the core rock. Therefore, the dynamic evolution of 3D fractures, including the initiation, propagation, and coalescence of micro-cracks in real time can be observed under different loading (Ketcham and Carlson 2001; Renard et al., 2009; Sun et al., 2020; Zhang et al., 2020).

A 148 kV MicroXCT-510 X-ray CT system was used to scan core the samples in real time under uniaxial load. The samples were rotated *via* a rotary table during scanning, thereby avoiding the disturbance of unloading on fracture evolution. Therefore, the simulation was closer to fracture evolution with a buried reservoir. Approximately 870–890 CT slices of each sample were scanned; thus, the precision of the reconstructed three-dimensional model by these images allowed full visualization of the fracture initiation and propagation (Sun et al., 2020).

The voxel size of the CT images were $0.0512 \times 0.0512 \times 0.0512$ mm and $0.0573 \times 0.0573 \times 0.0573$ mm, respectively; thus, each CT image was 0.0512 or 0.0573 mm thick. Therefore, cracks larger than 0.05 mm in width could be detected as relatively large and wide fractures, which appear as black areas (representing air), while small and narrow cracks appeared as gray cracks (Figure 6). Avizo software was used to reconstruct the dynamic evolution of the 3D fractures. In image processing, grayscale values of 0–255 were assigned to reveal the sample densities. Grayscale values less than 10 were marked as fractures and were represented in red.

Experimental procedures

The simulated experiment based on X-ray three-dimensional scanning was as follows: first, two samples were scanned to obtain the original fracture characteristics before loading. The detailed data are listed in Table 3. Second, the samples were loaded in uniaxial compression with quasi-static loading at 25, 50, 75, or 90% of the maximum stress. Two factors determined the maximum stress loading for each sample: lithology and confining pressure. The uniaxial compressive strength of siltstone is 60 MPa and the confining pressures of the two samples were 61 and 62 MPa, respectively (Table 4). Therefore, the maximum value of stress loading of each sample was 60 MPa, respectively. Third, real-time CT scanning was performed following the sample load-unload-scan procedure. Briefly, each sample was first loaded, then taken out and scanned. The procedures were repeated at different stresses until reaching the expected stress. Finally, low-density areas of each sample were marked in red in Avizo software to trace the fractures. Thus, the characteristics of fracture geometry, initiation, propagation, and density were obtained. Dynamic evolution of the 3D fractures was also reconstructed.
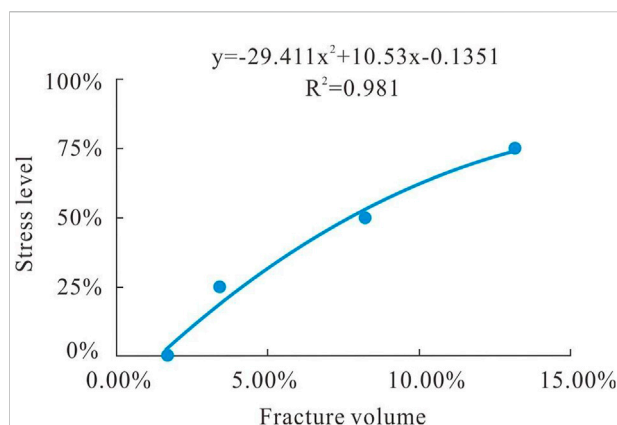
FIGURE 8
Relationship between fracture volume and stress level in strong-heterogeneity reservoir in sample CC05.

Results

Fracture evolution of a low-permeability reservoir with strong heterogeneity

The fracture evolution of a low-permeability reservoir with strong heterogeneity was analyzed using sample CC05 under uniaxial compression. The results in real-time based on CT scanning are as follows (Figure 7).

CT images before loading

The CT images revealed many bed-parallel and low-angle fractures inside sample CC05, the characteristics of which are shown in Figure 7. The left (YZ profile, slice from left to right) and front (XZ profile, slice from front to back) view slices showed many horizontal low-angle fractures inside the core. These features were also observed in the horizontal slice (XY profile). Most were small fractures with a zigzag shape in gray. The CT images showed fracture development along the bedding in profile, resulting in the formation of bed-parallel fractures. Therefore, the bedding, as an inhomogeneous surface, was crucial to the formation of the bed-parallel fracture.

In the three-dimensional perspective of the fracture represented by the red trace, the fractures were layered and not connected vertically. Before loading, the fracture volume density accounted for 1.72% of the total volume of the rock sample.

CT images at 15 MPa load and 25% stress level

Horizontal CT slices (XY slices) can reveal fracture development in the plane. In XY image showed the initiation of many small visible net-shaped fractures along one existing fracture and the formation of large visible fractures with a zig-zag shape at the top of the sample. The fractures propagated along
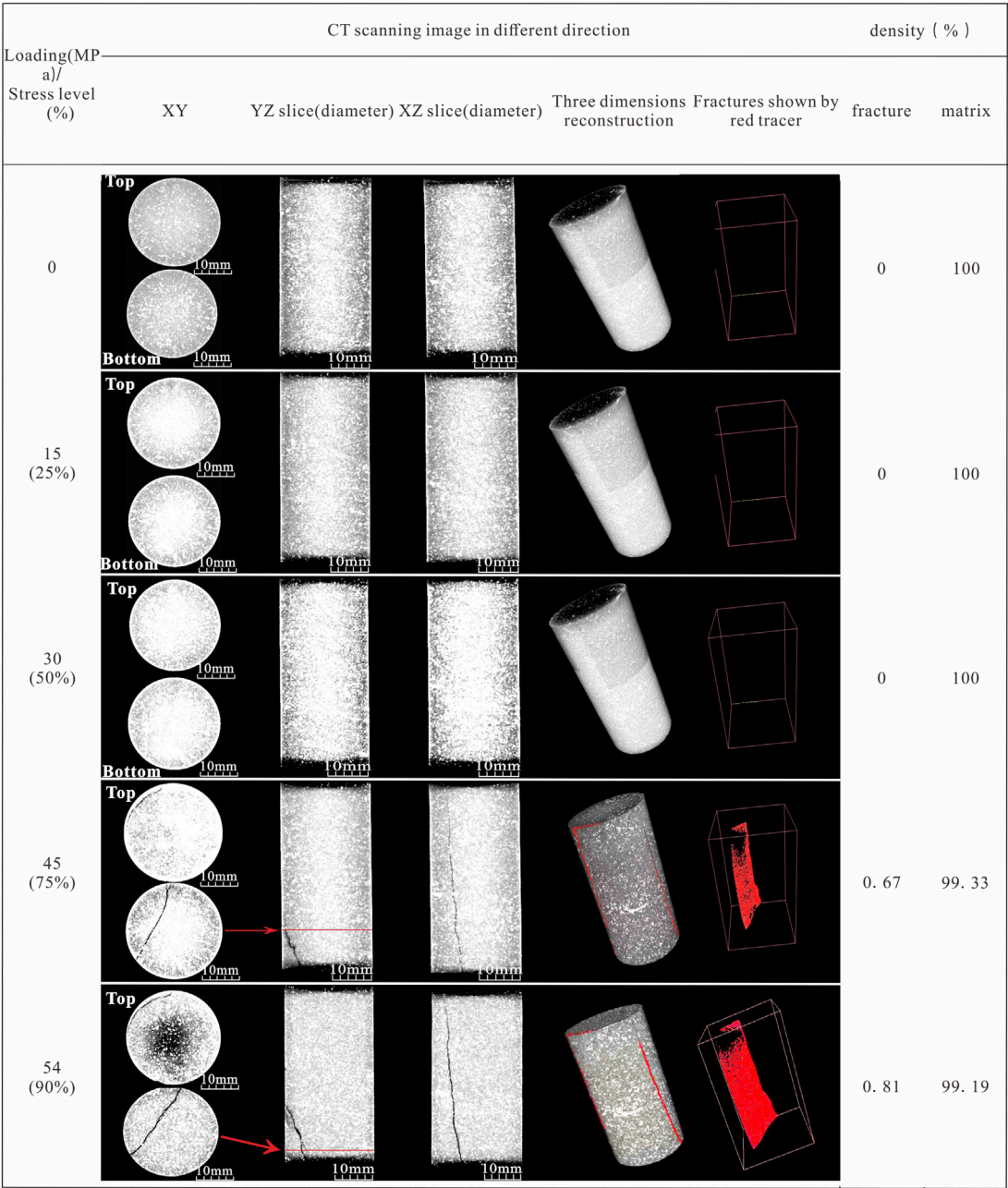
FIGURE 9
CT image of the fracture evolution of sample CC02 in weak-heterogeneity reservoir.

the termination of the pre-existing fractures (yellow circle) and connected to two nearly parallel large black fractures. One of the two nearly parallel large fractures terminated with many small fractures (red circle) in gray.

XZ profile (front view) slices are obtained vertical to the fractures to it better reveal fracture development during stress. Fracture ① developed in several tensile fractures with a dip angle of approximately 90°. These fractures terminated as

horizontal fractures and developed in the left lateral en-énchelon. Fracture ② was a shear fracture with a dip angle of 70°, at 20° to σ_1 (loading direction). It crossed the pre-existing bed-parallel fractures, consistent with the results observed in tri-axial tests (Lee et al., 2015). Fracture ③ developed at the upper portion of the sample. Thus, the fractures initiated from the top of the sample. The fractures labeled in the yellow circle corresponded to the yellow circles
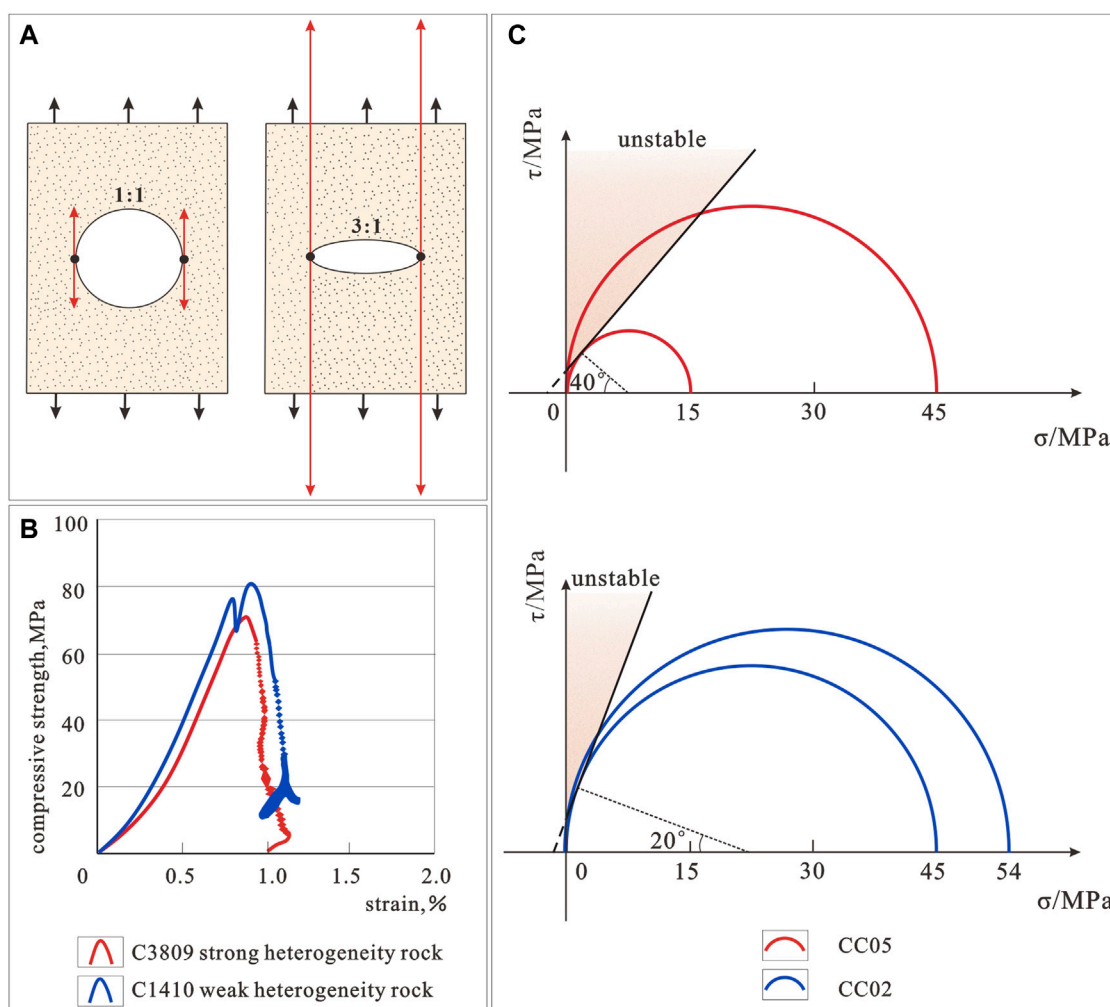
FIGURE 10
Effects of heterogeneity on the fracture mechanisms. **(A)** Illustration of local stress concentrations in a material with circular and elliptical holes (Fossen, 2016). Black arrows: remote stress. **(B)** Uniaxial compressive strength. **(C)** Mechanisms of fractures and heterogeneity.

in the XY slice (Figure 7). These indicated that fracture development was related to the preexisting weak surface.

Foliation-parallel extensional fractures also developed along the preexisting fracture. YZ (left view) slice images can reveal the development of fracture surfaces along the strike (length direction). The fractures in the YZ slice in the present study showed similar evolution, with large cracks across-bedding and small cracks terminating at the bedding surface. However, the large cracks were not as obvious as those that developed in the XZ plane. The fractures labeled in the red circle corresponded to the red circle in the XY slice (Figure 7).

The fractures in the three-dimensional perspective appeared as red traces. They were connected by layered and across-bedding fractures and formed a bright red image. However, other fractures were observed as bed-parallel fractures that

propagated *via* preexisting layered fractures. The fracture volume density accounted for 3.42% of the total volume of the rock samples, which was approximately two-fold that of that measured without loading (1.72%).

CT images at a 30 MPa load and 50% stress level

The fractures generally propagated faster than the former conditions and showed a distinct fracture style (Figure 7). On the plane, fractures continued to develop and new fractures were initiated (red and yellow circles). They propagated and developed toward the center of the sample, connecting into a network system of cracks covering almost the entire sample.

In the XZ slice, fracture ① continued to dilate, fracture ② developed a little, and fracture ③ almost healed. The obvious new cracks were the initiation of fractures ④ and ⑤. Fracture ④ appeared at the beginning of each lenticular crack of fracture ①

and formed a tensile-shear fracture. The most obvious was the formation of shear fracture ⑤. Fractures ⑤ and ④ formed in a Y shape with an angle of 40°, at 20° to σ_1. Moreover, certain small fractures, ⑥, began to develop opposite fractures ①-② and ④-⑤. The foliation-parallel extension fractures along the preexisting fracture continued to develop, but the aperture decreased.

In the YZ slice, the fractures showed evolution like those two slices. Large cracks were observed in the upper portion of the sample, propagated by the former small cracks. Smaller fractures occurred at the lower part and opposite the large fractures.

The three-dimensional CT images revealed that the across-bedding cracks continued to develop into through-going macro fractures. In the three-dimensional perspective, the fracture network continued to expand with increasingly large fractures in strong bright red. Other fractures further developed and were connected by small and across-bedding fractures. Under this loading condition, the increases in fracture opening and extension length jointly contributed to the fracture volume, which increased from 3.42 to 8.20% (more than two-fold).

CT images at a 45 MPa load and 70% stress level

Under a loading press of 45 MPa and a stress level of 75%, fractures propagated inside and down the sample (Figure 7). In the XZ slice, a new crack (No. ⑦), parallel to fracture ④), was initiated. To the right side, fracture ⑧ was initiated and a long shear crack (No.⑨) occurred, which extended almost to the bottom of the sample. Moreover, many near-parallel small cracks developed in the middle of the sample, connecting fractures ⑦ and ⑨ via a "soft linkage." At this stage, the opening of many bed-parallel extensional fractures decreased or even healed.

In the YZ cross-section slice, the fractures showed an evolution like that in the XZ slice. In the left part (back of the sample), large cracks (below the red circle) developed downward; in the front of the sample, cracks appeared deep in the sample. Therefore, the fracture images showed increasingly large cracks around the circle and increasingly small cracks at the center (Figure 7). Furthermore, the bedding-parallel fractures that existed before loading were almost healed.

The three-dimensional CT images showed that the cracks continued to expand and extend as penetrating cracks. The longest penetrated vertically down the entire sample. The number of fractures increased significantly, the crack spacing became increasingly smaller, and the density of network cracks increased.

The three-dimensional red trace perspective showed that the net fracture ran through the upper part of the sample and partially reached the bottom. Moreover, no crack development was observed in the black area. At this stress level, the proportion of fracture volume increased from 8.20% to the final 13.17% of the test, although it was not an exponential increase.

Binomial fitting was performed between the obtained fracture volumes of sample CC05 under the above uniaxial loading pressure. The load and scan were performed four times, providing a total of four data points. Despite the lack of data, it still showed a parabolic result (Figure 8). The correlation coefficient between the fracture volume ratio and the axial pressure, 0.981, indicated that these factors were highly correlated. In general, the fracture volume increased with increasing uniaxial loading pressure, indicating the gradual initiation, propagation, and penetration of micro-fractures during continuous loading, thereby generating a fracture network system. However, the two were not directly proportional. After the axial pressure increased to 50%, the slope of the fitting curve gradually decreased, indicating that the fracture volume increased slowly after reaching a certain value.

Dynamic fracture development and evolution in a low-permeability reservoir with weak heterogeneity

The relatively tight rock in low-permeability reservoirs such as sandstone and siltstone, with no bed-parallel or diagenetic fractures, is a type of reservoir showing weak heterogeneity. Sample CC02 was selected for fracture development and evolution tests as a representative of weak heterogeneous reservoirs (Figure 9).

Scanning of the slice images showed no bedding or fractures inside the sample before loading. In addition, no cracks were initiated in the uniaxial compression with compression pressure values of 15 and 30 MPa and stress levels of 25 and 50%, respectively.

When the loading pressure was increased to 45 MPa and the stress level to 75%, a shear fracture with a high dip angle of 85° was finally initiated in the XZ slice. This shear fracture was long and straight, with a decreasing width from the bottom to the top. In the YZ slice, two fractures were initiated; whereas in the plane, two shear fractures were observed: stepping in en-énchelon in the middle with another terminating with horse-tailing microfractures (Figure 9).

The three-dimensional red tracer revealed the three-dimensional characteristics of the fracture. The fracture was not continuous in the upper sample (black image). The proportion of the fracture volume was only 0.67%, indicating a very undeveloped fracture in the sample.

When the loading pressure increased to 54 MPa, the fracture became straighter and wider. The three-dimensional red perspective, showed continuous connection of the fracture in the middle and lower parts of the sample, indicated with a bright red color. However, this fracture did not propagate toward the upper part of the sample. Moreover, although the proportion of fracture volume increased from 0.67% to 0.81%, it remained an undeveloped fracture in the sample.

Overall, the above tests revealed the fracture evolution law at different heterogeneities (Figures 7, 9). Fractures in the relatively
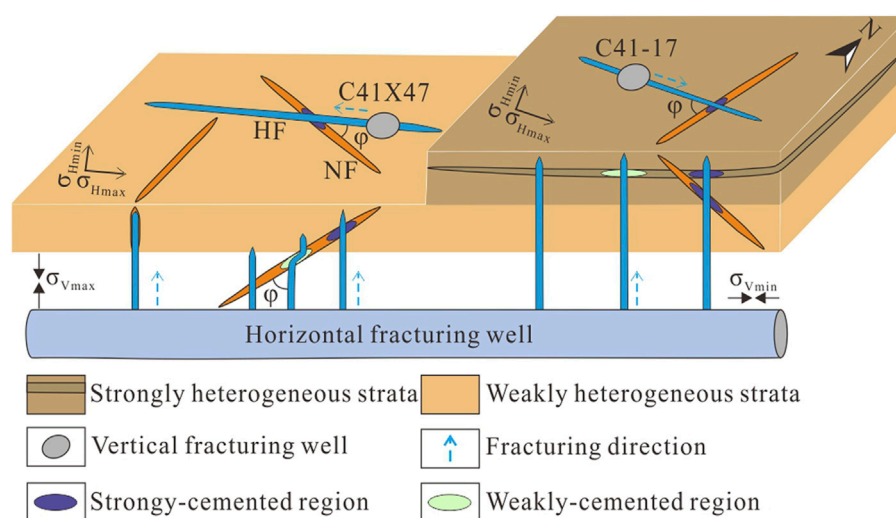
FIGURE 11
Effects of natural fracture characteristics in different heterogeneity reservoirs on fracturing.

strong heterogenetic low-permeability reservoir gradually initiated, propagated, and penetrated from top to bottom. Consequently, they formed a macroscopic crack and a vertical and horizontal network system. In contrast, fractures were difficult to form in the relatively weak heterogenetic low-permeability reservoir and formed as relatively large and long fractures once the loading exceeded the compressive strength of the rock. These results help to clarify the role of fractures in the hydraulic fracturing of oil wells.

Discussion

Effects of heterogeneity on fracture mechanisms

Griffith reported that randomly oriented and distributed intragranular microfractures in rock controlled the brittle strength of rock. Microscopic cracks, pores, and other flaws weaken rocks. Stress is generally concentrated at the tips of open microfractures in a rock, and the concentration increases with decreasing thickness/length ratio of the microfracture (Figure 10A) (Fossen, 2016). Local atomic bonds can be broken by this concentration, causing microcrack growth and further increasing the stress concentration at its tips to promote continued crack propagation (Fossen, 2016). Thus, microscale heterogeneities in the form of microfractures reduce rock strength. Mechanical weak layers, such as bedding, pre-existing bedding-parallel fractures, or mudstone layers in the reservoir make it thinner. Compared to weakly heterogeneous rocks, strongly heterogeneous rocks show lower uniaxial compressive

strength (Figure 10B). In uniaxial compression tests, fractures were more likely to occur (Figure 7).

Preexisting mechanic weak surfaces such as bedding, diagenetic fractures, and preexisting fractures lead to rock anisotropy stemming from sedimentary factors. The differences in critical differential stress may vary by several hundred percent, depending on the orientation (Fossen, 2016). Therefore, rock with a planar anisotropy will fail either along or across the weak surface. In sample CC05, the preexisting mechanically weak surfaces decreased the critical differential stress (Figure 10B) and the fractures occurred at 15 MPa. Most of the preexisting mechanically weak surfaces in CC05 were oriented perpendicular to σ_1; thus, across-bedding shear fractures formed at 20° to σ_1. New fractures were formed with gradually increasing loading. Therefore, fractures have a relatively large density and long development period (Figure 7, Figure 10C). Meanwhile, foliation-parallel extension fractures along the preexisting fracture developed at low stress (15 and 30 MPa) and were undeveloped or healed at high stress levels (45 MPa) (Figure 7). In contrast, without mechanically weak surfaces, the fractures were initiated only in relatively large differential stress (Figure 9, Figure 10C). Thus, fractures have a relatively small density and short development period (Figure 9).

Natural fracture development laws in oil well fracturing

The core observations and calculations showed that natural fracture (NF) volume densities of relatively strong

and weak heterogeneity in $E_2s_4^u$ were 0.28 and 0.15 m^2/m^3, respectively. This result indicated an undeveloped fracture in the study area. Furthermore, enhanced oil and gas production can be achieved by fracturing. Fracturing efficiently provides a faster and higher conductivity pathway into the reservoir (Gil et al., 2011). Discontinuities such as faults, unbounded bedding planes, and joints may significantly influence fracture shape during fracturing (Warpinski and Teufel 1987). Moreover, the HF may terminate, cross, or bypass the NF (Kolawole and Ispas 2020). Furthermore, the height constraint of the NF within stress barriers may impede the HF from crossing and cause arrest (Morris et al., 2016; Huang et al., 2018), leading to NF dilation, reactivation by shearing, and both shearing and dilation (Kolawole and Ispas 2020). The HF crosses the NF in the high and medium-to-high approach angles by propagating, dilating, or not dilating the NF in high-normal confining stress and strong NF interface bonding (Meng & de Pater, 2010). During fracturing, the HF propagates from the tip of the NF and diverts parallel to the HF, which terminates to the HF or is constrained by the NF in unidirectional and bidirectional stepping (Potluri et al., 2005; Kolawole and Ispas 2020). Therefore, the heterogeneity of low-permeability reservoirs plays an important role in hydraulic fracturing.

These results and those of the natural fracture analysis demonstrate that a strong-heterogeneity reservoir is more favorable to the fracturing effect compared to a weak-heterogeneity reservoir. The results based on the CT scans showed that fractures initiated and propagated easily in the strong-heterogeneity reservoir with bedding or pre-existing bedding-parallel fractures (Figure 7). Therefore, HF is produced more easily compared to a weak-heterogeneity reservoir under the same fracturing pressure. Although fractures are arrested when their tips propagate to the weak layer, which constrains expansion in the length direction, further fractures are produced in the production layer to enhance the oil channel. In contrast, in low-permeability reservoirs with relatively weak heterogeneity, fractures are hard to initiate. Therefore, the heterogeneity and mechanical properties of reservoirs of the kick-off point play a vital role in fracturing.

Experimental and numerical investigation showed that the approach angle affected the HF and NF interaction table (Zhu et al., 2018). A high approach angle (larger than 60°) between the HF and NF caused the HF to more easily cross the NF compared to angles ≤60°. Moreover, when the angle decreased, the HF was arrested at the NF plane (Fatahi et al., 2017; Wang et al., 2018). Therefore, bedding parallel fractures and NFs with dip angles ≤30° made it easier for hydraulic cracks to pass through and form long hydraulic cracks, whereas natural fractures with dip angles ≥30° arrested HFs at the NF plane.

When a fracture is initiated, it grows in the vertical and planar directions (Figures 7, 9). Compared to the fracture vertical growth, fractures may grow efficiently in other directions in planar. A high approach angle (≥50°) and low differential horizontal stresses (≤10 MPa) resulted in the HF crossing the NF (Zhu et al., 2018). Therefore, the strike of the NF can affect the propagation and termination of the HF.

Considering the approaching angle and horizontal differential stress, the results of this study proposed an actual model of fracturing to illustrate the effects of natural fracture characteristics in different heterogeneity reservoirs to fracturing (Figure 11). The best fracturing direction was along approach angles of 50°–90° to the dominant natural fracture, together with low differential horizontal stresses.

As mentioned above, the preferred direction of the NF in the study area was 15° (Figure 3B). Hence, the best fracturing direction was 65°–105°, with an approach angle of 50°–90° (Figure 11). Wells C41-17 and C41X47 in the C41 block were selected for fracturing work. The simulated minimum principal stress in Well C41-17 was 55 MPa, while the maximum principal stress measured by acoustic emission was 66 MPa (Liu et al., 2003). Thus, the horizontal differential stress was 11 MPa, which met the needs for the best fracturing effect. As mentioned above, the HF will cross the NF easily at a high approach angle and small differential horizontal stresses. The hydraulic fracturing produced HFs in strikes of 64.1°and 51° in Wells C41-17 and C41X47, respectively (Figure 1B), which was consistent with the theoretical findings.

Conclusion

This study investigated the three-dimensional evolution of fracture initiation and propagation in different heterogeneity conditions of low-permeability reservoirs by analysis of the core fractures and X-ray computed tomography scans in uniaxial compression tests with loading and unloading. The following conclusions resulted from these analyses:

1) The heterogeneity of low-permeability reservoirs affects the development of natural fractures. In strong-heterogeneity reservoirs with a pre-existing mechanical weak surface (bedding, diagenetic, etc.), many structural fractures develop and the fracture density is high. In contrast, structural fractures do not develop in weakly heterogeneous reservoirs without a pre-existing mechanical weak surface. These cases develop few fractures and show a low fracture density.

2) The development and evolution of 3D fractures are controlled by reservoir heterogeneity, load value, and direction. CT scans of strong-heterogeneity reservoirs showed that the fractures initiated and propagated from shallow to deep depths under

relatively small loading values. The initial crack was often a tensile fracture, which propagated into hybrid and shear fractures. These fractures intersected to form a complex and interconnected three-dimensional fracture body. In contrast, in weak-heterogeneity reservoirs with only large load values, the initial fractures often occur as large shear fractures. In addition, they step into the en-énchelon in the middle, terminating with horse-tailing microfractures in the plane. Therefore, a relatively simple 3D fracture system develops.

3) The reservoir heterogeneity controls the fracture stage and density. In strong-heterogeneity reservoirs, the fractures show long propagation and growth stages with large fracture densities. The fracture increase rate is positively correlated with the uniaxial loading value. In contrast, microfracture initiation is difficult in weak-heterogeneity reservoirs. Therefore, the fracture development period is relatively short, the formation period starts relatively later, and the fracture density is low.

4) A better fracturing effect can be achieved by selecting a reservoir with strong heterogeneity, along the direction at an angle >50° with respect to the natural fracture with small differential horizontal stresses.

Data availability statement

The original contributions presented in the study are included in the article/Supplementary material. Further inquiries can be directed to the corresponding author.

Author contributions

LL coordinated the core observations; developed the initial study concept; contributed to the conceptualization, data curation, original writing, experimental analysis, revisions, and editing; and submitted the article. GS developed the initial study concept and performed the formal analysis, sample collection, and experimental analysis. YZ and XL contributed to data reduction and editing and also prepared the figures. All authors contributed to the article and approved the submitted version.

Conflict of interest

GS was employed by Henan Geological Investigation and Designing Institute Co., Ltd.

The remaining authors declare that the research was conducted in the absence of any commercial or financial relationships that could be construed as a potential conflict of interest.

Publisher's note

All claims expressed in this article are solely those of the authors and do not necessarily represent those of their affiliated organizations, or those of the publisher, the editors, and the reviewers. Any product that may be evaluated in this article, or claim that may be made by its manufacturer, is not guaranteed or endorsed by the publisher.

References

Cao, G. (2005). "Experiment on microfractures initiation and propagation and seepage properties of sandstone samples by using X-ray scan," (Xi'an: Xi'an University of technology). master's thesis.

Chen, Y., Li, N., Han, X., Pu, Y., and Liao, Q. (2005). Research on crack development progress on non-interpenetrated media by using CT (In Chinese with English abstract). *Chin. J. Mech. Eng.* 24 (15), 2665–2670. doi:10.3321/j.issn:1000-6915.2005.15.011

Cnudde, V., Boone, M., Dewanckele, J., Dierick, M., Van Hoorebeke, L., and Jacobs, P. (2011). 3D characterization of sandstone by means of X-ray computed tomography. *Geosph. (Boulder).* 7, 54–61. doi:10.1130/ges00563.1

Ding, W., Wang, X., Hu, Q., Yin, S., Cao, X., and Liu, J. (2015). Progress in tight sandstone fractures reservoir (In Chinese with English abstract). *Prog. Geoscience* 30 (7), 737–750. doi:10.11867/j.issn.1001-8166.2015.07.0737

Fatahi, H., Hossain, M. M., and Sarmadivaleh, M. (2017). Numerical and experimental investigation of the interaction of natural and propagated hydraulic fracture. *J. Nat. Gas Sci. Eng.* 37, 409–424. doi:10.1016/j.jngse.2016.11.054

Fossen, H. (2016). *Structural Geology*. United Kingdom: Cambridge University Press.

Gale, J. F. W., Reed, R. M., and Ho1der, J. (2007). Natural fractures in the Barnett Shale and their importance for hydraulic fracture treatments. *Am. Assoc. Pet. Geol. Bull.* 91 (4), 603–622. doi:10.1306/11010606061

Germanovich, L. N., Salganik, R. L., Dyskin, A. V., and Lee, K. K. (1994). Mechanisms of brittle fracture of rock with pre-existing cracks in compression. *Pure Appl. Geophys.* 143 (1-3), 117–149. doi:10.1007/BF00874326

Gil, I., Nagel, N., Sanchez-Nagel, M., and Damjanac, B. (2011). "The effect of operational parameters on hydraulic fracture propagation in naturally fractured reservoirs-getting control of the fracture optimization process," in Proceedings of the 45th US Rock mechanics/geomechanics symposium, San Francisco, California, June 2011. ARMA-11-391.

Huang, J., Morris, J. P., Fu, P., Settgast, R. R., Sherman, C. S., and Ryerson, F. J. (2018). Hydraulic-fracture-height growth under the combined influence of stress barriers and natural fractures. *SPE J.* 24 (1), 302–318. doi:10.2118/189861-PA

Jin, Y., Zhang, X., and Chen, M. (2005). Initiation pressure models for hydraulic fracturing of vertical wells in naturally fractured formation (In Chinese with English abstract). *Acta Pet. Sin.* 26 (6), 113–114. doi:10.3321/j.issn.0253-2697.2005.06.026

Ketcham, R. A., and Carlson, W. D. (2001). Acquisition, optimization and interpretation of X-ray computed tomographic imagery: Applications to the geosciences. *Comput. Geosci.* 27, 381–400. doi:10.1016/S0098-3004(00)00116-3

Kolawole, O., and Ispas, I. (2020). Interaction between hydraulic fractures and natural fractures: Current status and prospective directions. *J. Pet. Explor. Prod. Technol.* 10 (4), 1613–1634. doi:10.1007/s13202-019-00778-3

Lee, H. P., Olson, J. E., Holder, J., Gale, J. F. W., and Myers, R. D. (2015). The interaction of propagating opening mode fractures with preexisting discontinuities in shale. *J. Geophys. Res. Solid Earth* 120, 169–181. doi:10.1002/2014jb011358

Li, D. P. (1997). *Development of low permeability sandstone oilfield.* Beijing: Petroleum Industry Press.

Li, H., Fan, C. W., Jiang, Z. X., Li, J., Li, C., Xu, X. H., et al. (2022). Natural fractures in low-permeability sandstone reservoirs in the LD-A HPHT gas field, yinggehai basin: Implications for hydrocarbon exploration and development. *Front. Earth Sci. (Lausanne).* 10, 934097. doi:10.3389/feart.2022.934097

Li, H., Tang, H., Qin, Q., Zhou, J., Qin, Z., Fan, C., et al. (2019). Characteristics, formation periodsand genetic mechanisms of tectonic fractures in the tight gas sandstones reservoir: A case study of xujiahe formation in YB area, sichuan basin, China. *J. Petroleum Sci. Eng.* 178, 723–735. doi:10.1016/j.petrol.2019.04.007

Li, J., Kong, X., Song, M., Wang, Y., Wang, H., and Liu, X. (2019). Study on the influence of reservoir rock micro-pore structure on rock mechanical properties and crack propagation (In Chinese with English abstract). *Rock soil Mech.* 40 (11), 4419–4156, 4164. doi:10.16285/j.rsm.2018.1866

Li, L., Sang, X., and Chen, X. (2017). Research and progress on fracture of low-permeability reservoir (In Chinese with English abstract). *Prog. Geophys.* 32 (6), 2472–2484. doi:10.6038/pg20170626

Li, L., Zhong, D. L., Shi, X. P., Tang, Z. B., Hu, Q. Y., Xu, Y., et al. (2009). Late Mesozoic–Cenozoic decollement structure and its deep geological background in Western Shandong, China. *Prog. Nat. Sci.* 19 (05), 603–613. doi:10.1016/j.pnsc.2008.08.006

Liu, X. T., Dai, J. S., Xu, J. C., and Wang, B. F. (2003). Finite element simulation of the present ground stress field of Sha-4 Member in the Chun-41 fault block. *Petroleum Explor. Dev.* 30 (3), 126–128. doi:10.3321/j.issn.1000-0747.2003.03.035

Meng, C., and de Pater, J. L. (2010). "Hydraulic fracture propagation in pre-fractured natural rocks," in Proceedings of the American Rock Mechanics Association, Nagasaki. ARMA-10-318. doi:10.2118/140429-MS

Morris, J. P., Fu, P., Settgast, R. R., Sherman, C. S., Friedrich, M., and Leonard, P. (2016). The combined influence of stress barriers and natural fractures upon hydraulic fracture height growth. *Am. Rock Mech. Assoc.* 4, 2871–2876.

Potluri, N. K., Zhu, D., and Hill, A. D. (2005). "The effect of natural fractures on hydraulic fracture propagation," in SPE European Formation Damage Conference, Sheveningen, The Netherlands, May 2005. SPE 94568. doi:10.2523/94568-MS

Renard, F., Bernard, D., Desrues, J., and Ougier-Simonin, A. (2009). 3D imaging of fracture propagation using synchrotron X-ray microtomography. *Earth Planet. Sci. Lett.* 286 (1-2), 285–291. doi:10.1016/j.epsl.2009.06.040

Shi, G. Y., Li, L., Yu, S. Q., and Xu, C. (2021). Development characteristics and stages of fractures in the Low-permeability reservoir of the Fourth Member of Shahejie Formation of Chun-41 fault block (In Chinese with English abstract). *Geol. Sci.* 56 (03), 854–866. doi:10.12017/dzkx.2021.044

Sun, X., Li, X., Zheng, B., He, J., and Mao, T. (2020). Study on the progressive fracturing in soil and rock mixture under uniaxial compression conditions by CT scanning. *Eng. Geol.* 279, 105884. doi:10.1016/j.enggeo.2020.105884

Van Golf-Racht, T. D., and Chen, Z. (1989). *The engineering fundament of fractured reservoir (Chinese version).* Beijing: Petroleum industry press.

Wang, R., Chen, M., and Sun, W. (2008). Quantitative research on the characteristics of microfracture and parameters for micro cracks in ultra-low permeability sandstone reservoir: Taking yan 25 and Zhuang 40 areas in ordos basin for example (in Chinese with English abstract). *Acta Mineral. Sin.* 28 (2), 215–220. doi:10.3321/j.issn:1000-4734.2008.02.016

Wang, W., Olson, J., Prodanovi, M., and Schultz, R. A. (2018). The impact of natural fracture thickness on hydraulic fracture interaction mechanics. Proceedings of the Unconventional Resources Technology Conference. Houston, Texas, USA, July 2018, doi:10.15530/urtec-2018-2902343

Warpinski, N. R., and Teufel, L. W. (1987). Influence of geologic discontinuities on hydraulic fracture propagation (includes associated papers 17011 and 17074). *J. Petroleum Technol.* 39 (2), 209–220. doi:10.2118/13224-pa

Zabler, S., Rack, A., Manke, I., Thermann, K., Tiedemann, J., Harthill, N., et al. (2008). High-resolution tomography of cracks, voids and micro-structure in greywacke and limestone. *J. Struct. Geol.* 30 (7), 876–887. doi:10.1016/j.jsg.2008.03.002

Zeng, L. (2004). Fissure and its seepage characteristics in low permeability sandstone reservoir (In Chinese with English abstract). *Geoscience* 39 (1), 11–17. doi:10.3321/j.issn:0563-5020.2004.01.002

Zeng, L., and Xiao, S. (1999). Fractures in the mudstone of tight reservoirs (In Chinese with English abstract). *Exp. Pet. Geol.* 21 (3), 266–269. doi:10.3969/j.issn.1001-6112.1999.03.015

Zhang, Y., Niu, S., Du, Z., Hao, J., and Yang, J. (2020). Dynamic fracture evolution of tight sandstone under uniaxial compression in high resolution 3D X-ray microscopy. *J. Petroleum Sci. Eng.* 195, 107585. doi:10.1016/j.petrol.2020.107585

Zhou, X., Zhang, L., and Fan, K. (2006). The research situation and progresses of natural fracture for low permeability in oil and gas basin (In Chinese with English abstract). *Geol. Rev.* 52 (6), 777–782. doi:10.16509/j.georeview.2006.06.008

Zhu, G., Sousa, R. L., Abdulla, M., Al-Rub, R., and Sassi, M. (2018). "Numerical investigation of the interaction between hydraulic fractures and nature fractures at reservoir scale," in Proceedings of the 2Nd International Discrete Fracture Network, Seattle, Washington, USA, June 2018. ARMA-DFNE-18-0774.

Study on the influence of natural cracks on the mechanical properties and fracture mode for shale at the microscale: An example from the Lower Cambrian Niutitang Formation in northern Guizhou

Chao Yang, Zhonghu Wu*, Wentang Wang, Heng Qu, Nuo Ren and Hai Li

College of Civil Engineering, Guizhou University, Guiyang, China

A large number of natural cracks exist in shale reservoirs, and the presence of natural cracks weakens the integrity of shale, which is an important factor governing the effectiveness of shale gas extraction. In this paper, shales from the Lower Cambrian Niutitang Formation in northern Guizhou were scanned by electron microscopy, their microstructures were selected for digital image processing, and uniaxial compression numerical tests were conducted on shale models containing different natural crack dips using the rock fracture process system RFPA2D-DIP to study the effects of natural cracks on the mechanical properties and fracture patterns of shales at the microscopic scale. The study shows that the peak strength and elastic modulus of shale increase with increasing natural crack inclination angle. The fracture modes of shale at the microscopic scale can be roughly divided into four categories: similar to I-type fractures (0°), oblique I-type fractures (15°, 45°, 60°, 75°), folded line fractures (30°), and V-type fractures (90°). Natural cracks within shale are found to have a significant effect on the distribution of stress. Acoustic emission can reflect the stress change and rupture process for shales containing natural cracks with different dip angles at the microscopic scale. The presence of natural cracks has a significant effect on the AE energy and fractal dimension. The magnitude of the AE energy increases with increasing stress level and reaches a maximum value at 90°, while the value of the fractal dimension is found to zigzag upwards because the value of the fractal dimension is jointly influenced by both newborn cracks and native natural cracks.

KEYWORDS

natural crack, peak stress, rupture mode, stress distribution, acoustic emission, fractal dimension

1 Introduction

Shale gas, as an unconventional natural gas resource, has a large resource potential and wide distribution area, and is, thus, of wide interest to scholars at home and abroad (Wang et al., 2016a; Wang et al., 2016b; Shrestha et al., 2016; Nezhad et al., 2018; Liu et al., 2020a; Ban et al., 2021; Yu et al., 2021; Zhu et al., 2021). Compared with conventional natural gas, shale gas has the advantages of a long extraction life and long production cycle, and along with the consumption of conventional oil and gas, shale gas is expected to take its place in the future (Lisjak et al., 2014; Heng et al., 2015; Wu et al., 2017; Hu et al., 2020; Xu et al., 2020; Jin et al., 2021). Currently, the United States leads the world in the commercial production of shale gas (Wang et al., 2019). According to the results of exploration, China has the highest amount of shale gas in the world, and the difficulty in extracting shale gas is largely due to the low porosity and poor permeability of shale formations (Zou et al., 2016; Lan et al., 2018; Wu et al., 2018; Liu et al., 2019). For shale gas extraction, hydraulic fracturing is the preferred technology in most countries (Wang et al., 2014; Ju et al., 2018; Zhao et al., 2020; Feng et al., 2021). Therefore, studies of the mechanical properties of shale and its fracture pattern provide important theoretical support for the design of commercial shale gas extraction schemes.

Shales often contain complex natural fractures, and the presence of natural fractures affects the mechanical properties and fracture patterns of shales. Natural fractures, due to their irregularity, lead to a difficult problem in theoretically studying the damage mechanism for shales containing natural fractures. To solve this challenge, domestic and international scholars have carried out relevant mechanical tests in the laboratory. Chen et al. used the RTR-1000 triaxial rock mechanical test system to perform triaxial experiments on shales containing different fractures (controlling a single variable so that the number of fractures, dip angle, depth and filling are different) to investigate the peak stress, elastic modulus and damage forms for shales under different fracture patterns (Chen et al., 2020). Lee H et al. described the initiation, extension and coalescence of cracks at or near preexisting open cracks or defects in specimens under uniaxial compression (Lee and Jeon, 2011). Wei et al. conducted an experimental study into the deformation and fracture characteristics of brittle shales containing natural fractures under uniaxial cyclic loading in Pengshui, Chongqing, using the RMT-150C rock mechanics test system (Wei et al., 2015). Wang et al. carried out Brazilian splitting tests with disc specimens containing prefabricated fractures and monitored the

FIGURE 1
Area map of the Fenggang No.3 Block, Qianbei, Guizhou (Liu et al., 2019).
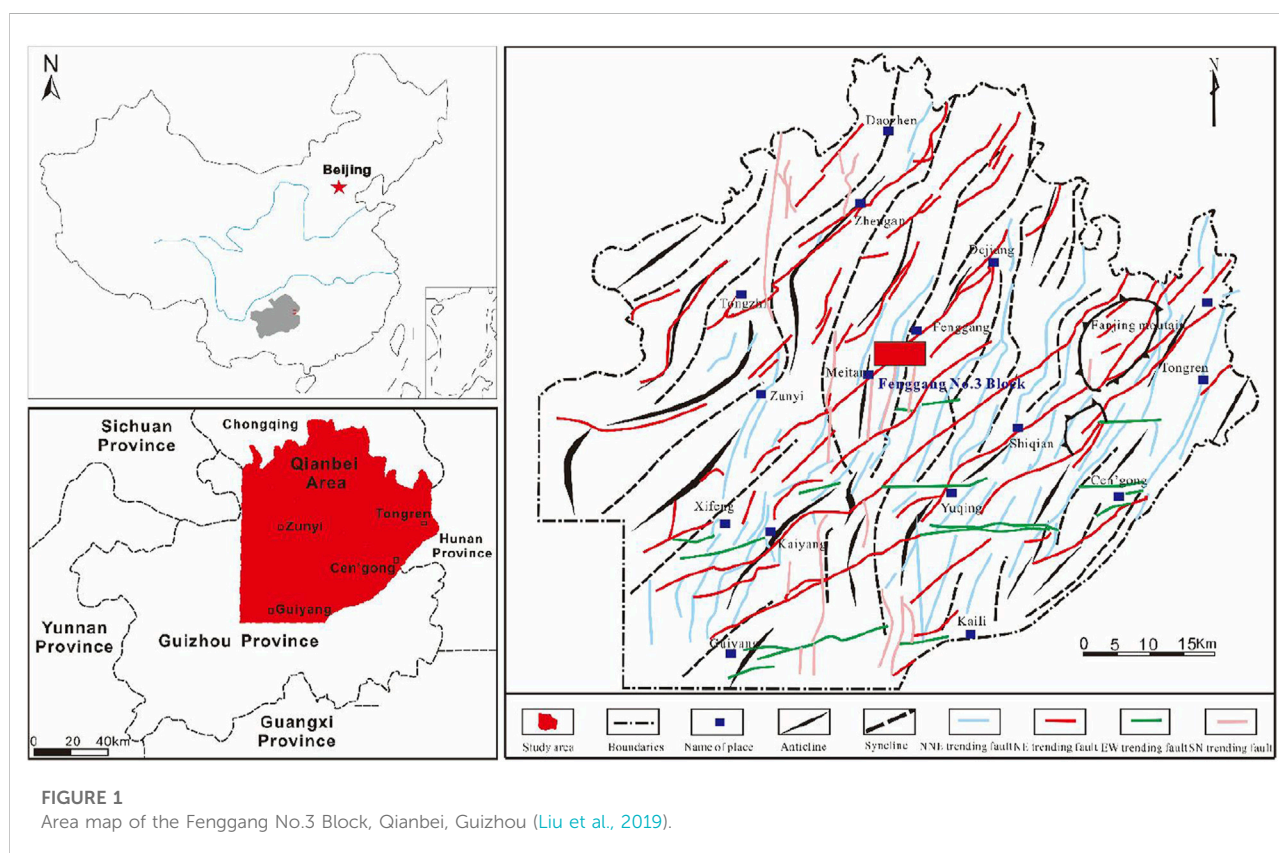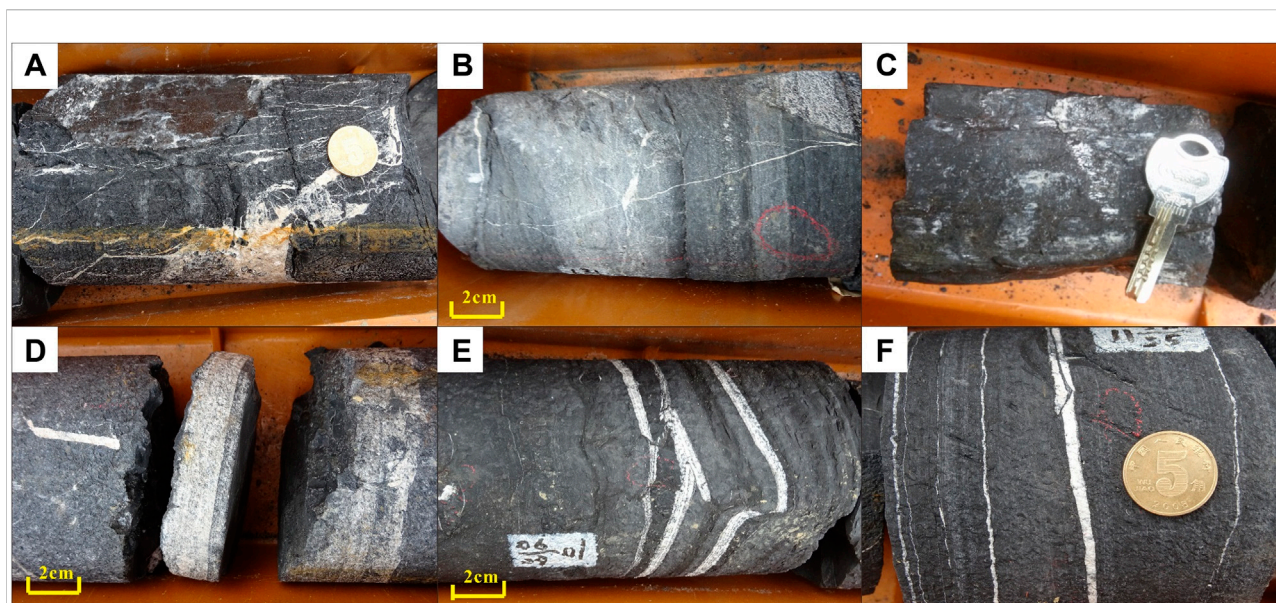
FIGURE 2
Niutitang Formation shale fracture photos in Fenggang No.3 block. **(A)** Tectonic fractures. **(B)** High-angle shear fractures. **(C)** Low-angle slip fractures. **(D)** Construct pressure solution suture. **(E)** Tensile fracture formed by crumping. **(F)** Horizontal interlayer seam.

damage process for the specimens using a high-speed camera and an acoustic emission monitoring device, aiming to investigate the fracture characteristics and breaking mechanism for black shale under the combined effect of laminations and prefabricated fractures. Numerous scholars have studied the damage mechanisms for shales containing defects through tests such as triaxial, uniaxial and Brazilian splitting (Wang et al., 2020). However, in the laboratory, the damage mechanism for naturally fractured shales is studied by the pre-preparation of fractures. It is difficult to prepare shale specimens with variable defects, especially for testing shales with natural fractures at the microscopic scale, which is basically impossible to do in the laboratory, and numerous factors limit researchers to study the damage mechanism of shales with natural fractures.

Numerical tests are sought after by academics as an alternative research tool because they enable more control over more variables and make it easier to perform tests that are otherwise difficult to carry out in the laboratory. Yu et al. studied the interaction mechanism between hydraulic and natural fractures and proposed a new numerical method called 2P-IKSPH (Yu et al., 2021). Zheng et al. developed a damage-stress-seepage coupled hydraulic fracture extension model based on the extended finite element method to investigate the interaction mechanism between hydraulic fracturing and natural fractures (Zheng et al., 2019). Liu et al. proposed a mixed-phase field approach and used the mixed-phase field model to numerically investigate the behavior of hydraulically

fractured shale specimens containing prefractured laminae (Liu et al., 2020b). He et al. developed a model based on a validated particle flow program (PFC2D) to investigate the indirect tensile mechanical behavior of shales containing two central parallel cracks under Brazilian cleavage test conditions (He et al., 2021). Shi et al. developed numerical models for five different sets of prefabricated fractures with laminar dip angles to study the mechanism of fracture extension in black shale by hydraulic fracturing (Shi et al., 2018).

In summary, both indoor and numerical tests have focused on the effect of macroscopic cracking on the damage mechanism for shale, and few studies have been carried out that address the effect of natural cracking on the mechanical properties and fracture mode of shale at the microscopic scale due to the specificity of natural cracking.

To further study the microstructure, shale samples were observed by scanning electron microscopy. A natural crack was selected by electron microscopy, and the microstructure of shale with natural cracks was obtained by correlation processing. Seven groups of digital images of shale with natural cracks at different dip angles and a control group without cracks were imported by RFPA2D-DIP. Numerical models were established in turn, and numerical tests (uniaxial compression) were carried out for each of the eight groups. The mechanical properties and fracture patterns for shale specimens containing natural fractures at different dip angles are discussed and analyzed. The results of this study provide theoretical support and have
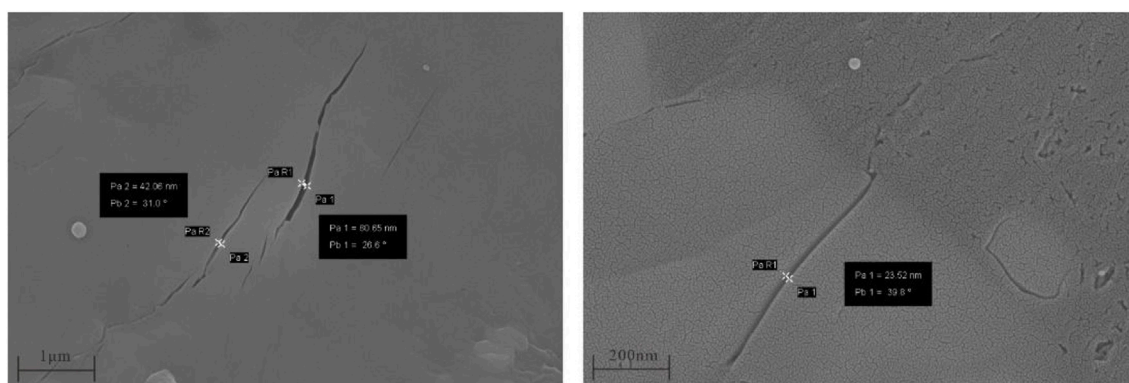
FIGURE 3
Scanning electron microscope.

important implications for the design of commercial shale gas extraction schemes.

2 Geological background

2.1 Overview of the study area

Fenggang Shale Gas No.3 Block in Guizhou is an important part of the National Shale Gas Resources Strategic Investigation Pilot Project, which has a good geological research foundation and resource development prospects (Figure 1). The area is located in the northern part of Guizhou Province, and the administrative division is under the jurisdiction of Meitan County, Fenggang and Sinan County of Tongren Region in the southeastern part of Zunyi District, Guizhou Province. The geotectonic position of the study area is located in the eastern part of the Upper Yangzi platform area, and the tectonic evolution is consistent with the regional tectonic evolution of the Yangzi platform. The tectonic evolution of the Yangzi platform occurred during the Xue Feng movement period, the Early-Middle Garidon period, the Late Garidon period, the Haixi period, the Indo-Chinese period, the Yanshan period and the Xishan period. The superposition of multiple tectonic movements has resulted in a complex tectonic pattern for the Yangzi Plateau.

The study area is located in the southern section of the Wuling tectonic zone, and north-south, north-northeast and northeast fractures and folding structures are developed in the area and are superimposed on each other for transformation. The north-south, northeast and north-northeast folded axial surfaces and punching faults constitute the main tectonic skeleton in the area. Folds and fractures are commonly developed in the area, the folds mainly consist of north-east and north-northeast spreading "spaced trough" structures, and a series of north-east-directed

compound backslopes and compound oblique structures are developed. The fractures are formed by the joint action of multiple fractures, mainly north–northeast and northeast torsional fractures. Among these tectonic traces, the north-south oriented tectonic zone is formed at the earliest stage, the north-east oriented tectonic zone is formed at the latest stage, and the north-north-east oriented tectonic zone is formed in between the earliest and latest stages.

2.2 Crack development characteristics of the study area

2.2.1 Macroscopic crack development characteristics

Observation of the fractures in the shale cores of the shale of the Niutitang Formation under the Cambrian System in Fenggang No. Three Block shows that the fracture types in the shale cores of the Niutitang Formation are mainly tectonic fractures (Figure 2A), high-angle shear fractures (Figure 2B), low-angle slip fractures (Figure 2C), construct pressure solution suture (Figure 2D), tensile fracture formed by crumping (Figure 2E) and horizontal interlayer seam (Figure 2F), among which the main fractures consist of tectonic fractures and shear fractures (Figures 2A,B).

2.2.2 Macroscopic crack development characteristics

Scanning electron microscopy reveals that micron-to-nanoscale microfractures are developed in black shale (Figure 3). The fracture lengths are approximately 1 μm–10 μm, and the widths range between 24 nm–942 nm. A few of the microfractures are filled with pyrite and clay minerals, etc., and most of them belong to the effective fractures that are not filled. For shale reservoirs with low porosity and low
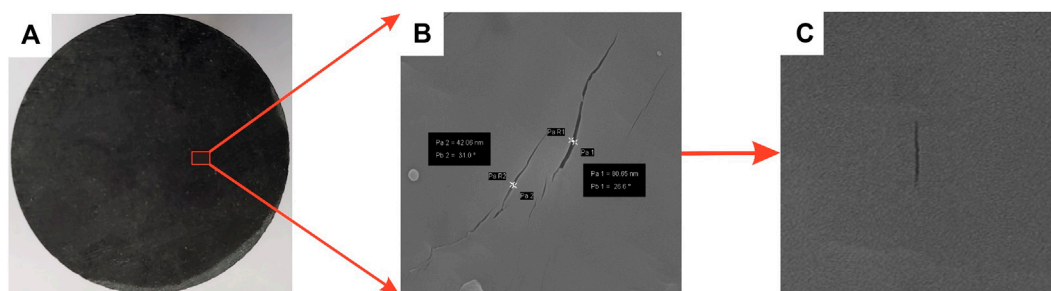
FIGURE 4
Shale macro and micro structure. **(A)** Macro structure of shale. **(B)** Scanning electron microscopy of shale. **(C)** Micro structure of natural fractured shale containing.

permeability, the development of natural fractures is of great significance for increasing shale gas production.

3 Test program

3.1 Test material

The shale sample used in this experiment was obtained from the Lower Cambrian Niutitang Formation stratum in the Qianbei area, and the sample color was black (Figure 4A). Scanning electron microscopy was used to further study the microstructure of the shale sample, and an electron microscope scan of the shale of the Niutitang Formation was obtained (Figure 4B). A natural fracture was selected from the electron microscope scan, and the microstructure of the shale containing natural fractures was determined by correlation processing (Figure 4C). The gray–black color in the figure shows the shale matrix, and the dark black part shows the natural fracture inside the shale. The natural fractures in shale will affect the mechanical properties and fracture pattern of shale under uniaxial compression.

3.2 Microstructure digital image processing characterization

During the processing of the microstructure images of shale by RFPA2D-DIP, the selected shale microstructure images were first imported, and the differences in color and brightness were used to characterize the differences in the material and its inhomogeneity. By the threshold segmentation method, the image segmentation threshold for shale microstructure was selected based on the change in the magnitude of the I-value (which characterizes the magnitude of the brightness in the image) (Liu et al., 2020a). Figure 5A shows the selected shale microstructure image containing natural cracks under electron microscopy scanning, and in the digital image processing

process, a scan line was used through the shale microstructure image containing natural cracks to obtain the curve for the change in the I value (Figure 5B). A I value threshold of 68 was obtained by multiple scanning and synthesis, which was divided into two intervals of 0–68 and 68–110, with natural cracks and the shale matrix lying in the range of 0–68 and 68–110, respectively. Figure 6 shows the digital characterization image of the processed shale from which the shape and distribution of natural cracks can be clearly observed.

3.3 Numerical model

In the process of digital image processing for the shale microstructure containing natural cracks, the image consists of a large number of pixel points and each pixel point is considered as a cell; the mapping method was used to convert the cell and grid, with each small grid representing a cell, characterizing a pixel point; then, the color characteristics of each pixel point, i.e., I value, were used to classify each pixel point into different material types and assign different mechanical parameters, generating a digital image characterizing the shale. Digital images of the matrix and natural cracks were generated to establish a numerical model that corresponds to the real situation (Cui et al., 2020).

To consider the nonuniformity of shale, in RFPA2D-DIP, it was assumed that each mechanical parameter of the shale model microcell obeys a Weibull statistical distribution (Weibull, 1951):

$$\phi(\alpha) = \frac{m}{\alpha_0} \cdot \left(\frac{\alpha}{\alpha_0}\right)^{m-1} \cdot e^{-\left(\frac{\alpha}{\alpha_0}\right)^m} \quad (1)$$

In Eq. 1, the mechanical property parameters of the unit are characterized by α, such as the modulus of elasticity and compressive strength, where α0 characterizes the average value of the mechanical property parameters for the unit and m
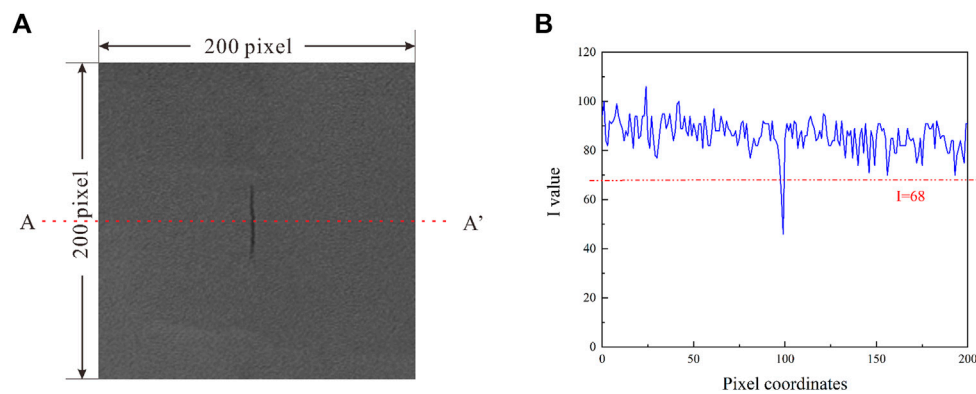
FIGURE 5
Numerical image characterization. **(A)** Position of scan line AA'. **(B)** Curve of l value on scan line AA'.
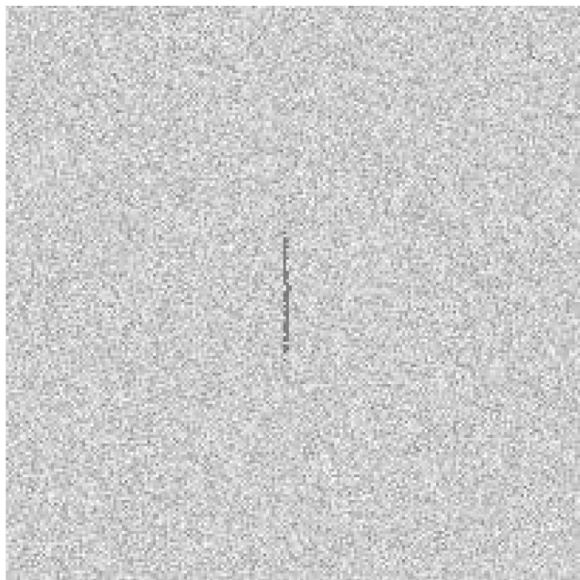
FIGURE 6
Image after threshold segmentation

characterizes the homogeneity of the material; the more homogeneous the material, the larger the m. According to the literature (Zhu et al., 2011; Lou et al., 2020; Wu et al., 2020), each known mechanical parameter for the shale is shown in Table 1. In

order to study the mechanical properties, rupture process and acoustic emission signal evolution characteristics of shale containing different inclination angles of natural cracks at microscopic scale, so as to establish numerical models of shale specimens with internal natural crack inclination angles of 0°, 15°, 30°, 45°, 60°, 75°, 90° and control group without natural cracks under uniaxial compression conditions, a total of 8 groups, were tested numerically by RFPA2D-DIP, and the mechanical loading model is shown in Figure 7, loaded by displacement control volume.

4 Experimental results and analysis

4.1 Mechanical properties

Figure 8 shows the stress–strain curves for shale containing natural cracks with different inclination angles under uniaxial compression. The stress–strain curves for the 90° and control specimens show good consistency, except that the peak compressive strength of the control specimens is higher than that of the 90° specimens, and the stress–strain curves can be summarized in four stages: linear elastic stage, yield stage, rupture stage, and stability stage, which are typical of brittle damage.

The stress–strain curves corresponding to 0°, 15°, 30°, 45°, 60°, and 75° specimens show inconsistency with the corresponding curves obtained for the control group, which can be mainly divided into two types: 0°, 60°, and 15°, 30°, 45°, and 75°. Both
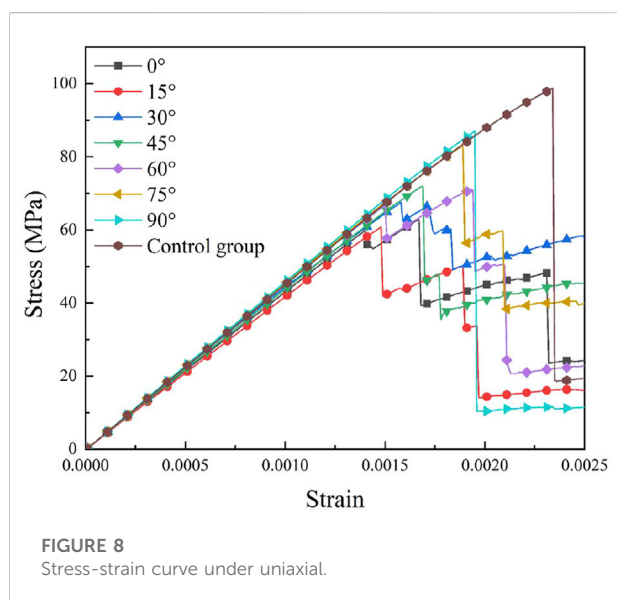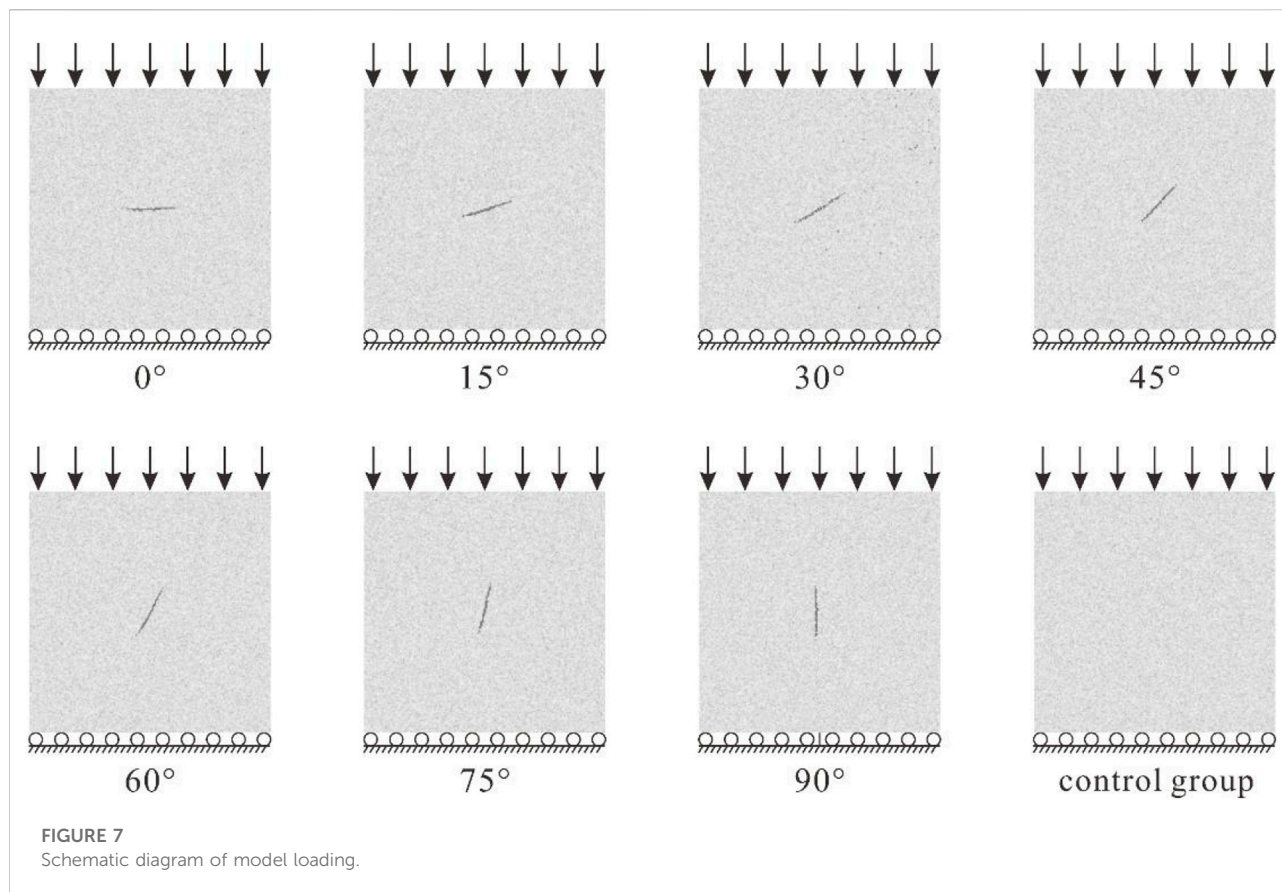
TABLE 1 Mechanical parameters of shale matrix.

Material	Homogeneity	Elastic modulus/MPa	Compressive strength/MPa	Possion ratio ν	Compression tension ratio	Internal friction angle/(°) angle/(°)
Shale substrate	5	51,600	145	0.22	14	35

FIGURE 7
Schematic diagram of model loading.

FIGURE 8
Stress-strain curve under uniaxial.

Taking 60° as an example, the first stage is the linear elastic stage, where with an increase in displacement loading, the stress increases linearly; the second stage is the first yielding stage, where the continued loading leads to a gradual nonlinear increase in the stress until it reaches the initial stress peak and the rock ruptures; the third stage is the initial rupture stage, where the rock ruptures for the first time, which leads to a linear decline in the stress; and the fourth stage is the second stressing. The fourth stage is the secondary stress stage, where after the initial rupture of the rock with increasing displacement loading, the stress again increases nonlinearly until the second time to reach the peak stress, with the second peak stress being higher than the peak stress of the first rupture; the fifth stage is the repetition stage, where with increasing displacement loading, the phenomenon of multiple stress drops occurs; the sixth stage is the stability stage, where the stress tends to stabilize and no longer change with increasing displacement loading stress size.

This is because the shale fractures in the 0°–75° tests were initiated by natural fractures in the shale, and after the first stress peak in the fracture process, the stress drops and then rises again, reciprocating until the fracture is complete. The shale can continue to withstand the load after the initial stress drop, and the existence of this phenomenon is related to the inclination of the natural fractures and the way the shale is

types undergo multiple stress drops during the rupture process, and the peak stresses for 0° and 60° all occur at the second stress drop, while 15°, 30°, 45°, and 75° peak stresses all occur at the first stress drop.

FIGURE 9
Peak stress and modulus of elasticity at different angles.
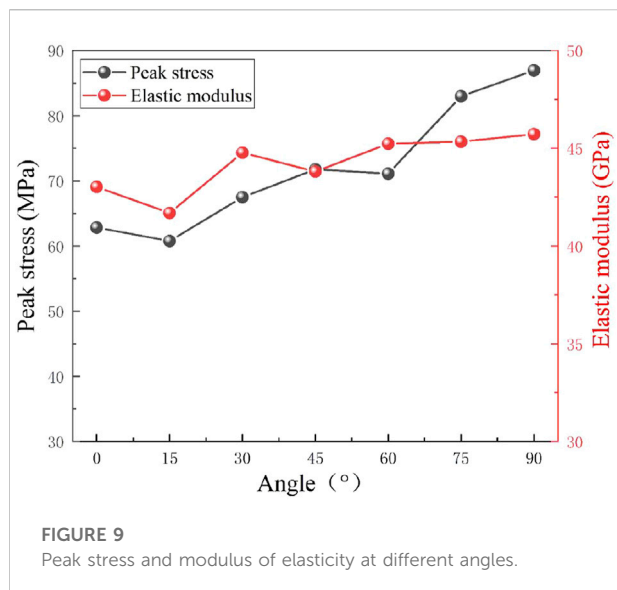
fractured. The 90° test was not initiated by a natural fracture in the shale, so only one stress drop is found to occur.

The relationship between the peak stress, elastic modulus and different crack inclination angles was obtained by simulating numerical experiments with different crack inclination angles, as shown in Figure 9. The overall trend for the peak stress and elastic modulus of shale increases with increasing natural crack inclination angle, which is basically consistent with the conclusion obtained in the literature (Liu et al., 2020c). Only the 15° and 60° shale specimens show a decrease in peak stress, while the 15° and 45° shale specimens show a decrease in elastic modulus. The peak stress is found to occur at 62.8 MPa at 0°, 60.8 MPa at 15°, 67.5 MPa at 30°, 71.8 MPa at 45°, 71.1 MPa at 60°, 82.9 MPa at 75°, 86.9 MPa at 90°, and 98.7 MPa in the control group; the control group shows clearly different behavior due to the presence of natural cracks. The overall trend is that as the angle of the natural cracks contained in the shale increases, the stress loss that occurs in the uniaxial compression process for the shale is 36.4% for 0°, 38.4% for 15°, 31.6% for 30°, 27.3% for 45°, 27.9% for 60°, 16% for 75°, and 11.9% for 90°. The overall trend is that as the natural fracture angle in the shale increases, the stress loss that occurs in uniaxial compression decreases. In general, the peak stress and elastic modulus of shale increase as the natural crack angle in shale increases, and, conversely, the stress loss that occurs in shale decreases.

4.2 Rupture mode

Figure 10 shows the fracture process and acoustic emission diagram for the microstructure of naturally fractured shale with different dip angles under uniaxial compression. It is obvious

from the rupture process of natural fractured shale containing different inclination angles that the rupture process for natural fractured shale containing different inclination angles is mainly divided into three processes: crack initiation, crack expansion and crack penetration. Figure 10A shows the crack initiation stage for the shale damage process, Figure 10B shows the crack expansion stage, Figure 10C shows the crack penetration stage, and Figure 10D shows the shale crack. The acoustic emission map corresponds to the penetration stage due to the different angles of the natural fracture, which leads to different fracture initiation points, different fracture extension processes, and, finally, different fracture patterns. There are four main categories as follows:

1) Cracking perpendicular to the natural crack and finally forming a similar I-type crack (0°): In the uniaxial compression state where the natural crack is inclined at an angle of 0°, first, the natural crack in the middle of the shale is gradually compressed with increasing displacement loading, and tiny cracks sprout up and down from the middle of the natural crack. As the crack gradually expands upward and downward, new cracks begin to sprout on the right side of the lower sprouting crack and mainly along the new crack. The upper side is mainly located along the initial sprouting crack until penetration and finally connects and penetrates to form a similar I-type crack, producing more microcracks in the lower half of the main crack and fewer in the upper half.

In the process of the natural crack being compacted, due to the irregularity of the natural crack (wide in the middle and narrow at the ends), the middle of the natural crack is cracked by tension, and tensile damage occurs in the unit. As the natural crack is compacted, the crack tip is gradually extended up and down by tension, while the rest of the unit undergoes sporadic shear damage until the crack penetrates the specimen.

2) Inclined or along both sides of the natural crack, eventually forming oblique I-type cracks (15°, 45°, 60°, 75°): taking 45° as an example, in the uniaxial compression state where the natural crack is inclined at an angle of 45°, the cracks sprout at both ends of the natural crack, close to perpendicular to the natural crack, and then expand upward and downward with the starting crack, and it can be observed in the crack expansion stage that the cracks on the sitting side extend upward. The crack on the upper right side only extends upward along the emergent crack, and the natural crack with an inclination of 45° is gradually compacted in the crack extension stage, and finally extends upward and downward along the emergent crack on the lower left side to expand into a through crack. Meanwhile, the crack on the upper right side only extends partly in the extension

FIGURE 10
Fracturing process of microstructure of shale. **(A)** Crack initiation. **(B)** Crack propagation. **(C)** Fracture mode. **(D)** Acoustic emission.
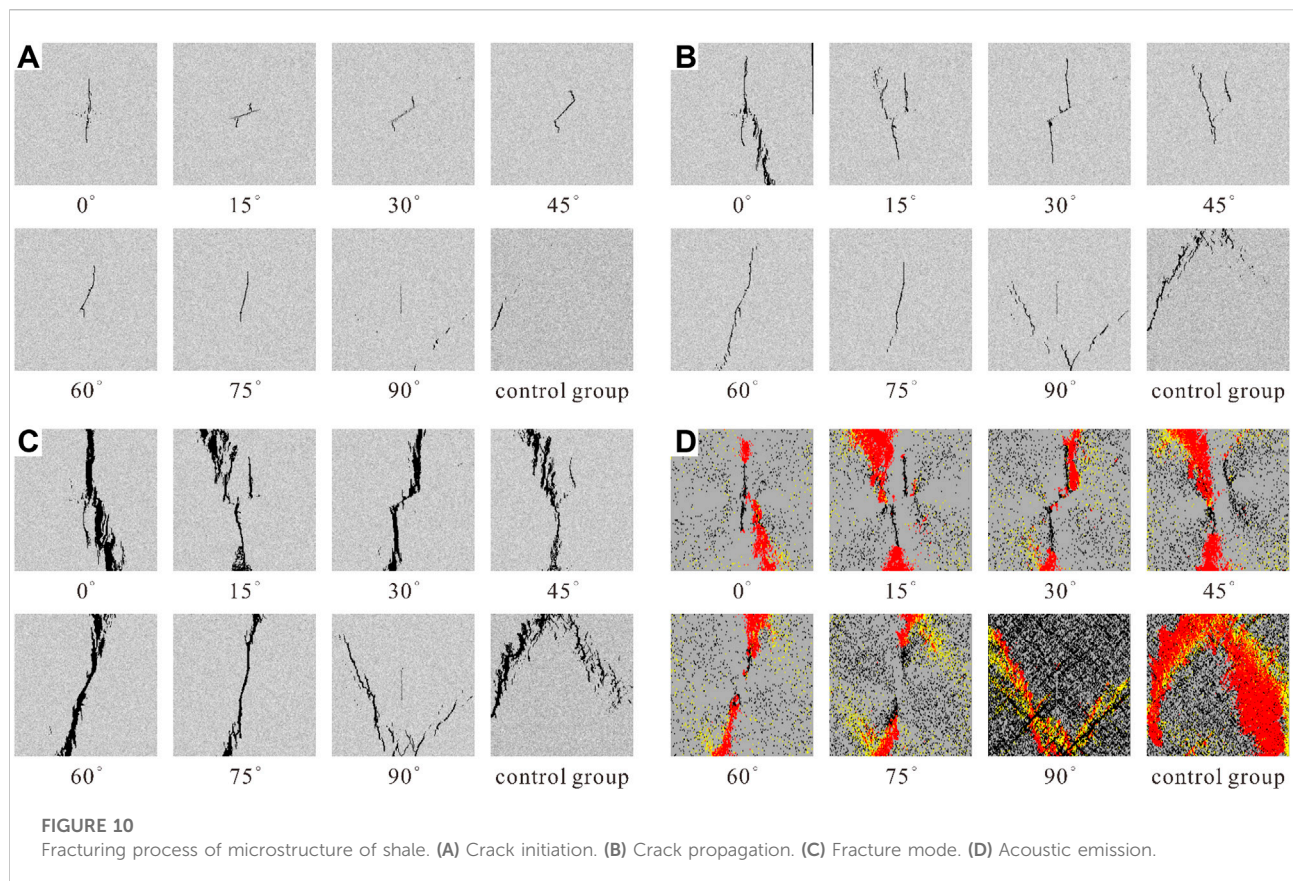
stage and does not form a through crack, and the rupture process for the specimen at 15° is similar to that described above, which is only the initial emergent crack, which does not start at the two ends of the natural crack, but at a distance from the two ends of the natural crack. For the 60° and 75° specimens, it is obvious that the emergent crack starts from the natural crack, and the angle and direction of the crack extension is located nearly up and down along both sides of the natural crack. With continuous loading, the crack extends continuously to form an oblique I-type through crack, and more tiny cracks are produced at the upper and lower ends of the crack near the penetration cracks.

With an increase in displacement loading, tensile damage occurs at both ends of the natural crack, cracks sprout, and with the extension of the sprouted crack, in addition to tensile damage at the extended crack, the rest of the sporadic units show shear damage. When the sporadic rupture of the unit leads to the formation of a crack, crack extension occurs when tensile damage occurs, and the cracks formed penetrate each other to form the main crack and penetration.

3) Tilted cracking on both sides of the natural crack, eventually forming a folding crack (30°): in the uniaxial compression state with a natural crack tilt angle of 30°, the crack starts to form along both sides of the natural crack, the starting angle is nearly vertical, the lower left side starts cracking downward, the upper right side starts cracking upward. With continuous loading until the crack penetrates, a folding through crack is formed, with the natural crack and the sprouting crack around sprouting many tiny secondary cracks, especially with a short vertical crack sprouting in the middle of the natural crack, which does not extend and expand again.

For a natural crack inclination of 30°, with ab increase in loading, tensile damage occurs at both ends of the natural crack, sprouting cracks and expansion, sporadic shear damage units do not form through cracks, and with the extension of the crack, the formation of tensile damage mainly occurs *via* cracking.

4) Crack initiation not along the natural crack, eventually forming V-shaped cracks (90°) and inverted V-shaped cracks (control group): in the uniaxial compression state with a natural crack inclination angle of 90°, it is obvious that the crack initiation does not occur from the natural crack but involves the sprouting of tiny cracks on the lower right side and the lower left side of the specimen, respectively, and with continuous loading, the cracks on the left and right sides

extend continuously, forming penetration cracks that are nearly V-shaped. With continuous loading, the cracks on the left and right sides are extended, forming a penetration crack that is nearly V-shaped and more micro cracks appear on the lower part, while the control specimen is cracked from the left side, and the cracks are extended diagonally upward to the top and then extended along the lower right side, finally forming an inverted V-shaped penetration crack and more secondary cracks along the main crack.

For a natural crack inclination angle of 90°, crack initiation and expansion are not affected by the natural crack. With an increase in displacement loading, unit shear damage occurs, and with an increase in the number of damaged units, cracks gradually form under tensile and shear extension and expansion.

The fracture pattern diagrams and acoustic emission diagrams for naturally fractured shale with different dip angles show good agreement between acoustic emission and the fracture pattern of the shale. In the acoustic emission diagrams of natural fractured shale with different inclination angles, the red characterized unit is damaged in tension at the current loading step, the yellow characterized unit is damaged in compression shear at the current loading step, and the black characterized unit is completely damaged at the current loading step. In the uniaxial compression state when the natural crack inclination angle is 0°, 15°, 30°, and 45°, it can be found that most of the cells in the main crack part of the rupture process suffer from tensile damage, and the rest of the cells are accompanied by a small amount of compression shear damage. In the uniaxial compression state when the natural crack inclination angle is 60° and 75°, it can be found that most of the cells in the main crack part of the rupture process suffer from tensile damage. However, for the uncracked uniaxial compression, when the natural crack inclination is 90°, it can be found that the cracking process is accompanied by tensile and compression shear damage in the main cracked units.
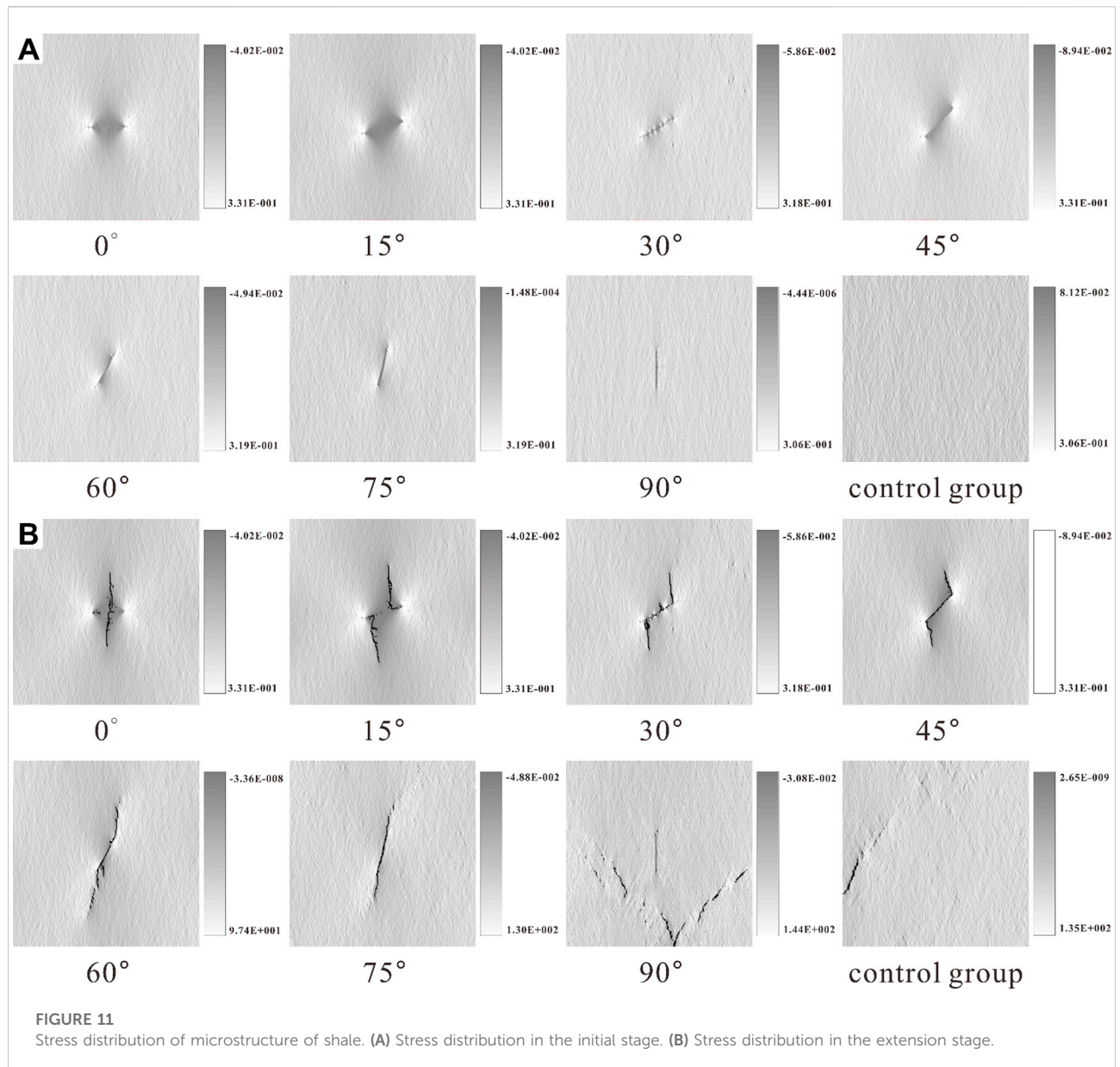
4.3 Stress distribution characteristics

The stress distribution characteristics of the microstructure of naturally cracked shale containing different inclination angles under uniaxial compression are shown in Figure 11, and the color brightness in the stress distribution diagram represents the magnitude of the stress; the brighter the color, the higher the stress. In the initial stage (Figure 11A), when the natural crack inclination angle is 0°, it is obvious that there is an obvious stress concentration effect at the ends of both sides of the natural crack, while the middle of the crack has less stress; for a natural crack inclination angle of 15°, 45°, 60° and 75°, it is obvious that the stress is mainly concentrated on the left end and the right end of the natural crack; for a natural crack inclination angle of 30°, the stress is concentrated on the ends of

both sides of the crack, and the stress is concentrated on the upper and lower sides of the crack, followed by the formation of irregular cracks distributed in a jagged pattern; for a natural crack inclination of 90°, the stress distribution is similar to that of the control group test, which has little relationship with the vertical natural crack, and the crack mainly affects the overall strength size of the shale. In the extension stage (Figure 11B), the 0° specimen cracks vertically upward and downward from the middle, and the stress is still concentrated at both ends of the natural crack; the 15° specimen cracks upward and downward not far from the end of the crack, and the stress is still mainly concentrated at both sides of the end of the crack; the 30°, 45°, 60°, and 75° specimens crack from both ends of the crack, and the stress follows the distribution of the new crack as the crack opens; the 90° specimen cracks from the lower part of the specimen, and the stress is mainly concentrated at both sides of the new cracks. This indicates that the presence of natural cracks within the shale has a significant effect on the stress distribution.

4.4 Evolutionary characteristics of acoustic emission distribution

Figure 12 shows the relationship between the stress, loading step, acoustic emission and cumulative acoustic emission for different natural crack inclination angles. In the RFPA2D-DIP numerical test, one acoustic emission event characterizes the microrupture of a cell, and the cumulative acoustic emission is the cumulative sum of acoustic emission events, which characterizes the overall number of cell microruptures (Liu et al., 2020c). As shown in Figure 12, the stress-loading step and the acoustic emission-loading step show good agreement, and the change phase for acoustic emission basically coincides with the change phase for shale stress.

In the eight sets of tests described in this paper, the tests with a natural crack inclination of 90° show the same trend as that for the control group (Figures 12G,H). Taking the uniaxial compression natural crack of 90° as an example (Figure 12G), in the first stage, the specimen shows a flat - nonlinear the accumulated acoustic emission. In the initial stage of loading (loading steps of 0–63), with increasing number of loading steps, the stress gradually increases, the number of acoustic emission events is 0, the accumulated acoustic emission number is also 0, showing a flat acoustic emission. In the process of gradual loading (loading steps of 64–196), with an increase in displacement loading, the stress continues to increase, the internal units of the shale begin to gradually undergo damage, the acoustic emission events gradually increase from 0, the accumulated acoustic emission exhibits nonlinear growth, and the stress magnitude gradually approaches the peak stress; In the second stage, the cumulative acoustic emission shows a sudden change—flat, as the loading step is further increased (loading step

FIGURE 11
Stress distribution of microstructure of shale. **(A)** Stress distribution in the initial stage. **(B)** Stress distribution in the extension stage.

is 196), the stress reaches a peak, and the number of acoustic emission events also reaches a peak, the shale cracks expand rapidly, and the cumulative acoustic emission grows abruptly, then the shale is completely destroyed. At this time, upon a further increase in the loading step (loading step is 197-), the stress magnitude shows a smooth change, and the number of acoustic emission events is close to 0. The cumulative acoustic emission shows a flattening. During the whole process for the natural crack dip angle of 90° and the control group, only one stress drop occurs, i.e., the stress instantaneously levels off after reaching the peak, and the acoustic emission and cumulative acoustic emission also level off after showing abrupt changes at the same loading step.

In six sets of tests with natural crack inclination angles of 0°, 15°, 30°, 45°, 60°, and 75° in uniaxial compression (Figures 12A–F), a minimum of two stress drops occur during loading, and a minimum of two sudden changes in acoustic emission and cumulative acoustic emission are observed. For the example of natural cracking in uniaxial compression at 75° (Figure 12F), the first stage of cumulative acoustic emission shows a flat—nonlinear response; in the initial stage of loading (loading steps 0–32), with an increasing number of loading steps, the stress gradually increases, the number of acoustic emission events is 0, the number of cumulative acoustic emission is also 0, showing a flat response. In the process of gradual loading (loading steps 33–189), with an increase in

FIGURE 12
Relationship among stress, AE count, cumulative AE count and loading steps under different angle. **(A)** 0˚, **(B)** 15˚, **(C)** 30˚, **(D)** 45˚, **(E)** 60˚, **(F)** 75˚, **(G)** 90˚, **(H)** Control group.
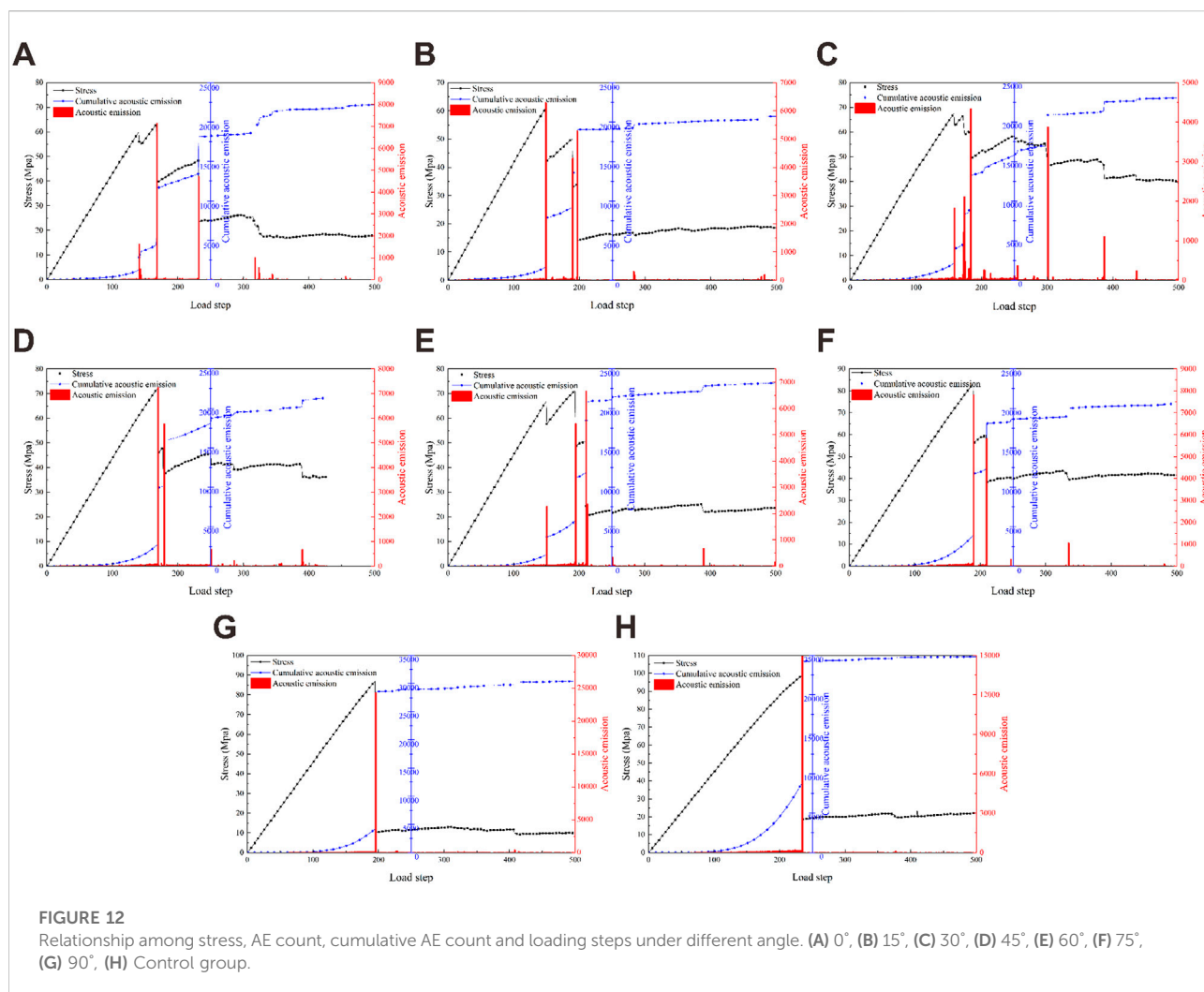
displacement loading, the stress continues to increase, the shale internal unit is gradually damaged, acoustic emission events gradually increase from 0, the cumulative acoustic emission shows a nonlinear growth, and the stress magnitude gradually approaches the peak stress observed for the first stress drop phenomenon; The cumulative acoustic emission in the second stage shows abrupt - nonlinear - abrupt - nonlinear - abrupt—flat behavior. With a gradual increase in the number of loading steps (190-), the specimen shows a total of three stress drop phenomena, and three abrupt changes in the corresponding acoustic emission and cumulative acoustic emission are observed to occur at loading steps of 190, 210, and 335, respectively, and the number of acoustic emission events is 7808, 5812, and 1040, corresponding to stress values of 82.97, 59.79, and 39.43 MPa, respectively, before leveling off.

Therefore, it is concluded that the acoustic emission signal shows good agreement with the variation in the mechanical properties and fracture process for naturally fractured shale containing different dip angles, as discussed above, and the

acoustic emission can reflect the stress variation and fracture process for naturally fractured shale containing different dip angles at the microscopic scale.

Fractal theory can be used to quantitatively describe irregularities and complexities, which naturally includes the evolution of rock fractures. The fractal dimension DS can be used to quantitatively describe the intensity and complexity of rock fractures (Zhang et al., 2018). In this paper, images of rock fractures at different stress levels with different natural crack inclinations were imported into a MATLAB calculation program to determine their corresponding fractal dimensions. The fractal dimension DS is solved as follows (Zhang et al., 2015):

$$D_S = -\lim_{\frac{1}{r} \to 0} \frac{\log N(r)}{\log \frac{1}{r}} \tag{2}$$

where Ds is the fractal dimension of the damaged region, r is the side length of the square box, and N(r) is the number of square boxes with side length r needed to cover the damaged region therein.

TABLE 2 AE energy and fractal dimension Ds at different stress levels for different natural crack inclination angles.

Stress level		10%	20%	30%	40%	50%	60%	70%	80%	90%	100%
Angle											
0°	AE energy	0	0.0001	0.0004	0.007	0.0014	0.006	0.0147	0.0376	0.095	0.6059
	Ds	0.6164	0.614	0.6979	0.7675	0.7616	0.787	0.7786	0.8144	0.8202	1.1812
15°	AE energy	0	0.0002	0.0012	0.0019	0.0014	0.0074	0.0412	0.1011	0.2188	0.7078
	Ds	0.6341	0.7233	0.8248	0.7859	0.8032	0.8034	0.8003	0.8	0.7923	1.2167
30°	AE energy	0	0	0.0001	0.0011	0.0027	0.0211	0.0703	0.1555	0.3415	0.6998
	Ds	0.6446	0.6478	0.6464	0.6773	0.7115	0.7506	0.7886	0.7866	0.8125	1.1843
45°	AE energy	0	0.0002	0.0003	0.0006	0.0061	0.0244	0.0821	0.1971	0.4453	2.0445
	Ds	0.5984	0.6545	0.6686	0.6953	0.6923	0.7169	0.7184	0.7037	0.7235	1.1943
60°	AE energy	0	0	0	0.0001	0.0029	0.0235	0.067	0.1442	1.5265	3.9967
	Ds	0.8092	0.8032	0.7807	0.8331	0.8673	0.897	0.9348	0.9121	0.9909	1.3873
75°	AE energy	0	0	0	0.0004	0.0089	0.0446	0.1431	0.3609	1.3555	2.957
	Ds	0.5935	0.5906	0.5794	0.5918	0.5889	0.6001	0.6276	0.6401	0.6376	0.995
90°	AE energy	0	0	0	0.0009	0.0117	0.0484	0.1415	0.3944	1.3997	6.3681
	Ds	0.6852	0.6872	0.9026	0.6872	0.6811	0.9026	0.6745	0.6745	0.6684	1.4219
Control group	AE energy	0	0	0	0.0063	0.0383	0.1444	0.4176	1.1289	3.9514	14.22
	Ds	0	0	0	0	0	0	0	0	0	1.5577

Table 2 shows the values for the AE energy and fractal dimension DS for different stress levels at different natural crack inclination angles, and Figure 13 shows the relationship between the stress level and AE energy and fractal dimension at different natural crack inclination angles. As shown in the figures, the AE energy increases with increasing stress level at any natural crack inclination angle; the overall trend is that the AE energy value corresponding to the peak stress increases with increasing natural crack inclination angle but decreases at a natural crack inclination angle of 75°, which is because at a natural crack inclination angle of 75°, the specimen extends along the direction of the crack inclination angle at both ends of the natural crack without extending the complex crack, the rupture form is simple, and the number of ruptured units is small.

As shown in the graph, the fractal dimension of the specimens from 0° to 90° is not 0 at a stress level of 10% due to the presence of natural cracks, while the fractal dimension values for the control group specimens, are 0 at the 10%–90% stress level due to the absence of natural cracks, and only when the stress level is 100% is the fractal dimension value 1.5577, which also shows the brittleness of the rock. For example, for a natural crack inclination of 0°, the fractal dimension value is 0.6164 at a stress level of 10%; due to the unevenness of the natural crack (wide at the middle and narrow at the ends), the shale is stressed to split from the middle of the natural crack up and down; when the stress level is 20%, the fractal dimension value is 0.614, which is slightly less than that at a stress level of 10%, which is because although the stress is increased (the crack splitting from the middle of the natural crack also expands) the increase in the stress also leads to compression of the natural
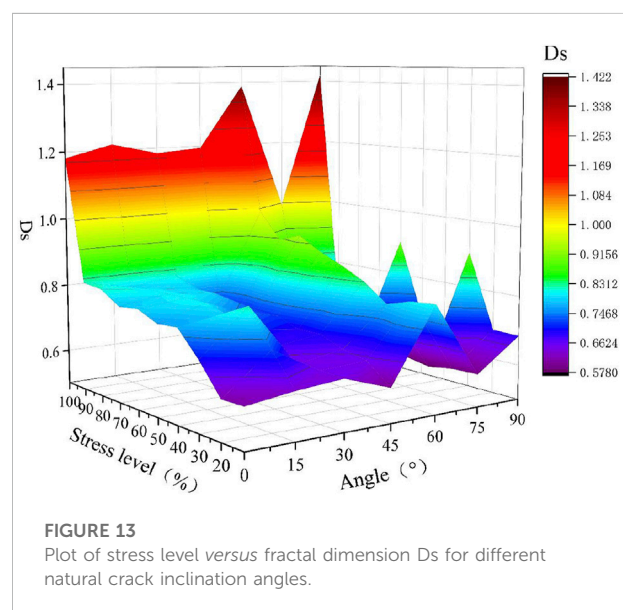
FIGURE 13
Plot of stress level *versus* fractal dimension Ds for different natural crack inclination angles.

crack to a certain extent, so the fractal dimension value is slightly reduced; in the process of increasing the stress level from 20% to 100%, the fractal dimension value zigzags upwards, which is because although the stress-induced crack expands, the natural crack is also gradually compressed, and the new cracks and the native natural cracks together affect the fractal dimension. In the test where the natural crack inclination angle ranges from 30°–90°, the value of fractal dimension is also influenced by the new cracks and the native natural cracks.

With an increase in the natural crack inclination angle, the fractal dimension value at the peak stress under the overall trend also increases, and the fractal dimension value at 90° is 1.4219, which is the maximum value of the fractal dimension in the test from 0° to 90°. However, for a natural crack inclination angle of 75°, the fractal dimension value is only 0.995, which is the same as the change law for the AE energy value because it cracks with both ends of the natural crack, and the fractal dimension value is only 0.995 for a natural crack inclination angle of 75°.

In summary, the magnitude of the AE energy is increased with increasing stress level in 0°–90° tests and reaches a maximum value at 90°, while the fractal dimension value zigzags upwards, which is due to the joint influence of the newborn cracks and the native natural cracks. In the process of increasing the stress level, the natural cracks are compacted, and the compacting phenomenon is decreased with increasing inclination angle of the natural cracks. In the control test, both AE energy and fractal dimension values are increased with increasing stress level. The overall trend for the AE energy and fractal dimension values under peak stress show a continuous increase with increasing inclination angle of the natural crack, while the maximum value is reached in the control test, and only a significant decrease is observed in the 75° test, which is because the 75° specimen extends along the direction of the crack inclination angle at both ends of the natural crack without extending the other cracks, i.e., the rupture form is simple.

5 Conclusion

Shale specimens obtained from the Lower Cambrian Niuhuitang Formation of the Qianbei region were studied in this paper. The shale samples were observed by scanning electron microscopy, a natural crack was selected, and the microstructure of the shale with natural cracks was obtained by correlation processing. Seven groups of digital images of shale with natural cracks at different dips and a control group without cracks were imported using RFPA2D-DIP. Numerical models were built in turn, numerical tests (uniaxial compression) were carried out for each of the eight groups of specimens, and the following conclusions were obtained:

1) The dip angle for the natural fracture has an important influence on the mechanical characteristics of shale. As the natural fracture inclination angle increases, the peak stress and modulus of elasticity of shale as a whole tend to increase; however, compared to the intact specimens, the strength loss due to the natural fracture tends to show an overall decrease, and during fracture, the damage is more complex compared to that for the control group, except for the specimens with a natural fracture inclination angle of 90°, where one or two stress drops occur after the peak stress.

2) The dip angle of the natural fracture has an important influence on the fracture pattern of the shale. The fracture patterns for shales containing natural fractures at the microscopic scale can be broadly divided into four categories: when the natural fracture inclination angle is 0°, the central part of the fracture is cracked in tension and is accompanied by the compression of the natural fracture to extend in the direction of loading, eventually forming a similar I-shaped fracture; when the natural fracture inclination angle is 15°, 45°, 60°, and 75°, tensile damage occurs at the ends of the natural fracture, accompanied by the extension of the budding fracture and microfracture connection. When the natural crack inclination angle is 30°, the natural crack end produces a wing-shaped crack and continues to stretch and break along the wing crack, eventually forming a folded crack; when the natural crack inclination angle is 90°, the crack initiation and expansion is not affected by the natural crack, and a V-shaped crack is eventually formed as the microcrack expands, connects and penetrates.

3) The microstructure of shale has an important influence on the main stress distribution. In the initial stage, the stresses in the 0°–75° specimens are mainly distributed at the ends of the fractures or at the top and bottom sides, while the 90° specimens show no obvious stress distribution at the natural fractures; in the rupture stage, the stresses in the 0° and 15° specimens are still mainly distributed at the ends of the fractures, while the stresses in the 30°–90° specimens are distributed in the direction of fracture expansion, and the stress concentration phenomenon is obvious. This indicates that the presence of natural cracks within the shale has a significant influence on the distribution of the principal stresses.

4) Acoustic emission can reflect the stress changes and rupture process for naturally fractured shales containing different dip angles at the microscopic scale. In the 0°–90° test, the magnitude of the AE energy is positively correlated with the stress level, and the overall trend for the AE energy increases with increasing inclination angle of natural fractures at peak stress, with a significant decrease observed only in the 75° test.

5) The presence of natural cracks has a significant effect on the fractal dimension. The fractal dimension is controlled by both natural and nascent cracks and is increased with increasing stress level, with the fractal dimension at peak stress increasing with the natural crack inclination, except for the 75° test, where it shows a significant decrease.

Data availability statement

The original contributions presented in the study are included in the article/supplementary material, further inquiries can be directed to the corresponding author.

Author contributions

Writing-original draft preparation, CY; writing-review and editing, ZW; methodology, CY; software, CY; formal analysis, CY; investigation, WW; resources, HL; data curation, HQ and NR; funding acquisition, ZW All authors have read and agreed to the published version of the manuscript.

Funding

Conflict of interest

Publisher's note

References

Ban, Y., Fu, X., Xie, Q., Duan, J., and Abdullah, R. (2021). Failure characteristics of obliqued-layers shale specimens from ex-perimental observation. *Arab. J. Sci. Eng.* 46, 10757–10770. doi:10.1007/s13369-021-05538-2

Chen, J., Li, Y., Ma, H., Wang, X., and Li, S. (2020). Experimental study on the three-axis compression of shale considering the influence of the crack. *Sci. Technol. Eng.* 20 (26), 10778–10782.

Cui, H., Wu, Z., Lou, Y., Zuo, Y., Sun, W., and Liu, H. (2020). Numerical experiment on damage and fracture of shale based on micro-scale. *Coal Geol. Explor.* 48 (5), 137–143.

Feng, X., Ma, F., Zhao, H., and Guo, J. (2021). Numerical simulation of hydraulic fracturing in shale gas reservoirs under fault influence. *J. Eng. Geol.* 29 (3), 751–763.

He, B., Liu, J., Zhao, P., and Wang, J. (2021). PFC2D-based investigation on the mechanical behavior of anisotropic shale under Brazilian splitting containing two parallel cracks. *Front. Earth Sci.* 15 (4), 803–816. doi:10.1007/s11707-021-0895-8

Heng, S., Yang, C., Zhang, B., Guo, Y., Wang, L., and Wei, Y. (2015). Experimental research on anisotropic properties of shale. *Rock Soil Mech.* 36 (03), 609–616.

Hu, Y., Li, X., Zhang, Z., He, J., and Li, G. (2020). Numerical investigation on the hydraulic stimulation of naturally fractured Longmaxi shale reservoirs using an extended discontinuous deformation analysis (DDA) method. *Geomech. Geophys. Geo-energ. Geo-resour.* 6, 73. doi:10.1007/s40948-020-00195-5

Jin, J., Zheng, X., Fu, Y., Chen, T., Yang, D., and Zhong, H. (2021). Experimental study of acidization impact to pore topo-logical structure variation of Niutitang shale. *J. Eng. Geol.* 29 (3), 891–900.

Ju, W., Wu, C., and Sun, W. (2018). Effects of mechanical layering on hydraulic fracturing in shale gas reservoirs based on numerical models. *Arab. J. Geosci.* 11, 323. doi:10.1007/s12517-018-3693-1

Lan, H., Chen, J., and Wu, Y. (2018). Spatial characterization of micro- and nanoscale micro-cracks in gas shale before and after triaxial compression test. *J. Eng. Geol.* 26 (1), 24–35.

Lee, H., and Jeon, S. (2011). An experimental and numerical study of fracture coalescence in pre-cracked specimens under uniaxial compression. *Int. J. Solids Struct.* 48, 979–999. doi:10.1016/j.ijsolstr.2010.12.001

Lisjak, A., Grasselli, G., and Vietor, T. (2014). Continuum–discontinuum analysis of failure mechanisms around unsupported circular excavations in anisotropic clay shales. *Int. J. Rock Mech. Min. Sci. (1997).* 65, 96–115. doi:10.1016/j.ijrmms.2013.10.006

Liu, H., Zuo, Y., Wu, Z., Sun, W., and Xi, S. (2020). Study of concrete internal crack growth deformation law and fracture process using digital images. *Concrete* (01), 32–37+40.

Liu, J., Cao, X., Xu, J., Yao, Q., and Ni, H. (2020). A new method for threshold determination of gray image. *Geomech. Geophys. Geo-energ. Geo-resour.* 6, 72. doi:10.1007/s40948-020-00198-2

Liu, J., Liang, X., Xue, Y., Fu, Y., Yao, K., and Dou, F. (2020). Investigation on crack initiation and propagation in hydraulic fracturing of bedded shale by hybrid phase-field modeling. *Theor. Appl. Fract. Mech.* 108, 102651. doi:10.1016/j.tafmec.2020.102651

Liu, Y., Gao, D., Li, Q., Wan, Y., Duan, W., Zeng, X., et al. (2019). Mechanical frontiers in shale-gas development. *Adv. Mech.* 49 (00), 1–236.

Lou, Y., Wu, Z., Sun, W., Yin, S., Wang, A., Liu, H., et al. (2020). Study on failure models and fractal characteristics of shale under seepage-stress coupling. *Energy Sci. Eng.* 8, 1634–1649. doi:10.1002/ese3.621

Nezhad, M., Fisher, Q., Gironacci, E., and Rezania, M. (2018). Experimental study and numerical modeling of fracture propagation in shale rocks during Brazilian disk test. *Rock Mech. Rock Eng.* 51, 1755–1775. doi:10.1007/s00603-018-1429-x

Shi, X., Zhang, X., Wang, B., Tang, T., and Han, W. (2018). Hydraulic fracturing test with prefabricated crack on anisotropic shale, Laboratory testing and numerical simulation. *J. Petroleum Sci. Eng.* 168, 409–418. doi:10.1016/j.petrol.2018.04.059

Shrestha, N., Chilkoor, G., Wilder, J., Gadhamshetty, V., and Stone, J. J. (2016). Potential water resource impacts of hydraulic fracturing from unconventional oil production in the Bakken shale. *Water Res.* 108, 1–24. doi:10.1016/j.watres.2016.11.006

Wang, G., Xiao, Y., Zhao, H., Wang, Y., and Chen, Y. (2019). Application of microseismic monitoring technology to re–fracturing of shale gas horizontal wells. *Geol. Explor.* 55 (5), 1336–1342.

Wang, H., Li, Y., Cao, S., Pan, R., Yang, H., Zhang, K., et al. (2020). Brazilian splitting test study on crack propagation process and macroscopic failure mode of pre-cracked black shale. *Chin. J. Rock Mech. Eng.* 39 (05), 912–926.

Wang, R., Gu, Y., Ding, W., Gong, D., Yin, S., Wang, X., et al. (2016). Characteristics and dominant controlling factors of organic-rich marine shales with high thermal maturity, A case study of the Lower Cambrian Niutitang Formation in the Cen'gong block, southern China. *J. Nat. Gas Sci. Eng.* 33, 81–96. doi:10.1016/j.jngse.2016.05.009

Wang, S., Zhao, J., and Li, Y. (2014). Hydraulic fracturing simulation of complex fractures growth in naturally fractured shale gas reservoir. *Arab. J. Sci. Eng.* 39, 7411–7419. doi:10.1007/s13369-014-1221-5

Wang, Y., Li, X., Zhang, Y., and Zheng, B. (2016). Gas shale hydraulic fracturing, a numerical investigation of the fracturing network evolution in the Silurian Longmaxi formation in the southeast of Sichuan Basin, China, using a coupled FSD approach. *Environ. Earth Sci.* 75, 1093. doi:10.1007/s12665-016-5696-0

Wei, Y., Yang, C., Guo, Y., Liu, W., Wang, L., and Heng, S. (2015). Experimental investigation on deformation and fracture characteristics of brittle shale with natural cracks under uniaxial cyclic loading. *Rock Soil Mech.* 36 (06), 1649–1658.

Weibull, W. (1951). A statistical distribution function of wide applicability. *J. Appl. Mech.* 18, 293–297. doi:10.1115/1.4010337

Wu, Z., Lou, Y., Yin, S., Wang, A., Liu, H., Sun, W., et al. (2020). Acoustic and fractal analyses of the mechanical properties and fracture modes of bedding-containing shale under different seepage pressures. *Energy Sci. Eng.* 8, 3638–3656. doi:10.1002/ese3.772

Wu, Z., Zuo, Y., Wang, S., Chen, J., Wang, A., Liu, L., et al. (2017). Numerical study of multi-period palaeotectonic stress fields in Lower Cambrian shale reservoirs and the prediction of fractures distribution, A case study of the Niutitang Formation in Feng'gang No. 3 block, South China. *Mar. Pet. Geol.* 80, 369–381. doi:10.1016/j.marpetgeo.2016.12.008

Wu, Z., Zuo, Y., Wang, S., Sun, W., and Liu, L. (2018). Experimental study on the stress sensitivity and influence factors of shale under varying stress. *Shock Vib.* 2018, 1–9. doi:10.1155/2018/3616942

Xu, X., Shen, B., Li, Z., Zhang, W., Yu, L., and Ma, Z. (2020). Status and prospect of experimental technologies of geological evaluation for shale gas. *Reserv. Eval. Dev.* 10 (1), 1–8.

Yu, S., Ren, X., Wang, H., Zhang, J., and Sun, Z. (2021). Numerical simulation on the interaction modes between hydraulic and natural fractures based on a new SPH method. *Arab. J. Sci. Eng.* 46, 11089–11100. doi:10.1007/s13369-021-05672-x

Zhang, R., Dai, F., Gao, M., Xu, N., and Zhang, C. (2015). Fractal analysis of acoustic emission during uniaxial and triaxial loading of rock. *Int. J. Rock Mech. Min. Sci. (1997).* 79, 241–249. doi:10.1016/j.ijrmms.2015.08.020

Zhang, S., Shou, K., Xian, X., Zhou, J., and Liu, G. (2018). Fractal characteristics and acoustic emission of anisotropic shale in Brazilian tests. *Tunn. Undergr. Space Technol.* 71, 298–308. doi:10.1016/j.tust.2017.08.031

Zhao, P., Xie, L., Ge, Q., Zhang, Y., Liu, J., and He, B. (2020). Numerical study of the effect of natural fractures on shale hydraulic fracturing based on the continuum approach. *J. Petroleum Sci. Eng.* 189, 107038. doi:10.1016/j.petrol.2020.107038

Zheng, H., Pu, C., and Tong, I. (2019). Study on the interaction mechanism of hydraulic fracture and natural fracture in shale formation. *Energies* 12, 4477. doi:10.3390/en12234477

Zhu, Y., Liu, K., Zhong, X., Wang, Y., Chen, C., Zhang, H., et al. (2021). Experimental investigation on the anisotropic behaviors induced by bedding planes in mechanical properties of ma'quan oil shale. *Arab. J. Sci. Eng.* 47, 11385–11403. doi:10.1007/s13369-021-06027-2

Zhu, Z., Xiao, P., Sheng, Q., Liu, J., and Leng, X. (2011). Numerical simulation of fracture propagation of heterogeneous rock material based on digital image processing. *Rock Soil Mech.* 32 (12), 3780–3786.

Zou, Y., Zhang, S., Ma, X., Zhou, T., and Zeng, B. (2016). Numerical investigation of hydraulic fracture network propagation in naturally fractured shale formations. *J. Struct. Geol.* 84, 1–13. doi:10.1016/j.jsg.2016.01.004

Fracture development and controlling factors at metamorphic buried-hill reservoirs of Bozhong 19-6 gas field in Bohai Bay, East China

Lijun Mi[1], Tingen Fan[1], Hongjun Fan[1], Tao Niu[1], Lei Gong[2]*, Xiaocen Su[2], Yonghe Sun[2] and Yuqi Cheng[2]

[1]CNOOC Research Institute Ltd., Beijing, China, [2]Bohai-Rim Energy Research Institute, Northeast Petroleum University, Qinhuangdao, China

Fractures of multi-scales and multi-origins are primary storage space and effective seepage channels for metamorphic buried-hill reservoirs. They not only allow communication between various pores to enhance storage and seepage capacity, but also are essential for high yields. Fracture development and controlling factors at metamorphic buried-hill reservoirs of Bozhong 19-6 Gas Field were investigated based on imaging log, core data, experiments, e.g., thin sections and scanning electron microscope, and outcrop description. Results show that structural fractures, weathering fractures and dissolution fractures were developed in the metamorphic buried-hill reservoirs in the study area, among which structural fractures and weathering fractures are the most popular ones. However, fracture types varied obviously among different structure positions. Lithology, fault, weathering crust and ancient landform are primary factors affecting fracture distribution. Fractures were prone to be developed at lithology with high bright mineral contents. Faults were characterized by a dual structure including fault core and damage zone. Fracture density followed a decreasing trend with increasing distance from faults. Damage zone could be identified when fracture density was consistent with regional fracture density. The width of the damage zone was determined by factors such as fault scale and structure location. Well-connected weathering fractures were popular at the leached unit, with structural fractures of secondary importance. The unweathered unit was dominated by structural fractures with low density.

Introduction

Continuing oil and gas exploration activities at deep and ultra deep basins have made buried-hill reservoirs important exploration targets in recent years (Hou et al., 2013; Wang et al., 2015; Zhou et al., 2022). A large number of buried-hill reservoirs have been discovered in metamorphic rocks or granite basement at Baihu Oilfield in Vietnam and Bongor Basin in Chad (Dou et al., 2015; Wang et al., 2019; Luo et al., 2020; Luo et al., 2021; Zhou et al., 2022). Recently, major breakthroughs have also been made at the Archeozoic metamorphic buried-hill reservoirs at the Bohai Bay Basin, China, e.g., reserves of 100 million tons have been discovered at Jinzhou 25-1 metamorphic buried-hill, Xinglongtai buried hill at Liaohe Basin and Bozhong 19-6 metamorphic buried hill (Luo et al., 2014; Luo et al., 2016; Wang et al., 2019; Xu et al., 2020; Ye et al., 2021). Multiple types of buried-hill reservoirs were developed in petroliferous basins, where a large number of structural fractures and weathering fractures grew due to multi-stage tectonic movements and long-term weathering. These fractures were developed into complex fracture networks, complicating structure of metamorphic buried-hill reservoirs with strong heterogeneity (Luo et al., 2014; Xu et al., 2020; Ye et al., 2021). As a result, oil and gas enrichment was not only controlled by lithologies and reservoir properties, etc., but also was directly determined by fracture development [(Zhou et al., 2022), (Zhou et al., 2005; Luo et al., 2014; Deng, 2015; Luo et al., 2016; Hu et al., 2017; Zhou et al., 2017; Xu et al., 2020; Fan et al., 2021; Ye et al., 2021)]. Previous studies show that natural fractures can not only provide storage space for oil and gas accumulation at metamorphic buried-hill reservoirs, but also are effective seepage channels (Gao et al., 2015; Gong et al., 2016), since they not only communicate pores and enhance permeability of metamorphic buried-hill reservoirs, but also govern high yields (Huang et al., 2016; Hu et al., 2017; Xue et al., 2020). However, as suggested by increasing exploration and development activities, fracture characteristics and development mechanism at buried-hill reservoirs as well as primary controlling factors are poorly understood (Zeng et al., 2016; Chen et al., 2018), which brings considerable challenge for fracture distribution prediction and exerts significantly negative impact on drilling and reservoir development (Gong et al., 2017). Taking metamorphic buried-hill reservoirs at Bozhong 19-6 Gas Field as an example, this paper used imaging log, core data, and experiments, e.g., thin sections and scanning electron microscope (SEM) images, etc., to investigate genetic types and distribution of fractures in metamorphic reservoirs. After that, primary controlling factors of fractures development at metamorphic buried-hill reservoirs were analyzed based on weathering crust and fault system on outcrops as well as fracture distribution under different landforms.

FIGURE 1
Structure location of Bozhong 19-6 Gas Field (Gong et al., 2019a).
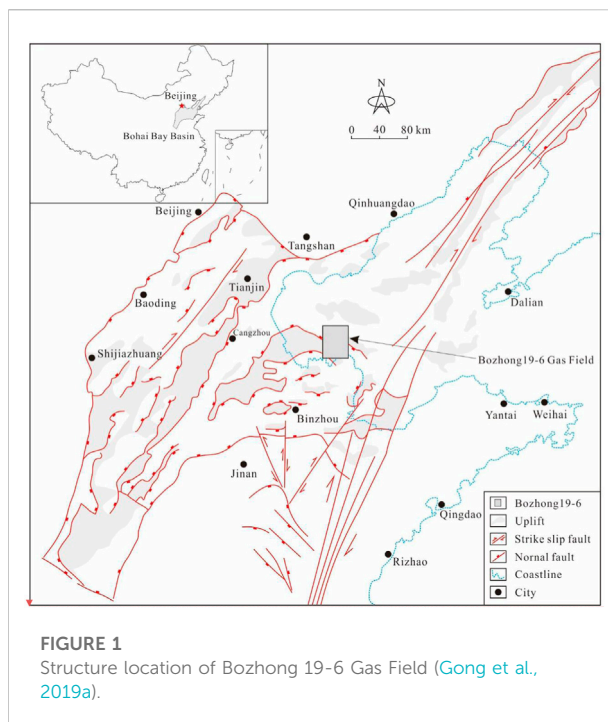
Geological setting

Bozhong 19-6 Gas Field is located at the southwest of Bozhong Sag, bounded by Bozhong Sag, Shanan Sag and Huanghekou Sag. It is a faulted anticline complicated by strike slip faults and associated faults, with a structure pattern of "a high-in-sag" (Figure 1) (Dou et al., 2015; Xie, 2020; Xue et al., 2020; Fan et al., 2021). The strata drilled in Bozhong 19-6 Gas Field are: the Quaternary Pingyuan Formation, the Neogene Minghuazhen Formation and the Guantao Formation, the Paleogene Dongying Formation, the Shahejie Formation and the Kongdian Formation, and the Archaeozoic buried hill, from top to bottom. Drilling data shows that, except the Pingyuan Formation, hydrocarbon intervals are developed in all these Formations, with oil intervals at the shallow and gas intervals at the deep (Hou et al., 2019; Xu et al., 2019; Chen et al., 2021; Luo et al., 2021). The Archaeozoic buried hill is complicated in lithology, which can be divided into two types, i.e., metamorphic rocks and intrusive rocks, with six sub types. The metamorphic rocks can be further divided into regional metamorphic rocks, dynamic metamorphic rocks and migmatite. The regional metamorphic rocks include metamorphic granite and gneiss. The dynamic metamorphic rocks are cracked gneiss and cataclasite. The migmatite is primarily migmatite gneiss and migmatite granite. The magmatite can be divided into acidic intrusion-granite, intermediate intrusion-diorite porphyry and basic intrusion-diabase.

The metamorphic rocks are minerally composed of bright quartz, plagioclase and potassium feldspar. The feldspar and quartz account for 20.0%–100.0%, with an average of 91%. The dark minerals, mainly biotite, white mica, hornblende, with a small
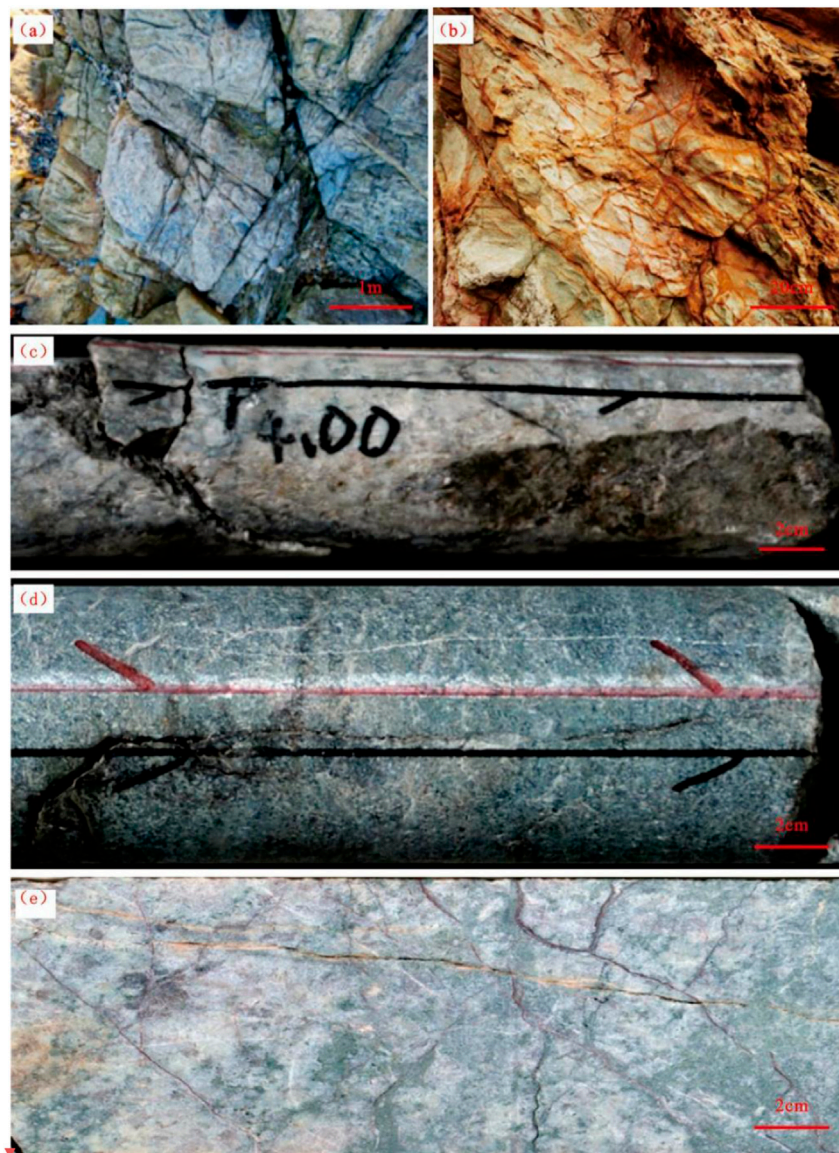
FIGURE 2
Fracture types and development characteristics in the study area. **(A)** Structural fractures. **(B)** Weathering fractures. **(C)** Shear fractures. **(D)** Extensional fracture. **(E)** Weathering fractures.

amount of siderite. Pyrite and ankerite, are low in content, between 5% and 15%, with an average of 9%. The buried-hill reservoirs are commonly dual media those are primarily composed of macro fractures, micro fractures, intergranular pores, intragranular solution pores, etc. (Zhou et al., 2022) They are primarily fractured-porous ones and porous-fractured ones, followed by fractured ones and porous ones. Core analysis shows that, the Archaeozoic buried hill is 0.8 %–15.8% in porosity, with an average of 6.4% and a median of 6.7%. The permeability ranges from 0.02 mD to 508.61 mD, with an average of 8.90 mD and a median of 0.24 mD. Log interpretation suggests, the porosity is 1.0%–25.8%, with an average of 4.5% and a

median of 3.8%, and the permeability is between 0.003 mD and 696.10 mD, with an average of 4.24 mD and a median of 0.02 mD.

Fracture development

Fracture types and characteristics

Structural fractures, weathering fractures and dissolution fractures can be identified from the study area based on outcrops, imaging log, cores, thin sections and SEM images.

FIGURE 3
Fracture characteristics on imaging log.
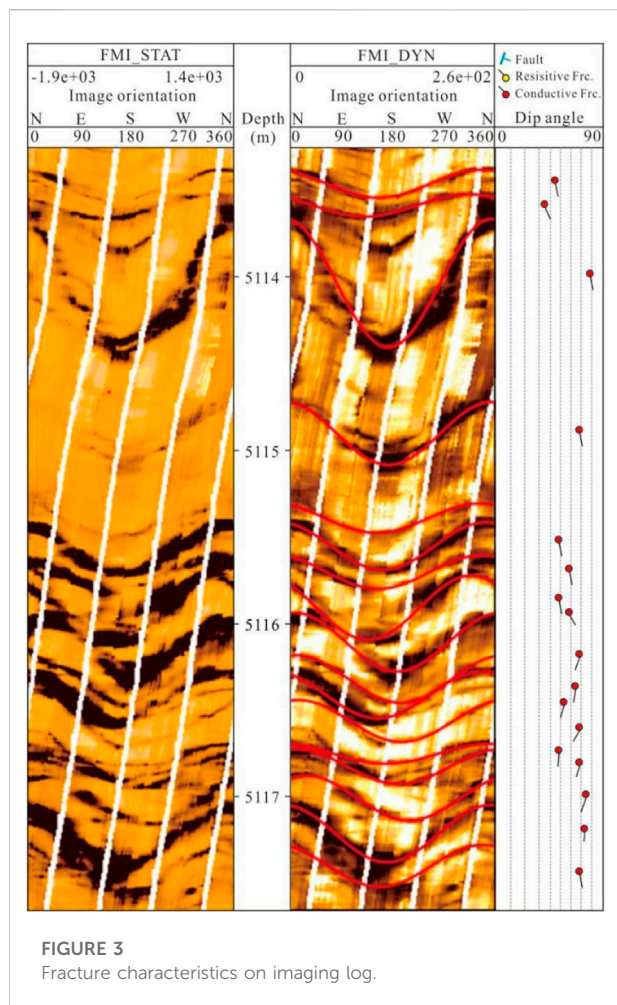
Among them, structural fractures and weathering fractures are the primary ones, while some of them were dissolved to form dissolution fractures (Figure 2).

Structural fractures are referred to natural fractures derived from regional or local tectonic stress field, which are well developed in all kinds of metamorphic rocks and granites, with large scale and long extension. They are generally several meters to tens of meters in length, with the maximum up to hundreds of meters (Figure 2A). These fractures often appear in groups with obvious regularity and orientation but no obvious variation in occurrence. Structural fractures are the most popular ones in metamorphic reservoirs in the study area, which are characterized by multi-phases, multi-orientations, uneven development with various scales and filling behaviors. They can also be divided into shear fractures and extensional fractures based on their mechanical properties. Shear fractures, mainly oblique fractures and high-angle fractures, are generally conjugated in various lithologies with flat and smooth surfaces. Slips and steps can be observed in some samples, which are partly filled by calcite (Figure 2C). They

are extended widely with large length, which can cut through several layers. Some shear fractures are slipped obviously (with displacement of 2–5 cm) to form small-scale faults with small fault cores, including structural lenses, breccias and fault gouges, etc. Extensional fractures have rough and uneven surfaces, which are often filled with minerals. They are irregularly distributed in the study area with high dip angle and small length (Figure 2D).

Weathering fractures are commonly extensional ones derived from physical or chemical weathering of exposed rocks, in honeycomb or network pattern with high density. However, they are irregularly distributed with bend or arc-shaped surface and unstable occurrence. These fractures are relatively small in extension, generally centimeter-scale to decimeter-scale with dip angles of 0–90°, but some can be up to meter-scale. They are commonly filled with clay minerals, or are contaminated by iron (oxidized to red) (Figures 2B,E). Dissolution fractures mainly occur along early weathering fractures and/or structural fractures, which widens fracture apertures and are accompanied by dissolution holes locally (Figure 3).

Quantitative fracture characterization

Two types of resistive fractures and conductive fractures were identified from imaging logs (Figure 3), among which conductive fractures (effective fractures) are the main ones (Figure 4A), indicating good fracture effectiveness. Imaging log interpretation suggests that fractures in the study area are complex in orientation, which are primarily extended along NE-SW, near E-W, near N-S and NW-SE trending (Figure 4B). Fracture orientation varies greatly among different structure positions, especially at the structure high, near faults and at fault intersections, where orientations are generally consistent with fault strikes. They are mainly oblique fractures with dip angle of 30°–60°, followed by bedding-parallel fractures and subvertical fractures (Figure 4C). The fracture density identified by imaging log is 1–5 m^{-1}, which is higher in the semi-weathered zone compared with unweathered zone (Figure 4D). However, multiple fractured units are also developed in the unweathered zone.

Core observations show that, the dip angle of fractures is distributed between 0° and 90°, with the peak value at 30°–70°. It varies significantly among different fracture types. e.g., 60°–90° for structural fractures, and 30°–60° for weathering fractures (Figure 5A). The fracture length on cores is about 5–15 cm, with an average of 9.39 cm and a maximum of 45 cm (Figure 5B). The structural fractures are large in length, generally about 12–20 cm, with an average of 17.09 cm. Different from that, weathering fractures are short, with length of 4–7 cm and an average of 5.81 cm. Fractures are popular on cores, especially in the weathering zone. The areal density of weathering fractures is about 30–70 m/m², with an
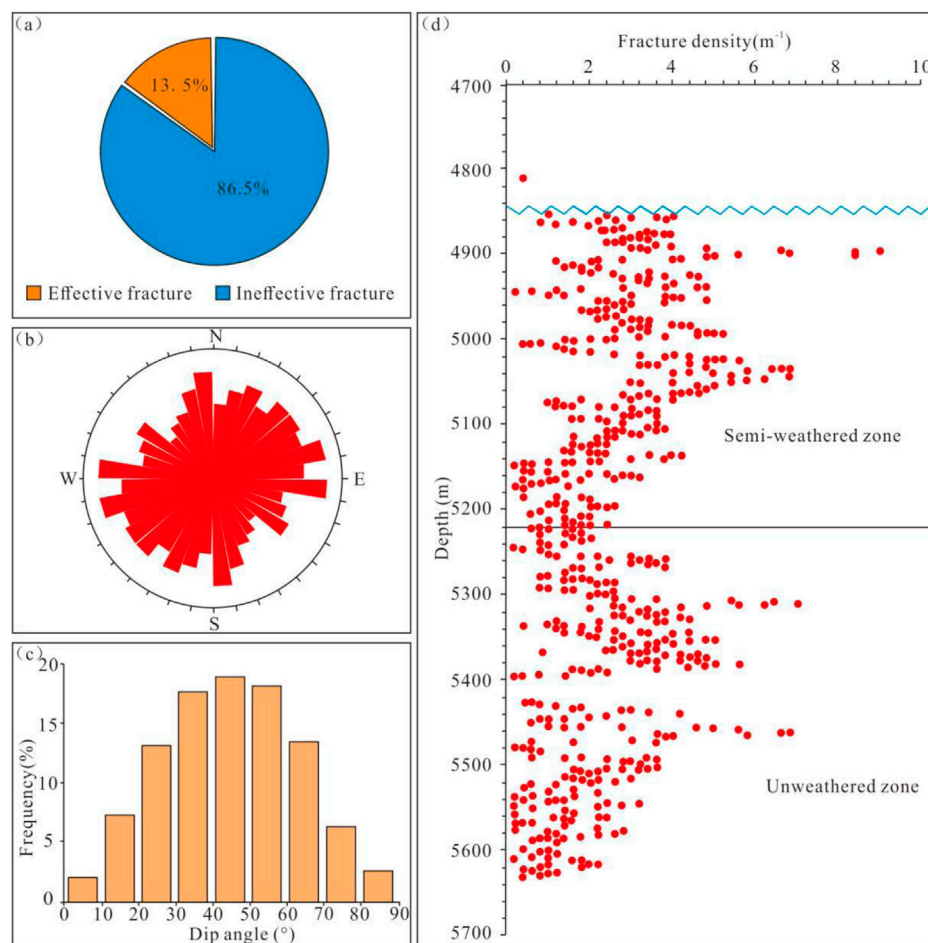
FIGURE 4
Quantitative characterization of fracture parameters and fracture distribution on imaging log. **(A)** Pie chart of fracture effectiveness. **(B)** Rose diagram of fracture strikes. **(C)** Diagram of dip angle distribution. **(D)** Fracture intensity and distribution in vertical.

average of 53.0 m/m^2, and it is up to 93 m/m^2 at local position (Figure 5C). The value of structural fractures is about 10–30 m/m^2, with an average of 20.1 m/m^2. These fractures are highly filled by mudstone, iron and a small amount of calcite, where 68% of weathering fractures are completely filled, 15% are half filled, 17% are not filled, and thereby only 32% are effective fractures (Figure 5D).

Discussion

The Bozhong 19-6 buried-hill reservoirs were developed at early stage and experienced multiple and complex geological events at later stage, resulting in strong heterogeneity in natural fracture distribution. Investigation on weathering crusts and fault zones on outcrops and fracture distribution at underground as well as another data shows that nature fracture development at

buried-hill reservoirs in the study area is mainly controlled by lithology, weathering crusts, faults and ancient landform, etc.

Lithology

Lithology is the primary factor regulating fracture development under the same tectonic stress (Gong et al., 2019b; Lyu et al., 2019; Gong et al., 2021a; Cao et al., 2021; Gong et al., 2022), since mechanical properties of rocks vary as a function of mineral compositions, structures and textures. The influence of lithology and mineral compositions on fracture development was analyzed based on similar outcrops, cores and thin sections. Fractures are well developed at six lithologies in the study area, e.g., cataclasite, with a linear density of 43.46 m^{-1}, followed by metamorphic granite and granite gneiss, while they are poorly developed at rocks with
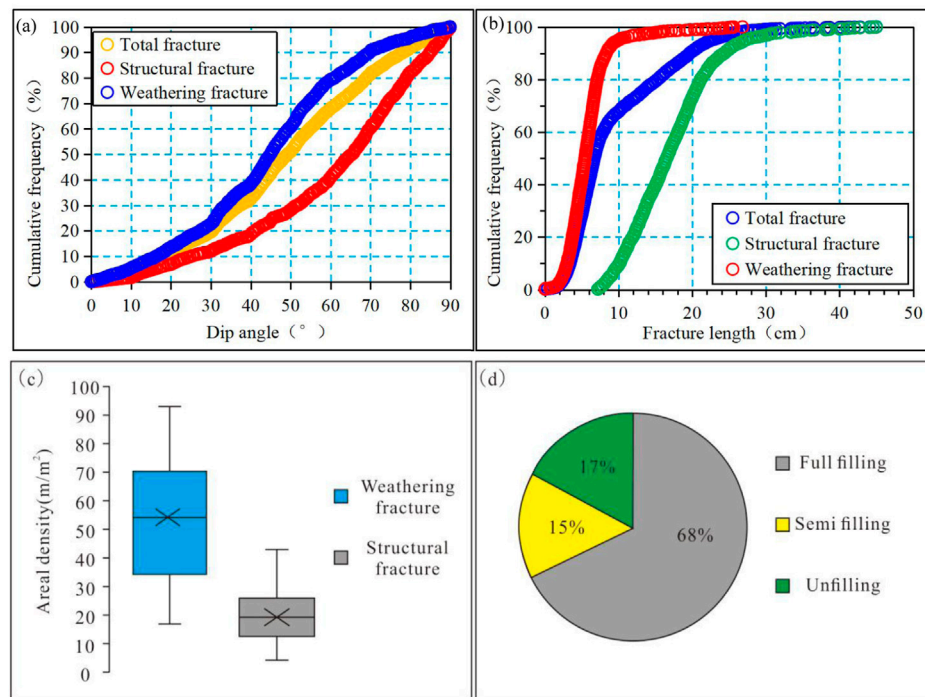
FIGURE 5
Quantitative characterization of fracture parameters and fracture distribution on cores. **(A)** Dip angle of fracture. **(B)** Fracture length. **(C)** Fracture intensity. **(D)** Fracture effectiveness.
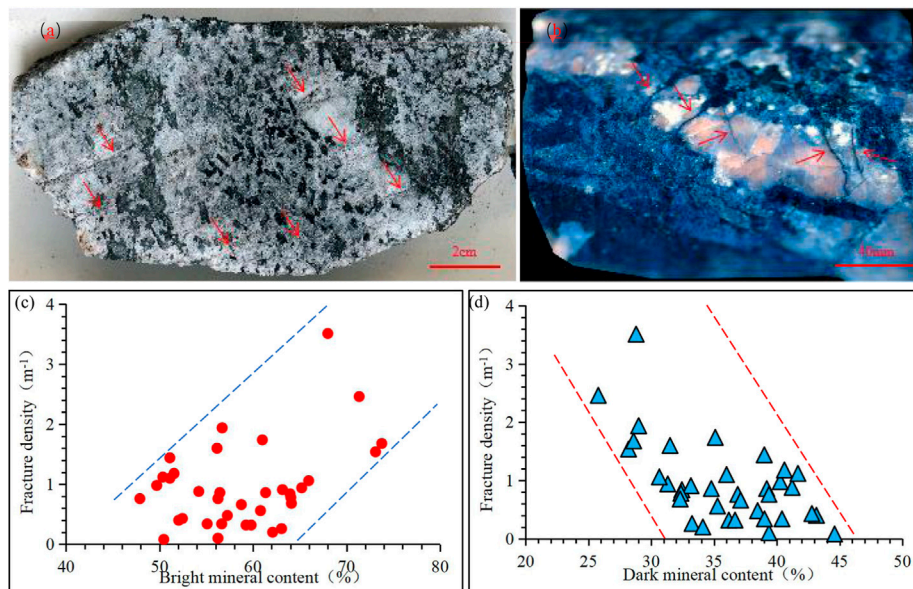
FIGURE 6
Controlling of lithology on fracture distributions. **(A,B)** Variation in fracture development with mineral types. **(C)** Relationship between bright mineral contents and fracture development. **(D)** Relationship between dark mineral contents and fracture development.
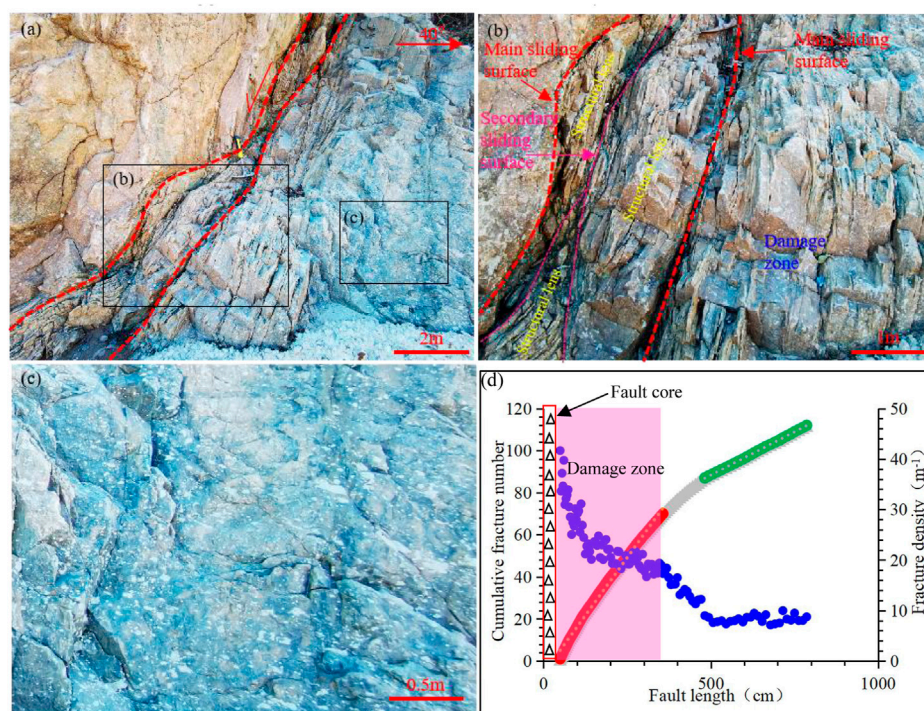
FIGURE 7
Internal structure of fault zone at Gushiyu village. **(A)** The overall characteristics of Gushiyu fault; **(B)** characteristics of the fault core; **(C)** characteristics of fracture development in the host rock; **(D)** distribution characteristics of fractures near faults.

high dark mineral content, e.g., amphibole and pyroxene, with linear density of 6.65 m^{-1}.

Mineral compositions are important elements to determine fracture development under the same geological conditions (Wang et al., 2022). Samples from outcrops and cores show that, fractures are mainly developed in rocks with high bright mineral contents (quartz, feldspar, etc.), with density up to 40-50 m^{-1}) (Figure 6). These fractures generally terminate abruptly at the boundary between light and dark minerals, and only a small number of large structural fractures pass through this boundary. Ductile deformation is commonly occurred to the units with high dark mineral content (biotite, hornblende, etc.), where fractures are poorly developed, with density less than 5 m^{-1}. The comparison between mineral contents derived from XRD analysis and fracture development shows that the bright mineral contents are significantly positively correlated with fracture development, whereas the dark mineral contents are negatively correlated with fracture development (Figure 6).

Fault structure

Faults those can regulate stress distribution at different structure units (Gong et al., 2021b; Ferrill et al., 2021; Zeng

et al., 2022) *via* stress disturbance can significantly control fracture development at metamorphic buried-hill reservoirs. Generally, obvious stress concentration along faults can enhance fracture development. Considerable previous studies confirm that fault system is characterized by a dual structure that can be divided into two units, i.e., fault core and damage zone (Zeng et al., 2022; Gong et al., 2021b; Peacock et al., 2017). The fault core is generally composed of sliding surface, fault gouge, breccia, structure lens and cataclasite, and the damage zone is composed of fractures and secondary faults with different scales (Choi et al., 2016). Figure 7 shows a typical fault at metamorphic rocks at the Gushiyu village in the north of Qinhuangdao city. The hanging wall is dominated by sandstone and the footwall is slate or schist. It is a normal fault with occurrence of 165°<80°and displacement of 8–10 m.

Fault core and damage zone can be identified from this fault system. The core is 10–50 cm in thickness, mainly composed of primary sliding surface, secondary sliding surface and structure lens. The structure lens are large in scale, with size of 0.25 m×2.0-0.1 m×0.3 m. Fractures in the structure lens are well developed, with density up to 30–40 m/m². The fault core is an open one with no fillings, which can act as a predominant seepage channel. Fractures are densely developed near the sliding surface, with average density of 20–30 m/m² and fracture spacing as low as
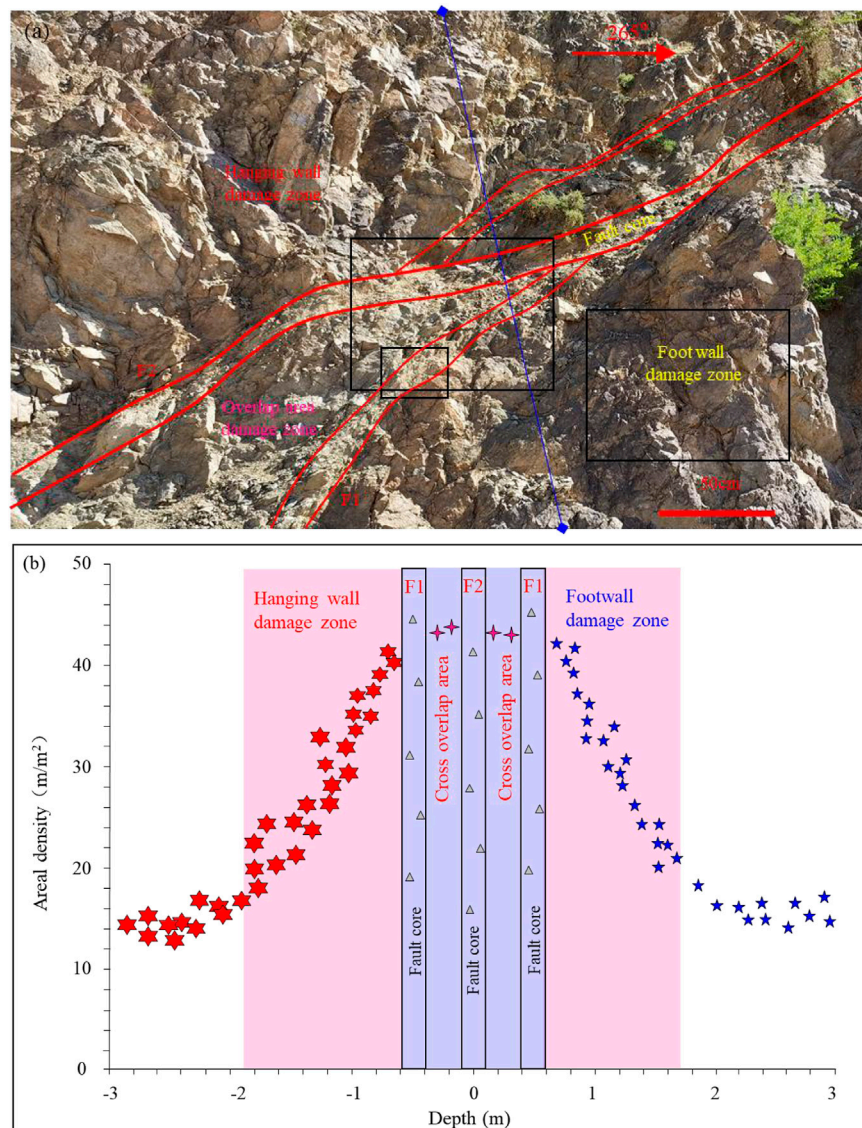
FIGURE 8
Fault structure and distribution of associated fractures at Huoqing Road. **(A)** The overall characteristics of Huoqing Road fault; **(B)** internal structure of fault zone and distribution of associated fractures.

1–2 cm. Two groups of fractures are developed in the damage zone. One group is parallel to the sliding surface, with small fracture spacing and high density, while another group is at an angle of 75° with the sliding surface, which has large fracture spacing (10–30 cm). They are intersected to form a fracture network with good connection. Another two groups of fractures occur far from the sliding surface (Figure 7), where they are weakly developed, with spacing of 30–40 cm and density of 3–5 m/m². The width of the damage zone can be identified when the fracture density is consistent with the regional fracture density. Relationship between distance and cumulative fracture numbers suggests that it is about 3.48 m for the Gushiyu fault.

The damage zone can be divided into tip damage zone, wall damage zone and linkage damage zone based on its location (Kim and Sanderson, 2010; Choi et al., 2016; Luo et al., 2018; Zhu et al., 2021). The tip damage zone refers to the subseismic faults and fractures at the end of faults, also known as process zone. Wall damage zone is distributed on two sides of sliding surface. The linkage damage zone is developed at the position where two or more faults are interacted with each other, e.g., fault intersection or overlapping zone. Figure 8 shows two faults at the Huoqing Road of Wulate, Bayannur City, Inner Mongolia, where F1 fault was developed at early stage and was cut by F2 fault. The dual structure with similar core
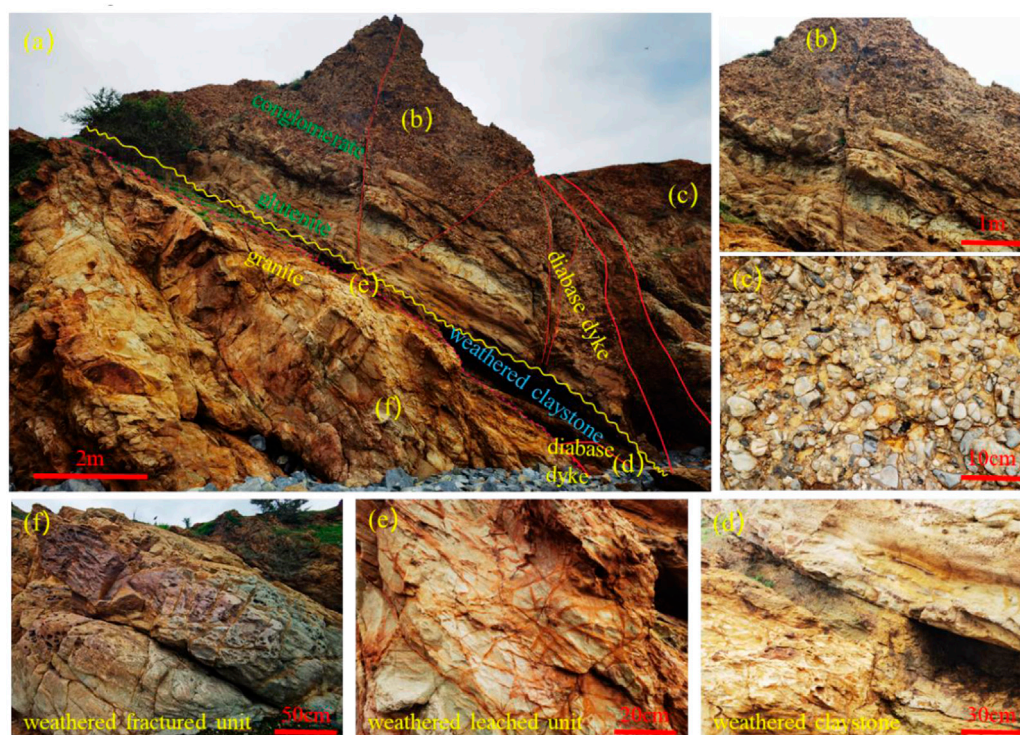
FIGURE 9
Paleo-weathering crust structure and fracture distribution at Longhuitou scenic spot. **(A)** Overall characteristics of weathering crust and fractures; **(B)** fracture characteristics in glutenite; **(C)** fracture characteristics in conglomerate; **(D)** fracture characteristics in weathered claystone; **(E)** fracture characteristics in semi-weathered leached unit; **(F)** fracture characteristics in semi-weathered fractured unit.

structures can be observed from both these two faults, including fault breccia and a small amount of fault gouge. F1 is a normal fault with occurrence of 195°∠48°, core width of 10–20 cm and displacement of 1.2 m F2 is also a normal fault with occurrence of 206°∠53°, core width of 20–30 cm and displacement of 1.5 m. Fractures are well developed at damage zone, especially at positions overlapped by these two faults, where multiple sets of fractures are interacted to form networks, with density up to 40 m/m². The density decreases to about 10 m/m² with increasing distance from the fault, and thereby, the identified width of the damage zone is 0.8–1.5 m.

Weathering crust structure

Structures of two paleo-weathering crusts were described in detail to clarify fracture distribution in vertical at metamorphic buried-hill reservoirs. The first weathering crust is located at the top of the Archaeozoic granite at Longhuitou scenic spot, Xingcheng City, Liaoning Province, and is overlaid by the Middle Jurassic Haifanggou polymict conglomerate. It can be divided into weathered claystone, semi-weathered leached unit and semi-weathered fractured unit based on weathering degree

and fracture development (Figure 9). The weathered claystone is 20–30 cm in thickness. Most was converted into brownish-red and loose clay minerals under intensive weathering and erosion with weak fracture development, where the structure and texture of the parent rock were completely destroyed. Some claystone was washed away by rain or sea water to form grooves. The semi-weathered leached unit remains original mineral framework under general weathering and leaching, where both weathering fractures and structural fractures can be observed. The weathering fractures have extremely high density, with an average of 30–50 m/m², as a result, fracture networks can be formed with length of 10–30 cm, indicating high-quality seepage channel. Both sides of fractures are iron red, with a width of 3–6 cm. Structural fractures and weathering fractures were developed at the semi-weathered fracture unit. However, different from semi-weathered leached unit, it is dominated by structural fractures, with low density but large scale (meter-scale). Trans-gravel fractures, gravel-edge fractures and intra-gravel fractures can be found at overlaid sandy conglomerates, where the trans-gravel fractures are mainly large-scale shear ones (3–6 m in length). However, fracture density is significantly lower than that of three units at weathering crust.

FIGURE 10
Paleo-weathering crust structure and fracture distribution at Jiashan. **(A)** Overall characteristics of weathering crust and fractures; **(B)** fracture characteristics in gravelly sandstone; **(C)** fracture characteristics in weathered claystone; **(D)** fracture characteristics in weathered broken unit; **(E)** fracture characteristics in semi-weathered leached unit; **(F)** fracture characteristics in semi-weathered fractured unit.

The second paleo-weathering crust is situated at the top of Archaeozoic granite at Jiashan, Xingcheng City, Liaoning Province, which is overlaid by the Changzhougou gravelly coarse sandstone of the Changcheng System. The weathering crust can be divided into weathered claystone, weathered broken unit, semi-weathered leached unit and semi-weathered fractured unit (Figure 10). The weathered claystone, which is dominated by soil-like secondary minerals, is 15–25 cm in thickness. Part of the claystone was washed by rain to form grooves. The weathered broken unit is mainly composed of cataclasite and mudstone, with high argillaceous content. Strong weathering and dissolution resulted in vaguely-visible fracture networks, where fractures were obviously dissolved with smooth surface. Weathering fractures and structural fractures were developed at the semi-weathered leached unit, while the former was popular, with an average density of 30–50 m/m^2 and length of 10–30 cm. Minerals are difficult to be identified in this unit because of strong weathering and dissolution, with abundant dissolution pores and enlarged fractures. Most fractures are not filled and are widened by dissolution, with uneven surfaces and dissolution pores at local positions. As a result, fracture network is developed with good connection. Structural fractures and weathering fractures were

developed at the semi-weathered fractured unit, with low density but large size, commonly in meter-scale. The overlaid gravelly coarse sandstone intervals are dominated by strata-bounded fractures and through-strata fractures of tectonic-origin.

Therefore, a well-developed weathered crust can be divided into weathered claystone, weathered broken unit, semi-weathered leached unit, semi-weathered fractured unit and unweathered unit (Kim and Sanderson, 2005; Hou et al., 2013; Chen et al., 2021; Fan et al., 2021) (Figure 11). The weathered claystone is typical compacted rock with no fracture. From the weathered broken unit to the unweathered unit, fracture types change from weathering ones to structure ones, with decreasing fracture density. Factors affecting unit thickness and fracture development are lithology, weathering period and weathering degree of the bedrock as well as ancient landform.

Ancient landform

Weathering and leaching, playing an important role in controlling weathering crust structure and vertical zoning of

FIGURE 11
Weathered crust structure pattern and fracture distribution in vertical.

reservoirs, are depended on ancient landform (Zou et al., 2011; Zeng et al., 2017). Exploration activities show that new and thin strata above buried hills are good indicators of high positions, where long-term weathering and leaching can contribute positively to high-quality reservoir development. The location of ancient landform also affects fracture types and fracture development. Structural fractures, extensional fractures associated with stress releasing under gravity and weathering fractures can be developed at the high of the landform, especially at high mountains with large slopes. The former two are large in extension and cutting depth, up to hundreds of meters, providing channels for weathering and leaching. The latter is small in scale, but have large density, up to 50–100 m/m^2. These fractures are commonly well connected, contributing to strong weathering and leaching. Weathering fractures and structural fractures can be developed at small ridges and steep slopes, where weathering fractures are popular, cutting rocks into fragments and promoting weathering and leaching. Structural fractures are popular at most gentle slopes covered by sediments, e.g., colluvium and slope wash, with a few weathering fractures, where weathering and leaching are relatively weak. Weathering is also weak at gully that is covered by flowing water or sediment throughout the year, but faults can be well developed, especially structural fractures. Sedimentation is the primary geological event at low positions, where no significant weathering and leaching are developed.

Conclusion

Structural fractures, weathering fractures and dissolution fractures are developed at metamorphic buried-hill reservoirs in the study area, where structural fractures and weathering fractures are the most popular ones. Fracture types vary greatly among different structure positions. Four fracture groups were mainly developed in the study area, i.e., NEE-SWW trending, near EW trending, near NS trending and NW-SE trending. Oblique fractures are prevailing with dip angle of 30°–60°, with bedding-parallel fractures and subvertical fractures of secondary importance. The fracture density identified by imaging log is about 1–5 m^{-1}. Vertically, the overall fracture density at the semi-weathered unit is higher than that in the unweathered unit, and multiple fractures are also developed in the unweathered unit. Fractures are well developed yet are significantly filled on cores, especially in the weathering unit, where areal density of weathering fractures is about 30–70 m/m^2, with an average of 53.0 m/m^2. The areal density of structural fractures is mainly distributed at 10–30 m/m^2, with an average of 20.1 m/m^2.

Lithology, fault, weathering crust and ancient landform are primary elements governing fracture distribution. Fracture density is high in lithology with high bright mineral contents. Faults have a typical dual structure including fault core and

damage zone. The fracture density decreases with increasing distance from faults. Damage zone will be ended when the density is consistent with the regional fracture density. The width of the damage zone is generally determined by factors, e.g., fault scale and structure location. The semi-weathered leached unit is dominated by well-developed and well-connected weathering fractures, with structural fractures of secondary importance. Different from that, the semi-weathered damage zone is dominated by structural fractures, followed by weathering fractures, with low fracture density. Structural fractures are prevailing at the unweathered unit, where fracture density is high for certain lithology at local positions. Ancient landform primarily controlled the distribution of weathering fractures, which were well developed at high positions (e.g., ridges and slopes), while sedimentation was the primary geological event at gentle slopes and low positions.

Data availability statement

The original contributions presented in the study are included in the article/supplementary material, further inquiries can be directed to the corresponding author.

Author contributions

Funding

Conflict of interest

LM, TF, HF, and TN were employed by CNOOC Research Institute Ltd., China.

The remaining authors declare that the research was conducted in the absence of any commercial or financial relationships that could be construed as a potential conflict of interest.

Publisher's note

All claims expressed in this article are solely those of the authors and do not necessarily represent those of their affiliated organizations, or those of the publisher, the editors and the reviewers. Any product that may be evaluated in this article, or claim that may be made by its manufacturer, is not guaranteed or endorsed by the publisher.

References

Cao, D., Zeng, L., Lyu, W., Xu, X., and Tian, H. (2021). Progress in brittleness evaluation and prediction methods in unconventional reservoirs. *Petroleum Sci. Bull.* 1, 31–45. doi:10.3969/j.issn.2096-1693.2021.01.003

Chen, X., Wei, A., Wang, Y., Gao, S., Ye, T., and Li, X. (2018). Controlling effect of archaean metamorphic rocks on fractures in southwest Bohai Sea. *Geol. Sci. Technol. Inf.* 37, 165–173. doi:10.19509/j.cnki.dzkq.2018.0223

Chen, X., Zhao, Z., Hui, G., Yue, J., and Zhao, J. (2021). Characteristics of weathered metamorphic rocks crust in bohai sea and its quantitative prediction. *Mar. Geol. Front.* 37, 33–41. doi:10.16028/j.1009-2722.2020.168

Choi, J., Edwards, P., Ko, K., and Kim, Y. (2016). Definition and classification of fault damage zones: A review and a new methodological approach. *Earth-Science Rev.* 152, 70–87. doi:10.1016/j.earscirev.2015.11.006

Deng, Y. (2015). Formation mechanism and exploration practice of large-medium buried-hill oi fields in Bohai Sea. *Acta Pet. Sin.* 36, 253–261. doi:10.7623/syxb201503001

Dou, L., Wei, X., Wang, J., Li, J., Wang, R., and Zhang, S. (2015). Characteristics of granitic basement rock buried-hill reservoir in Bongor Basin, Chad. *Acta Pet. Sin.* 36, 897–904. doi:10.7623/syxb201508001

Fan, T., Niu, T., Fan, H., Wang, S., Xiao, D., and Luo, J. (2021). Geological model and development strategy of Archean buried hill reservoir in BZ19-6 condensate field. *China Offshore Oil Gas* 33, 85–92. doi:10.11935/j.issn.1673-1506.2021.03.009

Ferrill, D., Smart, K., Cawood, A., and Morris, A. (2021). The fold-thrust belt stress cycle: Superposition of normal, strike-slip, and thrust faulting deformation regimes. *J. Struct. Geol.* 148, 104362. doi:10.1016/j.jsg.2021.104362

Gao, S., Zeng, L., Ma, S., He, Y., Gong, L., Zhao, X., et al. (2015). Quantitative prediction of fractures with different directions in tight sandstone reservoirs. *Nat. Gas. Geosci.* 26, 427–434. doi:10.11764/j.issn.1672-1926.2015.03.0427

Gong, L., Cheng, Y., Gao, S., Gao, Z., Feng, J., Wang, H., et al. (2022). Fracture connectivity characterization and its controlling factors in the Lower Jurassic tight sandstone reservoirs of eastern Kuqa. *Earth Sci.*. doi:10.3799/dqkx.2022.066

Gong, L., Fu, X., Wang, Z., Gao, S., Jabbari, H., Yue, W., et al. (2019). A new approach for characterization and prediction of natural fracture occurrence in tight oil sandstones with intense anisotropy. *Bulletin* 103, 1383–1400. doi:10.1306/12131818054

Gong, L., Gao, M., Zeng, L., Fu, X., Gao, Z., Gao, A., et al. (2017). Controlling factors on fracture development in the tight sandstone reservoirs: A case study of jurassic-neogene in the kuga foreland basin. *Nat. Gas. Geosci.* 28, 99–208.

Gong, L., Gao, S., Liu, B., Yang, J., Fu, X., Xiao, F., et al. (2021). Quantitative prediction of natural fractures in shale oil reservoirs. *Geofluids* 2021, 1–15. doi:10.1155/2021/5571855

Gong, L., Liu, B., Fu, X., Jabbari, H., Gao, S., Yue, W., et al. (2019). Quantitative prediction of sub-seismic faults and their impact on waterflood performance: Bozhong 34 oilfield case study. *J. Petroleum Sci. Eng.* 172, 60–69. doi:10.1016/j.petrol.2018.09.049

Gong, L., Wang, J., Gao, S., Liu, B., Miao, F., Meng, Qi., et al. (2021). Characterization, controlling factors and evolution of fracture effectiveness in shale oil reservoirs. *J. Petroleum Sci. Eng.* 203, 108655. doi:10.1016/j.petrol.2021.108655

Gong, L., Zeng, L., Chen, S., Gao, S., Zhang, B., Zu, K., et al. (2016). Characteristics of micro-fractures and contribution to the compact conglomerate reservoirs. *Geotect. Metallogenia* 40, 38–46. doi:10.16539/j.ddgzyckx.2016.01.004

Hou, M., Cao, H., Li, H., Chen, A., Wei, A., Chen, Y., et al. (2019). Characteristics and controlling factors of deep buried-hill reservoirs in the BZ19-6 structural belt, Bohai Sea area. *Nat. Gas. Ind.* 39, 33–44. doi:10.3787/j.issn.1000-0976.2019.01.004

Hou, L., Luo, X., Wang, J., Yang, F., Zhao, X., and Mao, Z. (2013). Weathered volcanic crust and its petroleum geologic significance: A case study of the carboniferous volcanic crust in northern xinjiang. *Petroleum Explor. Dev.* 40, 257–265. doi:10.11698/PED.2013.03.01

Hu, Z., Xu, C., Yang, B., Huang, Z., and Su, W. (2017). Reservoir forming mechanism of Penglai 9-1 gra nite buried-hills and its oil geology significance in Bohai Sea. *Acta Pet. Sin.* 38, 274–285. doi:10.7623/syxb201703004

Huang, J., Tan, X., Cheng, C., Li, Z., Ma, L., Zhang, H., et al. (2016). Structural features of weathering crust of granitic basement rock and its petroleum geological significance: A case study of basement weathering crust of dongping area in qaidam basin. *Earth Sci.* 41, 2041–2060. doi:10.3799/dqkx.2016.528

Kim, Y., and Sanderson, D. J. (2005). The relationship between displacement and length of faults: A review. *Earth-Science Rev.* 68, 317–334. doi:10.1016/j.earscirev.2004.06.003

Kim, Y., and Sanderson, D. (2010). Inferred fluid flow through fault damage zones based on the observation of stalactites in carbonate caves. *J. Struct. Geol.* 32, 1305–1316. doi:10.1016/j.jsg.2009.04.017

Luo, Q., Fariborz, G., Zhong, N*., Wang, Y., Qiu, N., Skovsted, C. B., et al. (2020). Graptolites as fossil geo-thermometers and source material of hydrocarbons: An overview of four decades of progress. *Earth-Science Rev.* 200, 103000. doi:10.1016/j.earscirev.2019.103000

Luo, Q., George, S., Xu, Y., and Zhong, N. (2016). Organic geochemical characteristics of the mesoproterozoic hongshuizhuang formation from northern China: Implications for thermal maturity and biological sources. *Org. Geochem.* 99, 23–37. doi:10.1016/j.orggeochem.2016.05.004

Luo, Q., Gong, L., Qu, Y., Zhang, K., Zhang, G., and Wang, S. (2018). The tight oil potential of the Lucaogou Formation from the southern Junggar Basin, China. *Fuel* 234, 858–871. doi:10.1016/j.fuel.2018.07.002

Luo, Q., Zhang, L., Zhong, N., Wu, J., Goodarzi, F., Sanei, H., et al. (2021). Thermal evolution behavior of the organic matter and a ray of light on the origin of vitrinite-like maceral in the Mesoproterozoic and Lower Cambrian black shales: Insights from artificial maturation. *Int. J. Coal Geol.* 244, 103813. doi:10.1016/j.coal.2021.103813

Luo, Q., Zhong, N., Qin, J., Li, K., Zhang, Y., Wang, Y., et al. (2014). Thucholite in Mesoproterozoic shales from northern north China: Occurrence and indication for thermal maturity. *Int. J. Coal Geol.* 125 (1), 1–9. doi:10.1016/j.coal.2014.01.009

Lyu, W., Zeng, L., Zhou, S., Du, X., Xia, D., Liu, G., et al. (2019). Natural fractures in tight-oil sandstones: A case study of the upper triassic yanchang formation in the southwestern ordos basin, China. *Bulletin* 103, 2343–2367. doi:10.1306/0130191608617115

Peacock, D., Dimmen, V., Rotevatn, A., and Sanderson, D. (2017). A broader classification of damage zones. *J. Struct. Geol.* 102, 179–192. doi:10.1016/j.jsg.2017.08.004

Wang, D., Wang, Q., Liu, X., Zhao, M., Hao, Y., and YiWei, H. (2019). Characteristics and developing patterns of gneiss buried hill weathering crust reservoir in the sea area of the Bohai Bay basin. *Acta Petrol. Sin.* 35, 1181–1193. doi:10.18654/1000-0569/2019.04.13

Wang, J., Hu, C., Pan, Y., Huang, Q., Yuan, H., Gong, L., et al. (2022). Fracture development characteristics and comprehensive evaluation of buried hill metamorphic reservoir in Jihua 1 area. *Chin. J. Geol.* 57, 463–477. doi:10.12017/dzkx.2022.027

Wang, X., Zhou, X., Xu, G., Liu, P., Gao, K., and Guan, D. (2015). Characteristics and controlling factors of reservoirs in Penglai 9-1 large-scaleoilfield in buried granite hills, Bohai Sea. *Oil Gas. Geol.* 36, 262–270. doi:10.11743/ogg20150211

Xie, h. (2020). Gas resources and accumulation model of BZ19-6 Archean buried-hill large-scale gas reservoir in Bozhong Sag, Bohai Bay Basin. *Pet. Geol. Exp.* 42, 858–866. doi:10.11781/sysydz202005858

Xu, C., Du, X., Liu, X., Xu, W., and Hao, Y. (2020). Formation mechanism of high-quality deep buried-hill reservoir of Archaean metamorphic rocks and its significance in petroleum exploration in Bohai Sea area. *Oil Gas. Geol.* 41, 235–247. doi:10.11743/ogg20200201

Xu, C., Yu, H., Wang, J., and Liu, X. (2019). Formation conditions and accumulation characteristics of Bozhong 19-6 large condensate gas field in offshore Bohai Bay Basin. *Petroleum Explor. Dev.* 46, 27–40. doi:10.1016/s1876-3804(19)30003-5

Xue, Y., Wang, Q., Niu, C., Miao, Q., Liu, M., and Yin, J. (2020). Hydrocarbon charging and accumulation of BZ 19-6 gas condensate field in deep buried hills of Bozhong Depression, Bohai Sea. *Oil Gas. Geol.* 41, 891–902. doi:10.11743/ogg20200501

Ye, T., Niu, C., Wang, Q., Dai, L., and Li, F. (2021). Characteristics and controlling factors of large bedrock buried-hill reservoirs in the bohai Bay Basin—A case study of the BZ19-6 condensate field. *Acta Geol. Sin.* 95, 1889–1902.

Zeng, L., Gong, L., Guan, C., Zhang, Be., Wang, Q., Zeng, Q., et al. (2022). Natural fractures and their contribution to tight gas conglomerate reservoirs: A case study in the northwestern sichuan basin, China. *J. Petroleum Sci. Eng.* 210, 110028. doi:10.1016/j.petrol.2021.110028

Zeng, L., Zhao, X., Zhu, S., and Zhao, J. (2017). Waterflood-induced fractures and its significance for development of low-permeability sandstone oil reservoirs. *Petroleum Sci. Bull.* 3, 336–343. doi:10.3969/j.issn.2096-1693.2017.03.031

Zeng, L., Zhu, R., Gao, Z., Gong, L., and Liu, G. (2016). Structural diagenesis and its petroleum geological significance. *Petroleum Sci. Bull.* 2, 191–197. doi:10.3969/j.issn.2096-1693.2016.02.015

Zhou, X., Wang, Q., Feng, C., Ye, T., Liu, X., Hao, Y., et al. (2022). Formation conditions and geological significance of large Archean buried hill reservoirs in Bohai Sea. *Eart. Scie.* 47, 1534–1548. doi:10.3799/dqkx.2021.249

Zhou, X., Xiang, H., Yu, S., Wang, G., and Yao, C. (2005). Reservoir characteristics and development controlling factors of JZS Neo-Archean metamorphic buried hill oil pool in Bohai Sea. *Petroleum Explor. Dev.* 2005, 17–20.

Zhou, X., Zhang, R., Li, H., Wang, B., and Guo, Y. (2017). Major controls on natural gas accumulations in deep-buried hills in Bozhong Depression, Bohai Bay Basin. *J. China Univ. Petroleum* 41, 42–50. doi:10.3969/j.issn.1673-5005.2017.01.005

Zhu, H., Song, Y., and Tang, X. (2021). Research progress on 4-dimensional stress evolution and complex fracture propagation of infill wells in shale gas reservoirs. *Petroleum Sci. Bull.* 3, 396–416. doi:10.3969/j.issn.2096-1693.2021.03.032

Zou, C., Hou, L., Tao, S., Yuan, X., Zhu, R., Zhang, X., et al. (2011). Hydrocarbon accumulation mechanism and structure of large-scale volcanic weathering crust of the Carboniferous in northern Xinjiang, China. *Sci. China Earth Sci.* 41, 221–235. doi:10.1007/s11430-011-4297-8

Time-dependent deformation of Wufeng-Longmaxi shale and its implications on the *in situ* state of stress

Wei Cheng[1,2], Xiaowen Zhang[1,2], Juan Jin[1,2], Jiandong Liu[1,2]*, Weidong Jiang[1,2], Guangming Zhang[1,2], Shihuai Zhang[3]* and Xiaodong Ma[3]

[1]Research Institute of Petroleum Exploration & Development, PetroChina, Beijing, China, [2]Key Laboratory of Oil & Gas Production, CNPC, Beijing, China, [3]Department of Earth Sciences, ETH Zürich, Zürich, Switzerland

The stress-strain relationship in shales is generally time-dependent. This concerns their long-term deformation in unconventional reservoirs, and its influence on the *in situ* stress state therein. This paper presents an experimental investigation on the time-dependent deformation of the Longmaxi shale gas shale. A series of creep experiments subject the shale samples to long-term, multi-step triaxial compression. It is found that the shale samples exhibit varying degrees of time-dependent deformation, which can be adequately described by a power-law function of time. The experimental results establish the relationship between the elastic Young's modulus and viscoplastic constitutive parameters, which are different from previous those derived from North American shales. Based on this viscoplastic constitutive model, the stress relaxation and the differential stress accumulation over geologic time scales can be estimated. It is found that linear elasticity substantially overestimates the differential stress accumulation predicted in the context of viscoplastic relaxation. The characterized viscoplasticity and stress relaxation are of vital importance for various geomechanical problems in shale reservoirs.

1 Introduction

The boom in unconventional plays in recent decades requires deeper understanding of the geomechanical properties and *in situ* stress characteristics of shale gas reservoirs. The refined understanding of the rock properties and *in situ* stress facilitates reservoir evaluation, drilling, wellbore stability, and well stimulation (Britt and Schoeffler, 2009; Britt, 2012; Zheng et al., 2018; Clarke et al., 2019; Wang et al., 2019; Zoback and Kohli, 2019). The mechanical properties of shales are significantly different from those of common rock types (e.g., sandstones and carbonates) characterized by heterogeneity,

time-dependency and anisotropy. Challenges remain when conventional concepts and models (such as linear elasticity) are applied to infer the geomechanical properties and *in situ* stress in shale reservoirs.

Shales typically consist of rich compliant components, e.g., clay minerals and total organic carbon content (TOC), which promote significant time-dependent deformation. Such time-dependence may affect a variety of mechanical processes *in situ*. For instance, hydraulic fractures opened by proppants can eventually close over time, leading to reservoir permeability loss and thus production reduction (Guo and Liu, 2012; Li and Ghassemi, 2012; Rybacki et al., 2017). The time-dependent deformation of shales is often invoked as one of the main mechanisms for the reservoir compaction or surface subsidence (Hagin and Zoback, 2007; Chang et al., 2014; Musso et al., 2021). In addition, the time dependence of shales has also been closely related to the evolution of the state of *in situ* stress. For example, in a normal or normal/strike-slip faulting regime, it has been observed that the least principal stress (quantifying the frac gradient) can increase markedly in a viscoplastic formation, rendering a more isotropic state of stress than that in the more elastic/brittle formations above and below (Warpinski and Teufel, 1989; Sone and Zoback, 2014b; Ma and Zoback, 2017). Plausibly due to viscoplastic stress relaxation (Yang et al., 2015; Xu et al., 2019), the increased magnitude of the least principal stress may act as a stress barrier with a higher frac gradient, limiting the propagation of vertical hydraulic fractures. Predicting the variations of the least principal stress at different depths can facilitate the optimization of drilling and the control of fracture propagation (hydraulic fracturing and seismicity mitigation). However, it has been demonstrated that the observed variations of the least principal stress within shale formations cannot be well explained by the frictional equilibrium concept (Townend and Zoback, 2000; Sone and Zoback, 2014b; Ma and Zoback, 2020). Therefore, quantifying the time-dependent response of shales is of vital importance to *in situ* stress prediction and other geomechanical applications.

In order to investigate the time-dependent response of shales, a lot of uniaxial and triaxial creep experiments have been carried out (Chang and Zoback, 2009; 2010; Li and Ghassemi, 2012; Sone and Zoback, 2014a; Yang and Zoback, 2016; Rassouli and Zoback, 2018). It is found that creep can be enhanced, to different extent, in the presence of high differential stress, high content of compliant components, and water and loaded in the direction perpendicular to bedding orientation. In order to describe the laboratory-derived creep behavior, the empirical laws for rocks, soils, and other solids can generally be used, including power-law, logarithmic, exponential, and hyperbolic functions (Gupta, 1975; Findley et al., 1976; Karato, 2008; Paterson, 2012). Among them, the power-law model has been successfully used to quantify the linear viscous behavior of North America shales under primary creep stage and its long-term effect on the *in situ* state of stress (Sone and Zoback 2014a; Sone and Zoback 2014b; Yang et al., 2015; Ma and Zoback, 2020). Considering the different tectonic environments, however, it is not clear if the empirical relations derived from North

America shales can be directly applied to other shale types, such as the Wufeng-Longmaxi shale investigated in this paper.

In this study, we performed a series of multi-step creep experiments on the shale samples from the Longmaxi formation, a major unconventional play in southwestern China (Zou et al., 2015; Dong et al., 2018). Based on the laboratory triaxial creep experiments, the time-dependent behavior of the Longmaxi shale samples was investigated considering the effect of hydrostatic loading, differential stress, and deformational anisotropy. Utilizing the theory of linear viscoelasticity, the time-dependent constitutive relation was established for the Wufeng-Longmaxi shale samples. According to the experimental data, a new empirical relation was proposed to relate the constitutive parameters to the elastic properties. Then the laboratory-derived viscoplastic stress relaxation response was extrapolated, facilitating an estimation of the *in situ* stress over geologic time scales.

2 Shale samples and laboratory methodology

2.1 Longmaxi shale lithofacies—Taking Well 1 as an example

Shale cores tested in this study are from three vertical appraisal wells, referred to as Well 1, 2, and 3, respectively. The three wells are all located in a shale gas reservoir at the southern margin of the Sichuan Basin, China. Tectonically, the shale gas reservoir is located in the Changning anticline area, which is essentially a large basement fault-bend fold. Its tectonic location is the transition zone between the south Sichuan low-slow fold belt and the Daliangshan-Daloushan fault fold belt (He et al., 2019). Although characterized by complex structural deformation in the geologic history, the *in situ* stress data, mostly from World Stress Map (Hu et al., 2017; Heidbach et al., 2018; Kong et al., 2021) and focal mechanism inversions of historic earthquakes (Lei et al., 2019), consistently indicate the regional NW-W trend of the SHmax and the reverse faulting/strike-slip stress environment in this region (Ma et al., 2022). Among the three wells, a series of integrated well logs are available from the depth of 1950–2300 m in Well 1, characteristic of the regional geology and reservoir lithofacies. It has been confirmed that the clay-rich Wufeng-Longmaxi formations are the target of the shale gas play, showing the potential to yield economic hydrocarbon production.

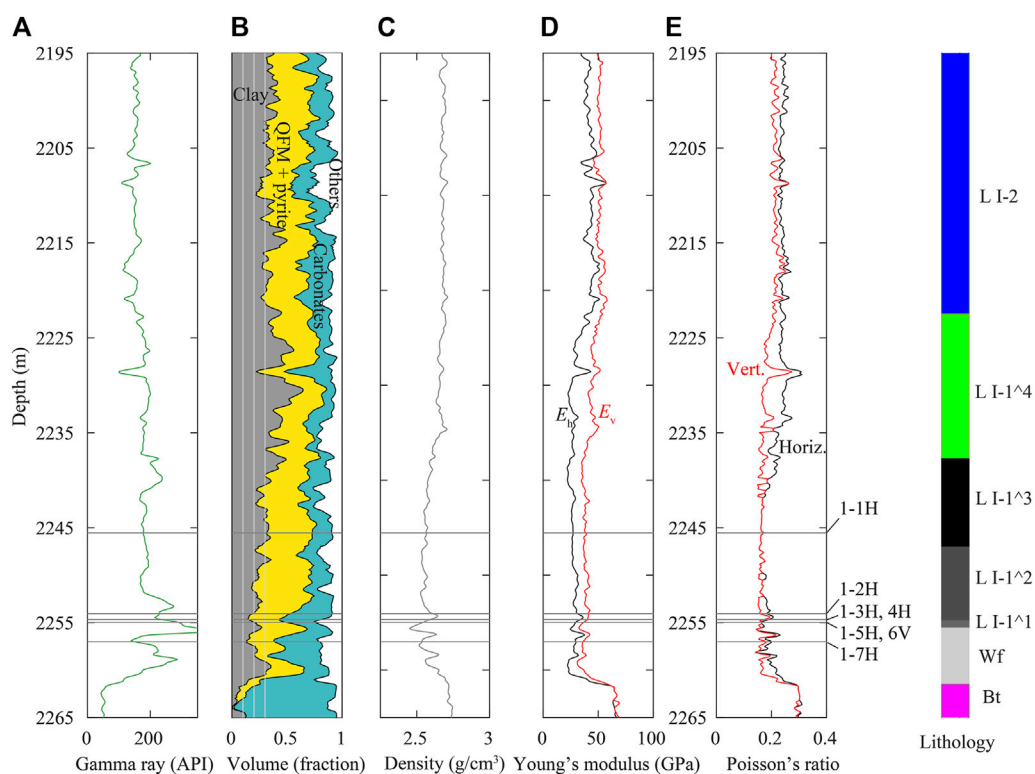In Figure 1, the integrated geophysical logs corresponding to part of the Wufeng-Longmaxi formations and the underlying Baota Formation are shown (depth: 2195–2265 m). The gamma ray logs show high values (>100 GAPI) within the reservoir depths, indicating the high content of clay (Figure 1A). After entering the Baota formation, the gamma ray value decreases abruptly to a low level, consistent with the diminishing clay

shown in compositional log in Figure 1B. Overall, the clay-rich Wufeng-Longmaxi formations have a marked contrast in mineralogy to the underlying carbonate-rich Baota formation. The lower Longmaxi formation is further divided into several lithofacies according to their characteristic physical properties, which is evident in terms of mineral composition (e.g., clay content) and mechanical properties (e.g., sonic log derived Young's modulus and Poisson's ratio). The stratigraphic column in Figure 1, from top to bottom, shows the successive lithofacies of the Longmaxi formation: Longmaxi-I2 ("L-I2"), L-I1⁴, L-I1³, L-I1², and L-I1¹. The variations in mineral composition and physical properties among the lithofacies clearly show that the Longmaxi shale is highly heterogenous. To further study the mechanical behavior of the Longmaxi shale, several shale samples were retrieved within the target formation in each well. Figure 1 shows the extracted core depths in Well 1.

2.2 Sample preparation and description

The shale cores from the three wells were prepared into cylindrical samples with nominal diameter of 25 mm and nominal length of 50 mm. These samples have cylindrical axes either perpendicular or parallel to the bedding planes, which are referred to as vertical (denoted as "V") and horizontal (denoted as "H") samples, respectively. Note that samples from the same lithofacies have significantly different depths across wells, as shown in Table 1, indicating a highly inclined formation in the shale gas play. For each well, there is one pair of vertical and horizontal samples cored from the same depth, i.e., 1–5H and 1–6V in Well 1, 2–1V and 2–2H in Well 2, and 3–2H and 3–3V in Well 3. Those samples have also been analyzed for the mineral composition using powder X-ray diffraction (XRD) method after the creep experiments. In Figure 2, the mineral composition results are summarized as squares in a ternary plot with clay, QFP (quartz, feldspar, pyrite), and carbonate content, which are further provided in Table 1. The shown samples, except for 1–7H, are from the same lithofacies. From Figure 2, the ternary diagram indicates that samples 1–5H and 1–6V are relatively clay-rich, and 2–1V and 2–2H are relatively silicate-rich. For sample 1–7H, its mineral composition departs significantly from that of samples 1–5H and 1–6V, although its coring depth is only 3 m deeper. For comparison, the mineral composition data in Figure 1B are also plotted as dots in the ternary diagram.

FIGURE 1
Integrated geophysical logs of Well 1: **(A)** Gamma ray; **(B)** Element Capture Spectroscopy (ECS); **(C)** Density; **(D)** Sonic log derived Young's modulus; **(E)** Sonic log derived Poisson's ratio. The coring depths of seven shale samples from Well 1 are shown with "H" and "V" denoting horizontal and vertical samples, respectively. For reference, the stratigraphic column is also shown where "L", "Wf", and "Bt" denote Longmaxi, Wufeng, and Baota formations, respectively.
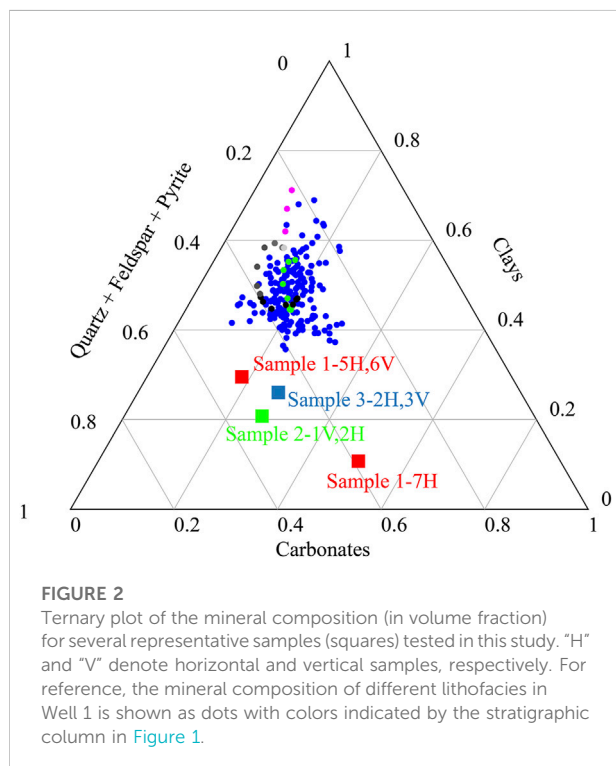
TABLE 1 Mineral composition and experimental data of the shale samples used in the multi-step creep experiments. "H" and "V" denote horizontal and vertical samples, respectively.

Well	Sample[a]	Coring depth (m)	Lithofacies	Confining pressure (MPa)	Differential stress levels (MPa)	Material composition (vol%)[b]						
						Qtz	Kfs	Pl	Cal	Dol	Py	Clay
—	S1	—	—	20	40	—	—	—	—	—	—	—
—	S2	—	—	20	20/40/60	—	—	—	—	—	—	—
1	1-1H	2245.55	L-I-1̄3	20	20/40/60	—	—	—	—	—	—	—
	1–2H	2254.06	L-I-1̄2	20	20/40/60	—	—	—	—	—	—	—
	1–3H	2254.68	L-I-1̄1	20	60	—	—	—	—	—	—	—
	1–4H	2254.68	L-I-1̄1	20	60	—	—	—	—	—	—	—
	1–5H	2254.97	L-I-1̄1	20	20/40/60	42.2	0.5	6.0	11.1	7.2	3.2	29.8
	1–6V	2254.97	L-I-1̄1	20	40/60							
	1–7H	2257.02	Wf	20	60	—	—	—	—	—	—	—
2	2-1V	1033.23	L-I-1̄2	15	20/40/60	46.3	0.6	2.1	21.9	4.7	3.4	21.0
	2-2H	1033.23	L-I-1̄1	15	20/40/60							
	2–3H	1028.58	L-I-1̄1	15	20/40/60	—	—	—	—	—	—	—
	2–4H	1036.8	Wf	15	20/40/60	—	—	—	—	—	—	—
3	3-1H	2999.59	L-I-1̄2	40	60	—	—	—	—	—	—	—
	3-2H	3004.83	L-I-1̄1	40	40/60	39.4	0.0	4.9	17.9	9.2	2.3	26.3
	3-3V	3004.83	L-I-1̄1	40	20/40							
	3–4H	3005.93	L-I-1̄1	40	20/40/60	—	—	—	—	—	—	—

[a]For samples from Wells 1, 2, and 3, the first number in the sample name denotes the well number.
[b]Qtz, Quartz; Kfs, K-feldspar; Pl, Plagioclase; Cal, Calcite, Dol, Dolomite; Py, Pyrite.

FIGURE 2
Ternary plot of the mineral composition (in volume fraction) for several representative samples (squares) tested in this study. "H" and "V" denote horizontal and vertical samples, respectively. For reference, the mineral composition of different lithofacies in Well 1 is shown as dots with colors indicated by the stratigraphic column in Figure 1.

Apparently, the compositional log *via* Element Capture Spectroscopy (ECS) indicates systematically higher clay contents and lower QFP contents (volume percentage) than those of the samples from Well 1. Such inconsistency may be attributed to the differences in scale and measurement methods. Before performing the creep experiments on these samples, two shale samples (S1 and S2) without detailed coring information were tested for calibration purposes.

2.3 Experimental procedures

Multi-step creep experiments were performed using a servo-controlled triaxial apparatus to investigate the time-dependency of the shale samples. Previous studies on North America shales reveal that the confining pressure effect seems to be absent or slightly affecting creep rates (e.g., Sone and Zoback, 2014a). In this study, the confining pressure applied to the samples from each well is approximately estimated according to the coring depth (Table 1) and the shale density (2.5–2.7 g/cm³), although overpressure might be present in the reservoir depths (He et al., 2019). In general, three differential stress levels (20, 40, and 60 MPa) were designated to subject the samples to various stress conditions pertinent to the *in situ* effective differential stress. In
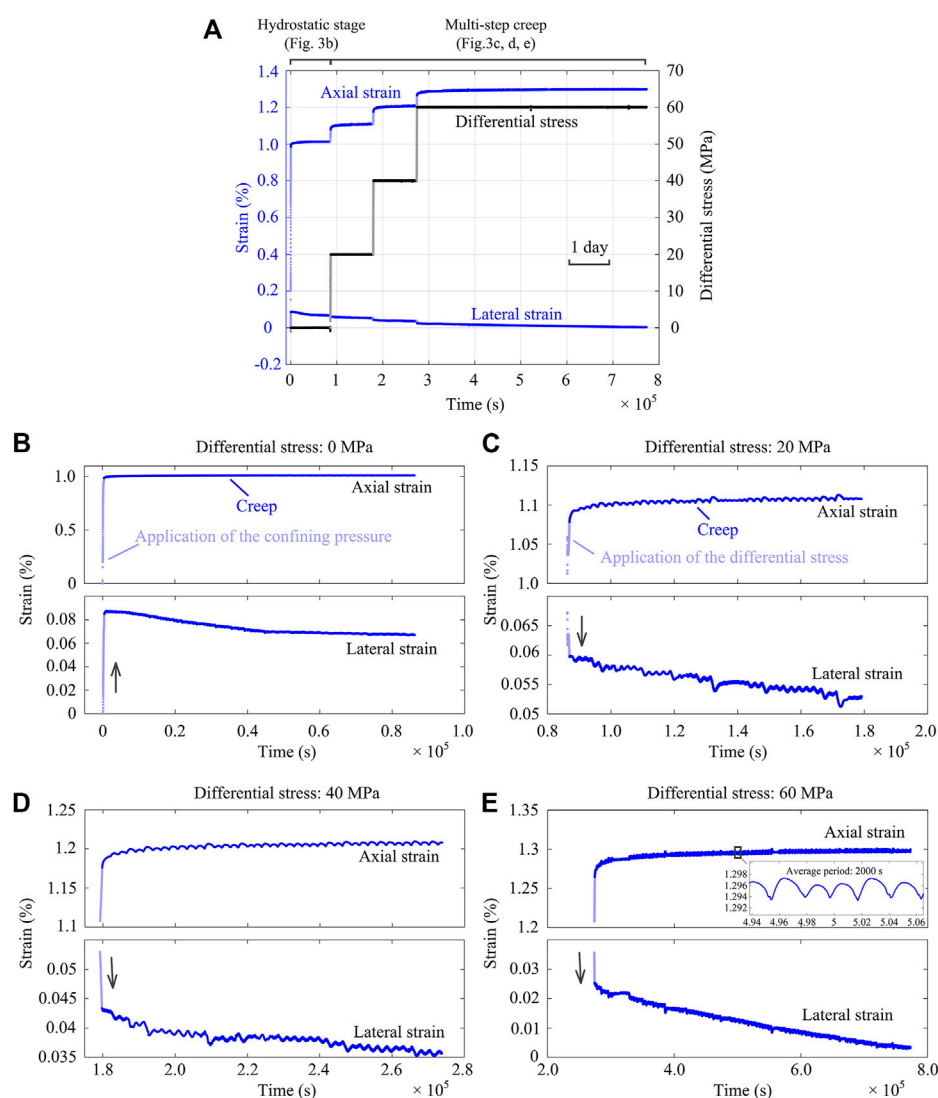
FIGURE 3
(A) Differential stress and axial/lateral strains evolving with time during the multi-step creep experiment (Sample: S2, confining pressure: 20 MPa). For the first three steps, the stress was held for about 1 day (24 h), while the stress for the last step was held for about 6 days. Detailed information of the strains evolving with time is shown in **(B–E)**: **(B)** hydrostatic stage, **(C–E)** differential stress stages with differential stresses of 20, 40, and 60 MPa, respectively. Arrows represent the increase or decrease of the lateral strain during the "instantaneous" loading. Note that data with light color denote the application of the confining pressure or differential stresses. Also note the scale difference for the axial and lateral strain in **(B–E)**.

what follows, we take the multi-step creep experiments on Sample S2 as an example to present the experimental procedure. As shown in Figure 3A, the creep response of Sample S2 was measured at three differential stress levels (20, 40, and 60 MPa) under the confining pressure of 20 MPa.

Specifically, the sample was first subject to confining pressure. The increase of confining pressure lasted around 400 s to reach the prescribed level. The sample then stayed in the hydrostatic stage for ~24 h to reach its thermal equilibrium. Differential stress P_{diff} was then raised consecutively to three

levels (i.e., 20, 40, and 60 MPa) at a loading rate of 2 MPa/min in the subsequent three steps. For the first two steps, the differential stress (20 and 40 MPa) was held constant for ~24 h. For the last step, differential stress (60 MPa) was held constant for about 6 days. During the creep process, the applied differential stress was recorded by the pressure transducer and the strains were measured by the linear variable differential transducer (LVDT). In Figure 3A, the recorded differential stress and strains of Sample S2 are shown as a function of time during the multi-step creep experiment.

Note that, the *in situ* stress in the upper crust is typically limited by the rock frictional strength (Townend and Zoback, 2000), which is generally much lower than the ultimate compressive strength of the intact rock. To characterize the time-dependence of the shale samples, the applied differential stresses are less than 50% of the ultimate strength. Under such relatively low stress levels, we can obtain the viscoplastic behavior of the shale samples while preventing the transition into tertiary creep. In Table 1, the applied confining pressures and differential stresses of the tests in this study are detailed.

3 Experimental results

3.1 Mechanical characteristics during the multi-step creep experiments

During each experiment, the shale sample experienced "instantaneous" deformation and "long-term" creep in each step. From Figure 3A, three main features can be observed: 1) significant deformation takes place under hydrostatic loading; 2) creep strain is most prominent in the axial direction; and 3) creep induces dilatant lateral strain that cannot be overlooked. In the hydrostatic stage, as presented in Figure 3B, contraction (positive) occurs in both the axial and lateral directions. As in the subsequent creep stages, the deformation in the axial direction is more pronounced than that in the lateral direction when increasing the confining pressure to the prescribed value. While the hydrostatic state is maintained for

FIGURE 4
Axial strain responses of the samples from three wells under hydrostatic conditions. For each curve, the sample name and the corresponding confining pressure are explicitly indicated. For comparison, each pair of the samples are from the same depth, i.e., 1−3 H and 1−4 H, 1−5 H and 1−6 V, 2−1 V and 2−2 H, 3−2 H and 3−3 V (see Table 1 for more details).

a period of ~24 h, the axial strain is almost constant while the lateral strain first decreases (dilates) and then reaches a constant value. This may be due to the intrinsic anisotropy of the samples or the different methods for measuring the axial and lateral strains. Based on this observation, it is argued that the sample should stay in the hydrostatic stage for sufficiently long period (e.g., 12 h as suggested by Figure 3B) to reach a state of equilibrium in terms of deformation and temperature.

Similarly, the shale sample in the differential stress stage also shows a combination of instantaneous elastic response and time-dependent creep response. In Figures 3C–E, it can be observed that, upon each differential stress step, most of the axial strain (light blue data) occurs during the 'instantaneous' application of the differential stress. In contrast, the lateral strain first decreases in response to the "instantaneous" loading and then undergoes more deformation at an almost constant rate during the creep stage. In addition, when the differential stress is held, both the axial and lateral strains show significant "cyclic" fluctuations, which may be due to the loading system artefact during the long-time creep period or the temperature fluctuations in the testing environment. In Figure 3E, the close-up of a time interval around 5×10^5 s clearly shows the details of the data fluctuations. Regression to the data yields an average period of about 2000 s.

3.2 Comparative observations between shale samples

In Section 3.1, anisotropy can be observed for a single sample from the different strain responses in the axial and lateral directions. In this section, we further compare the mechanical responses of different samples under the hydrostatic stage and differential stress stage. In Figure 4, the axial strain data of several representative shale samples under hydrostatic stage are shown. These samples can be divided into different pairs, and each pair are from the same depth, i.e., 1–3H and 1–4H (2254.68 m), 1–5H and 1–6V (2254.97 m), 2–1V and 2–2H (1033.23 m), 3–2H and 3–3V (3004.83 m). Under hydrostatic condition, samples 1–3H and 1–4H, featuring the same coring depth and orientation, display considerably different response to the "instantaneous" loading of the confining pressure, indicative of significant heterogeneity of these shale samples. For the effect of sample orientation, it is observed that the horizontal sample 1–5H shows more significant amount of axial strain than the vertical sample 1–6V. In contrast, the horizontal samples show less axial strain than the vertical samples for Well 2 and Well 3. As reported by previous studies, e.g., Wong et al. (2008), shale samples are typically stiffer in the horizontal direction (bedding parallel) than in vertical direction (bedding perpendicular), consistent with their assumptions being transverse isotropy materials. Therefore, it is generally expected more pronounced creep behavior for vertical samples. Comparison between 1 and 5H and 1–6V shows the mechanical features of shale samples are not
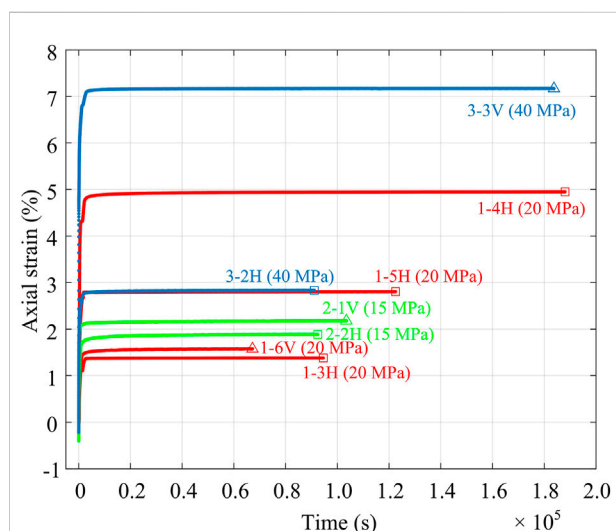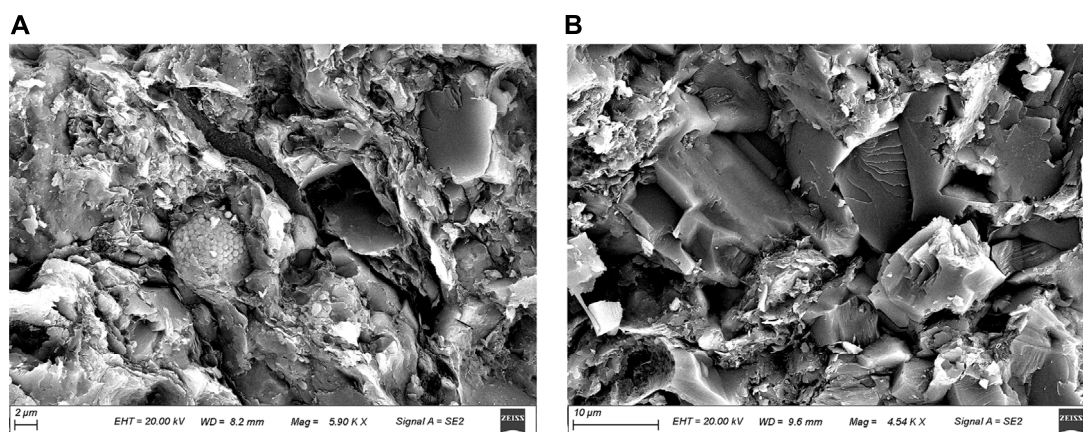
FIGURE 5
SEM micrographs of two thin-sections corresponding to the same depth as the samples 1−5 H and 1−6 V. **(A)** Micrograph shows flake illite, clastic grains, pelletized pyrite, organics, and micro-pores. **(B)** Micrograph shows the abundance of calcite wrapped by clay minerals, and inter-/intra-grain pores.

always consistent with a transverse isotropy model, which may be due to its complex microstructure. As shown in Figure 5, the two thin-sections taken from the same depth as samples 1–5H and 1–6V exhibit either the abundance of flaking clay minerals or abundant calcite, which strongly support the high heterogeneity of the Wufeng-Longmaxi shale. It can thus be inferred that the horizontal sample 1–5H contains more clay minerals than the vertical sample 1–6V, leading to a more compliant horizontal sample as also suggested by the logging-derived Young's modulus shown in Figure 1D. As anther result, the compositional difference could mask the orientation effect predicted by the transverse isotropy model.

As aforementioned, the "instantaneous" response of the sample to the differential stress may also be largely elastic. In Figure 6, we plot the cumulative differential stress *versus* the cumulative axial strain after each differential stress step. It appears that the main difference between the two samples of a pair is the axial strain accumulated in the hydrostatic stage. After applying the differential stress, all samples regardless of the well and depth show similar stress-strain relations. Specifically, for each sample, the relationship between the differential stress and the cumulative axial strain is approximately linear, plausibly justifying the linear elastic behavior of the sample under the relatively low differential stresses. The dependence of the cumulative axial strain on differential stress can then be quantified by the slope, which is effectively the Young's modulus. For each sample, the applied several differential stress steps yield individual values of Young's modulus. In addition, combining all differential stress steps, an average Young's modulus can be further obtained as indicated by the dashed line in Figure 6. In Table 2, the Young's modulus values of each sample are summarized.
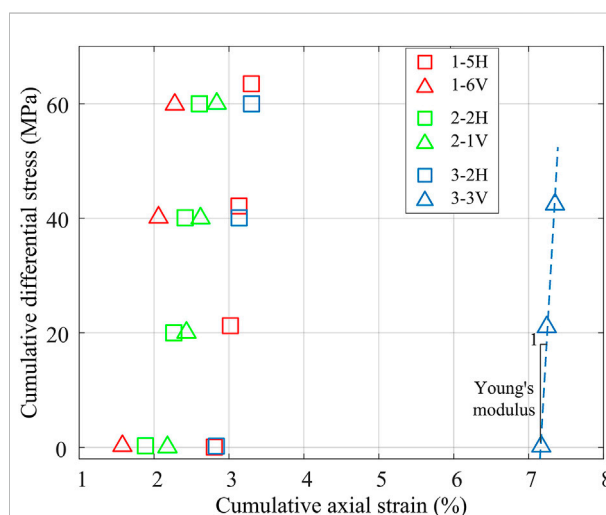

FIGURE 6
Relationship of the cumulative differential stress and total axial strain for three pairs of shale samples. Each pair of samples were retrieved from the same depth.

3.3 Viscoplastic constitutive relationship

In the framework of linear viscoelastic theory (see Appendix A), we can quantitatively calculate the creep compliance $J(t)$ describing the time-dependent strain response to a unit input (Heaviside step) of differential stress. Specifically, $J(t)$ can be obtained by dividing the measured strain by the magnitude of differential stress in laboratory investigations. In Appendix B, we have tested different functions to fit the experimental results. It is found that the power-law function and logarithmic function can

TABLE 2 Power-law constitutive parameters for Longmaxi shale sample.

| Sample	Coring depth (m)	n under different P_{diff} (MPa)			B (GPa^{-1}) under different P_{diff} (MPa)			E (GPa) under different P_{diff} (MPa)			Fitted E (GPa)
		20	40	60	20	40	60	20	40	60	
S1	—	—	0.018	—	—	0.0306	—	—	41.90	—	41.90
S2	—	0.045	0.022	0.016	0.0378	0.0389	0.0290	20.96	20.47	20.88	20.79
1-1H	2245.55	0.030	0.024	0.017	0.0387	0.0344	0.0386	18.04	22.09	21.32	21.73
1–2H	2254.06	0.028	0.022	0.018	0.0386	0.0397	0.0427	39.91	41.92	41.39	41.63
1–3H	2254.68	—	—	0.030	—	—	0.0145	—	—	50.40	50.40
1–4H	2254.68	—	—	0.022	—	—	0.0430	—	—	18.40	18.40
1–5H	2254.97	0.010	0.012	0.016	0.0904	0.0693	0.0668	9.88	12.79	12.83	13.05
1–6V	2254.97	—	0.003	0.014	—	0.116	0.0991	—	8.27	8.52	8.48
1–7H	2257.02	—	—	0.017	—	—	0.0486	—	—	16.48	16.48
2-1V	1033.23	0.023	0.016	0.015	0.0973	0.0920	0.0925	7.87	9.04	9.11	9.21
2-2H	1033.23	0.021	0.022	0.016	0.0769	0.0664	0.0733	10.05	11.46	11.13	11.28
2–3H	1028.58	0.039	0.022	0.015	0.0454	0.0511	0.0530	15.61	17.22	18.01	18.07
2–4H	1036.8	0.110	0.032	0.026	0.0685	0.0338	0.0435	41.01	20.53	17.27	13.39
3-1H	2999.59	—	—	0.017	—	—	0.0173	—	—	45.76	45.76
3-2H	3004.83	—	0.027	0.014	—	0.0541	0.0649	—	13.07	12.73	12.77
3-3V	3004.83	0.038	0.010	—	0.0220	0.0398	—	28.66	23.08	—	22.78
3–4H	3005.93	0.019	0.020	0.018	0.0460	0.0317	0.0365	17.93	25.88	22.37	22.95
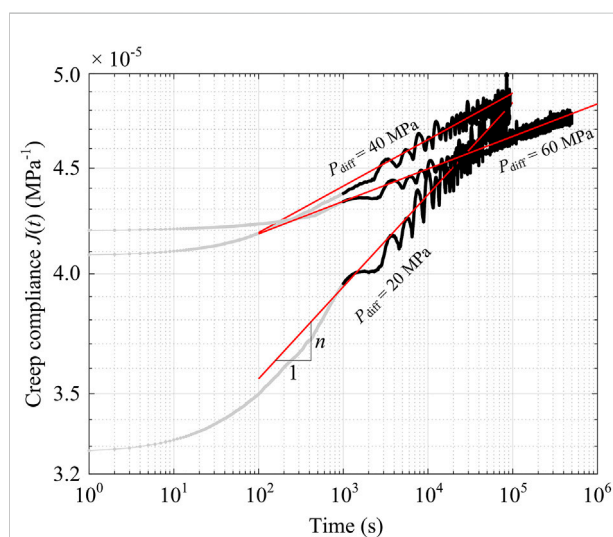
FIGURE 7
Relationships of creep compliance (J) and time (t) for three differential stress levels (20, 40, 60 MPa) shown in the log-log space (Sample: S2, confining pressure: 20 MPa). The grey data is the first 1000 s which is not considered in the linear regression. Red solid lines are the fitted results.

functions. In particular, the power-law function is simple and capable of predicting long-term creep behavior, which has been extensively used in previous studies (Sone and Zoback, 2014a; Yang and Zoback, 2014; Yang et al., 2015; Rassouli and Zoback, 2018; Xu et al., 2019; Mandal et al., 2021).

In Figure 7, the creep compliance data for the three differential stress steps of Sample S2 are plotted *versus* time in the log-log space. Each set of data shows an increasing trend with the logarithm of time. As with the strain data in Figure 3, the creep compliance data also feature fluctuations with decreasing degree with time. When the holding time is sufficiently long, the compliance data starts to show a linear trend. For the same sample under different differential stresses, it displays remarkably different creep compliance responses by the individual slopes. Quantitatively, the experimental data can be fitted by the widely-used power-law function:

$$J(t) = Bt^n \tag{1}$$

where B and n are viscoplastic constitutive parameters. As illustrated in Figure 7, each set of the creep compliance data can be well fitted by a straight line based on linear regression. Accordingly, n is the slope of the line and B is related to the intercept of the vertical axis. In the multi-step creep experiments, note that, the application of differential stress is not ideally "instantaneous". However, compared with the long creep period, the application of differential stress can be
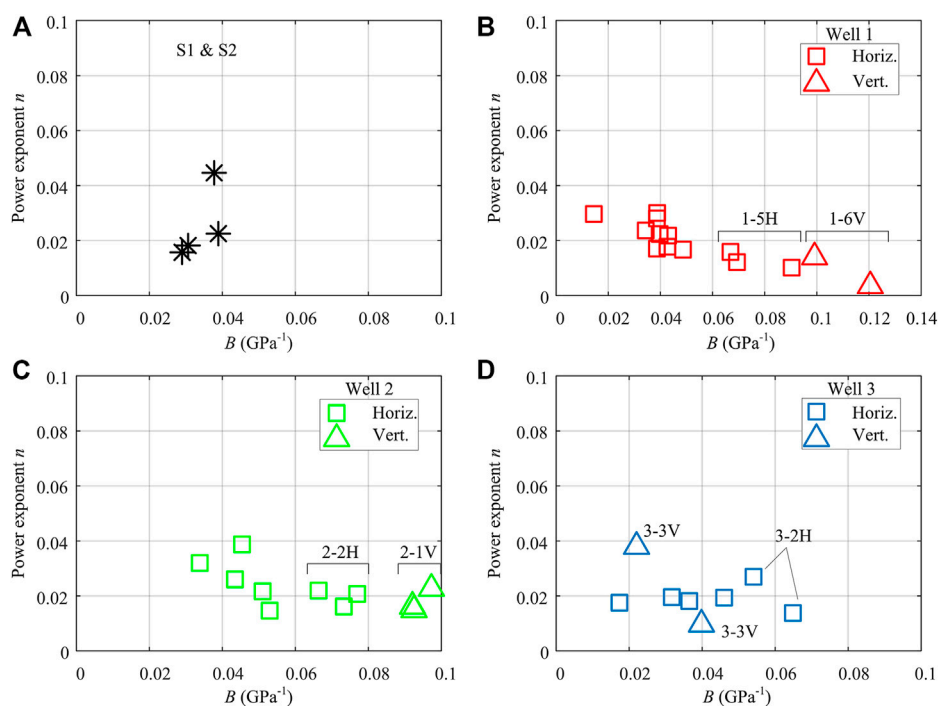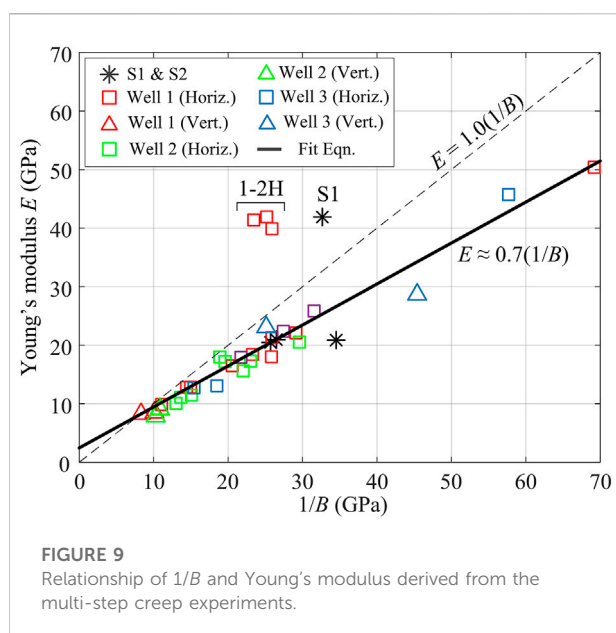
best fit the experimental data. As explained by Sone and Zoback (2014a), the creep compliance generally shows self-similar characteristics in time, which can be well described by both

FIGURE 8
Summary of the constitutive parameters of all shale samples.

FIGURE 9
Relationship of 1/B and Young's modulus derived from the multi-step creep experiments.
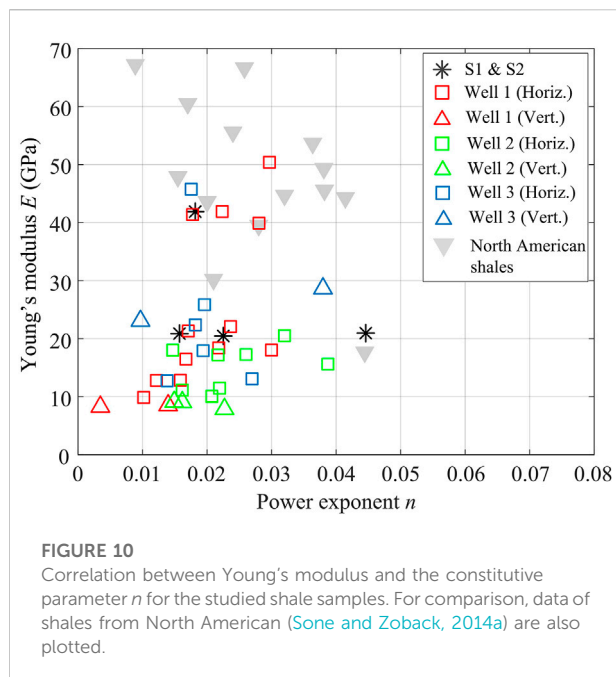
approximately regarded as an instantaneous Heaviside step. Therefore, it is general to discard the initial portion of the experimental data associated with the stress application when determining the creep compliance function $J(t)$. As

shown in Figure 7, the first 1000 s data are not included in the linear fitting. In Table 2, the determined B and n values, together with Young's modulus, of all tested samples are listed.

3.4 Constitutive parameters of the shale samples

The determined viscoplastic constitutive parameters (B and n) listed in Table 2 are now plotted in Figure 8. Comparison between each well shows that these samples, although collected from different wells and depths, fall within a similar range of n value, i.e., 0 to 0.04. For values of B, however, Samples S1 and S2 and Well 3 samples possess relatively lower B values, whereas the B values of Well 2 samples span a higher range (0.04–0.1) and Well 1 samples possess the widest range of B values (0.01–0.12). In addition, both Well 1 samples and Well 2 samples show that the vertical samples have higher B values and lower n values than horizontal samples, indicating anisotropy in their viscoplastic properties. However, the samples from Well 3 do not show apparent anisotropy from the laboratory results.

According to Eq. 1, it could be interpreted that B is the creep compliance corresponding to the initial 1 s of creep deformation (Sone and Zoback, 2014a). Essentially, B is intimately related to the instantaneous elastic modulus of the shale sample. In

FIGURE 10
Correlation between Young's modulus and the constitutive parameter *n* for the studied shale samples. For comparison, data of shales from North American (Sone and Zoback, 2014a) are also plotted.

previous studies (Sone and Zoback, 2014a; Yang et al., 2015), the relationship between $1/B$ and the calculated Young's modulus E of a variety of shales consistently shows a one-to-one correlation, despite some dispersion. To examine the relationship between $1/B$ and E of the Longmaxi shale, the experimental data are plotted in Figure 9. Excluding the data (Samples S1 and 1–2H) above the diagonal line, the Young's modulus E derived from the multi-step creep experiments is approximately 0.7 times of $1/B$, which is different from the empirical relations of the shales from North America (Sone and Zoback, 2014a). From Figures 8, 9, it can be seen that the vertical samples are more compliant than the horizontal samples, except for Well 3 samples, which is generally consistent with the theoretical prediction of the transverse isotropy model.

The power exponent *n* is a parameter associated with time-dependency, describing the relative contribution of the creep strain to the total strain observed at a given time. In other words, a larger value of *n* corresponds to more pronounced creep behavior. As an end-member, the value of $n = 0$ corresponds to an elastic behavior independent of time. Another interesting observation is that, for samples from Wells 1 and 2, higher values of B are accompanied by lower values of *n*. In other words, samples with lower Young's modulus have a lower creep tendency. In Figure 10, this trend is further observed by plotting the correlation between Young's modulus and the constitutive parameter *n*. By contrast, data of several North American shales (Sone and Zoback, 2014a) show that *n* generally decreases with *E*. The observation of the studied shale samples appears to be counterintuitive, since one would generally expect larger amount of creep deformation for samples

with lower Young's modulus due to more compliant components (Yang et al., 2015; Rassouli and Zoback, 2018; Xu et al., 2019). As indicated by Figure 5B, the abundance of stiff minerals (e.g., calcite) is likely accompanied by the abundant micro-pores, which may often contain fluids as suggested by the overpressure in the Wufeng-Longmaxi formation. Consequently, it is inferred that the abundance of stiff minerals contributes to high Young's modulus as a short-term response. At the same time, pore reduction/collapse and drainage could take place over a long time, leading to significant creep deformation as a long-term response. Such an inference could plausibly explain the observation that the stiffer samples feature more significant creep behavior, which, however, still warrants further investigation.

4 Long-term effect of viscoplasticity

4.1 Expected stress relaxation of the shale samples

Following the theory of linear viscoelasticity, we first obtain the relaxation modulus function by performing Laplace transform operations (Lakes, 2009; Sone and Zoback, 2014a):

$$E(t) \approx \frac{1}{B}t^{-n} \qquad (2)$$

Eq. 2 implies that $1/B$ is effectively the Young's modulus at $t = 1$ s, $E(1s)$. Note again that, the fitted relation in Figure 9 yields that the Young's modulus E is 0.7 times of $E(1s)$ for the studied shale samples. The difference from the empirical relation for the North American shales (Sone and Zoback, 2014a) may be due to the limited shale samples or the special microstructure. Therefore, it should be cautious to directly apply the empirical relation of the North American shales to other shales. Based on the fitted relation between B and Young's modulus, one can derive B values from Young's modulus values which are more accessible from static experiments.

With the relaxation modulus function, we can further calculate the stress response with time based on Eq. (A2). Assuming a constant strain rate $\dot{\varepsilon}$, we have:

$$\sigma(t) = \int_0^t E(t-\tau)\frac{d\varepsilon(\tau)}{d\tau}d\tau = \frac{\dot{\varepsilon}}{B}\frac{t^{1-n}}{1-n} = \frac{\varepsilon_0 E}{0.7}\frac{t^{-n}}{1-n} \qquad (3)$$

where ε_0 is the accumulated strain over time t, the constant 0.7 is from the relation between $1/B$ and E shown in Figure 9. In particular, the term $\frac{t^{-n}}{1-n}$ is referred to as stress relaxation factor, which quantifies the fraction of the applied elastic stress that remains unrelaxed after a certain time t (Ma and Zoback, 2020).

In Figure 11, the variation of the stress relaxation factor with the constitutive parameter *n* for different time scales ranging from several days (0.01 years) to years and to millions of years. For all time scales, the stress relaxation factor
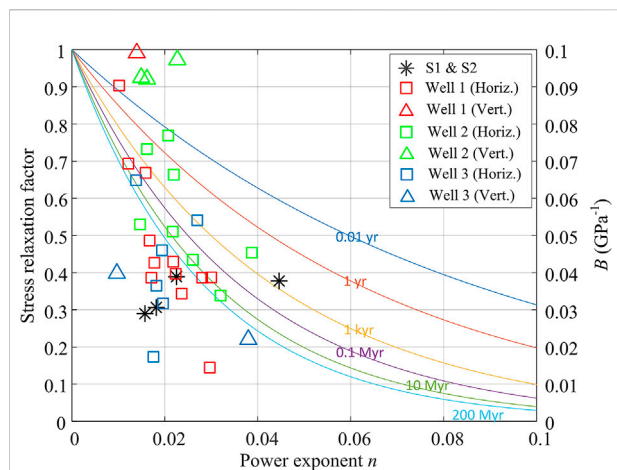
FIGURE 11
Stress relaxation factor as a function of the power exponent n for several time scales from several days up to 200 millions of years (Myr). For comparison, the constitutive parameters of all the samples are plotted.
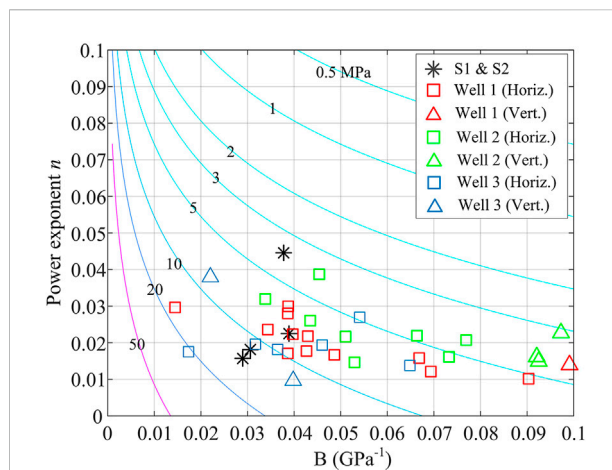

FIGURE 12
Stress accumulation (contours) as a function of the constitutive parameters (B and n). In the calculation, a constant strain rate of 10^{-19} and a deformation duration of 150 Myr are assumed. The constitutive parameters of all studied samples are also plotted.

decreases continuously with the increase of n, quantifying the tendency of viscous relaxation. For a certain value of n, the unrelaxed stress decreases with time scales and the effect of time gradually diminishes. For example, the difference between 10 Myr and 200 Myr for any value of n is much smaller than that between 0.01 years and 1 year. In other words, a significant amount of stress relaxes within an initial short period of time, which is insignificant compared with the geologic time scales. As indicated by Eq. 3, as long as the accumulated strain ε_0 and Young's modulus E are reasonably constrained, it is able to estimate the *in situ* stress without knowing the exact tectonic strain history. For all the studied shale samples, in addition, the mean value of n is about 0.02. Therefore, it is expected that 20% of the applied differential stress relaxes after 0.01 years (about 3–4 days) and 50% of the applied stress relaxes after 200 Myr.

4.2 Estimation of differential stress accumulation over geological time scales *in situ*

To estimate the accumulation of differential stress over a certain period of time, a constant strain rate of 10^{-19} and a deformation duration of 150 Myr are prescribed. Note that it is not easy to constrain a reasonable tectonic strain for the studied shale gas play located near the southern margin of the Sichuan Basin due to the complex geologic and tectonic history. The strain rate and deformation duration are only used for illustrative purpose.

As shown in Figure 9, most of the horizontal samples have the Young's modulus (E_{hori}) of 10–30 GPa. Over the deformation duration of 150 Myr, the accumulated differential stresses for the horizontal samples are expected to be between 6.8 and 20.3 MPa in the absence of viscoelastic relaxation. Taking the time-dependency of shales into consideration, the differential stress accumulated over the deformation duration is estimated and shown as contours in Figure 12. The predicted magnitude of the differential stress for all samples ranges from 3 up to 20 MPa. Note that, the values where the contours intercept with the horizontal axis ($n = 0$) correspond to the elastic stress accumulation without viscous relaxation. For a certain B value, stress relaxation becomes more pronounced as n increases, indicating less accumulation of the differential stress.

For most of the horizontal samples, the magnitude of the cumulative differential stress is predicted to be 3–10 MPa. Compared with the differential stress in the absence of viscoelastic relaxation, the stress reduction after 150 Myr is about 50%, which is similar to the percentage corresponding to 200 Myr as shown in Figure 11. In other words, the stress reduction rate decreases significantly with time. Therefore, if a perfectly isotropic state of *in situ* stress is observed in at the reservoir depths, two main reasons could be present: 1) The shale experiences a sufficiently long period of viscoplastic deformation; 2) other mechanisms, such as frictional slips (Zhang and Ma, 2021) and overpressure (Miller et al., 2004), can also be operative so that a more isotropic stress state is attainable over a shorter time scale.

5 Concluding remarks

In this study, a series of laboratory multi-step creep experiments were performed on several Longmaxi shale samples to investigate their time-dependent deformation properties. It is found that studied shale samples exhibit varying degrees of time-dependent strain response, which can be adequately described by a power-law function of time. Based on this viscoplastic model, we extrapolated the stress relaxation of the tested samples and calculated the differential stress accumulation over geologic time scales. Specifically, the following conclusions can be obtained:

1) Under the applied differential stress levels (20–60 MPa), the instantaneous response of all samples is approximately linear and elastic.
2) The studied samples, collected both from the same well and from different wells, exhibit varying degrees of time-dependent deformation. The time-dependent strain response can be well described by a power-law function of time with only two parameters (B and n).
3) From the experimental results, it is found that Samples S1 and S2 and Samples from Well 3 possess relatively lower values of B, whereas the B values of Well 2 samples are higher. For the constitutive parameter n, all samples fall within the same ranges (0–0.04). Samples from Wells 1 and 2 show that the vertical samples have higher values of B and lower values of n, indicating the anisotropy in the viscoelastic properties. However, samples from Well 3 do not show apparent anisotropy from the laboratory results.
4) The elastic Young's modulus E correlates with both constitutive parameters (B and n). As indicated by the experimental data, it is found that $E \approx 0.7$ (1/B). For the correlation between E and n, it is found that higher E generally corresponds to higher n, which means that a stiffer sample (with higher Young's modulus) tends to exhibit more pronounced time-dependent deformation. Such observation is counterintuitive since one would expect larger creep deformation for samples with lower Young's modulus due to more compliant components. Therefore, further investigation is required in the future, particularly for the microstructure of the samples.
5) The degree of stress relaxation over certain time periods is positively related to the constitutive parameter n. For a certain value of n, the unrelaxed stress decreases with time but the effect of time gradually diminishes so that a significant amount of differential stress relaxes in the initial short period of time.
6) Linear elasticity is not adequate to predict the differential stress accumulation over time. The predicted differential stress accumulation is much larger in the absence of viscoelastic relaxation. As an example, for most of the horizontal samples, the magnitude of differential stress is predicted to be 3–10 MPa over 150 Myr at a constant strain rate of 10^{-19}. In contrast, the accumulated differential stress is predicted to be 6.8–20.3 MPa by linear elasticity.

To summarize, our laboratory experiments reveal the tendency of the long-term deformation of the Longmaxi shale. The viscoplastic parameters, characterizing the long-term behavior, can be correlated with the elastic Young's modulus, quantifying the transient behavior that can be measured *in situ* with logs and *ex situ* in the laboratories. The viscoplastic properties of the Longmaxi shale can be readily extrapolated to the *in situ* stress estimation over geologic time scales, facilitating a variety of geomechanical applications in the development of unconventional reservoirs. Specifically, characterizing the *in situ* state of stress, especially the "bed-to-bed" lithology-controlled stress variations, is critical to optimizing horizontal well trajectory, improving hydraulic fracturing effectiveness, and controlling fracture propagation. The workflow presented here for the Longmaxi shale reservoir can be potentially applied to other unconventional plays.

Data availability statement

The original contributions presented in the study are included in the article/Supplementary Material, further inquiries can be directed to the corresponding authors.

Author contributions

WC, XZ, JJ, JL, WJ, and GZ contributed in conceiving this research, laboratory experiments, original draft preparation. SZ and XM contributed in formal analysis, validation, and reviewing.

Funding

Acknowledgments

Conflict of interest

Publisher's note

References

Britt, L. (2012). Fracture stimulation fundamentals. *J. Nat. Gas Sci. Eng.* 8, 34–51. doi:10.1016/j.jngse.2012.06.006

Britt, L. K., and Schoeffler, J. (2009). "The geomechanics of a shale play: What makes a shale prospective!," in Proceeding of the SPE Eastern Regional Meeting, Charleston, West Virginia, USA, September 2009. doi:10.2118/125525-ms

Chang, C., Mailman, E., and Zoback, M. (2014). Time-dependent subsidence associated with drainage-induced compaction in Gulf of Mexico shales bounding a severely depleted gas reservoir. *Am. Assoc. Pet. Geol. Bull.* 98 (6), 1145–1159. doi:10.1306/11111313009

Chang, C., and Zoback, M. D. (2009). Viscous creep in room-dried unconsolidated Gulf of Mexico shale (I): Experimental results. *J. Pet. Sci. Eng.* 69 (3–4), 239–246. doi:10.1016/j.petrol.2009.08.018

Chang, C., and Zoback, M. D. (2010). Viscous creep in room-dried unconsolidated Gulf of Mexico shale (II): Development of a viscoplasticity model. *J. Pet. Sci. Eng.* 72 (1–2), 50–55. doi:10.1016/j.petrol.2010.03.002

Clarke, H., Soroush, H., and Wood, T. (2019). "Preston new road: The role of geomechanics in successful drilling of the UK's first horizontal shale gas well," in Proceeding of the Society of Petroleum Engineers - SPE Europec Featured at 81st EAGE Conference and Exhibition 2019, London, England, UK, June 2019. doi:10.2118/195563-ms

Dong, D., Shi, Z., Guan, Q., Jiang, S., Zhang, M., Zhang, C., et al. (2018). Progress, challenges and prospects of shale gas exploration in the Wufeng–Longmaxi reservoirs in the Sichuan Basin. *Nat. Gas. Ind. B* 5 (5), 415–424. doi:10.1016/j.ngib.2018.04.011

Findley, W. N., and Davis, F. A. (2013). *Creep and relaxation of nonlinear viscoelastic materials.* Courier corporation.

Findley, W. N., Lai, J. S., and Onaran, K. (1976). *Creep and relaxation of nonlinear viscoelastic materials with an introduction to linear viscoelasticity.* NewYork: Dover. doi:10.1115/1.3424077

Guo, J., and Liu, Y. (2012). "Modeling of proppant embedment: Elastic deformation and creep deformation," in Proceeding of the SPE Production and Operations Symposium, Proceedings, Doha, Qatar, May 2012. doi:10.2118/157449-ms

Gupta, V. B. (1975). The creep behavior of standard linear solid. *J. Appl. Polym. Sci.* 19 (10), 2917. doi:10.1002/app.1975.070191028

Hagin, P. N., and Zoback, M. D. (2007). Predicting and monitoring long-term compaction in unconsolidated reservoir sands using a dual power law model. *Geophysics* 72 (5), E165–E173. doi:10.1190/1.2751501

He, D., Lu, R., Huang, H., Wang, X., Jiang, H., and Zhang, W. (2019). Tectonic and geological setting of the earthquake hazards in the Changning shale gas development zone, Sichuan Basin, SW China. *Petroleum Explor. Dev.* 46 (5), 1051–1064. doi:10.1016/S1876-3804(19)60262-4

Heidbach, O., Rajabi, M., Cui, X., Fuchs, K., Muller, B., Reinecker, J., et al. (2018). The World Stress Map database release 2016: Crustal stress pattern across scales. *Tectonophysics* 744, 484–498. doi:10.1016/j.tecto.2018.07.007

Hu, X., Zang, A., Heidbach, O., Cui, X., Xie, F., and Chen, J. (2017). Crustal stress pattern in China and its adjacent areas. *J. Asian Earth Sci.* 149, 20–28. doi:10.1016/j.jseaes.2017.07.005

Karato, S. I. (2008). *'Deformation of earth materials', an introduction to the rheology of Solid Earth.* Cambridge University Press, 463.

Kong, W., Huang, L., Yao, R., and Yang, S. (2021). Review of stress field studies in Sichuan-Yunnan region. *Prog. Geophys.* 36 (5), 1853–1864. doi:10.6038/PG2021FF0171

Lakes, R. (2009). *Viscoelastic materials.* Cambridge University Press. doi:10.1017/CBO9780511626722

Lei, X., Wang, Z., and Su, J. (2019). The December 2018 ML 5.7 and January 2019 ML 5.3 earthquakes in South Sichuan basin induced by shale gas hydraulic fracturing. *Seismol. Res. Lett.* 90 (3), 1099'1110. doi:10.1785/0220190029

Li, Y., and Ghassemi, A. (2012). "Creep behavior of barnett, haynesville, and marcellus shale," in Proceeding of the 46th US Rock Mechanics/Geomechanics Symposium 2012, Chicago, Illinois, June 2012.

Ma, X., Zhang, S., Zhang, X., Liu, J., Jin, J., Cheng, W., et al. (2022). Lithology-controlled stress variations of Longmaxi shale–Example of an appraisal wellbore in the Changning area. *Rock Mech. Bull.* 1, 100002. doi:10.1016/j.rockmb.2022.100002

Ma, X., and Zoback, M. D. (2017). Lithology-controlled stress variations and pad-scale faults: A case study of hydraulic fracturing in the woodford shale, Oklahoma. *Geophysics* 82 (6), ID35–ID44. doi:10.1190/GEO2017-0044.1

Ma, X., and Zoback, M. D. (2020). Predicting lithology-controlled stress variations in the woodford shale from well log data via viscoplastic relaxation. *SPE J.* 25 (5), 2534–2546. doi:10.2118/201232-PA

Mandal, P. P., Sarout, J., and Rezaee, R. (2021). Specific surface area: A reliable predictor of creep and stress relaxation in gas shales. *Lead. Edge* 40 (11), 815–822. doi:10.1190/tle40110815.1

Miller, T. W., Luk, C. H., and Olgaard, D. L. (2004). *The interrelationships between overpressure mechanisms and* in-situ *stresses.* Texas: AAPG Memoir, 76. doi:10.1306/m76870c2

Musso, G., Volonte, G., Gemelli, F., Corradi, A., Nguyen, S., Lancellotta, R., et al. (2021). Evaluating the subsidence above gas reservoirs with an elasto-viscoplastic constitutive law. Laboratory evidences and case histories. *Geomechanics Energy Environ.* 28, 100246. doi:10.1016/j.gete.2021.100246

Paterson, M. S. (2012). *Materials science for structural geology.* London: Springer. doi:10.1007/978-94-007-5545-1

Rassouli, F. S., and Zoback, M. D. (2018). Comparison of short-term and long-term creep experiments in shales and carbonates from unconventional gas reservoirs. *Rock Mech. Rock Eng.* 51 (7), 1995–2014. doi:10.1007/s00603-018-1444-y

Rybacki, E., Herrmann, J., Wirth, R., and Dresen, G. (2017). Creep of posidonia shale at elevated pressure and temperature. *Rock Mech. Rock Eng.* 50 (12), 3121–3140. doi:10.1007/s00603-017-1295-y

Sone, H., and Zoback, M. D. (2014a). Time-dependent deformation of shale gas reservoir rocks and its long-term effect on the *in situ* state of stress. *Int. J. Rock Mech. Min. Sci.* 69, 120–132. doi:10.1016/j.ijrmms.2014.04.002

Sone, H., and Zoback, M. D. (2014b). Viscous relaxation model for predicting least principal stress magnitudes in sedimentary rocks. *J. Petroleum Sci. Eng.* 124, 416–431. doi:10.1016/j.petrol.2014.09.022

Townend, J., and Zoback, M. D. (2000). How faulting keeps the crust strong. *Geology* 28 (5), 399–402. doi:10.1130/0091-7613(2000)028<0399:hfktcs>2.3.co;2

Wang, W., Wen, H., Jiang, P., Zhang, P., Zhang, L., Xian, C., et al. (2019). "Application of anisotropic wellbore stability model and unconventional fracture model for lateral landing and wellbore trajectory optimization: A case study of shale gas in jingmen area, China," in Proceeding of the

International Petroleum Technology Conference 2019, March 2019. doi:10.2523/19368-ms

Warpinski, N. R., and Teufel, L. W. (1989). *In-situ* stresses in low-permeability, nonmarine rocks. *JPT, J. Petroleum Technol.* 41 (4), 405–414. doi:10.2118/16402-pa

Wong, R. C. K., Schmitt, D. R., Collis, D., and Gautam, R. (2008). Inherent transversely isotropic elastic parameters of over-consolidated shale measured by ultrasonic waves and their comparison with static and acoustic *in situ* log measurements. *J. Geophys. Eng.* 5 (1), 103–117. doi:10.1088/1742-2132/5/1/011

Xu, S., Singh, A., and Zoback, M. D. (2019). "Variation of the least principal stress with depth and its effect on vertical hydraulic fracture propagation during multi-stage hydraulic fracturing," in Proceeding of the 53rd U.S. Rock Mechanics/Geomechanics Symposium, New York City, New York, June 2019.

Yang, Y., Sone, H., and Zoback, M. D. (2015). "Fracture gradient prediction using the viscous relaxation model and its relation to out-of-zone microseismicity," in Proceedings - SPE Annual Technical Conference and Exhibition, Houston, Texas, USA, September 2015. doi:10.2118/174782-ms

Yang, Y., and Zoback, M. D. (2014). The role of preexisting fractures and faults during multistage hydraulic fracturing in the Bakken Formation. *Interpretation* 2 (3), SG25–SG39. doi:10.1190/INT-2013-0158.1

Yang, Y., and Zoback, M. D. (2016). Viscoplastic deformation of the bakken and adjacent formations and its relation to hydraulic fracture growth. *Rock Mech. Rock Eng.* 2 (49), 689–698. doi:10.1007/s00603-015-0866-z

Zhang, S., and Ma, X. (2021). Global frictional equilibrium via stochastic, local coulomb frictional slips. *JGR. Solid Earth* 126 (7), 1404. doi:10.1029/2020JB021404

Zheng, W., Xu, L., Pankaj, P., Ajisafe, F., and Li, J. (2018). "Advanced modeling of production induced stress change impact on wellbore stability of infill well drilling in unconventional reservoirs," in Proceeding of the SPE/AAPG/SEG Unconventional Resources Technology Conference 2018, Houston, Texas, USA, July 2018. doi:10.15530/urtec-2018-2889495

Zoback, M. D., and Kohli, A. H. (2019). *Unconventional reservoir geomechanics*. Cambridge University Press.

Zou, C., Dong, D., Wang, Y., Li, X., Huang, J., Wang, S., et al. (2015). Shale gas in China: Characteristics, challenges and prospects (I). *Petroleum Explor. Dev.* 42 (6), 753–767. doi:10.1016/S1876-3804(15)30072-0

Appendix A: Theory of linear viscoelasticity

For a linear viscoelastic medium, the strain (or stress) response scales linearly with the applied stress (or strain), which favors the use of linear superposition (often referred to as "Boltzmann superposition") (Lakes, 2009; Findley and Davis, 2013). In other words, the total strain (or stress) response to a multiple-step stress (or strain) input can be simply obtained as the sum of individual strain (or stress) responses to each step.

Assuming the stress (or strain) inputs are infinitesimal, Boltzmann superposition allows us to calculate the strain (or stress) response in an integral form:

$$\varepsilon(t) = \int_0^t J(t - \tau) \frac{d\sigma(\tau)}{d\tau} d\tau \tag{A1}$$

$$\sigma(t) = \int_0^t E(t - \tau) \frac{d\varepsilon(\tau)}{d\tau} d\tau \tag{A2}$$

in which $J(t)$ is the creep compliance function describing the time-dependent strain response to a Heaviside input of unit stress. $E(t)$ is the relaxation modulus function describing the time-dependent stress response to a Heaviside input of unit strain.

If $J(t)$ and $E(t)$, kernel functions, are known, one can obtain the responses to any arbitrary input history by convolving the kernel functions with the derivative of the input history. The relation between $J(t)$ and $E(t)$ is given by taking the Laplace transforms of Eq. (A1) and Eq. (A2):

$$\varepsilon(s) = sJ(s)\sigma(s) \tag{A3}$$

$$\sigma(s) = sE(s)\varepsilon(s) \tag{A4}$$

Eliminating ε and σ from both equations further gives:

$$J(s)E(s) = \frac{1}{s^2} \tag{A5}$$

This equation allows us to obtain one kernel function if the other one is known. For example, if $E(t)$ is known, $J(t)$ can be calculated by the following steps: 1) taking the Laplace transform of $E(t)$ to obtain $E(s)$; 2) using Eq. (A5) to solve for the corresponding creep compliance $J(s)$ in the Laplace domain; and 3) performing the inverse Laplace transform to obtain the creep compliance $J(t)$ in the time domain. Such operations require that the Laplace and inverse Laplace transform are manageable. Similarly, $E(t)$ can be obtained according to the known $J(t)$.

Appendix B: Comparison of different functions applied to creep data

Figures B1A–E show the regression of five simple functions to the creep compliance data from the differential stress (60 MPa) stage of Sample S2, including polynomial function with three parameters, exponential function with three parameters, hyperbolic function with three parameters, power-law function with two parameters, and logarithmic function with two parameters. From the values of R^2, the power-law function and logarithmic function can best fit the experimental data. A further comparison between the power-law and logarithmic functions in Figure B1F shows that both functions have trivial differences in the fitting performance. As shown in Figure 7, considering the self-similar characteristics of the creep compliance, power-law function is adopted in this study due to its simple expression and the capability of predicting long-term creep behavior.
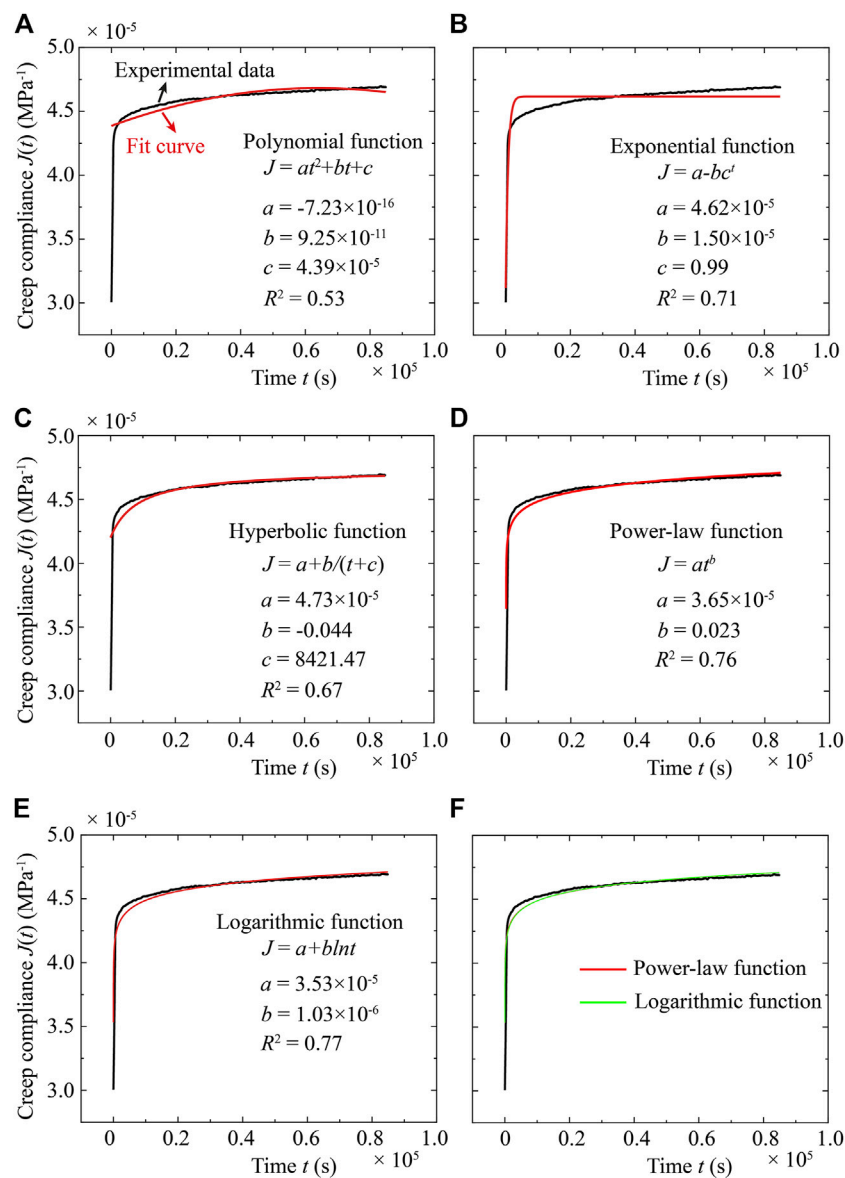
FIGURE B1
Comparison of different functions fit to the creep experimental data: **(A)** Polynomial function with three parameters; **(B)** Exponential function with three parameters; **(C)** Hyperbolic function with three parameters; **(D)** Power-law function with two parameters; **(E)** Logarithmic function with two parameters; **(F)** Comparison between the power-law and logarithmic functions. The experimental data are from the differential stress (60 MPa) stage of Sample S2.

Quantitative prediction of multistage fractures of ultra-deep tight sandstone based on the theory of minimum energy dissipation

Shuizhen Liu[1], Jianwei Feng[1]*, Josephine Anima Osafo[1], Guisheng Li[2] and Gang Li[2]

[1]School of Geosciences, China University of Petroleum, Qingdao, China, [2]No. 5 Oil Production Plant, PetroChina Dagang Oilfield, Tianjin, China

Due to strong reservoir heterogeneity and low-resolution limit of geophysical data, it is difficult to predict fractures in ultra-deep reservoirs by conventional methods. In this research, we established a novel geomechanical model for prediction of fracture distribution in brittle reservoirs, especially for ultra-deep tight sandstone reservoirs. Methodologically, we intended to introduce the minimum energy dissipation principle considering time variable, combined with the generalized Hooke's law containing damage variable, and obtained the energy dissipation rate expression corresponding to the energy dissipation process of brittle rocks. Combined with the three-shear energy yield criterion, the Lagrangian multiplier was introduced to deduce and construct the constitutive model and the failure criterion of rocks under the framework of the theory of minimum energy dissipation. Based on the law of conservation of energy, the stress-energy coupling characterization model of fracture density parameter was derived. Finally, all the improved geomechanical equations were incorporated into a finite element software to quantitatively simulate the distributions of tectonic stress filed and fractures based on paleo-structure restoration of Keshen anticline during the middle and late Himalayan periods. Its predictions agreed well with measured fracture density from reservoir cores and image logs.

1 Introduction

As an important unconventional resource and clean-burning fuel, tight sandstone gas has been widely distributed in many countries in the world, such as the U.S., Canada, Australia, Mexico, Russia, and China (Conti et al., 2016; Lu et al., 2016; Song et al., 2017; Zhou et al., 2021). In general, tight sandstone reservoirs distinctively differ from

conventional reservoirs due to their unique geological features including great burial depth, strong diagenesis, strong heterogeneity, abnormal overpressure, low porosity and developed fractures (Shrivastava and Lawatia, 2011; Walderhaug et al., 2012; Xue et al., 2014; Ding et al., 2015; Wang et al., 2016). In these tight low-permeability sandstones, the majority of reservoir spaces and seepage channels for hydrocarbon are primarily provided by widely distributed natural fractures, especially structural fractures, which can significantly and effectively improve the permeability of a reservoir and enhance hydrocarbon delivery to wellbores (DeJarnett et al., 2001; Laubach, 2003; Cumella and Scheevel, 2008; Taylor et al., 2010; Solano et al., 2011; Shanley and Cluff, 2015; Ju et al., 2017). Therefore, understanding and interpreting where and when structural fractures develop within a geological structure, along with their orientation, intensity and porosity are important in both exploration and production of tight sandstone reservoirs. However, how to predict fractures effectively is still a worldwide challenge. Three-dimensional (3-D) characterization and modeling of subsurface structural fractures pose a greater challenge in deep tight sandstone gas reservoirs with complex tectonism and diagenesis (McLennan et al., 2009; Olson et al., 2009; Deng et al., 2013; Zeng et al., 2017; Ay et al., 2019).

Models based on geometry and/or kinematics such as analyses of fault-related folds and fold curvature (Lisle, 1994; Hennings et al., 2000; Sanz et al., 2008; Ju et al., 2014; Feng et al., 2020), seismic techniques or logging methods are commonly used in fracture reservoir exploration and production and fracture prediction or modeling. In recent years and advancement of artificial intelligence technology based on a large amount of drilling measurement data, some researchers have employed the use of neural networks or deep-learning methods to predict the space of subsurface fractures. These approaches which aims to acquire the attributes of inter-well fracture networks, rely on measured data and relate the deformation to corresponding structural position (Smart et al., 2012). They are commonly tied to ideal geometric models or simplified assumptions that may not completely reflect the multi-phase deformation behaviors and mechanical properties of underground rocks (Laubach, 2003; Olson et al., 2009; Smart et al., 2012).

Generally, tectonic stress field is the most important factor in controlling development and distribution of structural fractures in reservoirs (Mckinnon and Barra, 1998; Tuckwell et al., 2003; Jiu et al., 2013; Ju et al., 2014; Liu, et al., 2017). Therefore, important and efficient geomechanical modeling strategies used in recent exploration and development of brittle reservoirs are; 1) studying concentrations and changes in paleo-tectonic stress field, 2) determining critical process involved in fracture development, and 3) combining various rupture criteria to predict favorable zones of fractures (Sanz et al., 2008; Zeng, 2010a; Smart et al., 2012; Zhao et al., 2013; Wu et al., 2017; Feng, et al., 2021).Since the 1960's, many studies have been published

on the mechanisms of fracture-generating structural movement including rock constitutive relation, failure criterion, indicator of comprehensive rupture rate, and strain energy density (Price, 1966; Hoek, 1980; Song, 1999; Tan, 1999; Zhou, 2003; Olson & Laubach, 2009). Currently, commonly used rock strength criteria such as the maximum stress theory, the maximum strain theory, the Tsai-Hill criterion, the Hoffman criterion, the Tsai-wu criterion, the Mises-Schleicher criterion (i.e., AMS criterion), the single-shear criterion and the double-shear strength criterion, are mostly for surface rock or metal materials (Luo et al., 2009). Moreover, most of the existing rock constitutive relations and strength criteria are phenomenological views based on experiments. They are based on certain theoretical assumptions and rely on a large number of accurate, small dispersion and reasonable experimental data in each quadrant lacking a unified theoretical framework (Luo et al., 2009). In particular, various rock strength criteria have certain applicable conditions and limitations. For example, Rankine's strength theory is only applicable to brittle rock under 2-D stress conditions, and the maximum shear stress strength theory is only applicable to the shear-slip failure of plastic rocks, where the influence of the intermediate principal stress is not considered. The Coulomb failure criterion only works on materials with compressive strength greater than tensile strength, such as rocks under low confining pressure and temperature.

The theory of minimum energy dissipation (i.e. the principle of minimum entropy generation), as a general natural law existing in the systems with and without life, linear equilibrium and non-equilibrium mechanical systems has many applications in material mechanics, life science and even social science. According to this basic theory, the material or rock failure process always occurs in the weakest place, that is, the primary condition of the minimum energy dissipation rate must be satisfied at any time during the rock deformation process (Tabarrok and Leech, 2002). The complexity and particularity of deep geological conditions, faults, folds, lithology, temperature and pressure affect the formation deformation behavior and fracture development to varying degrees. Therefore, this basic theory is necessary to solve the problem of rock failure in essence and predict the spatial distribution of fractures more accurately. In this study, the theory of minimum energy dissipation was first considered, then the damage variable, energy consumption rate expression and Lagrange multiplier was applied in the process of rock deformation. In addition, the combine yield criteria of three-shear energy was used to derive and construct the rock constitutive model and failure criterion under the framework of minimum energy consumption theory. Furthermore, taking the energy conversion and conservation law as constraints, and the instantaneous energy dissipation rate as a link, the stress-energy coupling characterization model of fracture density parameter was derived. Finally, the Keshen gas reservoir in the Kuqa Depression of the Tarim Basin was selected as the
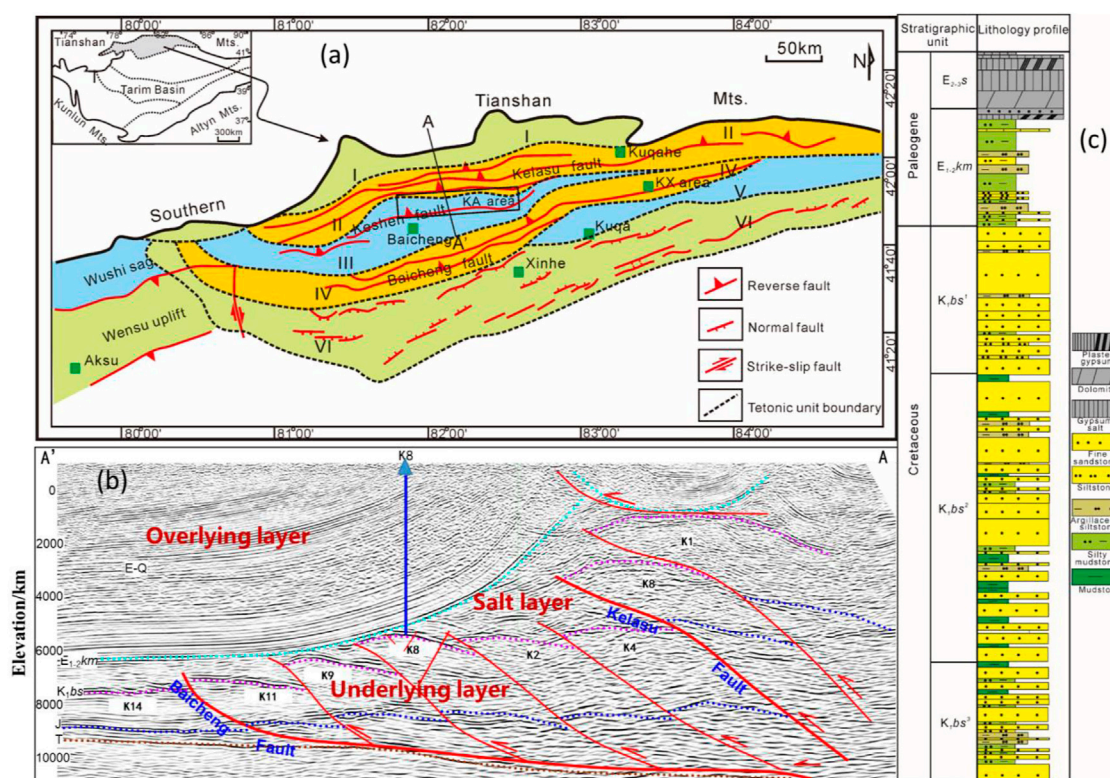
FIGURE 1
Maps show the elementary structural features of the Kuqa Depression. **(A)** Location of the study area (from Zhang et al., 2006),I-Northern monocline tectonic zone; II-Kelasu tectonic zone; III-Baicheng sag; IV-Qiulitage tectonic zone; V-Yangxia sag; VI-Northern Tarim Uplift; **(B)** Tectonic cross-section of the location shown in **(A)**.Pre-T: Silurian to Triassic; J: Jurassic; K_1y-K_1s-K_1b: Yageliemu Formation+ Shushanhe Fromation-Baxigai Fromation; $E_{1-2}km$:Kumugeliemu Formation; $E_{2-3}s$:Suweiyizu Formation; N_1j: Jidike Formation; N_1k: Kangcun Formation; N_2k−Q_1x: Kuqa Formation to Quaternary; **(C)** Schematic stratigraphy of the Kuqa Depression.

study area. By establishing the paleo-tectonic model and geomechanical model of the key tectonic movement period, we performed the paleo-tectonic stress field simulation and quantitatively predicted the spatial distribution of multistage structural fractures, which were effectively verified by the measured fracture density from drilled cores and imaging logs.

2 Geological setting

The Keshen gas reservoir, located in Kuqa Depression, the northern margin of the Tarim Basin is an important tight gas-producing area in China. (Figure 1A). Structures that developed widely in the Kuqa Depression during the Cenozoic Period are dominated by thrust faults and related folds. Laterally, the Kuqa Depression can be divided into three structural belts and two sags, which are the northern monocline belt, the Kelasu structural belt, the Baicheng sag, the Kuqa depression, and the Qiulitage structural belt from north to south. The Keshen gas reservoir is situated in the footwall of Kelasu tectonic belt, south of Kela fault and displays a narrow anticline with a structure

amplitude of less than 500 m, which is mainly developed in the Pliocene Kuqa period (Zhang et al., 2006; Zeng et al., 2010b; Sun et al., 2017).The top of the Keshen gas reservoir is cross-cut by a series of subsidiary faults striking E-W, making the structural architectural complex with moderate dips in the southern wing ranging from 19° to 23° and in the northern wing ranging from 16° to 20° (Figure 1B). The major fracture intervals in the Keshen gas reservoir consist of Cretaceous delta front rocks (the Lower Bashijiqike Formation, i.e., K_1bs) which are dominated by fine sandstone, siltstone, and mudstone with limited sandy conglomerate (Figure Figure1C). These beds reach a total thickness of up to 320 m within the study area and are divided into three members (e.g., K_1bs^1, K_1bs^2 and K_1bs^3) from top to bottom according to lithological cycles and interbeds (Chu et al., 2014). The K_1bs^1 and K_1bs^2 can further be divided into two sand groups (e.g. K_1bs^{1-1}, K_1bs^{1-2} and K_1bs^{2-1}, K_1bs^{2-2}), respectively. The relevant geological data is scarce because only few wells have been drilled in the K_1bs_3 member. The K_1bs is a typical low-permeability tight sandstone reservoir, which is deeply buried ranging from depth of 6,000 to 8,000 m with fracture-pore dual medium. The porosity of the
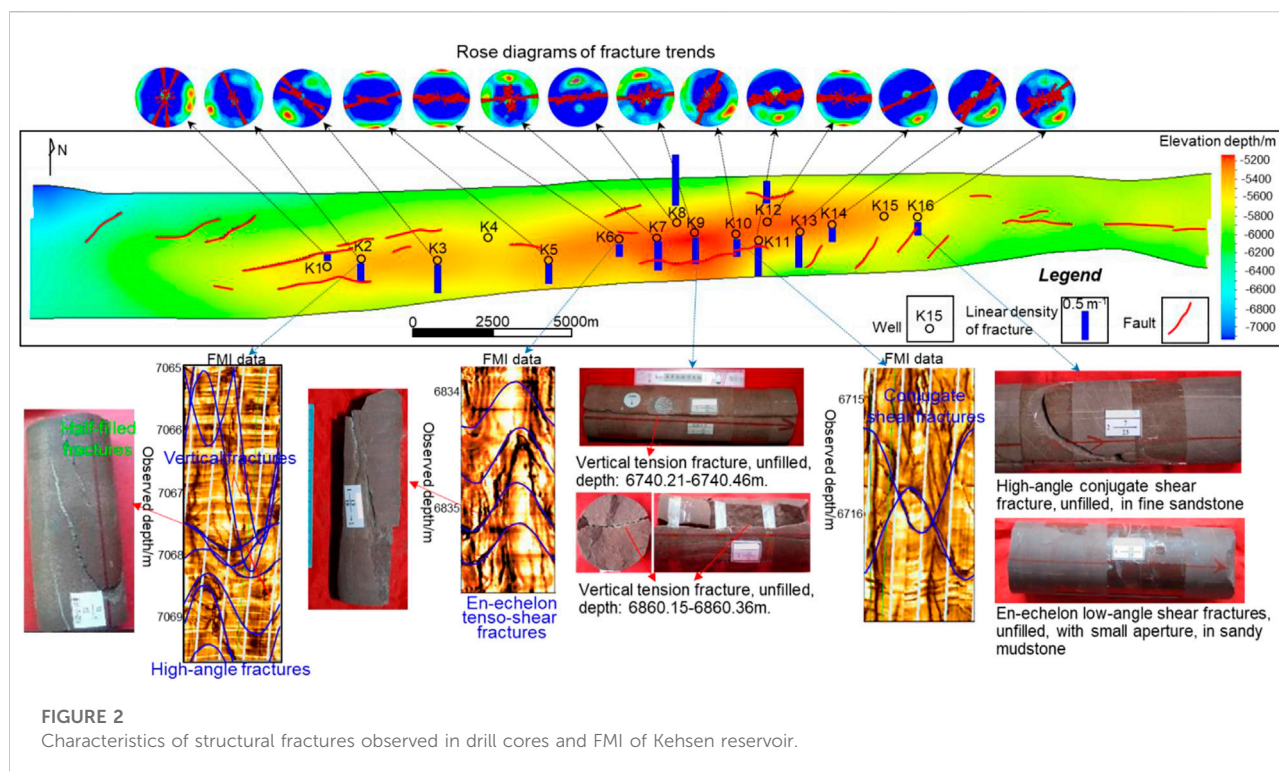
FIGURE 2
Characteristics of structural fractures observed in drill cores and FMI of Kehsen reservoir.

Bashijiqike reservoir as determined by core tests, mainly ranges from 3% to 5%. The reservoir matrix permeability mainly lies in the range of $(0.035–0.1) \times 10^{-3}$ μm², while the tested permeability of reservoir reaches $(0.035–0.1) \times 10^{-3}$ μm², much higher than the former. Structural fractures are widely distributed in the Kela gas reservoir, which greatly improve the connectivity of the reservoir and make the K$_1$bs the most important target zone of oil and gas.

3 Fracture's characteristics and formation timing

3.1 Development characteristics of fractures

Structural fractures in the K$_1$bs of the Keshen gas reservoir were mainly identified and analyzed from core observation, thin section study and formation micro-imaging (FMI) interpretations. The fractures present in the six cored wells could be subdivided based on their orientation into six distinct, mutually abutting fracture sets oriented nearly EW (Set I), NNW-SSE (Set III), NE–SW (Set IV), NNE-SSW (Set V) and SN (VI) (Figure 2). Some of these shear fractures constituted three conjugate fracture systems, and the corresponding bisectors of shearing angles pointed to 310°, 347° and 13° respectively. It could be inferred from the theory of structural geology that these three orientations respectively indicated the three stages of tectonic movement from the

southern margin of the Tianshan Mountains since the Cenozoic period. Observations from cores and analysis from FMI showed that the dip angle of fractures in Keshen gas reservoir mainly ranged from 75-90 (i.e., vertical fractures), followed by 45-75 (i.e., high-angle fractures) and 15-45 (i.e., low-angle fractures). Low dip-angle and horizontal fractures were almost not developed, accounting for only about 0.1% of the total number of fractures, generally located in the limb and saddle areas of the anticline. The statistical results showed that the macrofracture apertures after correction mainly ranged from 0.1 to 0.4 mm, except for some fractures in the eastern anticline exceeding 0.69 mm. As a result of geological paleo-fluid action (Olson et al., 2009), most fractures in K$_1$bs were unfilled and semi-filled, in which the filled fractures accounted for less than half of the total (approximately 27%), with anhydrite and dolomite as the main fillings. Macroscopically, the strong deformation of the high part of the anticline made the fracture aperture relatively large and the filling degree low, thus making the high part of the anticline a high-yield area of natural gas. For example, the absolute open flow (AOF) of single wells in the high part of Keshen anticline reached $397 \times 10^4–523 \times 10^4$ m³/d, while the productivity in the limbs were relatively poor and the relative AOF was only $272 \times 10^4–328 \times 10^4$ m³/d.

The structural fractures most frequently encountered in the reservoir of the area were planar discontinuities that are sub-perpendicular to the bedding and can be divided into three basic types namely tension fracture, tenso-shear fracture, and shear
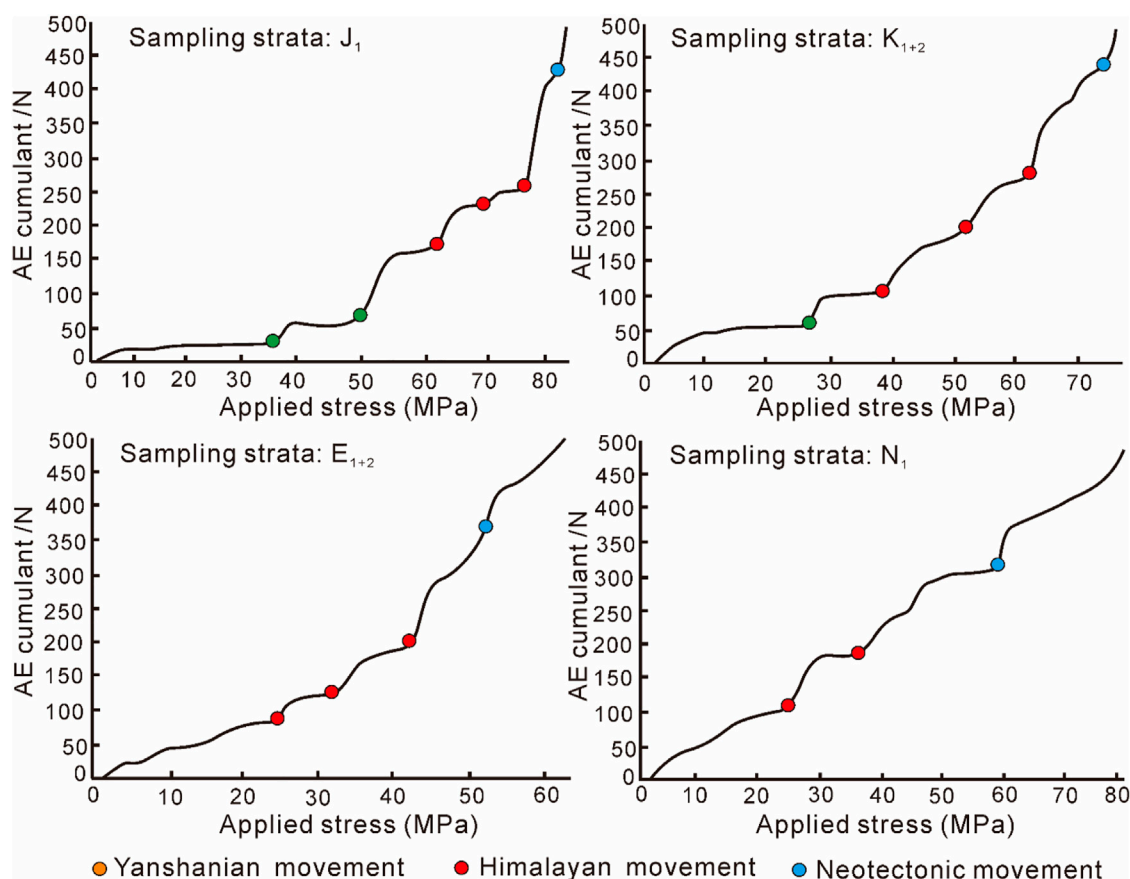
FIGURE 3
Typical response curves of AE experiment of rocks in different formations of Keshen gas reservoir (Note that this is only part of the data).

fracture, respectively accounting for 67%, 17%, 16% of the total number of fractures. As an important indicator for revealing the development degree of fractures in reservoirs, the fracture density can be divided into linear density (D_{lf}), areal density (D_{sf}) and volume density (D_{vf}). Among the three, the D_{lf} is defined as the number of fractures per unit length, which is a kind of parameter that can most directly and effectively characterize the fracture development degree (Golf-Racht, 1982; Ju et al., 2014). The results from core observations and FMI interpretations suggested that, the average D_{lf} of fractures in K_1bs mainly ranged from 0.2 m^{-1} to1.2 m^{-1}, showing strong differences and heterogeneity both in plane and vertical. For example, fractures were the most developed in siltstone, with a linear density of ~1.52 m^{-1}, followed by fine sandstone and medium sandstone, with a D_{lf} of 1.01 m^{-1} and 0.61 m^{-1}, respectively. In contrast, fractures were not developed in mudstone, and the D_{lf} was generally below 0.51 m^{-1}. Structurally, the fracture D_{lf} of the high parts of the anticline was obviously higher than that of the low part and higher than that of the limb. The average fracture density at the eastern highs of the Keshen anticline reached 1.19 m^{-1}, which was significantly higher than that at the western highs (0.61 m^{-1}) (Figure 2).

3.2 Generation timing of fractures

Currently, rock AE test and structural trace analysis are the most common and effective techniques for determining paleo-tectonic stress value and fracture formation period. Combining previous studies and the results of this analysis, it is concluded that since the late Cretaceous three regional tectonic movements in Kuqa depression and Keshen gas reservoir are recorded, i.e., the Late Yanshanian-Early Himalayan period, the middle and late Himalayan movements, which controlled the development of a series of folds, faults and fractures (Zhang et al., 2020; Zhao et al., 2021). The early Cretaceous strata encountered four paleo-tectonic movements after eliminating the influence of current tectonic movements from acoustic emission (AE) tests (Figure 3). The Paleogene and Neogene strata recorded three and two paleo-tectonic movements, respectively. Furthermore, referring to the regional tectonic background, the two major paleo-tectonic movements expressed by Neogene rocks correspond to the tectonic movements in the middle and late Himalayan periods, while the other two major tectonic movements correspond to the early
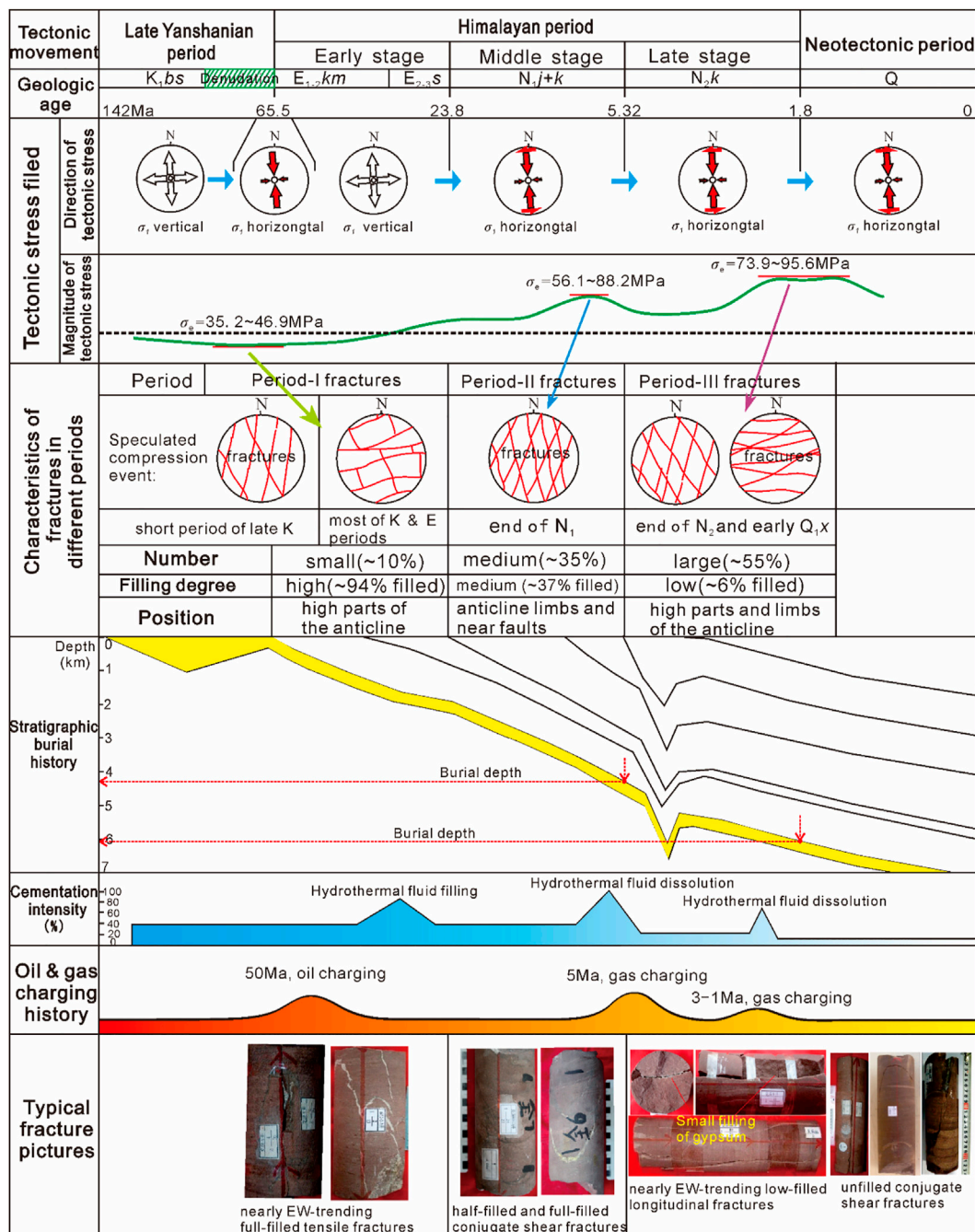
FIGURE 4
Sequence of fracture formation and cementation relative to regional tectonic events and burial history and for the Kuqa Depression. Part of the paleostress data from Zeng et al. (2004) and Li et al. (2015). And, the statistics of diagenetic cementation and fracture filling are derived from a large number of microscopic thin slices and drilling core data, respectively.

Himalayan and late Yanshanian tectonic movements, respectively.

Furthermore, the combination of Andersonian faulting modes and Geomechanics Theory can effectively analyze the formation stage and time problems of complex fracture networks. As shown in Figure 2, nearly 6,000 fracture data from FMI and cores indicated that the number of NW-trending fractures account for 52.18% of the total and the NE-trending fractures account for about 35.1%. In contrast, the number of nearly EW-trending fractures account for
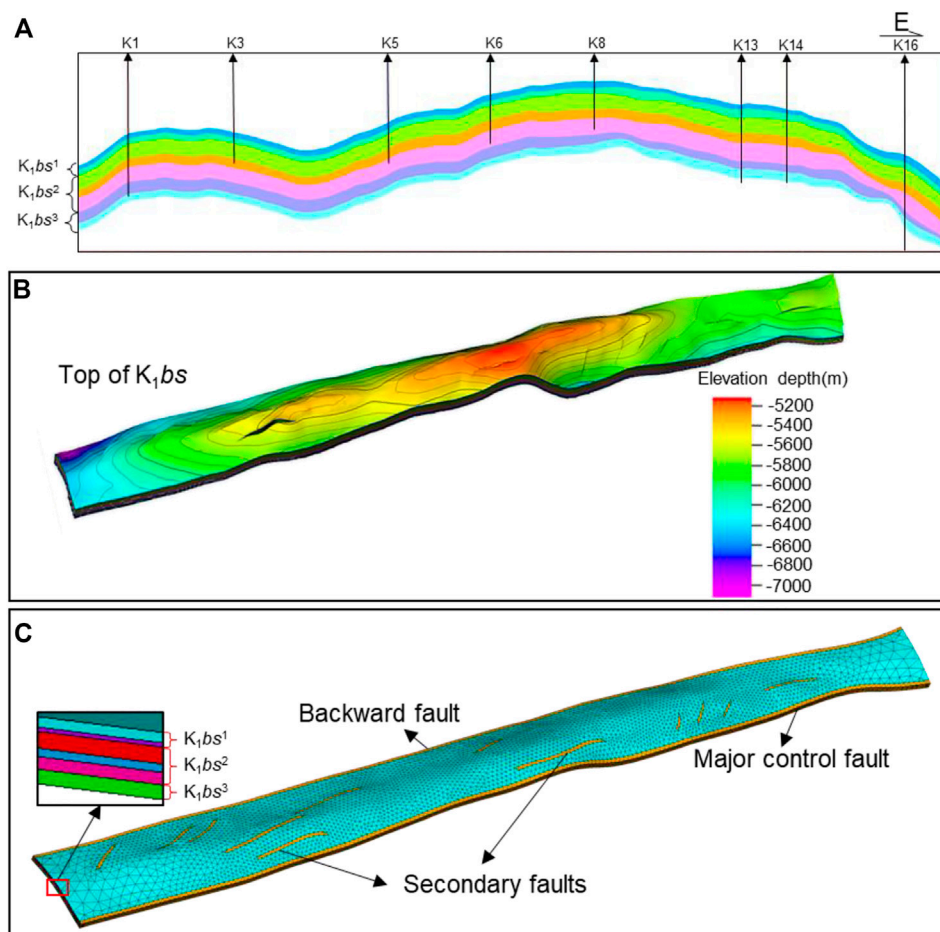
FIGURE 5
(A) Horizon model of post-stack seismic interpretation; **(B)** 3D geological model based on corner point grid; **(C)** Simplified 3D FE models of the Bashenjiqike Formation in the Keshen gas reservoir.

approximately 9.78% of the total number, while the nearly SN-trending fractures account for only 2.93%. In the Kuqa depression, both the statistical results of folds, faults, conjugate joints and the experimental results of rock AE shows that the maximum principal compressive stress of paleotectonic stress field during the late Yanshan movement to Himalayan movement is nearly SN-trending (specifically, ~NNW350°). However, a series of en-echelon faults had been developed in Keshen gas field, which is a secondary structural unit in the Kuqa depression, indicating that there existed a local torsional stress field at the same time (Figure 2). In other words, the major faults on the boundary of Keshen gas field experienced left-lateral and right-lateral shear movements during the Himalayan movements, which caused the change of fracture orientation on the plane. It can be inferred from the above that, in the late Yanshanian and early Himalayan periods, a series of nearly EW-trending tensile fractures were mainly developed in the Keshen area under the environment of long-term weak

extension and short-term weak compression (Figure 4). During the middle Himalayan period, the anticline was initially in shape under the strong compression and local left-lateral shear stress field. In the Keshen area, some NE-trending conjugate fractures and a small amount of nearly EW- trending tensile fractures were formed. In the initial folded framework, the anticline was strongly uplifted and an obvious tensile stress environment appeared at the top due to the combined action of the strong compression of the Tianshan Mountains and the dextral stress field of the boundary fault. With this information, only a series of conjugated fractures developed on the limbs, whereas a large number of tensile fractures/faults with parallel hinges developed at the top (Figure 4).

According to the results of the diagenetic evolution sequence of the reservoirs in the Keshen area, from the Late Cretaceous to the present, the diagenesis and compaction of the K_1bs reservoir has a tendency to become weaker (Li et al., 2017; Li et al., 2018). Under the influence of mantle thermal activity during the
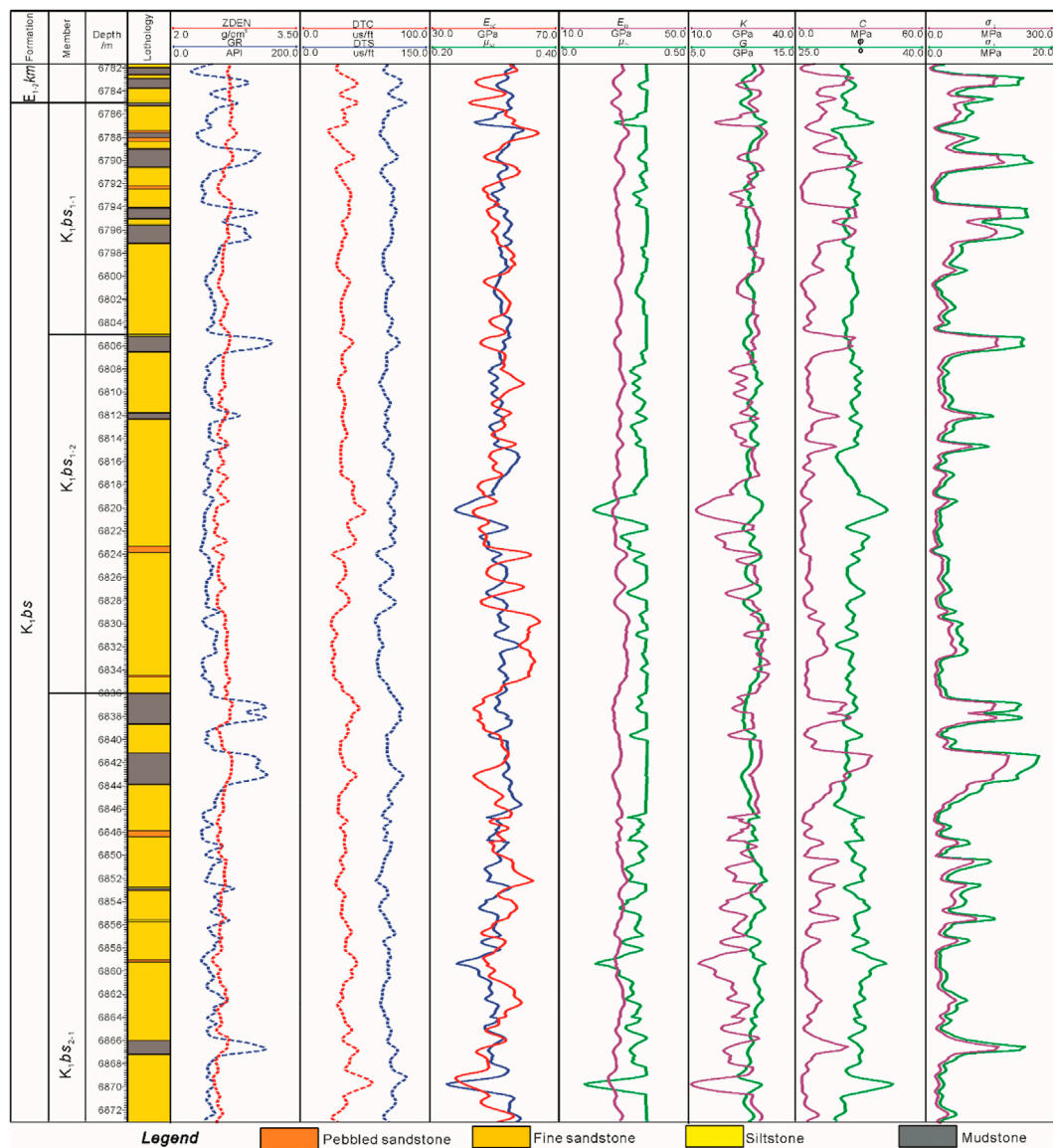
FIGURE 6
Comprehensive columnar section of rock mechanics parameters in the K_1bs of the K15 well. Here, ZDEN is the litho-density logging, GR is the natural gamma logging, DTC is the P-wave time difference logging, DTS is the S-wave time difference logging, E_{td} is the dynamic Young's modulus of rock, μ_{td} is the dynamic Poisson's ratio of rock, E_{td} is the corrected static Young's modulus of rock, μ_{ts} is the corrected static Poisson's ratio of rock, K is the bulk modulus of rock, and $K = E/[3 \times (1-2\mu)]$, G is the shear modulus of rock, and $G = E/[2 \times (1 + \mu)]$, φ is the internal friction angle of rock, σ_c is the compressive strength of rock; σt is the tensile strength of rock.

Paleogene period, a large-scale deep thermal fluid diagenetic event occurred in the Kuqa Depression and the diagenesis occurred in the early diagenetic stage-A from the epigenetic stage (Li et al., 2018). The core statistics showed that under the influence of this hydrothermal fluid diagenesis, the extensional fractures in the Keshen gas field are basically filled with calcite and gypsum, with an average filling degree of 94%. On the contrary, during Miocene to Pleistocene, the overall burial depth of the Keshen gas field increased and the storage space

of reservoir was dominated by lateral and vertical compaction under strong thrust action. During this period, the reservoir reached the middle diagenetic stage-A, the deep thermal fluid was dominated by extensive acid dissolution and the porosity of the fractures developed during the same period increased. However, due to the existence of the overlying Paleogene gypsum-salt layer, a large amount of anhydrite and dolomite minerals were transported into the K_1bs reservoir under the action of stratum water, making some fractures partially filled

(Figure 4). It can be seen that for the exploration and development of the Keshen gas field, the structural fractures developed in the middle and late Himalayan Movement are effective and also the focus of our research.

4 Methods and theory

4.1 Simulation of multistage paleotectonic stress field

4.1.1 Establishment of geological model

An accurate and reasonable 3D geological model (e.g., paleo-tectonic model) is crucial to numerical simulation of tectonic stress field and fractures. Generally, horizon data and fault data related to geological and geomechanical models were derived from the interpretation of the post-stack 3D seismic data (Figures 5A,B). The traditional corner grid modeling process, may lead to drastic changes in the thickness of the same small layer and even unreasonable interleaving between layers. Therefore, a deterministic modelling method was used to establish the geological model of the study area based on the corner point gridding (Figure 5C). After transforming the corner point grid model into key points, a finite element (FE) model close to the real underground geological structure was established the in the ANSYS software. In detail, the construction of 3D geologic model incorporated three horizons of K_1bs^1, K_1bs^2, K_1bs^3 or several isolated blocks (Figures 5A,B). Since there were few wells drilled in the K_1bs^3 and the geological stratification data were relatively scarce, K_1bs^3 can only be combined into a set of strata in modeling. As a result, the average thickness of six layers K_1bs^{1-1}, K_1bs^{1-2}, K_1bs^{2-1}, K_1bs^{2-2}, K_1bs^{2-3} and K_1bs^3 within geologic model was set to 25 m, 25 m, 70 m, 40 m, 70 m and 80 m, respectively. However, due to the quality of ultra-deep seismic data, the reliability of some low-order faults in Keshen anticline is debatable. In this study, by combining the comparison and verification of various seismic attributes, such as original seismic amplitude volume, maximum positive curvature attribute, variance attribute, and ant tracking attribute, 12 relatively reliable large-scale faults were retained for geological modeling among the 23 originally interpreted faults.

4.1.2 Geomechanical modelling

Rock mechanics parameters are key parameters characterizing the degree of formation brittleness and possible fracture development. Two methods can be used to obtain rock mechanics parameters: rock mechanical experiments on core samples or calculation of well logging curves. The former obtains the static mechanical parameters of rock, while the latter obtains the dynamic parameters with large errors between them. Therefore, it is necessary to construct the correlation between them based on laboratory data. In this study, conventional uniaxial and triaxial compression tests were conducted to obtain static rock

mechanical parameters. A total of 48 rock samples were drilled from K_1bs Formation, involving different lithology and horizons to ensure the rationality and practicability of the data. All samples were processed according to International System for Rock Mechanics (ISRM)-suggested methods with a core diameter of 25 mm and length of 50mm, ends ground flat to 0.01 mm with vertical deviation of less than 0.25°. In order to meet the underground formation conditions and consider the safety problems, the confining pressures during the Triaxial experiments could be set to 35 MPa, 45 MPa, and 55 MPa, respectively, and the loading rate could be set to 0.01 mm/s. In this way, the complete stress-strain curves and mechanical parameters of sandstone were acquired, including the uniaxial/triaxial compression strength or peak strength (σ_c), Young's modulus (E) and Poisson's ratio (μ), cohesive strength (C_0) and friction angle (φ). Prior to this, corrections should be made between uniaxial and triaxial experimental data, i.e., uniaxial results are corrected to triaxial conditions and then used to calibrate the log calculation results (Figure 6) to determine the relationship between log dynamic parameters and triaxial static parameters. Based on the corrected triaxial test data, the dynamic-static relationship of rock mechanical parameters can be obtained by further modifying the depth of rock samples, as shown below:

$$\begin{cases} E_{ts} = 0.125 \cdot E_{td} + 7.8215, R = 0.728 \\ U_{ts} = 3.968 \cdot U_{td} - 0.7551, R = 0.855 \end{cases} \quad (1)$$

where, E_{ts} is the triaxial static Young's modulus; E_{td} is the triaxial dynamic Young's modulus; U_{ts} is the triaxial static Poisson's ratio; U_{td} is the triaxial dynamic Poisson's ratio; R is the correlation coefficient. By using the continuous logging interpretation method and combining the above dynamic-static relationship, the triaxial static mechanical parameters of multiple wells can be calculated, and the average value of six sand groups in K_1bs can be obtained as the basis for numerical simulation.

The mechanical parameters of the fault zone directly affect the numerical simulation results, which is the basis of modeling (Liu et al., 2017). Before the formation of faults or folds, the overall Young's modulus was about 115–135% of the sedimentary strata in the model, while the Poisson's ratio was the opposite whereas the faults correspond to the weak zones after the formation. According to the above dynamic-static correction results, the average static Young's modulus, Poisson's ratio, rock cohesion, internal friction angle, bulk modulus of rock, and shear modulus of each geological unit were summarized as shown in Figure 6 and Table 1.

4.1.3 Boundary conditions

Based on the tectonic evolution, paleostress reconstruction and related tests, boundary conditions of two formation periods of fractures were defined, including the load application and

TABLE 1 Average mechanical properties of the K_1bs tight sandstones from triaxial compressional tests. In the table, E is the rock Young's modulus; μ is the Poisson's ratio; σ_c is the rock compressive strength; ρ is the rock density; φ is the rock internal friction angle; C_0 is the rock cohesion, K is the rock bulk modulus, and G is the rock shear modulus.

Sand group	E/GPa	μ	ρ/g/cm^3	C_0/MPa	φ/°	K/GPa	G/GPa
K_1bs^{1-1}	37.7	0.215	2.60	81.61	32.45	22.05	15.51
K_1bs^{1-2}	36.8	0.22	2.61	82.51	34.27	21.90	15.08
K_1bs^{2-1}	38.2	0.21	2.54	83.69	36.74	21.95	15.79
K_1bs^{2-2}	37.5	0.215	2.59	87.88	36.14	21.93	15.43
K_1bs^{2-3}	38.4	0.21	2.57	85.14	37.72	22.07	15.87
K_1bs^3	34.65	0.233	2.65	89.905	30.26	21.59	14.06
Fault zone	29.5	0.274	2.57	68.65	27.19	21.76	11.58
Boundary rocks	36.84	0.219	2.60	85.81	33.98	21.85	15.11
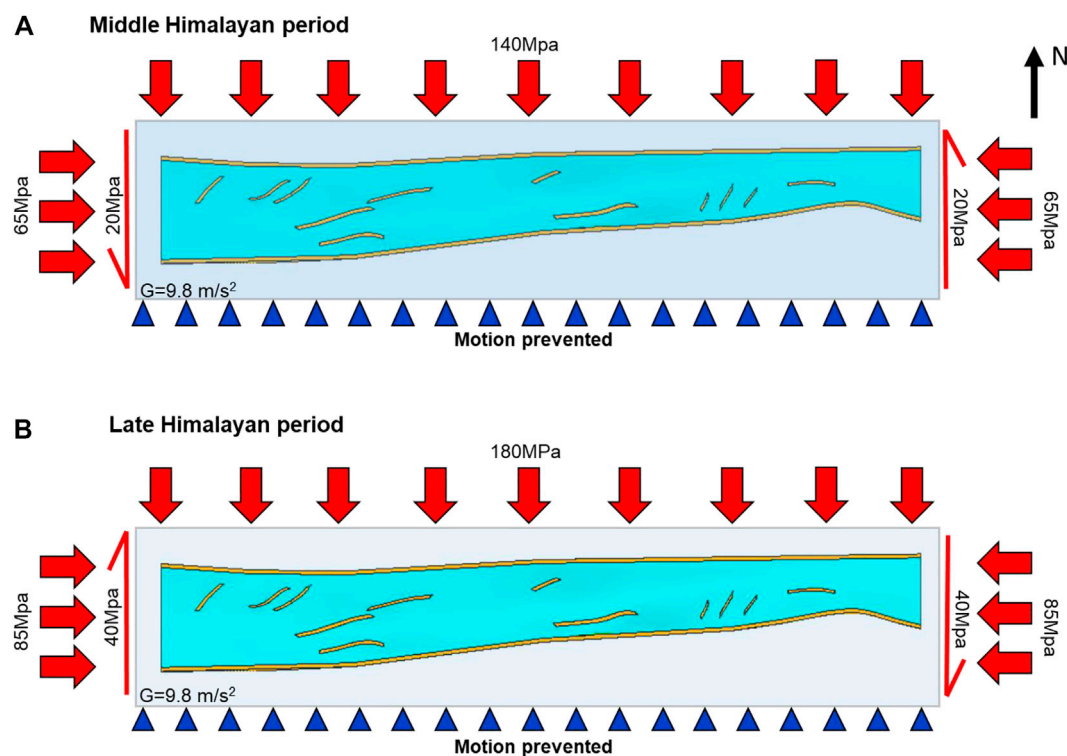
FIGURE 7
Mechanical model of tectonic stress field simulation of study area. **(A)** Boundary condition in middle Himalayan period; **(B)** Boundary condition in late Himalayan period.

displacement constraint. The determination of stress magnitude was based on the AE tests (Figure 3), and the maximum principal stress in different tectonic periods were summarized. Due to the occurrence of tectonic movements, fluids generally exists in the formations, that is, the interaction between the pore pressure and the tectonic stress forms an effective stress field. However, the samples used for rock AE experiments do not contain fluid, so the value of the paleo-maximum principal stress obtained by the experiment is an effective paleostress value. Consequently, in Kuqa Depression, the tectonic stress intensity from the late Yanshanian to early Himalayan was relatively weak, located in range of 35.2–46.9 MPa. In contrast, the tectonic stress intensity of the middle Himalayan movement at

the end of the Paleogene became stronger, reaching 56.1–88.2 MPa (Figure 3, Figure 4). When entering the late Himalayan and Neotectonic period, the tectonic stress intensity reached its peak, located in the range of 73.9–95.6 MPa. According to the Mohr-Coulomb strength criterion, the horizontal compression force of less than 100 MPa under deep formation conditions are not enough to generate so many high-angle structural fractures, which cannot be directly used for FE numerical simulation. As showed in Figure 4, during the middle Himalayan, the burial depth of the top of K_1bs formation was ~−4,250 m, and the corresponding vertical stress (i.e., σ_v) reached 108 MPa. In contrast, under the strong compression in the late Himalayan period, the burial depth of the top surface of K_1bs reached ~-6,100 m, and the corresponding vertical stress reached 155 MPa.

Since most of the wells in Keshen gas field are located at the top of an anticline, in terms of Andersonian faulting and Mohr-Coulomb theory, a series of sub-vertical shear fractures (as shown by core observation results) can only be developed under the Type-III stress environment (i.e.,$\sigma_H>\sigma_v>\sigma_h$). It can be inferred that in the middle and late Himalayan movements, only when the horizontal tectonic stress exceeded 108 MPa or 155 MPa can the Type-III stress state be satisfied. According to the AE experiment results and the concept of equivalent paleo-stress, a reasonable boundary condition scheme for the Keshen model was finally determined after repeated attempts. For the middle Himalayan model, pressures of approximately 140 MPa and 65 MPa were applied on the north and east-west sides, respectively, and 20 MPa of sinistral shear stress was applied on the east-west boundary (Figure 7A). For the late Himalayan model, pressures of approximately 180 MPa and 85 MPa were applied on the north and east-west sides, respectively, and 40 MPa of dextral shear stress was applied on the east-west boundary (Figure 7B). For these two models, the southern edge was set as a fixed boundary to appropriately reflect the blocking effect of the South Tarim Basin. Simultaneously, the bottom boundary of the model was also fixed and gravity load was automatically applied by the software, to maintain the system in equilibrium.

The deformation and destruction of geological structures, especially the uplift of folds, occurs under the action of long-term tectonic movements and is no longer a simple elastic mechanics problem. The general-purpose elastic-plastic FE method based on ANSYS software was selected for this study. This software is well-suited for analyzing large-deformation problems in geomechanics over a wide range of scales in one, two, and three dimensions (Smart et al., 2012; Kim et al., 2015; Ass & Mat, 2021; Tojaga et al., 2021). In order to eliminate the boundary effect of the stress field simulation as much as possible, it was necessary to nest a larger rectangular parallelepiped outside the Keshen geologic model with planar area of ~1.5 times (Figure 7). The geomechanical model was segmented using a triangular mesh, allowing a large number of elements and nodes to be subdivided. Particularly, the meshing of the target layer and fault zone needed to be much finer than that of

the surrounding rock. The geologic models of middle and late Himalayan periods were finally divided into 34,577 nodes, 129,576 elements and 46,327 nodes, 199,846 elements respectively.

4.2 Calculation of fracture linear density

4.2.1 Rock constitutive model

According to the theory of minimum energy dissipation, the material or rock failure process always occurs in the weakest place and in the most destructible way, that is, the theory of minimum energy dissipation rate is always satisfied in the energy consumption process (Luo et al., 2009; Leykin, 2015).

Following the damage mechanics theory, the continuous damage variable D ($0 \leqq D \leqq 1$) can be used to directly measure the damage degree of rock mass (Luo et al., 2009). Essentially, the damage of brittle rock is an energy-consuming process under the action of load, which should also be constrained by the principle of minimum energy consumption. In the process of rock failure or energy dissipation, the infinite small unit will produce irreversible strain ε_i ($i = 1, 2, 3$) before reaching complete destruction. If other factors were not considered, and the principal strain ε_i caused by the force was regarded as the only energy dissipation mechanism of the rock mass in failure process, the corresponding expression of the energy dissipation rate is as follows (Li, 2011; Peng et al., 2016):

$$\varphi = \sigma_i \cdot \dot{\varepsilon}_i \tag{1a}$$

where, φ is the energy dissipation rate (J/s); σ_i ($i = 1, 2, 3$) are the three principal stress (MPa); $\dot{\varepsilon}_i$ ($i = 1, 2, 3$) are the three strain rate tensor (s^{-1}).

Combined with the generalized Hooke's law including the damage variable D, the irreversible strain rate tensor $\dot{\varepsilon}_i$ was obtained using the formula below:

$$\begin{cases} \dot{\varepsilon}_1 = -\dfrac{\dot{D}}{[1-D]^2 E}\left[\sigma_1 - \mu(\sigma_2 + \sigma_3)\right] \\ \dot{\varepsilon}_2 = -\dfrac{\dot{D}}{[1-D]^2 E}\left[\sigma_2 - \mu(\sigma_1 + \sigma_3)\right] \\ \dot{\varepsilon}_3 = -\dfrac{\dot{D}}{[1-D]^2 E}\left[\sigma_3 - \mu(\sigma_1 + \sigma_2)\right] \end{cases} \tag{2}$$

Substituting equation (2) into equation (1), the energy consumption rate expression is shown below:

$$\varphi = -\dfrac{\dot{D}}{[1-D]^2 E}\left[\sigma_1^2 + \sigma_2^2 + \sigma_3^2 - 2\mu(\sigma_1\sigma_2 + \sigma_2\sigma_3 + \sigma_1\sigma_3)\right] \tag{3}$$

where, φ is the energy dissipation rate (J/s); D is the damage variable; $\dot{D}$ is the damage rate; E, μ are the elastic modulus (GPa) and Poisson's ratio of the rock mass before failure, and the values could be measured by experiments; σ_i ($i = 1, 2, 3$) are the three principal stress (MPa); $\dot{\varepsilon}_i$ ($i = 1, 2, 3$) are the three strain rate tensor (s^{-1}).The

unified energy yield criterion for rock expresses the relationship between shear strain energy and volumetric strain energy and can be used as a constraint condition for the process of rock damage and energy dissipation (Sun et al., 2018), so the constraint under triaxial stress conditions are as below:

$$F(\sigma_1, \sigma_2, \sigma_3) = \frac{1}{2G}\left[\frac{\sigma_1 - \sigma_2}{2\cos\varphi_{12}} - \frac{(\sigma_1 + \sigma_2)}{2}\tan\varphi_{12}\right]^2$$
$$+ \frac{1}{2G}\left[\frac{\sigma_2 - \sigma_3}{2\cos\varphi_{23}} - \frac{(\sigma_2 + \sigma_3)}{2}\tan\varphi_{23}\right]^2$$
$$+ \frac{1}{2G}\left[\frac{\sigma_1 - \sigma_3}{2\cos\varphi_{13}} - \frac{(\sigma_1 + \sigma_3)}{2}\tan\varphi_{13}\right]^2$$
$$+ \alpha\frac{(\sigma_1 + \sigma_2 + \sigma_3)^2}{18K} + \beta \quad (4)$$

where, α and β are material parameters that characterize the relationship between shear strain energy and volumetric deformation energy during rock yield; φ_{12}, φ_{23}, φ_{13} are the internal friction angles of rock (o); G and K are the bulk modulus and shear modulus (GPa) respectively. The above parameters can be measured experimentally.

According to the minimum energy consumption theory (Tabarrok & Leech, 2002), in the damage evolution process of rock, the consumption rate has the stationary value under the corresponding conditions. Therefore, Lagrange multiplier was introduced and the following expression was obtained:

$$\begin{cases} \dfrac{\partial(\varphi + \lambda F)}{\partial\sigma_1} = 0 \\ \dfrac{\partial(\varphi + \lambda F)}{\partial\sigma_2} = 0 \\ \dfrac{\partial(\varphi + \lambda F)}{\partial\sigma_3} = 0 \end{cases} \quad (5)$$

Combining formulas (Eqs 1–5, the rock damage equation under triaxial condition is expressed as:

$$D = 1 - exp\left[\frac{\lambda A}{2(\varepsilon_1 + \varepsilon_2 + \varepsilon_3)} + C_0\right] \quad (6)$$

and

$$\dot{D} = -\frac{\lambda A}{2(\varepsilon_1 + \varepsilon_2 + \varepsilon_3)}exp\left[\frac{\lambda A}{2(\varepsilon_1 + \varepsilon_2 + \varepsilon_3)} + C_0\right] \quad (7)$$

As the Damage Mechanics Theory (Krajcinovic, 1989) states: when the strain reaches the threshold, the rock damage begins to develop and is in the elastic deformation stage before the damage threshold. Thus, the rock damage equation after introducing damage threshold strain ε_0 is:

$$D = \begin{cases} 0, \varepsilon_1 < \varepsilon_0 \\ 1 - exp\left[\dfrac{\lambda A}{2(\varepsilon_1 + \varepsilon_2 + \varepsilon_3)} + C_0\right], \varepsilon_1 \geq \varepsilon_0 \end{cases} \quad (8)$$

where, $A = \frac{E}{4G}\left[\frac{(1-\sin\varphi_{12})^2}{(\cos\varphi_{12})^2} + \frac{(1-\sin\varphi_{13})^2}{(\cos\varphi_{13})^2} - \frac{1}{2G} + \frac{\alpha}{3K}\right]\varepsilon_1$
$+ \frac{1}{4G}\left[\frac{(1+\sin\varphi_{12})^2 + \mu(1-\sin\varphi_{12})^2}{(\cos\varphi_{12})^2} + \frac{(1-\sin\varphi_{23})^2}{(\cos\varphi_{23})^2} + \frac{\mu(1-\sin\varphi_{13})^2}{(\cos\varphi_{13})^2}\right]\sigma_2$
$+ \frac{1}{4G}\left[\frac{(1-\sin\varphi_{12})^2}{(\cos\varphi_{12})^2} + \frac{(1+\sin\varphi_{23})^2}{(\cos\varphi_{23})^2} + \frac{(1+\sin\varphi_{13})^2 + \mu(1-\sin\varphi_{13})^2}{(\cos\varphi_{13})^2}\right]\sigma_3$
$+ \left(-\frac{1}{2G} + \frac{\alpha}{3K}\right)(\mu + 1)(\sigma_2 + \sigma_3)$

; λ and C_0 were the constants related to lithology. Therefore, combined with the generalized Hooke's law containing damage variables, the constitutive model of rock was obtained:

$$\sigma_t = \begin{cases} E\varepsilon_1 + \mu\sigma_2 + \mu\sigma_3, \varepsilon_1 < \varepsilon_0 \\ E\varepsilon_1\,exp\left[\dfrac{\lambda A}{2(\varepsilon_1 + \varepsilon_2 + \varepsilon_3)} + C_0\right] + \mu\sigma_2 + \mu\sigma_3, \varepsilon_1 \geq \varepsilon_0 \end{cases} \quad (9)$$

4.2.2 Rock failure criterion

The previous experimental results show that when the axial stress reaches 0.75, 0.85 and 0.92 times the peak strength, a large number of micro-cracks in the brittle rock begin to expand and connect (Eberhardt et al., 1998; Dai et al., 2011; Ju et al., 2017). Finally, macroscopic fractures are formed at the peak strength, followed by slipping along the fracture planes to form faults (Gudmundsson, 2010). Therefore, using the peak point of the stress-strain curve to identify the model parameters can make the parameters have clear physical meanings for the deep tight sandstone with strong brittle characteristics. Assuming that the stress and strain at the peak point of stress-strain curve under confining pressure were σ_{1s}, σ_{2s}, σ_{3s}, ε_{1s}, ε_{2s}, ε_{3s}, respectively, then there were:

$$\frac{d\sigma_t}{d\varepsilon_1} = 0 \quad (10)$$

The formula (6) was arranged and substituted into the peak condition to obtain the values of constants λ a nd C_0:

$$\begin{cases} \lambda = \dfrac{2(\varepsilon_{1s} + \varepsilon_{2s} + \varepsilon_{3s})^2}{A_0\varepsilon_{1s}} \\ C_0 = ln[\sigma_{1s} - \mu\sigma_{2s} - \mu\sigma_{3s}] - ln[E\varepsilon_{1s}] - A_0(\varepsilon_{1s} + \varepsilon_{2s} + \varepsilon_{3s}) \end{cases} \quad (11)$$

The damage threshold could also be obtained as follows:

$$\varepsilon_0 = -\frac{\lambda A_0}{2C_0} - \varepsilon_{2s} - \varepsilon_{3s} \quad (12)$$

where, $A_0 = E/4G[(1 - \sin\varphi_{12})^2/(\cos\varphi_{12})^2$
$+ (1 - \sin\varphi_{13})^2/(\cos\varphi_{13})^2 - 1/2G + \alpha/3K]\varepsilon_{1s}$

$+ 1/4G[(1 + \sin\varphi_{12})^2 + \mu(1 - \sin\varphi_{12})^2/(\cos\varphi_{12})^2$

$+ (1 - \sin\varphi_{23})^2/(\cos\varphi_{23})^2 + \mu(1 - \sin\varphi_{13})^2/(\cos\varphi_{13})^2]\sigma_{2s}$

FIGURE 8
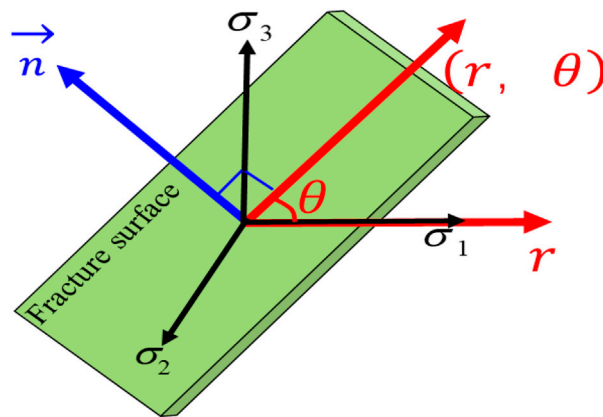Diagram of calculating the fracture angle in polar coordinate system.

$$+ 1/4G \left[(1 - sin\,\varphi_{12})^2 / (cos\,\varphi_{12})^2 + (1 + sin\,\varphi_{23})^2 / (cos\,\varphi_{23})^2 \right.$$

$$+ (1 + sin\,\varphi_{13})^2 + \mu (1 - sin\,\varphi_{13})^2 / (cos\,\varphi_{13})^2] \sigma_{3s}$$

$$+ (-1/2G + \alpha/3K)(\mu + 1)(\sigma_2 + \sigma_{3s}).$$

From above we could get:

$$\varphi_0 = \left[E\varepsilon_0\,exp\left[\frac{\lambda A_0}{2(\varepsilon_1 + \varepsilon_2 + \varepsilon_3)} + C_0 \right] + \mu\sigma_2 + \mu\sigma_3 \right] \varepsilon_0 \qquad (13)$$

Finally, the consumption rate expression under the framework of minimum energy consumption principle could be obtained:

$$\varphi = \begin{cases} \left(E\varepsilon_1 + \mu\sigma_2 + \mu\sigma_3 \right)\varepsilon_1, \varepsilon_1 < \varepsilon_0 \\ \left(E\varepsilon_1\,exp\left[\frac{\lambda A}{2(\varepsilon_1 + \varepsilon_2 + \varepsilon_3)} + C_0 \right] + \mu\sigma_2 + \mu\sigma_3 \right)\varepsilon_1, \varepsilon_1 \geq \varepsilon_0 \end{cases}$$
$$(14)$$

It can be seen from the formula that when $\varphi > \varphi_0$, the rock lost its steady state and broke, that is, the tensile fracture or shear fracture was formed.

4.2.3 Geomechanical models of fracture parameters

4.2.3.1 Fracture dip angle

As shown in Figure 8, under the principal stress coordinate system with the coordinate origin as the pole and the positive semi-axis of the maximum principal stress as the polar axis, the appropriate polar coordinate system was established. The angle between the fracture surface and the maximum principal stress was the rupture angle. First, the stress function expression $F(r, \theta)$

of fracture surface (r, θ) point needed to be determined (Peng et al., 2019), that is:

$$F = r^2 (acos\,2\theta + bsin2\theta + c\theta + d) \qquad (15)$$

where, a, b, c and d were arbitrary constants. After substituting it into the equation $(\frac{\partial^2}{\partial r^2} + \frac{1}{r}\frac{\partial}{\partial r} + \frac{1}{r^2}\frac{\partial^2}{\partial \theta^2})\varphi = 0$, it was found that this function satisfied the compatibility equation. Therefore, the stress component can be expressed as (Peng et al., 2020):

$$\begin{cases} \sigma_r = \frac{1}{r}\frac{\partial F}{\partial r} + \frac{1}{r^2}\frac{\partial^2 F}{\partial \theta^2} = -2(acos\,2\theta + bsin2\theta - c\theta - d) \\ \sigma_\theta = \frac{\partial^2 F}{\partial r^2} = 2(acos\,2\theta + bsin2\theta + c\theta + d) \\ \tau_{r\theta} = -\frac{\partial}{\partial r}\left(\frac{1}{r}\frac{\partial F}{\partial \theta} \right) = 2asin\,2\theta - 2bcos2\theta - c \qquad (16) \end{cases}$$

where, σ_r and σ_θ are the stress components along both radial and annular directions in polar coordinate systems (MPa); $\tau_{r\theta}$ is the shear stress component in polar coordinate system (MPa).

Next, substitute (Eq. 16) into the boundary conditions:

If $\theta = 0°$, $\begin{cases} \sigma_r = 0 \\ \tau_{r\theta} = 0 \end{cases}$, if $\theta = 90°$, $\begin{cases} \sigma_r = -\sigma_{max} \\ \tau_{r\theta} = 0 \end{cases}$ (17)

Where, σ_{max} is the maximum principal stress (MPa).

Thus, the corresponding values of the constants a, b, c, and d were obtained, namely:

$$\begin{cases} a = d = -\frac{\sigma_{max}}{4}r^2 \\ b = c = 0 \end{cases} \qquad (18)$$

At the same time, the stress function expression could be expressed as:

$$F = -\frac{\sigma_{max}}{4}r^4 cos\,2\theta - \frac{\sigma_{max}}{4}r^4 \qquad (19)$$

Further combined with Eq. 2, the energy consumption rate expression in the polar coordinate system was obtained:
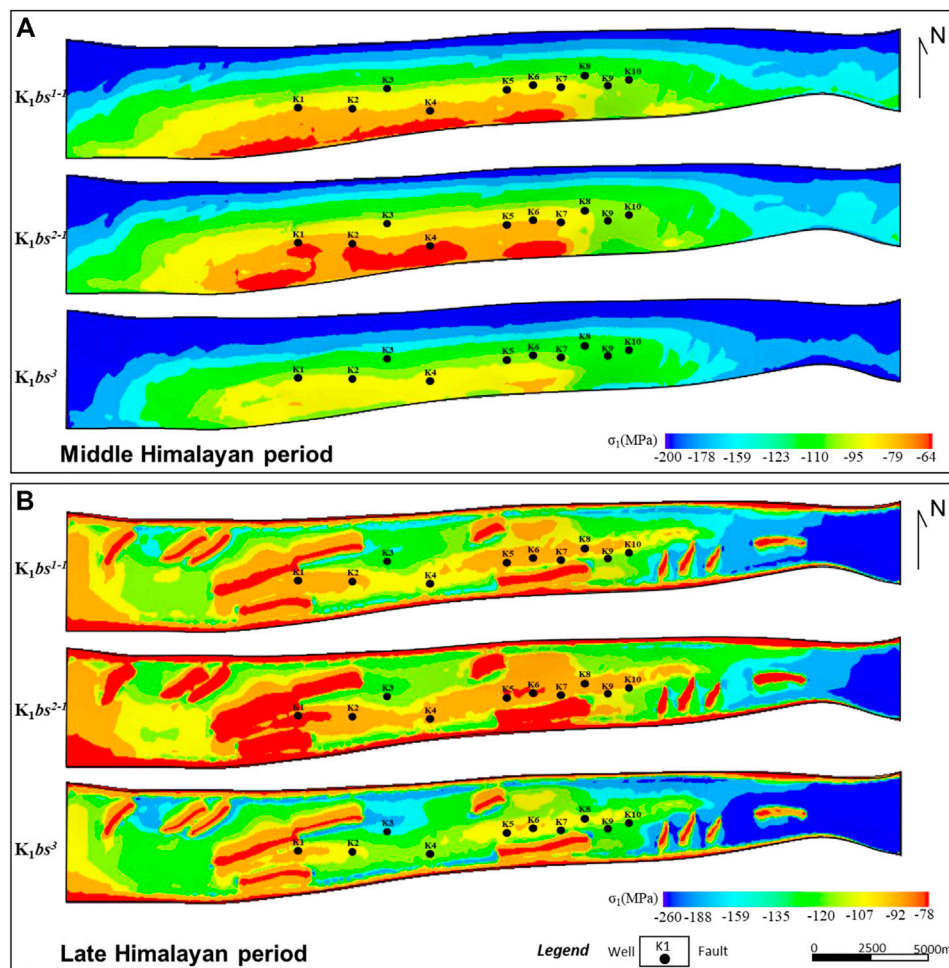
FIGURE 9
Distribution of paleo-tectonic stress field in different period. **(A)** Maximum principal stress in middle Himalayan period of target layer; **(B)** Maximum principal stress in late Himalayan period of target layer.

$$\varphi = -\frac{\dot{D}}{(1-D)^2 E}\left(-\frac{\sigma_{max}}{4}\cos 2\theta - \frac{\sigma_{max}}{4}\right)^2 \qquad (20)$$

Finally, the rupture angle expression obtained by the minimum energy dissipation principle was:

$$\theta = \frac{1}{2}\arccos\left[\sqrt{\frac{16E\varphi(1-D)^2}{\dot{D}\sigma_{max}^2}} - 1\right] \qquad (21)$$

where: $D = 1 - exp\left[\frac{\lambda A}{2(\varepsilon_1+\varepsilon_2+\varepsilon_3)} + C_0\right]$;

$\dot{D} = -\frac{\lambda A}{2(\varepsilon_1+\varepsilon_2+\varepsilon_3)}exp\left[\frac{\lambda A}{2(\varepsilon_1+\varepsilon_2+\varepsilon_3)} + C_0\right]$.

(2) Fracture linear density

For a brittle material such as deep tight sandstone, when the stress state reaches its failure strength, the rock will break

to produce macroscopic fractures and release energy (Gdoutos, 2012; Kravchenko et al., 2014). Combined with (Eq. 14), the dissipated energy in the process of crack formation can be derived (assuming that the initial phase energy dissipation is 0):

$$\omega = \int \varphi dt = \int\left\{\left(E\varepsilon_1 exp\left[\frac{\lambda A}{2(\varepsilon_1+\varepsilon_2+\varepsilon_3)}+C_0\right]+\mu\sigma_2+\mu\sigma_3\right)\varepsilon_1\right\}dt$$
$$= \frac{2E\varepsilon_1^2(\varepsilon_1+\varepsilon_2+\varepsilon_3)}{\lambda A}exp\left[\frac{\lambda A}{2(\varepsilon_1+\varepsilon_2+\varepsilon_3)}+C_0\right]+\mu\varepsilon_1(\sigma_2+\sigma_3)-\frac{2E\varepsilon_1^2(\varepsilon_1+\varepsilon_2+\varepsilon_3)}{\lambda A}e^{C_0} \qquad (22)$$

where, ω is the strain energy released by new fractures (J); t is the moment of stress applied (s).

Generally, brittle macro-fractures occur with strain energy releasing, especially when the surrounding three-dimensional stress state reaches the rock's strength. At this time, part of the strain energy will be released as the surface energy of the new fractures while the rest will be released in the form of elastic waves (Barton et al., 1977). Nonetheless, compared with the fracture surface energy, elastic wave energy was so weak that it
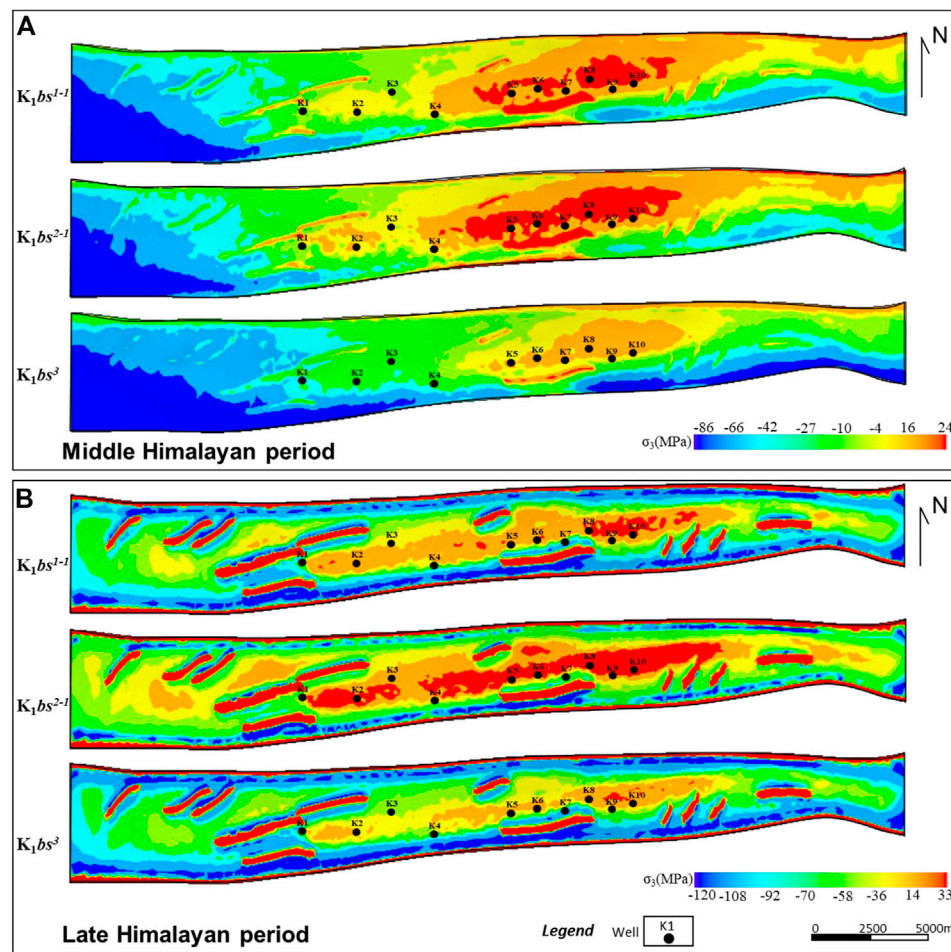
FIGURE 10
Distribution of paleo-tectonic stress field in different period. **(A)** Minimum principal stress in middle Himalayan period of target layer; **(B)** Minimum principal stress in late Himalayan period of target layer.

can be neglected. We assume that all of the fractures in this study were caused by the releasing energy and therefore, the law of conservation of energy must be satisfied:

$$\omega = \omega_s V = SJ \tag{23}$$

where ω is the strain energy released by new fractures (J); ω_s is the strain energy density of the new fracture surface area (J/m³); V is the unit cell volume (m³); S is the surface area of the new fractures (m²); J is the energy per unit area required for fractures, i.e., fracture surface energy (here, this energy was different from and had a far lower value than the theoretical value of molecular dissociation).

Further transformation of Eq. 23, the fracture density expression under the theory of minimum energy consumption can be obtained by the formula below:

$$D_v = \frac{S}{V} = \frac{\omega_s}{J} = \frac{2E\varepsilon_1^2}{\lambda AVJ}(\varepsilon_1 + \varepsilon_2 + \varepsilon_3) \, exp\left[\frac{\lambda A}{2(\varepsilon_1 + \varepsilon_2 + \varepsilon_3)} + C_0\right]$$
$$+ \frac{\mu\varepsilon_1}{VJ}(\sigma_2 + \sigma_3) - \frac{2E\varepsilon_1^2}{\lambda AVJ}(\varepsilon_1 + \varepsilon_2 + \varepsilon_3)e^{C_0} \tag{24}$$

where, D_v is the fracture volume density per unit volume (m²/m³). Further, combined with the fracture density formula established in the previous stage (Dai et al., 2011), the fracture linear density model under the framework of the principle of minimum energy consumption was obtained:

$$D_l = \begin{cases} \dfrac{2D_v L_1 L_3 \sin\theta\cos\theta - L_1 \sin\theta - L_3 \cos\theta}{L_1^2 \sin^2\theta + L_3^2 \cos^2\theta}, \theta \neq 0 \\ D_v, \theta = 0 \end{cases} \tag{25}$$
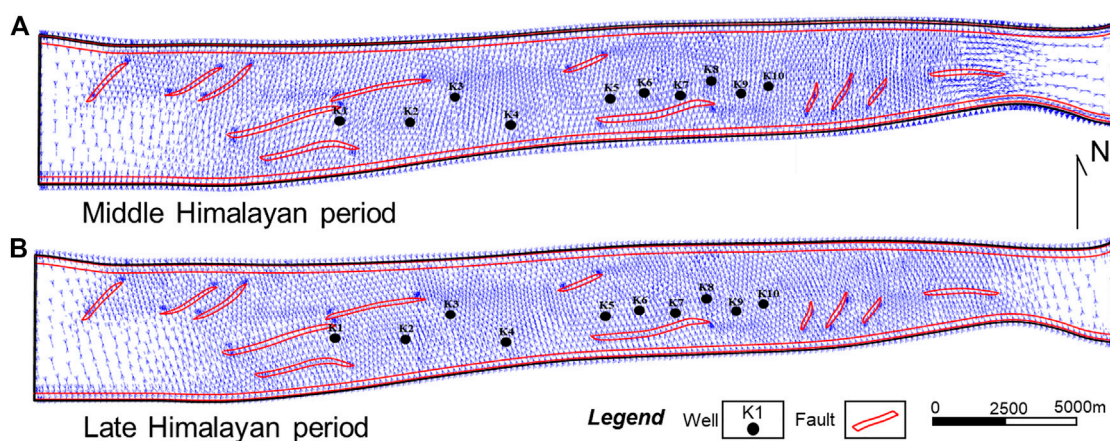
FIGURE 11
Distribution characteristics of maximum principal stress direction of tectonic stress field in different periods. **(A)** Direction of maximum principal stress in middle Himalayan period of target layer; **(B)** Direction of maximum principal stress in late Himalayan period of target layer.

where, $\theta = \frac{1}{2}arccos[\sqrt{\frac{16E\varphi(1-D)^2}{D\sigma_{max}^2}} - 1]$; D_l is the fracture linear density (1/m); L_1, L_3 were the side length of the selecting representing element volume (m).

After establishing geomechanical models through ANSYS software, the 3D paleotectonic stress field simulation was carried out in Keshen area. Then, the rock failure criterion and geomechanical models of fracture parameters were implanted into the FE platform to predict spatial distribution of fractures. As a general principle, tectonic movement is a slow process in which stress fields and energy dissipation rates are constantly changing and fractures may occur at each stage. Therefore, the coupling effect between late stress and cracks will exist where the early fractures occur. The principle of minimum energy consumption can solve this problem, that is, reaching the condition of minimum energy consumption rate will produce new fractures.

5 Results and discussion

5.1 Paleo-tectonic stress field

As shown in Figure 9, Figures 10, 11, the maximum principal stress, minimum principal stress, and stress direction of the middle and late Himalayan periods were calculated. Generally, the distribution of the maximum principal stress (σ_1) is the main factor controlling the thrust fault and anticline deformation in the compression basin whereas the minimum principal stress (σ_3) is the main factor controlling whether there is a local tensile zone at the top of the anticline. The σ_1 during the Middle Himalayan period was generally between -200 and -64 MPa (the negative sign represents the compressive stress, the positive sign represents the tensile stress) (Figure 9), and the minimum principal stress was generally between -86 and 44 MPa (Figure 10). The high-value areas

were mainly concentrated in the east and west ends and north limb of Keshen anticline and distributed around the fault core, particularly at the en-echelon faults and the tip of the faults (Figure 9A). Vertically, the values of σ_1 increased with the increase of depth, for example, the expression strength of section K_1bs^3 was obviously greater than that of K_1bs^2 and K_1bs^1. As shown in Figure 10A, the tensile-stress zones (i.e. positive values) were concentrated in the middle and east of the study area and the top of the anticline, and distributed around the fault cores. In particular, at the high parts of central Keshen anticline, the tensile stress values reached 24 MPa, indicating a relatively strong local extensional environment. Vertically, the tensile stress at the top of the anticline was significantly higher than that at the bottom, which was consistent with the neutral surface effect of flexural folding. In contrast, in the late Himalayan period, the maximum principal stress was generally between −260 and −78 MPa, the minimum principal stress was generally between −120 and 33 MPa. Compared with the middle Himalayan tectonic stress field, the intensity of σ_1 increased, and high-value areas migrated to the east of the study area. In addition, low values of σ_1 can easily occur in the high positions of anticline core and the fault cores, which was the result of concentrated release of tectonic stress (Figure 9B). Interestingly, similar to σ_1, the positive values (i.e., tensile stress) of σ_3 were concentrated at the top of the anticline and fault cores, indicating where a large number of tensile fractures occurred (Figure 10B). Generally, the distribution of the maximum principal stress (σ_1) direction is closely related to the occurrence of the fractures. According to the simulation results, from west to east of the anticline, the direction of σ_1 changed significantly, that is, from the SN to the NE, and then to the SN and EW (Figure 11). Specifically, the direction of σ_1 varied obviously at the intersection of faults and the tip of faults, especially at the position of anticline-syncline transition. Based on seismic
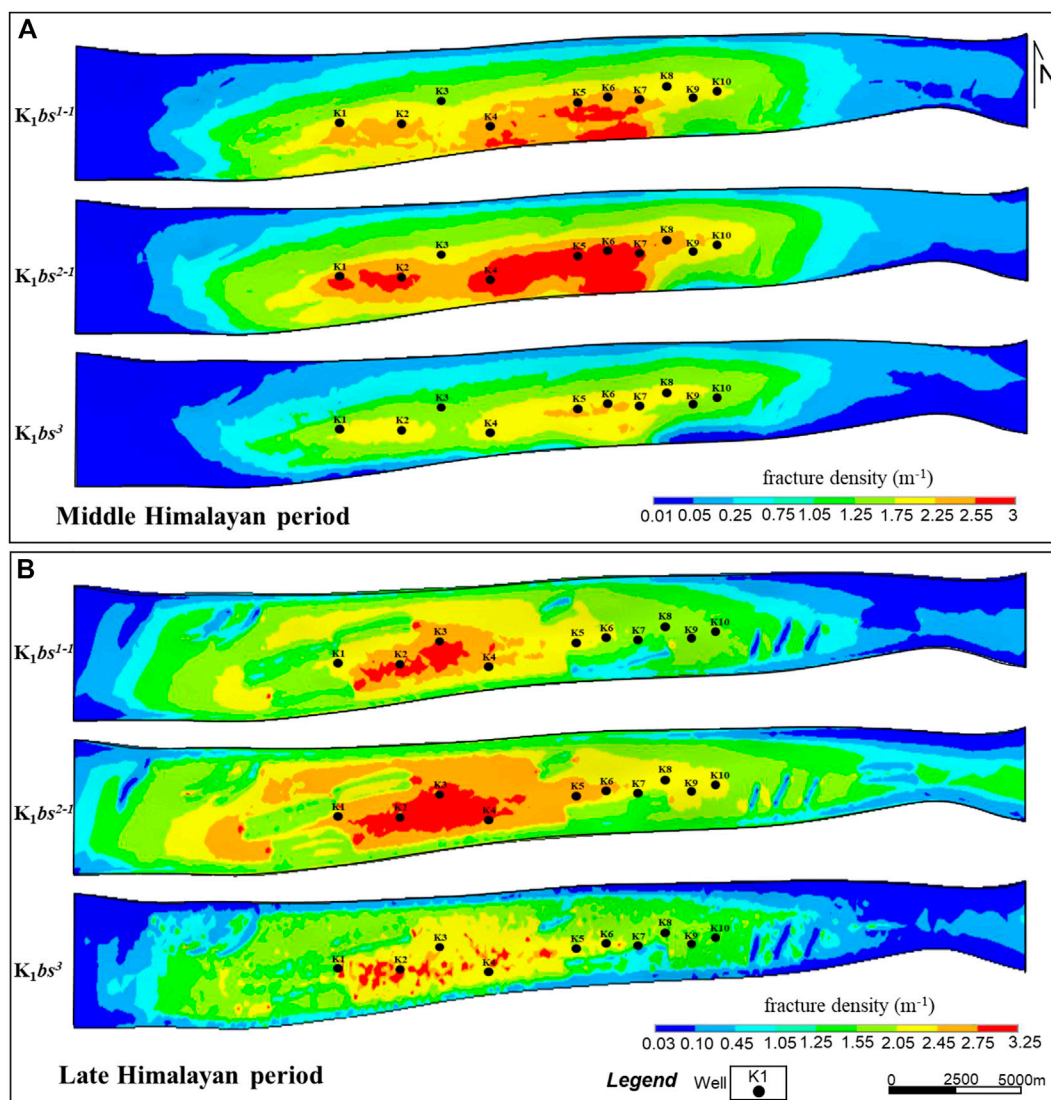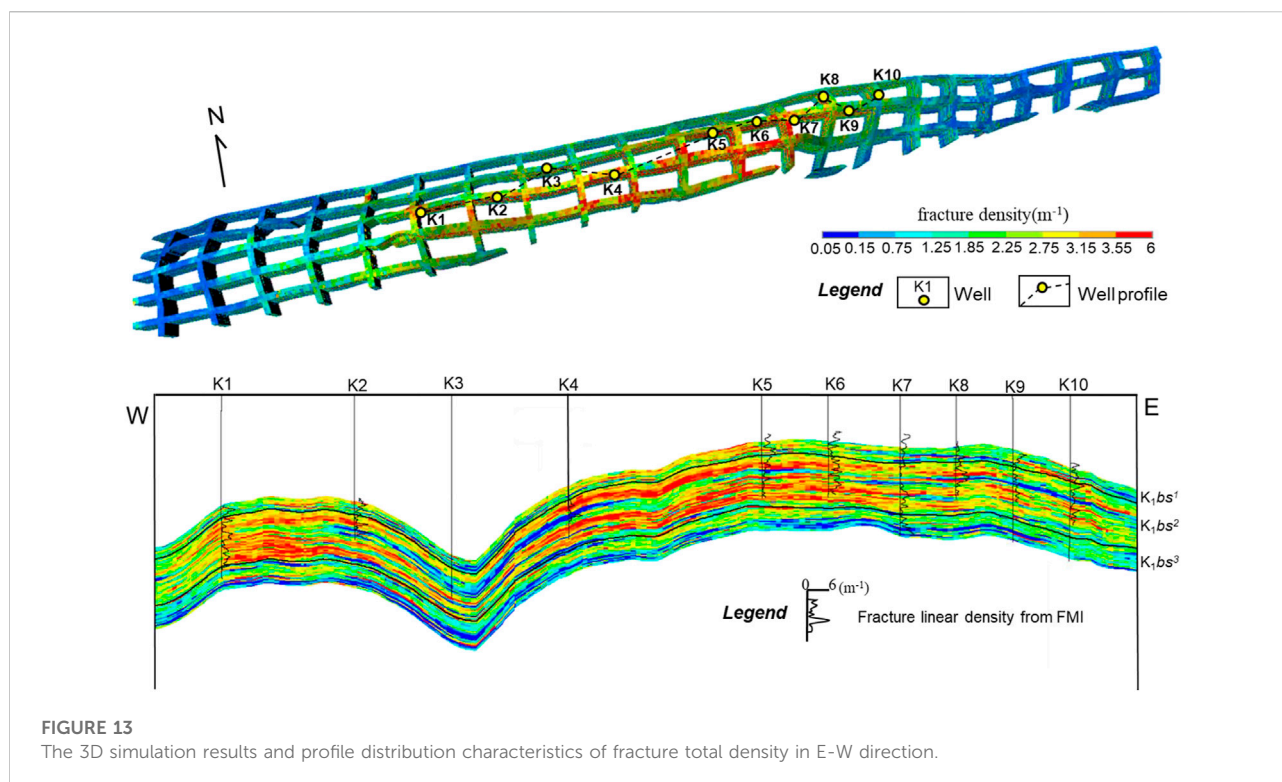
FIGURE 12
Spatial distribution of fracture development degree in different period. **(A)** Fracture linear density in Middle Himalayan period; **(B)** Fracture linear density in late Himalayan period.

interpretation results, this sudden change of stress direction was basically consistent with the position of NW-trending accommodation zones which jointly affected the spatial difference of stress state and the generation of fractures in different groups.

5.2 Fracture distribution and its controlling factors

The spatial predictions showed that the fracture linear density (D_{lf}) of Keshen gas field was significantly different in the two periods of tectonic movement. As shown in Figure 12A, the well-developed

fracture areas under middle Himalayan movement were primarily located on (1) the central part of Keshen anticline; (2) the structural high parts of fold core; (3) the southern major fault zone and the hanging wall of large-scale faults; and (4) along the long axis of anticline. Vertically, the D_{lf} of fractures at the top of the anticline was higher than 2.25 m^{-1} in most areas of K$_1$bs^2, higher than 2.25 m^{-1} in only some areas of K$_1$bs^1 and widely lower than 2.25 m^{-1} in K$_1$bs^3. Locally, the distribution of D_{lf} was still different at the top of the anticline of three lithologic members. For example, the D_{lf} in the east was higher than that in the west, the south was higher than the north, and the saddle between the two high points was lower. Nevertheless, the development and distribution of fractures in the

FIGURE 13
The 3D simulation results and profile distribution characteristics of fracture total density in E-W direction.

middle Himalayan were mainly controlled by folding, followed by buried depth or lithofacies, and then by faulting.

Compared with the middle Himalayan, the D_{lf} of fractures in the late tectonic movement increased significantly, reaching more than 3.25 m^{-1}, and the high-value areas were widely distributed (Figure 12B). On the plane, the high-value areas of D_{lf} in this period gradually migrated to the west of anticline, and concentrated to the core of anticline. For example, in K$_1$bs^2, the D_{lf} near wells K1, K2, K3 and K4 of the anticline core was mostly above 3.25 m^{-1}. For example, the D_{lf} in the core of the anticline or near wells K1, K2, K3, and K4 was more than 3.25 m^{-1}. Interestingly, contrary to the characteristics of the middle Himalayan period, the D_{lf} around the secondary faults, especially the en-echelon faults, presented as low values. For this reason, combined with the tectonic evolution history and acoustic emission results, it can be concluded that most of the secondary faults of Keshen anticline formed in middle Himalayan and inherited activities in late Himalayan. In other words, these faults were where stress was easily concentrated when they were formed, controlling the development of local fractures. However, these faults were not easy to cause stress concentration as weak zones in later activities, and thus did not no longer control the generation of more fractures. As mentioned above, the development of Keshen anticline was mainly controlled by the strong thrusting of the southern major fault during the early stage, and by the combined action of the northern backward fault and southern major fault in the late

stage. Under this background, the high-value areas of D_{lf} was mainly located near the southern major and secondary faults during the early stage, and migrated northward and westward along with the fold hinge in the late stage.

After superposition calculation of D_{lf} in two stages, it was found that, the well-developed fracture areas were primarily located on (1) around the fold core or along the hinge line; (2) the structural and stratigraphic high parts; and (3) shared hanging wall of two EW-striking thrust faults (Figure 13). Based on the west-east section of 3D simulation results, the total D_{lf} of K$_1$bs^1 and K$_1$bs^2 in Keshen gas field was significantly higher than that of K$_1$bs^3, and that of K$_1$bs^2 was slightly higher than that of K$_1$bs^1. Among them, the total D_{lf} exceeded 3.15 m^{-1} in many areas of K$_1$bs^2, while only a few areas of K$_1$bs^3 exceeded 3 m^{-1}. As shown in Figure 13, on the whole, the distribution of the predicted total D_{lf} was highly consistent with the FMI interpretations of wells.

5.3 Validation of geomechanical models

As can be seen from Figure 13 and Figure 14, the overall numerical simulations in wells were in good agreement with the results of core observations and FMI interpretations. Comprehensively, the relative error of simulation results for fracture density was mostly less than 20% and the individual exceeded 30%, such as well K8 (Figure 14A). In fact, a series of soft or weak argillaceous interbeds are developed in continental
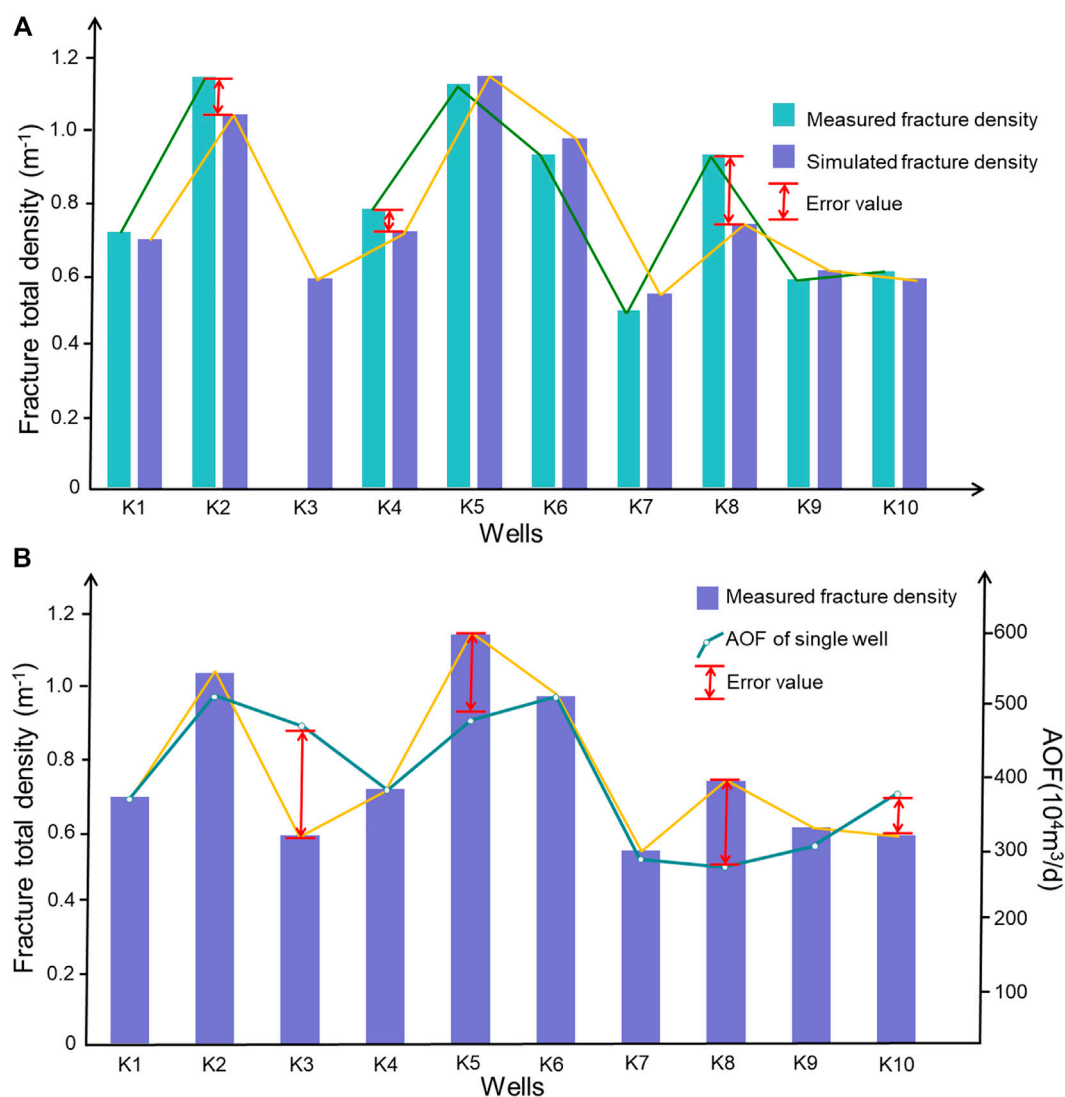
FIGURE 14
Comprehensive validation of the prediction results of 3D fracture distribution. **(A)** Comparison of the measured fracture density and simulated fracture density in wells of study area; **(B)** Relationship between gas well productivity and fracture contribution in Keshen gas field.

tight sandstones, which have strong plastic characteristics and are difficult to produce fractures. However, due to the limitation of the grid size of geological modeling and FE software, it is difficult to take such small or thin interlayer into account, which leads to the error of numerical simulation results. Numerous production practices prove that fractures are not only the important seepage channels but also determine the high and stable yield of the tight sandstone reservoir. As shown in Figure 14B, the high-productivity wells of gas reservoir were basically consistent with the high-value areas of fracture density, except for individual wells. For example, the productivity or absolute open flow (AOF) of well K3 at the western high point of Keshen anticline reached $491 \times 10^4 \mathrm{~m}^3/\mathrm{d}$, but its fracture

density was less than 0.7 m^{-1}, and there was a mismatch. Core observation showed that the fracture dip angle of well K3 was nearly 90° and the mineral filling rate of core statistics was only 0.14. It can be inferred that the fracture effectiveness or connectivity of the target layer of this well was better, which is probably the main factor for higher productivity. All the above descriptions show that the fracture mechanics models and prediction results based on the principle of minimum energy consumption in this study are reasonable and reliable. Nevertheless, affected by the degree of geological knowledge and the limitations of modeling software, there is still a long way to go to achieve a complete, accurate and quantitative prediction of the spatial distribution of deep fractures.

6 Conclusion

1) The spatial distribution of multi-stage fractures in ultra-deep Keshen gas field was clarified. The geological analysis method based on drilling core and FMI, rock mechanics experiment, and the FE numerical simulation based on principle of minimum energy consumption were adopted to carry out fracture prediction study. This novel method can help further understand the spatial distribution of fractures in complex ultra-deep tight sandstone reservoirs.

2) There were three main periods of structural fractures in the study area, and the fractures in the middle and late Himalayan periods were the most important for oil and gas migration and accumulation. The fractures in the latter two stages accounted for about 90% of the total number, most of which were unfilled and semi filled, and were important factors influencing the productivity of gas reservoirs.

3) The heterogeneity of fracture development and distribution in the Keshen gas reservoir was extremely strong. The primary factor of fracture development was folding, followed by lithofacies and buried depth, and finally thrust faulting. On the whole, the high-value areas of fracture density were mainly located at the top of fold and complicated by secondary faults and local topography, which was mainly reflected in the variation of stress field.

4) Two FE models of Keshen gas field during the middle and late Himalayan periods incorporating various lithologies, multiscale faults, mechanical parameters, constitutive model, failure criterion and fracture mechanics models was constructed to simulate the spatial fracture distributions. The overall geomechanical modeling results were in agreement with *in-situ* core observations, FMI analysis and AOF of wells. The novel method presented in this study is also applicable to quantitative prediction of fractures in deep reservoirs in other areas.

Data availability statement

The original contributions presented in the study are included in the article/supplementary material, further inquiries can be directed to the corresponding author.

Author contributions

JF: Conceptualization, Methodology, Writing-Reviewing and Editing, Supervision. SL: Data curation, Writing-Original draft preparation. JO: Software, Visualization, Investigation, Validation. GuL: Actual production data collection. GaL: Actual production verification.

Conflict of interest

Authors GuL and GaL were employed by the company PetroChina Dagang Oilfield.

The remaining authors declare that the research was conducted in the absence of any commercial or financial relationships that could be construed as a potential conflict of interest.

Publisher's note

All claims expressed in this article are solely those of the authors and do not necessarily represent those of their affiliated organizations, or those of the publisher, the editors and the reviewers. Any product that may be evaluated in this article, or claim that may be made by its manufacturer, is not guaranteed or endorsed by the publisher.

References

Ass, A. S., and Mat, M. A. (2021). Finite element simulation of elastoplastic behavior of nanoporous metals using bicontinuous RVE models. *Procedia Struct. Integr.* 32, 230–237. doi:10.1016/j.prostr.2021.09.033

Ay, A., Sn, A., Hk, A., Ps, A., Ap, A., and Rc, B. (2019). A case study of azimuthal fracture characterization in Cambay Basin, India. *J. Appl. Geophys.* 169, 239–248. doi:10.1016/j.jappgeo.2019.07.003

Barton, N., Bandis, S., and Bakhtar, K. (1985). Strength, deformation and conductivity coupling of rock joints. *Int. J. Rock Mech. Min. Sci. Geomechanics Abstr.* 22, 121–140. doi:10.1016/0148-9062(85)93227-9

Chu, G. X., Shi, S., Shao, L. Y., Wang, H. Y., and Guo, Z. H. (2014). Contrastive study on geological characteristics of cretaceous Bashijiqike Formation in Keshen2 and Kela2 gas reservoirs in kuqa depression. *Geoscience* 28 (3), 604–610.

Conti, J., Holtberg, P., Diefenderfer, J., Larose, A., Turnure, J. T., and Westfall, L. (2016). *International energy outlook 2016 with projections to 2040*. United States: OSTI. doi:10.2172/1296780

Cumella, S. P., and Scheevel, J. (2008). "The influence of stratigraphy and rock mechanics on Mesaverde gas distribution, Piceance Basin, Colorado," in

Understanding, exploring, and developing tight-gas sands. AAPG hedberg series. Editors S. P. Cumella, K. W. Shanley, and W. K. Camp, 3, 137–155.

Dai, J. S., Feng, J. W., Li, M., and Wang, J. (2011). Discussion on the extension law of structural fracture in sand-mud interbed formation. *Earth Sci. Front.* 18 (2), 277–283.

De Jarnett, B. B., Lim, F. H., Krystinik, L. F., and Bacon, M. L. (2001). *Greater green river basin production improvement project* (U S A: U. S. Department of Energy, Federal Energy Technology Center). Contract no. DE-AC21-95MC31063 (final report.

Deng, S. G., Wang, Y., Hu, Y. Y., Ge, X. M., and He, X. Q. (2013). Integrated petrophysical log characterization for tight carbonate reservoir effectiveness: A case study from the longgang area, sichuan basin, China. *Pet. Sci.* 10 (3), 336–346. doi:10.1007/s12182-013-0282-5

Ding, W. L., Wang, X. H., Hu, Q. J., Yin, S., Cao, X. Y., and Liu, J. J. (2015). Progress in tight sandstone reservoir fractures research. *Adv. EARTH Sci.* 30 (7), 737–750. doi:10.11867/j.issn.1001-8166.2015.07.0737

Eberhardt, E., Stead, D., Stimpson, B., and Read, R. S. (1998). Identifying crack initiation and propagation thresholds in brittle rock. *Can. Geotech. J.* 35 (2), 222–233. doi:10.1139/t97-091

Feng, J. W., Sun, J. F., Zhang, Y. J., Dai, J. S., Wei, H. H., Quan, L. S., et al. (2020). Control of fault-related folds on fracture development in kuqa depression, Tarim Basin. *OIL & Gas. Geol.* 41 (3), 15.

Gdoutos, E. E. (2012). Crack growth instability studied by the strain energy density theory. *Arch. Appl. Mech.* 82 (10-11), 1361–1376. doi:10.1007/s00419-012-0690-9

Golf-Racht, T. D. V. (1982). *Fundamentals of jointed reservoir engineering.* New York, NY, USA: Elsevier Scientific.

Gudmundsson, A., Simmenes, T. H., Larsen, B., and Philipp, S. L. (2010). Effects of internal structure and local stresses on fracture propagation, deflection, and arrest in fault zones. *J. Struct. Geol.* 32, 1643–1655. doi:10.1016/j.jsg.2009.08.013

Hennings, P. H., Olson, J. E., and Thompson, L. B. (2000). Combining outcrop data and three-dimensional structural models to characterize fractured reservoirs. *AAPG Bull.* 84, 830–849.

Hoek, E., and Brown, E. T. (1980). *Underground excavations in rock.* London, UK: The Institution of Mining and Metallurgy, 80–101.

Jiu, K., Ding, W. L., Huang, W. H., You, S. C., Zhang, Y. Q., and Zeng, W. T. (2013). Simulation of paleotectonic stress fields within Paleogene shale reservoirs and prediction of favorable zones for fracture development within the Zhanhua Depression, Bohai Bay Basin, east China. *J. Pet. Sci. Eng.* 110, 119–131. doi:10.1016/j.petrol.2013.09.002

Ju, W., Hou, G. T., and Zhang, B. (2014). Insights into the damage zones in fault-bend folds from geomechanical models and field data. *Tectonophysics* 610, 182–194. doi:10.1016/j.tecto.2013.11.022

Ju, W., Wu, C. F., Wang, K., Sun, W. F., Li, C., and Chang, X. X. (2017). Prediction of tectonic fractures in low permeability sandstone reservoirs: A case study of the Es3m reservoir in the block shishen 100 and adjacent regions, dongying depression. *J. Pet. Sci. Eng.* 156, 884–895. doi:10.1016/j.petrol.2017.06.068

Kim, J. S., Lee, K. S., Cho, W. J., Choi, H. J., and Cho, G. C. (2015). A comparative evaluation of stress-strain and acoustic emission methods for quantitative damage assessments of brittle rock. *Rock Mech. Rock Eng.* 48, 495–508. doi:10.1007/s00603-014-0590-0

Krajcinovic, D. (1989). Damage mechanics. *Mech. Mater.* 8 (2-3), 117–197. doi:10.1016/0167-6636(89)90011-2

Kravchenko, S. G., Kravchenko, O. G., and Sun, C. T. (2014). A two-parameter fracture mechanics model for fatigue fracture growth in brittle materials: Eng. *Eng. Fract. Mech.* 119, 132–147. doi:10.1016/j.engfracmech.2014.02.018

Laubach, S. E. (2003). Practical approaches to identifying sealed and open fractures. *Am. Assoc. Pet. Geol. Bull.* 87, 561–579. doi:10.1306/11060201106

Leykin, V. Z. (2015). Basic laws of the processes and the principle of minimum energy consumption during pneumatic transport and distribution of pulverized fuel in direct pulverized fuel preparation systems. *Therm. Eng.* 62 (8), 564–571. doi:10.1134/s0040601515080042

Li, L., Tang, H. M., Wang, Q., Tang, S. L., Feng, W., and Wang, Z. F. (2017). Diagenetic evolution of cretaceous Ultra-Deep reservoir in keshen belt, Kelasu thrust belt, kuqa depression. *XINJIANG Pet. Geol.* 38 (01), 7–14.

Li, Z. J. (2011). *Research on the law of fracture initiation and propagation based on principle of minimum consume energy.* Daqing, China: Northeast Petroleum University.

Li, Z., Luo, W., Zeng, B. Y., Liu, J. Q., and Yu, J. B. (2018). Fluid-rock interactions and reservoir formation driven by multiscale structural deformation in basin evolution. *Earth Sci.* 43 (10), 3498–3510. doi:10.3799/dqkx.2018.323

Lisle, R. S. (1994). Detection of zones of abnormal strains in structures using Gaussian curvature analysis. *AAPG Bull.* 78, 1811–1819.

Liu, J. S., Ding, W. L., Yang, H. M., Wang, R. Y., Yin, S., Li, A., et al. (2017). 3D geomechanical modeling and numerical simulation of *in-situ* stress fields in shale reservoirs: A case study of the lower cambrian niutitang Formation in the cen'gong block, south China. *South China Tectonophys.* 712-713, 663–683. doi:10.1016/j.tecto.2017.06.030

Lu, H., Lu, X. S., Fan, J. J., Wang, X. H., Fu, X. F., Zhang, B., et al. (2016). Controlling effect of fractures on gas accumulation and production within the tight sandstone: A case study on the jurassic dibei gas reservoir in the eastern part of the kuqa foreland basin, China. *J. Nat. Gas Geoscience* 1, 61–71. doi:10.1016/j.jnggs.2016.05.003

Luo, Y. S., Tang, S. H., Liu, C. W., and Zhou, Z. B. (2009). Advances on the least energy consumption principle and its application. *Ournalofrailw. Sci. Eng.* 2, 82–89.

Mckinnon, S. D., and Barra, I. G. (1998). Fracture initiation, growth and effect on stress field: A numerical investigation. *J. Struct. Geol.* 20, 1663–1672.

McLennan, J. A., Allwardt, P. F., Hennings, P. H., and Farrell, H. E. (2009). Multivariate fracture intensity prediction: Application to Oil Mountain anticline, Wyoming. *Am. Assoc. Pet. Geol. Bull.* 3 (11), 1585–1595. doi:10.1306/07220909081

Olson, J. E., Laubach, S. E., and Lander, R. H. (2009). Natural fracture characterization in tight gas sandstones: Integrating mechanics and diagenesis. *Am. Assoc. Pet. Geol. Bull.* 93 (11), 1535–1549. doi:10.1306/08110909100

Peng, Y., Li, Y. M., and Zhao, J. Z. (2016). A novel approach to simulate the stress and displacement fields induced by hydraulic fractures under arbitrarily distributed inner pressure. *J. Nat. Gas Sci. Eng.* 35, 1079–1087. doi:10.1016/j.jngse.2016.09.054

Peng, Y., Zhao, J. Z., Sepehrnoori, K., and Li, Z. L. (2020). Fractional model for simulating the viscoelastic behavior of artificial fracture in shale gas. *Eng. Fract. Mech.* 228, 106892. doi:10.1016/j.engfracmech.2020.106892

Peng, Y., Zhao, J. Z., Sepehrnoori, K., Li, Z. L., and Xu, F. (2019). Study of delayed creep fracture initiation and propagation based on semi-analytical fractional model. *Appl. Math. Model.* 72, 700–715. doi:10.1016/j.apm.2019.03.034

Price, N. J. (1966). *Fault and joint development in brittle and semi-brittle rock.* Oxford, UK: Pergamon Press, 133–164.

Sanz, P. F., Pollard, D. D., Allwardt, P. F., and Borja, R. I. (2008). Mechanical models of fracture reactivation and slip on bedding surfaces during folding of the asymmetric anticline at Sheep Mountain, Wyoming. *J. Struct. Geol.* 30, 1177–1191. doi:10.1016/j.jsg.2008.06.002

Shanley, K. W., and Cluff, R. M. (2015). The evolution of pore-scale fluid-saturation in low-permeability sandstone reservoirs. *Am. Assoc. Pet. Geol. Bull.* 99, 1957–1990. doi:10.1306/03041411168

Shrivastava, C., and Lawatia, R. (2011). "Tight gas reservoirs: Geological evaluation of the building blocks," in *SPE Middle East unconventional gas conference and exhibition, 31 january-2 february* (Oman: Muscat).

Smart, K. J., Ferrill, D. A., Morris, A. P., and McGinnis, R. N. (2012). Geomechanical modeling of stress and strain evolution during contractional fault-related folding. *Tectonophysics* 576 (577), 171–196. doi:10.1016/j.tecto.2012.05.024

Solano, N., Zambrano, L., and Aguilera, R. (2011). Cumulative-gas-production distribution on the nikanassin tight gas formation, alberta and British columbia, Canada. *SPE Reserv. Eval. Eng.* 14, 357–376. doi:10.2118/132923-PA

Song, H. Z. (1999). An attempt of quantitative prediction of natural fracture on brittle rock reservoir. *J. Geomech.* 5, 76–84.

Song, Z. Z., Liu, G. D., Yang, W. W., Zhou, H., Sun, M., and Wang, X. (2017). Multi-fractal distribution analysis for pore structure characterization of tight sandstone-A case study of the Upper Paleozoic tight formations in the Longdong District, Ordos Basin. *Mar. Petroleum Geol.* 92, 842–854. doi:10.1016/j.marpetgeo.2017.12.018

Sun, M. C., Xu, W. Y., Wang, S. S., Wang, R. B., and Wang, W. (2018). Study on damage constitutive model of rock based on principle of minimum dissipative energy. *J. Central South Univ. Sci. Technol.* 49 (08), 2067–2075.

Sun, S., Hou, G. T., and Zheng, C. F. (2017). Fracture zones constrained by neutral surfaces in a fault-related fold: Insights from the Kelasu tectonic zone, Kuqa Depression. *J. Struct. Geol.* 104, 112–124. doi:10.1016/j.jsg.2017.10.005

Tabarrok, B., and Leech, C. M. (2002). Hamiltonian mechanics for functionals involving second-order derivatives. *J. Appl. Mech.* 69 (6), 749–754. doi:10.1115/1.1505626

Tan, C. X., and Wang, L. J. (1999). An approach to the application of 3_D tectonic stress field numerical simulation in structural fissure analysis of the oil-gas-bearing basin. *Acta Geosci. Sin.* 20, 392–394.

Taylor, T. R., Giles, M. R., Hathon, L. A., Diggs, T. A., Braunsdorf, N. R., Birbiglia, G. V., et al. (2010). Sandstone diagenesis and reservoir quality prediction: Models, myths, and reality. *Am. Assoc. Pet. Geol. Bull.* 94 (8), 1093–1132. doi:10.1306/04211009123

Tojaga, V., Kulachenko, A., Stlund, S., and Gasser, T. C. (2021). Modeling multi-fracturing fibers in fiber networks using elastoplastic timoshenko beam finite elements with embedded strong discontinuities-formulation and staggered algorithm. *Comput. Methods Appl. Mech. Eng.* 384, 113964. doi:10.1016/j.cma.2021.113964

Tuckwell, G. W., Lonergan, L., and Jolly, R. J. H. (2003). The control of stress history and flaw distribution on the evolution of polygonal fracture networks. *J. Struct. Geol.* 25, 1241–1250. doi:10.1016/s0191-8141(02)00165-7

Wlderhaug, O., Eliassen, A., and Aase, N. E. (2012). Prediction of permeability in quartz-rich sandstones: Examples from the Norwegian continental shelf and the Fontainebleau sandstone. *J. Sediment. Res.* 82 (12), 899–912. doi:10.2110/jsr.2012.79

Wang, R., Ding, W., Zhang, Y., Wang, Z., Wang, X., He, J., et al. (2016). Analysis of developmental characteristics and dominant factors of fractures in lower cambrian marine shale reservoirs: A case study of niutitang Formation in cen'gong block, southern China. *J. Pet. Sci. Eng.* 138, 31–49. doi:10.1016/j.petrol.2015.12.004

Wu, Z. H., Zuo, Y. J., Wang, S. Y., Chen, J., Wang, A. L., Liu, L. L., et al. (2017). Numerical study of multi-period palaeotectonic stress fields in lower cambrian shale reservoirs and the prediction of fractures distribution: A case study of the niutitang formation in feng'gang No. 3 block, south China. *Mar. Petroleum Geol.* 80, 369–381. doi:10.1016/j.marpetgeo.2016.12.008

Xue, Y. C., Cheng, L. S., Mou, J. Y., and Zhao, W. (2014). A new fracture prediction method by combining genetic algorithm with neural network in low-permeability reservoirs. *J. Petroleum Sci. Eng.* 121, 159–166. doi:10.1016/j.petrol.2014.06.033

Zeng, L. B., and Li, Y. G. (2010a). Tectonic fractures in tight gas sandstones of the upper triassic xujiahe formation in the western sichuan basin, China. *Acta Geol. Sin. - Engl. Ed.* 84 (5), 1229–1238. doi:10.1111/j.1755-6724.2010.00293.x

Zeng, L. B., Wang, H. J., Gong, L., and Liu, B. M. (2010b). Impacts of the tectonic stress field on natural gas migration and accumulation: A case study of the kuqa depression in the Tarim Basin, China. *Mar. Pet. Geol.* 27, 1616–1627. doi:10.1016/j.marpetgeo.2010.04.010

Zeng, Q. L., Zhang, R. H., and Lu, W. Z. (2017). Fracture development characteristics and controlling factors based on 3D laser scanning technology: An outcrop case study of Suohan village, Kuqa foreland area. *Tarim. Basin Nat. Gas. Geosci.* 28 (3), 397–409.

Zhang, Y. Z., Feng, J. W., Luo, R. L., and Liu, Z. L. (2020). Study of controlling factors on productivity of keshen gas field: A deep tight sandstone reservoir in kuqa depression. *IOP Conf. Ser. Earth Environ. Sci.* 555 (1), 012107. (5pp). doi:10.1088/1755-1315/555/1/012107

Zhang, Z. P., Wang, Q. C., and Wang, Y. (2006). Brittle structure sequence in the Kuqa Depression and its implications to the tectonic paleostress. *Earth Science-Journal China Univ. Geosciences* 31 (3), 310–316.

Zhao, G. J., Li, X. Q., Liu, M. C., Dong, C. Y., Li, J., Liu, Y., et al. (2022). Fault activity and hydrocarbon accumulation significance of structural belt in northern Kuqa Depression. *J. Min. Sci. Technol.* 7 (01), 34–44. doi:10.19606/j.cnki.jmst.2022.01.004

Zhao, W. T., Hou, G. T., and Sun, X. W. (2013). Influence of layer thickness and lithology on the fracture growth of clastic rock in East Kuqa. *Geotect. Metallogenia* 37 (4), 603–610.

Zhou, G. X., Ye, Y., and Zhou, F. J. (2021). Research progress in damage assessment methods for tight sandstone gas reservoirs. *J. Phys. Conf. Ser.* 1, 12033. doi:10.1088/1742-6596/2009/1/012033

Zhou, X. G., Cao, C. J., and Yuan, J. Y. (2003). The status and prospects of quantitative structural joint prediction of reservoirs and research of oil and gas seepage law. *Adv. Earth Sci.* 18, 398–404.

Development or absence of conjugate fractures in low-permeability sandstones

Haimeng Yang[1], Jifeng Yu[1]*, Peng Chen[2], Caifu Hu[3] and Peng Dai[4]

[1]College of Earth Sciences and Engineering, Shandong University of Science and Technology, Qingdao, China, [2]School of Earth Resources, China University of Geosciences, Wuhan, China, [3]Tongren Zhongneng Natural Gas Co, Ltd, Tongren, China, [4]Institute of Geophysical and Geochemical Exploration, Chinese Academy of Geological Science, Tianjin, China

Natural fractures are ubiquitous in rocks. The Coulomb law of Mohr's failure theory predicts that the angle between conjugate failure surfaces is a constant. In the Ordos Basin, observing the development of two groups of conjugate fractures in the field, cores and imaging logging is very difficult. In this paper, the directions of paleocurrents in the Upper Triassic Yanchang Formation of the Ordos Basin are determined by measuring the orientations of field bedding**.** Through the correlation analysis of paleocurrent and natural fracture orientations, when the sediment comes from a single source, a group of fractures with a large angle between conjugate fractures and the paleocurrent direction is found not to develop. When the sediments in the study area have two provenances, both provenance directions affect the development of conjugate fractures. In the southern Ordos Basin, influenced by the direction of paleocurrent flow in the near-north direction, fractures in the near N–S direction develop. Through rock mechanics experiments in different directions, the planar anisotropy in rock mechanics parameters caused by the direction of paleocurrent flow is found to be the geological factor leading to various degrees of fracture development in different directions within the Ordos Basin.

1 Introduction

The occurrence of fractures plays a decisive role in quantifying the anisotropy of fractured reservoirs. The orientation of fractures is indicative for determining the migration and accumulation of oil and gas in different geological periods and is a prerequisite for accurately predicting the current fracture opening pressure, effective opening, permeability and other parameters (Zeng et al., 2008a; Liu et al., 2021; Li et al., 2022). The Coulomb law of Mohr's failure theory predicts that the angle between conjugate failure planes is a constant, which is independent of the magnitude

of the stress difference in rock failure, and that the maximum principal stress divides the angle equally (Muehlberger, 1961; Palchik, 2006; Li et al., 2019,2022; Chai and Yin, 2021; Wood, 2022). Experimental results show that the angle actually decreases with decreasing confining pressure (Muehlberger, 1961). A single group of fractures may have similar properties (types, mineral fillers, etc.) and specific direction range. Natural fractures are ubiquitous in rocks. Because of sedimentary changes, differential diagenesis and uneven stress distribution in sandstone reservoirs, the degrees of fracture development for different formations are different (Nelson, 2001; Zeng et al., 2008a; Laubach et al., 2009; Liu et al., 2018; Gong et al., 2019; Liu et al., 2022b, c). The vertical anisotropy of rock also affects the propagation paths of fractures, which are terminated, penetrated or turned near structural planes (Hutchinson, 1996; Gudmundsson, 2006; Gudmundsson et al., 2010; Larsen et al., 2010; Liu et al., 2019). According to the published literature (Zeng et al., 2008b; Jiang et al., 2016; Lyu et al., 2016; Gong et al., 2019; Fan et al., 2020; Fan et al., 2022), observing conjugate fracture development in the Ordos Basin is very difficult, whether in the field, cores or imaging logging. However, in the margin of the basin, where the value of tectonic differential stress is large, tectonic stress may be the dominant factor controlling the directions and paths of fracture propagation, and conjugate fractures can be seen in the field (Zhao and Hou, 2017a).

The Ordos Basin is one of the main areas of low-permeability sandstone reservoirs and is a key region for the exploration and development of low-permeability reservoirs in China (Liu et al., 2005; Yao et al., 2013; Zou et al., 2013; Tao et al., 2016). In the Ordos Basin, due to the influences of sedimentation, diagenesis and tectonism, the heterogeneity of low-permeability reservoirs is strong, and natural fracture development is affected by lithology, thickness and rock mechanics parameters (Zhao et al., 2014; Ju et al., 2017). Natural fractures control the seepage systems of low-permeability reservoirs, thus affecting the deployment of low-permeability oilfield development plans and their development (Zeng et al., 2007; Zeng et al., 2008a; Zeng and Li, 2009; Ju et al., 2015; Zhao and Hou, 2017a; Liu et al., 2022a; Chen et al., 2022). Therefore, studying the orientations of natural fractures and the factors that influence fracture orientation is very important for the deployment of an injection-production well pattern, the direction of water seepage in the reservoir, and the formulation of a reasonable development plan. In this paper, we provide an example of how the planar anisotropy of rock mechanics caused by sedimentation (paleocurrent direction) leads to variable fracture development in different directions in the Ordos Basin. Controlled by the direction of the paleocurrent, the planar anisotropy of reservoir mechanical parameters shows the lowest compressive strength parallel to the direction of the paleocurrent, which is an important factor affecting the diverse degrees of fracture development in different directions.

2 Geological settings and stratigraphy

The Upper Triassic Yanchang Formation in the Ordos Basin developed delta plains, delta fronts, semideep lakes and deep lake deposits (Liu and Yang, 2015). Controlled by sedimentary facies, the sand bodies are distributed in large areas on the plane. On the whole, the structural deformation of the reservoir in the basin is weak, the strata dips are gentle, and faults and folds have not developed (Figure 1). Outcrop observations around the basin indicate that the fractures in the Triassic and Jurassic strata are relatively developed. Therefore, although folds and faults are not present in the basin, the regional stress acting on the periphery of the basin has an impact on the interior of the basin, which is characterized by extensive regional fractures in the basin (Zeng et al., 2008a).

According to the sedimentary cycle and oil-bearing properties, the Yanchang Formation can be divided into 10 oil-bearing formations, named Chang 10 to Chang one from bottom to top. The strata in which low-permeability reservoirs have developed are mainly the Chang 4 to Chang 8 oil-bearing formations, with permeabilities less than 1×10^3 μm^2 and porosities generally between 4% and 12%, and the rocks have fine grains and compact lithology (Guo, 2016). As the bottom stratum of the Triassic Yanchang Formation, the Chang 10 oil-bearing formation is generally composed of gray–white coarse sandstone, medium sandstone and fine sandstone, with gray–black mudstone. The Chang 9 oil-bearing formation is in the rapid subsidence period of the Ordos Basin. Large-scale lake transgression occurred in the basin. The lake basin is developed, and a set of gray–black mudstone, gray–black siltstone and gray–white fine sandstone are deposited. The Chang 8 oil-bearing formation is a set of interbedded gray–black mudstone, gray siltstone, fine sandstone and gray–white medium sandstone. The Chang 7 oil-bearing formation is mainly a set of dark mudstone deposits of semideep shallow lake facies. The Chang 6 oil-bearing formation is a set of interbedded deposits of gray–white siltstone, gray, gray–black mudstone and gray–white fine sandstone. The sedimentary Chang 4+5 oil-bearing formation in the Ordos Basin is a small-scale lake transgression event in the study area. Therefore, compared with the Triassic Chang 6 oil-bearing formation, the Triassic Chang 4+5 oil-bearing formation has more argillaceous content and higher mudstone and siltstone content. Fractures can not only be used as channels for oil and gas migration but also increase the permeability of reservoirs and the connectivity of pores, thus improving reservoir performance.
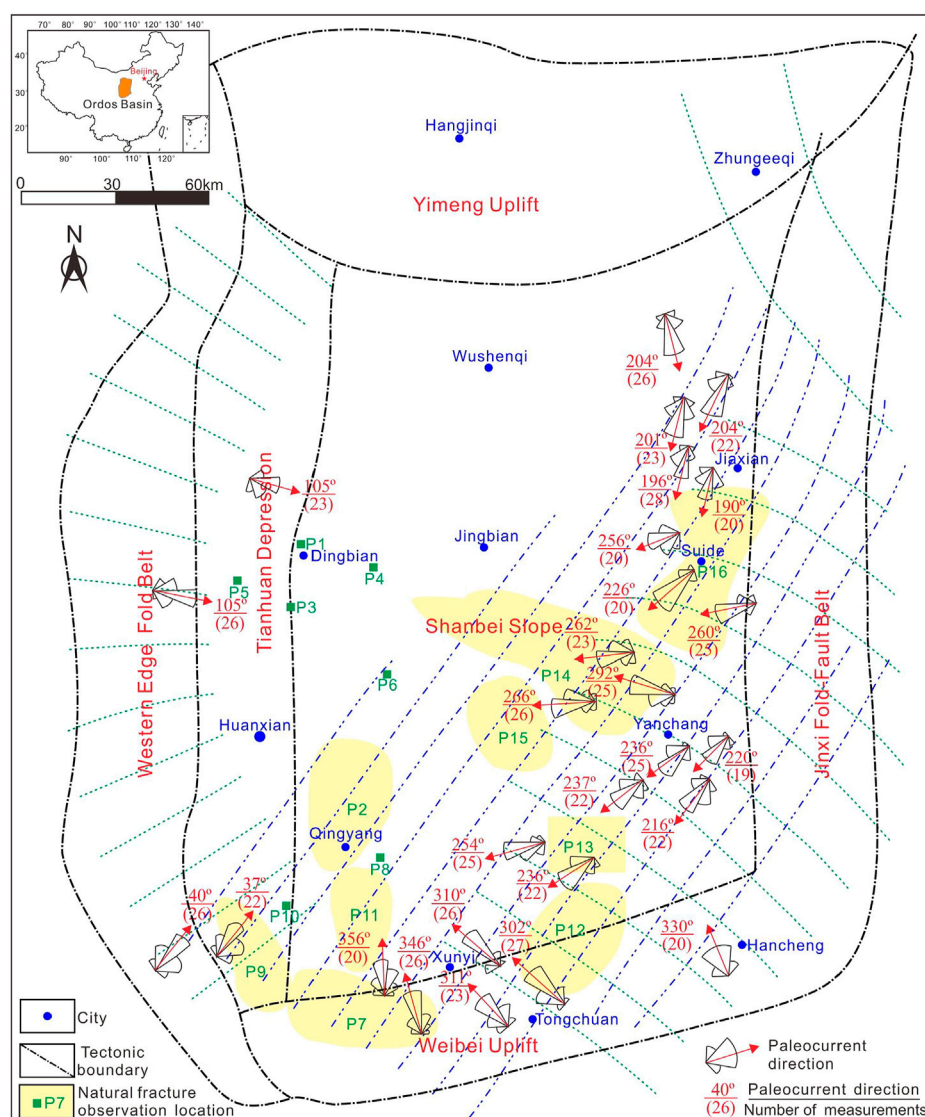
FIGURE 1
Distribution of the tectonic stress field and paleocurrents in the Ordos Basin. The paleocurrent directions in the Yanchang Formation are shown for the early and middle stages of sedimentation (Chang 4 to Chang 10 oil-bearing formations). The paleocurrent data were provided by Guo (2016), and the tectonic stress field data were provided by Xu et al. (2006). The blue dashed line is the direction of the maximum horizontal principal stress in the Himalayan period, and the green dashed line is the direction of the maximum horizontal principal stress in the Yanshanian period.

3 Data and methods

The orientation of natural fractures is mainly determined by field observations, core paleomagnetic orientation and imaging logging. A core paleomagnetism experiment was completed in the Paleomagnetism and Paleotectonic Reconstruction Laboratory, Institute of Geomechanics, Chinese Academy of Geological Sciences. The directions of paleocurrents are determined mainly by measuring the orientation of bedding, such as tabular cross-bedding, trough cross-bedding and wedge cross-bedding. Through detailed observations of field profiles

around the Ordos Basin, the directions of paleocurrents in different areas can be restored.

To study the variations in the mechanical properties of rocks in different directions and their relationships with fracture development, uniaxial and triaxial rock mechanics tests were carried out on rocks in different directions. The confining pressures set in the rock mechanics experiment were 20 MPa, 30 MPa and 40 MPa. The rock mechanics experiment was completed with a WGE-600 universal testing machine in the Rock Mechanics Laboratory of Beijing University of Science and Technology. Rock samples were taken from low-permeability sandstone reservoirs of the Upper Triassic Yanchang

FIGURE 2
Structural fractures in the Yanchang Formation: photographs from the field. **(A)** Structural fractures are developed in sand–mud interbeds at Jiaxian, but fractures are basically not developed in the in the lower mudstone. **(B)** The shear fractures developed in mudstone at Suide have a small spacing and short extension distance. **(C)** The shear fractures developed in the sandstone at Xunyi have a large spacing and long extension distance. **(D)** This shear fracture developed in the dense sandstone at Dingbian is filled with calcite and has a width of 2.0 cm. See the locations in Figure 1.

Formation in the Ordos Basin. To ensure a sufficient number of samples, drilling samples were selected from fine sandstone sections with thicknesses over 20 cm (Zeng et al., 2008b). First, the relative coordinate system of the core was established. Samples were taken at 30-degree intervals parallel to the bedding plane, clockwise and counterclockwise from a certain marked direction. Samples in six directions were taken from each part from bottom to top. Three parallel samples were drilled on the same plane and processed into standard cylindrical samples of 25 mm×(45–60) mm (Zeng et al.,

2008b). The number of samples in each position was 18. Finally, the direction of the marker line in the samples was determined by the paleomagnetic orientation of the core.

4 Results and discussion

A single joint group or orthogonal joint system is formed in a stable stress field. In the field, the time of formation can be
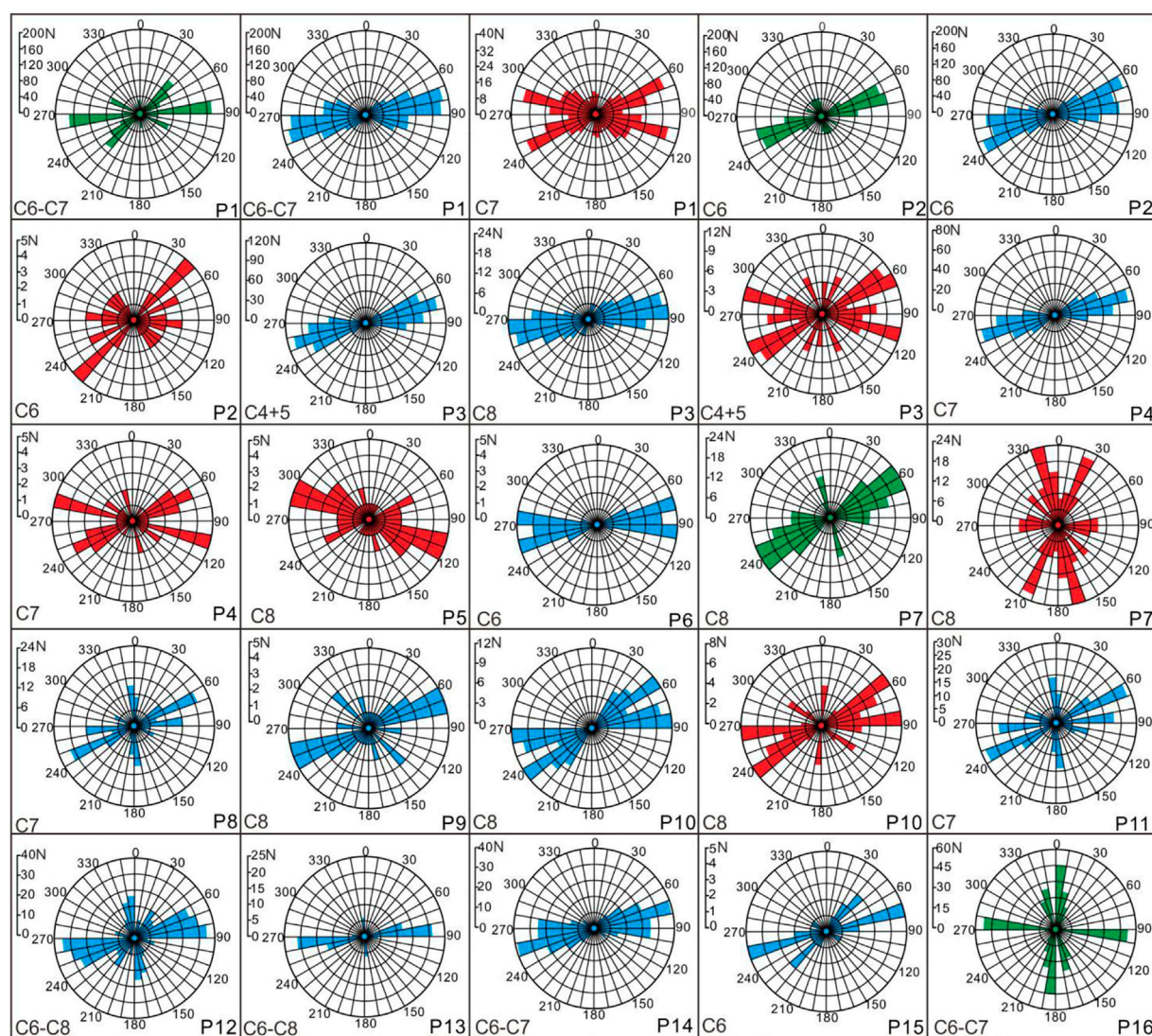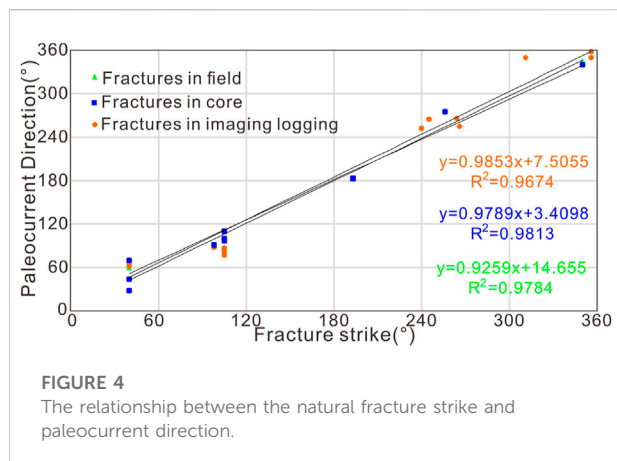
FIGURE 3
Fracture strike rose diagrams for different areas. Green represents fractures in field statistics, red represents fractures determined by core paleomagnetism, and blue represents fractures in imaging logging statistics. P1-P16 are the locations of the fracture observation points, and C4-C8 are the different oil-bearing formations of the Yanchang Formation. C4+5 = Chang 4+5 oil-bearing formations; C6 = Chang 6 oil-bearing formation; C7 = Chang 7 oil-bearing formation; C8 = Chang 8 oil-bearing formation. See Figure 1 for the P1-P16 locations. Some imaging logging and paleomagnetic data in the western Ordos Basin were provided by Fan et al. (2016).

judged by the mutual contact relationship of joints. According to the cross-cutting relationship of fractures, the four groups of fractures developed in the Ordos Basin mainly formed in two stages. In surface outcrops, cores and imaging logging, the E–W- and NW–SE-trending fractures can be seen to restrict the N–S- and NE–SW-trending fractures, and NE–SW- and N–S-trending fractures cut NW–SE- and E–W-trending fractures, reflecting the two main stages of formation for fractures in the Ordos Basin. The E–W- and NW–SE-trending fractures are a group of conjugate shear fractures that formed in the early stage, while the N–S- and NE–SW-

trending fractures are a group of conjugate shear fractures that formed in the late stage. Combining this information with the paleostress distribution (Figure 1), the early fractures mainly formed under horizontal compressive stress in the WNW–ESE direction, while the late fractures mainly formed under horizontal compressive stress in the NNE–SSW direction. The directions of the above two stages of the tectonic stress field are identical to those of the Yanshanian and Himalayan stages (Figure 1), which indicates that the Late Jurassic and the Late Cretaceous-Paleogene were the main periods of fracture formation in the Ordos Basin, and the results are the same as

FIGURE 4
The relationship between the natural fracture strike and paleocurrent direction.

FIGURE 5
Uniaxial compressive strength of the rock in different directions for low-permeability sandstone in the P3 area (according to Tang et al., 2012).

FIGURE 6
Uniaxial compressive strength of the rock in different directions for low-permeability sandstone in the Longdong area (P2, P8, and P10) (according to Zeng et al., 2008b).

those obtained from the analysis of inclusions in fracture fillings (Zhao et al., 2017b).

Field fracture observations show that the outcrops are dominated by high-angle fractures with an inclination greater than 75°, and 90% of the fractures have an inclination greater than 80°. The study of rock fracture mechanics shows that the dip angle of the fractures is closely related to the mechanical properties of the rock (Liu et al., 2021). Field observations show that the dip angle of the high-angle fractures in the tight sandstone decreases when continuing into the mudstone. As shown in Figure 2, the spacing distribution of natural fractures of the same scale is relatively uniform. The overall finding is that the fracture spacing increases with increasing fracture size. The fracture spacing is less than 1 m for fractures with an extension length of less than 2 m, 3–5 m for fractures with a length of 2–10 m, and 6–10 m for fractures with a length of more than 10 m. In the west central Ordos Basin, the orientations of fractures are mainly ENE–WSW and near E–W; NW–SE-directed fractures did not develop in the Yanshanian period, N–S (or NNE–SSW)-directed fractures did not develop in the Himalayan period, and the direction of the paleocurrent was near ESE 100° (Figure 3, P1, P3, P4, and P5). In the southwestern Ordos Basin (Figure 3, P2, P6, P9, and P10), the same pattern is observed. In the southern Ordos Basin, due to a change in the paleocurrent direction, especially the development of a northward paleocurrent, the Himalayan fractures (Figure 3, P7, P8, P11, P12, and P13) developed in the N–S direction. In the middle and eastern Ordos Basin, the directions of paleocurrents are mainly WSW 260° and SW 220°, and the directions of fractures are mainly E–W and ENE–WSW (Figure 3, P14 and P15). The SSE–NNW-trending fractures did not develop in the Yanshanian period, and the N–S-trending fractures did not develop in the Himalayan period. In the northeastern part of the Ordos Basin, the directions of the paleocurrents are SSW 190° and WSW 256°. Field fracture observations show that the orientations of fractures are mainly N–S and E–W (Figure 3, P16); in the Yanshanian
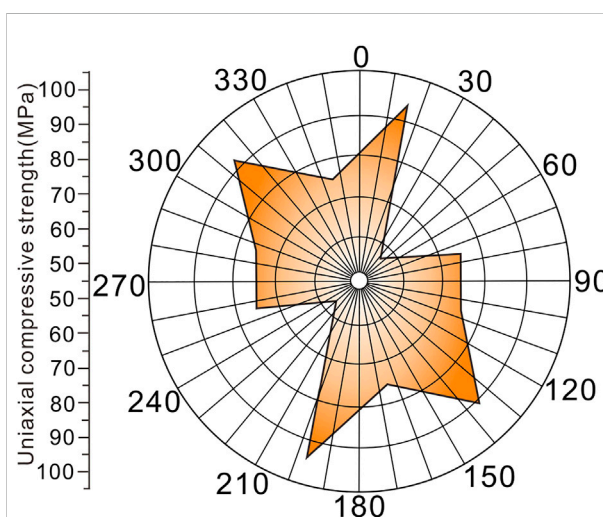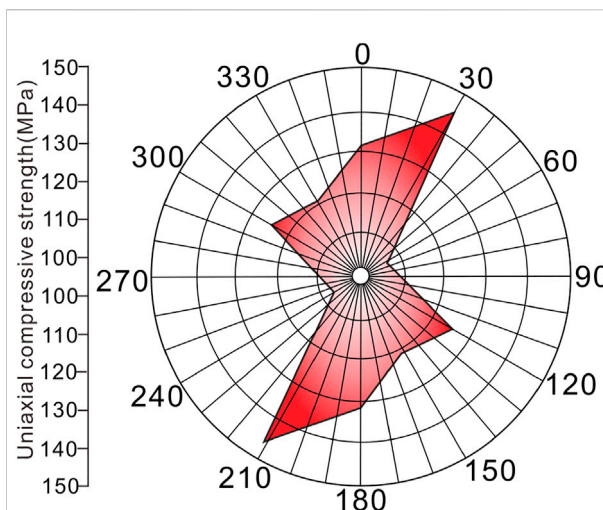
period, SE-directed fractures did not develop, while in the Himalayan period, NE–SW-directed fractures did not develop.

Field observations, core statistics and imaging logging statistics show that the fracture orientation is basically consistent with the direction of the paleocurrent, and the relationship between them is linear (Figure 4). In the P3 area, the paleocurrent direction is ESE 105°, and the uniaxial compressive strength of the rock is the lowest in the E–W
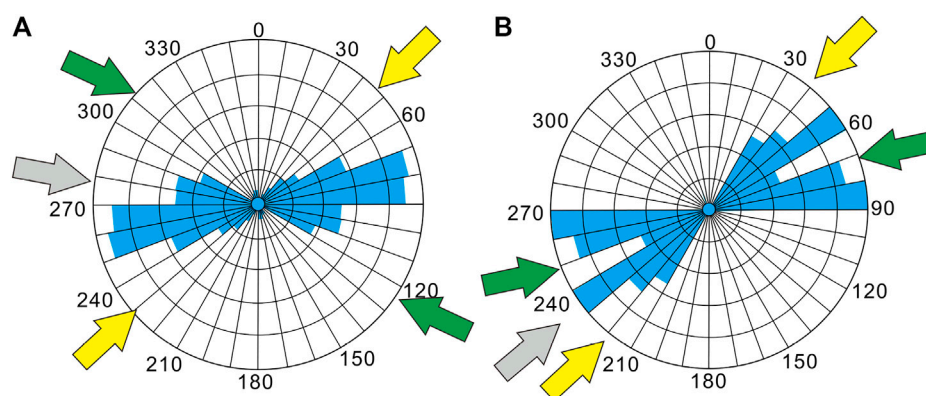
FIGURE 7
(A) The relationship between the strike of natural fractures and the direction of the paleocurrent and paleostress field in the western central Ordos Basin; **(B)** the relationship between the strike of natural fractures and the direction of the paleocurrent and paleostress field in the southwestern Ordos Basin. The yellow arrow is the direction of the maximum horizontal principal stress in the Himalayan period, and the blue arrow is the direction of the maximum horizontal principal stress in the Yanshanian period; the light gray arrow is the main paleocurrent direction, and the dark gray arrow is the secondary paleocurrent direction.
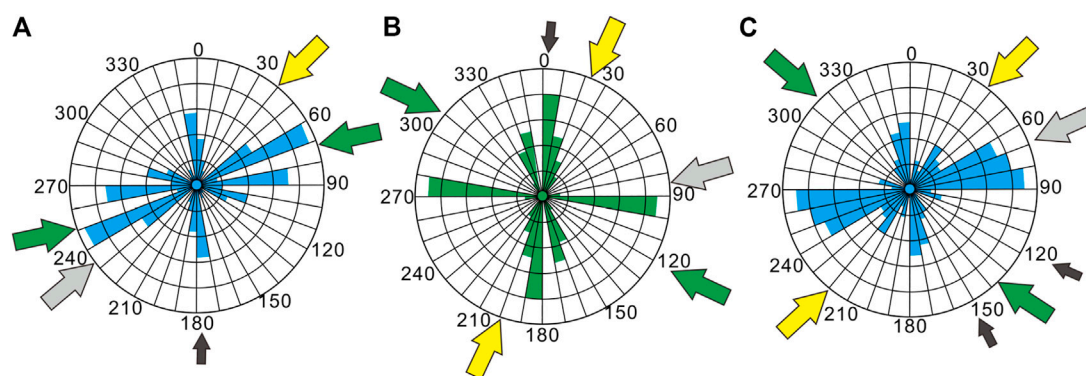
FIGURE 8
(A) The relationship between the strike of natural fractures and the direction of the paleocurrent and paleostress field in the southern Ordos Basin; **(B)** the relationship between the direction of the paleocurrent and paleostress field in the east central Ordos Basin; **(C)** the relationship between the strike of natural fractures and the direction of the paleocurrent and paleostress field in the southeastern Ordos Basin. The yellow arrow is the direction of the maximum horizontal principal stress in the Himalayan period, and the blue arrow is the direction of the maximum horizontal principal stress in the Yanshanian period; the light gray arrow is the main paleocurrent direction, and the dark gray arrow is the secondary paleocurrent direction.

direction (Figure 5). The anisotropy in the uniaxial compressive strength of the rock leads to the nondevelopment of SE–NW-directed fractures in the Yanshanian period and the nondevelopment of NNE–SSW-directed fractures in both groups of fractures in the Himalayan period. In the P2, P8 and P10 areas, the direction of the paleocurrent is NE 40°, and the uniaxial compressive strength of the rock is the lowest in the NE–SW direction, which results in a group of undeveloped conjugate fractures in the Yanshanian and Himalayan periods (Figure 6). Anisotropy in the rock mechanics parameter plane is

caused by the distribution of bedding or grain orientations in the rock developed by the paleocurrent, which is the main factor that determines the different degrees of fracture development in different directions.

When the sediments in the study area come from a single source, a group of fractures with a small angle between the conjugate fracture and the source direction develops, while a group of fractures with a large angle between the conjugate fracture and the source direction does not develop (Figures 7A,B). The normal stress and shear stress curves of rocks

under different confining pressures were fit, and the internal friction angle of tight sandstone in the study area is 40–45° (Liu et al., 2021). When there are two paleocurrent currents in the study area, both source directions affect the orientation of natural fractures. In the southern Ordos Basin, influenced by the direction of paleocurrent currents in the near N–S direction, fractures in the near N–S direction developed (Figures 8A,B). As the number of paleocurrent directions increases, the orientations of natural fractures become more complicated (Figure 8C).

5 Conclusion

In this paper, we present an example of a group of undeveloped conjugate fractures caused by paleocurrents. The main controlling factors of fracture development in the Ordos Basin are lithology, stratum thickness and tectonic stress. The fractures in the study area are mainly high-angle fractures, showing typical structural genetic characteristics. Due to the heterogeneity of reservoir rocks, conjugate fractures are characterized by one group of relatively developed fractures and another group of relatively weak fractures.

The direction of the paleocurrent results in anisotropy in the rock mechanics plane; the rock compressive strength parallel to the direction of the paleocurrent is the smallest, which means that a group of conjugate fractures did not develop in the Ordos Basin, and the direction of the paleocurrent led to undeveloped fractures. The main reason for the difference is the rock mechanics parameters in the same direction. When the differential stress at the basin margin is large, the tectonic stress is the dominant factor controlling the direction and path of fracture propagation, and conjugate fractures can be seen in the field profiles. In the Ordos Basin, the stress difference is small, and the anisotropy in the rock mechanics parameters of reservoirs affects the propagation of fractures, resulting in various degrees of fracture development in different directions.

The direction of the paleocurrent combined with the distribution of the paleostress field can be used to predict which group of conjugate fractures develop. Conversely, the direction of the paleocurrent can be inferred by combining the orientation of developed fractures with the distribution of the paleostress field.

Data availability statement

The original contributions presented in the study are included in the article/supplementary material, further inquiries can be directed to the corresponding author.

Author contributions

HY and JY contributed in writing, reviewing, and editing, datacuration, writing—original draft preparation; PC, CH, and PD contributed in formal analysis, validation, and reviewing.

Conflict of interest

Author CH was employed by Tongren Zhongneng Natural Gas Co, Ltd.

The remaining authors declare that the research was conducted in the absence of any commercial or financial relationships that could be construed as a potential conflict of interest.

Publisher's note

All claims expressed in this article are solely those of the authors and do not necessarily represent those of their affiliated organizations, or those of the publisher, the editors and the reviewers. Any product that may be evaluated in this article, or claim that may be made by its manufacturer, is not guaranteed or endorsed by the publisher.

Supplementary material

The Supplementary Material for this article can be found online at: https://www.frontiersin.org/articles/10.3389/feart.2022.1058768/full#supplementary-material

References

Chai, Y., and Yin, S. (2021). 3D displacement discontinuity analysis of *in-situ* stress perturbation near a weak faul. *Adv. Geo-Energy Res.* 5 (3), 286–296. doi:10.46690/ager.2021.03.05

Chen, C., Ji, G., Wang, H., Huang, H., Baud, P., and Wu, Q. (2022). Geology-engineering integration to improve drilling speed and safety in ultra-deep clastic reservoirs of the Qiulitage structural belt. *Adv. Geo-Energy Res.* 6 (4), 347–356. doi:10.46690/ager.2022.04.09

Fan, C. H., Li, H., Qin, Q. R., He, S., and Zhong, C. (2020). Geological conditions and exploration potential of shale gas reservoir in Wufeng and Longmaxi Formation of southeastern Sichuan Basin, China. *J. Petroleum Sci. Eng.* 191, 107138. doi:10.1016/j.petrol.2020.107138

Fan, C. H., Xie, H. B., Li, H., Zhao, S. X., Shi, X. C., Liu, J. F., et al. (2022)., 2022. China. Lithosphere, 8035106. doi:10.2113/2022/8035106Complicated fault characterization and its influence on shale gas preservation in the southern margin of the sichuan basin, China

Fan, J., Qu, X., Wang, C., Lei, Q., Cheng, L., and Yang, Z. (2016). Natural fracture distribution and a new method predicting effective fractures in tight oil reservoirs in Ordos Basin, NW China. *Petroleum Explor. Dev.* 43 (5), 806–814. doi:10.1016/s1876-3804(16)30096-9

Gong, L., Fu, X., Wang, Z., Gao, S., Jabbari, H., Yue, W., et al. (2019). A new approach for characterization and prediction of natural fracture occurrence in tight oil sandstones with intense anisotropy. *Bulletin* 103 (6), 1383–1400. doi:10.1306/12131818054

Gudmundsson, A. (2006). How local stresses control magma-chamber ruptures, dyke injections, and eruptions in composite volcanoes. *Earth-Science Rev.* 79 (1-2), 1–31. doi:10.1016/j.earscirev.2006.06.006

Gudmundsson, A., Simmenes, T. H., Larsen, B., and Philipp, S. L. (2010). Effects of internal structure and local stresses on fracture propagation, deflection, and arrest in fault zones. *J. Struct. Geol.* 32 (11), 1643–1655. doi:10.1016/j.jsg.2009.08.013

Guo, Y. (2016). *Characteristics of tight reservoirs and reservoir enrichment in the triassic Yanchang Formation in the Ordos Basin.* China: Petroleum Industry Press.

Hutchinson, J. W. (1996). *Notes for a dcamm course.* Lyngby: Technical University of Denmark.Stresses and failure modes in thin films and multilayers.

Jiang, L., Qiu, Z., Wang, Q., Guo, Y., Wu, C., Wu, Z., et al. (2016). Joint development and tectonic stress field evolution in the southeastern Mesozoic Ordos Basin, west part of North China. *J. Asian Earth Sci.* 127, 47–62. doi:10.1016/j.jseaes.2016.06.017

Ju, W., Shen, J., Qin, Y., Meng, S., Wu, C., Shen, Y., et al. (2017). *In-situ* stress state in the linxing region, eastern Ordos Basin, China: Implications for unconventional gas exploration and production. *Mar. Petroleum Geol.* 86, 66–78. doi:10.1016/j.marpetgeo.2017.05.026

Ju, W., Sun, W., and Hou, G. (2015). Insights into the tectonic fractures in the yanchang formation interbedded sandstone-mudstone of the ordos basin based on core data and geomechanical models. *Acta Geol. Sin. - Engl. Ed.* 89 (6), 1986–1997. doi:10.1111/1755-6724.12612

Larsen, B., Grunnaleite, I., and Gudmundsson, A. (2010). How fracture systems affect permeability development in shallow-water carbonate rocks: An example from the gargano peninsula, Italy. *J. Struct. Geol.* 32 (9), 1212–1230. doi:10.1016/j.jsg.2009.05.009

Laubach, S. E., Olson, J. E., and Gross, M. R. (2009). Mechanical and fracture stratigraphy. *Bulletin* 93 (11), 1413–1426. doi:10.1306/07270909094

Li, H., Tang, H., Qin, Q., Zhou, J., Qin, Z., Fan, C., et al. (2019). Characteristics, formation periods and genetic mechanisms of tectonic fractures in the tight gas sandstones reservoir: A case study of xujiahe formation in YB area, sichuan basin, China. *J. Petroleum Sci. Eng.* 178, 723–735. doi:10.1016/j.petrol.2019.04.007

Li, J., Li, H., Yang, C., Wu, Y., Gao, Z., and Jiang, S. (2022). Geological characteristics and controlling factors of deep shale gas enrichment of the Wufeng-Longmaxi Formation in the southern Sichuan Basin, China. *Lithosphere* 2022, 4737801. doi:10.2113/2022/4737801

Liu, C., Zhao, H., and Wang, F. (2005). Attributes of the mesozoic structure on the west margin of the ordos basin. *Acta Geol. Sin.* 79 (6), 747.

Liu, J., Chen, P., Xu, K., Yang, H., Liu, H., and Liu, Y. (2022a). *Fracture stratigraphy and mechanical stratigraphy in sandstone: A multiscale quantitative analysis.* Netherlands: Marine and Petroleum Geology. 145, 105891. doi:10.1016/2022/105891

Liu, J., Ding, W., Dai, J., Wu, Z., and Yang, H. (2018). Quantitative prediction of lower order faults based on the finite element method: A case study of the M35 fault block in the Western hanliu fault zone in the gaoyou sag, east China. *Tectonics* 37 (10), 3479–3499. doi:10.1029/2017tc004767

Liu, J., Ding, W., Xiao, Z., and Dai, J. (2019). Advances in comprehensive characterization and prediction of reservoir fractures. *Prog. Geophys.* 34 (6), 2283–2300.

Liu, J., Ding, W., Yang, H., and Liu, Y. (2021). Quantitative multiparameter prediction of fractured tight sandstone reservoirs: A case study of the Yanchang Formation of the Ordos Basin, central China. *SPE J.* 26 (05), 3342–3373. doi:10.2118/205495-pa

Liu, J., Mei, L., Ding, W., Xu, K., Yang, H., and Liu, Y. (2022b). Asymmetric propagation mechanism of hydraulic fracture networks in continental reservoirs. *GSA Bull.* doi:10.1130/B36358.1

Liu, J., Yang, H., Xu, K., Wang, Z., Liu, X., Cui, L., et al. (2022c). Genetic mechanism of transfer zones in rift basins: Insights from geomechanical models. *GSA Bull.* 134 (9-10), 2436–2452. doi:10.1130/b36151.1

Liu, S., and Yang, S. (2015). Upper triassic – jurassic sequence stratigraphy and its structural controls in the Western ordos basin, China. *Basin Res.* 12 (1), 1–18. doi:10.1046/j.1365-2117.2000.00107.x

Lyu, W., Zeng, L., Liu, Z., Liu, G., and Zu, K. (2016). Fracture responses of conventional logs in tight-oil sandstones: A case study of the upper triassic Yanchang Formation in southwest Ordos Basin, China. *Bulletin* 100 (9), 1399–1417. doi:10.1306/04041615129

Muehlberger, W. R. (1961). Conjugate joint sets of small dihedral angle. *J. Geol.* 69 (2), 211–219. doi:10.1086/626729

Nelson, R. (2001). *Geologic analysis of naturally fractured reservoirs.* Netherlands: Elsevier.

Palchik, V. (2006). Application of mohr–coulomb failure theory to very porous sandy shales. *Int. J. Rock Mech. Min. Sci.* 43 (7), 1153–1162. doi:10.1016/j.ijrmms.2006.03.007

Tang, X., Zeng, L., He, Y., Fan, J., Xu, W., Gong, L., et al. (2012). Effect of deposition and diagenesis on tectonic fractures of sandstone reservoirs with ultra-low permeability in jiyuan oilfield. *J. Oil Gas Technol.* 34 (4), 21–25.

Tao, S., Yuan, X., Hou, L., Zhu, R., Yang, F., Li, C., et al. (2016). Play types, geologic characteristics and exploration domains of lithological reservoirs in China. *Petroleum Explor. Dev.* 43 (6), 941–953. doi:10.1016/s1876-3804(16)30112-4

Wood, D. A. (2022). Predicting brittleness indices of prospective shale formations from sparse well-log suites assisted by derivative and volatility attributes. *Adv. Geo-Energy Res.* 6 (4), 334–346. doi:10.46690/ager.2022.04.08

Xu, L., Zhou, L., Zhang, Y., and Dang, B. (2006). Characteristics and tectonic setting of tectono-stress field of Ordos Basin. *Geotect. Metallogenia* 30 (4), 455–462.

Yao, J., Deng, X., Zhao, Y., Han, T., Chu, M., and Pang, J. (2013). Characteristics of tight oil in triassic Yanchang Formation, Ordos Basin. *Petroleum Explor. Dev.* 40 (2), 161–169. doi:10.1016/s1876-3804(13)60019-1

Zeng, L., Gao, C., Qi, J., Wang, Y., Li, L., and Qu, X. (2008a). The distribution rule and seepage effect of the fractures in the ultra-low permeability sandstone reservoir in east Gansu Province, Ordos Basin. *Sci. China Ser. D-Earth. Sci.* 51 (2), 44–52. doi:10.1007/s11430-008-6015-8

Zeng, L., and Li, X. (2009). Fractures in sandstone reservoirs with ultra-low permeability: A case study of the upper triassic Yanchang Formation in the Ordos Basin, China. *Bulletin* 93 (4), 461–477. doi:10.1306/09240808047

Zeng, L., Li, Z., Shi, C., Wang, Z., Zhao, J., and Wang, Y. (2007). Characteristics and origin of fractures in the sandstone reservoirs of ultra-low permeability of the upper triassic yancheng formation in the Ordos Basin. *Acta Geol. Sin.* 81 (2), 174–180.

Zeng, L., Zhao, J., Zhu, S., Xiong, W., He, Y., and Chen, J. (2008b). Impact of rock anisotropy on fracture development. *Prog. Nat. Sci.* 18 (11), 1403–1408. doi:10.1016/j.pnsc.2008.05.016

Zhao, J., Zhou, X., Lei, Q., Zhao, G., He, Y., Shi, J., et al. (2017b). Study on paleo-tectonic and present tectonic stress in chang 7 tight reservoir of Maling oilfield, Ordos Basin. *J. Geomechanics* 23 (6), 810–820.

Zhao, W. T., and Hou, G. T. (2017a). Fracture prediction in the tight-oil reservoirs of the triassic Yanchang Formation in the Ordos Basin, northern China. *Pet. Sci.* 14 (1), 1–23. doi:10.1007/s12182-016-0141-2

Zhao, X., Liu, L., Hu, J., Zhou, X., and Li, M. (2014). The tectonic fracture modeling of an ultra-low permeability sandstone reservoir based on an outcrop analogy: A case study in the wangyao oilfield of Ordos Basin, China. *Pet. Sci.* 11 (3), 363–375. doi:10.1007/s12182-014-0350-5

Zou, C., Tao, S., Yang, Z., Hou, L., Yuan, X., Zhu, R., et al. (2013). Development of petroleum geology in China: Discussion on continuous petroleum accumulation. *J. Earth Sci.* 24 (5), 796–803. doi:10.1007/s12583-013-0373-7

Frontiers in
Earth Science

Investigates the processes operating within the major spheres of our planet

Advances our understanding across the earth sciences, providing a theoretical background for better use of our planet's resources and equipping us to face major environmental challenges.

Discover the latest Research Topics

See more →

Frontiers

Avenue du Tribunal-Fédéral 34
1005 Lausanne, Switzerland
frontiersin.org

Contact us

+41 (0)21 510 17 00
frontiersin.org/about/contact

frontiers | Research Topics